International Conference

ICCST/2

1998

9 - 11 June 1998
Durban ▪ South Africa

Composite Science and Technology

Edited By:
S. Adali
E.V. Morozov &
V.E. Verijenko

19980928 053

PROCEEDINGS

Second International Conference
on
Composite Science
and
Technology

9 - 11 June 1998
Durban
South Africa

Edited by: S. Adali, E.V. Morozov and V.E. Verijenko
Department of Mechanical Engineering
University of Natal, Durban
South Africa

[illegible] [illegible]LITY INSPECTED 3

REPORT DOCUMENTATION PAGE	Form Approved OMB No. 0704-0188

Public reporting burden for this collection of information is estimated to average 1 hour per response, including the time for reviewing instructions, searching existing data sources, gathering and maintaining the data needed, and completing and reviewing the collection of information. Send comments regarding this burden estimate or any other aspect of this collection of information, including suggestions for reducing this burden to Washington Headquarters Services, Directorate for Information Operations and Reports, 1215 Jefferson Davis Highway, Suite 1204, Arlington, VA 22202-4302, and to the Office of Management and Budget, Paperwork Reduction Project (0704-0188), Washington, DC 20503.

1. AGENCY USE ONLY (Leave blank) ADA353971	2. REPORT DATE 4 August 1998	3. REPORT TYPE AND DATES COVERED Final Conference Proceedings 9-11 June 1998

4. TITLE AND SUBTITLE International Conference on Composite Science and Technology (2nd) (ICCST/2). Held in Durban, South Africa on 9-11 June 1998. Proceedings.	5. FUNDING NUMBERS F61708-W-0011 N68171-98-M-5331
6. AUTHOR(S) Adall, S.; Morozov, E. V.; Verijenko, V. E.	
7. PERFORMING ORGANIZATION NAME(S) AND ADDRESS(ES) Source Code: 413809 Department of Mechanical Engineering University of Natal Durban, South Africa	8. PERFORMING ORGANIZATION REPORT NUMBER
9. SPONSORING/MONITORING AGENCY NAME(S) AND ADDRESS(ES) European Office of Aerospace Research and Development PSC 802 Box 14 FPO 09499-0200	10. SPONSORING/MONITORING AGENCY REPORT NUMBER CSP-98-1007

11. SUPPLEMENTARY NOTES
This work relates to Department of the Air Force Grant under Contract No.F61708-W-0011, issued by the European Office of Aerospace Research and Development. The United States has a royalty-free license throughout the world in all copyrightable material contained herein.

12a. DISTRIBUTION/AVAILABILITY STATEMENT Approved for Public Release; distribution is unlimited.	12b. DISTRIBUTION CODE A

ABSTRACT (Maximum 200 words) In recent years there have been remarkable developments and advances in the field of composites involving all majors aspects, namely materials, structures and manufacturing. The new techniques have been developed as a result of extensive experimental, computational and analytical studies, adding a new dimension to tailor-made materials which are suitable not only for applications involving aerospace but also civilian structures. As research papers presented at this conference indicate, the continuous integration of advanced technology, processes and computational methods are collectively helping the composites become truly the material of the future by cutting the cost of materials and processes and time-to-market. ICCST/2 follows the highly successful ICCST/1 held in 1996. The conference provides a forum for the presentation of the latest research results and technology applications in composites and brings scientists, engineers and technologists together on African soil. It is hoped that the present conference will contribute to the ongoing advancement of science and technology in Southern Africa as well as to the upliftment of the communities and populations of the region. In the last decade, substantial progress has been made in smart materials and structures technology, primarily due to developments in shape memory alloys, piezoelectric materials and fiber optics. This is presently an emerging field of technology combining know-how from physics, electronics, mechanics and chemistry and with applications ranging from vibration control to damage detection. A section of the conference is now devoted to this field. 80 papers appear in these proceedings.

12. SUBJECT TERMS *SYMPOSIA, *COMPOSITE MATERIALS, MECHANICAL PROPERTIES, CERAMIC MATRIX COMPOSITES, COMPOSITE STRUCTURES, METAL MATRIX COMPOSITES, COMPUTER AIDED MANUFACTURING, SOUTH AFRICA, SANDWICH CONSTRUCTION, SMART TECHNOLOGY, ICCST/2 FOREIGN REPORTS, PROCEEDINGS, EOARD	15. NUMBER OF PAGES 16. PRICE CODE

17. SECURITY CLASSIFICATION OF REPORT	18. SECURITY CLASSIFICATION OF THIS PAGE	19, SECURITY CLASSIFICATION OF ABSTRACT	20. LIMITATION OF ABSTRACT
UNCLASSIFIED	UNCLASSIFIED	UNCLASSIFIED	UNCLASSIFIED

NSN 7540-01-280-5500

Standard Form 298 (Rev. 2-89)
Prescribed by ANSI Std. 239-18
298-102

PREFACE

In recent years there have been remarkable developments and advances in the field of composites involving all majors aspects, namely materials, structures and manufacturing. The new techniques have been developed as a result of extensive experimental, computational and analytical studies, adding a new dimension to tailor–made materials which are suitable not only for applications involving aerospace but also civilian structures. As research papers presented at this conference indicate, the continuous integration of advanced technology, processes and computational methods are collectively helping the composites become truly the material of the future by cutting the cost of materials and processes and time–to–market.

ICCST/2 follows the highly successful ICCST/1 held in 1996. The conference provides a forum for the presentation of the latest research results and technology applications in composites and brings scientists, engineers and technologists together on African soil. It is hoped that the present conference will contribute to the ongoing advancement of science and technology in Southern Africa as well as to the upliftment of the communities and populations of the region.

In the last decade, substantial progress has been made in smart materials and structures technology, primarily due to developments in shape memory alloys, piezoelectric materials and fiber optics. This is presently an emerging field of technology combining know–how from physics, electronics, mechanics and chemistry and with applications ranging from vibration control to damage detection. A section of the conference is now devoted to this field.

The response to the call for papers has resulted in over 100 papers. However, to ensure that the papers are of a high standard and to provide a relatively small forum for the delegates to meet each other, the technical committee limited the number of papers to 80, which appear in these proceedings. For this reason all the papers were subjected to a careful screening before being accepted.

The fact that 27 countries are represented in this volume bears testimony to the international nature of the conference and to composites research. We thank all the authors and delegates who contributed to the success of ICCST/2. Our special thanks go to the keynote speakers, session chairpersons and reviewers for their contribution and efforts.

Sarp Adali
Evgeny V Morozov
Viktor E Verijenko

Durban
May 1998

Acknowledgements

The organizers gratefully acknowledge the support of University of Natal and the Foundation for Research Development, and thank the United States Airforce, European Office of Aerospace Research and Development for their contribution to the success of ICCST/2. The support by the European Research Office of the US Army under Contract No. N68171–98–M–5331 is gratefully acknowledged.

We would like to express our sincere thanks to Congress International for their contribution to the organisation of ICCST/2, to Portia Redmond for her expert advice and help with the publication of the Proceedings volume, and to our postgraduate students for helping with numerous tasks.

International Advisory Board

C W Bert	University of Oklahoma, USA
V Birman	University of Missouri-Rolla, USA
A Bogdanovich	AdTech System Research, USA
A H Cardon	Free University of Brussels, Belgium
E Demuts	Wright Laboratory, USA
W P De Wilde	Free University of Brussels, Belgium
G Duvaut	Universite de Paris, France
H Eschenauer	University of Siegen, Germany
M S Found	Sheffield University, UK
Z Gurdal	VPISU, USA
D Hui	University of New Orleans, USA
T-Y Kam	National Chiau Tung University, Republic of China
K T Kedward	University of California, USA
I Kimpara	Tokyo University, Japan
F Lene	Ecole Normale Superieure de Cachan, France
L Librescu	VPISU, USA
G. Long	Co-op Research Centre for Adv Comp Struct, Australia
I H Marshall	University of Paisley, Scotland
V Middleton	Nottingham University, UK
A Miravete	University of Zaragoza, Spain
H Ohtsubo	Tokyo University, Japan
P Pedersen	Technical University of Denmark, Denmark
S L Phoenix	Cornell University, USA
V G Piskunov	Ukraine Transport University, Ukraine
J N Reddy	Texas A&M University, USA
R D Sanderson	University of Stellenbosch, SA
B Schrefler	University of Padova, Italy
M L Scott	Royal Melbourne Inst of Technology, Australia
T R Tauchert	University of Kentucky, USA
V V Vasiliev	University of Aviation Technology, Russia

Local Organising Committee

R Hacking	Technikon Natal, Durban
P Haupt	Mattek, CSIR, Pretoria
J Huston	Aerotek, CSIR, Pretoria
T le Roux	Somchem, Cape Town
A Parsons	Somchem, CapeTown
T Raman	Aircraft Division, Pretoria
S Shaikh	Defence Secreteriat, Pretoria
D Twomey	Kentron, Pretoria
F Vandeput	Kentron, Pretoria
M Walker	Technikon Natal, Durban

CONTENTS

1. KEYNOTE LECTURES

Recent developments in the modelling and behaviour of advanced sandwich construction (Abstract)
L. Librescu........1
Modeling the statistical lifetime of glass fibre/polymer matrix composites in tension
S.L. Phoenix........3
Development in thermopiezoelasticity with relevance to smart composite structures
T.R. Tauchert, F. Ashida, N. Noda, S. Adali, and V.E. Verijenko........17
Modern conceptions of plate theory
V.V. Vasiliev........31

2. COMPOSITE MATERIALS AND PHYSICAL PROPERTIES

Determination of filler content of wood-based composites by thermogravimetric analysis
M.Y. Ahmad Fuad, S. Rahmad, and M.R. Nor Azlan........51
Highly loaded catalytic grafting thermoplastic/poly(para-phenylene-terephtalamide) (kevlar) composites
A. Ait-Kadi and A. Yousefi........57
Effects of different fillers on polypropylene
C. Albano, L. Marquez, and G. Ronca........63
Wetting analysis of natural sisal fibres with polymeric matrix
H.A. Al-Qureshi and J.L.G. Silva........69
DuPont's aramid fibres for advanced composite materials: from past experiences and recent developments to future applications
R. Pinzelli and D. Blomert........75
Layerwise reinforcement of carbon fibre triaxial woven fabrics
Y. Sato........83
Composite materials for wear resistance coatings using thermal spraying
S. Steinhauser, B. Wielage, T. Schnick, A. Ilyuschenko, and T. Azarova........89
Prediction and measurement of the anisotropic thermal expansion behaviour of oriented polyoxymethylene
R.R. Zahran and S.S. Shenouda........95

3. MECHANICAL PROPERTIES

Impact resistance of microwave cured epoxy/glass composites
S. Adanur and B. Xu........101
Behaviour of polyolefin blends in the presence of $CaCO_3$
C. Albano, J. Gonzales, M. Ichazo. C. Rosales, R. Perera, R. Navas, C. Urbina, and C. Parra........107
Influence of metallic fillers on the thermal and mechanical behaviour in composite of epoxy matrix
Z. Brito and G. Sanchez........113
A comparison between the tensile properties of injection molded and compression molded sand-reinforced polyethylene
A.Y. Kandeil and R.R. Zahran........119

The effect of strain rate and fibre content on the Poisson's ratio of glass/epoxy composites
O.I. Okoli and G.F. Smith..........125
The effect of polyamide coatings on the mechanical properties of unidirectional carbon/epoxy composites
C.D. Papaspyrides, P.C. Varelidis, and R.L. McCullough..........133

4. MECHANICS OF COMPOSITES

Homogenization of multilayered elastomer composites
M. Brieu, F. Devries, and F. Lene..........139
Study of near-surface buckling of composite materials in zones of compression (model of a piecewise-uniform medium)
Yu.N. Lapusta..........145
Effect of drying on properties of ceramic composite precursors: analytical model
I.B. Sevostianov, V.M. Levin, and W. Pompe..........151
Prediction of residual thermal stresses of laminated composite tubes
A.C. Seibi and M.F. Amateau..........157
Strength and stiffness of braided fiber composites
S.R. Swanson..........163

5. METAL MATRIX AND CERAMICS COMPOSITES

Particulate composites with the TZP matrix and (Ti, W) additive
M. Faryna, Z. Pedzich, W. Pyda, and K.Haberko..........169
Mechanical properties and evaluation of magnesium matrix composites
Q. Gaofeng, S. Yujiu, and T. Mingjing..........175
Interfacial stress and strength analysis of metal matrix composites in thermal shock process
D.Y. Ju..........181
Internal stresses in metal matrix composites reinforced by particles
R. Paskaramoorthy..........187
TiC inclusions synthesized in-situ in the zirconia matrix
W. Pyda..........195

6. SANDWICH STRUCTURES

Closed-form analysis of the thickness effect of regular honeycomb core material
W. Becker..........201
High-precision modelling of deformation of sandwich structures under bilateral symmetric and oblique--symmetric loading
O.G. Gurtovy..........207
Buckling and failure analysis of FRP faced sandwich plates
A. Muc and P. Zuchara..........213
Stress concentration in bending of sandwich panels under point forces
V.A. Polyakov..........219

7. COMPOSITE STRUCTURES: DESIGN

Optimization of angle-ply laminates for min--max deflection under imprecisely specified dynamic loads
J.C. Bruch Jr, S. Adali, J.M. Sloss, and I.S. Sadek 227
Optimization of fibre reinforced composites
G. Duvaut and G. Terrel 233
Analysis and design of reinforced composite structures
A.L. Kalamkarov 239
Optimum dome contour of composite shell wound with a roving of finite width
A.A. Krikanov 245
Design and analysis of a lightweight frigorific semitrailer by means of a numerical simulation procedure
E. Larrode, L. Castejon, M.A. Jimenez, and R. Clemente 253
Design of composite plates under cyclic loading
A. Muc and Z. Krawiec 259
Design/optimization of isogrid cylindrical structures
D. Slinchenko, V.E. Verijenko, S. Adali, and I.B. Sevostianov 265
Fibre composite intra-modullary nails: design considerations
C.J. von Klemperer and R. Bodger 271
Design for manufacture and optimization of laminates using generic algorithms and finite element analysis
M. Walker 277
Minimum weight design of laminated plates subjected to fatigue loads using a cumulative damage rule constraint
M. Walker and D. Jonson 287

8. COMPOSITE STRUCTURES: ANALYSIS

Aspects of structural design and manufacture of an all composite motorglider wing
W.M. Banks and J.A. Russell 295
Influence of plastic coating of radial plain bearings on contact stress
A.V. Chigarev and A.S. Kravchuk 301
On response of functionally graded cylindrical panels to thermal loading
E. Feldman and I. Belostotsky 307
Semi-analytical study of composite containers under internal and external pressure
N. Le Bris, H. Dumontet, and F. Lene 313
Performance evaluation of composite tube reinforced concrete columns
Z. Li, R. Lee, M. Chen, and P. Tong 319
Response of composite isogrid cylinders under axial compression
H. Mahfuz, M. Rahman, E. Foster, P.S. Das, and S. Jeelani 325
High-order model of the stress-strain state for the composite beams
V.G. Piskunov, A.V. Goryk, and A.L. Lyakhov 333

Solution of dynamic boundary problems in a continuous elastic curvilinear anisotropic medium with a spherical cavity
Y.A. Rossikhin and M.V. Shitikova 339

9. LAMINATED PLATES AND SHELLS

Exact elasticity solution for investigation peculiarities in deformations of thick plates and shells in composite materials
S.M. Galileev, A.V. Matrosov, N.N. Gubin, and I.N. Miroshnichenko 345

Composite plates with undulating surfaces
M. Kashtalian 353

Thermoelasticity of spatially reinforced composite plates
E.V. Morozov 359

Analysis of stress-strain state of composite laminated shells and plates by the second order shear theory
V.G. Piskunov, A.O. Rasskazov, and S.G. Burihyn 365

Buckling behaviour of laminated composite plates under thermal loading
P.S. Simelane and B. Sun 371

Linear analysis of laminated composite plates using single layer higher order discrete models
D. Vuksanovic 377

10. SMART MATERIALS AND STRUCTURES

Vibration control of thermally loaded orthotropic plates with piezoelectric stiffeners
S. Adali, T.R. Tauchert, and V.E. Verijenko 383

Minimization of deflection using piezo effect and ply angles for thick laminated plates
S. Adali, V.E. Verijenko, T.R. Tauchert, and A. Richter 389

Vibration analysis of laminated composite beams with piezoelectric layers using a higher order theory
D. Huang and B. Sun 395

Dynamics and buckling of a multilayer composite plate with embedded shape memory alloy wires
W. Ostachowicz, M. Krawczuk, and A. Zak 403

Some problems of piezoelectric sensor mechanics
B. Sun 409

11. COMPUTATIONAL STUDIES

Development of a numerical model for the damage identification on composite plate structures
J.V. Araujo Santos, C.M. Mota Soares, C.A. Mota Soares, and H.L.G. Pina 417

"RIOJA 95" numerical testing correlation: America's Cup Spanish challenge ship
J. Cuartero, A. Perez de Lucas, M. Lopez Rodriguez, and L. Castejon 423
Dynamic analysis of orthotropic shells by grid-characteristic method
E.G. Evseev and E.V. Morozov 429
Higher order boundary elements: exact influence formulae and their asymptotics
M.A. Kayupov and G. Kuhn 435
Finite elements for the analysis of vibrations of laminated composite plates and solid bodies
A.V. Marchuk and V.K. Prisjaznuk 441

12. COMPOSITES MANUFACTURING

Software for the simulation and the control of the filament winding of ellipsoidal structures
A.J. Atangana, N.H. Essoh, S.J. Kingue, and, A.D. Dzonang 447
Quick-welding in filament winding of thermoplastics prepregs
A.J. Atangana, E.P. Belinga, P.G. Pekego, N.P. Samba, J.B. Fouda, and A.P. Owono 453
Integrally stiffened RTM composite panel
V.S. Avva, R.L. Sadler, and K.N. Shivakumar 457
Optimisation of composite curing process for minimum residual stress
A.K. Gopal, S. Adali, and V.E. Verijenko 463
Six axes fittings winder: high speed production of "T" and elbow parts
W.S. Kozak (Presented by J. Green) 469
Fabrication and mechanical properties of glass fibre reinforced polyester filled with copper particles - Part I
A.C. Seibi and S. Al-Zadjali 477
Cost comparison of RTM hand--lay and cast tooling
G. Veldsman and A.H. Basson 483
Void formation during resin film infusion process and optimum temperature profile
V.E. Verijenko, S. Adali, and I.B. Sevostianov 489

13. FRACTURE AND FATIGUE OF COMPOSITES

Theoretical foundations for nondestructive detection of cracks in ceramic matrix composites based on surface temperature
L.B. Byrd and V. Birman 495
On continuum approximation in compressive fracture theory for metal matrix composites: asymptotic accuracy
I.A. Guz 501
Nonlinear fracture analysis of hybrid polymer composite materials and structures
E.V. Morozov, S.A. Sylantiev, E.G. Evseev, and H.G. Lessmann 507
A new approach to fatigue analysis in composites based on residual strength degradation
D. Revuelta, J. Cuartero, A. Miravete, and R. Clemente 513

14. EXPERIMENTAL STUDIES

Impact perforation of thin stiffened CRFP panels
M.S. Found, I.C. Howard, and A.P. Paran........519
Damage development assessment in grp pipes under biaxial loading conditions
L. Golaski, J. Schmidt, and I. Baran........525
Effect of trigger geometry on energy absorption in composite profiles
M.A. Jimenez, A. Miravete, E. Larrode, and D. Revuelta........531
Experimental validation of refined models of composite plates
M. Karama, S. Mistou, J.P. Faye, S. Caperaa, and J.L.Lacassagne........537
What we can expect from ultrasonic method for composite materials
E.G. Nesvijski........543
On the application of the acoustic emission and infrared thermography to fracture process evaluation in short fibre reinforced plastics
J. Schmidt and I. Baran........549

Author index........557

RECENT DEVELOPMENTS IN THE MODELING AND BEHAVIOR OF ADVANCED SANDWICH CONSTRUCTIONS

Liviu Librescu
Engineering Science and Mechanics Department
Virginia Polytechnic Institute and State University
Blacksburg, VA 24061, USA

The design and development of supersonic/hypersonic flight vehicles, of Future reusable space transportation systems, launch vehicles and of advanced propulsion systems constitute challanging issues for the aeronautical engineers and the research workers insolved in these problems.

It is a well-known fact that during their flight missions, the structure of flight vehicles has to with stand severe aerodynamic, aeroacoustic and thermomechanical loads. The temperatures involved are likely to range from the extreme lows of cryogenic fuels and radiation to space, to the highs associated with aerodynamic heating, heat from propulsion unit and radiation from the sun. In spite of the increased flexibility which is likely to characterize the structure of these flight vehicles, they have to be able to fulfill a multitude of missions in complex environmental conditions and feature an expanded operational envelope. The same is valid with the resuable space vehicles, which, for evident reasons, require a prolongation of their operational life, without impairing upon the security of flight.

A problem of evident importance towards the rational design of advanced supersonic/ hypersonic flight vehicles lies on the possibility to accurately determine the load carrying capability of their structure. Moreover, a better understanding of conditions yielding an enhancement of the load carrying capacity, can dramatically contribute to the increase in performance of these flight vehicles.

For curved panels such an investigation has a special relevance. Indeed, in contrast to flat panels which experience a considerable amount of additional load-carrying capability in the postbuckling range, the curved panels exhibit a highly unstable postbuckling behavior, manifested by snap-through jumps toward a state of stable equilibrium. In addition, the load carrying capacity of curved panels is imperfection sensitive.

It appears evident that reduction of the intensity of the snapping phenomenon and of the sensitivity to initial geometric imperfection is a matter of considerable importance toward a prolonged use of curved panels in the postbuckling range, without impairing upon their structural integrity.

One of the modern trends in the construction of next generation of flight vehicles capable of operating in a high temperature environment, consists of the ongoing incorporation in their structure of advanced composite materials.

A typical laminated structure which is highly used in these projects and is likely to play an increased role in the design of advanced flight vehicles is the sandwich type construction.

In its simplest form the sandwich construction can be viewed as a structure composed of two stiff layers (face-sheets), separated by a thick mid-layer of low density material (core layer). This type of structure encompasses a number of properties of exceptional importance toward fulfilment of the high exigencies imposed upon the advanced flight vehicles. Among other features there are i) high bending stiffness characteristics with little resultant weight penalty, ii) provide a smoother aerodynamic surface in a higher-speed range, iii) provide excellent thermal and sound insulation, and increased strength at elevated temperatures, and iv) provide a longer operational time as compared to stiffened-reinforced structures which are weakened by the appearance of stress concentration. In a continuing effort for higher stiffness and strength to weight ratios, the raditional materials have evolved from metallic face-sheets and aluminum honeycomb core to composite materials. In this sense, the face-sheets are likely to be composed of anisotropic fibre-reinforced composite laminates, whereas the core from non-metallic honeycomb and plastic foam materials.

Due to all these new features, in order to predict accurately their response behavior under mechanical and thermal loading systems, refined models of sandwich-type constructions are needed.

The goal of this paper is to review some of the modern developments which have taken place in the last several years, and connect these with the prior achievements in the field. At the same time, problems related with the use of this structural model toward investigating the buckling strenght and its behavior in the post-buckling range by taking into account the effect of the initial geometric imperfections will be also addressed.

Another problem included in this lecture and which presents a considerable practical importance is related with the enhancement of the buckling strength and of the postbuckling behavior, and with the reduction of sensitivity to initial geometric imperfections as featured by the curved panels. Results addressing these issues are displayed and pertinent conclusions are outlined.

The provided list of references is not exhaustive in the sense that it is mainly connected with the topics presented in this review, in which the author himself has been directly involved.

MODELING THE STATISTICAL LIFETIME OF GLASS FIBER/ POLYMER MATRIX COMPOSITES IN TENSION

S. LEIGH PHOENIX
DEPARTMENT OF THEORETICAL AND APPLIED MECHANICS
CORNELL UNIVERSITY
ITHACA, NY 14853, USA
e-mail: slp6@cornell.edu

ABSTRACT

In this paper we present a viewpoint on modeling the lifetime of glass fiber/polymer matrix composite structures loaded primarily in tension along the fiber axis. In many applications such components may sustain, over many years and in deleterious environments, stress levels that are a significant fraction of their ultimate tensile strength. Thus the failure phenomenon of concern is creep rupture. Ideally, a comprehensive model should incorporate such features as environmentally driven, statistical degradation mechanisms in the glass fiber (such as stress corrosion cracking), creep and microcracking of the polymer matrix, slip at the fiber/matrix interface near fiber breaks, local residual stresses from processing, including their complex micromechanical interactions. Such a model should yield overall distributions for lifetime in terms of the overall applied stress field, the overall volume of material, and boundary effects. Parameters of the model should reflect subtle scaling relationships among microstructural variables (e.g., fiber packing geometry), parameters of the statistics of fiber strength and degradation, matrix and interface creep exponents, rate factors in the stress-corrosion chemistry, and applied stress level. Particular attention must be paid to the character of the extreme lower tails of the strength and lifetime distributions since these are crucial in establishing load levels that result in the extremely high reliability levels important in life-safety applications. For example, the model should be able to predict the steady load level in a composite specimen with an effective loaded volume that yields a given lifetime (e.g., 25 years) at an extremely low probability of failure (e.g., 10^{-6}). This essentially rules out mean field approaches so prevalent in the mechanics and physics community. A model of this sort would also be useful in the development of strategies for effective accelerated testing and data interpretation using special time-temperature scalings and master curves. Lastly, the model would have value in guiding strategies for quality control, materials processing, and component architecture during manufacture. Of course, such a comprehensive model is well beyond the present state of the art. Nevertheless, a surprising amount of progress has been made in developing the necessary conceptual and computational framework including the micromechanics, chemistry and physics of the fundamental failure mechanisms. In this paper we will review some of the relevant literature and suggest directions that should be fruitful in yielding useful models.

INTRODUCTION

In many applications in civil engineering [1-6], a composite component must sustain, for many years, stress levels that are a significant fraction of its ultimate tensile strength, and often in deleterious environments. Various applications in new construction are: (i) reinforcement of concrete using 1D rods, 2D grids and 3D networks, (ii) tension members for prestressing concrete, (iii) bridge cables, stays, hangers and roof support cables, (iv) pultruded beams and bridge superstructures, and (v) storage tanks and piping. Interest also exists in using composites for repair and rehabilitation of deteriorating structures. Further applications also include pressure vessels and flywheels in aerospace and automotive applications, and centrifuges in medical and nuclear power. A generally recognized problem is creep fracture (also known as creep rupture, stress rupture, and static fatigue), a catastrophic failure event that typically occurs with little or no warning [6]. Thus, establishing load levels that yield long lifetimes at acceptable reliability levels becomes a major challenge. To this end considerable research is being carried out in the US [7] and internationally [8]. Many recent works report basic lifetime tests on the performance of composite components in various environments and over limited time-frames (e.g. [9-12] in [8]). These works, however, rarely consider governing micromechanical, statistical and chemical mechanisms at the fiber scale, and rarely draw on the vast experimental and modeling literature developed over the past 50 years in connection with national defense and space exploration. Often crucial information on properties of the constituent materials, and test conditions is not documented. Thus, it is problematic to extrapolate the results to other settings.

A common methodology is to use a 'brute force' testing approach. In this method, a large number of lifetime tests are performed on basic composite specimens at each of several load levels, and the results are fitted to a lifetime model based on phenomenology, such as a Weibull distribution. Scale and shape parameters are chosen to reflect sensitivity to stress level through power law or exponential laws (producing linearity on log-log and semi-log coordinates, respectively), which sometimes may contain an Arrhenius factor to account for temperature or environmental effects. While such tests are very important, their utility is greatly diminished in the absence of an accurate model to allow extrapolation of the data to other time and size scales, chemical concentrations, and especially load levels that result in low failure probabilities. Studies in the literature suggest some key lessons: The precise values of creep-rupture parameters cannot be predicted through simple averaging rules based on bulk measurements on the fibers and epoxies; in fact, similar systems can yield puzzlingly different results, pointing to the need for understanding the basic micromechanisms.

Glass fiber/polymer matrix composites have been of interest for military and aerospace applications for about 50 years, and a vast literature has developed. This literature covers failure mechanisms in glass fibers, polymer creep and interface failure mechanisms including environmental aspects. In addition there exists extensive lifetime data on failure of composite specimens under long term loading. Let us now review various aspects of this literature.

REVIEW OF EXPERIMENTAL LITERATURE

Experiments on single glass fibers. The mechanisms of failure in E-glass, S-glass and other glass fibers, with respect to short-term strength and long-term static fatigue conditions, have been extensively studied both theoretically and experimentally, and considerable data has been carefully generated. The classic works of Taylor [13], Stuart and Anderson [14], Charles [15,16], Mould and Southwick [17], and Charles and Hillig [18] have resulted in a fundamental understanding of the chemical and kinetic mechanisms involved, including the effects of stress-corrosion in humid and alkali environments. Kies [19], and Schmitz and Metcalfe [20, 21] carried out extensive studies of the flaw types, their sources during processing and handling, and especially their statistical distributions. Hillig and Charles [22] further advanced understanding of stress dependence in surface reactions and how flaws geometrically evolve to form cracks. Metcalfe *et al.* [23] studied spontaneous flaw growth in alkali environments, and provided some spectacular micrographs of periodic cracking along glass fibers. In the fiber optics area, more recent work has considered the protection of the surface of glass fibers using polymer coatings. Schonhorn *et al.* [24], for example, showed how to improve the performance of optical glass fibers in static fatigue by coating with a uv-curable epoxy-acrylate coating, but interestingly certain degradation exponents remained unchanged. Many key ideas in the failure of glass fibers are reviewed in Kelly and Macmillan [25].

Based on this literature we believe it is possible to build a statistical, mechanistic model of the failure of individual glass fibers under steady and mildly cyclic stresses that is much more advanced and comprehensive than has been attempted to date. Such a model can incorporate effects of temperature, alkali (and acid) species and concentrations, probability distribution shapes, and scaling laws for lifetime (scale parameter or mean) versus stress level. Much of the fiber lifetime data can be resolved fairly linearly on power-law coordinates with slope exponents ranging from about 30 on downward as the environment becomes more aggressive (e.g. higher temperature, increased moisture and alkaline concentration). Some of the above works show how data for various cases and materials can be reduced onto one master or universal fatigue curve. Surprisingly, many recent studies on the failure of glass fiber/polymer matrix composites have made virtually no reference to this extensive literature.

Experiments on unidirectional glass fiber/epoxy composites. Extensive experiments on the strength and stress rupture of S-glass/epoxy unidirectional composites (mostly resin impregnated strands), were carried out at Lawrence Livermore National Laboratory (LLNL) in the late 60's through the '70's. The results are reported in several publications and internal reports [26-31], and some data is shown in Figure 1. (Kevlar and carbon fiber composites were also studied [32,33].) The most extensive experiments were on epoxy-impregnated strands containing several hundred filaments in two basic epoxies. Data is available for hundreds of strands loaded for over five years at several load levels above 33% of the short terms strength. (The experiments were unfortunately destroyed by an earthquake in 1979.) Strength retention tests were performed on specimens removed after surviving for various times in an attempt to study degradation in strength versus time [28]. Strength retention was also performed on unloaded specimens that had been stored under ambient conditions for up to 4 years, with only about a 4% drop in strength, most of which occurred during the first year. While the data base generated was massive, the modeling employed was minimal with respect to relating strand performance to that of virgin glass fibers and the epoxy matrix.

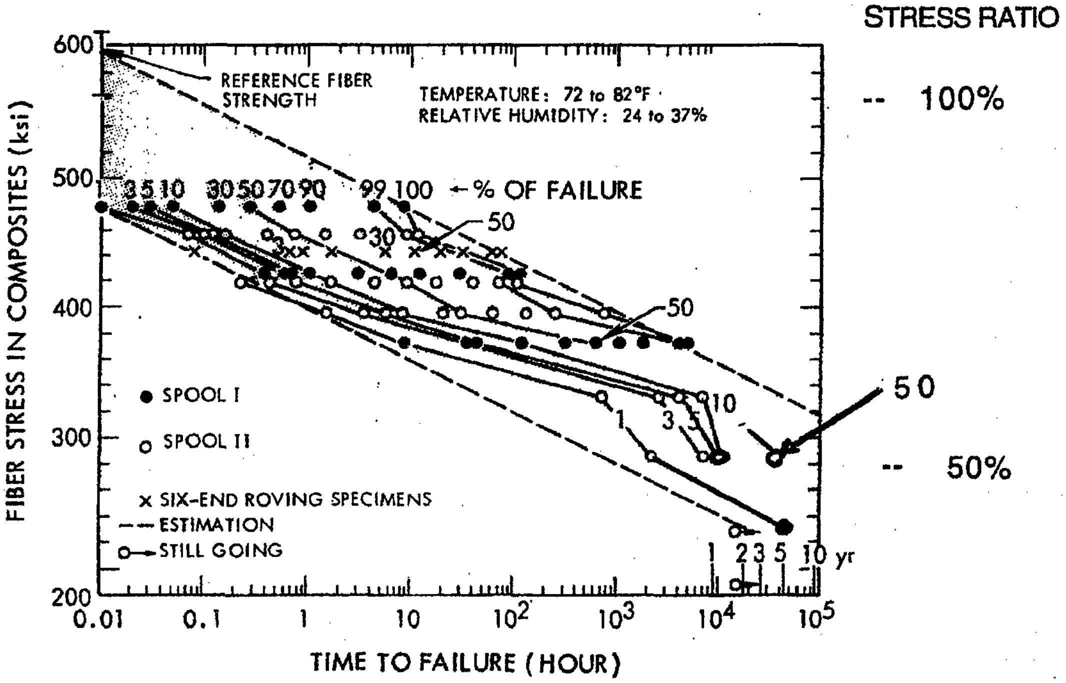

Figure 1. Time to failure quantiles (% probabilities of failure) for S-glass/epoxy strands tested in stress rupture at LLNL in the 1970's [27]. The last two data points were added by the author from data generated just before an earthquake destroyed the experiments.

Studies have also been performed at laboratories outside of the US. In Israel, Lifshitz and Rotem [34], performed experiments on glass fiber/epoxy and glass fiber/polyester composites, and built a simple micromechanical model to explain the results. Lifshitz [35] reviewed the literature on stress-rupture in many materials including single E-glass fibers tested at 50% RH and various temperatures. In England, Kelly and colleagues [36,37] studied the failure of bundles of glass fibers and composites by stress-corrosion mechanisms in hot, wet environments. In these cases models built on micromechanical and statistical mechanisms were developed to explain the results. In the mid 1980's work was conducted in England by several workers [38-43] including much work on polyester matrix composites in aggressive environments, including both acids and bases, and at various temperatures. These works underscore the importance of fiber-matrix interactions, including the importance of matrix cracking in allowing aggressive chemical species to enter the composite and attack the fiber surface.

In the US. during the 1970's and early 1980's long-term stress rupture of glass fiber composites appears to have received little attention. A compilation by Hilado [43] has no papers devoted to the subject, though effects of moisture on strength and fracture energy are covered.

Experiments on creep behavior of polymer matrices. Lifshitz and Rotem [34] showed that matrix creep in shear between the fibers plays an important role in the breakdown of the composite, by altering over time the stress redistribution from broken to surviving fibers. Long-term creep data for polyesters and epoxies is difficult to find, but there are references to other polymers and general time-temperature scaling principles. Findley and Tracy [44] reported creep data for PVC under loadings lasting 16 years. Kibler and Carter [45] gave some creep results for 5208 epoxy resin at various temperatures from 296 K to 435 K, and fit a power-law creep function (in the context of linear viscoelasticity) with corresponding exponents increasing from 0.1 to 0.4. Master curves and shift factors for net creep compliance were also given. Kibler [46] developed results for creep of various graphite epoxy laminates from which creep parameters for the epoxy alone could be extracted. Viscoelasticity theories for such applications were given by Schapery in a review paper [47] and in a special appendix to Kibler's report [46]. In the case of crack growth connected to local polymer creep and breakdown at the tip, relevant theories were given by Schapery [48]. A well known monograph on molecular based aging and creep mechanisms in polymers is due to Struik [49].

MICROMECHANICS AND STATISTICS OF MECHANISMS IN CREEP FRACTURE

Creep fracture of unidirectional fibrous composites results from evolving microstructural damage in the form of statistically accumulating fiber breaks over time, eventually resulting in rapid localization at some location forming a catastrophic crack. When such composites are loaded at a substantial fraction of their instantaneous strengths, it is important to appreciate the magnitudes of the stress levels involved. At a fiber volume fraction of 65%, for example, composite specimens such as resin impregnated strands or rods, can have mean tensile strengths of the order of 1.75 to 2.5 GPa (250 to 350 ksi). Under, ideal, ambient laboratory conditions, composites loaded at 40% of these values, namely 0.7 to 1.0 GPa (100 to 140 ksi) can have mean lifetimes of the order of 10 years. The variability in time to failure, however, is typically very large with coefficients of variation on the order of 100% to 500% depending on the fiber type, as indicated in Figure 1. In the final stages of life, within such structures, a rapid increase in strain rate (tertiary creep) may occur in a few highly localized regions, but at the macroscale this is very difficult to detect. In fact, the amount of overall creep observed is very small and even a secondary creep stage may be obscured. This is because creep is mostly due to break opening displacements since the matrix carries negligible tensile load and the brittle fibers creep negligibly. Continuous graphite fibers, for example, typically show no creep at room temperature [50]. (When the load-bearing fibers are aligned off-axis in a composite, the situation is quite different as matrix creep and failure may dominate, as shown by Raghavan and Meshii [51,52].)

The high variability in strength found in brittle fibers is well modeled by Weibull-Poisson statistics. This variability, due to various random flaws on the fiber surface and in the fiber interior, means that many fiber breaks are inevitable in the composite as time passes or as load is increased, especially in glass fibers, where flaw growth due to stress corrosion mechanisms occurs. Initial fiber breaks may be fiber discontinuities due to processing or breaks due to initial loading, and at loads well below the composite mean strength are typically widely spaced relative to the fiber diameter. A few, however, may be in small clusters. These breaks create local stress concentrations in both the matrix and the neighboring intact fibers as the matrix, through shear, transmits the tensile loads of broken fibers to neighboring fibers.

Near these initial breaks, especially those in small clusters, the local tensile stress levels in the fiber can approach 5 GPa or even higher, whereas the maximum shear stresses in the matrix are of the order of 35 MPa, more than 100 times lower. At such stress levels the matrix will creep in shear, or, progressively debond from the fiber (as a propagating cylindrical mode II crack) followed by time dependent slip. The effective shear strains even before slip can reach as much as 30 or 40 percent. Thus, the length scale of overloading of neighboring intact fibers increases over time, and the probability of subsequent failure of these fibers also increases. The resulting additional fiber breaks further increase local fiber and matrix stress concentrations, and further accelerate the local matrix shear creep, interface debonding and slip processes, again increasing the local stresses and probabilities of failure of neighboring fiber elements. Generally there will be many small, stochastically growing clusters of fiber breaks distributed throughout the loaded composite. Eventually one of them will become large enough, possibly through cluster linking, to initiate a catastrophic crack.

In summary, there is an interaction of such factors as the statistics of fiber flaw growth, matrix creep, interface debonding and slip, local fiber packing, fiber volume fraction and overall composite volume under load. Local stress level, temperature, moisture concentration, and acid or alkali concentration, will affect the rates of these processes in different ways. Overall composite breakdown rates and statistics crucial to life-prediction will reflect non-trivial interactions of these rates and shape parameters of the statistical fiber flaw distributions as they change over time. One can expect extremal statistical processes over the loaded volume to play a crucial role. This means that mean field concepts will play a minor rôle in understanding failure.

CURRENT MODELS FOR CREEP FRACTURE

A detailed mathematical description of the above viewpoint can be found in Phoenix *et al.* [53] and Otani *et al.* [54] who developed a model of failure backed up with experimental results on model microcomposites of seven carbon fibers (Hercules IM6) in an epoxy. It was shown that, whereas the carbon fibers underwent negligible creep rupture, that of the composites was appreciable; the lifetime scale parameter versus stress level on a log-log plot showed a power-law exponent of about 55, about one-fifth the 294 value for individual fibers, as shown in Figure 2. Moreover, this composite exponent was shown to depend explicitly on the Weibull shape parameter for fiber strength, ρ, the creep/debond exponent for the matrix, β, and the critical fiber break cluster size, k following $[k/(k-1)]2\rho/\beta$.

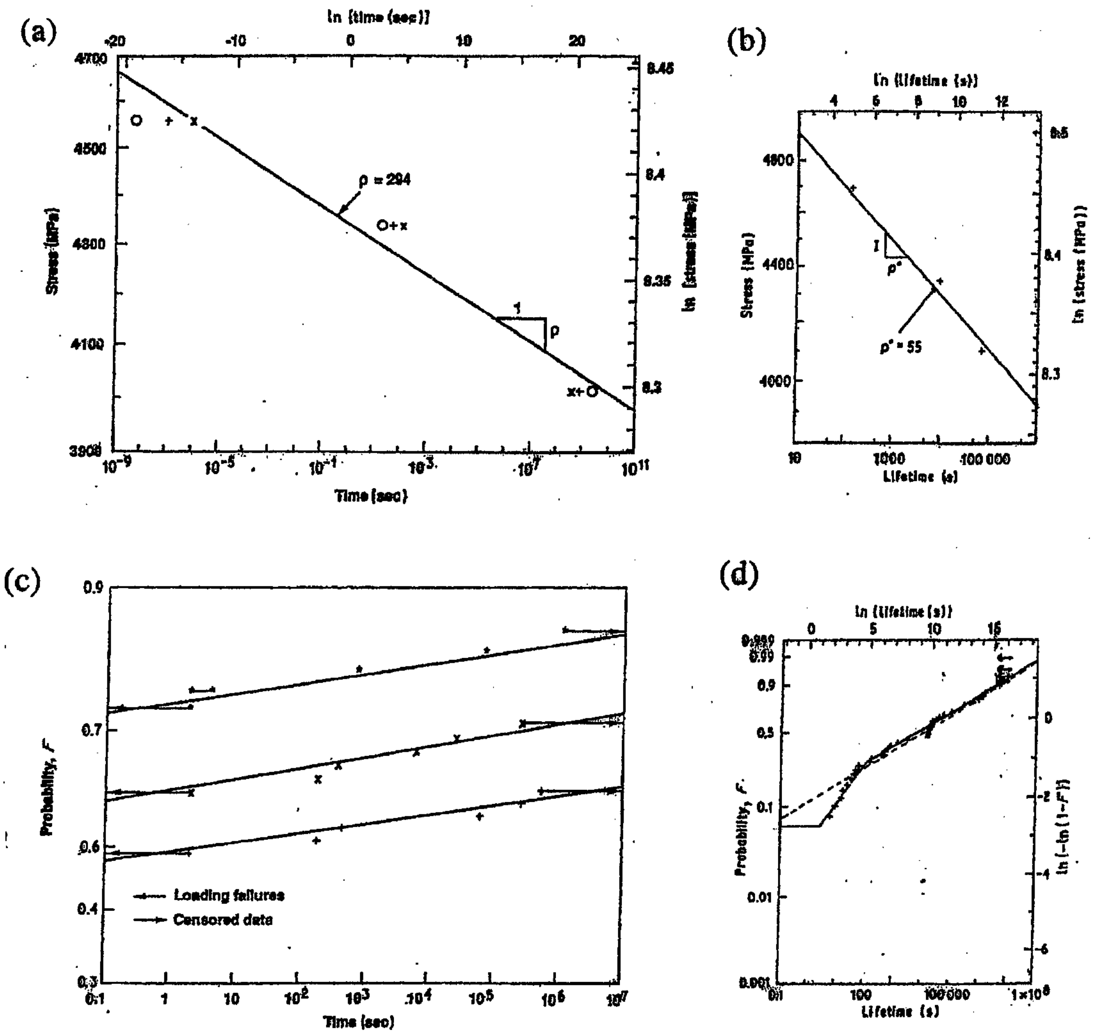

Figure 2. Lifetime data for Hercules IM6 graphite fibers and 7-fiber/epoxy: (a) Weibull scale parameter for lifetime versus stress level for single fibers on power-law coordinates; (b) corresponding data for 7-fiber microcomposites; (c) distributions for lifetime of single fibers at stress ratios (stress divided by Weibull scale parameter for strength) 0.925, 1.00 and 1.05, plotted on Weibull coordinates; (d) corresponding data for 7-fiber microcomposites at the stress ratio 0.83.

A related aspect was the distribution for lifetime of the composite as compared to the fibers. Farquhar *et al.* [51] plotted lifetime data for individual IM6 graphite fibers, on Weibull coordinates for various normalized stress ratios (stress divided by Weibull scale parameter for strength) as shown in Figure 2. The fit was excellent and the Weibull shape parameter for lifetime was about 0.02 representing huge variability (>1,000%). In comparison, the lifetime distributions for the 7-fiber, IM6 graphite fiber/epoxy microcomposites [53,54] showed Weibull shape parameter values more than 10 times larger, as shown in Figure 2. In fact, the lifetime distribution was not truly Weibull but showed bimodal behavior as the model predicted; the Weibull shape parameter for the upper tail was about 0.2 and for the lower tail was about 0.4. These higher values corresponded to greatly *decreased* variability in composite lifetime versus the fibers, and the variability decreased even further deep into the lower tail of the lifetime distribution especially at lower loads. The kink in the bimodal distribution was shown to be caused by a change in the critical cluster size at shorter times.

In connecting their results to other work, Phoenix *et al.* [53] reference experimental work on graphite fiber/epoxy strands at Lawrence Livermore National Laboratory in the '70's and '80's [32], at Oak Ridge National Laboratory in the '80's, and in Japan [55], again following a direct experimental approach. Slightly larger power-law exponents were measured in those cases (probably because of reduced boundary or surface effects due to having many more fibers, reducing the effects of slip), but the values were still far lower than values above for single fibers. Also the Weibull exponents for lifetime were comparable to the values for the 7-fiber composites.

In glass fiber/polymer matrix composites, stochastic flaw growth in the individual glass fibers also plays a critical role [34-42], making the failure process and modeling much more complicated than in the carbon fiber composites. The breakdown parameters depend subtly on interactions of the statistics of fiber flaw growth, matrix creep and debonding mechanisms. Similar processes also occur in metal matrix and glass matrix composites reinforced with ceramic fibers. In recent modeling efforts [56-59] stress redistribution among fibers was assumed to follow 'global load-sharing'. (See Iyengar and Curtin [59] and references therein to Curtin's earlier landmark work.) Calculation of the mean lifetime has been carried out, but not the variability nor the distribution shape. Thus, distributions for lifetime (especially the reliability associated with lower-tail behavior), and size effects have not been obtained as yet. These latter issues may be treated, however, by extending recent work on time-independent, global load-sharing models by Phoenix *et al.* [60].

BASIS FOR IMPROVEMENTS IN MODELING

Computational micromechanics techniques. Up to now statistical models for creep fracture involving micromechanics have used highly idealized stress redistribution rules. This has been done in large part to simplify the probability calculations but also because more sophisticated micromechanical calculations are computationally too intensive, especially using standard techniques such as the finite element method. One extreme has been equal load-sharing (ELS) among fibers [34-36], which has recently been extended to the concept of global load-sharing (GLS) [59]. The other is local load-sharing (LLS) where the stress of failed fibers is redistributed equally onto its nearest surviving neighbors following geometrically prescribed patterns [53,54]. Matrix creep has usually been captured by increasing with time the characteristic length of the local stress transfer region, using simple scalings from problems with an isolated fiber break in an array of fibers. These rules have led to considerable insight through scaling relationships involving fiber Weibull moduli, matrix creep exponents, load-sharing constants and fiber break cluster sizes, but for larger 3D composites they are not realistic enough to yield precise quantitative predictions of the lifetime scale parameters and distribution shapes.

In creep fracture, various micromechanical features occur, that require more sophisticated treatment. As mentioned, when a fiber breaks the stress at the fiber discontinuity drops to zero, but over a characteristic length recovers gradually along the fiber to the remotely applied fiber stress. Also corresponding to this length is an overstress length on neighboring fibers, where nominally the maximum overstress occurs directly adjacent to the fiber. The shear deformation near broken fibers, may reflect elastic, plastic and viscoelastic effects in the matrix and frictional sliding effects at the interface acting together to determine the growth of the characteristic length of stress transfer in time, and the actual shape of the overstress profiles on neighboring intact fibers. This characteristic overstress length will grow to become many times the length based on initial elasticity, but the stress concentration peaks may be lowered somewhat also (though on more distant neighbors they will increase). Interestingly, these peak values are unchanged when only matrix creep under linear viscoelasticity occurs; decreases in the peak turn out to result from matrix deformation that is nonlinear in stress such as plasticity and time dependent slip. Nevertheless the probability of additional fiber failures occurring locally in time will increase, resulting in clusters of breaks that increase in size.

To improve the modeling, there have recently been concerted efforts at Cornell University and elsewhere to develop computational micromechanics techniques that are much faster and more realistic. The most successful framework has been built upon the idealized, shear-lag framework of Hedgepeth [61,62]. (See the monograph of Chou [63] for a review and many applications.) In these models the fibers carry the tensile loads and the matrix primarily transmits loads in shear, allowing load transfer from fiber to fiber near breaks. Extension of these models to include additional stress tensor information may seem desirable and is reasonably straightforward, but numerical studies have shown that the gains in accuracy and realism are surprisingly small and rarely worth the greatly increased computational cost. In fact, the shear-lag approach yields realistic and accurate stress and displacement results that are consistent with those from experiments using micro-Raman spectroscopy and finite element calculations [64,65]. But the greatest advantage is that the shear-lag model can model stress redistribution in complex, random fiber break patterns including crack-like formations. In the latter case, when compared to classical continuum results for cracks in orthotropic media, the stress results agree remarkably down to the length scale of one fiber diameter [66]. Also shear-lag models show promise of modeling complex process zones ahead of crack tips not amenable to classical continuum treatments since crucial, discrete statistical features are lost (which surprisingly do not smooth out as the crack grows large relative to the fiber diameter).

The simplest, purely elastic version developed at Cornell is called break influence superposition (BIS) [66], and it can handle rapidly hundreds of arbitrarily placed fiber breaks [67,68] on a small workstation. A more advanced version called quadratic influence superposition (QIS) [69] uses quadratic order corrections to allow for localized matrix yielding, interfacial debonding and frictional sliding around many, arbitrarily located fiber breaks. The QIS technique can compute the extent and shape of the yield and debond zones, and the stress and strain distributions everywhere. In the time dependent case, the newest version is called the viscous break interaction (VBI), which can handle fiber break arrays in viscous and viscoelastic matrices following a power-law creep function [70]. This new model builds on influence functions based on earlier work at Cornell [71,72]. All these versions show promise of being up to three orders of magnitude more powerful than full discretization schemes such as finite difference or finite element methods. Finally we note that Curtin and coworkers [73] used lattice Green's functions to solve problems similar to those treated by the BIS and QIS method. However, high accuracy requires fine discretization along the fibers, reducing computational efficiency.

STOCHASTIC FAILURE MODELS FOR FIBERS AND BUNDLES

In addition to the computational micromechanics aspects described above, there is also long-standing experience in stochastic modeling of the failure of fiber bundles, and chains of bundles under ELS, GLS [74-80] and LLS [81,82] among fibers. Experiments have also been performed on fibers and composites to support the basis for these models [83-85]. Several works, for example, have dealt with the failure of bundles where the failure of the individual fibers depends stochastically on their individual load histories [74-77,81] and reflects fiber strength degradation kinetics. This is a crucial aspect to modeling failure in glass fibers. As discussed, an important aspect has been to capture time dependent creep in the matrix and debonding at the interface, and how it affects stress transfer mechanisms and probabilities of local fiber failure. These works incorporate this feature crudely [53,54,70]. Also, an important theme has been the treatment of long chains of finite bundles. In these cases, the mathematical framework of the statistical theory of extremes is crucial [76,77,81,82,83].

FUTURE PROSPECTS IN MODELING

The goal of building a comprehensive model will be accomplished by incorporating: i) fiber mechanical properties and flaw statistics at the length scale of local fiber load transfer, including any stochastic stress-time dependency, ii) matrix plasticity and creep in shear around fiber breaks, iii) interface debonding and viscous frictional sliding in terms of local shear stress, iv) local fiber and matrix packing geometry (2D planar, 3D hexagonal and random) and associated residual stresses from processing, and v) multiple matrix cracking insofar as it affects penetration of the environment to the fiber surface. Major aspects will be to use these theoretical models and supporting numerical analyses to determine key scalings, such as: a) the shapes of resulting strength and lifetime distributions, effective Weibull shape parameters (in cases where the Weibull distribution is an accurate approximation) as a function of load level and distribution, and composite volume, b) sensitivity of lifetime to load level in power-law (log-log), exponential (semi-log) and other functional frameworks motivated by the physics and micromechanics of stochastic flaw growth in the composite, c) critical cluster size and 'crack threshold' parameters. An important goal should be to uncover new functional forms for strength and lifetime distributions when relevant, rather than assume Weibull forms *a priori*. This is particularly important when modeling sensitivity to stress level and lower tail behavior.

A long term goal should be to implement the model in a Monte Carlo framework to: i) validate key analytical scalings and determine certain proportionality constants not accessible by analytical methods alone, and ii) perform many more replications (say 1,000 samples per stress level) on realistic structures than can be handled by physical experiments alone. The ultimate objective should be to generate computational tools to 'design' material microstructures and determine processing routes towards enhancing lifetime and reliability through proper quality control tests and handling procedures for the glass fibers, and tailoring of fiber-matrix interface and local matrix creep properties. For validation, predictions should be compared to experimental results on actual composite specimens (resin impregnated strands or coupons) as well as on microcomposite specimens [53,54].

For example, with respect to the fiber we already have stochastic models for its failure based on Weibull/Poisson statistics and fracture mechanics concepts for flaws [25,36,37,51,81,84,85], but these do not take full advantage of early knowledge on chemical mechanisms of stress-corrosion [13-18,22,23] and flaw statistics [19-21]. These ideas should be revisited to better couple chemistry, temperature, flaw statistics and crack-growth mechanisms into a stochastic fracture model for fibers. This is essential to understanding the chemical interactions of the glass and the environment at the fiber-matrix interface. Versions of the model should be comprehensive and suitable for numerical simulation codes for composite creep fracture, but simplified, parametric versions will be necessary and desirable for asymptotic and scaling analysis. One goal should be to asses the extent to which the simplified models can be used without significantly compromising the accuracy of predictions.

With respect to the matrix, as mentioned earlier, at a fiber break the load is transmitted to neighboring fibers, and the cross-linked polymer matrix locally undergoes large shear stresses and strains. As time passes the matrix creeps and eventually work hardens, resulting in interface failure and a slowly propagating debond or shear crack [86]. Furthermore the extent of interface sliding will depend on friction controlled by the balance in normal stresses resulting from thermal shrinkage during curing (compression) versus swelling from moisture absorption (tension), these also depending on the fiber packing geometry and volume fraction. This process needs to be better modeled. Also moisture and aggressive chemical species (alkalis) may penetrate the matrix to the fiber surface by diffusion through the matrix, or transport along the debonded fiber/matrix interface, or along transverse matrix cracks. We believe the tools are available to model these effects.

With respect to stress and strain evolution around large arbitrary arrays of fiber breaks in 3D, recent computational mechanics techniques are sophisticated, weighted superposition methods where the calculations are tied to the amount of damage (fiber breaks, nonlinear matrix deformation zones) rather than to the full composite size. Solving multiple fiber break problems involves an appropriately weighted, superposition of certain basis or influence functions obtained from certain unit solutions. An important advance is the very recently developed version, VBI to handle fiber break arrays in viscous and viscoelastic creeping matrices following a power-law creep function [69]. We believe this method is adaptable to a viscoelastic matrix with nonlinearities involving a power law in both stress and time, or to an interface slipping in time. It also can be extended to include 3D fiber arrays, variable fiber spacing and arbitrary sequences of fiber failures. This is needed to efficiently calculate evolving fiber and matrix stress and strain profiles at any stage of the composite failure process. In particular it is necessary to model what happens in growing clusters of breaks as they coalesce to form a catastrophic crack. We should note that there is a strong indication that when these nonlinear processes are particularly strong as is often the case, GLS becomes a very accurate model once the effective bundle size is determined [58,59]. A basis exists for a model that could be adapted for this task [80].

The stochastic models for failure of fiber bundles and fibrous composites, discussed earlier [74-82], have shortcomings that need to be addressed. Much more realistic stress-redistribution calculations in 3D are necessary and these can be achieved by the methods just discussed Second, there is a need to pursue scaling concepts with respect to volume effects in the strength distributions that have been pursued in the physics literature [87,88]. Perhaps most important is the need to combine stochastic decay in fiber strength with matrix creep in one unified framework, leading to lifetime distributions, size scalings and stress dependencies that are realistic and can be used to interpret real composite lifetime data in the context of the mechanisms involved. Thus, using enhanced computational capability for micromechanics, probability analysis and combinatorics in an extreme value setting, it will be possible to develop more advanced functional forms of failure distributions, including size and stress gradient effects, effects of stress level, and effects of temperature and environment.

With respect to accelerated testing, questions to consider through modeling are: To what extent is it possible to be misled by apparent good performance early in tests? To what extent do paradoxical phenomena occur? How sensitive are such tests to factors known to eventually reduce long-term lifetime according to the models above or to data in the literature? And lastly, can parameters be estimated from accelerated tests on simple composite specimens that can be used in predicting the lifetime of larger specimens in service?

Finally such models could be used to assess manufacturing approaches, materials processing, quality control and component architecture insofar as they affect durability and reliability. Questions are: What quality control tests on the fiber, matrix and composite strands or coupons are necessary to ensure reliable components? Is proof loading useful as a strategy to 'weed out' weak components and 'condition' the material, or, does it introduce large numbers of fiber breaks that subsequently accelerate the creep fracture process? Should yarns and rovings be clustered in the material or should the fibers be distributed as much as possible throughout the material? Should components be continuous or arrays of smaller components as in bridge strands, and what is the optimal number. If material or components are removed from service and residual strength tests performed can this be converted into a meaningful measure of remaining life? In large applications should material be put on test in laboratories under conditions similar to the actual application, and should material be periodically removed for testing? In quality control tests of strength coupons, what signs in the failure modes and distributions are indicative of material that will have poor reliability? In engineering practice these may well be the most relevant questions. We believe modeling plays a crucial role in answering them.

REFERENCES

1. F. Seible and V. Karbhari. "Advanced Composites Build on Success", *Civil Engineering,* August, 44-47, 1996.
2. K.S. Fisher and S. Bassett. "Cables, strands and rods keep tension high", *High Performance Composites*, July/August, 23-29, 1997.
3. *Composites for Infrastructure; A Guide for Civil Engineers.* Ray Publishing, 4891 Independence St., Suite 270, Wheat Ridge, CO 80033, 1997.
4. A. Nanni and C.W. Dolan (editors). "FRP Reinforcement for Concrete Structures", *Proc. ACI SP-138, American Concrete Institute, Detroit MI,* page 997, 1993
5. R.E. Chambers. "ASCE Design Standard for Pultruded Fiber-Reinforced-Plastic (FRP) Structures", *ASCE Journal of Composites for Constructions* , 26, 1997.
6. A. Nanni. "Coordinated Program for Research on Advanced Composites in Construction (RACC)", *Final Report to NSF,* Dept. of Architectural Engineering, The Pennsylvania State University, University Park, PA 16802, 1994
7. L.C. Bank, T.R. Gentry and A. Barkatt. "Accelerated test methods to determine the long-term behavior of FRP composite structures: Environmental effects", *J. Reinforced Plastics and Composites*, **14**, 559, 1995.
8. *Non-Metallic (FRP) Reinforcement for Concrete Structures.* Proceedings of the Second International RILEM Symposium (FRPRCS-2), edited by L. Taerwe, RILEM, E & FN Spon, London, 1995.
9. A. Gerritse and J.A. Den Uij. "Long-term behavior of Arapree" (Ref. 8, pp 57-66), 1995.
10. M. Scheibe and F.S. Rostasy. "Stress-rupture of AFRP subjected to alkaline solutions and elevated temperatures-experiments" (Ref. 8, pp 67-71), 1995.
11. F. Katsuki, T. Uomoto. "Prediction of deterioration of FRP rods due to alkali" (Ref. 8, pp 82-89), 1995.
12. C. Arya, F.K. Ofori-Darko and G. Pirathapan. "FRP rebars and elimination of reinforcement corrosion in concrete structures" (Ref. 8, pp 227-234), 1995.
13. N.W. Taylor. "Mechanism of fracture of glass and similar brittle solids", *J. Appl. Physics*, **18**, 943-954, 1947.
14. D.A. Stuart and O.L. Anderson. "Dependence of ultimate strength of glass under constant load and temperature, ambient atmosphere, and time", *J. Amer. Ceram. Soc.*, **36**, 416-424, 1952.
15. R. J. Charles. "Static fatigue of glass. I". *Journal of Applied Physics*, **29**, 1549-53, 1958.
16. R. J. Charles. "Static Fatigue of glass. II". *Journal of Applied Physics*, **29**, 1554-60, 1958.
17. R.E. Mould and R.D. Southwick. "Strength and static fatigue of abraded glass under controlled ambient conditions," Part I, *J. Amer. Ceram. Soc.*, **42**, 542-581; Part II, **42**, 582-607, 1959.
18. R.J. Charles and W.B. Hillig. "The kinetics of glass failure by stress corrosion", published as part of the *Symposium on the Mechanical Strength of Glass and Ways of Improving It,* Union Scientifique Continentale du Verre, 1961.
19. J.A. Kies. "The Strength of Glass Fibers and the Failure of Filament Wound Pressure Vessels", *NRL Report 6034,* U.S. Naval Research Laboratory, 1964.
20. G.K. Schmitz and A.G. Metcalfe. "Characterization of flaws on glass fibers", *Proc. 20th Anniversary Technical Conference,* The Society of the Plastics Industry, 1965.
21. G.K. Schmitz and A.G. Metcalfe. "Stress-corrosion of E-glass fibers", *I&EC Product Res. & Dev.*, **5**, 1-6, 1966.
22. W.B. Hillig and R.J. Charles. "Surfaces, stress-dependent surface reactions, and strength", in *High Strength Materials* (ed. V.F. Zackay), pp. 682-705. Wiley, New York, 1965.
23. A.G. Metcalfe, M.E. Gulden and G.K. Schmitz, "Spontaneous cracking of glass filaments", *Glass Technology*, **12**, 15-23, 1971.

24. H. Schonhorn, T.T. Wang, H.N. Vazirani and H.L. Frisch. "Static and dynamic fatigue of high-strength glass fibers coated with uv-curable epoxy-acrylate", *J. Appl. Phys.*, **49**, 4783-87, 1978.
25. A. Kelly and N.H. Macmillan. *Strong Solids* (3rd ed.) Oxford University Press, 1986.
26. E.Y. Robinson and T.T. Chiao. "Analysis of Stress-Rupture Data from S-Glass Composites", *UCRL-73358*, Lawrence Livermore National Laboratory, Livermore, California, 1971.
27. T.T. Chiao, J.K. Lepper, N.W. Hetherington and R.L. Moore. "Stress-rupture of simple S-glass/epoxy composites", *J. Composite Materials*, **6**, 358-370, 1972.
28. T.T. Chiao and R.L. Moore. "Strength retention of S-glass/epoxy composites", *J. Composite Materials*, **6**, 156-159, 1972.
29. T.T. Chiao and R.L. Moore. "Stress-rupture of S-glass/epoxy multifilament strands: Time-to-break data", *UCRL-51220*, Lawrence Livermore National Laboratory, Livermore, CA, 1972.
30. T.T. Chiao, C.C. Chiao and R.J. Sherry. "Lifetime of fiber composites under sustained tensile loading", *UCRL-78367*, Lawrence Livermore National Laboratory, Livermore, CA, 1976.
31. H.T. Hahn and T.T. Chiao. "Long-term behavior of composite materials", in *Advances in Composite Materials,* " *Advances in Composite Materials, Vol. 1*, (edited by A.R. Bunsell *et al.*) Pergamon, Oxford, UK, 1978.
32. R.L. Moore, M.A. Hamstad, and T.T. Chiao. "Stress-rupture behavior of graphite fiber/epoxy strands", *Fukugo Zairyo: Composite Materials and Structures*, **3**, 19-23, 1974.
33. S.L Phoenix and E.M. Wu. Statistics for the time-dependent failure of Kevlar-49/epoxy composites: Micromechanical modeling and data interpretation." *Report UCRL-53365*, Lawrence Livermore National Laboratory, Livermore, California, 1983.
34. J.M. Lifshitz and A. Rotem. "Time-dependent longitudinal strength of unidirectional fibrous composites", *Fibre Sci. and Technol.* **3**, 1-20, 1970.
35. J.M. Lifshitz, Time-dependent fracture of fibrous composites, in *Composite Materials, Volume 5*, edited by L.J. Broutman, Academic Press, New York, 1974.
36. J. Aveston, A. Kelly and J.M. Sillwood. "Long-term strength of glass reinforced plastics in wet environments", *Advances in Composite Materials, Vol. 1*, (edited by A.R. Bunsell *et al.*) Pergamon, Oxford, UK, 1980.
37. A. Kelly and L.N. McCartney. "Failure by stress-corrosion of bundles of fibers", *Proc. R. Society*, **A 374** (1981) 475, 1981.
38. M.G. Phillips. "Prediction of long-term stress-rupture life for glass fibre-reinforced polyester composites in air and in aqueous environments", *Composites*, **14**, 270-275, 1983.
39. F.R. Jones, J.W. Rock and A.R. Wheatley. "Stress-corrosion cracking and its implications for the long-term durability of E-glass fibre composites", *Composites*, **14** 262-269, 1983.
40. P.J. Hogg. "Factors affecting the stress-corrosion of GRP in acid environments", *Composites*, **14**, 254-261, 1983.
41. G. Pritchard and S.D. Speake. "The use of water absorption kinetic data to predict laminate property changes", *Composites*, **18**, 227-232, 1987.
42. G. Pritchard and S.D. Speake. "Effects of temperature on stress-rupture times in glass/polyester laminates", *Composites*, **19**, 29-35, 1988.
43. C.J. Hilado (editor). "Glass Reinforced Polyester Systems", *Materials Technology Series Vol. 14*, Technomic Publishing Co., Lancaster PA, 1984.
44. W.N. Findley and J.F. Tracy. "16-year creep of polyethylene ands PVC", Report MRL E-88, EMRL-57, Brown University, Providence, RI, 1973.
45. K.G. Kibler and H.G. Carter. "Viscoelastic parameters of epoxy resin from thermomechanical and electrical conductivity measurements" *Composite Materials: Testing and Design (5th Conference)*, ASTM STP 674, S.W. Tsai, ed., American Society for Testing and Materials, 282-288, 1979.
46. K.G. Kibler. "Time-Dependent Environmental Behavior of Graphite/Epoxy Composites", Technical Report AFWAL-TR-80-4052. Materials Laboratory, Wright-Patterson Air Force Base, OH 45433 (see also Appendix C. therein by R.A. Schapery), 1980.
47. R.A. Schapery. "Viscoelastic behavior and analysis of composite materials," in *Composite Materials*, 2, G.P. Sendeckyj editor, pp. 85-165, Academic Press, New York, 1974.
48. R.A. Schapery. "Correspondence principles and a generalized *J* integral for large deformation and fracture analysis of viscoelastic media, *Int. J. Fracture*, **25**, 195-223, 1984.

49. L.C.E. Struik. "*Physical Aging in Amorphous Polymers and Related Materials*", Elsevier, New York, 1979.
50. D.S. Farquhar, F. M. Mutrelle, S.L. Phoenix and R.L. Smith. "Lifetime statistics for single graphite fibers in creep rupture". *Journal of Materials Science*, **24**, 2131-2164, 1989.
51. J. Raghavan and M. Meshii. "Prediction of creep rupture of unidirectional carbon fiber reinforced polymer composite", *Materials Science and Engineering*, **A197**, 237-249, 1994.
52. J. Raghavan and M. Meshii. "Creep of polymer composites", *Composites Science and Technology*, **57**, 1707-1725, 1998.
53. S.L. Phoenix, P. Schwartz and H.H. Robinson IV. "Statistics for the strength and lifetime in creep-rupture of model carbon/epoxy composites", *Compos. Sci. Tech.*, **32**, 81-120, 1988.
54. H. Otani, S.L. Phoenix and P. Petrina. "Matrix effects on lifetime statistics for carbon fiber/epoxy microcomposites in creep-rupture", *J. Materials Science*, **26**, 1955-1970, 1991.
55. Y. Kawazu, T. Norita and M. Fujiwara. "Static fatigue behavior of carbon fiber/epoxy strands", *Sen-i Gakkai-shi*, **31**, 67-72, 1975.
56. K.W. Kelly and E. Barbero. "The effect of fiber damage on the longitudinal creep of a CFMMC". *Int. J. Solids Struct.*, **30**, 3417-3429, 1993.
57. R.M. McMeeking. "Models for the creep of ceramic matrix composite materials", in *High Temperature Mechanical Behavior of Ceramic Composites* (S. V. Nair and K. Jakus, eds.) Butterworth Heinmann, Boston, 409-436, 1995.
58. N. Ohno and T. Miyake. "Relaxation in broken fibers in unidirectional composites: modeling and application to creep rupture analysis", *J. Mech. Phys Solids*, to appear, 1997.
59. N. Iyengar and W.A. Curtin. "Time-dependent failure in fiber-reinforced composites by matrix creep and interface shear creep", *Acta. Mater.* (1997) to appear, 1997.
60. S.L. Phoenix, M. Ibnabdeljalil and C.-Y. Hui. "Size effects in the distribution for strength of brittle matrix fibrous composites", *Int. J. Solids Struct.*, **34**, 545-568, 1997.
61. J.M. Hedgepeth. *Stress Concentrations in Filamentary Structures*, NASA TND-882, 1961.
62. J.M. Hedgepeth and P. Van Dyke. "Local stress concentrations in imperfect filamentary composites", *J. Composite Mater*, **1**, 294-309, 1967.
63. T.W. Chou. *Microstructural Design of Fiber Composites*, Cambridge University Press, Cambridge, UK, 1992.
64. L.S. Schadler and C. Galiotis. "A Review of The Fundamentals and Applications of Laser Raman Spectroscopy Microprobe Strain Measurements in Composite Materials", Invited paper for *J. International Materials Reviews*, **40**, 116-134, 1995.
65. L.S. Schadler, M.S. Amer, and B. Iskandarani. "Experimental Measurement of Fiber/Fiber Interaction Using Micro-Raman Spectroscopy", *Mechanics of Materials*, **23**, 205-216, 1996.
66. I.J. Beyerlein, S.L. Phoenix and A.M. Sastry. "Comparison of shear-lag theory and continuum fracture mechanics for modeling fiber and matrix stresses in an elastic cracked composite lamina", *Int. J. Solids and Structures*, **33**, 2543-2574, 1996.
67. I.J. Beyerlein and S.L. Phoenix. "Statistics of fracture for an elastic notched composite lamina containing Weibull fibers - Part I: Features from Monte Carlo simulation", *Engineering Fracture Mechanics*, **57**, 241-265, 1996.
68. I.J. Beyerlein and S.L. Phoenix. "Statistics of fracture for an elastic notched composite lamina containing Weibull fibers - Part II: Probability models of crack growth", *Engineering Fracture Mechanics*, **57**, 267-299, 1996.
69. I.J. Beyerlein and S.L. Phoenix. "Stress concentrations around multiple fiber breaks in an elastic matrix with local yielding or debonding using quadratic influence superposition", *Journal of the Mechanics and Physics of Solids* , **44**, 1997-2039, 1996.
70. I.J. Beyerlein, S.L. Phoenix and R. Raj. "Time evolution of stress distributions around arbitrary arrays of fiber breaks in a composite with a creeping viscoelastic matrix", *Int. J. Solids Structures*, to appear, 1998.
71. D.C. Lagoudas, C.Y. Hui and S.L. Phoenix. "Time evolution of overstress profiles near fiber breaks in a composite with viscoelastic matrix", *International Journal of Solids and Structures*, **25**, 45-66, 1988.

72. D.D. Mason, C.-Y. Hui and S.L. Phoenix. "Stress profiles around a fiber break in a composite with a nonlinear, power-law creeping matrix", *International Journal of Solids and Structures*, **26**, 2829-2854, 1992.
73. S.J. Zhou and W.A. Curtin. "Failure of fiber composites: a lattice Green function model", *Acta Metall. Mater.*, **43**, 3093-3104, 1995.
74. S.L. Phoenix. "Stochastic strength and fatigue of fiber bundles", *International Journal of Fracture*, **14**, 327-344, 1978.
75. S.L. Phoenix. "The asymptotic distribution for the time to failure of a fiber bundle", *Advances in Applied Probability*, **11**, 153-187, 1979.
76. R.L. Smith and S.L. Phoenix. "Asymptotic distributions for the failure of fibrous materials under series-parallel structure and equal load sharing", *Journal of Applied Mechanics*, **103**, 75-82, 1981.
77. M. Ibnabdeljalil and S.L. Phoenix. "Creep-rupture of brittle matrix composites reinforced with time dependent fibres: Scalings and Monte Carlo simulations", *J. Mechanics and Physics of Solids*, **43**, 897-931, 1995.
78. M. Ibnabdeljalil and S.L. Phoenix. "Scalings in the statistical failure of brittle matrix composites with discontinuous fibers: Analysis and Monte Carlo simulations", *Acta Metallurgica et Materialia*, **43**, 2975-2983, 1995.
79. C.-Y. Hui, S.L. Phoenix and L. Kogan. "Analysis of fragmentation in the single filament composite: roles of fiber strength distributions and exclusion zone models", *Journal of the Mechanics and Physics of Solids*, **4**, 1715-1737, 1997.
80. L. Kogan, C.-Y. Hui, and S.L. Phoenix. "Formulation for fragmentation of fibers in a single filament composite when the matrix is history dependent or no exclusion zone exists", under revision, 1998.
81. S.L. Phoenix and L.J. Tierney. "A statistical model for the time dependent failure of unidirectional composite materials under local elastic load-sharing among fibers", *Engineering Fracture Mechanics*, **18**, 193-215, 1983.
82. R.L. Smith, S.L. Phoenix, M.R. Greenfield, R.B. Henstenburg, and R.E. Pitt. "Lower-tail approximations for the probability of failure of 3-D fibrous composites with hexagonal geometry", *Proceedings of the Royal Society*, London **A388**,353-391, 1983.
83. I.J. Beyerlein and S.L. Phoenix. "Statistics for the strength and size effects of microcomposites with four carbon fibers in epoxy", *Composites Science and Technology*, **56**, 75-92, 1996.
84. H.D. Wagner, P. Schwartz and S.L. Phoenix. "Lifetime statistics for single Kevlar 49 filaments in creep-rupture", *Journal of Materials Science*, **21**, 1868-1878, 1986.
85. H.F. Wu, S.L. Phoenix and P. Schwartz. "Temperature dependence of lifetime statistics for single Kevlar 49 filaments in creep-rupture", *Journal of Materials Science*, **23**, 1851-1860, 1988.
86. R. Gulino, P. Schwartz and S.L. Phoenix. "Experiments on shear deformation debonding and local load transfer in a model graphite/glass/epoxy composite" *Journal of Materials Science*, **26**, 6655-6672, 1991.
87. P.M. Duxbury, P.L. Leath and P.D. Beale. "Breakdown properties of quenched random systems: The random-fuse network", *Physical Review B*, **36**, 367-380, 1987.
88. P.D. Beale and D.J. Srolovitz. "Elastic fracture in random materials", *Physical Review B*, **37**, 5500-5507, 1988.
89. J. He, I.J. Beyerlein, and D.R. Clarke. "Load transfer from broken fibers in continuous fiber Al_2O_3-Al composites and dependence on local volume fraction." *J. Mech. Phys. Solids*, 1998.

DEVELOPMENTS IN THERMOPIEZOELASTICITY WITH RELEVANCE TO SMART COMPOSITE STRUCTURES

T. R. Tauchert[1], F. Ashida[2], N. Noda[3], S. Adali[4] and V. Verijenko[4]

[1]Department of Mechanical Engineering, University of Kentucky, Lexington, KY 40506-0046, USA
[2]Department of Electronics and Control Engineering, Tsuyama National College of Technology, Okayama 708, JAPAN
[3]Department of Mechanical Engineering, Shizuoka University, Johoku 3-5-1, Hamamatsu, 432, JAPAN
[4]Department of Mechanical Engineering, University of Natal, Durban 4041, Republic of South Africa

ABSTRACT

A review of theoretical developments in thermopiezoelasticity having relevance to smart composite structures is presented. The equations governing linear response of piezothermoelastic media are outlined, and a general solution procedure based on potential functions is described. Sensor applications aimed at predicting thermal loads and corresponding responses from measurements of electric potential distributions are described; studies on the control of composite structures (beams, plates and shells) via piezoelectric actuation are reviewed.

INTRODUCTION

Due to their special characteristics, piezoelectric materials can function effectively as distributed sensors and actuators for controlling structural response. In sensor applications, mechanically or thermally induced disturbances can be determined from measurement of the induced electric potential difference *(direct piezoelectric effect)*, whereas in actuator applications deformation or stress can be controlled through the introduction of an appropriate electric potential difference *(converse piezoelectric effect)*. By integrating piezoelectric elements and advanced composite materials, the potential exists for forming high-strength, high-stiffness, light-weight structures capable of self-monitoring and self-controlling. Such "smart" structural systems, characterized by sensors and actuators that are attached or embedded within a laminate and regulated by feedback control, have been the focus of considerable recent attention. While the majority of the research has been directed at behaviors of structures subject to isothermal conditions, an increasing number of investigations have addressed thermo-electro-mechanical responses. The purpose of this article is to report on the status of piezothermoelasticity and its relevance to intelligent composite structures.

Among the early investigations in this area, Tiersten [53] derived the differential equations and boundary conditions governing the behavior of an electrically polarizable, finitely deformable, heat conducting medium in interaction with an electric field. Thereafter, Mindlin [36] deduced the equations describing small vibrations of piezoelectric plates, including the coupling between the deformation, temperature and electric fields. A uniqueness theorem was presented in [36] to establish the face and edge conditions sufficient to assure unique solutions of the two-dimensional equations. W. Nowacki [39] provided a uniqueness theorem for the solution of the three-dimensional equations of thermopiezoelectricity . He also generalized Hamilton's principle and the theorem of reciprocity of work to include thermoelectric effects. J.P. Nowacki [38] derived a reciprocity theorem for static thermopiezoelectricity, and utilized the theorem to generalize Maysel's (Green's function) formula. Uniqueness and reciprocity results for quasistatic and dynamic thermopiezoelectricity were established by Iesan [24].

Kalpakidis and Massalas [28] extended Tiersten's theory, by including in addition to dipole moments the quadrupole moments, and by considering the constitutive equations to be dependent on the time rate of change of absolute temperature. A generalized linear theory of thermoelasticity for piezoelectric materials, which includes heat-flux among the independent constituent variables, was proposed by Chandrasekharaiah [19]. Thermal effects in piezoelectric composite structures, including temperature-dependent material properties and heat generation due to electric loading, were studied by Rao and Sunar [41]. Bert and Birman [15] investigated both stress and temperature dependency of the constitutive properties; they showed that as a consequence of temperature dependency, the thermal expansion and piezoelectric coefficients must be stress dependent.

While the governing equations of themopiezoelectricity are normally expressed in differential form, they may alternatively be stated in variational form. Variational principles were deduced by Altay and Dokmeci [1] for discontinuous fields. The principles were shown to generate the divergence equations (stress equations of motion, charge equation of electrostatics, and equation of heat conduction), the gradient equations (strain-displacement equations, electric field-electric potential relations and Fourier's law of heat conduction), the constitutive equations, boundary conditions and jump conditions for a medium with or without a surface of discontinuity. These variational principles provide a useful means for deriving lower order theories and approximate solutions for piezothermoelastic bodies.

The present authors have proposed general solution procedures for stationary three-dimensional [12] and two-dimensional [5] problems of piezothermoelastic solids in Cartesian coordinates, for axisymmetric problems [13] in cylindrical coordinates, and for transient two-dimensional [21] and axisymmetric [10] problems.

In the following sections of this article we review the equations governing piezothermoelastic behaviors, describe a potential function solution procedure, discuss a number of inverse problems having relevance to piezoelectric sensors, and review various investigations dealing with the control of composite structures via piezoelectric actuation.

EQUATIONS GOVERNING PIEZOTHERMOELASTIC RESPONSE

The differential form of the equations governing the linear response of a piezothermoelastic medium, written in terms of general curvilinear coordinates, is as follows.

Motion:

$$\sigma^{ij}\big|_j + f^i = \rho\, \ddot{u}^i \qquad (1)$$

Electrostatics:

$$D^i\big|_i = 0 \qquad (2)$$

Heat conduction:

$$q^i\big|_i = -\rho c \dot{T} + Q \qquad (3)$$

Constitutive relations:

$$\sigma^{ij} = c^{ijk\ell}\varepsilon_{k\ell} - e^{mij}E_m - \beta^{ij}T \qquad (4)$$

$$D^i = e^{ik\ell}\varepsilon_{k\ell} + \eta^{im}E_m + p^i T \qquad (5)$$

$$q^i = -\lambda^{ij}T_{,j} \qquad (6)$$

in which σ^{ij} is the stress tensor; $\varepsilon_{k\ell} = 1/2(u_k\big|_\ell + u_\ell\big|_k)$ is the strain tensor, with u_k denoting the displacement vector; D_i is the electric displacement vector; $E_m = -\Phi_{,m}$ is the electric field vector, given by the gradient of the electric potential Φ; T is the temperature rise from the stress-free temperature. Also, c^{ijkl} denote elastic moduli; e^{mij} are piezoelectric coefficients; β^{ij} are stress-temperature coefficients; η^{im} are permittivities; p^i are pyroelectric coefficients; λ^{ij} are coefficients of thermal conductivity; f^i is the body force vector; ρ denotes density; c is the specific heat; Q is the rate of heat generation per unit volume; $(\dot{\ })$ denotes a time derivative; and $(\ |_j)$ represents covariant differentiation with respect to a curvilinear coordinate θ^j.

The above equations of motion and electrostatics can alternatively be expressed in variational form as [1]

$$\int_V [(\sigma^{ij}|_i - f^j - \rho\, \ddot{u}^j)\delta u_j - D^i\Big|_i \delta\Phi]\, dV - \int_S [(n_i\sigma^{ij} - \bar{t}^j)\delta u_j - (n_i D^i - \bar{q})\delta\Phi] dS = 0 \qquad (7)$$

in which $\bar{t}^j$ and $\bar{q}$ denote, respectively, the prescribed stress traction and electric charge on surface S of a body of volume V.

A GENERAL SOLUTION PROCEDURE FOR PIEZOTHERMOELASTIC BODIES

A solution procedure based upon potential functions has been developed for analyzing the quasistatic piezothermoelastic response of a three-dimensional body of crystal class 6mm in Cartesian [12] or cylindrical coordinates [13], a two-dimensional problem [5] for a plate of class mm2, and a plate of class 6mm under axisymmetric heating [14]. For simplicity we consider here the latter two cases, wherein the body is subject to a transient temperature field expressible as

$$T(\zeta, z, t) = T_0(z, t) + T_1(\zeta, z, t) \qquad (8)$$

in which ζ represents x in the two-dimensional problem in Cartesian coordinates, or the radial coordinate r in the axisymmetric problem.

Solutions to the equations of equilibrium (1) and electrostatics (2) are found by expressing the displacements and electric field vector in terms of potential functions as [5,10,14]

$$E_\zeta = -(\Phi_1)_{,\zeta} \ , \quad E_z = -(\Phi_0 + \Phi_1)_{,z} \qquad (9)$$

$$\begin{aligned} u_\zeta &= (\phi_1 + \phi_2 + \sum_{i=1}^{3} \ell_i \psi_i)_{,\zeta} \\ u_z &= (\phi_0 + k_1\phi_1 + j\phi_2 + \sum_{i=1}^{3} m_i \psi_i)_{,z} \end{aligned} \qquad (10)$$

For the temperature field $T_0(z,t)$, the potential functions Φ_0 and ϕ_0 are given by

$$\Phi_0 = \int \gamma_2 T_0(z, t) dz + C_1 \qquad (11)$$

$$\phi_{0,z} = \int \gamma_1 T_0(z, t) dz + C_2 \qquad (12)$$

while for $T_1(\zeta,z,t)$ the electric potential Φ_1 is expressed as

$$\Phi_1 = \chi + (\sum_{i=1}^{3} n_i \psi_i)_{,z} \qquad (13)$$

In this case the piezothermoelastic potentials ϕ_i $(i = 1,2)$, the piezoelastic potentials ψ_i $(i = 1,2,3)$, and the piezoelectric function χ are governed by the following equations:

$$(\Delta_\zeta + \mu_1 \frac{\partial^2}{\partial z^2})(\Delta_\zeta + \mu_2 \frac{\partial^2}{\partial z^2})(\Delta_\zeta + \mu_3 \frac{\partial^2}{\partial z^2})\phi_1 = d_2\Delta_\zeta\Delta_\zeta T_1 + d_1\Delta_\zeta T_{1,zz} + d_0 T_{1,zzzz} \qquad (14)$$

$$\Delta_\zeta \psi_i + \mu_i \psi_{i,zz} = 0 \qquad (15)$$

$$\phi_{2,zz} = \frac{1}{\xi_1}(\Delta_\zeta \phi_1 + \nu_1 \phi_{1,zz} - \delta_1 T_1) \tag{16}$$

$$\chi_{,z} = \frac{1}{\xi_2}(\Delta_\zeta \phi_2 + \nu_2 \phi_{2,zz} - \delta_2 T_1) \tag{17}$$

where

$$\Delta_\zeta = \begin{cases} \partial^2 / \partial x^2 & (\zeta = x) \\ \partial^2 / \partial r^2 + r^{-1} \partial / \partial r & (\zeta = r) \end{cases} \tag{18}$$

In the above equations the quantities $j, k_1, \ell_i, m_i, n_i, d_i, \gamma_i, \delta_i, \nu_i, \mu_i$ and ξ_i depend on the material properties as indicated in Ref. [5] for $\zeta = x$, or in Ref [14] for $\zeta = r$. Since equations (14) and (15) constitute uncoupled differential equations, solutions for ϕ_1 and ψ_i generally can be found. Once these functions have been determined, ϕ_2 and χ are obtained from equations (16) and (17).

PIEZOELECTRIC SENSOR APPLICATIONS

The direct piezoelectric effect, whereby an electric potential is generated when a piezoelectric material deforms, provides a mechanism for sensing thermomechanical disturbances. The concept of utilizing piezoelectric elements to predict unknown thermal loadings and the corresponding piezothermoelastic responses from measurement of induced electric potentials has been investigated by the present authors [3,6,8,9,11]. For example, an inverse problem was solved [9] using the potential function approach (equations (9)-(18)) to predict the axisymmetric stationary temperature distribution on the surface of a circular piezothermoelastic disk, based on measurements of the electric potential distributions on the faces of the disk. The problem of a disk subject to a spatially uniform, time-varying ambient surface temperature also has been considered [8]. For this situation an exact solution to the inverse problem was obtained corresponding to a particular analytical form of the electric potential difference. Also presented was a finite difference formulation that leads to a solution for the unknown temperature, without specification of a particular form for the electric potential. Reference [11] extended the earlier studies [8,9] to the case of transient axisymmetric response. A finite difference procedure was developed to determine the transient, radially-varying ambient temperature $\Theta(r,t)$ on the surface of a circular disk (Fig. 1), based on a knowledge of the induced electric potential difference across the disk thickness. The thermal loading was presumed to cause a difference in the electric potential given by $V(r,t) = [\Phi]_{z=b} - [\Phi]_{z=-b} = -V_0(1 - 2f\frac{r^2}{a^2} + f\frac{r^4}{a^4})(1 - e^{-\kappa t/a^2})$ where V_0 is a constant and f is a specified parameter. Figure 2 shows the radial distribution of nondimensionalized electric potential difference $[\overline{\Phi}]_{\bar{z}=\bar{b}} - [\overline{\Phi}]_{\bar{z}=-\bar{b}}$ at various times $\bar{t}$ for a disk of thickness-to-diameter ratio $\bar{b} = b/a = 0.1$, corresponding to a value of parameter $f = 1$. The ambient temperature distributions $\overline{\Theta}(\bar{r},\bar{t})$ that would produce such electric potential difference variations are illustrated in Fig.3; the corresponding surface radial stress is shown in Fig.4.

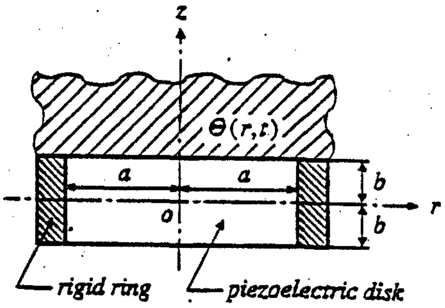

Fig. 1. Piezoelectric sensor [11].

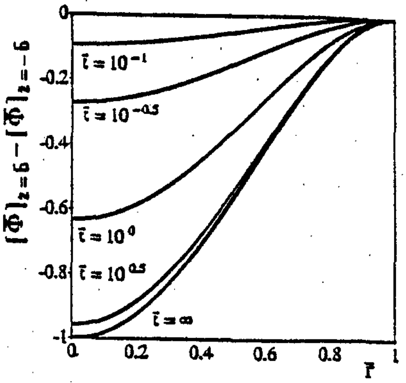

Fig. 2. Electric potential difference [11].

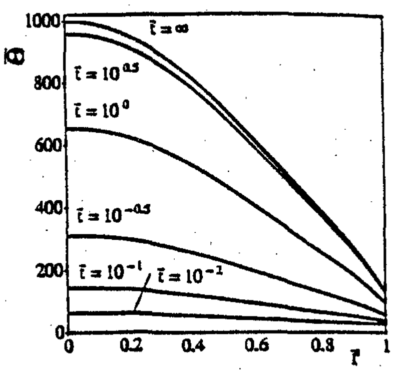

Fig. 3. Inferred ambient temperature [11].

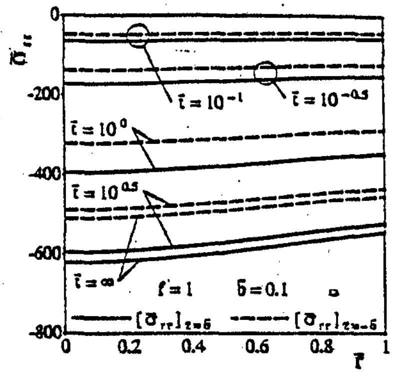

Fig. 4. Radial stress [11].

The inverse thermoelasticity problem of a structural plate to which a piezoelectric ceramic plate is perfectly bonded was considered by Ashida et al. [3]. The potential function approach again was utilized to determine the unknown stationary heating temperature θ(x,y) on the surface of the structural plate, based upon the induced potential distribution $\Phi = V_0\, v(x,y)$ on the free surface of the piezoelectric plate. Results such as those mentioned above indicate that time-varying and/or spatially-varying thermal loads and responses can be inferred from a knowledge of induced electric potential distributions.

Various other aspects of piezothermoelastic sensing are reported in Refs. [16,25]. Irschik et al. [25] considered the inverse problem of designing ("shaping") a sensor with a spatially-varying intensity of activity such that the measured signal can be interpreted in a desired manner. They examined the possibility of non-uniqueness of the inverse problems. Birman [16] examined the effect of temperature on accurate interpretation of data from piezoelectric sensors.

CONTROL OF COMPOSITE STRUCTURES VIA PIEZOELECTRIC ACTUATION

Displacements and stresses caused by temperature variations can affect significantly the performance and life of structures that operate in elevated or reduced temperature environments. By taking advantage of the converse piezoelectric effect of bonded or embedded piezoelectric elements within a composite structure, unwanted thermomechanical disturbances can be reduced or possibly eliminated. A review of published works dealing with the control of various composite structures, including laminated slabs/beams subject to cylindrical bending, and laminated plates and shells with general deformation behaviors, follows.

Cylindrical Bending of Laminates

Several studies have been carried out on the cylindrical bending of piezothermoelastic laminates subject to thermo-electro-mechanical loading [23,29,49,50]. In Ref. [49] for example, exact analytical solutions were derived for the stationary plane-strain response of a hybrid laminate consisting of orthotropic and/or isotropic structural layers and orthorhombic piezoelectric layers. For electric loading of the piezoelectric layers, consisting of either a large applied surface voltage or electric charge, it was assumed that the electric field resulting from variations in stress or temperature (the direct piezoelectric effect) is insignificant compared with that produced by the electric loading. In this case the electrostatics equation (2) governing the electric potential Φ becomes uncoupled and reduces to $\eta^{im}\Phi_{,mi} = 0$. Formulations that ignore the direct piezoelectric effect hereafter will be referred to as "uncoupled".

The analytical formulation of [49] was employed in [50] to obtain the solution for a "benchmark problem", consisting of a simply supported five-layer hybrid laminated slab (Fig. 5) subject to specified thermal and electric-potential surface loadings. Also presented was a high-order formulation in which both in-plane and out-of-plane displacement components were assumed to have cubic variations through the thickness of the laminate. The high-order theory, which accounts for transverse normal and shear deformations, reduces to first-order shear-deformation and classical (Kirchhoff) theories, as special cases. Numerical results for the benchmark problem indicate that the third-order theory yields results which are in better agreement with the piezothermoelasticity solution than those based upon classical bending theory.

Dube, Kapuria and Dumir presented three-dimensional exact piezothermoelastic solutions for cylindrical bending of simply supported orthotropic [23] and cross-ply laminated [29] panels. Solutions to the coupled equilibrium and electrostatic equations were obtained by Fourier expansion of the state variables. In [29], a laminate consisting of a graphite-epoxy substrate with a polyvinylidene fluoride (PVDF) layer bonded to one face, was determined for prescribed sinusoidal surface temperature distributions and electric potential difference applied to the piezoelectric layer. It was demonstrated that the maximum values of both the deflection and the stress due to thermal loading can be substantially reduced by applying an appropriate value of potential difference across the piezoelectric layer.

Response of composite beams to piezoelectric actuation has been investigated by several authors [17,18,33,41,45,56,57]. Rao and Sunar [41] derived a fully-coupled finite element formulation for thermopiezoelectric media, and applied the formulation to analyze vibration sensing and control of a cantilever beam having two PVDF layers functioning as the distributed sensor and actuator. Results indicate that heat generation resulting from feedback voltage applied to the actuator may have a significant influence upon the structural response. The authors also investigated the effect of actuator placement along the length of the surface of the cantilever beam [45]. Lee and Saravanos [33] investigated the thermopiezoelectric response of composite beams using a coupled, layerwise (piecewise continuous approximations through the laminate thickness for the state variables) formulation and linear finite elements. Results demonstrate the capability to actively compensate thermal deflections with piezoceramic actuators; the corresponding sensory response of the composite beam was also studied. Blandford, et al. [18]

employed first-order shear deformation theory and a hierarchical finite element representation to investigate the static response of laminated beams to thermal and electric loads. The electric potential was assumed to vary piecewise linearly through each piezoelectric layer. Both uncoupled and coupled (direct piezoelectric effect included) formulations were developed. A comparison was made of results with the thermoelasticity solution of [50] for the hybrid laminate of Fig. 5 subject to a spatially varying electric potential applied to the top surface. Displacements calculated using the coupled theory differ from the uncoupled theory values by less than 1 percent when the piezoelectric layers are PVDF, and by 5 percent in the case of lead-zirconate-titanate (PZT) layers. Stresses obtained by the coupled theory were found to be approximately 8 percent greater than those found using the uncoupled formulation.

Tzou and Howard [56] developed a piezothermoelastic thin shell theory, and showed that the theory could be simplified for a variety of configurations, including a composite beam. Tzou and Ye [57] then studied the dynamic behavior and control of a steel beam sandwiched between two PZT layers. Birman et al. [17] considered delamination detection in thermoelastic composite beams having piezoelectric layers.

Laminated Plates

Analytical solutions to the coupled three-dimensional equations of piezothermoelasticity for laminated plates are given in Refs. [2,4,22,60]. Control of stationary [22] and transient [4] thermoelastic displacements of an infinite isotropic plate to which is bonded a piezoelectric ceramic layer was investigated by Choi, Ashida and Noda. The potential function method (equations (9)-(18)) was employed to determine a surface electric potential $V_0v(x,y,t)$ required to achieve a prescribed displacement $u_0g(x,y,t)$ when the structural layer is exposed to a surface temperature $T_0f(x,y,t)$. An extension to this work for the case of a structural plate with two piezoelectric layers (Fig. 6) was presented by Ashida [2]. Use of multiple rather than single piezoelectric layers for the control of thermally induced deformations has the advantage that much lower electric potential differences are needed. Xu et al. [60] developed three-dimensional solutions in Fourier series form for analyzing rectangular plates consisting of fiber-reinforced cross-ply and piezoelectric layers. Sensitivity coefficients were evaluated and used to study sensitivity of the responses to variations in different geometric and material parameters of the plate.

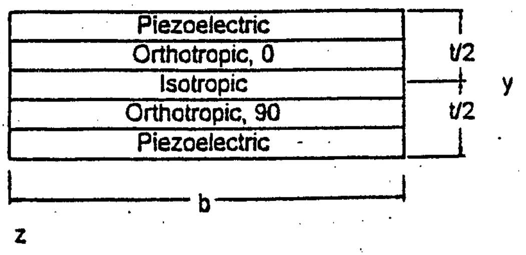

Fig. 5. Hybrid laminate [50].

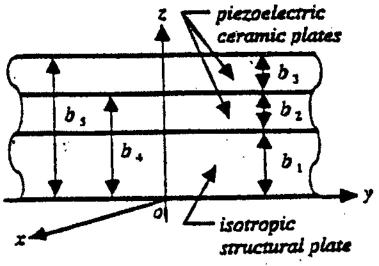

Fig. 6. Laminate configuration [2].

Two-dimensional plate formulations applied to piezothermoelastic laminates have included classical bending theory [48], first-order shear deformation theory [26], "equivalent-single-layer" high-order theories [27,62], layerwise theories [42,43], and predictor-corrector procedures [47]. Classical lamination theory was extended in [48] to include piezothermoelastic response of hybrid plates consisting of fiber-reinforced and piezoelectric materials. Solutions were obtained for a "free" plate of arbitrary contour and a simply supported rectangular plate, assuming in each case that the electric field induced by temperature and stress variations were negligibly small compared with applied electric loading. Noda and Kimura [37] utilized classical lamination theory, and investigated the importance of temperature/stress coupling in the equation of electrostatics. A comparison with Tauchert's solution [48] for a simply supported hybrid laminate indicated that the coupling may not be negligible. Jonnalagadda et al. [26] extended first-order shear deformation theory to include piezoelastic behavior, and obtained an analytic solution for a simply supported plate, and finite element results in the case of simply supported or fixed edge conditions. Third-order formulations that incorporate transverse normal and shear strains were applied to cross-ply and angle-ply plates having attached piezoelectric layers in Refs. [27] and [62], respectively. Inclusion of transverse and normal strain effects was found to be important in cases of electrically loaded thick plates.

Shen and Weng [44] employed a finite element formulation to study the effect of coupling between the strain and electric fields on deformation control of laminated composites. Sensor electrical outputs due to thermal loadings, as well as actuator voltages needed to reduce thermal deflections were analyzed. The results indicate that the larger the piezoelectric coefficient d_{31}, or the thinner the structural portion of the plate, the larger the coupling will be.

Lee and Saravanos [34,35] formulated a layerwise laminate theory to model both the active and sensory responses of piezoelectric composite plates. Results of their study demonstrate capabilities to achieve thermal shape control, and indicate the importance of temperature dependent nonlinearities on the displacement and stress distributions.

A comprehensive study assessing computational models for thermoelectroelastic multilayered plates was presented by Tang et al. [46]. Numerical results show that of the approaches considered (first-order, third-order and discrete layer theories, and predictor-corrector procedures), the predictor-corrector approach, in which first-order theory represents the predictor phase and the corrector phase modifies the functional dependence of the displacements on the thickness coordinate, provides the most accurate results.

Laminated Shells

A piezothermoelastic analysis of a circular cylindrical laminated shell subject to axisymmetric thermal or mechanical loading was presented by Chen and Shen [20]. Exact solutions were found using the power series expansion method. Both direct and inverse piezoelectric effects were considered. Numerical results for cross-ply laminates having attached piezoelectric layers demonstrated that certain commonly made assumptions (e.g., neglect of transverse normal and shear effects; the assumption of a linear variation of electric potential across a piezoelectric layer; etc.) are not always reasonable.

Xu and Noor [59] derived analytical three-dimensional solutions for the fully coupled thermoelectroelastic response of hybrid multilayered cylindrical shells. Sensitivity coefficients were employed to study the sensitivity of static shell response to variations in various shell parameters. Numerical results for graphite-epoxy/PZT laminates showed that the effects of the thickness ratios and locations of thermoelectroelastic layers on the shell response to thermomechanical and electric loads. The authors further derived three-dimensional solutions for free vibration problems of initially stressed laminated cylindrical shells [61]. Kapuria et al. [30] also presented three-dimensional solutions for simply supported cylindrical hybrid shells, including consideration of potential differences applied across piezoelectric layers. They also obtained exact solutions for a simply supported cross-ply cylindrical panel [32]. Feasibility of reducing thermal deflections and stresses by actuating a piezoelectric layer, and effectiveness of various actuating schemes for shape control, were also investigated.

A large-deformation piezothermoelastic thin shell theory was developed by Tzou and Bao [54]. Applications and simplifications of their generic theory to a laminated shell and other shell continua, e.g., shells of revolution, spherical shells, cylindrical shells, and conical shells, were demonstrated. They further considered a laminated cylindrical shell having distributed piezoelectric layers [55]. Their results for multi-field step and impulse responses showed that displacements induced by mechanical and temperature excitations are in-phase, and the electric induced displacement is out-of-phase; accordingly, electric excitation can be used to control thermomechanically induced excitations.

CONCLUDING REMARKS

Results from the investigations reviewed in this paper illustrate that thermal loads and resulting piezothermoelastic responses can be inferred from measurements of induced electric potential distributions in piezoelectric sensors. Likewise, through application of appropriate electric potentials to distributed piezoelectric actuators, thermal displacements and stresses can be controlled. The potential thus exists for forming high-strength, light-weight intelligent composite structural systems.

ACKNOWLEDGEMENT

This material is based upon work supported by the Division of International Programs of the National Science Foundation under Grant No. INT-9515326.

REFERENCES

1. Altay, G.A. and Dokmeci, M.C., Fundamental Variational Equations of Discontinuous Thermopiezoelectric Fields, *Int. J. Engineering Science*, vol.34, pp.769-782, 1996.

2. Ashida, F., Control of Thermally Induced Elastic Displacement of an Isotropic Plate Associated with Two Piezoelectric Ceramic Plates, *Proceedings of the Int. Conf. on Materials and Mechanics '97* (JSME), pp. 573-574, 1997.

3. Ashida, F., Choi, J.-S. and Noda, N., An Inverse Thermoelastic Problem in an Isotropic Plate Associated with a Piezoelectric Ceramic Plate, *J. Thermal Stresses*, vol. 19, pp.153-167, 1996.

4. Ashida, F. and Noda, N., Control of Transient Thermoelastic Displacement of an Isotropic Plate Associated with a Piezoelectric Plate, *J. Thermal Stresses*, vol. 20, pp. 407-427, 1997.

5. Ashida, F. A., Noda, N. and Tauchert, T. R., A Two-Dimensional Piezothermoelastic Problem in an Orthotropic Plate Exhibiting Crystal Class mm2, *JSME Int. J. -Series A*, vol. 37, pp. 334-340, 1994.

6. Ashida, F. A., Noda, N. and Tauchert, T. R., Inverse Problem of Two-Dimensional Piezothermoelasticity in an Orthotropic Plate Exhibiting Crystal Class mm2, *JSME Int. J. -Series A*, vol. 37, pp. 341-346, 1994.

7. Ashida, F. A., Noda, N. and Tauchert, T. R., Solution Method for Two-Dimensional Piezothermoelastic Problem of Orthotropic Solids, *Transactions of the Japan Society of Mechanical Engineers*, vol. 560, pp. 64-68, 1993.

8. Ashida, F. A. and Tauchert, T. R., An Inverse Problem for Determination of Transient Surface Temperature from Piezoelectric Sensor Measurement, *J. Applied Mechanics* (in press).

9. Ashida, F. A. and Tauchert, T. R., Temperature Determination for a Contacting Body Based on an Inverse Piezothermoelastic Problem, *Int. J. Solids and Structures*, vol. 34, pp.2549-2561, 1997.

10. Ashida, F. A. and Tauchert, T. R., Transient Response of a Piezothermoelastic Circular Disk Under Axisymmetric Heating, *Acta Mechanica*, vol. 128, pp.1-14, 1998.

11. Ashida, F.A. and Tauchert, T.R., A Finite Difference Scheme for Inverse Transient Piezothermoelasticity Problems, *J. Thermal Stresses* (forthcoming).

12. Ashida, F. A., Tauchert, T. R. and Noda, N., A General Solution Technique for Piezothermoelasticity of Hexagonal Solids of Class 6mm in Cartesian Coordinates, *Z. Angewandte Mathematik und Mechanik,* vol.74, pp.87-95, 1994.

13. Ashida, F. A., Tauchert, T. R. and Noda, N., Potential Function Method for Piezothermoelastic Problems of Solids of Crystal Class 6mm in Cylindrical Coordinates, J. *Thermal Stresses*, vol. 17, pp. 361-375, 1994.

14. Ashida, F. A., Tauchert, T. R. and Noda, N., Response of a Piezothermoelastic Plate of Crystal Class 6mm Subject to Axisymmetric Heating, *Int. J. Engineering Science*, vol.31, pp.373-384, 1993.

15. Bert, C.W. and Birman, V., Stress Dependency of the Thermoelastic and Piezoelectric Coefficients, *Analysis and Design Issues for Modern Aerospace Vehicles* – AD Vol. 55, ASME, pp.265-269, 1997.

16. Birman, V., Effect of Temperature on Accurate Interpretation of Data from Piezoelectric Sensors, *Proc. 10th ASCE Engineering Mechanics Conf.*, vol. 2, pp.762-765, 1995.

17. Birman, V., Saravanos, D. A. and Hopkins, D. A., Sensory Composite Beams for Delamination Detection in Thermal Environments, *Adaptive Structures and Composite Materials: Analysis and Application*, ASME AD45, pp.351-358, 1994.

18. Blandford, G. E., Tauchert, T. R. and Du, Y., Self-Strained Piezothermoelastic Composite Beam Analysis Using First-Order Shear Deformation Theory, submitted for publication.

19. Chandrasekharaiah, D.S., A Generalized Linear Theory for Piezoelectric Media, *Acta Mechanica*, vol. 71, pp. 39-49, 1988.

20. Chen, C.-Q. and Shen, Y.-P., Piezothermoelasticity Analysis for a Circular Cylindrical Shell under a State of Axisymmetric Deformation, *Int. J. Engineering Science*, vol.34, pp. 1585-1600, 1996.

21. Choi, J., Ashida, F. and Noda, N., Transient Piezothermoelasticity of a Hexagonal Plate of Class 6mm, *Archive of Applied Mechanics*, vol.65, pp.24-37, 1995.

22. Choi, J.-S., Ashida, F. and Noda, N., Control of Thermally Induced Elastic Displacement of an Isotropic Structural Plate Bonded to a Piezoelectric Ceramic Plate, *Acta Mechanica*, vol. 122, pp.49-63, 1997.

23. Dube, G.P., Kapuria, S. and Dumir, P.C., Exact Piezothermoelastic Solution of Simply-Supported Orthotropic Flat Panel in Cylindrical Bending, *Int. J. Mechanical Sciences*, vol. 38, pp.1161-1177, 1996.

24. Iesan, D., On Some Theorems in Piezothermoelectricity, *J. Thermal Stresses*, vol.12, pp.209-223, 1989.

25. Irschik, H., Belyaev, A.K., Krommer, M. and Schlacher, K., Non-Uniqueness of Two Inverse Problems of Thermally and Force-Loaded Smart Structures: Sensor Shaping and Actuator Shaping Problem, *Analysis and Design Issues for Modern Aerospace Vehicles* – AD Vol. 55, ASME, pp.119-131, 1997.

26. Jonnalagadda, K. D., Blandford, G. E. and Tauchert, T.R., Piezothermoelastic Composite Plate Analysis Using First-Order Shear Deformation Theory, *Computers and Structures*, vol.51, pp.79-89, 1994.

27. Jonnalagadda, K. D., Tauchert, T.R. and Blandford, G.E., High-Order Displacement Formulation for a Piezothermoelastic Laminate, *Mechanics of Electromagnetic Materials and Structures* - AMD Vol. 161, MD Vol. 42, ASME, pp.145-159, 1993.

28. Kalpakidis, V.K. and Massalas, C.V., Tiersten's Theory of Thermoelectroelasticity: An extension, *Int. J. Engineering Science*, vol.31, pp.157-164, 1993.

29. Kapuria, S., Dube, G.P., and Dumir, P.C., Exact Piezothermoelastic Solution for Simply Supported Laminated Flat Panel in Cylindrical Bending, *Z. Mathematik und Mechanik,* vol. 77, pp. 281-294, 1997.

30. Kapuria, S., Dumir, P.C., and Sengupta, S., Nonaxisymmetric Exact Piezothermoelastic Solution for Laminated Cylindrical Shell, *AIAA J.*, vol. 35, pp.1792-1795.

31. Kapuria, S., Dumir, P.C., and Sengupta, S., Exact Piezothermoelastic Axisymmetric Solution of a Finite Transversely Isotropic Cylindrical Shell, *Computers and Structures*, vol. 61, pp. 1085-1099, 1996.

32. Kapuria, S., Sengupta, S. and Dumir, P.C., Three-Dimensional Piezothermoelastic Solution for Shape Control of Cylindrical Panel., *J. Thermal Stresses*, vol. 20, pp.67-85, 1997.

33. Lee, H.-J., and Saravanos, D.A., Coupled Layerwise Analysis of Thermopiezoelectric Composite Beams, *AIAA J.*, vol.34, pp.1231-1237, 1996.

34. Lee, H.-J., and Saravanos, D.A., Generalized Finite Element Formulation for Smart Multilayered Thermal Piezoelectric Composite Plates, *Int. J. Solids and Structures*, vol. 34, pp. 3355-3371, 1997.

35. Lee, H.-J., and Saravanos, D.A., Thermal Shape Control of Active and Sensory Piezoelectric Composite Plates, *Analysis and Design Issues for Modern Aerospace Vehicles* – AD Vol. 55, ASME, pp.249-257, 1997.

36. Mindlin, R.D., Equations of High Frequency Vibrations of Thermopiezoelectric Crystal Plates, *Int. J. Solids and Structures*, vol. 10, pp. 625-637, 1974.

37. Noda, N. and Kimura, S., Deformation of Piezothermoelastic Composite Plate Considering Coupling Effect, *Proceedings of the Int. Conf. on Materials and Mechanics '97* (JSME), pp. 571-572, 1997.

38. Nowacki, J.P., Steady-State Problems of Thermopiezoelectricity, *J. Thermal Stresses*, vol. 5, pp. 183-194, 1982.

39. Nowacki, W., Some General Theorems of Thermopiezoelectricity, *J. Thermal Stresses*, vol. 1, pp.171-182, 1978.

40. Nowacki, W.,Thermoelasticity of Anisotropic and Piezoelectric Bodies, Ch.5, *Dynamic Problems of Thermoelasticity*, Noordhoff, 1975.

41. Rao, S.S., and Sunar, M., Analysis of Distributed Thermopiezoelectric Sensors and Actuators in Advanced Intelligent Structures, *AIAA J.*, vol. 31, pp.1280-1286,1993.

42. Reddy, J.N., and Mitchell, J.A., On Refined Nonlinear Theories of Laminated Composite Structures with Piezoelectric Laminae, *SADHANA (J.Indian Academy of Sciences)*, 1994.

43. Reddy, J.N., Refined Theories and Computational Procedures for the Modelling of Smart Composite Structures, *Composite Science and Technology* (Proceedings of the First International Conference on Composite Science and Technology), pp.421-429, 1996.

44. Shen, Y.C., and Weng, C.I., Deformation Control of Laminated Composite Plate Containing Piezoelectric Layers Under Thermal Loading, *J. Thermal Stresses*, vol.18, pp.449-464, 1995.

45. Sunar, M. and Rao, S.S., Thermopiezoelectric Control Design and Actuator Placement, *AIAA J.*, vol.35, pp.534-539, 1997.

46. Tang, Y. Y., Noor, A. K. and Xu, K., Assessment of Computational Models for Thermoelectroelastic Multilayered Plates, *Computers and Structures*, vol. 61, pp.915-933, 1996.

47. Tang, Y. Y and Xu, K., Dynamic Analysis of a Piezothermoelastic Laminated Plate, *J. Thermal Stresses*, vol.18, pp. 87-104, 1995.

48. Tauchert, T.R., Piezothermoelastic Behavior of a Laminated Plate, *J. Thetmal Stresses*, vol.15, pp.25-37, 1992.

49. Tauchert, T.R., Cylindrical Bending of Hybrid Laminates Under Thermo-Electro-Mechanical Loading, *J. Thermal Stresses*, vol.19, pp.287-296, 1996.

50. Tauchert, T.R., Plane Piezothermoelastic Response of a Hybrid Laminate – A Benchmark Problem, *Composite Structures* (in press) .

51. Tauchert, T.R., Adali, S., Verijenko, V.E. and Richter, A.A., Minimum Deflection Design of Piezothermoelastic Laminated Composite Plates, *Analysis and Design Issues for Modern Aerospace Vehicles* – AD Vol. 55, ASME, pp.259-264, 1997.

52. Tauchert, T.R., Ashida, F. and Noda, N., Recent Developments in Piezothermoelasticity: Inverse Problems Relevant to Smart Structures, *Proceedings of the Int. Conf. on Materials and Mechanics '97* (JSME), pp.3-8, 1997.

53. Tiersten, H.F., On the Nonlinear Equations of Thermoelectroelasticity, *Int. J. Engineering Science*, vol. 9, pp. 587-604, 1971.

54. Tzou, H.S. and Bao, Y., Nonlinear Piezothermoelasticity and Multi-Field Actuations, Part 1: Nonlinear Anisotropic Piezothermoelastic Shell Laminates, *J. Vibration and Acoustics*, vol. 119, pp.374-381, 1997.

55. Tzou, H.S. and Bao, Y., Spatially Filtered Multi-Field Responses of Piezothermoelastic Cylindrical Shell Composites, *J. Structural Engineering and Mechanics*, vol. 4, 1996.

56. Tzou, H.S. and Howard, R.V., A Piezothermoelastic Thin Shell Theory Applied to Active Structures, *J. Vibration and Acoustics*, vol. 116, pp.295-302, 1994.

57. Tzou, H.S. and Ye, R., Piezothermoelasticity and Precision Control of Piezoelectric Systems: Theory and Finite Element Analysis, *J. Vibration and Acoustics*, vol. 116, pp. 489-495, 1994.

58. Tzou, H.S. and Zhou, Y.H., Nonlinear Piezothermoelasticity and Multi-Field Actuations, Part 2: Control of Nonlinear Deflection, Buckling and Dynamics, *J. Vibration and Acoustics*, vol. 119, pp.382-389, 1997.

59. Xu, K., and Noor, A.K., Three-Dimensional Analytical Solutions for Coupled Thermoelectroelastic Response of Multilayered Cylindrical Shells, *AIAA J*, vol. 34, pp. 802-812, 1996.

60. Xu, K., Noor, A.K. and Tang, Y.Y., Three-Dimensional Solutions for Coupled Thermoelectroelastic Response of Multilayered Plates, *Computer Methods in Applied Mechanics and Engineering,* vol.126, pp.355-371, 1995.

61. Xu,K., Noor, A.K. and Burton, W.S., 3D Solutions for Free Vibration of Initially Stressed Thermoelectroelastic Multilayered Cylinders, *J. Engineering Mechanics*, vol. 123, pp.45-51, 1997.

62. Xu, Y., Tauchert, T.R. and Blandford, G.E., Piezothermoelastic Analysis of an Antisymmetric, Angle-Ply Laminate Using a High-Order Displacement Formulation, *Composite Materials and Structures* - AD Vol.37, AMD Vol. 179, ASME, pp.89-102, 1993.

63. Yang, X. X., Shen, S. and Kuang, Z.B., The Degenerate Solution for Piezothermoelastic Materials, *European J. of Mechanics A – Solids*, vol. 16, pp. 779-793, 1997.

MODERN CONCEPTIONS OF PLATE THEORY

V. V. VASILIEV

Department of Mechanics and Optimization of Processes and Structures
Moscow State University of Aviation Technology
Moscow 103767, Russia

INTRODUCTION

The classical plate theory traditionally called Kirchhoff theory (K-theory) was developed from 1811 to 1883 by S. Germain, J.L. Lagrange, S.D. Poisson, A.Navier, G.R. Kirchhoff, M.J. Bousinesq, M. Lévy, W. Thomson and P.G. Tait. Historical treatises [1, 2, 3] conclude that the main contribution to the plate theory was that of Poisson, Kirchhoff, Thomson and Tait. Brief discussion of the corresponding results is given below.

Decomposing stresses and displacements into power series with respect to the thickness coordinate Poisson was the first to derive the modern form of the plate theory equations (Lagrange was the first to write the biharmonic equation of the plate theory but his derivation is not known). Poisson [4] had formulated the boundary problem of the plate theory which included three boundary conditions at the boundary points while the governing equation, being of the fourth order, required only two conditions. This inconsistency was criticized by Kirchhoff [5] who developed the plate theory using variational approach and a system of physical assumptions which were the generalization of Bernoulli-Euler beam theory assumptions. Kirchhoff variational equation was the same that was derived directly by Poisson but it was accompanied with two natural force boundary conditions. One of them specifies bending moment M_n at the plate edge and the other one is associated now with the so-called generalized transverse shear force which is a combination of an actual transverse shear force Q_n and a derivative of a twisting moment M_{ns} along the boundary contour, i.e.

$$V_n = Q_n + \frac{\partial M_{ns}}{\partial s}. \tag{1}$$

Here, n is a normal to the boundary contour and s is a contour coordinate. Kirchhoff did not discuss the physical meaning of the boundary conditions and a problem of "reconciliation" of Poisson and Kirchhoff plate theories appeared later in the theory of elasticity. This problem was resolved by Thomson and Tait [6] who had constructed a generalized transverse shear force (1) using static transformation that, in general, was valid only for an absolutely rigid body. For an elastic plate, a moment effect is different from that of a force, and, as shown below, Kirchhoff boundary condition, being mathematically exact, is a formal result reflecting physical inconsistency of the K-theory assumptions. The fact that the generalized transverse shear force V_n does not represent completely Q_n and M_{ns} acting at a plate edge was cleared out in the nineteenth century. Lévy, Boussinesq, Thomson and Tait formulated a three-dimensional elasticity problem for a plate loaded at the edge with self-balanced nonzero force Q_n and moment M_{ns} such that $V_n = 0$. Solution of this problem has shown that such loading induces a specific stress state of the plate corresponding to the edge twisting which rapidly vanishes within a short distance from the edge. Modern interpretation of this approach was developed by Donnell [7]. Lévy was the first who introduced the idea to supplement the K-theory with the second-order equation describing the boundary layer stress state [8], but this idea was not supported [9, 10, 11] probably because the K-theory was a two-dimensional theory, while Lévy equation included derivatives with respect to all three coordinates. Instead of this, Saint-Venant principle was used to justify possibility of neglecting Lévy equation and the corresponding stressed state. However, Saint-Venant principle is only an intuitive statement that allows us to simplify boundary conditions ignoring self balanced local loads. As known, there exist problems to which it cannot be applied, and the plate problem is one of them.

Thus, the K-theory has become the classical plate theory, being successfully used to solve engineering problems for more than a century. Though the study of plates with the aid of three-dimensional elasticity equations never stopped [12], the next significant result in the plate theory was obtained by E. Reissner [13] who derived a set of two governing equations one of which was of the fourth order like the equation of the K-theory, while the second was of the second order and actually represented the two-dimensional version of Lévy equation. Thus, a sixth order Reissner plate theory (R-theory) has been developed. This theory allows us to formulate three independent force boundary conditions at the plate edge for bending moment M_n, transverse force Q_n, and twisting moment M_{ns} and Poisson-Kirchhoff paradox disappears. To evaluate Reissner's contribution to the plate theory, it is very important to emphasize that he was the first to show that in order to construct a sixth order plate theory, we actually need to supplement the existing fourth order equation for the plate deflection with an independent second order boundary layer equation. By now attempts are undertaken to derive a sixth order equation for the plate deflection, e.g. [11]

$$D\Delta\Delta W - C\Delta\Delta\Delta W = p. \tag{2}$$

Such an equation cannot exist in the plate theory under consideration (we discuss here only theories that represent the plate stresses in terms of through-the-thickness stress resultants and couples and ignore self-balanced stresses). Indeed, if we write eq.(2) for a beam, we arrive at the sixth order ordinary differential equation for the beam deflection that requires three force boundary conditions at the beam end, while the beam stress state is determined by two static factors only, i.e., by a bending moment and by a transverse shear force. Thus, the shear deformable beam theory is described by the fourth order equation and is entirely different from the corresponding plate theory which has an additional second order boundary layer equation. This actually means that the R-theory is not a generalization of Timoshenko beam theory [14] and should not be called "Timoshenko-type plate theory" as it is done in many publications. In general, association of the R-theory with a shear deformable beam theory based on the fact that both theories allow for transverse shear deformation is a common misunderstanding of the R-theory. Indeed, we can study transverse bending of a beam taking into account shear deformation or ignoring it, and in both cases this study can be consistent. However, in contrast to beams, plates under transverse loading experience not only bending but also torsion which cannot exist without transverse shear deformation. Ignoring this deformation we arrive, as shown further, at physically inconsistent plate theory. Thus, allowance for shear deformation is not optional for the plate theory, but follows from some consistency conditions that are not satisfied in the K-theory [15]. Another common misunderstanding of the R-theory according to which there exist several theories of such a type (e.g. Reissner theory, Mindlin theory and etc.), is caused by the method with the aid of which the R-theory was originally constructed [13]. To discuss this important problem, consider a plate shown in Fig.1.

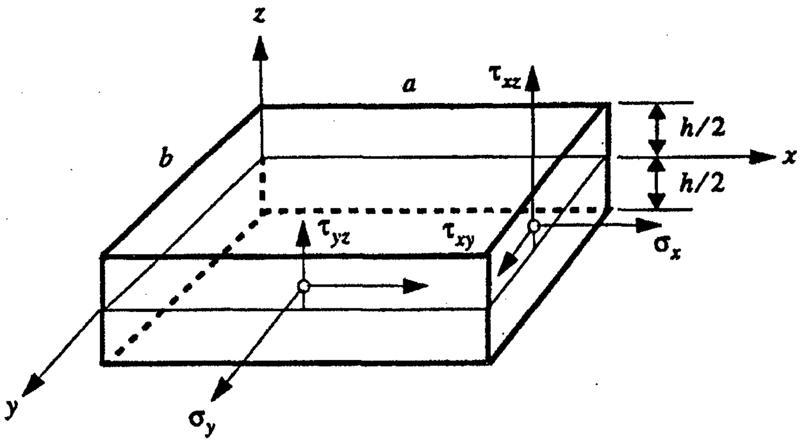

Figure 1. Stresses acting in the plate.

In contrast to traditional displacement formulation of the plate theory [12], Reissner used rather cumbersome stress formulation involving variational principle of minimum complementary energy and the following stress approximation with respect to the z-coordinate.

$$\sigma_x = z\,\frac{12}{h^3}\,M_x(x,y) \qquad \sigma_y = z\,\frac{12}{h^3}\,M_y(x,y) \qquad \tau_{xy} = z\,\frac{12}{h^3}\,M_{xy}(x,y) \tag{3}$$

$$\tau_{xz} = \frac{3}{2h}\left(1-\frac{4z^2}{h^2}\right)Q_x(x,y) \qquad \tau_{yz} = \frac{3}{2h}\left(1-\frac{4z^2}{h^2}\right)Q_y(x,y). \tag{4}$$

Here M_x, M_y and M_{xy} are bending and twisting moments and Q_x, Q_y are transverse shear forces acting in the plate. It should be noted that stresses (3) and (4) actually follow from the K-theory. In conjunction with equilibrium equations of this theory, i.e.

$$\frac{\partial M_x}{\partial x}+\frac{\partial M_{xy}}{\partial y}-Q_x=0 \qquad \frac{\partial M_y}{\partial y}+\frac{\partial M_{xy}}{\partial x}-Q_y=0 \tag{5}$$

$$\frac{\partial Q_x}{\partial x}+\frac{\partial Q_y}{\partial y}+p=0, \tag{6}$$

these stresses satisfy three-dimensional equilibrium equations of the elasticity theory and boundary conditions on the plate surfaces (see Fig.1), i.e.

$$\tau_{xz}\left(z=\pm\frac{h}{2}\right)=0 \qquad \tau_{yz}\left(z=\pm\frac{h}{2}\right)=0. \tag{7}$$

Displacement field corresponding to stresses (3) and coordinates shown in Fig.1 is as follows

$$u_x=z\theta_x(x,y) \qquad u_y=z\theta_y(x,y) \qquad u_z=w(x,y), \tag{8}$$

where w is the plate deflection and θ_x, θ_y are rotations of the plate element in xz and yz planes. Displacement approximation (8) was originally proposed by Hencky [16] who, following Kirchhoff, applied variational principle of minimum total potential energy to derive equations for θ_x, θ_y, and w. This approach was developed and enhanced by Bollé [9], Uflyand [17], Green [18], Mindlin [19] and many other authors of refined plate theories allowing for transverse shear deformation of the plate. However, Reissner in his numerous publications devoted to the R-theory did not use displacement formulation because of possible loss of accuracy associated with this approach [20]. Indeed, consider strain-displacement equations

$$e_x=\frac{\partial u_x}{\partial x} \qquad e_y=\frac{\partial u_y}{\partial y} \qquad e_{xy}=\frac{\partial u_x}{\partial y}+\frac{\partial u_y}{\partial x} \tag{9}$$

$$e_{xz}=\frac{\partial u_x}{\partial z}+\frac{\partial u_z}{\partial x} \qquad e_{yz}=\frac{\partial u_y}{\partial z}+\frac{\partial u_z}{\partial y} \tag{10}$$

and the Hooke's law for an isotropic plate

$$\sigma_x=\bar{E}(e_x+\nu e_y) \qquad \sigma_y=\bar{E}(e_y+\nu e_x) \qquad \tau_{xy}=Ge_{xy} \tag{11}$$

$$\tau_{xz} = Ge_{xz} \qquad \tau_{yz} = Ge_{yz}, \tag{12}$$

where

$$\bar{E} = \frac{E}{1-\nu^2} \qquad G = \frac{E}{2(1+\nu)}.$$

Substitution of displacements (8) into eqs. (9), (10) and then into eqs. (11), (12) yields

$$\begin{gathered} \sigma_x = z\bar{E}\left(\frac{\partial \theta_x}{\partial x} + \nu\frac{\partial \theta_y}{\partial y}\right) \qquad \sigma_y = z\bar{E}\left(\frac{\partial \theta_y}{\partial y} + \nu\frac{\partial \theta_x}{\partial x}\right) \\ \tau_{xy} = zG\left(\frac{\partial \theta_x}{\partial y} + \frac{\partial \theta_y}{\partial x}\right) \end{gathered} \tag{13}$$

$$\tau_{xz} = G\left(\theta_x + \frac{\partial w}{\partial x}\right) \qquad \tau_{yz} = G\left(\theta_y + \frac{\partial w}{\partial y}\right). \tag{14}$$

Comparing eqs.(3) and (13) we can see that for both stress and displacement formulations distribution of in-plane stresses through the plate thickness is linear. However, expressions (4) and (14) for transverse shear stresses are different. Displacement formulation yields stresses that do not depend on z and do not satisfy boundary conditions (7). In aforementioned publications devoted to displacement formulation of the plate theory, this inconsistency was either ignored or camouflaged with the aid of average through-the-thickness displacements, transverse shear strains, or strain energy. But irrespective of a particular derivation, final equations are in their essentials the same that follow from the R-theory. The difference is associated with different forms of the so-called shear correction factor which, as is shown later, should not exist in the plate theory under discussion. Based on foregoing discussion, one of the main objectives of this study is to demonstrate that the R-theory can be constructed using displacement formulation in a consistent and straightforward manner as simply as the K-theory is traditionally derived. From this derivation it should follow that the plate theories based on approximations (3), (4) or (8) are actually versions of one and the same theory which is the modern form of the classical plate theory.

EQUATIONS OF THE PLATE THEORY

Consider again a plate show in Fig.1. To construct an applied plate theory, we introduce a Basic Plate Element (BPE). This element is orthogonal to the plate mid-plane, its length is equal to the plate thickness h and its dimensions in the x

and the y directions are infinitely small. The theory that is considered below is based on the following two physical assumptions following from the fact that the plate thickness is relatively small.

1. Under plate bending the BPE (i) does not experience deformation in the z-direction ($e_z = 0$) and (ii) remains rectilinear and rotates at angles θ_x and θ_y in the xz and yz-planes, respectively.
2. Normal stress σ_z is negligible in comparison with stresses σ_x and σ_y.

These assumptions are not discussed here because they practically coincide with traditional assumptions of the K-theory that can be found in many textbooks. The only difference is that the BPE is not required to be orthogonal to the deformed mid-plane of the plate. Such a modification of the K-theory assumptions was proposed by Bollé [9] who introduced shear correction into rotation of BPE. It should also be noted that assumptions 1(i) and 2 can be formally avoided if we simulate the plate material with some orthotropic material having infinitely high stiffness in the z-direction. This interpretation was proposed in the plate theory by Kromm [21], but is not used here because we are aiming at the traditional straightforward derivation of the plate theory equations given in the textbooks.

Using the foregoing assumptions and traditional procedure of the K-theory we arrive at displacement field (8) and constitutive equations (11) which can be reduced to eqs.(13). Because stresses (13) are linear functions of z, they are statically equivalent to moments.

$$M_x = \int_{-h/2}^{h/2} \sigma_x z\, dz \qquad M_y = \int_{-h/2}^{h/2} \sigma_y z\, dz \qquad M_{xy} = \int_{-h/2}^{h/2} \tau_{xy} z\, dz. \tag{15}$$

Substituting stresses (13) into these equations we arrive at constitutive equations of the plate theory, i.e.

$$M_x = D(\kappa_x + \nu\kappa_y) \qquad M_y = D(\kappa_y + \nu\kappa_x)$$

$$M_{xy} = \frac{1}{2} D(1-\nu)\kappa_{xy}$$

where

$$\kappa_x = \frac{\partial\theta_x}{\partial x} \qquad \kappa_y = \frac{\partial\theta_y}{\partial y} \qquad \kappa_{xy} = \frac{\partial\theta_x}{\partial y} + \frac{\partial\theta_y}{\partial x} \tag{16}$$

are rates of BPE rotations and $D = Eh^3/[12(1-\nu^2)]$ is the plate bending stiffness.

Now consider transverse shear stresses τ_{xz} and τ_{yz} specified by Eqs.(12) and (10). Their particular form (14) that does not allow us to satisfy boundary conditions

(7) is a result of nonproper transformation. First, it should be taken into account that eqs.(8) specify approximate dependence of displacements on z. Second, in general, approximate expressions cannot be differentiated. Thus, substitution of eqs.(8) into eqs.(10) requiring differentiation with respect to z is not consistent and cannot be performed. Moreover, it is not necessary to perform it because we do not need to know τ_{xz} and τ_{yz} to construct the plate theory. Indeed, as follows from the first of the foregoing assumptions, BPE is absolutely rigid in the z-direction. So, according to the well known theorem of statics, the BPE motion does not depend on distribution of τ_{xz} and τ_{yz} along its length (plate thickness). The plate deflection depends only on resultant forces

$$Q_x = \int_{-h/2}^{h/2} \tau_{xz}\, dz \qquad Q_y = \int_{-h/2}^{h/2} \tau_{yz}\, dz. \tag{17}$$

Particularly, this means that the behavior of the plate whose displacements correspond to eqs. (8) does not depend on τ_{xz} and τ_{yz} distribution through the plate thickness. So, no shear correction factor which is traditionally used to take into account this dependence should exist in the plate theory under consideration.

Thus, instead of differentiating the displacements (8) we should perform integration. In conjunction with eqs.(8), (10), and (12), the first expression in eqs.(17) yields

$$Q_x = G\int_{-h/2}^{h/2}\left(\frac{\partial u_x}{\partial z}+\frac{\partial u_z}{\partial x}\right)dz = G\left[u_x\left(\frac{h}{2}\right)-u_x\left(-\frac{h}{2}\right)+\int_{-h/2}^{h/2}\frac{\partial u_z}{\partial x}\,dz\right] = Gh\left(\theta_x+\frac{\partial w}{\partial x}\right).$$

Then, we arrive at the following constitutive equations for transverse shear forces:

$$Q_x = C\left(\theta_x + \frac{\partial w}{\partial x}\right) \qquad Q_y = C\left(\theta_y + \frac{\partial w}{\partial y}\right), \tag{18}$$

where $C = Gh$ is the plate transverse shear stiffness.

Proceeding to construct the plate theory we should use equilibrium equations (5) and (6) of the K-theory and substitute moments and forces from constitutive equations (15) and (18). To derive the first equation, substitute forces Q_x and Q_y from eqs.(5) into eq.(6) to get

$$\frac{\partial^2 M_x}{\partial x^2} + 2\frac{\partial^2 M_{xy}}{\partial x \partial y} + \frac{\partial^2 M_y}{\partial y^2} + p = 0. \tag{19}$$

Expressing moments in terms of rotations with the aid of eqs.(15) and (16) we can reduce eq.(19) to the following form:

$$D\Delta\left(\frac{\partial\theta_x}{\partial x}+\frac{\partial\theta_y}{\partial y}\right)+p=0, \tag{20}$$

where

$$\Delta(\ )=\frac{\partial^2(\ )}{\partial x^2}+\frac{\partial^2(\ )}{\partial y^2}$$

Equation (20) allows us to introduce a potential function $\varphi(x,y)$ such that

$$\theta_x=-\frac{\partial\varphi}{\partial x}\qquad \theta_y=-\frac{\partial\varphi}{\partial y}. \tag{21}$$

Then, eq.(20) acquires its final form

$$D\Delta\Delta\varphi=p. \tag{22}$$

Consider now eqs.(5). Substituting moments and forces from eqs.(15) and (18) and taking into account eqs.(16) and (21) we arrive at

$$\frac{\partial F_\varphi}{\partial x}=0\qquad \frac{\partial F_\varphi}{\partial y}=0, \tag{23}$$

where

$$F_\varphi=\bar{D}\Delta\varphi-\varphi+w$$

and, $\bar{D}=D/C$. As follows from eqs.(23), $F_\varphi=$ constant, and since we need only derivatives of φ in eqs.(21), the constant can be included in φ. As a result, we get $F_\varphi=0$ or

$$w=\varphi-\bar{D}\Delta\varphi. \tag{24}$$

It looks like the theory is reduced to a fourth order equation (22). However, the theory has one more equation. Indeed, expressing θ_x and θ_y in terms of function φ we actually restrict a plate displacement field to a potential field with zero rotation in the xy plane, i.e.

$$\omega_z=\frac{1}{2}\left(\frac{\partial u_x}{\partial y}-\frac{\partial u_y}{\partial x}\right)=0. \tag{25}$$

This condition can be readily checked if we use eqs.(8) for displacements and eqs.(21) for rotations.

As follows from eq. (20), its homogeneous form ($p = 0$) has another solution, i.e.

$$\theta_x = \frac{\partial \psi}{\partial y} \qquad \theta_y = -\frac{\partial \psi}{\partial x}, \tag{26}$$

where $\psi(x, y)$ is a rotational potential or a stream function [22] specifying rotation in the xy plane. Indeed, using eqs.(8) for displacements and eqs.(26) for rotations we find from eq.(25).

$$\omega_z = z\,\frac{\partial^2 \psi}{\partial x\,\partial y}. \tag{27}$$

Rotation field (26), (27) corresponds to $p = 0$, which means that it can be induced only by forces and moments acting at the plate edges. If we repeat the derivation of eqs.(23) using eqs.(26) instead of eqs.(21), we arrive at

$$\frac{\partial F_\psi}{\partial x} = 0 \qquad \frac{\partial F_\psi}{\partial y} = 0$$

where

$$F_\psi = \Delta\psi - s^2\psi \qquad s^2 = \frac{2C}{D(1-\nu)}. \tag{28}$$

Resulting equation is derived in the same manner as eq.(24) and has the form

$$\Delta\psi - s^2\psi = 0. \tag{29}$$

Because the problem under consideration is linear, superposition of potentials yields the following general solution for eq.(20):

$$\theta_x = -\frac{\partial \varphi}{\partial x} + \frac{\partial \psi}{\partial y} \qquad \theta_y = -\frac{\partial \varphi}{\partial y} + \frac{\partial \psi}{\partial x}, \tag{30}$$

where potentials φ and ψ are the solutions of eqs.(22) and (29), respectively. The plate deflection is specified by eq.(24). Using eqs.(15), (16), (18), (24), and (30) we can write moments and forces in terms of potentials as

$$M_x = -D\left[\frac{\partial^2\varphi}{\partial x^2} + \nu\,\frac{\partial^2\varphi}{\partial y^2} - (1-\nu)\,\frac{\partial^2\psi}{\partial x\,\partial y}\right]$$

$$M_y = -D\left[\frac{\partial^2\varphi}{\partial y^2} + \nu\,\frac{\partial^2\varphi}{\partial x^2} + (1-\nu)\,\frac{\partial^2\psi}{\partial x\,\partial y}\right]$$

$$M_{xy} = -D\left[(1-\nu)\,\frac{\partial^2\varphi}{\partial x\,\partial y} + \frac{1}{2}\left(\frac{\partial^2\psi}{\partial x^2} - \frac{\partial^2\psi}{\partial y^2}\right)\right] \qquad (31)$$

$$Q_x = C\,\frac{\partial\psi}{\partial y} - D\,\frac{\partial}{\partial x}\,\Delta\varphi$$

$$Q_y = C\,\frac{\partial\psi}{\partial x} - D\,\frac{\partial}{\partial y}\,\Delta\varphi$$

Knowing moments and forces we can find stresses. The resulting expressions for stresses are, naturally, the same as those of the K-theory, and are specified by Eqs.(3) and (4). Equations of the K-theory formally follow from the foregoing equations if we assume that transverse shear stiffness C is infinitely high (in the limit, $C \longrightarrow \infty$) or $\bar{D} = 0$. The principle consequences of such transformation follow from eqs.(22), (24), (29), and (30) yielding

$$\psi = 0 \qquad \varphi = w \qquad \theta_x = -\frac{\partial w}{\partial x} \qquad \theta_y = -\frac{\partial w}{\partial y} \qquad D\Delta\Delta w = p. \qquad (32)$$

In conjunction with eqs. (8) this means that the K-theory restricts the plate displacements to a very particular and specific case. In-plane displacements u_x and u_y form a potential displacement field (without rotation), and the potential function is the plate deflection. As shown further, this is the actual reason because of which the K-theory is not consistent.

CONSISTENCY AND BOUNDARY CONDITIONS

Consistency of the boundary problem is an important (but not always necessary for applications) feature of a plate or shell theory constructed by reduction of three-dimensional elasticity theory equations to two-dimensional equations. Because a unique and conventional criterion of consistency does not exist, we use the following two conditions to evaluate the consistency of a plate theory formulated in terms of displacements [15].

1. Boundary conditions of a consistent theory should correspond to the order of the governing equations and, within the framework of the theory assumptions,

should provide zero stresses at the free edge and zero displacements at the fixed edge of the plate.

2. Equations derived by direct consideration of equilibrium and deformation of a plate element should provide stationarity of the corresponding two-dimensional total potential energy functional (Lagrange functional), and stationarity condition of this functional should provide equilibrium of a plate element as a solid.

As shown below, the sixth order theory described in the previous section satisfies both consistency conditions, while the K-theory (as well as the majority of nonclassical plate theories constructed by now) does not satisfy them.

Starting with the first consistency condition consider typical boundary conditions for a plate described by the sixth order theory and the fourth order K-theory. For the sake of brevity, boundary conditions are written only for the edge x = constant of a plate shown in Fig.1 (commutation rule can be used to write the corresponding conditions for the edge y = constant).

Let the plate edge be fixed (clamped or built in). According to the consistency condition, we have for this edge $u_x = 0,\ u_y = 0,\ u_z = 0$. Then, eqs.(8) and (32) yield conditions $\theta_x = 0,\ \theta_y = 0,\ w = 0$ for the sixth order theory and $w = 0,\ \partial w/\partial x = 0$ for the K-theory. These conditions correspond to the orders of equations for both theories.

For a plate with free edge, we get $\sigma_x = 0,\ \tau_{xy} = 0,\ \tau_{xz} = 0$, and eqs.(3), (4) give $M_x = 0,\ M_{xy} = 0,\ Q_x = 0$ for the sixth order theory. After some transformation with the aid of eqs.(31) and (29), these conditions can be presented in the following form [23]:

$$\frac{\partial^2 \varphi}{\partial x^2} + \nu \frac{\partial^2 \varphi}{\partial y^2} - (1-\nu) \frac{\partial^2 \psi}{\partial x\, \partial y} = 0 \tag{33}$$

$$\frac{\partial}{\partial x} \left[\frac{\partial^2 \varphi}{\partial x^2} + (2-\nu) \frac{\partial^2 \varphi}{\partial y^2} - \bar{D}(1-\nu) \frac{\partial^2}{\partial y^2} \Delta \varphi \right] = 0 \tag{34}$$

$$\bar{D} \frac{\partial}{\partial x} \Delta \varphi - \frac{\partial \psi}{\partial y} = 0. \tag{35}$$

For the K-theory, we should take $\varphi = w,\ \psi = 0$, and $\bar{D} = 0$ in these conditions. Then eq.(35) disappears and eqs.(33) and (34) yield the well known two boundary conditions of the K-theory [12]

$$\frac{\partial^2 w}{\partial x^2} + \nu \frac{\partial^2 w}{\partial y^2} = 0 \qquad \frac{\partial^3 w}{\partial x^3} + (2-\nu) \frac{\partial^3 w}{\partial x\, \partial y^2} = 0. \tag{36}$$

It should be emphasized that the second of these conditions corresponding to the generalized transverse shear force (1) is derived here without variational calculus used by Kirchhoff and without static transformation used by Thomson and Tait. It should also be noted that conditions (36) do not provide zero shear stresses at the free edge of a plate (only some combination of τ_{xy} and τ_{xz} is zero). So, the K-theory does not satisfy the first consistency condition formulated above.

Consider a classical simply supported plate with the following boundary conditions:

$$w = 0 \qquad \theta_y = 0 \qquad M_x = 0. \tag{37}$$

After some transformation [23] we can write them as

$$\varphi = 0 \qquad \frac{\partial^2 \varphi}{\partial x^2} = 0 \qquad \frac{\partial \psi}{\partial x} = 0. \tag{38}$$

For the edge $y = \text{const}$ (see Fig.1), the conditions under study have the form

$$\varphi = 0 \qquad \frac{\partial^2 \varphi}{\partial y^2} = 0 \qquad \frac{\partial \psi}{\partial y} = 0. \tag{39}$$

As can be shown [23], eq.(29) with boundary conditions (38) and (39) for ψ has only trivial solution $\psi = 0$. Thus, for a plate with simply supported edges, the sixth order theory yields the following boundary problem:

$$D\Delta\Delta\varphi = p \qquad \varphi_b = 0 \qquad \Delta\varphi_b = 0, \tag{40}$$

where φ_b corresponds to the boundary. Boundary conditions (37) imply that the plate is supported by boundary walls (diaphragms) that have infinitely high membrane stiffness and zero bending stiffness. Within the framework of the sixth order theory, there exists another set of boundary conditions for a simply supported plate, i.e.

$$w = 0 \qquad M_{xy} = 0 \qquad M_x = 0. \tag{41}$$

These conditions correspond to a plate with free edges resting on supports. Boundary problem with conditions (41) was studied by Kromm [21] and Donnell [7].

Now consider the second of the foregoing consistency conditions. The total potential energy of a plate loaded with normal pressure p can be written as

$$T=\iint\left\{\frac{1}{2}\left[M_x\kappa_x+M_y\kappa_y+M_{xy}\kappa_{xy}+Q_x\left(\theta_x+\frac{\partial w}{\partial x}\right)+Q_y\left(\theta_y+\frac{\partial w}{\partial y}\right)\right]-pw\right\}dx\,dy. \tag{42}$$

Stationarity condition $\delta T = 0$ provides equilibrium equations for a plate element and a set of natural boundary conditions. For the sixth order theory, variation with respect to θ_x, θ_y, and w yields all three classical equilibrium equations (5) and (6) and the associated boundary conditions discussed above. Thus, the consistency condition is satisfied. For the K-theory, on the other hand, θ_x and θ_y should be expressed in terms of w with the aid of eqs.(32), and we have only one kinematic variable, w. Variation with respect to w yields eq.(19) which is not an equilibrium equation. Equation (19) is only the result of a formal combination of the equilibrium equations. It should be emphasized that within the framework of the variational approach, eq.(19) appears irrespective of the equilibrium equations (5) and (6) and has no physical meaning.

Thus, the K-theory does not satisfy the consistency conditions. The reason for this is associated with eqs.(32) for θ_x and θ_y. Indeed, in the case of bending, the plate element as a solid has three degrees of freedom — two rotations, θ_x and θ_y and one displacement, w. Variational equations provide equilibrium of this element as a solid only if these kinematic variables are mutually independent which is not the case for the K-theory. This theory is based on physically inconsistent approximation of the plate displacement field which results in violation of equilibrium conditions for any problem of transverse bending to which the theory is applied.

EXAMPLES

As the first example demonstrating the difference between the sixth order theory and the K-theory, consider the most widely known problem of bending of a simply supported rectangular plate loaded with uniform pressure p. Boundary problem in eqs.(40) has a well known Navier-type solution in double trigonometric series [12] providing the following plate deflection:

$$w=\frac{16p}{\pi^6 D}\sum_m\sum_n\frac{1+\bar{D}(\lambda_m^2+\lambda_n^2)}{(\lambda_m^2+\lambda_n^2)^2}\sin(\lambda_m x)\sin(\lambda_n y), \tag{43}$$

where $\lambda_m = \pi m/a$, $\lambda_n = \pi n/b$ and a, b are the plate dimensions.

The term including $\bar{D}$ allows for transverse shear deformation. For thin plates, this term is relatively small and can be neglected. Then, eq.(43) reduces to the corresponding solution in the K-theory. However, there exists a principal difference between the two theories under consideration. In the sixth order theory, reactive forces at the supported edges of the plate are Q_x and Q_y. Their resultant force is $F = pab$ and provides the total force that balances the plate as a solid. In the K-theory, reactive forces are V_x and V_y specified by eq.(1), and their resultant force is larger than F. To maintain the balance, concentrated corner reactions are introduced [12]. However, there are no corner forces in this problem, and violation of the balance condition is a natural consequence of the K-theory. Navier-type solution that can be readily obtained for the corresponding three-dimensional elasticity problem shows no corner forces. It should also be mentioned that traditional interpretation of corner forces for a simply supported plate [12] is not adequate. Kromm's solution [21] which is used for this interpretation corresponds to a different problem, i.e., to a plate with boundary conditions (41), while solution (43) which is under discussion corresponds to boundary conditions (37). Thus, the solution following from the sixth order theory does not require any corner forces and is not only more accurate, but also simpler than the solution provided by the K-theory.

As another example, consider a problem of torsion of a rectangular plate by twisting moments m_{xy} uniformly distributed along the plate edges. This problem has a simple solution following directly from eqs.(37), i.e.

$$w = -\frac{m_{xy}xy}{D(1-\nu)} \qquad M_{xy} = m_{xy} \qquad M_x = M_y = Q_x = Q_y = 0. \tag{44}$$

However, the K-theory gives a different interpretation of this result. According to this interpretation, solution (44) corresponds to the plate twisted by four corner forces $P = 2m_{xy}$. This immediately leads to violation of equilibrium conditions. Indeed, if forces P are not the result of formal transformation but real forces, considering a quarter of the plate we can see that the only one remaining corner force cannot be balanced [24].

Now complicate the foregoing problem assuming that the twisting moment is distributed only along transverse edges $x = 0$ and $x = a$ (see Fig.1), while longitudinal edges $y = 0$ and $y = b$ are free. As can be readily seen, this problem cannot be solved within the framework of the K-theory. Meanwhile, the sixth order theory provides eq.(29) whose solution can be used in conjunction with solution (44) to satisfy boundary condition $M_{xy} = 0$ for $y = 0$ and $y = b$ [25].

As a more specific example, consider a contact problem. Let a plate be loaded through a shallow and absolutely rigid indenter whose surface is specified by a polynomial of the second order with respect to coordinates x and y. Then, the plate deflection within the contact area is also the polynomial of the second order, and therefore $\Delta\Delta w = 0$. As follows from the last equation of eqs.(32), in this case the K-theory yields $p = 0$. This means that, in contradiction with the common sense, there is no pressure between the plate and the indenter. The sixth order theory gives a different result. If we express φ in eq.(22) in terms of w with the aid of eq.(24) and take into account that $\Delta\Delta w = 0$, we arrive at the following equation:

$$\bar{D}\Delta p - p = 0.$$

Solution of this equation specifies a finite and nonzero contact pressure distribution between the plate and the indenter [23].

And finally, consider a numerical example. Let the plate be infinitely long in the x direction and its longitudinal edges $y = 0$ and $y = b$ be simply supported. The plate is loaded with pressure $p = p_0 \sin \lambda y$, where $\lambda = \pi/b$ and has the following parameters: $h/b = 0.05$, $\nu = 0.3$.

Substituting $\varphi = \varphi_0(x) \sin \lambda y$ and $\psi = \psi_0(x) \cos \lambda y$ into eqs.(22) and (29) we arrive at two ordinary differential equations for φ_0 and ψ_0. For a plate with free edge $x = 0$, solutions of these equation should satisfy the following boundary conditions at this edge: $M_x = 0$, $M_{xy} = 0$, $Q_x = 0$. For the K-theory, there is only two boundary conditions, i.e. $M_x = 0$ and $V_x = 0$, where V_x is specified by eq.(1). The theories under consideration yield the following solutions for the plate deflection [23].

$$w = \frac{p}{D\lambda^4}\left[1 + 0.178 e^{-\lambda x}\left(1 - 1.69\,\frac{x}{b}\right)\right] \sin \lambda y$$

$$w_K = \frac{p}{D\lambda^4}\left[1 + 0.169 e^{-\lambda x}\left(1 - 1.69\,\frac{x}{b}\right)\right] \sin \lambda y.$$

As can be seen, the results are very close. The difference shows itself for transverse shear force Q_x, for which the sixth order theory provides

$$Q_x = 0.64\,\frac{p\nu}{\lambda}\left(e^{-\lambda x} - e^{-sx}\right) \sin \lambda y, \tag{45}$$

where $s = 69.35/b$. It can be seen that s is much higher than $\lambda = 3.14/b$. Equation (45) consists of two parts — relatively slowly varying part which corresponds to potential φ and is called a penetrating solution and rapidly varying part which corresponds to rotational potential ψ and is referred to as a boundary layer solution. Expressions corresponding to the K-theory do not include a boundary layer solution and are as follows

$$Q_x = 0.606\,\frac{p\nu}{\lambda}\, e^{-\lambda x} \sin \lambda y \qquad V_x = 0.67\,\frac{p\nu}{\lambda b}\, x e^{-\lambda x} \sin \lambda y.$$

Distributions of normalized forces $\bar{Q} = Q\lambda/p\nu$ and $\bar{V} = V\lambda/p\nu$ along the supported edge are presented in Fig.2. As can be seen, generalized shear force V_x formally satisfying the boundary condition $V_x(x = 0) = 0$ is not a resultant of shear stress.

This conclusion is far from being only of an academic interest. In all existing textbooks, design guides, and computer codes, interaction between plates, plates and ribs, and plates and supports is described in terms of V which can be completely different from the actual interaction force. For example, if the edge $x = 0$ of the plate considered above is simply supported, the difference between maximum values of the actual reaction Q_x in eqs.(45) and force V_x is 35%.

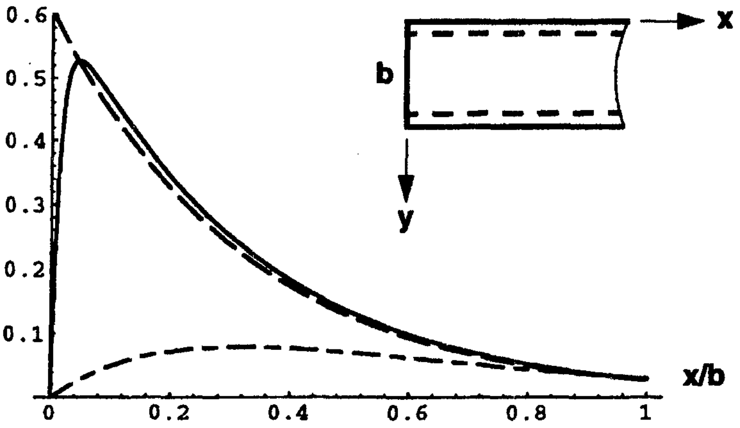

Figure 2. Variation of transverse shear forces with the longitudinal coordinate along the supported edge at the plate

———————— $\bar{Q}_x$, sixth order theory

— — — — $\bar{Q}_x$, K-theory

——·——·—— $\bar{V}_x$, K-theory

ASYMPTOTIC ANALYSIS

The boundary layer effect described above is typically ignored on the basis of asymptotic considerations. However, as it will be demonstrated in the following section, this effect may not be ignored, in the general case.

Equations describing thin-walled structural elements include a small parameter. For plate theories, this parameter is $\bar{h} = h/a$, where h is the plate thickness and a is the smallest in-plane dimension. For thin plates, $\bar{h} \ll 1$, and useful information can be obtained about the solution if we study its asymptotic behavior for $\bar{h} \longrightarrow 0$. To perform asymptotic analysis, introduce dimensionless coordinates $\bar{x} = x/a$ and $\bar{y} = y/a$. Then, eqs.(22), (24), and (29) can be presented in the following form:

$$\Delta\Delta\varphi = \frac{12pa}{\bar{E}\bar{h}^3} \tag{46}$$

$$w = \varphi - \frac{\bar{h}^2}{6(1-\nu)} \Delta\varphi \tag{47}$$

$$\bar{h}^2 \Delta\psi - 12\psi = 0. \tag{48}$$

Here, Δ is Laplacian operator in coordinates $\bar{x}$, $\bar{y}$.

Equation (46) shows that the asymptotic order of function φ is $\bar{h}^{(-3)}$ and that its derivatives are of the same order that of the function. The second term in the right-hand side of eq.(47) is of higher asymptotic order then the first term and can be neglected. So, asymptotic order of w is also $\bar{h}^{(-3)}$. From eq.(48), we see that the function ψ acquires large multiplier $\bar{h}^{(-1)}$ after each differentiation which means that ψ is a rapidly varying function. Thus, the solution of the problem under study, in general, consists of two parts — slowly varying penetrating solution (φ or w) and rapidly varying boundary layer solution (ψ). As can be shown by asymptotic analysis [26], for thin isotropic plates, the boundary layer solution can be neglected in comparison with penetrating solution.

Under this simplification, the sixth order theory formally provides the same equations that the K-theory. However, this simplified theory is not the K-theory because it does not include generalized shear forces V and corner forces. Numerous solutions of the plate theory problems obtained by now with the aid of the K-theory show that for many practical problems (usually for those that do not require us to introduce forces V) we can neglect the boundary layer solution.

However, there exist at least three reasons that do not allow us to neglect the boundary layer solution in the general case. First, as was shown above, the plate theory becomes physically inconsistent. Second, there is a class of plate problems for which penetrating solution degenerates, and only boundary layer solution describes the plate behavior (e.g., the torsion problem discussed above). And third, in some cases, boundary layer solution can affect penetrating solution through boundary conditions and change it. To demonstrate this, consider a square plate in the domain $-a/2 \le x < a/2$, $0 \le y \le a$ and having $\bar{h} = 0.01$ and $\nu = 0.3$. Plate edges $y = 0$ and $y = a$ are simply supported, and edges $x = \pm a/2$ are loaded with transverse shear force and twisting moment

$$Q_x = Q \sin \lambda y \qquad M_{xy} = \frac{M}{\lambda} \cos \lambda y,$$

where $\lambda = \pi/a$. The K-theory yields the following solution for the plate deflection [27]:

$$w_K = \frac{V}{E\bar{h}^3} \left(0.211 \cosh \lambda x - 0.155 \, \frac{x}{a} \, \sinh \lambda x \right) \sin \lambda y.$$

Here, $V = Q - M$ is, actually, the amplitude of the generalized transverse shear force specified by eq.(1). The solution following from the sixth order theory is

$$w = w_1 + w_2,$$

where

$$w_1 = \frac{V}{E\bar{h}^3}\left[0.211\cosh\lambda x - 0.156\left(\frac{x}{a}\sinh\lambda x - 1.5\bar{h}^2\cosh\lambda x\right)\right]\sin\lambda y$$

$$w_2 = \frac{Q}{E\bar{h}^2}\left[0.012\cosh\lambda x + 0.26\left(\frac{x}{a}\sinh\lambda x - 1.5\bar{h}^2\cosh\lambda x\right)\right]\sin\lambda y.$$

As can be seen, w_K and w_1 are practically the same and have asymptotic order $\bar{h}^{(-3)}$. However, w includes w_2 which is also a part of penetrating solution but is induced by a boundary layer solution (interacting with penetrating solution at the boundary) and has a higher asymptotic order ($\bar{h}^{(-2)}$). In general, $w_1 \gg w_2$, but if $V = 0$ and $Q \neq 0$, $w_K = 0$ and $w = w_2$. Thus, the plate deflection can be entirely different from what follows from the K-theory.

Asymptotic properties of the solution discussed above can be used to simplify the plate analysis in the sixth order theory. Following Reissner [28] we can assume that the solution of eq.(48) that exists only in the vicinity of the plate edge varies rapidly only in the direction normal to the edge and does not change significantly along the supported edge. For the edge x = constant, this means that $d^2\psi/dx^2 \gg d^2\psi/dy^2$, and eq.(48) is approximately reduced to

$$\bar{h}^2\frac{d^2\psi}{d\bar{x}^2} - 12\psi = 0. \qquad (49)$$

This equation can be readily solved, and its solution can be used in conjunction with solution for eq.(46) to satisfy three boundary conditions at the plate edge. Thus, the problem is actually reduced to eq.(46) which is the same that the governing equation of the K-theory.

However, there exists a problem associated with the sixth order theory. This is the so-called shear-locking problem in finite element analysis based on shear deformable plate theory [29]. This effect causing the loss of accuracy is associated with different asymptotic behavior of terms corresponding to bending and shear in energy functional (42). Shear-locking occurs because low-order polynomials used in finite element analysis as shape functions cannot approximate rapidly varying boundary layer solution. If this solution is singled out and described with the aid of eq.(49), shear-locking disappears [30].

CONCLUSIONS

The plate theory is shown to be physically consistent if it is reduced to a set of two partial differential equations. One of these equations corresponds to the governing equation of the classical Kirchhoff plate theory, and the other equation has been introduced into the plate theory by Reissner. According to the proposed interpretation, these equations compose a new plate theory that is entirely different from theories originally constructed by Kirchhoff and Reissner and can be referred to as a modern form of the classical plate theory.

REFERENCES

1. Todhunter, I., Pearson, K. *A History of the Theory of Elasticity and of the Strength of Materials.* Vol.1, 2, Dover Publications (1960).
2. Timoshenko, S.P. *History of Strength of Materials.* Dover (1983).
3. Jemielita, G. "On the Winding Paths of the Theory of Plates" *Mechanika Teoretyczna i Stosowana* **2**, 31, pp. 317–327 (1993).
4. Poisson, S. "Sur l'equilibre et le mouvement des corps elastiques" *Mem. l'Acad. Sci. Paris* **8**, pp. 357–570, 623–627 (1829).
5. Kirchhoff, G. "Über das Gleichgewicht und die Bewegung einer elastischen Scheibe" *J. reine und angew. Math.* **40**, S. 51–88 (1850).
6. Thomson, W., Tait, P. *Treatise on Natural Philosophy.* Cambridge University Press (1883).
7. Donnell, L. *Beams, Plates, and Shells.* McGraw-Hill, (1976).
8. Lévy, M. "Mémoire sur la théoric des plaques élastiques planes" *J. Math. Pures Appl.* **30**, pp. 219–306 (1877).
9. Bollé, L. "Contribution on probléme linéaire de flexion d'une plaque élastique" *Bull. Tech. Suisse Romander* **73**, S. 281–285, 293–298 (1947).
10. Reissner, E. "Review of Bollé" *Math. Revs.* **9**, p. 480 (1948).
11. Reissner, E. "Reflections on the theory of elastic plates" *Appl. Mech. Revs.* **38**, 11, pp. 1453–1464 (1985).
12. Timoshenko, S., Woinowsky-Krieger, S. *Theory of Plates and Shells.* McGraw-Hill (1959).
13. Reissner, E. "On the Theory of Bending of Elastic Plates" *Journal of Mathematical Physics* **23**, pp. 184–191 (1944).

14. Timoshenko, S.P. "On the correction for shear of the differential equations to transverse vibration of prismatic bars" *Phil. Mag.* Ser. 6, **41**, pp. 744–746 (1921).
15. Vasil'ev, V.V., Lur'e, S.A. "On refined theories of beams, plates, and shells" *J. of Comp. Mat.* **26**, 4, pp. 546–557 (1992).
16. Hencky, H. "Über die Berücksichugung der Schubverzerrung in ebenen Platten" *Ing. Arch.* Bd. 16, H.1, S. 72–76 (1947).
17. Uflyand, Ya. S. "The propagation of waves in the transverse vibrations of bars and plates" *Prikl. Mat. Mekh.* **12**, pp. 287–300 (1948, in Russian).
18. Green, A. "On Reissner's theory of bending of elastic plates" *Quart. of Appl. Math.* **7**, 2, pp. 223–228 (1949).
19. Mindlin, R.D. "Influence of rotatory inertia and shear on flexural motions of isotropic" elastic plates. *J. Appl. Mech.* **18**, pp. 31–38 (1951).
20. Reissner, E. Private Communications (1993).
21. Kromm, A. "Verallgemeinerte Theoric der Plattenstatik" *Eng. Arch.* **21**, S. 266–286 (1953)
22. White, F. *Fluid Mechanics.* McGraw-Hill (1986).
23. Vasiliev, V.V. "The theory of thin plates" *Mechanics of Solids (Mekhanika Tverdogo Tela)* **27**, 3, pp. 22–42 (1992).
24. Zhilin, P.A. "The plate theories of Poisson and Kirchhoff from the standpoint of contemporary plate theory" *Mechanics of Solids (Mekhanika Tverdogo Tela)* **27**, 3, pp. 43–58 (1992).
25. Reissner, E. "The effect of transverse shear deformation on the bending of elastic plates" *Transactions of ASME* **67**, pp. A69–A77 (1945).
26. Gol'denveizer, A.L. "On Reissner's plate theory" *Izv. Akad. Nauk SSSR, Otd. Tekh. Nauk* **4**, pp. 102–109 (1958, in Russian).
27. Vasiliev, V.V. "A discussion on classical plate theory" *Mechanics of Solids (Mekhanika Tverdogo Tela)* **30**, 4, pp. 130–138 (1995).
28. Reissner, E. "On the theory of transverse bending of elastic plates" *Int. J. Solids Struct.* **12**, 8, pp. 545–554 (1976).
29. Averill, R.C., and Reddy, J.N. "Behavior of plate elements based on the first-order shear deformation theory" *Engineering Computing* **7**, pp. 57–74 (1990).
30. Taylor, M.W., Vasiliev, V.V., Dillard, D.A. "On the problem of shear-locking in finite elements based on shear deformable plate theory" *Int. J. Solids Structures* **34**, 7, pp. 859–875 (1997).

DETERMINATION OF FILLER CONTENT OF WOOD-BASED COMPOSITES BY THERMOGRAVIMETRIC ANALYSIS

M. Y. AHMAD FUAD*, S. RAHMAD and M. R. NOR AZLAN
Polymer Technology Laboratory, SIRIM Berhad, P. O. Box 7035, 40911, Shah Alam, Malaysia

ABSTRACT

Oil palm wood flour (OPWF), a new type of wood-based filler for polypropylene composite has been investigated. One important characterisation of the OPWF composites involves the checking for the actual filler content and filler distribution within the matrix. The application of thermogravimetric (TG) analysis technique for evaluating filler content in composites have been described by many thermal analysts but the scope of analyses were often limited to mineral-based fillers or carbon black content determination. Filler content determination of wood-based filler using similar technique, however, poses a problem since the fillers themselves usually degrades earlier than the matrix material.

Here we report how filler content of wood-based fillers may be computed from selective thermogravimetric analyses. The computation of the OPWF content in the composites is based on a simple expression, $p_f = \Psi(m_d/m_c)$ derived from the analyses of the TG curves of the filler material and the resultant composite. Constant Ψ is a factor related to the mass losses of the filler and the matrix materials when subjected to a specified temperature range and is specific to the particular type of wood-based filler used. The technique has shown good agreement and consistency between the analysed and theoretical filler content and also has indicated that the composites have a uniform filler distribution.

INTRODUCTION

The applications of other wood-based fillers have been described by many workers.[8-10] The fillers were incorporated into the polypropylene matrix by various means such as by a two-roll mill or through an extruder. Accurate filler loadings and excellent filler dispersion were normally assumed. However, attempts were seldom made to support these assumptions scientifically. Filler losses during compounding or mixing processes and agglomeration of filler in the composites are not uncommon, thus the significance of the filler content and dispersion analyses.

For mineral-based filler that can stand substantially higher temperature than the matrix material, the matter is easily resolved by burning off the entire resin at high enough temperature leaving behind the inorganic filler behind for quantification. Glass fibre content of glass-reinforced plastics may be determined in this manner using furnace up to say 600 °C.

The choice of purging atmosphere in thermogravimetric (TG) analytical technique depends on the nature of fillers; for inert inorganic fillers such as glass, talc, silica and mica, flowing air or oxygen is preferred to virtually burn off the matrix materials. For organic fillers such as carbon black in polypropylene matrix, inert nitrogen atmosphere will be more suitable so that only the matrix polypropylene will disappear through thermal degradation without affecting the carbon content significantly.[11] If the matrix material does not completely volatilize and leaves behind some ash, then introduction of air is necessary at high enough temperature (550 °C) to oxidise the carbon component and thus separating it from the ash for quantification purpose.[12] Applications of this technique for evaluating filler content have been described by many thermal analysts but the scope of analyses were often limited to mineral fillers and carbon black determination .[13-14]

---

* To whom correspondence should be addressed.

Determination of wood-based fillers using similar technique, however, poses a problem since the fillers themselves usually degrade or carbonise together with the matrix plastics. In this present study, a relatively new type of wood-based filler is being investigated. The origin of the filler is from the trunk of an oil palm tree (*Elaeis Guineensis*), hence the term oil palm wood flour (OPWF) filler. Here we wish to report how filler content in wood-based composites may be calculated from simple expressions derived from selective thermogravimetric analyses. Filler contents of almost all the OPWF composites were conveniently determined with good accuracy and precision by these methods.

EXPERIMENTAL

The OPWF was compounded into polypropylene by means of a Brabender DSK 42/7 twin screw compounder having barrel temperatures of 170 to 190 °C from feeding zone to the die zone respectively. Four levels of loadings were prepared by compounding 20, 30, 40 and 50 parts filler to 100 parts resin resulting in theoretical filler content (by mass) of 16.7, 23.1, 28.6 and 33.3% respectively. The compositions and markings of the OPWF composites are as shown in Table 1. The compounds were extruded through a twin 4-mm rod die into a water bath, pulled and pelletized.

A highly filled composite at 50% filler content was also specially prepared using a Brabender W50E mixer to cross check for an apparent discrepancy in the analysed content of the OPC4 sample. While all the previous samples were prepared by the twin-screw compounder and injection moulding process, this sample (OPCM) is prepared solely using a *mixer* with a five-minute mixing time. Mixing was performed by a pair of counter rotating rotors at a temperature of 180 °C. Thermogravimetric analyses were performed on specimens taken from 3 different parts of the composite.

Thermogravimetric Analysis

The OPWF composite sample was scanned from 30 °C to 550 °C using a Mettler TG50 thermogravimetry analyser. The heating rate was 20 °C/min. and a nitrogen purge gas with a flow rate of 200 ml/min. was applied. Great care has to be exercised in the analysis of the OPWF filler content as the filler degrades earlier than the polypropylene matrix as shown by the thermogravimetric scans in Figure I. Whilst quite a substantial amount of degradation (carbonisation) of the OPWF has occurred at 380 °C, there seems to be hardly any significant degradation of the polypropylene matrix (as shown by the derivative thermogravimetric curve, DTG) up to this point.

Thus this temperature may serve as the upper limit of analysis in our subsequent computation for the OPWF content in the composites.

Step analysis of the neat OPWF thermogravimetric scan from 50 to 380 ^{o}C shows a percentage mass drop of 62.6%). If similar step analyses are carried out on the OPWF composites' samples within the above range, then the amount of filler present in each of the composites may be calculated. Basically there are two methods for calculating filler content. First, a simpler method where it is assumed at the mentioned temperature range, there is negligible mass loss due the matrix polypropylene and the entire mass loss is solely due to OPWF filler. The second method takes into account mass loss due to polypropylene component as well.

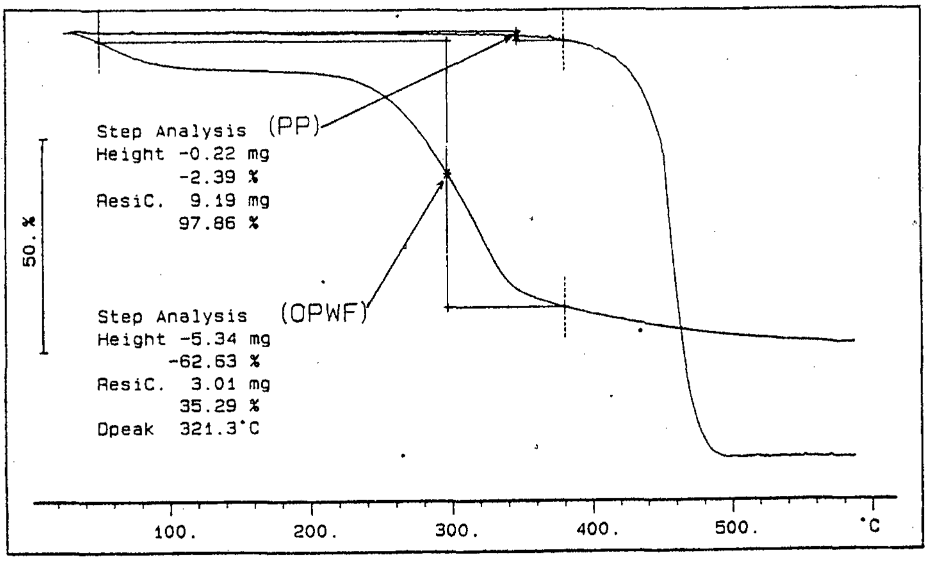

Figure 1 Step analyses of TG scans of PP and OPWF between 50°C and 380°C.

Method I

If the initial mass of the composite sample subjected to thermogravimetric scan is m_c and drop in mass at the above temperature range is m_d, then the amount of filler, m_f in the composite will be:

$$m_f = m_d(100/62.6) \qquad (1)$$

Percentage filler content, p_f will be:

$$p_f = 100(m_f/m_c) \qquad (2)$$

Combining equations (1) and (2), we get:

$$\mathbf{p_f = 160(m_d/m_c)} \qquad (3)$$

where

p_f is the percentage filler content,
m_d is mass loss in the thermogravimetric scan from 50 to 380 ^{o}C and
m_c is mass of composite sample in the thermogravimetric analysis.

Method II

In method II, loss of mass due to matrix polypropylene is taken into account. Between the 50 - 380 ^{O}C temperature range, it may be observed that there is a loss of 2.4% in case of the neat polypropylene (Figure II). Thus polypropylene contribution to the loss, m_p may be expressed as:

$$m_p = m_d(2.4/100) \tag{3}$$

Loss in mass due to filler only i.e., $m_{f'}$ will be:

$$m_{f'} = m_d - m_p \tag{4}$$

To calculate the amount of filler, equation (1) will then be:

$$m_f = m_{f'}(100/62.6) \tag{1a}$$

Substituting the value of $m_{f'}$ in equation (1a) will give the corrected filler content.

$$m_f = 1.56m_d \tag{5}$$

Combining equations (5) and (2) result in the percentage filler content in the OPWF composites after correction has been made to account for the polypropylene mass loss within the temperature range analysed.

$$\mathbf{p_f = 156(m_d/m_c)} \tag{6}$$

It may be seen clearly that the value for filler content after the correction is relatively lower than that calculated by method I. In general term, equation (6) may be expressed as

$$\mathbf{p_f = \Psi(m_d/m_c)} \tag{7}$$

where Ψ is a constant related to the mass losses of the filler and the matrix materials when subjected to a specified range of a temperature profile.

To check for filler distribution within the final composite samples, the OPWF residue levels were analysed at 3 different positions within the bar specimen: at the gate, midpoint and end positions of the bar. If the values are close to each other, they give good indication of uniform filler dispersion within the matrix.

RESULTS AND DISCUSSION

Results for the analysed OPWF contents in the composites are shown in Table I. The analyses reveal that the determined filler contents in all the OPWF composites (exception: OPC4 sample) are quite close to the percentage of the incorporated fillers. As expected, the mean filler contents of samples OPC1, OPC2 and OPC3 are slightly lower than the theoretical values due to filler losses during the compounding process. Sample with the highest filler loading, OPC4, however, when analysed gives a considerably lower value.

Table I. Filler content of OPWF composites at different locations in injected samples.

Composite Sample	Theoretical Filler Content (% by wt.)	Measured Filler Content (%)			
		Position of Sampling			
		Gate	Midpoint	End	Mean
OPC1	16.7	17.6	15.6	16.6	16.5 +/- 0.8[#]
OPC2	23.1	21.2	22.6	22.0	21.9 +/- 0.7
OPC3	28.6	25.7	25.3	25.6	25.5 +/- 0.2
OPC4	33.3	27.4	28.5	27.3	27.7 +/- 0.7
		Position 1	Position 2	Position 3	
OPCM	50.0	46.8	48.3	47.1	47.4 +/- 0.8

[#] standard deviation

This discrepancy may be attributed to higher filler losses relative to former samples. It was observed during the compounding process, at too high a filler content, the mixing process became less efficient, i.e. greater difficulty was encountered to incorporate the filler. As feeding of the filler and resin was assisted by a dozing screw feeder, occasionally at the earlier stage of compounding, higher proportion of the resin (than the filler) tend to be fed into the compounder. Hence this discrepancy may be attributed to inefficient mixing and not due to shortcomings in the analysing technique.

To cross check for this matter, a highly filled composite (50 % filler content) was specially prepared using an alternate processing technique, i.e., by a mixer. Analysed filler contents of this sample (OPCM) taken at the three different locations give good agreement to the theoretical value as shown in the last line of Table II. The mean value of 47.4 % may be considered quite close considering the inevitable filler losses during mixing process.

Uniform distribution of filler particles within the matrix in all the composite samples was also confirmed by the thermogravimetric analyses. Filler contents at 3 different locations of the specimen (at the gate, midway and at the end position away from injection gate) were in close agreement to one another. The standard deviation value for each sample was also noted to be small.

A typical plot of thermogravimetry scans for OPWF composites at various filler loadings is shown in Figure 3.

CONCLUSION

Strong evidence for the accuracy of the calculated filler content and the reliability of the described technique are supported by the good agreement and consistency between the analysed filler content and the theoretical incorporated values. The derived expression, $\mathbf{p_f} = \Psi(\mathbf{m_d}/\mathbf{m_c})$ may be applied to other wood-based composites to provide a simple and quick method for calculating the actual filler content. After determining the constant Ψ, all one have to do is to measure the mass drop, $\mathbf{m_d}$ and knowing the initial composite mass, $\mathbf{m_c}$, filler content, $\mathbf{p_f}$ is easily computed. The expression will enable workers to have a quick and convenient means of checking the actual filler contents of their composites and its dispersion within the matrix.

REFERENCES

1. Zaini, M. J., Fuad, M. Y. A, Ismail, Z., Mansor, M. S. and Mustafah, J. (1996). *Polym. Int.*, **40,** 51.
2. Fuad, M. Y. A, Zaini, M. J., Mustafah, J And Ismail, Z., Ishak, Z. A. M. and Omar, A. K. (1997), *Proceedings of ICCE/4*, pp 337, July 6-12, Hawaii.
3. Bramuzzo, M., Savadori, A. and Bacci, D. (1985). *Polym. Comp.*, **6**, 1 .
4. Jilken, L., Malhammar, G., and Selden, R. (1991). *Polym. Test.*, **10**, 329.
5. Kawalewski, T. and Galeski, A. (1986). *J. Appl. Polym. Sci.*, **32**, 2919 .
6. Weber, A. (1990). *Plast. Rubber Process. Appl.*, **14**, 65.
7. Bosshard, A.W. and Schlumpf, H.P. (1987). in *Plastics Additives Handbook*, R. Gachter and H. Muller, eds., Carl Hanser Verlag, Munich..
8. Maiti, S. N. and Subbarao, R. (1991). *Intern. J. Polymeric Mater.* **15,** 1.
9. Raj, R. G., Kokta, B. V., Groleau, G. and Daneault, C. (1989). *Plast. Rubber Process. Appl.*, **11**, 215.
10. Yap, M. G. S., Que,Y. T., Chia L. H. L. and Chan, H. S. O. (1991). *J. Appl. Polym. Sci.*, **43**, 2057.
11. Fuad, M. Y. A., Mustafah, J., Mansor, M. S., Ishak, Z. A. M. and Omar, A. K. (1995). *Polym. Int.*, **38,** 33.
12. Maurer, J. J., (1981) In: *Thermal Characterization of Polymeric Materials*. ed. Turi, E. A., Academic Press, Inc, San Diego. pp. 572
13. Cassel B., (1976). Recent Advances in Thermogravimetric Analysis of Polymer and Elastomer formulations. In: *Proceedings of the Sixth North American Thermal Analysis Society Conference,* Princeton, New Jersey.
14. Widmann, G. and Reisen, R. (1987) In: *Thermal Analysis - Terms, Methods, Applications.* ed. Huthig, Germany. pp 113.

HIGHLY LOADED CATALYTIC GRAFTING THERMOPLASTIC/POLY(PARA-PHENYLENE-TEREPHTALAMIDE) (KEVLAR) COMPOSITES

A. Ait-Kadi and A. A. Yousefi,
Chemical Engineering Department and CERSIM, Laval University
Quebec Canada G1K 7P4

INTRODUCTION

The conventional techniques of producing thermoplastic composites consists of heating the matrix until it softens or melts, and then incorporating the solid substrate (filler or reinforcement) at a given concentration. Strong mixing is often required to disperse the solid substrate in the relatively highly viscous matrix. Several problems must however be overcome when this simple and rather straightforward method is used. These problems are mainly related to solid dispersion in the viscous matrix ; solid/matrix interactions and solid wetting by the matrix. These are important parameters for a composite with desired properties to be obtained. Great efforts have been devoted to partially overcome these problems. Several advanced and rather complicated and expensive methods have been used to obtain better dispersion of solid substrates in viscous matrices. Chemical modification of the solid substrate surface using coupling agents (silanes or titanates) to promote adhesion at the polymeric/solid interface are used on a regular basis (Katz and Milewski, 1978). The optimum choice is however to create a chemical bond directly between the reinforcing agent and the polymeric matrix. In this paper we will present the results of such approach with ultra high molecular weight high density polyethylene and Thermoplastic/Poly(para-phenylene-terephtalamide) (Kevlar, a trade name of Du Pont)) composites. The technique called *Catalytic Grafting* consists of grafting the polymerization catalyst onto the surface of the solid substrate and proceed with the polymerization of the monomer of the composite's matrix. Before we get to the experimental procedure and experimental results, we shall first expose a brief review of the literature on the subject of catalytic grafting.

REVIEW OF THE LITERATURE

This technique has been first developed by Enikolopian (1976) and Howard *et al.*(1981). The technique consists of anchoring a polymerization catalyst (Ziegler-Natta catalysts in this case) onto the surface of the reinforcing agent and then polymerizing what would represent the matrix of the composite in the final product. Several reinforcements and fillers/polyolefin composites have been obtained with this technique (Enikolopian *et al.* 1990; Wang *et al.* 1992-a,b, 1993; Novokshnova *et al.* 1994; Casenave *et al.* 1996; Brahimi *et al.* 1996; Hyndricks *et al.* 1997-a,b). In essence, the solid substrate plays a double role in this so-called *Catalytic Grafting* technique: i) it plays the role of supported catalyst for the polymerization and ii) the role of filler or reinforcement in the final product. The chemical bond between the reinforcement surface and the synthesized polymer is easily hydrolysed in the steps following the polymerization. However, due to the fact that the catalyst reaches areas that cannot be reached by a molten polymer in the conventional technique, the resulting mechanical interactions in the catalytic grafting composites result in materials with enhanced overall properties as compared to their counterparts obtained by melt mixing. All the results of the above cited authors show the same trends. Moreover, the catalytic grafting can be used to "synthesize" highly filled and yet well dispersed composites. The purpose of the present work is to use the catalytic grafting technique to obtain highly filled Kevlar pulp/polyethylene composites. In the conventional technique, Kevlar pulp is not easy to incorporate in a highly viscous matrix (Rajabian, 1995). The method used here confirms the potential of the method to obtain composites even with difficult reinforcement and also to evaluate the properties of relatively highly filled composites obatined with such reinforcement.

EXPERIMENTAL AND MATERIALS

I-Materials

Kevlar pulp was graciously provided by DuPont Canada (Toronto, Canada). Ethylene and nitrogen gases were purchased from Prixair company (Quebec, Canada). Triethyl aluminum ($AlEt_3$) and titanum tetrachloride ($TiCl_4$) were purchased from Aldrich company (Milwaukee, USA). Ultra high molecular weight high density polyethylene (UMWHDPE) was synthesized in our laboratory as described below. The commercial high density PE (07105C) was provided by Dow Canada.

II-Experimental

Catalytic grafting of polymer on Kevlar fibers

Kevlar fibers have a relatively small amount of active sites on their surface for the first step of the catalytic grafting technique to be successfully completed. In order to increase the number of reactive groups on their surface, Kevlar fibers were chemically treated (hydrolysed) as described earlier by Chatzi *et al.* (1987). Accordingly, 80 grams of Kevlar fibers were immersed in 3200 ml of 10 w/w% aqueous solution of NaOH at ambient temperature for 10 minutes. Following the treatment, fibers were filtered and thoroughly washed with acetone and then dried under vacuum for 24 hours.

The catalytic grafting reaction was carried out on the surface of hydrolyzed Kevlar fibers in a home made reactor. The modified pulp was first charged in the reactor and allowed to dry under vacuum at 110 C overnight to exclude water and air from the reactor and Kevlar fibers. The temperature was then lowered to 60 and 2 liters of freshly distilled hexane (BDH co.) were added to the reactor under a continuous current of nitrogen gas. The required volume of $TiCl_4$ was injected into the reactor under continuous mixing and allowed to react with the fiber surface for one hour at 60 °C. The catalyst in excess was removed by washing repeatedly with freshly distilled hexane. The required volume of co-catalyst ($AlEt_3$) was injected into the reactor and was left for 5 minutes under mixing at 60 C in order to form the brownish complex of catalyst and co-catalyst. Thereafter, ethylene gas was purged into the reactor and the polymerization process starts and was maintained for 20 minutes. The reaction was then stopped by addition of ethyl alcohol and the final product recovered and washed and dried at

60 °C and under vacuum for 24 hours. The same reactor, materials and procedure were used to prepare ultra high density polyethylene to be used later with the "synthesized" composite.

Mixing and molding

When needed, UMWHDPE and grafted Kevlar fibers were melt blended in a batch mixer (Haake-Buchler Rheocorder System 40). Mixing was carried out at 180°C and 60 rpm for 10 minutes. Then, the resulting blend was removed and was air cooled to room temperature. The resulting composites were molded into rheological disks and plaques from samples for thermo-mechanical analysis were cut.

Rheological measurements

The dynamic measurements were isothermally carried out on a Bohlin CVO mechanical rheometer (stress controlled rheometer) using parallel plate geometry (25 mm plate diameter) at 180°C. The tests were performed at frequencies ranging from 0.004 to 62 rad/s. Stress sweep tests were first carried out to ensure that the rate sweep tests are performed in the linear viscoelastic zone of each material.

Thermo-mechanical measurements

Samples (42 x ~5 x ~1.3 mm) for this test were cut from a thin plaque prepared by melt molding of composites or neat polymers in a special mold. Thermo-mechanical properties of composite beams were measured using the Solid State Analyzer (RSAII from Rheometric Scientific) with a dual cantilever geometry at temperatures ranging from -140 to 140 °C at a constant frequency of 10 rad/s and a constant deformation of 0.2%.

Thermogravimetry

The percentage of the grafted PE on the surface of the Kevlar fibers was determined using a themogravimeter from Metller company (TG 50 + TC 11 TA processor). A small sample (10-15 mg) was put into a small crucible and was heated from 40 to 750 °C at a heating rate of 20 °C per minute. The test was repeated three times for the grafted Kevlar fiber sample. Analysis of the thermograms lead to the percentage of the grafted polyethylene since its decomposition temperature is different from that of Kevlar.

RESULTS AND DISCUSSION

The thermogravimetric tests revealed that there is about 50% of UMWHDPE grafted on the surface of the Kevlar fibers. The thermograms are not shown for the sake of brevity. These composites were characterized without further modification or else used as master batch to obtain lower fiber concentration composite when mixed with neat UMWHDPE. The thermomechanical properties of these materials as well as those obtained for a commercial HDPE and a neat UMWHDPE are shown on figures 1 and 2 for the storage modulus, E', and the loss tangent, tanδ, repectively (Ferry, 1987). The results of figure 1 show that blending the synthesized composite with neat polymer to obtain lower concentration composites leads to some complex behavior. Indeed, the results show that lowering the fibre concentration in the original composite does not necessarily lead to lower storage modulus. Moreover, the original composite seems to have a relatively higher storage modulus over the whole range of temperatures. The initial decrease of E' in the low temperature region is attributed to the glass transition (γ-transition) of the matrix. This is clearly shown on the loss tangent curves represented in Fig. 2. The glass transition temperature as extracted from this figure varies from - 117^{0}C to -122^{0}C. The glass transition temperature is slightly shifted towards lower temperatures as the fibre concentration is increased. This might be attributed to better interactions between the grafted polymer and the reinforcing fibers which limits the mobility of the grafted chains as the proportion of the grafted composite is increased. The only other transition that can be detected from Fig. 2 is the melt around 130 °C. This is typical behavior for high density polyethylenes (Kumar and Gupta, 1978). The results in the melt state (at 180^{0}C) are shown in Figs. 3 and 4 for the storage modulus, G', and the complex viscosity η^* respectively (Ferry, 1987). The results of these figures clearly show that the synthesized high density polyethylene is much more viscous than the commercial one supporting the fact that the low pressure Ziegler-Natta polymerization without chain transfer agents, such as hydrogen, invariably lead to ultra high molecular weight HDPE. The results also show that the storage modulus and the complex viscosity of the 50% composite are much more higher than the corresponding material functions for the neat UMWHDPE and the other composites. Again this indicate that the grafted polymer is intimately mixed with the reinforcing agent. For the other composites, the effect of fibre concentration is not very important. G' and η^* for the neat polymers also indicate that the synthesized polymer is of ultra high molecular nature. Indeed, the G' values for the synthesized polyethylene are almost constant (plateau) indicating the presence of a highly entangled network associated with molecular weights (or polymer chains lengths) much more above the critical molecular weight of the polymer (Ferry, 1987). The presence of high molecular weight chains results in a displacement of the terminal zone of the storage modulus toward lower frequencies. The amplitude of the displacement increases with increasing molecular weight. Based on the viscosity data obtained for the neat commercial and synthesized HDPE, and using the relation $\eta_0 = K\,M_w^{3.4}$ (Bird *et al.* 1987) where η_0 is the zero-shear viscosity and M_w the weight average molecular weight, M_w of the synthesized HDPE is estimated to be in the range of $1\text{x}10^6$ to $1.7\text{x}10^6$ (the M_w for the commercial HDPE is taken between 150000 and 250000, which are the numerical values generally encountered for such polymers).

Other results on this type of composites were also obtained by Rajabian on a similar composite (Rajabian, 1995). Even though the basic materials are slightly different, the general trends indicate that the overall mechanical properties (mainly impact properties) are much more important for the catalytic grafted composites as compared to their counterparts prepared by the conventional method. The rheological results of Rajabian (1995) also indicate that mixing grafted fibers with neat polymers does not change significantly the rheological properties of the composites as the fibre concentration increases. These results are similar to those obtained here when the 50 % composite (the synthesized composite) is diluted with the synthesized UMWHDPE. Here again, we attribute this difference to the difference in the mobility of the polymer chains on the fiber surface as compared to the free chains introduced by incorporating the synthesized UMWHDPE. These results are in agreement with those obtained in the solid state.

CONCLUSIONS

Highly loaded and yet well dispersed Kevlar pulp/Ultra high molecular weight composites can be produced using the *Catalytic Grafting* technique. The rheological data in the solid and the melt state indicate that the polymer is intimately mixed with the matrix. These conclusions were drawn from the difference in the rheological behavior observed when the composite recovered directly from the reactor is compared to composites at different concentrations obtained from further dilution of the original one.

REFERENCES

- Bird, R.B., R.C. Armstrong and O. Hassager, *Dynamics of Polymeric Liquids, Vol1: Fluid Dynamics*, 2nd Edition,John Wiley and Sons, New York, 1987.
- Brahimi B., B. Riedl and A. Ait-Kadi, Polymer Surfaces and Interfaces: Charcterization, Modification and Applications, K.L. Mittal and K.W. Lee (Eds), SPE008, 1-16, 1996.
- Casenave S., A. Ait-Kadi and B. Riedl, Can. J. Chem. Eng., 74, 308-315, 1996.
- Chatzi E.G., Tidrick S.L. and Koenig J.L., Am. Chem. Soc., Div. Polm. Prep., No.2, pp 13-14 (1987)
- Enikolopian N.S., M.L. Fridman, O. Stalnova and V.L. Popov, Adv. Polym Sci., 96, 42-67, 1990.
- Enikolopian, N.S., USSR pat. 763 379 (1976)
- Ferry, J. D., *Viscoelastic Properties of Polymers*, 3rd Edition, John Wiley and Sons, New York, 1987.
- Hindryckx, F., Ph. Dubois, R. Jérôme, Ph. Teyssié et M. Garcia Marti, J. Appl. Polym. Sci., 64, 423-438, 1997-a.
- Hindryckx, F., Ph. Dubois, R. Jérôme, Ph. Teyssié et M. Garcia Marti, J. Appl. Polym. Sci., 64, 439-457, 1997-b.
- Howard, E.G., R.D. Lipscomb, R.N. MacDonald, B.L. Glazard, C.W. Tullock and J.W. Colette, Ind. Eng. Echem. Prod. Res. Dev., 20, 421 (1981).
- Katz, Harry S. and Milewski, John V., *Handbook of fillers and reinforcements for plastics* Edited by Harry S. Katz, John V. Milewski, New York : Van Nostrand Reinhold, 1978
- Kumal, A. and S.K. Gupta, *Fundamentals of Polymer Science and Engineering*, Tata McGraw- Hill, Delhi, 1978.
- Novokshnova, L.A. and I.N. Meshkova, Polym. Sci. 36 517-525, 1994.
- Rajabian M., M.Sc. Thesis,Chem. Eng. Dept., Laval Univ.- Supervisor: A. Ait-Kadi, 1995.
- Wang, Q., S. Kaliaguine and A. Ait-Kadi, J. Appl. Polym. Sci., Vol. 48, 121-136, 1993.
- Wang, Q., S. Kaliaguine and A. Ait-Kadi, J. Appl. Polym. Sci, Vol. 45/6, 1023-1033, 1992-b.
- Wang, Q., S. Kaliaguine andA. Ait-Kadi, J. Appl. Polym. Sci., Vol. 44, 1107-1119,1992-a

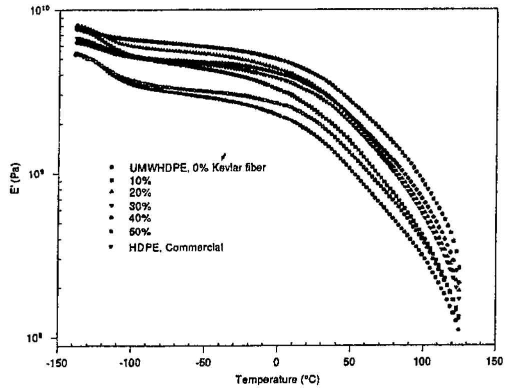

Figure 1 : Storage Modulus of Composites and Neat Polymers

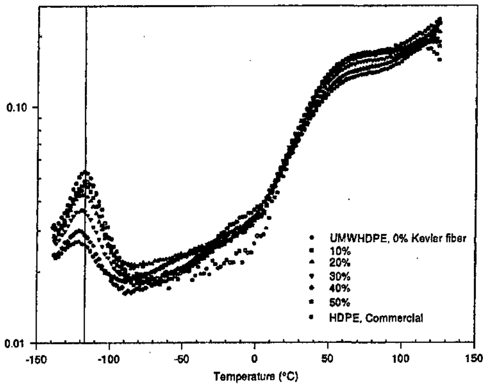

Figure 2 : Loss Tangent of Composites and Neat Polymers

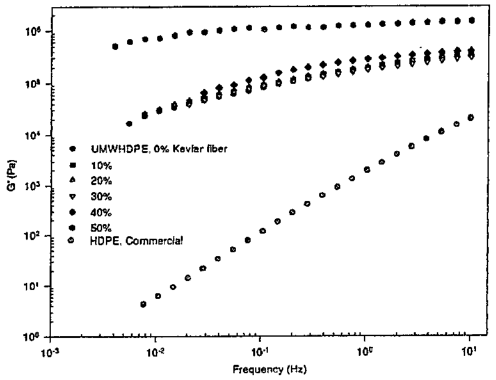

Figure 3 : Storage Modulus of Composites and Neat Polymers - T =180 ^{0}C

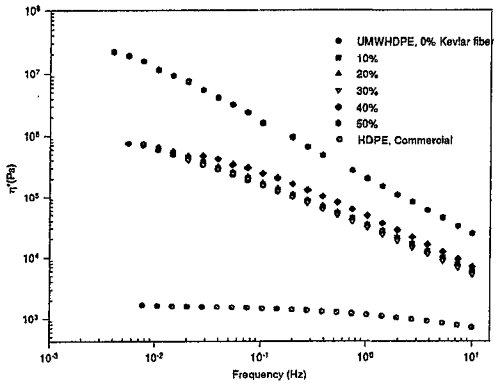

Figure 4 : Complex viscosity of Composites and Neat Polymers - T =180 ^{0}C

EFFECTS OF DIFFERENT FILLERS ON POLYPROPYLENE

C. Albano[1], L. Márquez[2], G. Ronca[2], O. Navarro[1] and A. Martínez[1].

[1]Universidad Central de Venezuela, Facultad de Ingeniería, Escuela de Ingeniería Química, Los Chaguaramos, PO Box: 48146, Caracas 1041 A; Venezuela, Fax: 58-2-6053178. E-mail: calbano@server1.ucv.edu.ve
[2]Universidad Simón Bolívar, Coordinación de Materiales, Laboratorio de Polímeros (B)

INTRODUCTION

In the last few years the development of new materials has been oriented towards composite materials, because they are more attractive systems with great significance for research and industrial application. The reasons for developing these compounds mainly consists of obtaining a material with specific properties and characteristics and low manufacture costs.

The addition of organic and inorganic substances (load) to polymers gives rise to changes in the mechanical properties of the blends. These properties frequently exhibit complex behavior, which depends on different factors, such as component properties, shape and size of the disperse phase (load), morphology of the system, load surface treatment, molecular weight, and polymer structure, among others, because both components are immiscible and incompatible. Deterioration of the properties of these composite materials is the result of the presence of two phases and the lack of adhesion in the interface.

Inorganic loads, such as glass, mica, talc, silica, calcium carbonate, are economically accessible, but they increase rigidity and bring about a loss of elongation at break and tensile strength [1,2,3].

Loaded PP is a plastic with low specific volume and there is a great deal of interest within the industry in analyzing the use of different loads to extend the range of applications of the product, which would result in lower raw material and finished product cost.

The focus of this work is using theoretical models to calculate the mechanical properties of the PP blends with different loads, such as talc, sodium benzoate and phthalocyanine, and then compare them to experimental values in order to explain the mechanical behavior of these blends.

The mechanical properties of the PP blend with the different loads are simulated by means of theoretical models and equations developed for heterogeneous systems. To apply the different models, they have to be combined with the nature of the matrix and of the dispersing phase, with the dimensions and distribution of the disperse particles and the extent and nature of the interfacial adhesion.

THEORETICAL MODELS

Models of Nielsen [4], Cohen-Ishai [5], Guth-Smallwood [6] and Mooney [7] predict the dependence of the yield module of heterogeneous blends on the composition.

Nielsen and Lewis [4] proposed the following model:

$$\frac{E_m}{E_b} = \frac{1 + AB_i\Phi_d}{1 - B_i\Psi\Phi_d} \tag{1}$$

where:

$$B_i = \frac{\left(\frac{E_m}{E_d} - 1\right)}{\left(\frac{E_m}{E_d} + A\right)} \qquad \Psi = 1 + \left(\frac{1 - \Phi_{max}}{\Phi_{max}^2}\right)\Phi_d \qquad A = \frac{(8 - 10\upsilon_m)}{(7 - 5\upsilon_m)}$$

where, E: Young's modulus (Kg/mm^2), ϕ_d: fraction in volume or mass of the discrete phase, v: Poisson radius. Subindices **b**, **m** and **d** refer to blend, matrix and disperse phase, respectively. ϕ_{max}: is the volumetric fraction of the maximum packing, and can be used as interaction parameter between both phases. A: constant related to the phase geometry, particularly for spherical inclusions and depends on the Poisson radius and ψ: factor which depends on the maximum packing fraction and on the disperse phase fraction.

The models developed by Cohen-Ishai, Guth-Smallwood and Mooney apply when the disperse phase is formed by rigid and spherical particles, whose functions consist of increasing rigidity in the matrix phase, because they restrict mobility of the polymer molecules.

Cohen- Ishai (C-I):

$$\frac{E_m}{E_p} = 1 + \frac{\Phi_d}{1 - \Phi_d^{\frac{1}{3}}} \tag{2}$$

Guth- Smallwood (G-S):

$$\frac{E_m}{E_p} = 1 + 2.5\Phi_d + 14.1\Phi_d^2 \tag{3}$$

Mooney:

$$\frac{E_m}{E_p} = \exp\left(\frac{2.5\varphi_d}{1 - s\varphi_d}\right) \tag{4}$$

where E_p: modulus of the pure polymer (Kg/mm^2) and E_m: modulus of the composite matrix (Kg/mm^2).

As with Young's modulus, studies have also been carried out on theoretical models to describe the phenomena occurring in the interface of the breaking point, where stress transference in discontinuities of a two-phase-blend is analyzed. According to Nielsen [4], Nicolais and Narkis [7] and others, strength properties are related to composition and volumetric fraction of a given sample in which both phases are observed.

Nielsen suggests an equation where an s factor is introduced, representing stress concentration:

$$\sigma = (1-\varphi^{2/3})s\,\sigma_0 \qquad (5)$$

Nicolais and Narkis suggest in the model presented by Nielsen, the incorporation of a weight factor of 1.21. The resulting expression is as follows:

$$\sigma = \sigma_0\left(1-1.21\Phi^{2/3}\right) \qquad (6)$$

where, φ and ϕ represent fraction in mass of the discrete phase, σ: the breaking strength of the blend (Kg/mm^2) and σ_o,: the strength of the matrix phase (Kg/mm^2).

The model applied to analyze the mechanical property of elongation at break offers qualitative information on the interfacial adhesion between the fillers and the matrix phase. The model used was Nielsen's [4].

According to Nielsen [4], there is a perfect adhesion and if a fracture tends to go from particle to particle, the proposed model is the following:

$$\frac{\varepsilon_b}{\varepsilon_m} = \left(1-\Phi_d^{1/3}\right) \qquad (7)$$

where, ε_b: elongation at break of the blend and ε_m: elongation at break of the matrix and ϕ_d: fraction in mass of the disperse phase.

EXPERIMENTAL

The material used in this work was polypropylene (PP) supplied by Pro-Fax (Tf: 436°K. MFI: 6.5gr/10 min, ρ: 0,903 gr/cm^3). The fillers used were talc, phthalocyanine and sodium benzoate. All the compounds were prepared in a co-rotating twin-screw extruder. Samples and specimens were prepared using state-of-the-art conditions (thermal, pressure) in this field. All tests were performed according to ASTM testing procedures. Then certain properties were simulated using the theoretical models that predict the different properties.

RESULTS AND DISCUSSION

The addition of a load to the polymer matrix produces a series of effects, among which the following can be mentioned: 1) the volume it occupies shows space discontinuity for the polymer it is crystallizing. 2) The polymer-load interface is a zone of discontinuities for the mechanical properties because of the wide properties disparity among the molecules.

A large number of properties of a loaded polymer are substantially different from the properties of an unloaded polymer. Drastic changes have been observed in the morphological structures of the polymer matrix, particularly when crystallization occurs [8,9]. These changes in the polymer microstructure are expressed through differences in the mechanical properties.

Mechanical properties of composite materials depend not only on the properties of the matrix, but also on the type of load, its concentration and the interfacial bond. In this research PP was mixed with concentrations lower than 10% load, therefore the additive does not act as a load but as a nucleating agent.

Figures 1, 2 and 3 show that Young's modulus increases as concentration of the different nucleating agents increases. The modulus of pure PP is lower than that of the loaded PP, because due to the fact that the load is a rigid substance, it presents a modulus higher than that of the polymer matrix.

Most of the models used that predict Young's modulus assume that for them to be applied there must be adhesion between load and polymer. It can be inferred from Figure 1, which represents PP modulus with talc, that although adhesion is not perfect, theoretical equations have proven to be effective at low concentrations (lower than 10%).

Figures 2 and 3, representing PP modulus with sodium benzoate and phthalocyanine, show that experimental values are higher than those predicted by the different models applied.

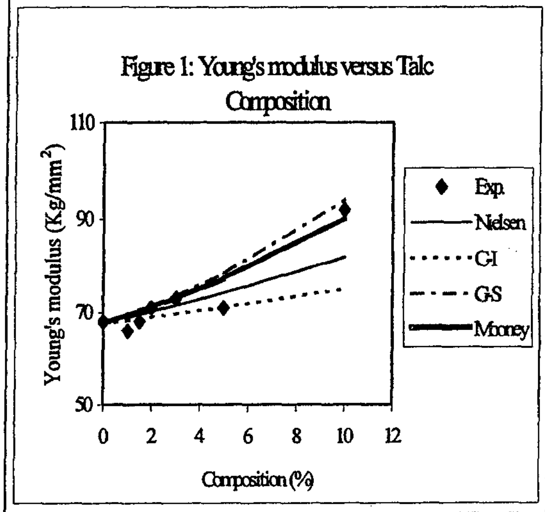
Figure 1: Young's modulus versus Talc Composition

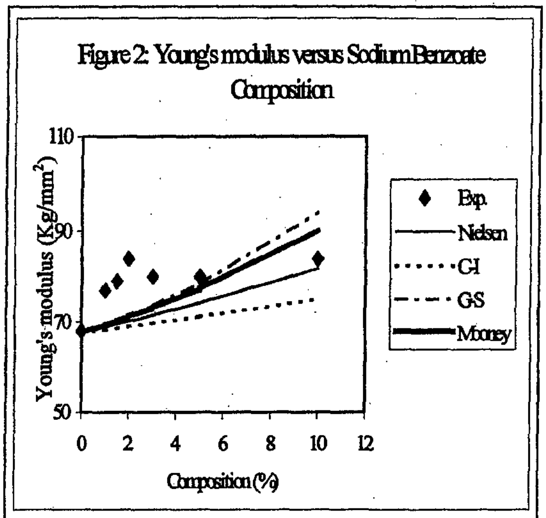
Figure 2: Young's modulus versus Sodium Benzoate Composition

The polymer modulus is affected by the added nucleating agents, because at determined concentrations they tend to form aggregates that can diminish the maximum packing volume (load) resulting in an increase in the modulus. This increase can also be attributed to the increase in the nucleation produced by the nucleating agent. When nucleation density increases, higher homogeneity and cohesion between spherulites are observed, and deformation strength of the material is therefore higher, i.e. a higher modulus. Moreover, the greater the contact between the spherulites, the fewer the empty spaces between them, and therefore the less the failure points. Hence, there are differences between experimental and predicted values, because the models applied do not consider these variables which affect Young's modulus.

Figures 4 shows both experimental and theoretical results for elongation at break. It can be observed that the experimental values corresponding to the polymer with the different loads show values up to 70% lower in comparison to the values obtained for pure PP.

This decrease is more pronounced with experimental values than with the theoretical ones. This behavior of experimental values is due to the fact that the presence of the load produces discontinuities in the stress transference, and weakening of the compound cause the fracture to occur at low elongation percentages. Also, this behavior affects the formation and grow of holes.

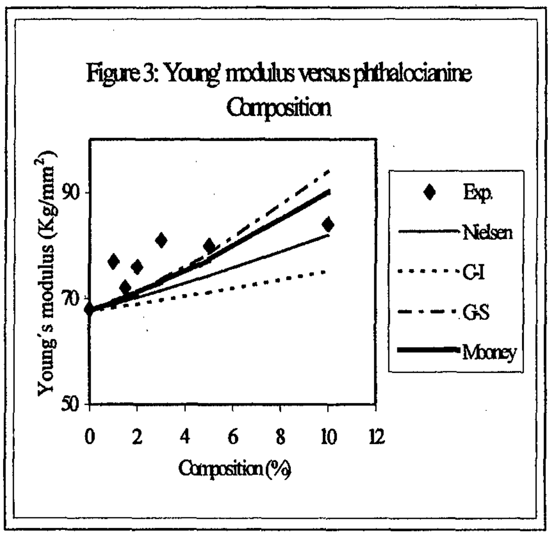
Figure 3: Young' modulus versus phthalocianine Composition

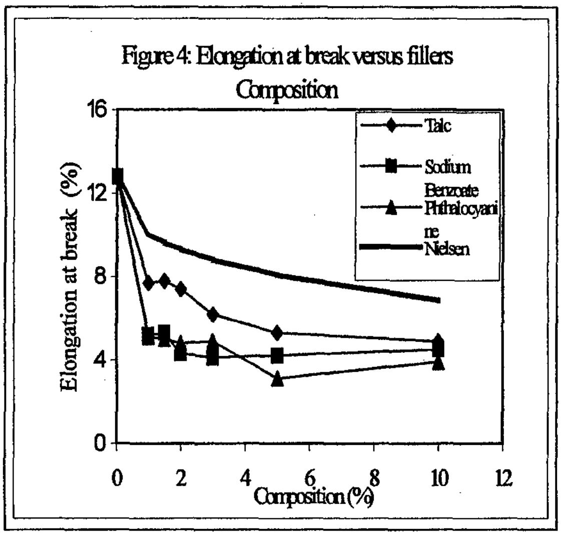
Figure 4: Elongation at break versus fillers Composition

Figure 5 presents the experimental results and the values of the different models applied to the breaking strength. It can be observed that experimental values are lower than those predicted by the different models employed, for concentrations up to 7% for all the loads used.

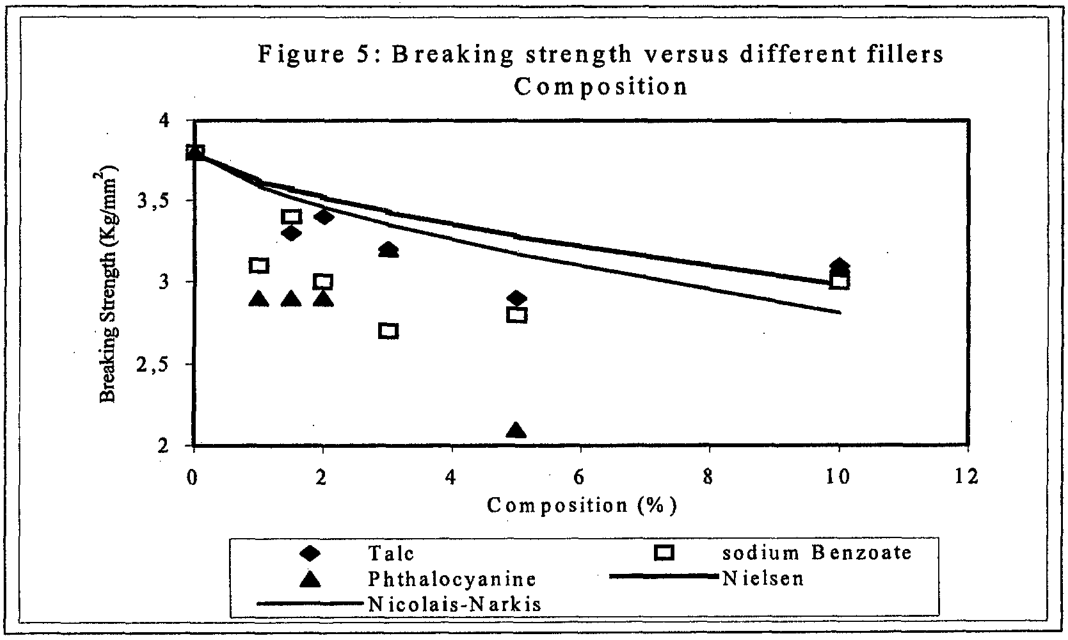
Figure 5: Breaking strength versus different fillers Composition

Field stresses near the particle are independent of its size and influence breaking strength. The polymer volume is influenced by a concentration of these stresses which increases as the size of the particle does (formation of aggregates) and, therefore, the probability of finding a greater imperfection inside the polymer volume is higher. According to the theory of Griffith [4], if there are imperfections inside the stress concentration area, breaking strength decreases.

CONCLUSIONS

Study of mechanical properties of PP blends with different loads shows that the modulus increases and breaking strength and elongation at break decreases as compared to pure PP.

The use of the models to analyze the different properties shows that there is not a good PP-load adhesion, due to the presence of holes in the interface, the stresses concentration and because the loads used are very rigid.

The applied models do not satisfactorily correlate the experimental values of the different mechanical properties analyzed, because they do not consider a series of characteristics of the polymers which can affect their solidification. Some of the most important are molecular weight and polymer crystallinity.

REFERENCES

[1] Sharma Y., Patel R., Dhimmar I., Bhardwaj I. "Study of the effect of titanate coupling agent on the performance of Polypropylene- Calcium carbonate composite. "*J. Appl. Polymer Sci.* 27, pp. 97-104 (1982).

[2] Nakagawa H., Sano H. " Improvement of Impact resistance of Calcium Carbonat filled polypropylene and propylene-ethylenen block copolymer." *Polymer Preprint.* 26, pp. 249-250 (1985).

[3] Mitsuishi K., Kodama S., Kawasaki H. "Mechanical properties of Polypropylene filled with Calcium Carbonate." *Polymer Eng. Sci.* 27(17), pp. 1069-1073 (1985).

[4] Nielsen L. E. "Mechanical Properties of Polymer and Composites." Marcel Dekker, INC, New York (1974).

[5] Maiti S., Lopez B. "Tensiles Properties of Polypropylene/Kaolin composites." *J. Appl. Polym. Sci.* 44, pp. 353-360 (1992).

[6] Guth E. "Theory of filler Reinforcement." *J. Appl. Phys.* 16, pp. 20-25 (1945).

[7] Theocaris P., Sideridis M. "The Elastic Moduli of Particulate- Filled Polymers." *J. Appl. Polym. Sci.* 29, pp. 2097-3011 (1984).

[8] Nicolais L., Narkis M. "Stress-Strain Behavior of Styrene-Acrylonitrile/Glass Bead Composites in the Glassy Region ." *Polymer Eng. Sci.* 11, pp. 194-199 (1991).

[8] Kowalewski T., Galeski A. "Crystallization of filled Polypropylene." *J. Appl. Polymer Sci.*32, pp. 2912-2934 (1982).

[9] Ronca G. " Heterogeneus Nucleation Polymer Crystallization". Brunel University. (1985).

WETTING ANALYSIS OF NATURAL SISAL FIBER WITH POLYMERIC MATRIX

H.A.AL-QURESHI and J.L.G.SILVA
Instituto Tecnológico de Aeronáutica, - CTA,
12.228-900 – São José dos Campos – SP – Brasil

INTRODUCTION

In recent years, due to the necessity for environmental protection, research has been directed towards the development of new materials. As a result, natural fibres have been the focus of interest. They have been employed as composite materials due to the low cost and density of the final product. Traditionally, sisal fibres are used as reinforcement, especially in the automotive industry.

Sisal is made up of 66-72% cellulose, 10-14% lignin, approximately 12% hemicellulose, 0.9% pectin and 10% water[1] .The relative quantity of cellulose and lignin directly influences the adhesive property of the fibre.

Generally in natural fibre reinforced composite, cellulose is responsible for the adherence to the polymer, while lignin inhibits the diffusion of the cellulose in the matrix, making the adherence of the fibre difficult, and also stopping the fibre from bonding extensively to the matrix. As a result of this, alkaline treatment on the surface of the sisal fibre becomes necessary, not only to remove grease and wax from the surface, but also to partially remove the lignin and the hemicellulose, thereby assisting the wettability mechanism.

The aim of this work was to study the wettability mechanism through surface changes in sisal fibre treated with an alkaline solution. An electron scanning microscope was utilised to calculate the angle of contact formed between a drop of the polymeric matrix (epoxy and polyester resins) and sisal fibre[2].

Other relevant properties will also be presented.

EXPERIMENTAL PROCEDURE

The present experiments were performed on sisal fibres which were initially washed in distilled water for one hour at 100°C and then immersed in 5% NaOH for a further hour at 100°C. NaOH was chosen as it did not influence the solubility of lignin, wax and grease.

Typical electron microscope images of epoxy and polyester drops on the untreated monofilament sisal fibres are shown in fig.1 and fig.2. Various geometrical measurements were taken from these images, to determine the contact angle, such as A_x , B_x and L. These values will be used to determine certain parameters given in Eq.1 and demonstrated in Table 1. A similar procedure was used for sisal fibre treated with NaOH. Experiments were also performed on tensile test laminate specimens produced from these fibres using conventional hand lay up (vacuum bag technique), to determine the mechanical properties[3] .

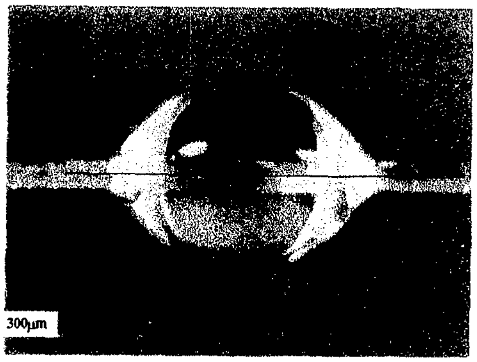

Fig.1 Photograph of epoxy resin resin drops attached to monofilament sisal fibre (treated NaOH 0%).

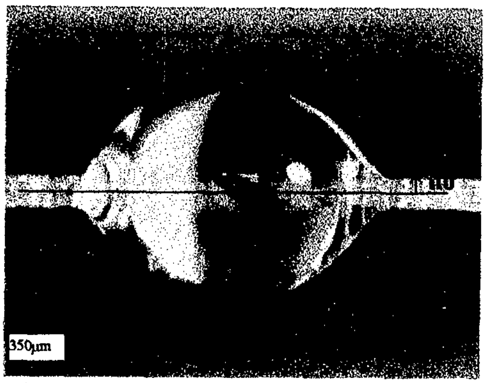

Fig.2 Photograph of polyester resin drops attached to monofilament sisal fibre (untreated NaOH 0%).

RESULTS AND DISCUSSION

Scanning Electron Microscope

Close examination of Fig.3 showing sisal fibre without any chemical treatment demonstrates the existence of electrons that cover the surface. These are possibly due to the formation of lignin, hemicellulose, wax and grease. The results caused by the alkaline treatment of the sisal fibres are shown in fig.4.

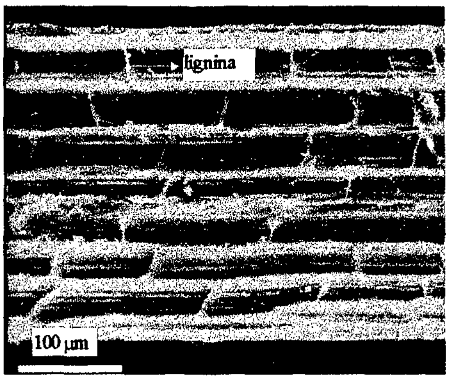

Fig.3 Sisal fibre without any chemical treatment

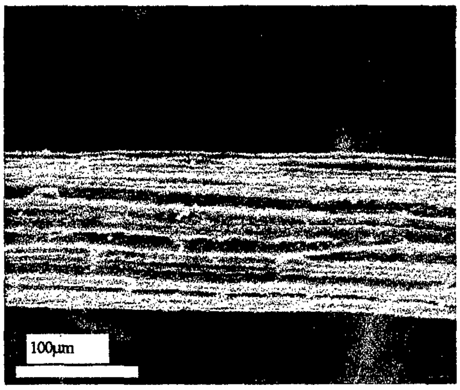

Fig.4 Sisal fibre with chemical treatment (NaOH 5%)

On comparison of the micrographs of Figs. 3 and 4, the surface changes caused by chemical treatment can be seen clearly. The surface elevation (fig.3) diminished considerably with the 5% NaOH (fig.4), from which the microfibres forming the sisal fibres can be seen clearly. Therefore it can be said that 5% NaOH treatment on sisal fibre, removed the superficial layer which covers the fibres.

Figs.5 and 6 show behaviour of a liquid drop of epoxy and polyester resin formed in a sisal fibre filament. From Figs. 5 and 6, is clear that the contour parameters (h_1 , L) can easily be measured. The parameters are used in Eq.1 to evaluate the contact angle[2].

$$\frac{d^2h}{dx^2} = -k\left[1+\left(\frac{dh}{dx}\right)^2\right]^{\frac{3}{2}} + \frac{\alpha^2}{h}\left[1+\left(\frac{dh}{dx}\right)^2\right]$$

eq.1

On closer examination of the values given in Table 2, it becomes evident that the length and height of drop vary inversely as the fibre is treated, see Figs. 5 and 6.

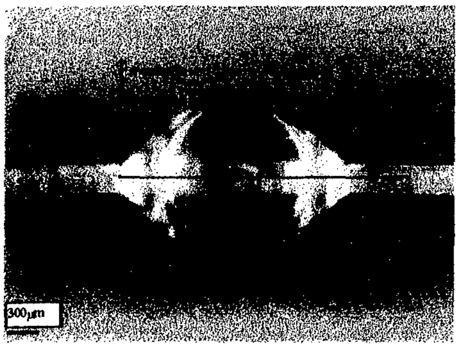

Fig.5 Liquid drop of epoxy resin formed in the sisal fibre treated with 5% NaOH

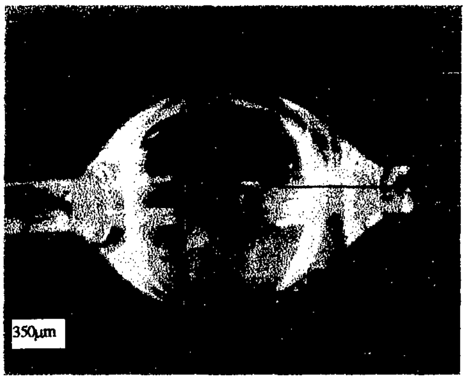

Fig.6 Liquid drop of polyester resin formed in the sisal fibre treated with 5% NaOH.

The inverse proportionality, is attributed to the fibres free surface energy, that is, as the sisal fibre was treated in alkaline solution of 5% NaOH, a larger proportion of the active sites were created on the fibre surface. Consequently, the surface free energy was increased, probably due to the decrease of either the height of drop (h) or the contact angle (table 1).

Table 1. Estimated contact angle between epoxy resin and monofilament sisal fibre (treated and untreated (0%)), polyester resin and monofilament sisal fibre (treated and untreated).

Solution NaOH (%)	Resin	L mx10^{-6}	h_o mx10^{-6}	h mx10^{-6}	(A_x / B_x) "α"	Angle θ
0	Epoxy	1830	105	690	0,592	47
5	Epoxy	1920	112	606	0,655	34
0	Polyester	1927	114	694	0,652	48
5	Polyester	1620	112	540	0,592	36

Mechanical Tests

Close examination of values given in Figs. 7 and 8 reveals that treated sisal fibre (5% NaOH) composites showed better tensile and flexural properties than untreated sisal fibre (0% NaOH) composite. It can be concluded that treated sisal fibre exhibits better wettability than untreated sisal fibre.

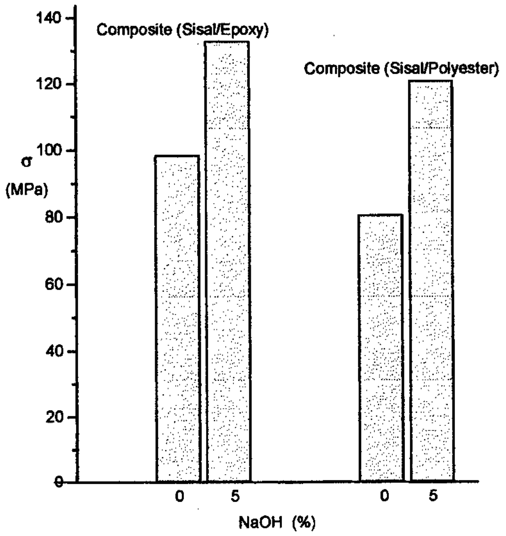

Figure 7. Tensile Strength of Sisal Fibre Composite

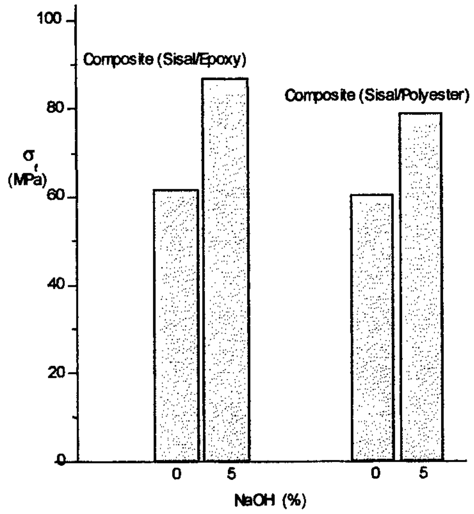

Figure 8. Flexural Strength of Sisal Fibre Composite

CONCLUSIONS

Analyses using an electron scanning microscope demonstrated that the chemical treatment removed substances from the surface (lignin) of the sisal fibre, which produced an improvement in the wettability property. The wettability tests, using values obtained for contact angles, can be expressed mathematically for fibres that have elliptical transverse section. These results demonstrated that smaller angles of contact can be obtained as a result of wettability. Consequently the rigidity and resistance of a laminated composite made from these fibres would demonstrate improved performance compared to composites using untreated ones.

REFERENCES

[1] KUMAR,R.P.; AMMA,M.L.G.; THOMAS,S. "Short Sisal Fiber Reinforced Styene – Butadiene Composite"; J. Appl. Poly. Sci., n.58, p.597-612, 1195.

[2] Silva,J.L.G.; AL-Qureshi,H.A, "Mechanics of Wetting Systems of Natural Fibers with Polymeric Resin", Proceedings of the Congress of Advances in Materials and Processing Technologies, AMPT'97, University of Minho, Guimarães – Portugal, 1997.

[3] AL-Qureshi, H.A., "16th Canadian Congress of Applied Mechanics – CANCAM – 97, Laval University, June 1-6, 1997.

DuPont's Aramid Fibers for Advanced Composite Materials

"From Past Experiences and Recent Developments to Future Applications".

René Pinzelli and Danielle Blomert

Advanced Fiber Systems. DuPont de Nemours Int,. SA. Geneva (CH).

1-Introduction.

During the last 20-25 years KEVLAR® brand fibre, and NOMEX® brand paper have been used for the production of numerous advanced composite parts or articles in many sectors: aerospace, defence, but also marine, automotive, sporting goods and other industrial applications.

This article briefly reviews key features and benefits of these two DuPont's products and provide examples of their uses in traditional advanced composite applications. The latest developments in terms of products (fibre and paper) are presented along with more recent applications and emerging new end-uses.

2-The Chemistry of KEVLAR ® and NOMEX®.

KEVLAR® is a para-aramid and NOMEX® a meta-aramid. Respectively invented and commercialised in 1965 and 1961, they are named aramids because their polymeric structures consist of a chain in which 85 % of the **amide** functional groups(-NH-C=O), are directly bonded to two **aromatic** benzene rings. The polymers used for the production of these **aramid** fibres are obtained by a poly-condensation between aromatic di-amines and aromatic acid chlorides. The molecular geometry of these two raw materials, explain largely the high strength of the para-aramid fibre KEVLAR® and the excellent thermal properties of the meta-aramid fibre NOMEX®, amongst other valuable characteristics used in many industrial applications.

3-The production of KEVLAR® and NOMEX®.

For KEVLAR®, the solution of the para-aramid polymer in concentrated sulphuric acid is an-isotropic and behaves like a liquid crystal. Its extrusion at high pressure through a spinneret results in highly orientated chains. The fibre is consolidated via a cold water quench, then washed, neutralised, and finally wound onto a bobbin.

This first step results in a high strength, low modulus fibre. The high modulus fibre known as KEVLAR® 49 is produced in a subsequent step during which the fibre is stretched under heat. For composite applications KEVLAR® 49 exists as yarns, and rovings of various decitex made of continuous filaments of 12 microns in diameter.

For composite materials, NOMEX® is not used as continuous fibre, but rather as paper, which in turn is the basic ingredient for the production of honeycomb cores. NOMEX® paper is produced from a combination of short-cut fibres and fibrils of NOMEX® fibre. These two constituents are brought together into a fibre/film hybrid sheet in a wet paper forming operation.

® DuPont's Registered Trademarks

The honeycomb cores for sandwich composite structures, are made by carefully placing parallel lines of adhesive on the flat paper sheets. The sheets are stacked together, then pressed and cured at high temperature and the resulting block is expanded so the adhesive-free areas open to form hexagonal cells. The expanded block then goes through a number of dips in phenolic resin, which are followed by oven curing cycles. These operations are continued until the honeycomb block reaches the desired density. Then the block is cut into sheets of the required core thickness.

4-The properties of KEVLAR® and NOMEX® for composite material designs.

4.1-The properties of KEVLAR®.

Below are presented the most relevant properties of KEVLAR® as continuous fibre reinforcement and of NOMEX® in a form of honeycomb cores for sandwich constructions.

The most common forms of reinforcing materials made of KEVLAR® are yarns, rovings (assembly of multiple ends of yarns), fabrics and unidirectional tapes. The yarns and rovings are used mainly for filament wound composite articles, and the fabrics or tapes for wet-lay-up, but also for materials pre-impregnated with epoxy, (so-called "prepregs"), for heat formed vacuum bag molding components.
In table 1 are summarised the major physical properties of KEVLAR® 49 in various forms: fibre, resin impregnated strands, unidirectional and fabric laminates.

Hybrid composites, in which two different reinforcing fibres are "jointly" used, are to composites what alloys are to metals. The properties of the hybrid reinforcements and therefore those of the composite materials made from it, are a compromise between those one gets if the reinforcing fibres were used separately, but in addition, each separate component is able to fulfill specific functions and provides additional benefits. For instance, when KEVLAR® and carbon fibres are used in hybrid composites, (the ideal volume ratio being 30:70), KEVLAR® copes with the damages created during processing (drilling and cutting) or in service (impacts), thus compensating for the brittle nature of carbon fibre. This concept is widely used in the aircraft industry as well as in marine and sporting goods related industries, as it enables the design engineer to get an optimum compromise between the technical and economical requirements.
The tensile modulus of hybrid composites follows the rule of mixture, as it is proportional to the content of each respective fibre used as shown in figure 1.
Figure 2 illustrates the benefits of using KEVLAR® in some parts for which carbon fibre has been selected for its high stiffness, but for which one needs to address the possible damage due to impacts, etc.

4.2-Other specific characteristics of KEVLAR®.

Though the bare fibre is sensitive to UV light, due to its organic nature, composites based on KEVLAR® on the other hand are not, as the fibre is protected by the resin around it, and by many others constituents such as paints, etc. Had this phenomenon been a real concern, KEVLAR® would not be used today in the aircraft industry for external components.

Table1: Physical properties of KEVLAR® 49 - Fiber and composite materials.(1)

Reinforcement	Fiber	Roving (2)	Unidirectional RT	 120 .C	Fabric
Tensile strength (MPa)	2760	3620	1380	1170	550
Tensile modulus (GPa)	120	130	80	65	30
Elongation at break (%)	2.1	2.5	--	--	--
Compressive strength (MPa)	--	--	275	220	170
Compressive modulus(GPa)	--	--	80	65	30
Shear strength(MPa)	--	--	45	33	28
Fiber volume (%)	--	--	60	60	45
Density (g/cm3)	1.44	1.44	1.38	1.38	1.33

(1) for epoxy resin matrix. (2) as per ASTM D-2343 Epoxy impregnated strand.

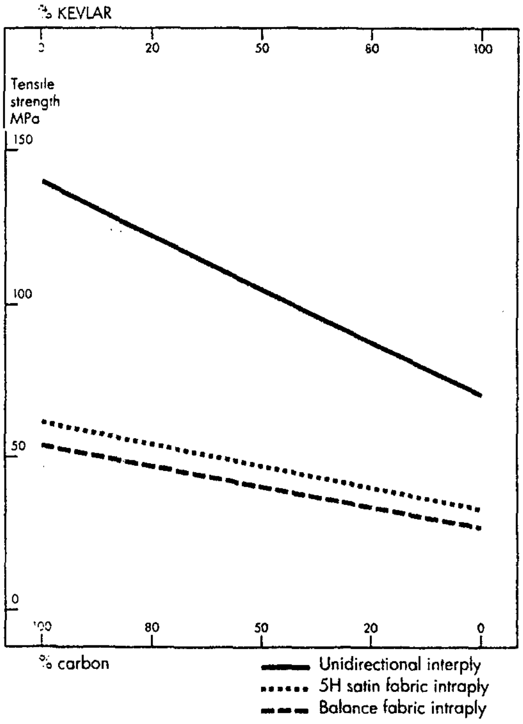

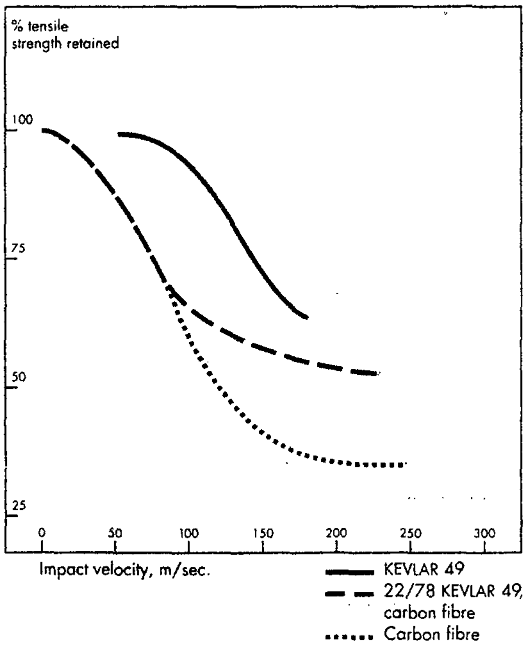

Figure1:Tensile modulus of hybrid laminates of KEVLAR® and Carbon.

Figure2:Residual tensile strength of quasi isotropic laminates after steel ball impact.

® DuPont's Registered Trademark.

The same argument can be used to address concerns one may have with respect to the moisture regain of KEVLAR®, specially when compared to other fibres such as glass and carbon. The moisture regain of KEVLAR® 49 is around 2 to 3 %. Considering that the equilibrium moisture level of the matrices used such as epoxy and polyester resins are of the same magnitude, the drying of the fibre before impregnation is in most cases neither required nor justified. Except for filament winding fabrication technique, when an acid anhydride is used to react with the liquid epoxy resin, and for which it is recommended to dry the fibre before impregnation, all the epoxy and polyester resins systems do not require pre-drying of the reinforcement.

As for high modulus aramid fibre, when compared to other fibres, the larger difference between the axial and the longitudinal thermal expansion coefficients, has led to the formation of resin micro cracks. This may occur for example, when the composite part is submitted to sudden and frequent changes of temperature, such as when an aircraft reaches fairly quickly an altitude of 30,000 feet. Consequently, when designing sandwich constructions based on honeycomb cores, one should use a sufficient number of plies, in order to avoid the subsequent migration of water or hydraulic fluid into the cells. This advice is equally valid for any fibre.

In the early days of composites reinforced with KEVLAR®, many have encountered difficulties with the cutting of the dry reinforcement or the cured laminates, and with their machining or drilling. Since that time, appropriate tools and methods have been developed and give satisfactory results, and information available.

4.3-Properties of the honeycomb core made of NOMEX® paper.

Sandwich composite constructions consist of a low density core separated by thin and stiff faces called skins. Under load the core is submitted to shear forces, and the skins will carry in-plane compressive and tensile loads.

These sandwich constructions, especially when NOMEX® honeycomb core is used, have a high strength for a minimum weight compared to other cores, a very attractive attribute in weight-sensitive applications. Shear and compressive properties of NOMEX® honeycomb core are presented in figures 3 and 4.

Because of its non-metallic nature, NOMEX® avoids galvanic corrosion, and provides a good resistance to impacts compared to aluminum core. Also, due to their good resistance to heat, sandwich panels based on NOMEX® core and skins of glass fabric and phenolic resin, meet the stringent fire resistance, smoke and toxicity requirements for interiors of aircraft and rail cars.

5-Recent Product Developments.

From the para-aramid polymer, DuPont produces KEVLAR® in many forms:

-high strength, low modulus (69 GPa) continuous yarns for ballistic protection, tyres, ropes, high pressure hoses.

-high strength, high modulus (125 GPa) continuous yarns and rovings for composite materials and for reinforcing elements of fibre optic cables.

-pulp for friction products such as brake pads, gaskets, and as staple for protective apparel, in particular cut and heat resistant gloves.

Figures 3 and 4: Comparison of Compression and Shear Strengths of Core materials.

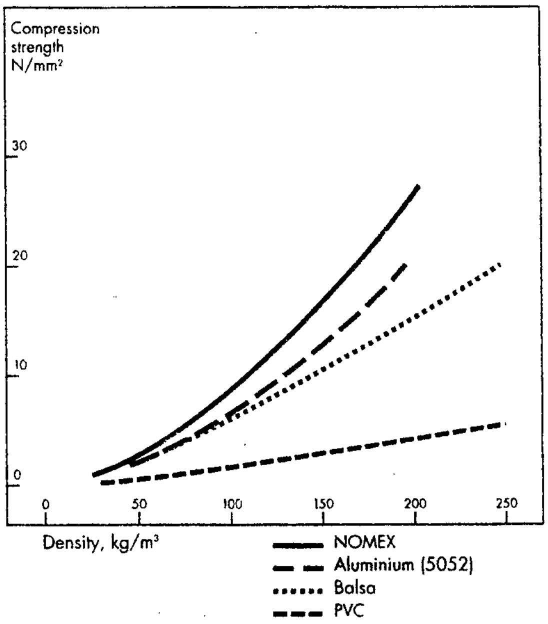

Figure 3: Compression strength

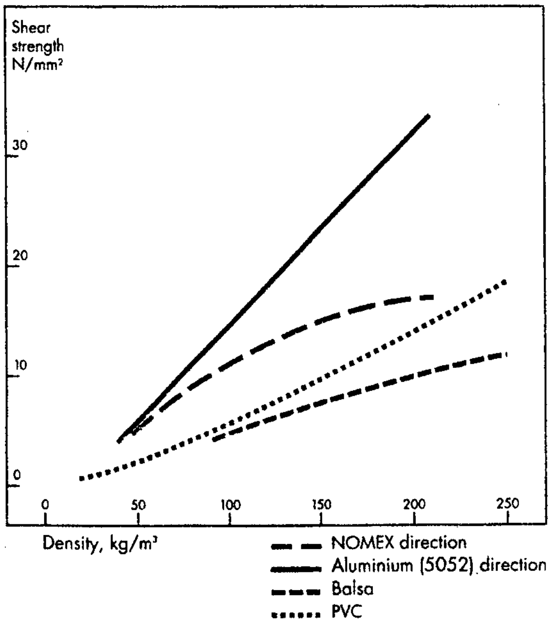

Figure 4: Shear strength.

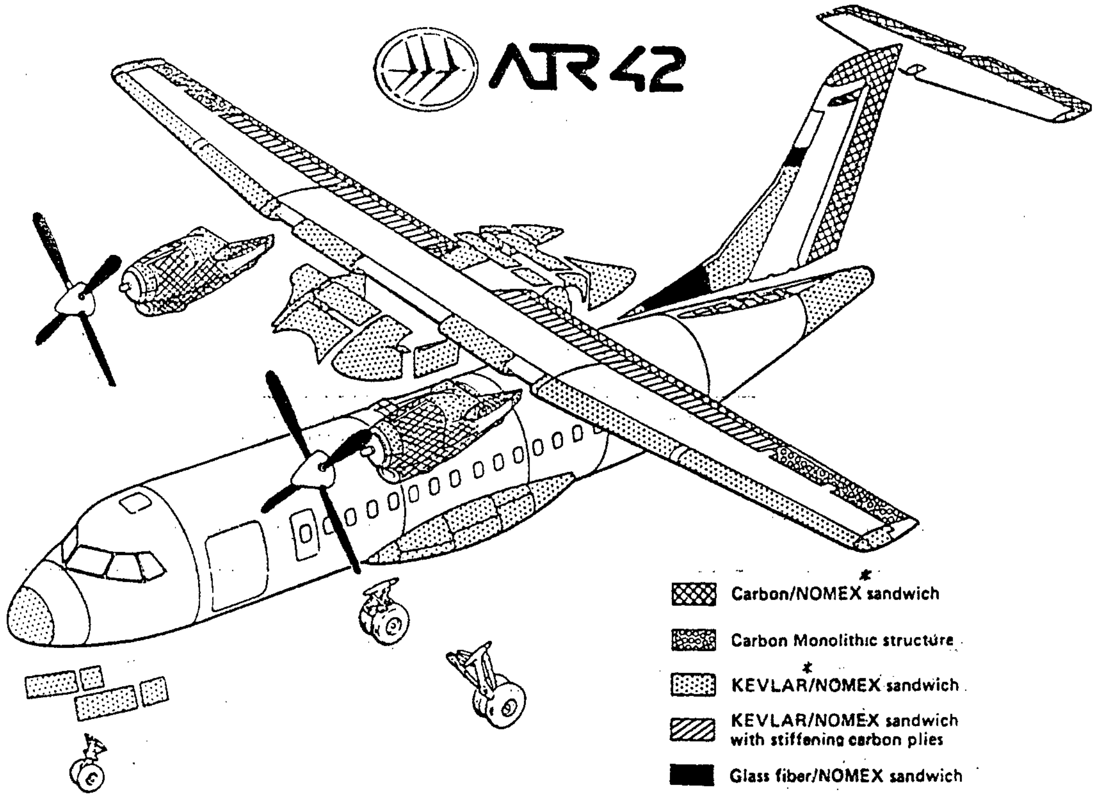
ATR 42
Carbon/NOMEX* sandwich
Carbon Monolithic structure
KEVLAR*/NOMEX sandwich
KEVLAR/NOMEX sandwich with stiffening carbon plies
Glass fiber/NOMEX sandwich

Figure 5: Composite materials in the ATR 42 Aircraft.(Document Aerospatiale -F).

®DuPont's Registered Trademarks

The properties of KEVLAR® can be modified by changes and/or improvements of, 1) production parameters, 2) spinning technology, 3) the structure of the polymer. Possibilities to make such a changes are limited tough, as a new fibre will be accepted by the aircraft industry only after expensive qualification programmes.

Recently, with a new spinning technology, the tensile strength of standard KEVLAR® 49 has been increased by 25 %. The new fibre named KEVLAR® 49 HS has been developed primarily for filament wound composite applications, especially for the production of light high pressure(200-300 bars) composite bottles and cylinders such as breathing apparatus, Natural Gas Vehicles, and transport of industrial gases.

With respect to aramid paper, DuPont has developed a new paper for a high performance core called KOREX®. This has been in response to requirements from the industry for honeycomb core material similar to NOMEX®, but with improved stiffness. KOREX® is a saturable aramid/phenolic core. “Saturable” means that the web material is impregnated with the dip resin rather than just being coated with it. The stiffness in shear and compression of KOREX® is twice that of core made with NOMEX® and compares favorably with those of core made of bias weave of glass fibre and phenolic resin. In addition, it has a lower equilibrium moisture content.

6-Applications of NOMEX® and KEVLAR® in composite materials.

The first adoptions of NOMEX® and KEVLAR® in advanced composites occurred in the early 70’s in the aircraft and aerospace sectors, thanks to the urgent need to save weight for meeting performance requirements and/or for reducing fuel consumption.

NOMEX® started its career in honeycomb composite structures more than 25 years ago, when aircraft producers decided to lower the weight of the floors, which at that time were made of balsa core and aluminum skins. A honeycomb core was selected but it had to be non-metallic as it was decided to use face skins made of carbon fibre. Carbon fibre had been produced especially for the composite fan blades of the RB-211 jet engine, but replaced in the end by heavier titanium due to fatigue problems.
Since then, the low weight, good compression, shear, impact and fire properties of NOMEX®, and the absence of galvanic corrosion, have allowed the aircraft composite designers to use this non-metallic core for many different components(see figure 5):
-for the interiors: side wall and ceiling panels, luggage compartments, galleys, floors for passengers and cargo areas.
-for the exteriors: flaps, fairing panels, rudders, elevators and radomes.
Cores made of NOMEX® paper are also used for blades, and many other parts of helicopters, some of the parts being classified as primary structures.
NOMEX® honeycomb cores has also been adopted for interiors of high speed trains such as the Pendolino of Fiat, ceiling panels for tramways of Bombardier, floor panels for metro cars of BART (USA), and for the double-decker shuttle tourist cars of the Trans-Channel trains between France and England. Competition maxi-sail boats for events such the America’s cup use core made of NOMEX® paper in the hulls. High performance cross country skis of renowned producers like Rossignol and Atomic, are also based on this light and high strength honeycomb core.

In the early 80's KEVLAR® 49 was adopted for the production of many internal and external components for new jet and propeller engines aircraft as well as for helicopters, often in reinforcing skins for sandwich composite constructions based on NOMEX® core. In many cases KEVLAR® was used in hybrid composite structures with carbon fibre in order to provide the required damage tolerance, in addition to the valuable weight saving. Today, KEVLAR® is still used in the aircraft industry, but due to its modest compression strength, it has been excluded from primary structures such as vertical stabilisers, elevators, rudders and other heavy-loaded components.

The high specific strength of KEVLAR® has been utilised for the production of weight-sensitive articles such as filament wound launching tubes, rocket casings, fuel tanks and aluminum lined composite pressure breathing bottles and cylinders.

KEVLAR® has been, and continues to be successfully used with glass fibre in hybrid reinforcements for marine applications, in hulls and in superstructures, especially when weight is critical as for patrol boats and for large yachts. The hybrid reinforcement offers to the shipyard a cost effective solution to achieve increase performance (speed) while retaining ease of lamination of the composite structures.

In sport articles such as alpine skis, tennis rackets, bicycle frames, KEVLAR® protects carbon fibre from local damages, acts as vibration dampening element. In addition, the name KEVLAR® is often utilized as a marketing promotional tool, a practice DuPont has began to control, and will authorise as required to avoid miss-uses.

The most relevant example of use of KEVLAR® in sport articles, is that of canoes and kayaks, for which the high strength and impact resistance are highly appreciated during both leisure and competition activities, so is its light weight when it comes to carrying the canoe or the kayak to and from the water.

7-New and future applications

NOMEX® as honeycomb core is mainly used for aircraft composite applications, and recently adopted for fast trains where it is in competition with other cores. For marine applications, DuPont is conducting a test programme towards the design of a cost effective sandwich panel system to be used for cladding and partition walls in fast passenger ferries, that can meet fire and thermal standards for fire restricting materials. NOMEX® DECORE® consists of sandwich panels based on a honeycomb core of NOMEX® and thin skins of ply wood. These panels are commercialised for furniture for leisure boats, and are up to 60 % lighter than solid ply wood. A specific and easy fabrication method has been developed to take into consideration the nature of NOMEX® DECORE® versus ply wood.

For KEVLAR®, there are two emerging new applications, both taking advantage of the high specific strength and impact resistance properties. These are: 1) high pressure composite cylinders for Natural Gas Vehicles(NGV), and for storage of industrial gases such as hydrogen, helium, and 2) reinforcement of concrete structures.

- Composite pressure cylinders.

The existence of large reserves of natural gas, and the need to reduce pollution created by vehicles running on diesel oil in large cities, are expected to result in increased demand for pressure tanks. Because of the heavy weight of metallic tanks, the demand for light composite pressure cylinders will be growing. Amongst the fibres which can be used to produce fully wrapped aluminium or thermoplastic lined composite cylinders, KEVLAR® 49HS will play its role due to its high specific strength and its notorious damage tolerance. Also, the adoptions of composite pressure cylinders for storage of industrial gases such as hydrogen, carbon monoxyde, will create additional business opportunities.

- Reinforcement of concrete structures.

The earth quakes which have occurred in California, in Japan, and more recently in Italy, have accelerated the adoption of composite materials both for strengthening and repair of concrete structures.

Over the last years one has seen the use of carbon fibre in pultruded laminates, as replacement of metal sheets in the so called plate bonding technique. This technique has been used around the world for some time. Unfortunately, there are many situations where this type of strengthening is not appropriate, such as adjacent to electrical and communications facilities. For such applications steel and other conductive reinforcement can contribute both to the risk of fire and the breakdown of communication lines.

The adoption of KEVLAR® expands the scope of deployment for bonded reinforcements. The ability to wrap KEVLAR® around circular columns and beams, for example, is an extremely efficient and cost-effective means of repair and support, which cannot so easily be achieved with metal components. Unidirectional tapes of various widths are impregnated with cold curing epoxy resin system, and wrapped around concrete structures requiring strengthening. The resulting laminated composite wall provides high strength, high tensile modulus, and a good resistance to impacts and damages.

This practical repair technique is faster than conventional repair methods, which are often disruptive, require demolition and bring additional disposal costs.

KEVLAR® has already been successfully used in Japan for repairing office blocks, piers of bridges, chimneys, and many other structures.

8-Requests for relevant documents on KEVLAR® and NOMEX®.

The reference list for relevant technical and commercial documents covering the uses of KEVLAR® and NOMEX® in composite applications, is too long to be included in this paper. Readers wishing to obtain from DuPont specific technical information on the design, fabrication, cutting and machining of composite materials based on KEVLAR® and NOMEX®, are encouraged to contact one of the authors of this review at the address below:

DuPont de Nemours International SA., Advanced Fiber Systems, 2 Chemin du Pavillon
1218-Le Grand Saconnex-:Geneva- Switzerland.(or by fax :00 41 22 717 62 18).

LAYERWISE REINFORCEMENT OF CARBON FIBER TRIAXIAL WOVEN FABRICS

Y. Sato

Gifu Prefectural Textile Research Institute ,Kitaoyobi 47, Kasamatsu, Hasimagun, Gifu pref, Japan.

1. INTRODUCTION

Triaxial Woven Fabric(TWF) was originally developed as base-material for space by NASA , it have high performance with carbon fiber.

How-ever in the case of molding laminated FRP , layerwise strength depends only on matrixes resin as well as regular fabric .

Nearly year at our research person even though laminated CFRP , are textile with a jet stream with the upper side , throw oneself for,non-woven fabric and TWF , and raised a strength for a layer of 70%.(1) For with this method ,it have taken time to throw spot with wide area and were necessary treatment water after task.

Here , I develop the method to make use of easily flocky technology and report the result.

2. EXPERIMENT

2.1 TWF weaving.

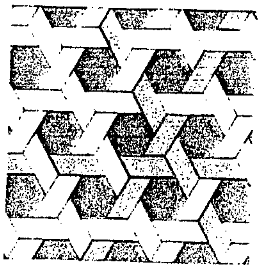

Fig1 Basic formations

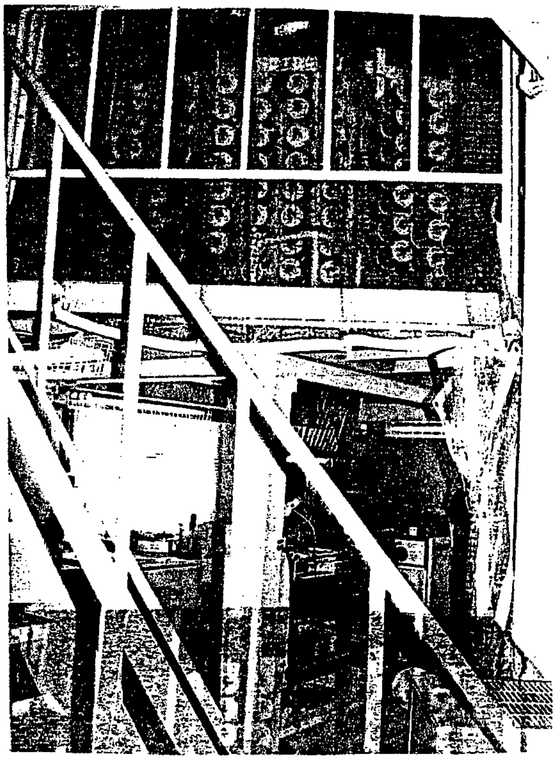

Fig2 TWC32C Machine

TWF weaving Table1 condition for a carbon fiber with a machine (Fig2)

Table1 TWF weaving condition

Machine	Howa Machinery LTD made TWM32C (Fig2)
Weaving speed	30 RPM
Formation	Basic (Fig1)
Filament	Torayca T300-1000

2.2 Layerwise reinforcement by flocky.

As basic formation of TWF have a large hexagonal gap ,it use to layerwise reinforcement. With a pre-experiment using a nylon pile , it can clearly throw a fiber itself into gap by flocky. However , a fiber suitable for flocky are conditions both an electric resistance and appropriate balance of length and thickness.

Though one doesn't become a problem case of a carbon fiber, another shows the condition Table2.

Table2 Most suitable for flocky length and thickness(2)

Length(mm)	Thickness(Denier)
-0.5	- 1.5
0.5-0.8	1.5 - 3.0
0.8-1.2	3.0 - 5.0

With this length and thickness are a ratio , because a pile not to get entangled.
In this condition, fiber length must be the worst less than 0.5 mm,in order to be 0.6d(T300) for a carbon fiber on the market. However,a fiber like a powder can't enough to reinforce Z-axis and we can't easily make a more thick carbon fiber.
Fig3 flow experimented as a fiber doesn't get entangled there.

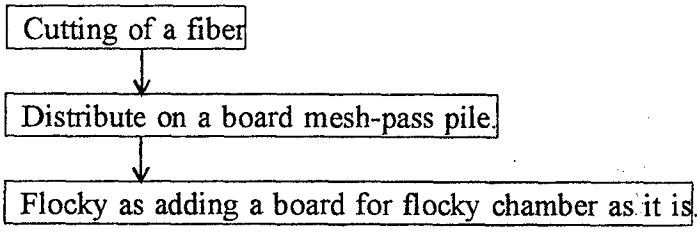
Cutting of a fiber
Distribute on a board mesh-pass pile.
Flocky as adding a board for flocky chamber as it is.

Fig3 Flocky flow

Show the condition for a Table4

As carbon fiber is well electricity, it occurs spark by short-circuited prevented a connection with an intermittent operation .

I left the object to make flocky in the incubator to be stiff epoxy resin 150 ℃ 2 hours.

Table4 Carbon pile flocky condition

Basis Sheet	PTFE SHEET
Volt	30 kV
Interval distance	10 cm
Glue	Epoxy resin Paint thickness 0.7mm by bar coat
Method	Up method intermittent operation (5-2sec on-off)
Time	180 sec

I made CFRP with a fig4 method and with a table 5 condition and molded as clipping PTFE film for a strength test for a layer.

Table5 Condition of CFRP make

Hot-press		Epoxy resin		rate
Pressure	980 kPa (10 kg / cm ^{2})	Main	Epicote828	100
Temp	150 ℃	Stiffness	Kayahard-MCD	80
		Stiff furtherance	Daito HD-acc-43	5

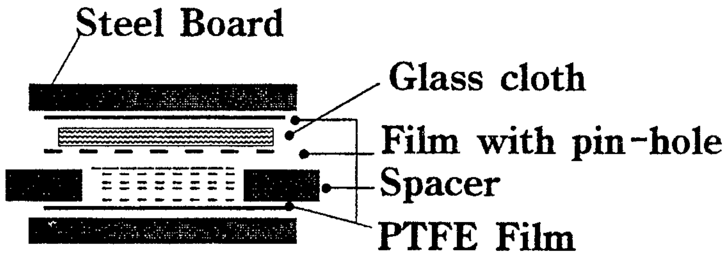
Steel Board
Glass cloth
Film with pin-hole
Spacer
PTFE Film

Fig4 Make CFRP (3)

2.4 Flocky with long carbon piles.

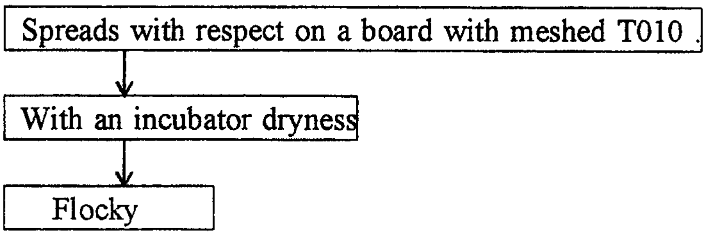
Spreads with respect on a board with meshed T010 .
With an incubator dryness
Flocky

Fig5 Long C pile flocky Flow

If a thick object can using CFRP board,it is a shortage with 1 mm. I examined it about the ready-made(T010-003) to cut T300 for 3 mm. As T010 have moderate moisture 5% ,the fiber stream is good, however when I make flocy as it is ,I wasn't able to make flocy almost without very small amount flew. I thought that moisture greatly passes and a method to remove moisture keeping a stream and make flocky.
I was able to make flocky well for this.

2.4 Reinforcement performance test
In order to confirm a CFRP of layer reinforcement strength ,I cut an piece with a diamond cutter., And after adding an introduction crack with a knife,it was made exfoliation test by universal tensile machine(Table5). In that case , an exfoliation direction tried to get certain , as inventing tool to show for Fig6.

Table5 Exfoliation strength tests

Layer number	8(4+4)
Test machine	Auto Graph(Shimadzu LTD)
Test pace width	25mm
Test speed	50mm/min

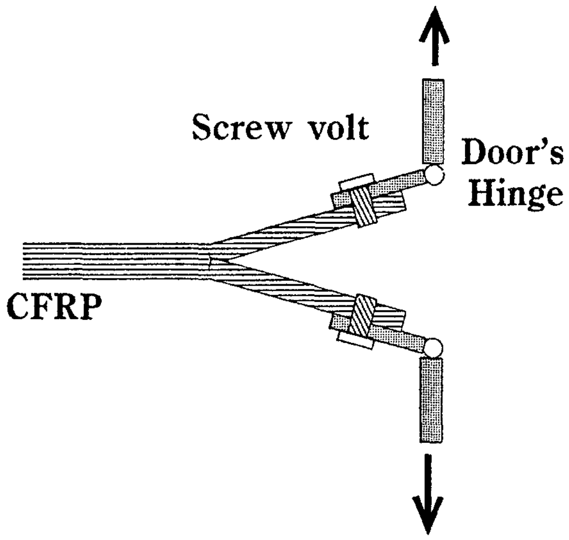

Fig6 Exfoliation tool for a layer

3. RESULT

3.1 Result of testing a layerwise reinforcement
Result of testing an exfoliation strength(Fig 7)
Compare max value ,it was made improvement in strength about 2times.
Though a blank showed typical layer exfoliation phenomenon, however, one of

reinforcement materials occurred break of base materials from introduction crack of a knife at once

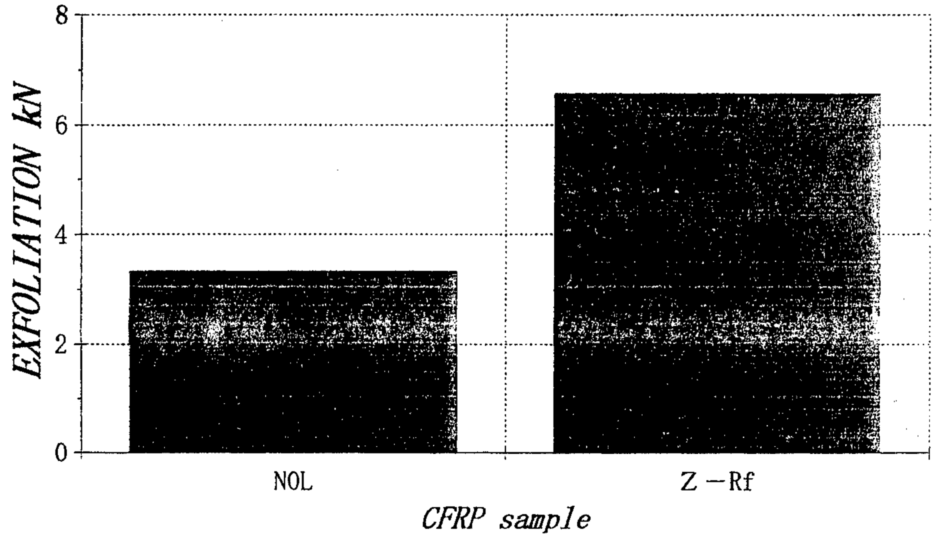

Fig7 Result of Exfoliation Strength..

The break part with an microscope show it for figure 8 and 9.

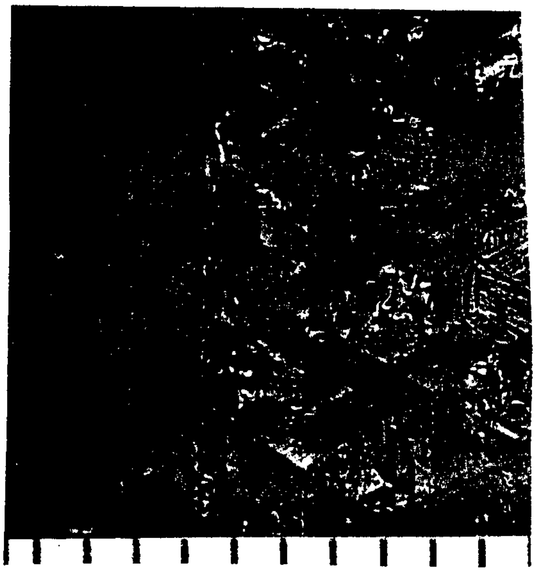
Fig8 Exfoliation Aspect of a Blank

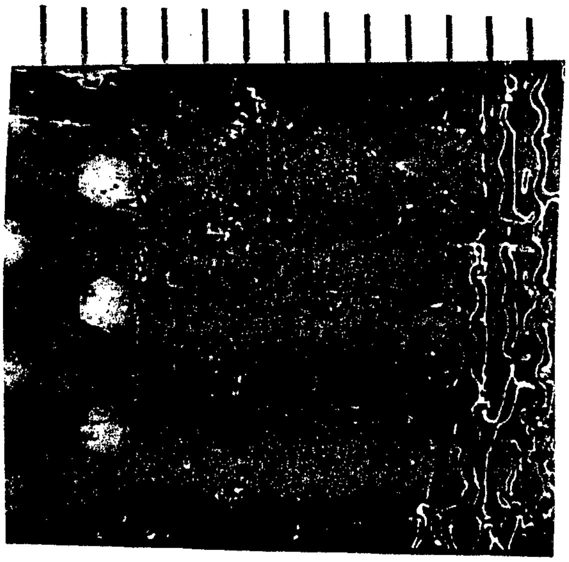
Fig9 Exfoliation Aspect of Reinforcement materials

By a microscope photograph of Fig8 and 9 a blank shows a beautiful tear section as leaving resin here and there , reinforcement materials ,the fiber remains as it is to have thrown itself into base materials except a portion of an introduction crack of a knife ,and it is guessed what it can reinforce steadily. I thought that an exfoliation strength will be really more great , 2-times numerical value was teared by a bend of base materials.

Though a tensile test itself of a carbon pile , differ from Z-axis of a direction as pulling , an approximately 30% strength improved. An advance of a crack is thought to be defended, as reinforcement materials is stuffed with a fiber.

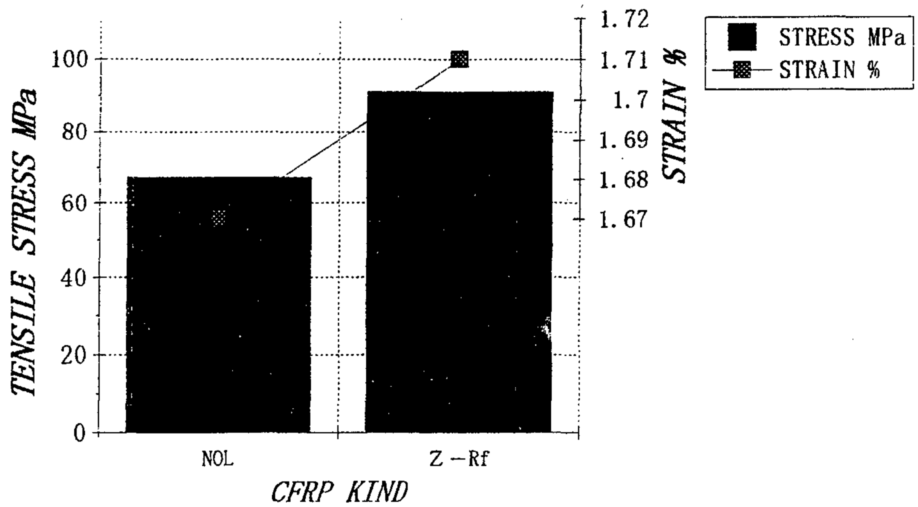

Fig10 Result of Tensile Strength.

REFERRENCE

1)K.Kawada :Gifu Prefecture Textile Research Institute report No.17, p33-37, 1994.

2)N.Iinuma:Fact of flocky processing, Koubunsikannkoukai co.LTD,p328-329,1985.

3)K.Matui:Expansion and evaluation method of a carbonic fiber,Realize INC,p292-297,1989.

COMPOSITE MATERIALS FOR WEAR RESISTANCE COATINGS USING THERMAL SPRAYING

S. Steinhäuser[1], B. Wielage[1] ,T. Schnick[1], A. Ilyuschenko[2] and T. Azarova[2].

[1]Institute of Composite Materials, Technical University, Chemnitz, Germany
[2]Powder Metallurgy Institute, Minsk, Republic of Belarus.

INTRODUCTION

The surface properties of structural units extremely influence their behaviour. In many cases the structural units are stressed in the surface range by a combination of mechanical, tribological, corrosive and thermal influences. The stress of materials causes a degradation of properties or even damages. Under these circumstances the deposition with coatings especially with composite coatings, is an effective surface protection - also applicable to composite materials. These deposits can be coated on steel, light metals, ceramics, plastics and others. The composite coatings consist of a matrix with, as a rule, nonmetal solid particles or - on a small scale - short and long fibres (Figure 1). These second phases are incorporated during the growth of the coating or later created inside the coatings (e. g. precipitation hardening). So the powders as well as the coatings can be composite materials.
The composite coatings depending on application consist of a matrix and various dispersal phases (see Figure 1). Material and structural interactions of different constituent phases induce modified composite properties. The dispersal phases can change the coating structure and the coating properties as well as the surface properties and the materials bond. Composite coatings are used for the primary coating and for repair coating. They effect

- increase of strength and support effect (hard phases in a tough matrix)
- formation of zones sensitive to absorb or scatter energy, relax stress and divert, catch or bridge cracks
- improvement of tribological properties (wear reduction, friction modification)
- improvement of corrosion resistance
- improvement of thermal resistance
- raising of porosity and roughness
- increase of catalyzing effects
- improvement of decorative effect
- barrier effects (e. g. thermal insulation).

The most important coating processes are the thermal spraying and the electrochemical or chemical (currentless) plating. The thermal sprayed composite coatings will be applied at high tribological and corrosive loads, e. g. for energy generation (e. g. gas turbines), steel manufacture and metal forming.
The composite coatings characterise a great improvement, particularly the wear resistance at high and complex stress. [1] - [3]

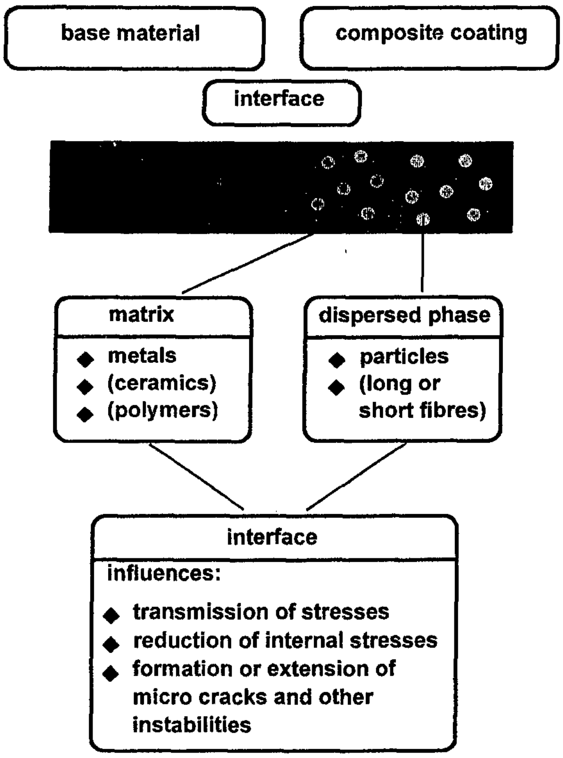
base material
composite coating
interface
matrix
◆ metals
◆ (ceramics)
◆ (polymers)
dispersed phase
◆ particles
◆ (long or short fibres)
interface
influences:
◆ transmission of stresses
◆ reduction of internal stresses
◆ formation or extension of micro cracks and other instabilities

Figure 1. Schematic depiction of a composite coating

PROBLEM STATEMENT

Up to now conventional materials for thermal spraying are based on scarce and expensive metals (e.g. Co, Cr, Ni, W), moreover these materials are harmful to health and environment [4]. There is a strong interest to substitute these materials by ecologically and economically beneficial powders. The aim of the investigation is to develop composite powders for thermal spraying with comparable tribological behaviour with respect to the ecologically and economically basis. Steel (Fe) / Titanium-carbide (TiC) based composite powders reveals a great opportunity for the substitution of conventional carbide powders.

Conventional powders convey Tungsten-carbide (WC) or Chromium-carbide (Cr_3C_2) and are proved effective as wear resistance particles however TiC offer a series of advantages: higher valence bonding resulting higher tensile strength, higher hardness (to 3.000 HV) however higher brittleness, higher melting point. The thermal coefficient of expansion (TiC - $7{,}95 \bullet 10^{-6}$ K) is closer to the coefficient of expansion of the steel matrix compared to WC ($3{,}9 \bullet 10^{-6}$ K), this causes a better thermal shock behaviour. The wear resistance of $TiC_{stoichiometric}$ is constant over a range from 20 - 1.200 °C. Because of high stress the addition of further elements (e.g. Cr, Ni, Mo) to the steel matrix is necessary to obtain the needed coating behaviour.

A new way of scientific and technical importance is to apply nanoscaled particles (second phases) with uniform shape and diameters below 500 nm to approximately 10 nm. Such nanoparticles are interesting dispersion hardened coatings. A further advantage is the spherical shape of the particles, which improves the wear stress (roll-off effect). But during the thermal spraying process there is the difficulty not to dissociate the small particles (not bound in the metal matrix).

The Self Propagating High Temperature Synthesis (SHS) is very promising as a method to obtain very small carbide particles finely dispersed in the metal matrix. It is based on the utilisation of the high exothermal reaction between titanium and carbon and proceeds without additional energy from an external source. SHS enables the production of TiC near to the stoichiometric composition intended to obtain in the Fe / TiC system [5]. The powders consist in a plastic phase acting as a binder (e. g. iron or iron-alloy) and spherical TiC-particles which are distributed homogeneously all over the binder phase (Figure 2). Applying different thermal spraying methods (atmospherically plasma spraying and vacuum plasma spraying) and varying the process parameters, dispersion hardened, wear resistant coatings could successfully be produced.

Because of the strong exothermic reaction of Ti and C, while the steel matrix reacts inert and reactions reflex with other components, the reactants are used completely and TiC is almost stoichiometric. The composite powder shows a homogenous texture construction (plastic metallic binder and uniformly distributed small TiC grains, dense and non-porous structure). The phase boundary forms via the molten state, which leads to good embedding and wettability of the titanium-carbides. This way a good protection against oxidation and disso- ciation during the thermal spray process is achieved.

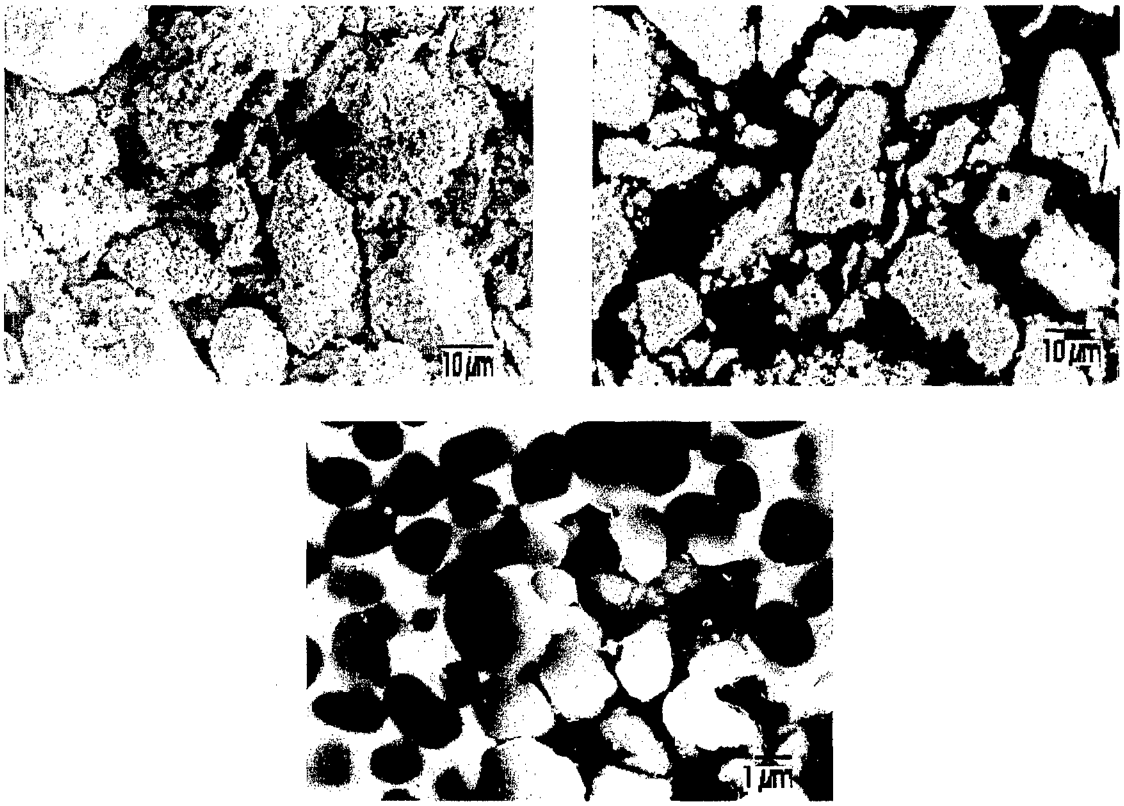

Figure 2. Scanning electron micrograph of SHS powder - Fe / 55 wt.-% TiC (small TiC-particles in the Fe-matrix)

Figure 5 shows the integral microhardness of different powders and different coatings. The coatings are sprayed with various plasma systems. The integral microhardness of the APS produced coatings is lower compared to the VPS coatings. The lower microhardness of the APS coatings is caused by higher porosity and different phase condition of the binder matrix. Further investigations are necessary for the phase identification.

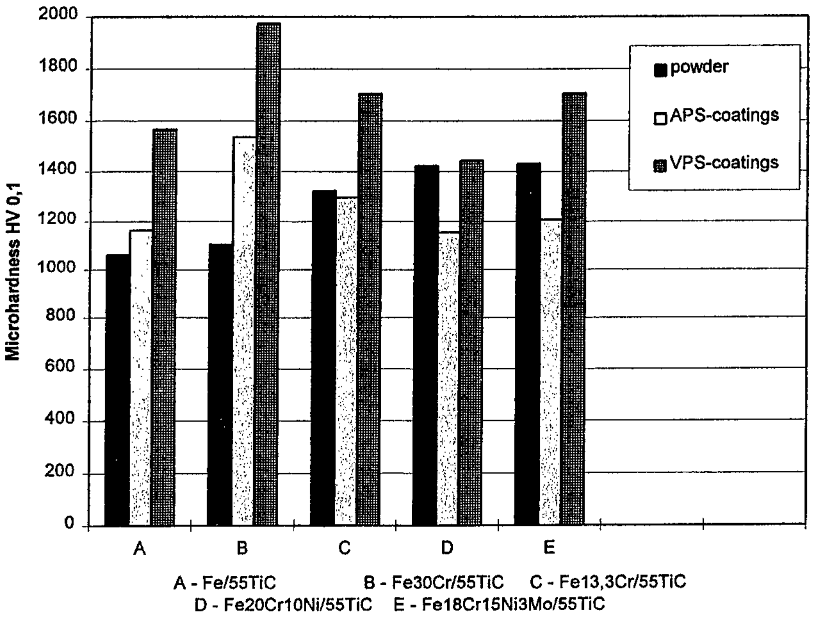

Figure 5. Integral - microhardness of different powders and plasma coatings

Comparative test results of APS and VPS coatings are presented in Figure 6, 7 and 8. The abrasion wear resistance of the plasma sprayed coatings shows an improvement in comparison to carbon steel.

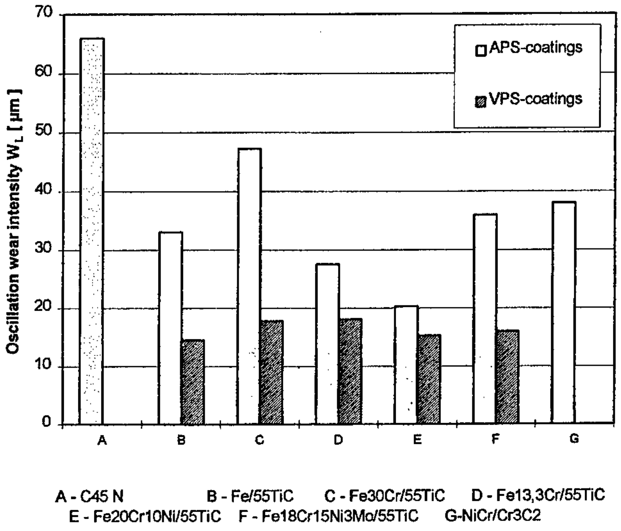

Figure 6. Oscillation wear-tests

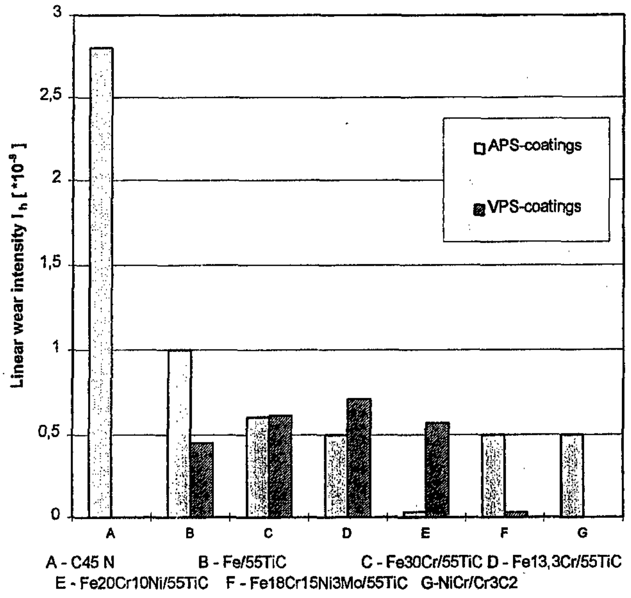

Figure 7. Sliding wear tests (disk / bush)

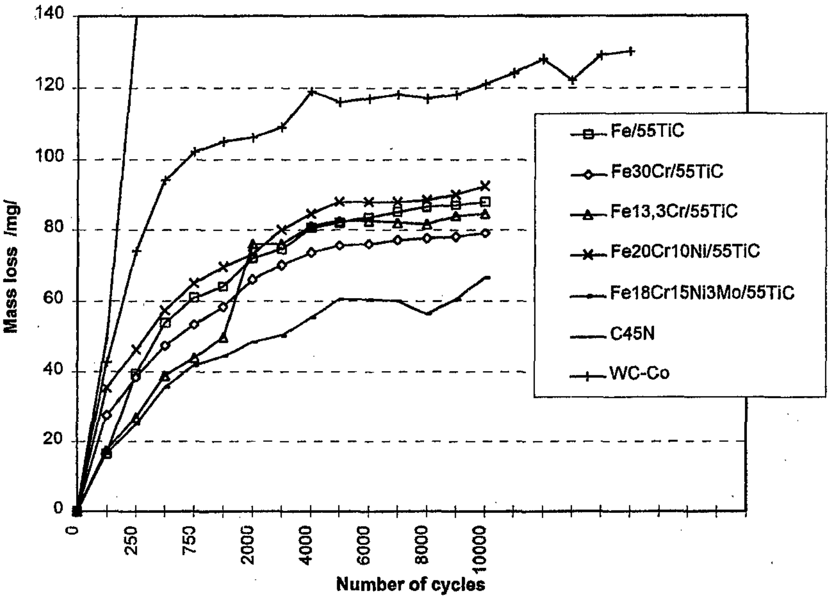

Figure 8. Comparitive Taber-Abraser tests of VPS-coatings (WC-Co-coatings were sprayed by HVOF)

CONCLUSIONS

Investigations carried out have revealed the great potential of plasma sprayed coatings based on the system Fe / TiC. The structure and the phase composition are dependent on the spraying conditions. Comparative wear tests indicate out the performance of these coatings [8] - [11]. First application test with APS coatings based on the system Fe / TiC at crank shaft bearings of diesel engines have shown an improvement of the wear resistance. Because of the first positive results further extensive tests are scheduled.

REFERENCES

[1]. Steinhäuser, S.; Wielage, B. Composite Coatings: Manufacture, Properties and Application Proceedings of the Tenth International Conference on Surface ModificationTechnologies, Singapure, September 2 - 4, 1996, Editors T.S. Sudarshan, K.A. Khor, M. Jeandin, published in 1997 by The Institute of Materials London, S. 436 - 450 and Surface Engineering 1997, Vol. 13, No. 4, S. 289 - 294

[2]. Steinhäuser, S. Disperse nichtmetallische Phasen in Oberflächenschichten (Compositschichten) Materialwissenschaft und Werkstofftechnik, 26 (1995), S. 608 - 614

[3]. Lugscheider,E.; Jokiel, P.; Remer, P.; Steinhäuser, S. u.a.Hard particle reinforced aluminium-alloys for aircraft applications (EWISCO) Tagungsband "1994 Thermal Spray Industrial Applications" (6th National Thermal Spray Conference) vom 20.-24. June 1994 in Boston, Mass., ASM International, S. 79 - 83

[4]. Steffens, H.D.; Lauterbach, R.; Thermisches Spritzen - Einführung und Übersicht Fortbildungsseminar,: Moderne Beschichtungsverfahren, 14.05. - 18.05.1990 dortmund, Seite 50 - 55

[5]. Yoon choi, shi-Woo Rhee, Effect of iron and cobalt assition on TiC com bustion synthesis, J. of Mat. Res., Vol. 8, Nr. 12, 3202 - 3209 (1993)

[6]. Steinhäuser, S.; Wielage, B.A contribution to the characterization of the wear protective oatings Tagungsband zur „14th International Thermal Spray Conference and Exhibition“ Mai 1995 in Kobe, Japan (5 Seiten)

[7]. Steinhäuser, S., Schmidt, G.: Characterization of wear protective coatings. Tribology international vol. 29 (1996) n.3, p. 207 - 214

[8]. Verstak, P. Vityaz, E. Lugscheider, E. Remer, P.Beljaev, T. Talako T. Azarova, V. oval:New coatings for elevated temperature erosion application.Conference TS 96, März 1996, Essen, 71 -75

[9]. Vityaz, A.A. Verstak, E. Lugscheider, P. Remer, S. Steinhäuser A.V. Borisov, T.A. Azarova, T.L. Belyaev, T.L. Talako: New metal and carbide coatings from synthesized powders for aluminium and titanum alloys wear protection. Collection Powder Metallurgy, Edition 17, Science and Technique, Minsk Belarusia, 1995, 101-108

[10]. Vityaz, A. Verstak, T. Azarova, T. Talako, E. Lugscheider: Titanium carbide in wear resistantcoatings. Conferencentsc 96, 7-11 October 1996, Cincinnati

[11]. Vitiaz, P.; Azarova, T.; Wielage, B.; Steinhäuser, S. et. al. Composite Fe/TiC - Powders forWear Resistance Coatings Using Plasma Spray Process ntsc 97 - National Thermal Spray Conference, Indianapolis, Indiana, USA, 15 - 19 September 1997

PREDICTION AND MEASUREMENT OF THE ANISOTROPIC THERMAL EXPANSION BEHAVIOR OF ORIENTED POLYOXYMETHYLENE

R.R. Zahran and S.S. Shenouda

Department of Chemical Engineering, Alexandria University
Alexandria, 21544 - Egypt

INTRODUCTION

Polyoxymethylene is a thermoplastic semicrystalline polymer. Such a polymer is known to be composed of a crystalline phase embedded in an amorphous phase. The spherulitic texture is a common morphological feature of semicrystalline polymers. A spherulite is composed of crystalline lamellae radiating in a twisting manner from the center of the spherulite to its boundary, and in between lies the amorphous phase. Therefore, POM is regarded as a being a molecular version of engineering composites [1].

The major objective of the present work is to implement the molecular composite model for the prediction and the analysis of the thermal expansion behavior of polyoxymethylene (POM). Therefore, isotropic and anisotropic POM samples are prepared and characterized morphologically. Their thermal expansion coefficients are measured and compared with the model prediction.

MOLECULAR COMPOSITE MODEL

The bulk polymer sheet is assumed to be reconstructed by stacking up unidrectionally oriented orthotropic plies, each of which contain tape-like lamellae, oriented in a predetermined manner. The resulting quasi isotropic laminate analogue is simulating the behavior of the bulk isotropic sheet [2]. The model calculations proceeds through two major steps: micromechanics and macromechanics [3]. In the micromechanics step, the true identity of the composite is recognized. The Halpin-Tsai equation is used to predict the unidirectionally oriented ply behavior. In the macromechanics step, the laminate analogy is used to build up the composite laminate by stacking up the plies in a predetermined manner. The model has been refined to account for the complex micromorphological changes taking place during solid-state deformation.

The accuracy, simplicity and versatility of the molecular composite model lie in the fact that its parameters are easily accessed experimentally. These parameters are the spherulite size, the thickness and the width of the crystallites and the volume fraction crystallinity. Drawing, however, results in a crystallite orientation distribution . The latter can be quantified using the so-called orientation parameter, λ, the value of which can vary from 0 for a randomly oriented system to ∞, for a perfectly aligned system [4].

EXPERIMENTAL

Isotropic and anisotropic POM samples were prepared. POM was compression molded into sheets of 16x16x0.3 cm in an electrically heated hydraulic press. After molding, three different cooling routes are adopted leading to three different thermal histories: 1) Slow cooling: the mold assembly is allowed to cool slowly to ambient temperature; 2) Quenching: the mold assembly is plunged into ice-cold water directly after molding and 3) Annealing: the mold assembly is allowed to cool slowly to 100°C, then heated to 150°C for 4 hours and cooled again to room temperature.

The isotropic squared sheets were cut into rectangular strips (15x2x0.3 cm). The strips were drawn at 150°C using an Instron tensile tester equipped with a temperature controlled environmental chamber. The gauge length and the cross head speed were adjusted to 3 cm and 2 cm/min respectively. Different draw ratios are obtained by varying the drawing time. The samples were held in the drawn state at the same drawing temperature for 15 minutes to prevent any shrinkage and to minimize any abrupt structural changes that may arise upon releasing the sample. Samples of draw ratios from 1 to 5 were prepared for each thermal history. After removing the samples they are stored at room temperature for 24 hours before any further measurement are performed.

The thermal strains were measured using an Orton Automatic Recording Dilatometer, model EK, furnished with a chromel-alumel thermocouple for temperature sensing. The sample length changes were transmitted through a fused silica push rod to the plunger of a linear variable differential transformer (LVDT). The thermal expansion coefficient "α" at any particular temperature "T" was calculated from the slope of the resulting thermal strain-temperature curve. The densities of the samples were obtained using pycnometry. The degree of crystallinity was obtained using differential scanning calorimetry. The degree of orientation was determined using wide angle x-ray scattering. The detailed morphological features of the spherulitic and the drawn texture were determined from scanning electron microscopy.

RESULTS AND DISCUSSION

Parametric Mapping Analysis

A parametric mapping analysis was performed to investigate the effect the model parameters on the thermal expansion behavior of POM. Pairs of model parameters were selectively varied, keeping the others constant. The results were expressed as 3-D structure-property maps. Such maps have shown potential use when designing oriented molecular composite structures [5]. A typical map is shown in Figure 1, which depicts the variation of the longitudinal and transverse thermal expansion coefficients (TEC) with the orientation parameter and the temperature. The figure shows that the alignment of the crystallites in the drawing direction is associated with a decrease in the longitudinal TEC and a simultaneous increase in the transverse TEC. It is also noticed that the longitudinal TEC becomes negative when the value of the orientation parameter is greater that 8. Such a behavior is expected because as the crystallites become oriented in the draw direction, the contribution of the c-axis properties in this direction increases and, in the meantime, the contribution of the properties of the a- and the b- axes in the transverse direction increases. It is also noticed that as long as the value of the orientation parameter is greater than 8, it does not have a significant effect on the longitudinal TEC. On the other hand, the transverse TEC increases slightly with orientation parameter at relatively higher temperatures. Figure 1 also shows that the orthogonal in-plane thermal expansion coefficients of POM are significantly sensitive to temperature fluctuations, and particularly α_{11} at lower values of λ : i.e. at low to moderate draw ratios. Furthermore, a slight change in the variation of both expansion coefficients with temperature is taking place around the glass transition temperature (-53°C), the change being more pronounced as we approach the isotropic state. Detailed discussion on the effect of volume fraction crystallinity and the crystalline phase geometry are given elsewhere [6].

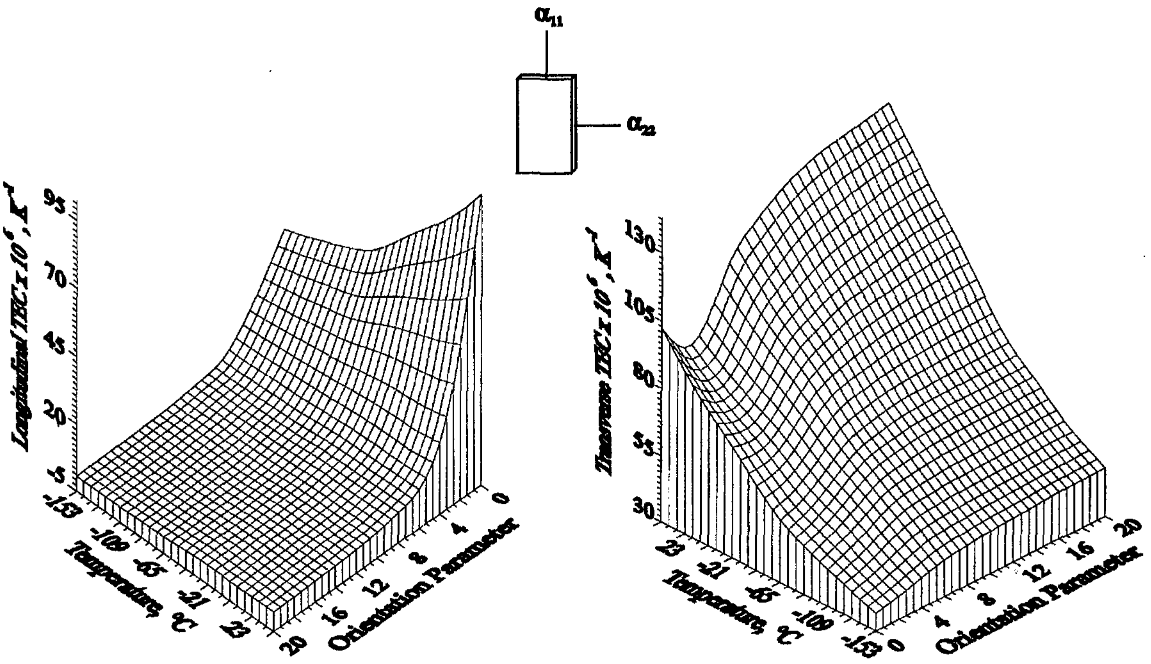

(a) (b)

Figure 1 Plot of (a) the longitudinal and (b) the transverse thermal expansion coefficients versus temperature and orientation parameter (Volume fraction crystallinity : 0.75; longitudinal and transverse aspect ratios: 60 and 5, respectively)

Comparison between Measurement and Model Prediction

Figure 2 depicts the predicted and measured thermal expansion coefficients dependence on temperature for isotropic annealed samples from 40 to 140°C. Obviously, the agreement between prediction and measurement is good It is noticed, however, that as the temperature increases above 100°C a poor agreement between the measurement and the prediction is observed. This is expected, since the viscoelastic nature of the matrix phase is not accounted for within the model calculations [5,6].

Figures 3 illustrates the predicted and measured thermal expansion coefficients at 45°C versus draw ratios from 1 to 5 for annealed samples. In general the agreement between predicted and experimental values is within 16 % for both the longitudinal and the transverse thermal expansion coefficients.

Another reason for the discrepancy between the two values (the predicted and measured values) is that the model does not account for the void effect, the interfacial effect and adherence between crystalline and amorphous phases [6]

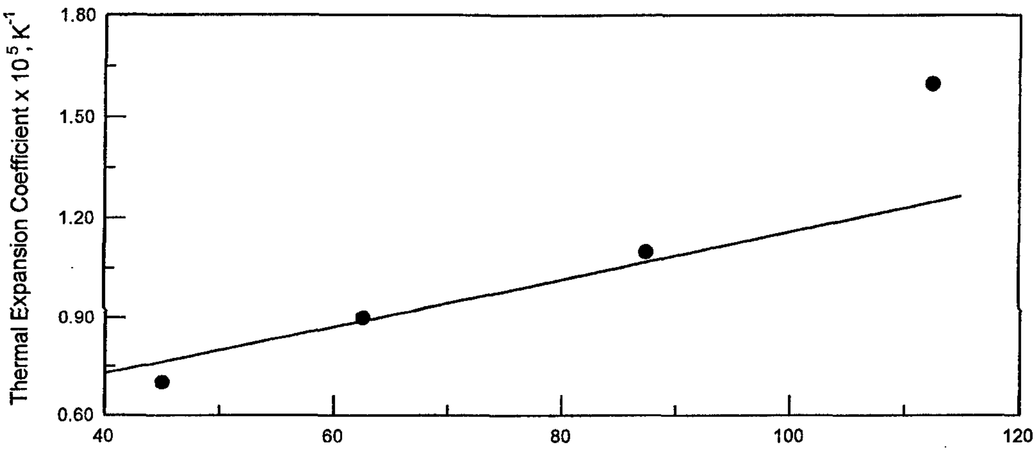

Figure 2 Comparison between the predicted ( ) and measured (●) thermal expansion coefficient of annealed isotropic POM samples at different temperatures.

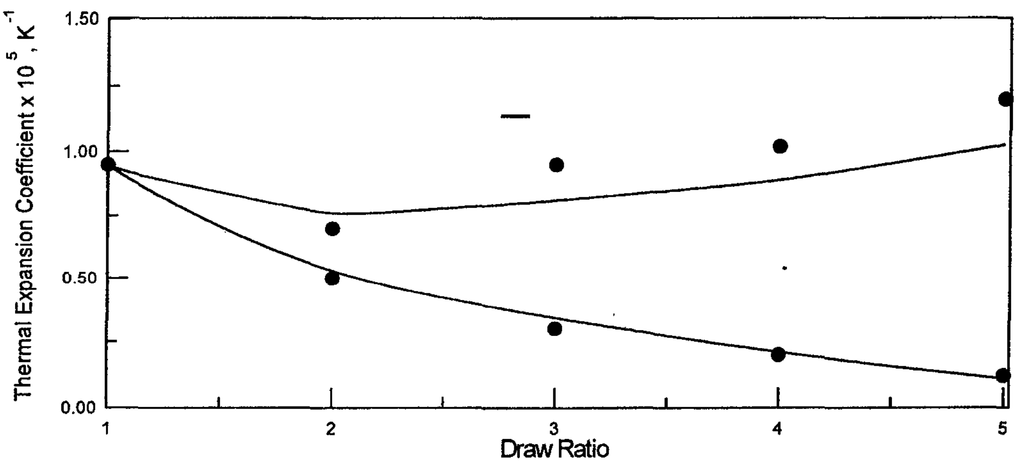

Figure 3 Comparison between the predicted ( ) and the measured (●) thermal expansion coefficients of annealed POM samples, of different draw ratios, at 45°C.

For the seek of a more complete comparison, the experimentally measured thermal expansion coefficients from other workers were also adopted. Choy *et al.* [7,8] measured the thermal expansion coefficients of isotropic and anisotropic POM at various temperatures. Figure 4 represents the comparison between the predicted and the measured thermal expansion coefficients of POM as reported in Reference 7. There is a very good agreement between both series of values specially at low temperature, where there is a good agreement for both the longitudinal and the transverse thermal expansion coefficients, measured at two different temperatures. The input parameters necessary for the model prediction were extracted from Reference 7.

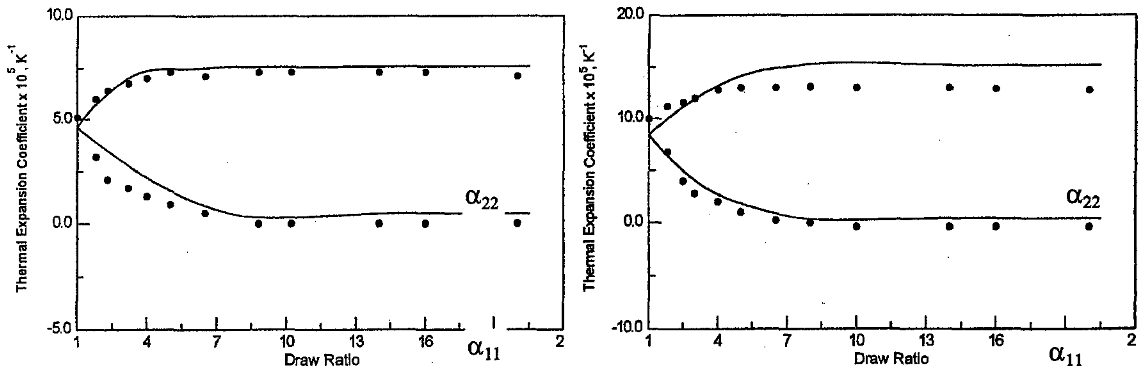

(a) (b)

Figure 4 Comparison between the measured (●) and the predicted ( ) orthogonal thermal expansion coefficients of POM at different draw ratios: (a) Temperature = -113°C and (b) Temperature = 27°C. (Data are adopted from Reference 7)

CONCLUSIONS

The parametric mapping analysis showed, that apart from the effect of temperature, the crystalline phase orientation distribution is a crucial parameter affecting the behavior of anisotropic polyoxymethylene. The best achievable thermal dimensional stability is of directional dependence: in the longitudinal direction, it is in the vicinity of $\lambda = 8$, while in the transverse direction it is in the vicinity of $\lambda = 2$ only above glass transition temperature. However, the ultimate anisotropy in the thermal expansion behavior oriented polyoxymethylene is attainable at an orientation parameter of 8 beyond which both thermal expansion coefficients are almost in variant to changes in levels of orientations.

Isotropic and anisotropic POM samples were experimentally prepared and fully characterized. The orthogonal thermal expansion coefficients of the obtained samples were experimentally measured. A good agreement was observed when comparing the theoretically predicted with the experimentally measured thermal expansion behavior of polyoxymethylene sheets. Therefore, the molecular composite model can be reliably utilized when designing with engineering, high-performance crystalline polymers.

REFERENCES

1. Halpin J.C. and Kardos J.L., "Modulus of Crystalline Polymers Employing Composite Theory", *Journal of Applied Physics,* **43**, pp. 5, (1972).
2. Kardos J.L., and Raisoni J., "The Potential Mechanical Response of Macromolecular Systems. A Composite Analogy", *Polymer Engineering and Science,* **15**, pp. 183, (1975).
3. Kardos J.L., "Structure Property Relation in Short Fiber Reinforced Plastics" *C.R.C. Critical Review in State Sciences,* pp. 419 (1973).
4. Kacir L., Narkis M. and Ishai O., "Oriented Short Glasss Fiber Composites; I, Prepration and Statistical Analysis of Aligned Fibers Mats" *Polymer Engineering and Science,* **15**, pp. 525 (1975).

5. Zahran R.R., and Kardos J.L. "A Molecular Composite Approach to the Thermal Expansion Behavior of Anisotropic Polyethylene", *Journal of Polymer Science Physics*, **33**, pp. 547 (1995).
6. Zahran, R.R. , Shenouda, S.S., El-Tawil, Y.A. and El-Kayar, A, "Analysis of the Thermal Expansion Behavior of Oriented Polyoxymethylene Sheets", *Polymer Engineering and Science*, **36**, pp. 1377 (1996)
7. Choy C.L. and Nakafuku C., "Thermal Expansion of Polyoxymethylene", *Journal of Polymer Science, Part B, Polymer Physics*, **26**, pp. 921 (1988).
8. Choy C.L., Chen F.C. Young K., "Negative Thermal Expansion in Oriented Crystalline Polymers", *Journal of Polymer Science, Polymer Physics Edition*, **19**, pp. 335 (1981).

IMPACT RESISTANCE OF MICROWAVE CURED GLASS/EPOXY COMPOSITES

Sabit Adanur and Baohua Xu
Auburn University, Department of Textile Engineering
115 Textile building
Auburn, AL 36849 USA

Abstract: To improve the impact resistance, a novel manufacturing process was developed to utilize microwave polymerization instead of conventional thermal method in processing glass/epoxy composite materials. The microwave processing is volumetric, direct, selective, and controllable. It was found that the composites cured by microwave hold an good impact properties and it changes with the microwave radiation time and microwave power setting. The glass transition temperature Tg and the crosslinked density of the polymer increase with the radiation time and power setting. The tough polymer and composite can be obtained through increasing the network homogeneity. A homogenous crosslinked matrix of the composite was obtained by microwave. polymerization process.

INTRODUCTION

Microwave is an electromagnetic wave characterized by wavelengths ranging between about 1 mm and 30 cm and frequency between 10^{8} and 10^{12} cycles per second [1,2]. Microwave heating is a form of dielectric heating, which is understood as the generation of heat in materials of either none or weak electric conductivity, mediated by the action of a high-frequency alternating electric field. It is conditional for the production of heat in an alternating electric field that a substance is present which possesses an asymmetrical molecular structure, as is the case in the water molecule. The molecules of polymers form electric dipoles which, when exposed to an electric field, assume an orientation relative to the direction of that field. The internal heat generated by the polar molecular oscillations will accelerate the crosslinking reactions. Under the influence of an alternating field the polymer dipole molecules display movements of rotational oscillation in time to the high frequency field's polarity changes. Due to the intermolecular friction thus produced high-frequent energy becomes first absorbed and then transformed into thermal energy [3-6].

Using microwave and epoxy resin systems, fast curing rates can be achieved. The microwave heating is volumetric, direct, selective, and controllable. The process reduces resin loss, improves fiber wet-out, fiber bonding with matrix, and mechanical properties of the composites, and provides precise fiber volume control. This paper addresses the effect of microwave curing on the impact resistance properties of glass/epoxy composite system and the relations among the microwave radiation parameters (such as radiation time and power setting) and network structures.

EXPERIMENTAL

For the composite reinforcement, a 0/90 degrees continuous cross woven fiber E-glass fabric was used. The resin system used was epoxy resin EPON®828/V-40 curing agent, from Shell Chemical Company. The resin and curing agent were mixed according to 3/1 weight ratio, respectively.

The work reported here is based on the results from four basic experiments: (1) Measurements of impact properties according to microwave radiation time and power setting. (2) Measurement of flexural strength according to the microwave radiation time and power setting. (3) Observation of changes in Tg according to radiation time and power setting. (4) Observation of changes in dynamic mechanical properties (tan δ and Log E') with the radiation time and power setting. The microwave equipment used was Panasonic microwave oven at a frequency of 2.45 GHz. The samples were radiated at different time spans and were cut according to ASTM D790M-84.I (Flexural three points bending) and test instrumented impact test [7].

RESULTS

Impact resistance: Figure 1 show the impact energy absorbed up to maximum load versus microwave radiation time at three power settings, which are obtained using instrumented impact tester. At high power setting (800 W), the absorbed impact energy of microwave cured glass/epoxy composite increase with radiation time, and after reaching maximum, the values have decreasing trend. Figure 2 shows the same trend for the impact maximum load. However, at low power settings (600 W and 400 W), the impact resistance properties do not change much more with the radiation time.

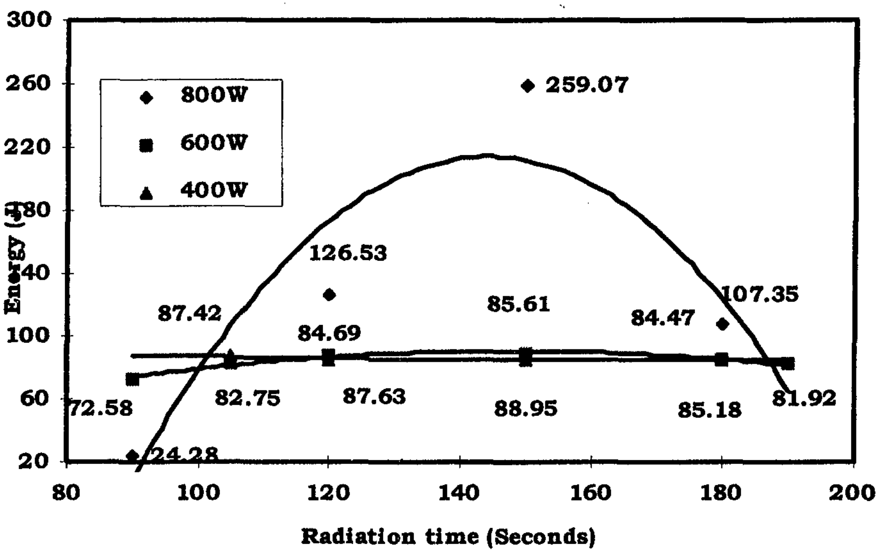

Figure 1. Impact energy absorbed up to maximum load at different radiation time and power setting

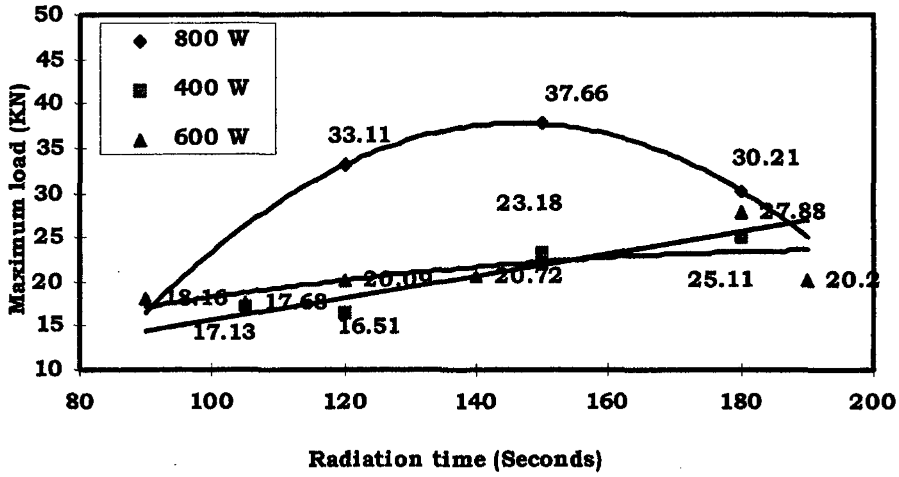

Figure 2. Impact maximum load at different radialton time and power setting

Glass transition temperature (Tg): Figure 3 shows that the Tg increases with the microwave radiation time at higher power settings (700 W and 1000 W).

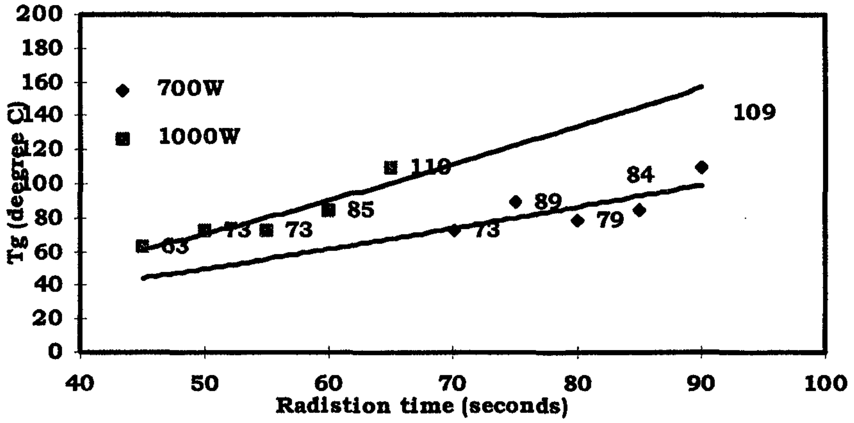

Figure 3. Relation between Tg and radiation time

Dynamic modulus (Log E'): Figure 4 shows that at a fixed power setting (1000 W), when the radiation time increases, the curves move to high temperature regions, and the modulus (Log E') increases. This indicates that the crosslinking density of the epoxy system cured by microwave increases with the radiation time [8] [9].

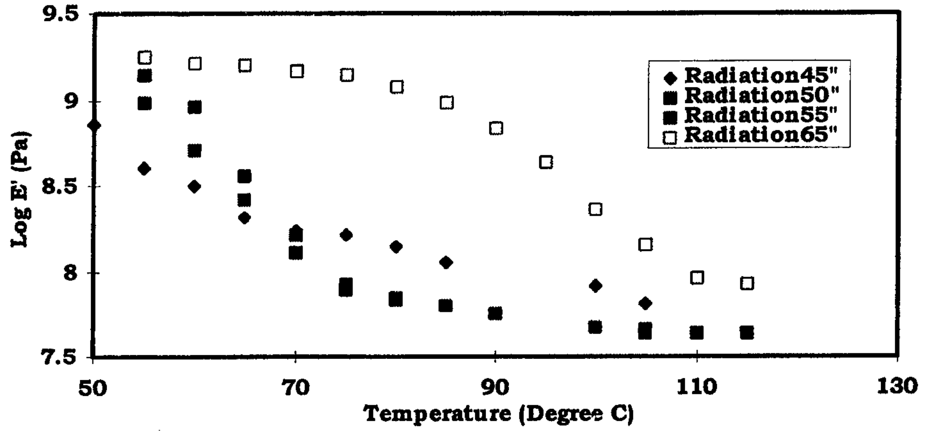

Figure 4. Relations between Log E' and radiation time at power setting 1000 W

Dynamic loss tangent (tan δ): Figure 5 indicate that at fixed power setting (1000 W), when the radiation time increase, the curve shifts to the high temperature areas. However, the damping peaks do not get wider. This indicates that the network of the epoxy system cured by microwave is homogenous [8] [12] [13].

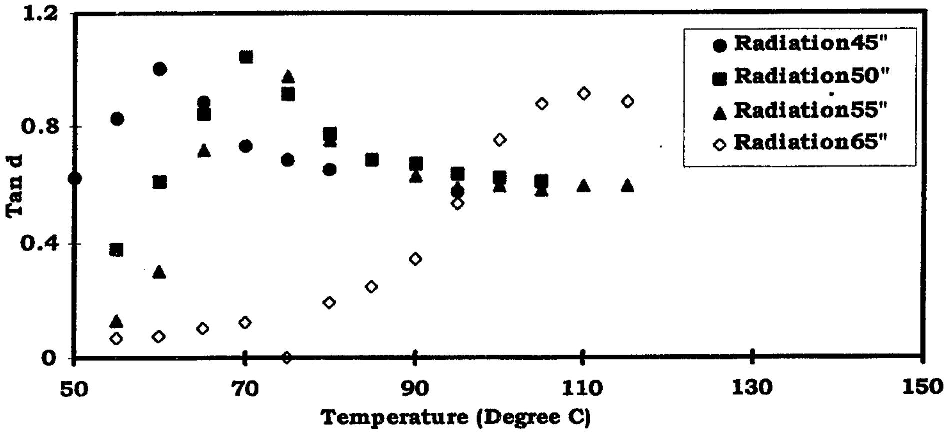

Figure 5. relations between tan d and radiationtime at power setting 1000 W

DISCUSSION

1. Glass transition temperature (Tg)

TMA (thermal mechanical analysis, which traces changes in polymer structure and mechanical properties) are one of the best methods for Tg measurement and analyzing structure and properties relations. TMA was chosen here, and the detailed explanation is presented in the following sections. Theoretically, Tg is a physical property only related to the sudden change of free volume of the material. Crosslinks reduce the available free volume, and hence Tg is expected to increase with increasing crosslink density.

In composite applications, increased toughness and Tg are simultaneously required. Crosslinking tends to increase a polymer's Tg, but decreases its toughness. Ways were sought to maintain high glass transition temperature of the matrix while keeping crosslink structure, thus increasing polymer's toughness at a given Tg [8]. In the case of microwave cured epoxy system, Tg increases with the increasing microwave radiation time and power setting as shown in Figure 3. The cross-linking density also increases.

2. Crosslinking density

Crosslinking theory [9,10,11] requires a high degree of crosslinking to result in a higher value of Log E' after the transition. In our results (Figures 4), the high Log E' was obtained at high power setting and more radiation time. High cross-linked epoxies tend to have high Tg but usually have less fracture toughness. For a low cross-linked thermoset polymer, the less rigid network architecture has the ability of producing higher amounts of plastic deformation, which may result in greater impact toughness. There is a maximum crosslinked density at which the toughness of matrix will reach its maximum value. In the case of microwave cured epoxy system at high power setting (Figures 1 and 2), the maximum cross-linked density was obtained with the maximum radiation time, at which the impact maximum load and impact energy absorbed up to maximum load reach its maximum values.

3. Dynamic mechanical properties

Variation of the dynamic storage modulus (E' or G') and the damping factor (tan δ) with temperature and frequency allow characterization of the viscoelastic properties of a particular material. This technique detects all motional transition and usually provides the most sensitive means of studying glass and secondary transitions, and of quantitatively deterring the effects of phase type crosslinking reactions and morphology properties [8].

In the case of microwave cured epoxy system (Figure 5), tan δ shifts to high temperatures with the radiation time increasing. The damping peaks and glass-rubber regions do not get wider. The broadening of the glass- to- rubber transition region seen in the property-temperature plots is often assumed to be due to a distribution in the molecular weight between cross-links or some other kind of heterogeneity in the network structure [12]. Mason [13] believes that the broadening is due to a broadening in the distribution of free volume between monomeric units.

4. Crosslinking homogeneity

A tough polymer and composite can be obtained through increasing the network homogeneity. Higher cross-linking homogeneity (in terms of less unreacted chain ends), which is the result of curing epoxy systems at higher conversion percentages, may be one important factor of toughening high Tg epoxy systems [8]. Network with greater homogeneity will have the uniform chain length between junctions. When the network with uniform chain lengths bears the stress, it will have better performance than a less homogeneous network. In low degree homogeneous network, the shorter chains may bear much stress individually before failure. The deformation property of less homogeneous network will be lower than the higher homogeneous one. The ultimate strain at failure will decrease because of shorter segments having greater elongation at break. The loading rates were relatively increased microscopically. The non-uniform deformation of network chain will yield more localized stress concentrations. The macroscopic failure rate will become faster, due to the localized stress concentration in low degree homogenous network.

CONCLUSIONS

We have shown that for the glass/epoxy system, the impact resistance properties, the glass transition temperature Tg and the crosslinked density of the polymer increase with the microwave radiation time at high power settings (700 - 1000W). There is a maximum crosslinked density at which the toughness of the matrix and composite will reach its maximum value. Microwave cured epoxy system has a higher cross-linked homogeneous network structure. A tough polymer and composite can be obtained through increasing the network homogeneity.

References:

[1] B. Ellis, "Chemistry and Technology of Epoxy Resins, BLACKIE ACADEMIC & PROFESSIONAL, 1993.

[2] Serway, Raymond A, "Physics For Scientist and Engineer", 2$^{\text{nd ed.}}$ pp785, CBS College Publishing, 1986.

[3] Mijovic, "Review of Cure of Poly.& Comp.by Microwave",Poly.Comp.June,90,p184

[4] Eva Marand, "Comparison of Reaction Mechanisms." Macromolecules 92,25,2242

[5] Boey, "Electro. Radiation Curing of a Epoxy/Glass.", Radiat.Phys.Chem.38,4,419,91

[6] Wei, "Comparison of Micro.& Therm. Cure." Poly.Eng.&Sci.1993.33.pp1132.

[7] Jang, Bor Z, "Advanced Polymer Composites", ASM International, 1994.

[8] CHARLES B. ARENDS, "POLYMER TOUGHENING", MARCEL DEKKER, INC, 1996.

[9] LAWRENCE E.NIELSEN AND ROBERT F. LANDEL, "MECHANICAL PROPERTIES OF POLYMERS AND COMPOSITES, Marcel dekker, INC, 1994.

[10] T. MURAYAMA, "Dynamic Mechanical Analysis of Polymeric Material", ELSEVIER SCIENTIFIC PUBLISHING COMPANY, 1978.

[11] P.J. Flory, Principles of Polymer Chemistry, Cornell U.P., Ithaca, N.Y., 1953, Chap.11.

[12] K. Ueberreiterand G. Kanig, J.Chem.Phys., 18, 399 (1950).

[13] P. Mason, Polymer, 5, 625 (1964).

BEHAVIOR OF POLYOLEFIN BLENDS IN THE PRESENCE OF $CaCO_3$

C. Albano[1], J. González[2], M. Ichazo[2], C. Rosales[2], R. Perera[2], R. Navas[1], C. Urbina[1] and C. Parra[1].

[1]Universidad Central de Venezuela, Facultad de Ingeniería, Escuela de Ingeniería Química, Los Chaguaramos, PO Box: 48146, Caracas 1041 A, Venezuela.
[2]Universidad Simón Bolívar, Grupo de Polímeros, Departamento de Mecánica.

INTRODUCTION

Polypropylene (PP) resins have found their way to use in a wide range of applications and technologies. Thanks to its properties, polypropylene is a good candidate for expanded use in the plastic industry. In order to fulfill a broad range of applications, resins have to demonstrate a wide range of properties. The long and time-consuming process of developing new resins for each application is not profitable nor logical. The use of fillers provides us with a means of adjusting the properties of the resins to each specific application.

Polyolefins have come to be the most used thermoplastic in the industry, representing almost 70% of the plastics used in the European Union and in Venezuela [1,2]. Polyolefin blends have attracted a great deal of attention [3], particularly those of PP with High Density Polyethylene (HDPE), because these plastics account for a significant percentage of waste material.

Compatibilization of two polymers (PP and recycled and non-recycled HDPE) with an EPR block copolymer made up of propylene and 8% ethylene, which can be used both functionalized (with 6% diethylmaleate (DEM) and 0.05% dicumile peroxide), and non-functionalized, as well as the effect of $CaCO_3$ (Calcium Carbonate), both non treated and treated with a coupling agent of the titanate type (LICA 12), were studied in this research.

Our work is aimed at optimizing certain mechanical and thermal properties and improving interface and processing in a composite material with a recycled component, specifically HDPE.

To improve the interaction of polymer blends, compatibilizing agents are added. Usually, these agents are block or grafting copolymers, because they can improve interaction between two polymers.

Incorporation of calcium carbonate, mica, barium sulfate or talc as fillers in thermoplastics is a common practice in the plastics industry to reduce the production costs of molded products. It is well known that mineral fillers improve the rigidity of the polymers, but they also decrease ductility and toughness, therefore, coupling agents are included in the formulae [4,5].

Mechanical properties of PP with $CaCO_3$ have been analyzed by different authors [4,6,7]. Maiti et al. [4] in studies on PP with modified $CaCO_3$ observed significant variations in mechanical properties. One of these variations is the 25% increase of impact strength with respect to the use of the unmodified charge. In the literature consulted, no study has been found on the loaded PP/HDPE blend, the object of this work. The only information found for loaded polyblends is for PP/LDPE with talc [8].

EXPERIMENTAL

The materials used in this work were PP (ρ: 0.91 g/cm^3; MFI: 7.0g/10 min; 230°C; and 2.16 load) supplied by PROPILVEN; HDPE (ρ: 0.96 g/cm^3; MFI: 7.3g/10 min; 190°C; and 2.16 load), supplied by RESILIN; and a recycled high density polyethylene (r-HDPE) supplied by Plásticos M y M. The blends were prepared in 80/20 wt.%, PP/HDPE and PP/r-HDPE. An ethylene-propylene copolymer (EPR) (8% ethylene) in 5wt.% with respect to the mixture was used as a modifier of the blends. $CaCO_3$ (ρ: 2.70 g/cm^3, particle size x 10^6: 5m; specific surface: 6.4 m^2/g) was used at 20, 30 and 40 wt.% with and without 1wt.% of LICA 12.

The blends were prepared in one stage in a W&P intermeshing co-rotating twin screw extruder. In this one-stage process, all materials were mixed simultaneously. The filler was incorporated through an additional feed port, located in a part of the extruder where complete fusion of the homopolymers was guaranteed. Specimens were prepared by injection molding at 200°C. A tensile test was performed using an Instron tester (model 1125) at room temperature. Measurements were taken at a crosshead speed of 50 mm/min according to ASTM D-638. Impact strength measurements were made on notched samples using a fractoscope (Zwick) in the Izod mode, according to ASTM D256-82. Differential scanning calorimetry (DSC, Perkin Elmer) was used to observe the behavior of melting and crystallization. To erase thermal history, the cooling and the second heating thermograms were detected with the following scanning rate: 5°C/min in the cooling and 10°C/min in the second heating.

RESULTS AND DISCUSSION

On the basis of the research carried out by Ichazo et al. [9] on the homopolymer and copolymer feeding and blending, and on extruder load, and on the comparison of the blends obtained in one stage with similar blends obtained in two stages (homopolymers were mixed first and in a second extrusion the filler was added subsequently), blending was optimized in one step and filler homogeneity was attained. Thus, the blends used in this research were prepared in one stage.

Table 1 shows mechanical properties of PP, PP/HPDE, PP/HPDE/functionalized and non-functionalized EPR, for blends with both recycled as well as non-recycled HDPE.

Table 1: Mechanical properties of PP, PP/HDPE blend, PP/HDPE/nf-EPR blend, PP/HDPE/f-EPR blend, PP/r-HDPE blend, PP/r-HDPE/nf-EPR blend

Polymers	E (MPa)	σ_r (MPa)	ε_r (%)	IR (J/m)	σ_f (MPa)	ε_f (%)
PP	1295±35	23.2±0.7	400	26±2	40.1±0.4	9.2±0.3
PP/HDPE	1337±175	21.5±0.6	65±11	29±4	39.0±0.2	8.3±0.1
PP/HDPE/nf-EPR	1639±253	37.5±0.6	12±1	46±4	41.0±0.3	8.6±0.3
PP/HDPE/f-EPR	1571±139	37.6±0.7	13±1	43±4	41.1±0.3	8.8±0.4
PP/r-HDPE	1379±95	18.3±1.8	18±4	28±3	39.6±0.3	8.0±0.2
PP/r-HDPE/nf-EPR	1380±78	35.2±1.2	15±1	36±4	40.2±0.1	8.1±0.2

The analysis of the results in Table 1 determined the significance of using a PP/HDPE (80/20) blend or a blend compatibilized with functionalized EPR (f-EPR) or non-functionalized EPR (nf-EPR) instead of using PP alone, particularly when the aim is utilizing waste materials, such as recycled HDPE (r-HDPE), and using loaded materials to reduce costs without impairing mechanical properties.

A slight increase in Young's modulus (E) for PP/recycled-HDPE and PP/non-recycled-HDPE blends as compared to pure PP can be observed in Table 1. The other mechanical properties, except for elongation at break (ε_r), show similar values within the range of experimental error. The results showed by elongation at break are due to the poor interfacial adhesion between these polymers because they are immiscible. This effect is more pronounced with recycled HDPE.

When nf-EPR and f-EPR are added to the PP/non-recycled-HDPE blend, a variation in mechanical properties is observed. In general, compatibilization of polymer blends represents a potential increase in these properties with respect to non compatibilized blends, particularly when there is poor interfacial adhesion between their components. In the case of Young's modulus, increases obtained amount to 23% when nf-EPR is added and 18% for blends with f-EPR compared to PP/HDPE blend. Also, at break point, strength (σ_r) increases by approximately 80%, whereas elongation at break drastically decreases by 80-85%.

When impact strength (IR) of compatibilized PP/HDPE blends is analyzed, increases of 59% and 48% for blends compatibilized with nf-EPR and f-EPR, respectively, are observed. At yield point (Yield strength, σ_f; Yield elongation, ε_f) variations between PP and PP/HDPE blend compatibilized with nf-EPR and f-EPR were not significant.

The results lead us to conclude that adding HDPE to PP does not significantly affect mechanical properties, except for elongation at break. When EPR is added, whether functionalized or non functionalized, similar behavior is observed, resulting in an increase in Young's module and in impact strength when compared to pure PP. Due to the specific use for which this blend is intended, an increase in elongation at break is not important whereas it is in mechanical properties such as modulus, tensile strength and impact strength.

The addition of non-functionalized or functionalized EPR to PP/non-recycled-HDPE blend possibly decreases the size of the minority phase, which results in an increase in the tensile strength of the composite material.

However, since no significant improvement in tensile and impact properties is observed in materials with f-EPR as compared to those with nf-EPR, it can be inferred that functionalization is not effective or that the functionalization percentage used is not appropriate. Therefore, the use of nf-EPR is favorable because costs are reduced since no functionalization is needed.

When non-recycled HDPE is replaced by recycled HDPE (r-HDPE), a comparison between PP/HDPE and PP/r-HDPE blends shows that the analyzed mechanical properties do not significantly vary, except for elongation at break, which reaches values of 65% and 18% respectively.

Regarding properties of the blends of PP with recycled and non-recycled HDPE with non-functionalized EPR, a slight decrease in the modulus and impact strength is detected when high density polyethylene is recycled. This phenomenon is due to the degradation processes which the material undergoes. These results lead us to conclude that recycled HDPE can be used in PP/r-HDPE/nf-EPR blend without significantly altering Young's modulus and impact strength.

In previous studies [9], mechanical behavior of PP/HDPE/non-functionalized EPR blend was analyzed, loaded at different concentrations (20, 30 and 40 wt. %), to determine the proper calcium carbonate concentration, treated or non treated with LICA 12. The results showed that optimal load concentration is 30% by weight.

Properties of PP/HDPE and PP/HDPE/nf-EPR blends and of pure PP when 30% treated or non treated filler is added, have to be compared to optimize mechanical properties and processing conditions and reduce raw material and processing costs.

The results obtained from the mechanical properties are shown in Table 2. They let us infer that adding treated filler at 30wt. % concentration to PP results in a increase of elongation at break when compared to that of PP/untreated-$CaCO_3$ blend. This is due to the interactions between the coupling agent and the polymer-filler interface, because one of its functions is to increase interfacial bond energy of the compound formed by the polymer matrix and filler, which inhibits the formation of micro-cracks on the surface or the material thus delaying its fracture. This behavior was not detected either in the PP/HDPE or the PP/HDPE/nf-EPR blends or in the blends with treated and untreated $CaCO_3$.

An increase in the modulus of PP, PP/HDPE and PP/HDPE/nf-EPR occurred also with the addition of treated and untreated filler. This behavior is the result of the restrictions imposed by the polymer matrix, which do not permit molecular movements. These results coincide with those obtained in the research by Maiti et al.[4,5], Arroyo et al.[8]; Yafit et al.[10]. With the treated filler, no significant improvement was attained in the modulus. According to the values reported in Table 2, filler treatment results in the PP/HDPE/nf-EPR blend with lower values for the tensile modulus as compared to the same blends with untreated load.

Table 2: Mechanical properties of PP, PP/HDPE blends and PP/HDPE/nf-EPR with 30% filler treated with LICA 12 (t) and untreated filler (ut.)

Blend	E (MPa)	σ_f(MPa)	ε_f (%)	σ_r (MPa)	ε_r(%)	IR(J/m)
PP/$CaCO_3$ ut.	1592±130	33.0±1.3	5.8±0.2	23.1±0.6	38±8	24±2
PP/$CaCO_3$ t	1613±191	30.5±0.4	5.5±0.2	21.9±0.4	83±7	28±1
PP/HDPE/$CaCO_3$ ut	1679±183	33.6±0.3	5.7±0.2	28.3±0.1	21±2	24±2
PP/HDPE/$CaCO_3$ t	1541±138	31.3±0.1	5.1±0.1	26.2 ±0.3	24±3	24±2
PP/HDPE/nf-EPR/$CaCO_3$ ut	2855±351	29.9±0.2	5.2±0.1	26.7±0.5	17±2	28±3
PP/HDPE/nf-EPR/$CaCO_3$ t	2065±300	32.3±0.9	5.7±0.3	29.5±1.1	13±3	29±3

As to variation of strength at the yield point and at the break point (Table 2) similar behavior is observed for PP/HDPE/nf-EPR with treated and with untreated filler, thus resulting in values lower than those obtained with the blends without filler (Table 1). Decrease in strength is due both to the inclusion of particles and their dispersion in the polymer matrix, which results in an increase in the stress concentration, which brings about, in turn, a decrease in material strength. In the case of PP/HDPE with treated filler, yield strength decreases and breaking strength increases as compared with the untreated filler. Whereas for loaded PP, breaking strength remains unchanged and yield strength decreases in relation to pure PP.

When untreated filler is added to the PP/HDPE/nf-EPR blend, values of elongation at break increase by almost 40% in comparison with the value for the PP/HDPE/nf-EPR blend without filler. This behavior is not very common for loaded compounds, because in experiments carried out with loaded pure polymers [4,5,10], the effect of rigidization on the polymer chains prevents it from being deformed. This means a decrease in elongation at break, as observed in PP and the PP/HDPE blend with treated and untreated filler. In this regard it is possible to infer that when a rigid filler is added to a matrix formed by two polymers and a copolymer, interactions produced are different, which could be the reason for this unusual behavior. On the other hand, the influence of treating the filler with a coupling agent of the titanate type, LICA 12, was not as expected for PP/HDPE and PP/HDPE/nf-EPR blends, because values for elongation at break should be higher than the values of the blends with untreated filler.

The results obtained lead us to conclude that the coupling agent does not produce the plastifying effect which improves elongation at break. This phenomenon occurs only in the case of PP with treated filler, because the increase in interfacial bond energy of the compound formed by the polymer matrix and the filler inhibits the formation of micro-cracks on the surface of the material and delays its fracture. Table 2 also shows the values for impact strength, which decrease in blends (PP/HDPE and PP/HDPE/nf-EPR) with treated filler as well as in blends with untreated filler. In the PP/$CaCO_3$ blend, impact strength values are similar, whether coupling agent is used or not.

These studies let us conclude that calcium carbonate can be used untreated at 30% concentration, because the use of LICA 12 does not produce the expected effects. This could be explained by means of the complexity of the systems studied, because many factors are in play which cannot be easily related in multicomponent systems. There is no comprehensive study on this kind of composite materials in the literature, except for the PP/LDPE blend with talc by Arroyo et al. [8].

Based on the fact that this research is aimed at reutilizing waste material, in this case recycled HDPE, an analysis of its properties is carried out to detect the possibility of its being used in the blends under study as a replacement for PP with treated and untreated filler.

Table 3: Mechanical properties of PP, PP/r-HDPE, PP/r-HDPE/nf-EPR with 30% filler treated with Lica 12 (t.) and untreated load (ut.).

Blends	E(MPa)	σ_r (MPa)	ε_r (%)	IR (J/m)
PP/CaCO3 t.	1592 ± 130	23.1 ± 0.6	38 ± 2	24 ± 2
PP/CaCO3 ut.	1613 ± 156	21.9 ± 0.4	83 ± 7	28 ± 1
PP/r-HDPE/CaCO3 ut.	1558 ± 156	29.3 ± 0.6	15 ± 2	14 ± 3
PP/r-HDPE/nf-EPR/CaCO3 ut.	1629 ± 106	26.9 ± 0.5	24 ± 1	20 ± 1

When the PP/r-HDPE blend is compared to PP (Tables 3 and 2), both with filler, deterioration in the impact strength and in elongation at break is observed. This phenomenon could be the result of the poor interaction between both polymers, which further decreases with the filler. The addition of EPR to the PP/r-HDPE blend with filler substantially improves its properties, which can be comparable to those of PP with untreated filler and shows an impact strength slightly lower for PP with treated filler. As far as elongation at break is concerned, its values are quite low for blends with recycled material, because the interaction between the different materials is not adequate.

In the analysis of the values obtained from the thermograms of the different compounds (Table 4), when $CaCO_3$ is used with a coupling agent fusion (T_f) and crystallization (T_c) temperatures and enthalpies (ΔH_f, ΔH_c) slightly decrease. This variation is not higher than three degrees when compared to the blends with untreated load, which could be considered negligible, therefore it is not necessary to treat the filler.

Table 4: Thermal Properties of the blends with $CaCO_3$ treated (t.) and untreated filler (ut.)

Blends	T_f(°C)	T_c(°C)	ΔH_f (J/mol)	ΔH_c(J/mol)
PP/$CaCO_3$ t.	167	122	53	71
PP/$CaCO_3$ ut.	163	120	54	68
PP/HDPE/$CaCO_3$ ut.	131-164	120	75	81
PP/HDPE/$CaCO_3$ t.	135-167	118	66	80
PP/HDPE/nf-EPR/$CaCO_3$ut.	132-165	121	66	77
PP/HDPE/nf-EPR/$CaCO_3$ t	131-163	118	66	74
PP/r-HDPE/$CaCO_3$ ut.	131-163	119	77	91
PP/rHDPE/nf-EPR/$CaCO_3$ ut.	131-163	118	76	87

Thus it could be concluded that it is possible to obtain a product with characteristics similar to loaded PP, treated and untreated, and to reduce raw material and processing costs.

CONCLUSIONS

Based on the results of this research, we can infer that the values of the mechanical and thermal properties analyzed for PP/r-HDPE, PP/r-HDPE/EPR blends with untreated $CaCO_3$ show that these can replace PP loaded with calcium carbonate, untreated and treated with the coupling agent (LICA 12). This is an optimal alternative for replacing part of the non-recycled material with recycled material, which would result in lower raw material and finished product costs and in a better benefit/cost relation.

ACKNOWLEDGEMENT: Plásticos M y M and Propilven.

REFERENCES

[1] Avipla, Boletín: "Reciclaje y Revalorización de desechos plásticos", May (1988).

[2] Buekens A. " Draft of the Study on Management of Plastic Wastes in the EEC region", Economic and Social Counsil United Nations, May (1992).

[3] Ichazo M., Gonzalez J., Albano C., Navas R. " Mechanical properties of PP/HDPE/EPR with Calcium Carbonate". *12th Bratislava International IUPAC/EPF Conference on Polymers. Modified Polyolefins for Advanced Polymeric Material. Bratislava. Slovak Republic.* pp. 99-100 (1997).

[4] Maiti S., Mahapatro P. " Mechanical Properties of iPP/$CaCO_3$ Composites". *J. Appl. Polymer Sci.* 42, pp. 3101-3110 (1991).

[5] Maiti S., Lopez B. "Tensiles Properties of Polypropylene/Kaolin Composites". *J. Appl. Polymer Sci.* 44, pp. 353-360 (1992).

[6] Tjong, S., Li R., Chueng T. "Mechanical Behavior of $CaCO_3$ Particulate-Filled B-Crystalline Phase Polypropylene Composites". *Polymer Eng. Sci.* 37(1), pp. 166-172 (1997).

[7] Mitsuishi K., Kodama S., Kawasaki H. "Mechanical properties of Polypropylene filled with Calcium Carbonate." *Polymer Eng. Sci.* 27(17), pp. 1069-1073 (1985).

[8] Arroyo M., Sánchez M., Vigo J. " Effect of Talc surface treatment on the mechanical properties of composites based on PP/LDPE blend matrices". *Polymer Eng. Sci.* 31(4), pp. 245-252 (1991).

[9] Ichazo M., Gonzalez J., Albano C., Rosales C., Perera R., Navas R. " Mechanical Behavior of PP/HDPE/EPR Blend with Calcium Carbonate". *Antec' 98.* (1998).

[10] Yafit S., Vega F. " Propylene filled compound, Why? ". *Antec' 97* (1997).

INFLUENCE OF METALLIC FILLERS ON THE THERMAL AND MECHANICAL BEHAVIOUR IN COMPOSITES OF EPOXY MATRIX

Z. Brito(1) and G. Sánchez(2).
(1)*Instituto Universitario de Tecnología de Valencia. Av. Cuatricentenario. La Manguita. Valencia. Edo. Carabobo. Fax: 58-41-231570.* E-mail: zullyb@telcel.net.ve
(2)*Universidad Central de Venezuela. Caracas. Venezuela.*

ABSTRACT

In this research the thermal behavior and the strain at rupture of a liquid epoxy resin (diglycidil ether of bisphenol A,DGEBA) crosslinked with ethylenediamine (ETDA) and filled with metals were analysed. The thermal treatment was carried out by thermogravimetric studies under nitrogen at high resolution (heating rate of 50°C/min) and temperature range at 25-500°C. Samples without and with several percents of metallic fillers (Cu, Zn and Al, respectively) were selected. The results from the thermal treatment showed a high influence of filler on the thermal stability of the epoxy matrix studied . The materials with filler presented decomposition temperature lower than those of the non-filled material.

The experimental results from the mechanical test showed the highest strain at rupture in absence of metallic filler for the 1:1 epoxy/amine ratio in contrast to the material with filler where mechanical behavior depended on filler type and the content. The composite with Cu presents strain at rupture of all.

INTRODUCTION

Polymer composite materials have been studied for many years and really constitute a very active area for researches in materials science. Such compounds present properties that should result by combination of the properties of its components, herald new industrial applications, which are not contemplated from each component alone.

It is well known that the thermal and mechanical behavior of polymers are strongly influenced by factors such as filler type, size, content and shape. Besides, such properties have a very complex dependence on the chemical structure and the crosslink density when thermoset resins and metallic fillers are combined.

Thermoset resins are very useful as matrix in high performance composite material. The epoxy resins form one of the most important groups among thermosets.

The objective of this work is to continue the study of the thermal degradation for DGEBA/ETDA systems. Previous researches about the thermal and kinetic behavior of DGEBA/ETDA composites had been published by the authors [1-4].

EXPERIMENTAL

The manufacturation of samples have been described in detail previously [5]. Three epoxy-amine molar ratios were used, namely, 1:1, 1:1.5 and 2:1. Composites with 10, 20 and 30% of various metallic fillers (Zn, Cu and Al) were employed. The metal particles having a size no more than 250 mesh were mixed with the epoxy/amine molar ratios mentioned.

The thermal treatment was carried out in a Dupont 1090 thermobalance, under nitrogen atmosphere, over the temperature range 25-500°C and at constant heating rate of 50°C/min.

In the mechanical test an Instron equipment was used. The samples were prepared according to ASTM DIN 53457 standard.

RESULTS AND DISCUSSION

Figure 1 shows the thermogravimetric curves (TG) for the epoxy/amine systems non-filled selected. Several steps were observed in the thermal decomposition of each material studied. For instance, the 1:1 and 1:1.5 epoxy/amine ratios showed three steps, in contrast to the 2:1 where five steps were carried out. Obviously, the crosslinking is a factor that concern to the thermal behavior of the resin. According to literature[6] at the stoichimetric ratio 1:1 there are a crosslink at every amine-epoxy junction in opposition to epoxy/amine ratio of 2:1 where the structure consists of four epoxy units connected to one amine molecule. The net result is an increasing number of crosslinked molecules. In the case of amine groups in excess (ratio 1:1.5) the thermal behavior was similar at the ratio 1:1.

On the other hand, from figure 1 we can see that when the ratio 2:1 is used, over 350°C, a higher thermal stability is achieved, together with a high amount of residue.

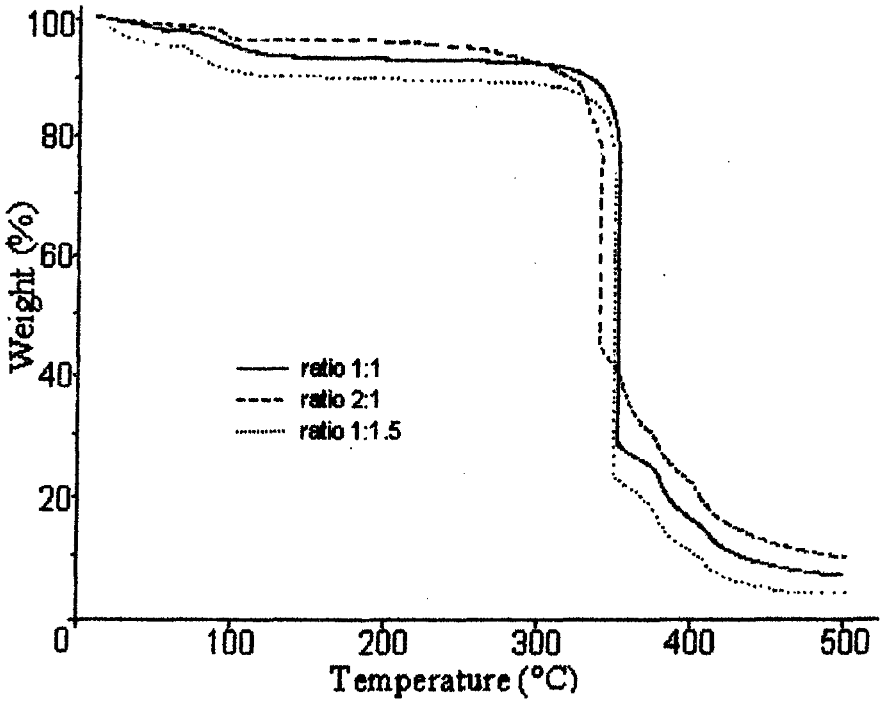

Figure 1. TG curves for DGEBA/ETDA non- filled.

Figure 2 shows TG curves for materials with ratio 1:1.5 and 30% of filler. In the case of the composite with Cu four different reaction mechanisms were observed and they are between 325-400°C or so. The presence of Zn in the DGEBA/ETDA matrix involved two different mechanisms over the range of 325-350°C and with Al there are three from 350 to 400°C.

The weight losses observed from 25 to 100°C were attributed to humidity adsorbed by the porous filler, water content in the matrix and ETDA volatilization.

The influence of the metallic filler on the thermal behavior of the studied epoxy/amine systems is evident and the complexities of the changes depend among others on characteristic of the filler used.

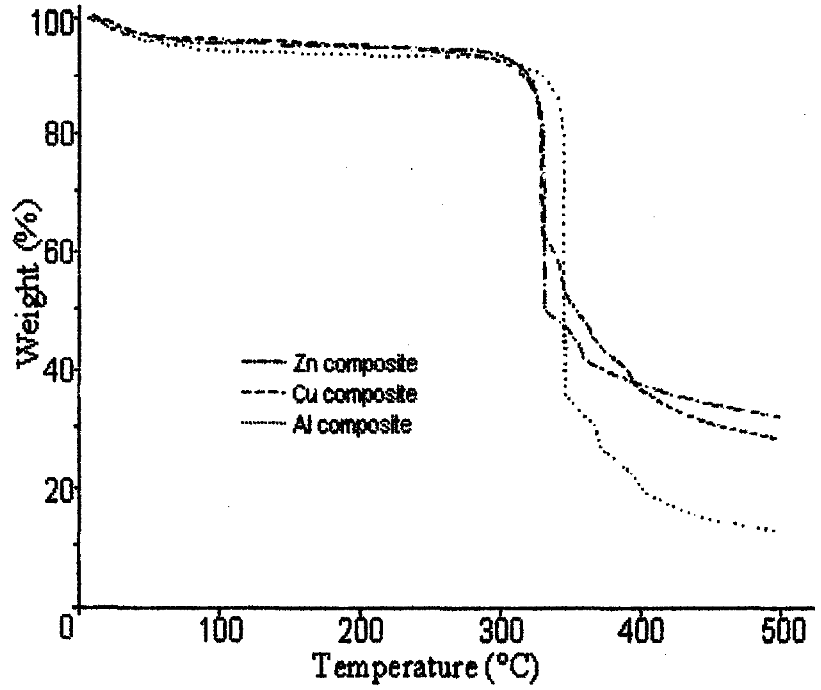

Figure 2. TG curves for DGEBA/ETDA filled.

The influence of the filler concentration on strain at rupture for all samples under investigation can be seen in figures 3, 4 and 5. In the compounds without metallic filler the values of strain at rupture were: 6.32 Kg/mm^2 for the epoxy/amine ratio 1:1, 2.09 Kg/mm^2 for the ratio 2:1 and 1.37 Kg/mm^2 for the 1:1.5.

Figure 3 shows the behavior of epoxy/amine ratio 1:1 composites, we can see in this one that the metallic filler caused a decrease on the strain at rupture. This effect was more pronounced for the composites with Zn and Al, respectively. Besides, a reduction in the studied mechanical property was observed at high filler concentration for all composites.

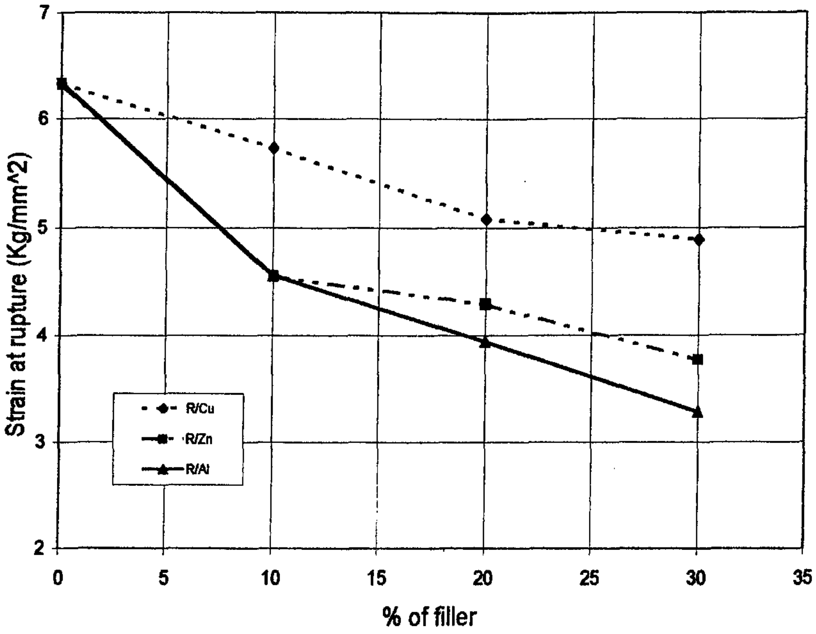

Figure 3.Strain at rupture Vs. % of filler.Epoxy/amine ratio 1:1.

Figure 4 presents the behavior of epoxy/amine ratio 2:1 composites. A similar behavior on the strain at rupture , up to 10% of filler, was observed in the materials with Cu and Al respectively, whereas, composite with Zn showed values of strain at rupture lower than those materials mentioned.

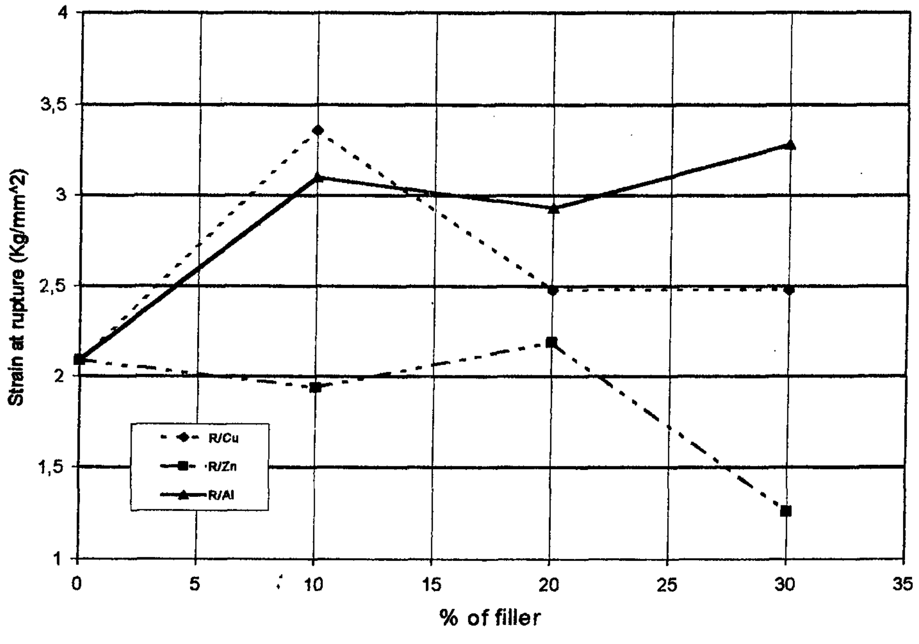

Figure 4. Strain at rupture Vs % of filler. Epoxy/amine ratio 2:1.

Finally, figure 5 shows the mechanical behavior of the ratio 1:1.5 composites under investigation. It becomes evident that Cu addition to the DGEBA/ETDA matrix greatly increases the composite's strain at rupture and that with the subsequent incorporation of Cu, up to 10%, the strain at rupture begins to fall due to poor ductility of the matrix. From this results, it can be concluded that high strain at rupture correspond to weak filler-matrix adhesion.

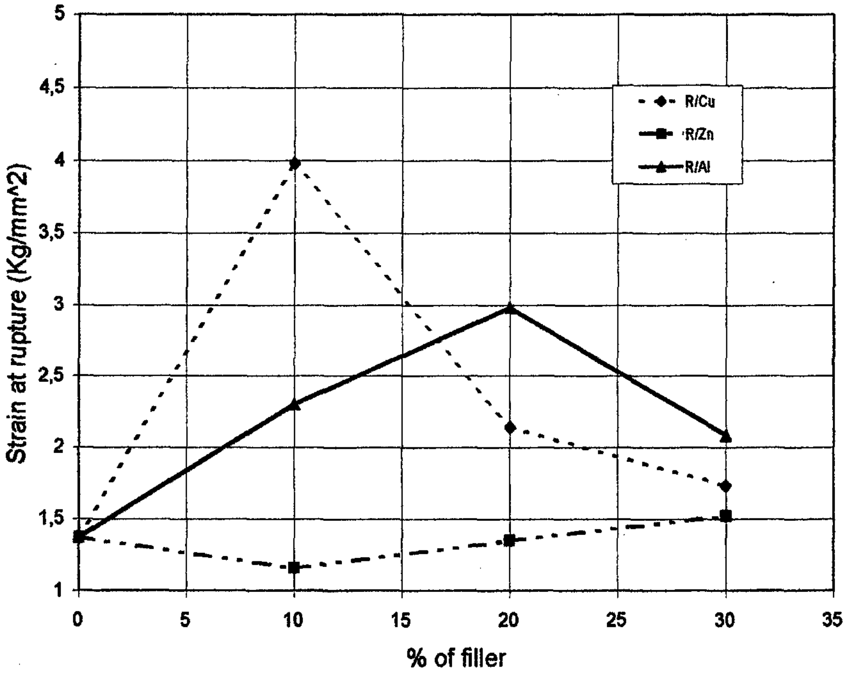

Figure 5. Strain at rupture Vs. % of filler. Epoxy/amine ratio 1:1.5.

CONCLUSIONS

A high influence of filler on the thermal stability of the DGEBA7ETDA matrix was observed. The materials with filler presented decomposition temperature lower than those of the non-filled material. Besides, the crosslinking is a factor that concern to thermal behavior of the resin.

The mechanical behavior of all composites was complex.The strain at rupture depended among others on type and content of filler. The composite with Cu showed the highest strain at rupture.This effect can be attributed to weak filler- matrix adhesion.

REFERENCES

[1] Brito .Z., V. Torrealba, G. Sánchez and L. Hernández.. *Numerical Methods in Engineering Simulation.* Computational Mechanics Publications.Boston. UK. 367-374 (1996).

[2] Brito. Z, V. Torrealba, G. Sánchez and L. Hernández. *Latin American Applied R. Research.* Vol. 26/S. 31-34 (1996).

[3] Brito. Z y G. Sánchez. *Revista Internacional Información Tecnológica.* Vol. 7. N°4. 117-120 (1996).

[4] Brito. Z., V. Torrealba, G. Sánchez and L. Hernández. *Acta of the 10TH International Symposium on Polymer Analysis and Characterization.* August 10-13, Canada. 28-29 (1997).

[5] Sánchez. G., Z. Brito., G. Perdomo and V. Mujica. *Polymer Degradation and Stability.* Vol. 40.109-114 (1993).

[6] Bell. J. *Journal of Polymer Science.* Part A-2. Vol. 8.417-436 (1970).

A COMPARISON BETWEEN THE TENSILE PROPERTIES OF INJECTION MOLDED AND COMPRESSION MOLDED SAND-REINFORCED POLYETHYLENE

A.Y. Kandeil[1] and R.R.Zahran[2]

[1] College of Engineering and Technology, Arab Academy for Science and Technology, P.O. Box 1029, Alexandria, Egypt

[2] Department of Chemical Engineering, Alexandria University, Alexandria - 21544, Egypt

INTRODUCTION

When particulate fillers are incorporated into a polymeric matrix, the mechanical and thermal behavior of the obtained composite system may critically change [1]. Work performed on such systems involved industrial fillers such as carbon black, calcium carbonate, mica and talc [2-4]. The effect of naturally occurring fillers such as river, mine and beach sand [5] on some properties of filled polymeric systems was also investigated. The nature and extent of interaction between the polymer matrix and the filler is decisive for many of the properties and applications of these composites. Among the naturally occurring fillers, sand is relatively cheap and is found more abundantly than the aforementioned industrial fillers. In the present work, an experimental investigation was designed to evaluate and to compare the tensile performance of sand-reinforced polyethylene (SRPE) composite samples, prepared by injection and compression molding.

EXPERIMENTAL

Low density polyethylene (LDPE) Lotrene FB 3003 (melt flow index = 0.25 - 0.23 g/10 min and specific gravity = 0.920) was used. Beach sand (specific gravity = 2.7203) was used as a filler. The sand was first washed with water at 22±1°C followed by soaking in distilled water for 24 hours. The sand was then dried at 105°C for 6 hours after decantation. The dry sand was sieved into five different cuts: 600, 425, 250, 150 and 75 μm.

Sand was slowly added and intimately mixed with the polymer to form a homogeneous mix. Dumb-bell shaped tensile specimens with 65 mm gauge length, 12.6 mm width and a thickness of 3.1 mm, were prepared using injection molding. The detailed procedure for sample preparation is explained elsewhere [6].

SRPE composite sheets were prepared by compression molding and rectangular plates of SRPE (170 x 70 x 5 mm) were obtained. They were then machined using a water saw to rectangular strips (70 x 15 x 5 mm), for tensile testing, as given in Reference 6

The SRPE composite samples were mechanically tested using a Lloyd Instrument Materials Testing Machine, equipped with a 5 kN load cell, with a cross-head speed of 100 mm/min, at 22±1°C. Five specimens were tested for each reported data point. The flow and fracture behavior of the prepared composite samples were analyzed by measuring the tensile modulus, yield stress, tensile strength and fracture strain obtained from the stress-strain diagrams.

RESULTS AND DISCUSSION

Figure 1-a shows that the tensile strength for the injection molded SRPE increases with sand content for all the examined melt temperatures. The rate of strengthening, however, is higher for samples prepared at lower melt temperatures. Similar effects were observed for different die temperatures, as shown in Figure 1-b. On the other hand, for compression molded samples, the tensile strength decreases linearly with the sand content. The sand particle size for all the results shown in Figures 1-a,b and c is 250 μm. It is clear that the effect of sand addition depends of the method of the sample preparation. A strengthening effect is observed for samples prepared by injection molding, while for compression molded samples, sand addition reduces the tensile strength.

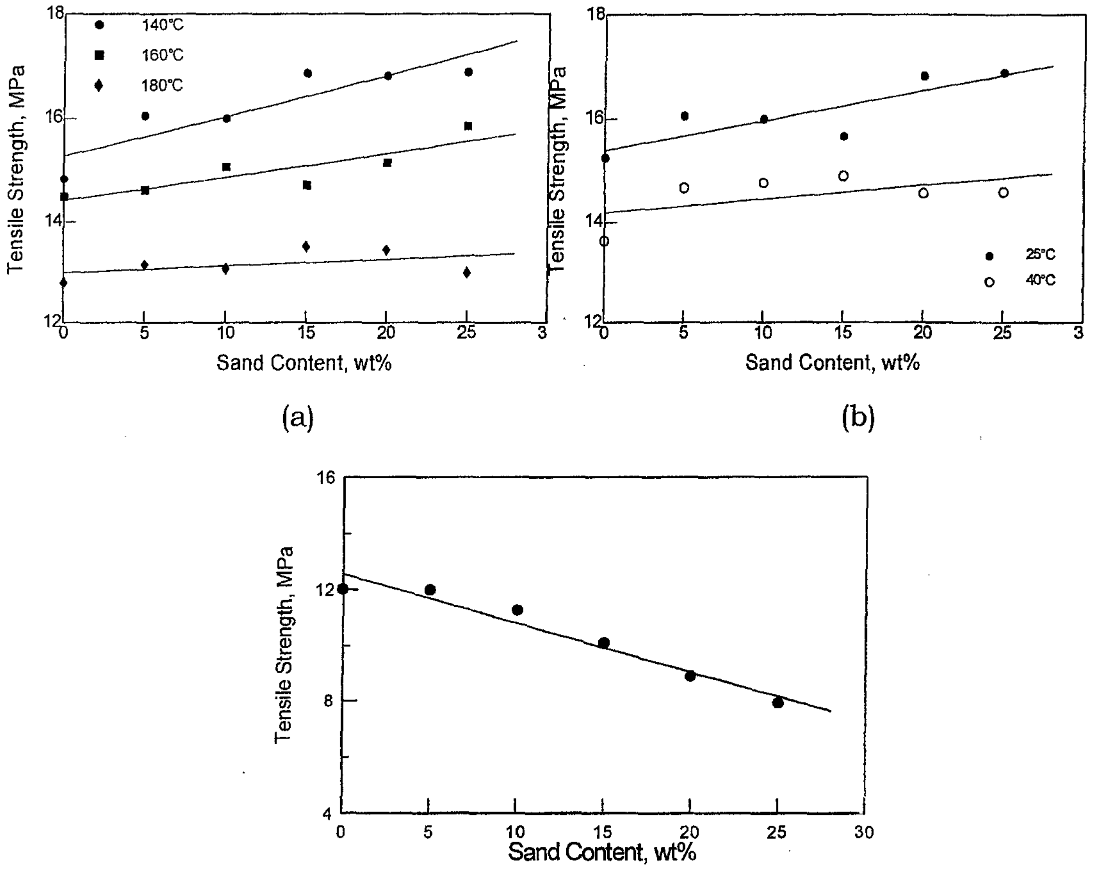

(a)

(b)

(c)

Figure 1 Variation of the tensile strength with the sand content at a sand particle size of 250 μm; (a) injection molding at different melt temperatures, (b) injection molding at different die temperatures and (c) compression molding.

The effect of sand content on the modulus of elasticity for injection molded and compression molded samples is shown in Figure 2. For injection molded samples, the modulus is an increasing function of the sand content, irrespective of the melt temperature. However, for compression molded samples, the effect of sand content on the modulus depends on the sand particle size. This will be explained later in terms of several structurally dominating mechanisms.

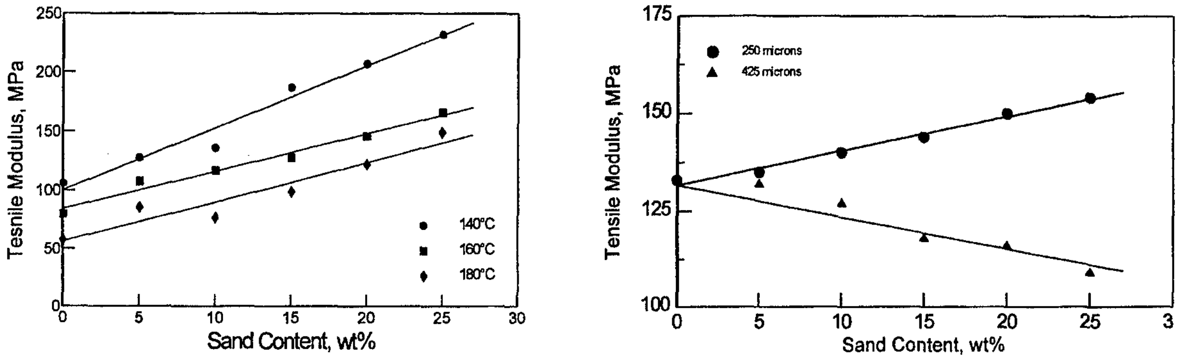

(a) (b)

Figure 2 Effect of sand content on the tensile modulus of (a) injection molded samples at different melt temperatures and (b) compression molded samples with two different particle sizes

The effect of sand particle size on the tensile strength for the injection and compression molded samples is shown in Figure 3. Figure 3-a indicates that the tensile strength increases with sand particle size until a peak at about 350 μm. Further increase in particle size results in a decrease in the tensile strength. This behavior was observed for the different melt temperatures, with the lower temperature producing the highest strength, as to be expected [6].

Figure 3-b shows that compression molded samples, show a slight increase in the tensile strength with sand particle size, for the 5wt% sand content only. A higher sand content, however, tends to decrease the tensile strength.

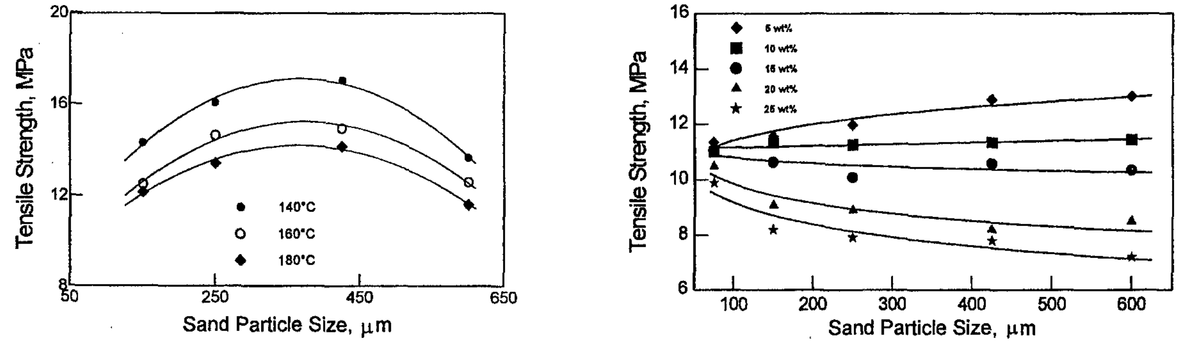

(a) (b)

Figure 3 Variation of the tensile strength of SRPE with sand particle size: (a) injection molding at various melt temperatures, and (b) compression molding..

Linear relationships between the tensile modulus and the sand particle size were observed for the injection molded samples, reinforced with 15wt% sand, at different melt temperatures , as seen from Figure 4-a. For the compression molded samples, reinforced with the same sand content, a non-linear behavior is observed, (Figure 4-b). A transition from a stiffening to a weakening effect occurs at a sand particle size of approximately 350 μm. In other words, below this critical sand size, the tensile modulus increases with sand content and above it, the modulus decreases with the sand content.

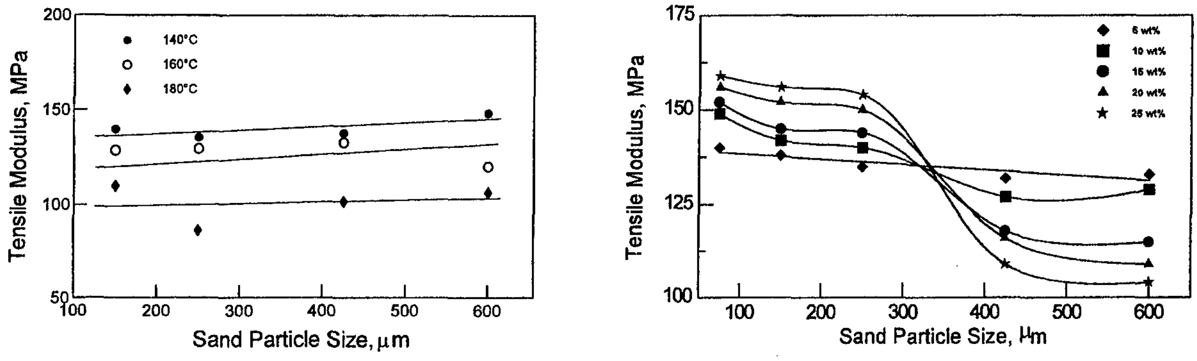

(a) (b)

Figure 4 Effect of sand particle size on the tensile modulus of SRPE: (a) injection molded at different melt temperatures; (b) compression molded at different sand contents

The variation of the fracture strain of injection and compression molded SRPE samples with the sand particle size, at different sand contents, is shown in Figures 5-a and 5-b, respectively. For injection molded samples, a maximum ductility is exhibited for a particle size of about 350 μm. In other words, ductility increases with sand particle size until about 350 μm, after which a drop in the ductility is observed. Such a behavior may be attributed to the nature of interaction between the filler and the polymer matrix,, as well as the filler's geometry [6]. For a given sand content -per unit volume- smaller particles provide relatively more sites for stress concentrations and possible void initiation and fracture origins. This leads to early fracture with deformation and consequently a decreased ductility. On the other hand, above 350 μm, the effect of decohesion is more pronounced and dominant [6].

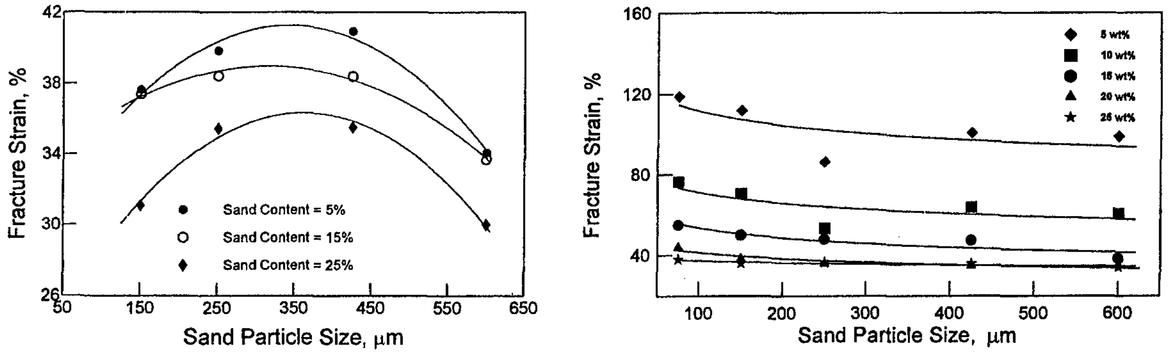

(a) (b)

Figure 5 Variation of fracture strain (ductility) with sand particle size at different sand contents for (a) injection molded samples; (b) compression molded samples.

For compression molded samples, the fracture strain decreases slightly with the sand particle size, within the entire range examined, as seen in Figure 5-b , and does not show the initial increase observed for injection molded samples.

The flow behavior of SRPE composites can be analyzed in terms of the superposition of more than one stress component, in addition to the matrix tensile strength. They are: the interfacial strength between the sand filler and the polymer matrix, the interlocking strength resulting from the mechanical interaction between the irregularly shaped filler and the matrix , and the induced matrix strengthening due to relatively higher strain rates imposed on the matrix because of the presence of the rigid sand particles [6]. At a given sand content, the increase in sand particle size is accompanied by a reduction in the number of sand particles. As mentioned earlier, smaller particles provide a relatively higher available interfacial surface area per unit volume of the composite sample, and consequently a greater chance for physical adhesion and wetting, in spite of the possible irregularities in the shape of the sand particles. Therefore, for a given sand particle size, at a relatively low sand content, the chances for possible irregularities in the particle's shape are lower when compared with higher sand content. So, at relatively low sand content, as the particle size increases, the number of sites available for sand/polymer adhesion is reduced. With a lower chance for the presence of irregularly shaped particles, the effect of mechanical interlocking increases slightly, and it overcomes the effect of internal friction and possible dewetting (decohesion) between the sand phase and the polymer phase.

At this point it is important to emphasize that compression molding allows the polymer melt/sand mix to solidify in a quiescent manner without any externally imposed forces on the mix to flow in a restricted conduit, as in injection molding. So, in injection molding, it is important to realize that if the sand particle size is greater than the critical size of 350 µm, a strength reduction will be excepted upon sand addition, as seen in Figure 3-a. On the other hand, for compression molding with relatively high sand content (e.g. > 10 wt%)and/or sand particle size, the interlocking will not be very much prevailing. Consequently, above a 10 wt% sand content, the effect of internal friction and decohesion, which are now more pronounced and dominant, overcomes the effect of interlocking. Accordingly, the possibility of vacuole formation and dewetting [6] is now more pronounced. The net result is a reduction in the tensile strength of the SRPE composites, with filler size and/or content. The diagram shown in Figure 6 summarizes the various prevailing mechanisms affecting the strengthening of SRPE samples prepared by either injection molding or compression molding. Such mechanisms explain the initial increase in the ductility for injection molded samples (see Figure 5-a), since more interlocking will promote the interfacial strength coupled with an enhanced ductility. The interlocking phenomenon is not significant for either injection molded samples with sand particle size greater than 350 µm, or compression molded samples (see Figures 5-a and 5-b). In the latter cases, dewetting coupled with less interfacial friction are the responsible mechanisms.

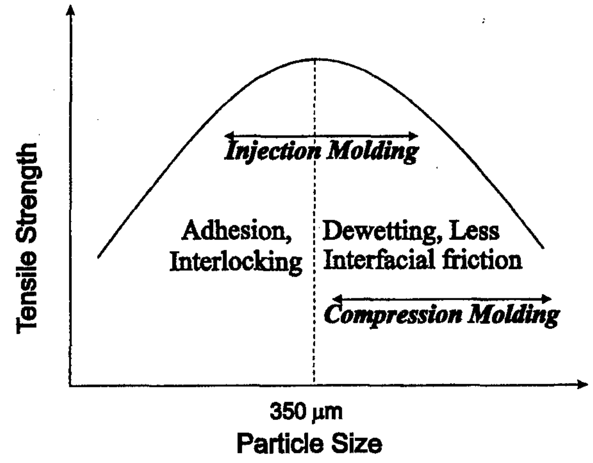

Figure 6 Dominating phenomena for the tensile behavior of SRPE

It is now pertinent to point out the incurred practical implications of using injection and compression molding for the preparation of SRPE. Table 1 shows the recommended methods of preparation for a given tensile behavior.

Table 1 Recommendations for preparing SRPE composites

Desired Property	Recommended Method of Fabrication	Condition
Strength	Injection molding	Lower melt/die temperature Sand particle size < 350 µm
Stiffness	Injection molding Compression molding	Lower melt/die temperature Sand particle size < 350 µm
Ductility	Injection molding	Lower melt/die temperature Sand particle size < 350 µm

CONCLUSIONS

A transition in the dominating mechanisms takes place at a critical sand particle size of about 350 µm for SRPE composites prepared by either injection or compression molding. A stiffening effect (increase in tensile modulus) is observed for all the samples prepared by injection molding irrespective of the sand particle size and/or content. If a strengthening effect is essential, only injection molding, at lower melt and/or die temperatures, is to be used, and the sand particle size should not exceed the critical size of 350 µm. On the other hand if stiffness is desired, either injection molding at lower melt and/or die temperatures, or compression molding with sand particle size less than the critical 350 µm size, is to be used. Compression molding is not suitable if ductility is desired. Furthermore, injection molding SRPE with a sand particle size less than the critical 350 µm, at lower sand content, will produce samples of relatively higher ductility.

REFERENCES

1. L. Sun and R. Salovey, in Advancements in Materials for Polymer Composites and Special Topics, Proceedings of the SPE Regional Technical Conference, Los Angeles, pp105 (1990)
2. M.R. Kamel and A. Mutel, J.Polym.Eng, **5**, pp. 293 (1985).
3. Y.K. Leong and D.V. Boger, J. Colloid and Interface Sci., **136,** pp. 249 (1990).
4. T.M. Malik, M.I. Farroqi and C. Vachet, Polym.Comp., **13,** pp. 174 (1992).
5. A.P. Padilla, A. Sanchez-Solis and O. Manero, J.Comp.Mater., **22**, pp. 616 (1988).
6. A.Y. Kandeil and R.R. Zahran in Polymers and other Advanced Materials: Emerging Technologies and Business Opportunities, Edited by P.N. Prasad, J.E. Mark and T.J. Fai, Plenum Press, NY (1995) pp. 125.
7. R.R. Zahran, Mater. Lett., **34**, pp. 161 (1998)

THE EFFECT OF STRAIN RATE AND FIBRE CONTENT ON THE POISSON'S RATIO OF GLASS/EPOXY COMPOSITES

Okenwa I. Okoli[1] and G.F. Smith[2]

[1,2]Warwick Manufacturing Group, University of Warwick, Coventry, CV4 7AL, UK

INTRODUCTION

The present engineering trend towards lean weight vehicle structures has paved the way for the increased utilisation of polymer composite materials in the automobile industry. Nevertheless, fibre reinforced composites (FRC) are still regarded as relatively new materials within the mechanical engineering field and often lack the the detailed material property data associated with metals. In particular, the use of composites in safety critical applications, leads to uneasiness since the mechanical response in crash applications is not well understood [1]. Many complex processes occur in crash situations. The material is subjected to rapid accelerations and rapid straining with large pressure shocks, often accompanied by huge temperature increases of several hundreds of degrees [2]. This further stresses the need for a full characterisation of the behaviour of fibre reinforced polymer composites under dynamic loading conditions and has prompted numerous investigations in recent years [3,4,5,6,7,8,9,10]. However, when compared to metals, relatively few studies have been conducted to investigate polymer mechanical properties at high strain rate [2].

Nevertheless, the strain rate effects of most polymers can be described by the Eyring theory of viscosity [11], which assumes that the deformation of a polymer involves the motion of a chain molecule over potential energy barriers. The Eyring model [11], suggests that yield stress varies linearly with the logarithm of strain rate. This is more so, since [12] at higher rates, the polymer matrix has less time to localise.

In the present study, tensile tests were performed on a glass epoxy laminate at different rates of strain to determine the effects of strain rate on the Poisson's ratio of the material. In addition, further tests were conducted at varying fibre contents to verify the relationship between fibre content and Poisson's ratio.

EXPERIMENTAL WORK

The apparatus and procedure used to obtain the tensile properties in the two laminates are described below.
The tensile tests were performed according to the method prescribed in ASTM D3039 [13].

The test specimens were cut from Tufnol grade 10G/40[a] glass/epoxy, 3 mm thick composite sheets. The glass was a cross-ply plain weave [0/90] fabric. The composite had a fibre weight fraction of 70% with 18 layers of glass. The specimens were cut 200 mm by 15 mm. Aluminium tabs 1 mm thick and 50 mm long were locally bonded on to the specimens with an adhesive, leaving a gauge section of 100 mm. Strain gauges (Measurement Group No. CEA-06-125UT-120) were bonded on either side of the specimens with (Measurement Group) M Bond 200 adhesive, to measure the axial and transverse strains on the material during testing. All data was logged on to a personal computer via a data logger. The low speed tensile tests were performed on a M30K Lloyds tensile testing machine at 4 cross head velocities (1.7, 8.3, 17.0, and 83.0 (x10^{-2}) mm.s^{-1}. Further tests were carried out at high speeds on an Instron 1343 tensile tester at 4 cross head velocities (10, 100, 1000, 2000 mm.s^{-1}).

The second material were locally manufactured random continuous glass/epoxy laminates with different fibre volume fractions (15.5, 20.7, 26.9, 38.0 and 41.2 %). They were also tested as with the previous material, but at a singular cross head velocity of 0.83 mm.s^{-1}.

RESULTS AND DISCUSSION

It was observed from Tables 1 and 2, and in Figure 1, that there was little variation in Poisson's ratio with log of strain rate. That is, the ratio of transverse strain to the corresponding axial strain below the proportional limit was not found to be rate sensitive for the material tested. This finding for reinforced thermoset is in contradiction to the observed behaviour of Poisson's ratio for unfilled thermoplastics which is non-linear with strain rate and is reported to decrease [14]. The absence of rate sensitivity in the Poisson's ratio of the composites tested as opposed to the reported rate sensitivity in thermoplastics can be attributed to the glass content in the composite laminates and the absence of glass or fibres in the thermoplastic as tested by Michaeli [14]. This is in agreement with the findings of other researchers [15,16,17,18,19,20,21,22,23,24,25].

Lakes [15] explains that composite properties may be linked with constituent properties by applying the corresponding principle of viscoelasticity to the elastic problem for the composite. However [15], when in a fibre dominated regime (as with the present case), the insensitivity of Poisson's ratio becomes imminent since the composite properties are much more sensitive to fibre stiffness than matrix stiffness [16,17]. Even a pure polymer may not change its Poisson's ratio with strain rate if it is in the glassy regime [18,19]. This is adduced by Ferry [20]. Caddock [21], Broughton [22], and Bader [23], agree with the findings of this work, since neither the polymer or the reinforcement would be expected to behave as viscoelastic materials.

This is further illustrated in this work, with the aid of photomicrographs. Figure 2 shows a magnified fracture surface of a Tufnol laminate tested in tension at a cross-head velocity of 1.7x10^{-2} mm.s^{-1}. The surface shows individual as well as group (bundle) fibre fracture. This may be attributed to translaminar tensile fracture [26] the fracture surface is rough with protruding broken fibres. The fibre ends indicate a brittle failure mode. However, there are signs of matrix adhering to the fibres which indicate a good bond in the fibre-matrix interface. This brings about brittle failure in the fibres since interfacial bonding influences the intralamina strength, the interlaminar shear strength and the interlaminar tensile strength [27]. The observed pull-out of fibres is dependent on the bond strength and the load transfer mechanism from matrix to fibre.

---

[a] Tufnol Birmingham, Birmingham B42 2TB, UK.

Figure 3 shows a magnified fracture surface of a Tufnol laminate tested in tension at a cross-head velocity of 10 mm.s^{-1}, with fibre bunch pull-out and signs of matrix adhesion. It was pointed out earlier that fibre-matrix adhesion brings about brittle failure. Increased damage in the matrix brought about by a combination of the increased test speed and the interfacial bond strength can be observed, and results in the bunch fibre pull-out shown. This bunch fibre pull-out implies that at this loading rate, the fibre-matrix interfacial bond strength was exceeded before the tensile failure strength of the composite was attained. It has been demonstrated, that the tensile modulus of elasticity [28], and tensile strength [29], of glass fibres increases with strain rate. It then follows that the observed rate dependence of the failure strength follows from the increased strength of the glass fibres.

The works of Saka and Harding [24,25], further establish the relationship between Poisson's ratio and strain rate, indicating a rather small change of 0.006% per decade between quasi-static ($10^{-3}s^{-1}$) and impact (1000 s^{-1}).

Furthermore, in Figure 4, it is shown that Poisson's ratio decreases marginally with an increase in fibre volume fraction (at fibre contents V_f of 15-40%). That is, once within the fibre dominated regime (as was observed by Lakes [15]), the composite properties are much more sensitive to fibre stiffness than matrix stiffness. Thus, as fibre content increases, the Poisson's ratio of the composite approaches that of an all glass specimen [30]. However, the extent to which fibre content affects the rate sensitivity of Poisson's ratio is yet to be established. Further work is needed in this area.

CONCLUSIONS

A comprehensive experimental study was conducted to ascertain the relationship between Poisson's ratio of a glass/epoxy composite and strain rate.

The findings from the tensile tests suggest that Poisson's ratio is not sensitive to strain rate. In addition, it was suggested that the absence of rate sensitivity in the Poisson's ratio of the laminates tested is due to the presence of fibres in the composites. However, the extent to which fibre content affects the rate sensitivity of Poisson's ratio is yet to be established. The lack of adequate experimental data to support this postulation necessitates the need for further work in this area.

REFERENCES

1. O.I. Okoli, G.F. Smith, "Overcoming inertial problems in the high strain rate testing of a glass/epoxy composite." Proc. SPE ANTEC, 2, pp. 2998-3002, (1995).

2. S.M. Walley, J.E. Field, P.H. Pope, N.A. Safford, "The rapid deformation behaviour of various polymers." J. Physics III France, 1, pp. 1889-1925, (1991).

3. D. Delfosse, G. Pageau, R. Bennett, A. Poursartip, "Instrumented Impact testing at high velocities.", JCTR, Vol. 15, No.1, pp. 38-45, (1993).

4. A.M.A. El Habak, "Compressive resistance of unidirectional GFRP under high rate of loading", JCTR, Vol. 15, No.4, pp. 311-317, (1993).

5. O.I. Okoli, "High speed performance of composite materials", in Engineering Polymers Integrated Capability (EPIC) Conference, work area 2d, University of Warwick, UK, March 1996.

6. O.I. Okoli, A. Abdul Latif, G.F. Smith, "The impact response of glass fibre reinforced composites: A comparison between finite element results and experimental data." Proc. of SPE ANTEC, 2, pp. 2504-2509, (1996).

7. O.I. Okoli, G.F. Smith, "The effects of strain rate on the failure energy of fibre reinforced composites." Proc. of the First Int. Conf. on Composite Science and Technology, Durban, South Africa, p. 359, (1996).

8. G. Zhou, "Characteristics of impact energy absorption during damage development in laminated composites." Proc. of the 4th Int. Conf. on Deformation and Fracture of Composites, IoM, Manchester, pp. 55-68, (1997).

9. O.I. Okoli, G.F. Smith, "The effects of strain rate and fibre volume fraction on the failure modes of fibre reinforced composites." Proc. of the 4th Int. Conf. on Deformation and Fracture of Composites, pp. 77- 88, (1997).

10. O.I. Okoli, G.F. Smith, "Semi-Empirical Relation for the Determination of Dynamic Young's Modulus in Woven Glass/Epoxy Reinforced Composites". Proc. SPE ANTEC, 2, pp. 237-2376, (1997).

11. H. Eyring, J. Chem. Phys. 4, p.283, (1936).

12. L.E. Govaert, H.J. Schellens, J.M.M. De Kok, T. Peijs, "Micromechanical modelling of time dependent failure in transversely loaded composites". Proc. 3rd Int. Conf. on Deformation and Fracture of Composites, IoM, pp. 77-85, (1995).

13. ASTM D 3039 - 76 (Reapproved 1989), Standard Test Method for Tensile Properties of Fiber-Resin Composites, Approved Aug. 27, 1976, Published October 1976, Annual Book of ASTM Standards, pp. 118-122.

14. W. Michaeli, J. Dassow, “Poisson's ratio of thermoplastics as a non-linear viscoelastic material parameter”. British Plastics and Rubber, pp. 21-24, (May 1995).

15. R.S. Lakes, Dept. of Mechanical Engineering, University of Iowa, Private Communication, August 1996.

16. R.M. Christensen, “Viscoelastic properties of heterogeneous media”. J. Mech. Phys. Solids, 17, pp.23-41, (1969).

17. L.V. Gibiansky, R.S. Lakes, “Bounds on the complex bulk modulus of a two-phase viscoelastic composite with arbitrary volume fractions of the components”. Mechanics of Materials, 16, pp.317-331, (1993).

18. V.J. Kopplemann, Ber das dynamische elastische Verhalten hochpolymerer Stoffe, Koloid Zeitschrift, 144, pp.12-41, (1955).

19. A. Tcharkhtchi, S. Faivre, L.E. Roy, J.P. Trotignon, J. Verdu, “Mechanical properties of thermosets. Part 1: Tensile properties of an anhydride cured epoxy”. Journal of Materials Science, pp.2687-2692, May 15 (1996).

20. J.D. Ferry, Viscoelastic properties of polymers, 3rd ed., J. Wiley, NY, 1980.

21. B.D. Caddock, University of Liverpool, Private Communication, September 1996.

22. W.R. Broughton, N.P.L. Private Communication, July 1996.

23. M.G. Bader, University of Surrey, Private Communication, September 1996.

24. J. Harding, K. Saka, M.E.C. Taylor, “Behaviour of fibre-reinforced composites under dynamic tension”. 3rd Progress Report, Oxford University Engineering Laboratory Report No. OUEL 1654/86, October 1986.

25. K. Saka, R.K.Y. Li, J. Harding , “Behaviour of fibre-reinforced composites under dynamic tension”. 4th Progress Report, Oxford University Engineering Laboratory Report No. OUEL 1714/87, 1987.

26. B.W. Smith, “Fractography for continuous fibre composites”, in Engineered Materials Handbook: Composites, 1, pp. 786-797, (1989).

27. P. Yeung, L.J. Broutman, “The effect of glass-resin interface strength of fibre reinforced plastics”. Polymer Engineering and Science, 18, 2, pp. 62-72, (1978).

28. A.E. Armenàkas, C.A. Sciammarella, “Response of Glass fibre reinforced epoxy specimens to high rates of tensile loading.” Experimental Mechanics, 13, pp. 433-440, October (1973).

29. L. M. Welsh, J. Harding, "Dynamic tensile response of unidirectionally reinforced carbon epoxy and glass epoxy composites. Proc. 5th Int. Conf. On Composite Materials ICCM V, TMS AIME, pp. 1517-1531, (1985).

30. R.M.V.G.K. Rao, M. Swaminadham, K. Rajanna, "Effect of moisture and glass contents on the Poisson's ratio of FRP plates as determined by laser interferometry". Fibre Science and Technology, 15, pp.235-242, (1981).

Cross-Head Velocity	Elastic Modulus Ex = Ey	Tensile Strength	Poisson's Ratio	Strain Rate	Log of Strain Rate
mm.s^{-1} (x10^{-2})	GPa	MPa	υ_{xy}	s^{-1} (*10^{-3})	s^{-1}
1.7	26.2	299	0.15	10.6	-3.9739
8.3	26.5	325	0.15	58.6	-3.2321
17.0	26.8	304	0.15	109.0	-2.9622
83.0	27.2	342	0.15	553.0	-2.2569

Table 1 Tensile properties of Tufnol Grade 10G/40 laminates at Low Strain Rates.

Cross-Head Velocity	Elastic Modulus Ex = Ey	Tensile Strength	Poisson's Ratio	Strain Rate	Log of Strain Rate
mm.s^{-1}	GPa	MPa	υ_{xy}	s^{-1}	s^{-1}
10	27.2	375	0.15	0.0363	-1.4407
100	28.0	403	0.16	0.2810	-0.5513
1000	35.6	412	0.16	1.5200	0.1829
2000	38.4	444	0.16	2.7200	0.4346

Table 2 Tensile properties of Tufnol Grade 10G/40 laminates at High Strain Rates.

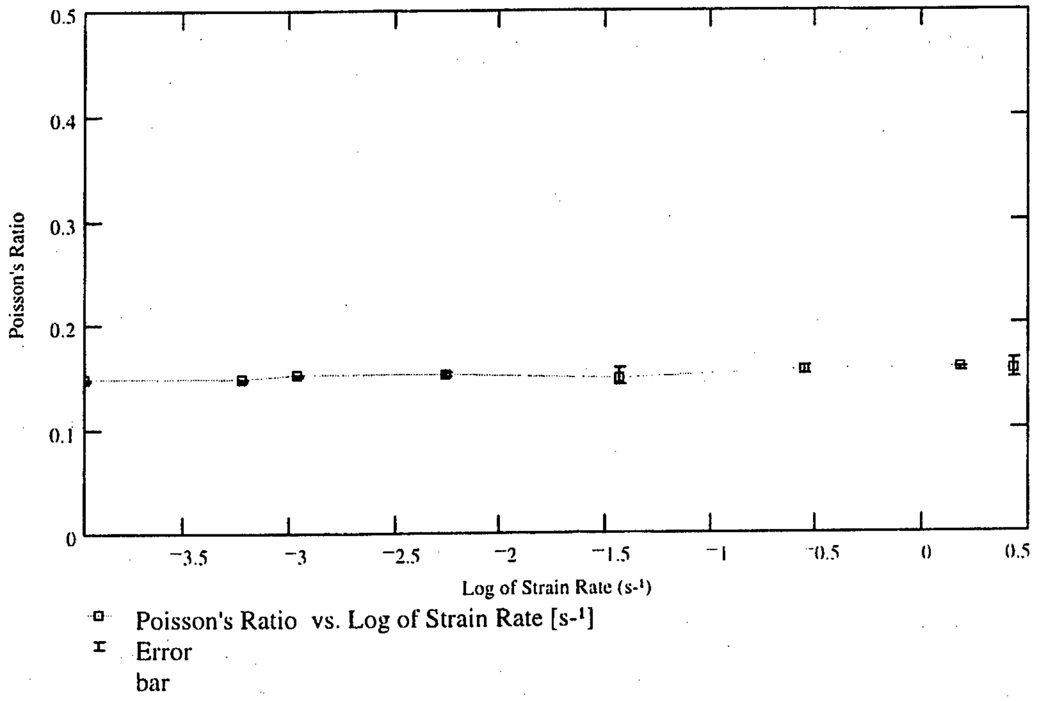

Figure 1 Poisson's Ratio vs. Log of Strain Rate.

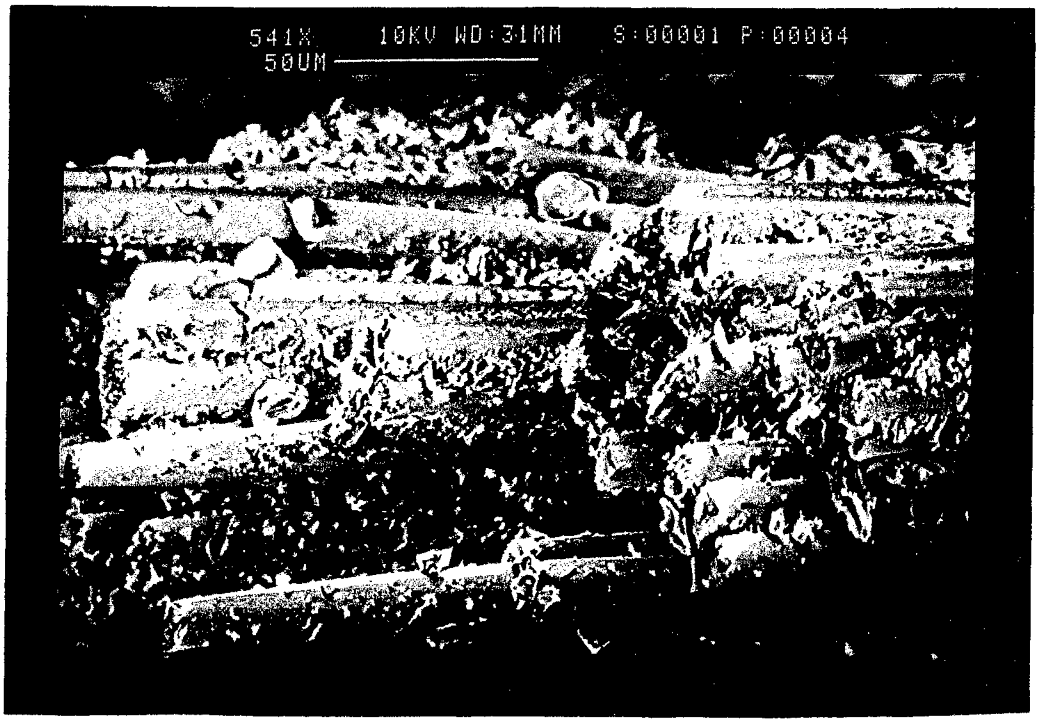
541X 10KU WD:31MM S:00001 P:00004
50UM

Figure 2 Tufnol 10G/40 Laminate showing brittle failure with fibre breakage (x541).

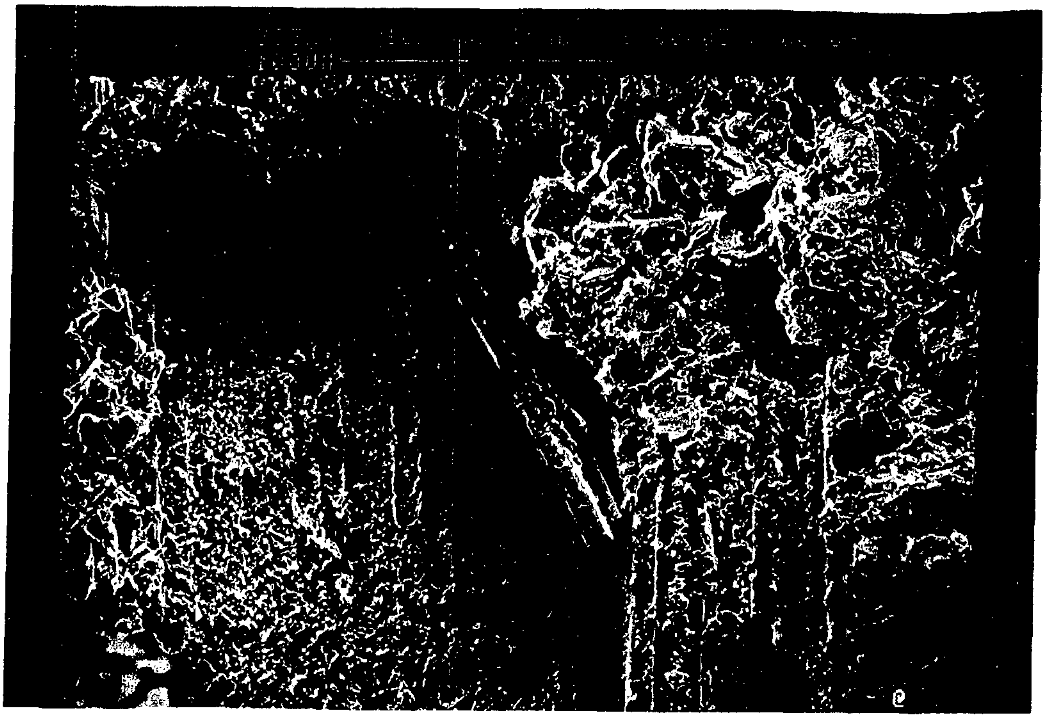

Figure 3 Tufnol 10G/40 Laminate showing fibre bunch pull-out with signs of fibre-matrix adhesion (x353).

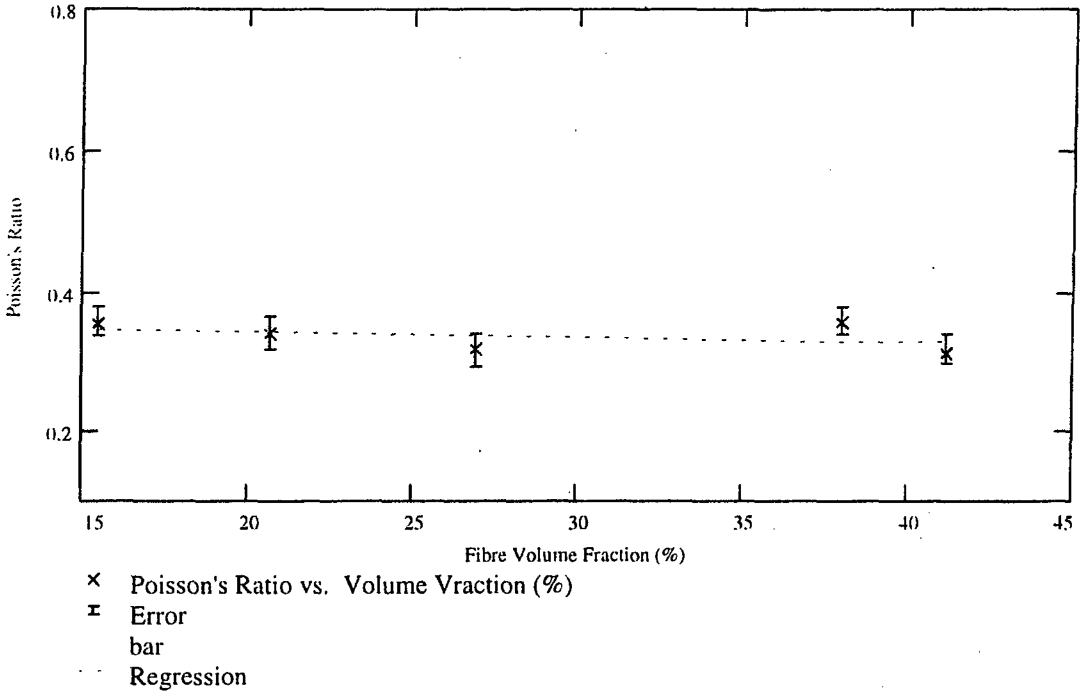

Figure 4 Poisson's Ratio vs. Fibre Volume Fraction.

THE EFFECT OF POLYAMIDE COATINGS ON THE MECHANICAL PROPERTIES OF UNIDIRECTIONAL CARBON/EPOXY COMPOSITES

C. D. PAPASPYRIDES[1], P. C. VARELIDIS[1] and R. L. MCCULLOUGH[2]

[1]Laboratory of Polymer Technology (Special Chemical Technology), Department of Chemical Engineering, National Technical University of Athens, Zographou, Athens 157 80, Greece
[2]Department of Chemical Engineering, Center for Composite Materials, University of Delaware, Newark, Delaware 19716, USA

INTRODUCTION

One of the major factors affecting the mechanical properties of carbon fiber composites is the fiber/matrix interphase. Stress transfer at the fiber/matrix interphase requires a strong interfacial bond between the two components. However, most of the times, an improvement of the coupling often causes a decrease in impact strength since too strong adhesion can limit the energy absorption mechanisms, making the composite more brittle [1, 2]. Furthermore, a characteristic of composite systems used for structural applications is that they show poor resistance to crack propagation. By tailoring the interphase through some kind of surface modification of the fibers, additional mechanisms can be introduced to hinder the crack propagation resulting in the increase of the propagation fracture energy [3-5].

Carbon fibers, are subjected to oxidative and nonoxidative treatments. Oxidative treatment of carbon fibers [1, 6] carried out in either gas or liquid phase, is the most commonly used modification method of fiber surface and is a standard treatment for commercially available carbon fibers. Unfortunately the reported improvement in the interlaminar shear strength is accompanied by a simultaneous decrease in toughness [6]. Another standard treatment for commercially available carbon fibers is to coat the fiber with a layer of sizing. They are supposed to enhance the wetting and impregnation characteristics of the fiber tow and to protect the fibers from damages during handling and processing. An increase in the interfacial shear strength of the composite has been reported for sized fibers [2, 7] but the effect of the sizing on the composite toughness remains unclear.

An alternative approach to the interface modification is to coat the fibers with a compliant and ductile layer. This layer can absorb more fracture energy by promoting localized plastic deformation around the crack tip and blunting the crack tip. It can also act as a stress relief medium reducing the stress concentration around the fiber caused by matrix shrinkage occurring during curing. Physical and mechanical properties of the coating along with its glass transition temperature and its thickness are key parameters affecting properties such as the interfacial and the transverse tensile strength and the fracture toughness [7]. There is a variety of coating techniques that have been employed such as electropolymerization [8, 9], solution dip-coating [10] or forms of interfacial polymerization starting from monomer reactants [11, 12].

In our previous work, long and short carbon fibers were coated with polyamide 6,6 by interfacial polyamidation in a batch process, resulting in composites with improved impact and tensile properties respectively [13, 14], while the interlaminar shear strength remained constant. In this study, a laboratory scale unit has been developed for the continuous coating based on the principles of interfacial polycondensation. The in-situ interfacial polyamidation of poly(hexamethylene adipamide) on carbon fibers is investigated as an example of interfacial polycondensation coating. Using the same apparatus with the proper modifications the same fibers were coated with Nylon® 6,6 by solution dip-coating. The present work is focused on the characterization of the coatings and the effect of the coatings on the adhesion and the fracture toughness of carbon/epoxy composites.

EXPERIMENTAL

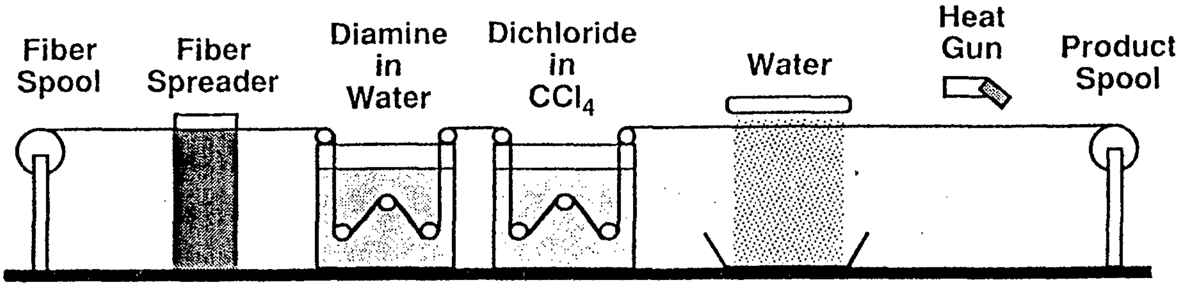

Figure 1. Schematic diagram of the experimental coating set-up used for the interfacial coating.

AS4 carbon fibers were continuously coated with polyamide 6,6 by interfacial polyamidation and solution dip-coating, using a laboratory scale unit that has been developed for this purpose. Figure 1 shows the process flow diagram for the system in the case of interfacial coating. The apparatus includes a spreader that separates the fiber tow apart before any coating process takes place so that the individual fibers can be coated. The impregnation of the fibers is achieved inside two baths. The fibers are first immersed in an aqueous solution of hexamethylenediamine and sodium carbonate. In a following step the fibers are immersed in adipoyl dichloride dissolved in carbon tetrachloride, where the polymerization reaction takes place. The ratio K of the molar reactant concentrations (diamine/dichloride) was kept constant at 2.5. The diamine concentration was chosen to be 1 % w/v. Next, the fibers are washed with water, dried in a stream of hot air and collected on a cylindrical spool. In the case of solution dip-coating polyamide 6,6 was dissolved in formic acid to make up a 3 % solution. The carbon filaments were separated by the spreader, immersed in the solution in an ultrasonic bath, and finally dried in a stream of hot air. This process produces unidirectional tows covered by a smooth polyamide sheath and bound together, forming sheets that resemble thermoplastic prepregs, i.e. the polyamide coating tends to fuse and act as a binder. Finally, the coated fibers were further dried in a vacuum oven at 80°C for 2h.

The nature of the coatings was identified by Fourier Transform Infrared Spectroscopy (FTIR) and Differential Scanning Calorimetry (DSC). Thermogravimetric Analysis (TGA) was used to measure the weight of polyamide deposited on the fibers. Scanning Electron Microscopy (SEM) revealed quite homogeneous coatings. Finally Gel Permeation Chromatography (GPC) was used to determine the molecular weight of the polymer coatings. Under the given processing conditions the interfacially formed polyamide coating was proven to have lower molecular weight, compared to the commercial Nylons™, and its molecular weight distribution (MWD) appears to be non-uniform as shown in Figure 2. Moreover as the diamine concentration increases the MWD becomes broader. This behavior is attributed to the fact that interfacial polymerization is a diffusion limited process [15, 16].

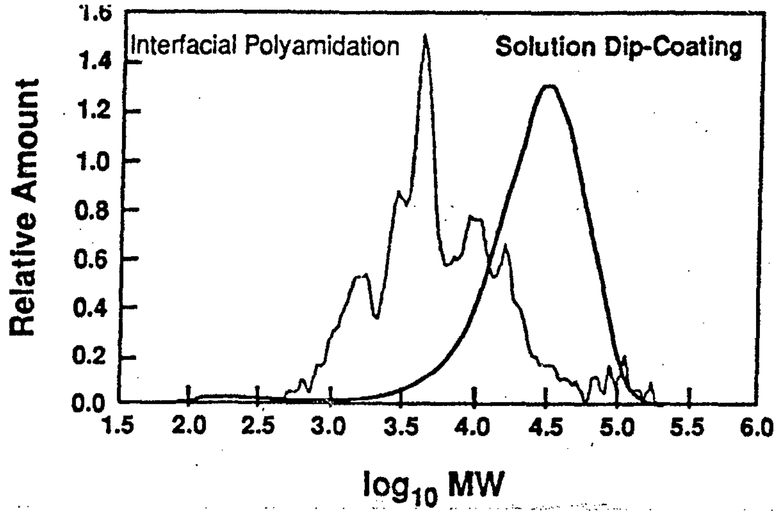

Figure 2. Molecular weight distribution of interfacially formed polyamide 6,6 in comparison with commercial Nylon™ 6,6.

Coatings of fibers have a strong influence on the fabrication processing characteristics and the process itself. Unidirectional prepregs were manufactured using, for the uncoated and the interfacially coated fibers, a filament winding mechanism (a modification of the coating set-up shown in Fig. 1). However, it was impossible to use filament winding technique, in the case of solution coated fibers, because of the formation of the aforementioned polyamide sheath that bounds together the solution coated fibers. Instead hand lay-up was employed resulting in prepregs with lower resin and volatile content. Solution coating makes the fibers stiffer and results in improved handling and processing ability, allowing better control of the fabrication process. On the contrary, interfacial coating is characterized by increased wettability and absorbs more resin making the accurate control of the composite fabrication process more difficult. Moreover, the use of filament winding instead of hand lay-up for the prepreg fabrication causes more damage (such as breaking or twisting) to the fibers due to the high tension and friction applied on the fibers. In a following step unidirectional composite panels were fabricated in an autoclave using 10 prepreg plies. The epoxy/hardener system was a mixture of EPON 828/PACM-20 (100/28). After a composite panel was fabricated, it was nondestructively inspected by the ultrasonic C-scan method. Furthermore, the fiber volume fraction (V_f) and the microstructure of the specimens was determined by optical microscopy.

Short beam shear tests showed that ILSS is independent of V_f for all three types of composite tested [17]. Moreover ILSS data show that dip-coating results in composites with improved adhesion, whereas interfacial coating results in the deterioration of the fiber/matrix bonding (Table 1). Similar conclusions are drawn by transverse tensile strength and strain data. The observed differences can be attributed to the introduction of the polyamide phase with its own physicochemical and mechanical properties between the matrix and the fibers [2, 7] and to obvious differences in the microstructure of the composites, resulting from the different prepreg fabrication process.

As far as the characteristics of the polyamide phase are concerned, it must be emphasized that the molecular weight and the morphology of the interfacially formed polyamide depend strongly on the reaction conditions [15, 16]. Moreover, even if the optimum reaction conditions are used and a high molecular weight polymer is produced, it is highly possible that there will still be some differences between the interfacially formed polyamide and the commercial polyamide due to the different morphology of these polymers. Even for polyamides of the same level of crystallinity, the spherulite size and distribution can be dramatically different not only between the two alternative polyamide coatings but also between interfacial coatings that are made under different conditions [18]. These possible differences in morphology may alter the mechanical properties of the coatings, resulting in composites with different mechanical properties.

Table 1. Apparent interlaminar shear strength (ILSS) and Mode I fracture toughness initiation (G_{ICinit}) and propagation (G_{ICprop}) values of different types of composites.

Type of composite	ILSS (MPa)	G_{ICinit} (kJ/m^2)	G_{ICprop} (kJ/m^2)
Uncoated	37.6 ± 0.7	0.40 ± 0.10	0.75 ± 0.12
Solution	47.8 ± 1.6	0.73 ± 0.19	1.01 ± 0.15
Interfacial	24.0 ± 1.3	0.45 ± 0.12	1.15 ± 0.19

The Mode I interlaminar fracture toughness (G_{IC}) was also determined from Double Cantilever Beam (DCB) test according to compliance method [5, 19] (Table 1). G_{ICinit} of interfacially coated fibers remains practically the same, while the increase observed in the case of solution coated fibers may be attributed to the better bonding (expressed by the increase of ILSS) [3-5]. In all cases, after some crack extension, a steady state was reached leading to a plateau, where the propagation values were determined (G_{ICprop}) (Table 1). Fiber bridging was much more intense in the case of interfacially coated fibers leading to the highest G_{ICprop} [3-5, 19].

CONCLUSIONS

A new process has been developed in which the concept of interfacial polycondensation has been modified in order to be suitable for continuous deposition of active polymer interlayers on the surface of reinforcing fibers. Also a laboratory scale unit has been manufactured based on this concept. The in-situ interfacial polyamidation of poly(hexamethylene adipamide) on carbon fibers is investigated as an example of interfacial polycondensation coating. The same unit, with the proper modifications, is suitable for continuous solution dip-coating. Presently, similar amounts of homogeneous polyamide layers are deposited on the surface of carbon fibers with both coating techniques. Under the given processing conditions the interfacially formed polyamide coating was proven to have lower molecular weight compared to the commercial Nylons™. Solution coating creates a polyamide sheath around the fiber tows and imposes the use of hand lay-up instead of filament winding for the prepregs fabrication. Solution coated fibers are stiffer and present improved handling and process ability.

Solution coated fibers exhibited improved transverse tensile and interlaminar shear strength (ILSS) performance over uncoated fibers, whereas interfacial coating (within our experimental conditions) caused deterioration in performance. These differences are attributed to the different nature of the two polyamides and to the microstructure differences induced because of the different manufacturing technique. Solution coating improves significantly G_{ICinit} because of the stronger bonding. Both polyamide coatings exhibit increased G_{ICprop} values compared to the uncoated samples due to fiber bridging. However, extensive fiber bridging was observed only for the interfacially coated samples, characterized by the highest propagation values.

As far as the interfacial coating is concerned, it must be strongly emphasized that by no means we claim that the process employed has been optimized. In order to achieve the "best" coating the role of all the important interfacial reaction conditions and coating fabrications conditions must be clarified. Still, it remains unclear if a "better" interfacial coating would lead to a different mechanical performance.

REFERENCES

1. Hull, D. "An Introduction to Composite Materials", Cambridge University Press, USA, pp. 145- 154 (1981).

2. Hughes, J. D. H. "The carbon fibre/epoxy interface-A review." *Composites Sci. Techn.*, **41**, pp. 13-45 (1991).

3. Madhukar, M. S., Drzal, L. R. "Fiber-matrix adhesion and its effect on composite mechanical properties: IV. Mode I and mode II fracture toughness of graphite/epoxy composites." *J. Compos. Mater.*, **26**(7), pp. 936-968 (1992).

4. Krawczak, P., Pabiot, J. "Fracture mechanics applied to glass fibre/epoxy matrix interface characterization. " *J. Compos. Mater.,* **29 (17)**, pp. 2230-2253 (1995).

5. Albertsen, H., Ivens, J., Peters, P., Wevers, M., Verpoest, I. "Interlaminar fracture toughness of CFRP influenced by fibre surface treatment: Part 1. Experimental results." *Composites Sci. Techn.*, **54,** pp. 133-145 (1995).

6. Jones, C. "The chemistry of carbon fibre surfaces and its effect on interfacial phenomena in fibre/epoxy composites."*Fib. Sci. Technol.*, **42,** pp. 275-298 (1991).

7. Kim, J.-K., Mai, Y.-W. "High strength, high fracture toughness fibre composites with interface control - A review. " *Composites Sci. Techn.*, **41**, pp. 333-378 (1991).

8. Dujardin, S., Lazzaroni, L., Rigo, L., Riga, J., Verbist, J. J. "Electrochemically polymer-coated carbon fibres: Characterisation and potential for composite applications." *J. Mater. Sci.*, **21**, pp. 4342-4346 (1986).

9. Rhee, H. W., Bell, J. P. "Effects of reactive and non-reactive fibre coatings upon performance of graphite/epoxy composites. " Polymer Comp., **12,** pp. 213-225 (1991).

10. Gerard, J. F. "Characterization and role of an elastomeric interphase on carbon fibers reinforcing an epoxy matrix. " Polym. Eng. Sci., **28**, pp. 568-577 (1988).

11. Cranmer, J. H., Tesoro, G. C., Uhlman, D. R. "Chemical modification of carbon fiber surface with organic polymer coating. " *Ind. Eng. Chem. Prod. Res Dev*, **21**, pp. 185-190 (1982).

12. M. Kodama, I. Karino and J. Kobayashi, "Interaction between the reinforcement and matrix in carbon-fibre-reinforced composite: effect of forming the thin layer of polyimide resin on carbon fibre by in situ polymerization. " *J. Appl. Polym. Sci.,* **33**, pp. 361-373 (1987).

13. Papaspyrides, C. D., Poulakis, J. G. "The effect of fiber Coating on the Tensile Properties of Ionomer-Based Composites.", *Polymer International,* **27**, 139-145 (1992).

14. Skourlis, T., Duvis, T., Papaspyrides, C. D. "The role of a polyamide interphase on carbon fibres reinforcing an epoxy matrix. " *Composites Sci. Techn.,* **48,** pp. 119-125 (1993).

15. Korshak, V. V., Frunze T. M. "Synthetic Hetero-chain Polyamides. " Israel Program for Scientific Translations Ltd., Jerusalem, (1964).

16. Morgan, P. W. "Condensation polymers : By Interfacial and Solution Methods", Interscience, New York, (1965).

17. King, T. R., Blackketter, D. M., Walrath, D. E., Adams, D. F. "Micromechanics prediction of the shear strength of carbon fiber/epoxy matrix composites: The influence of the matrix and interface strengths. " *J. Composite Materials*, **26(4)**, pp. 558-573 (1992).

18. Salehi-Mobarakeh, H., Ait-Kadi, A., Brisson, J. "Improvement of mechanical properties of composites through polyamide grafting onto Kevlar fibers" *Polym. Eng. Sci..*, **36(6),** pp. 778-785 (1996).

19. Friedrich, K. "Application of Fracture Mechanics to Composite Materials. " Elsevier, 1989.

HOMOGENIZATION OF MULTILAYERED ELASTOMER COMPOSITES

M. BRIEU[1], F. DEVRIES[1] and F. LÉNÉ[1]

[1] Laboratoire de Modélisation et Mécanique des Structures
U.P.M.C. / E.N.S.A.M. / E.N.S. Cachan – U.R.A. 1776 C.N.R.S.
Université Paris 6 - Tour 66 - Boite 161
4 place Jussieu - 75252 Paris cedex 05
France

INTRODUCTION

Because of the wide variety of behaviors which may be exhibited by rubber materials, their use in the development of structures having to assume suspension tasks is becoming more widespread. In order to extend the range of the use of such materials, it is now usual to dispose reinforcements inside them. The great difficulty encountered for the computation of the resulting reducing power and mechanical rigidity, arises from the material and geometrical nonlinearities to be accounted for, as well as the great number of heterogenities. A way for overcoming these difficulties consists of using homogenization techniques.

Because homogenization and linearization do not commute [4], when dealing with such composites, we briefly present the homogenization technique well-suited for such materials [4], [8]. It consists of solving two problems (one to be solved at the composite's microscopic scale, while the second allows for the computation of the researched homogenized behavior), coupled one another by the way of mean relations. For their solutions, incremental [4] and faster non-incremental [1], algorithms have been developed. They both allow for the computation on the one hand of the homogenized response of the composite, and on the other hand, of the microscopic stress and deformations fields, which allow to analyze the local damage's sensitiveness.

In order to assess the relevance of the homogenization technique considered, a comparison of the results furnished with finite elements results (corresponding to an heterogeneous model of the composite multilayered structure under consideration) is presented. It shows that this method leads to a very good description of the composite's behavior, provided the assumptions required for its use are satisfied.

PROBLEM STATEMENT

We consider a structure which occupies in its undeformed, stress-free state, a domain Ω of R^3, with respect to a system of axes denoted by $(0, x_1, x_2, x_3)$. This structure is constituted by a multilayered composite, and we assume that this material allows for a spatial and mechanical periodic distribution in such a way that it may be constructed by a periodic repetition of a representative volume element, hereafter called the basic cell and denoted by Y. Any point of Y is marked with respect to a system of axes denoted by $(0, y_1, y_2, y_3)$. Denoting the representative lengths of the composite structure and the basic cell Y by L and H respectively, we assume that the ratio $\epsilon = H/L$ is very small with respect to 1 (or in other words that the basic cell is much finer than the structure). The materials which constitute the layers of Y are chosen as nonlinear elastic in such a way that their behavior laws depend on a strain energy density, denoted by e.

We plan herein to compute the response of this composite structure as displacement loadings $\mathcal{U}$ are prescribed to a portion of its boundary, denoted by $\partial\Omega_1$, while the remaining part $(\partial\Omega_0)$ is, for instance, clamped in a rigid, fixed body. Denoting respectively by $\mathbf{\Pi}^\epsilon$, $\mathbf{U}^\epsilon$ and $\mathbf{F}^\epsilon$, the first Piola-Kirchhoff stress tensor, displacement field and deformation gradient tensor, and by $\mathbf{1}$ the dyadic tensor, the heterogeneous problem to be solved writes:

$$\left\{\begin{array}{lll} div_x\mathbf{\Pi}^\epsilon & = 0 & in\ \Omega \\ \mathbf{\Pi}^\epsilon & = \dfrac{\partial e^\epsilon(\mathrm{x},\ \mathbf{F}^\epsilon)}{\partial \mathbf{F}^\epsilon} & in\ \Omega \\ \mathbf{F}^\epsilon & = \mathbf{1}\ +\ \nabla_x\ \mathbf{U}^\epsilon & in\ \Omega \\ \mathbf{U}^\epsilon & = \mathcal{U} & on\ \partial\Omega_1 \\ \mathbf{U}^\epsilon & = 0 & on\ \partial\Omega_0 \end{array}\right. \tag{1}$$

where div_x and ∇_x stand for the divergence and gradient operators with respect to the macroscopic space variables (x_1, x_2, x_3).

As already pointed out the main difficulty encountered for the solution of this problem arises from the great number of heterogenities. The way we choose for overcoming this difficulty consists of using a homogenization technique, well-suited for accounting for the nonlinearities of this problem.

HOMOGENIZATION OF NONLINEAR ELASTIC COMPOSITES

As ϵ converges to zero, or in other words, as the number of heterogeneities becomes infinite, it may be shown [8], that the solution fields to problem (1) converge to $\mathbf{\Pi}$, $\mathbf{U}$ and $\mathbf{F}$, solution to the following coupled macroscopic-microscopic problems, when no instabilities (such as microbucklings) occur at the composite's microscale [6]:

$$\left\{\begin{array}{ll} div_x\mathbf{\Pi} = 0 & in\ \Omega \\ \mathbf{\Pi} = \dfrac{\partial E(\mathrm{x},\ \mathbf{F})}{\partial \mathbf{F}} & in\ \Omega \\ \mathbf{F} = \mathbf{1} + \nabla_x\mathbf{U} & in\ \Omega \\ \mathbf{U}\ = \mathcal{U} & on\ \partial\Omega_1 \\ \mathbf{U}\ = 0 & on\ \partial\Omega_0 \end{array}\right. \quad \left\{\begin{array}{ll} div_y\tau = 0 & in\ Y \\ \tau = \dfrac{\partial e(\mathrm{y},\ \mathbf{f})}{\partial \mathbf{f}} & in\ Y \\ \mathbf{f} = \mathbf{F} + \nabla_y\mathbf{u} & in\ Y \\ \mathbf{u} & Y-periodic \\ \tau(\mathbf{n}) & Y-antiperiodic \end{array}\right. \tag{2}$$

where the macroscopic strain-energy density $E(\mathbf{x}, \mathbf{F})$ is implicitly defined by the mean relations (3) and $\mathbf{n}$, div_y, ∇_y respectively stand for the unit external normal to ∂Y and the divergence and gradient operators with respect to the microscopic space variables (y_1, y_2, y_3):

$$\left\{\begin{array}{l} \mathbf{\Pi} =<\tau>_Y \\ \mathbf{F} =<\mathbf{f}>_Y \end{array}\right. \quad (<g>_Y\ \equiv \frac{1}{|Y|}\int_Y g(y)\ dy;\ |Y|\ \equiv \int_Y g(y)\ dy) \tag{3}$$

For the solution of these problems, incremental [4] and faster non-incremental [1], algorithms may be used.

ANALYSIS OF RELEVANCE OF THE HOMOGENIZATION TECHNIQUE

In order to assess the relevance of the homogenization technique, presented above, we compare in the sequel the results it furnishes to these obtained thanks to a finite element solution of problem(1) in the case of a multilayered composite structure. In order to limitate the numerical costs induced by the solution of problem (1) we consider that the loadings prescribed to the laminate induce plane strains. The finite element formulation that we have introduced, consists of using Ruas-like triangles [9] with 7 nodes by element. For the numerical solution of problem (1) we used a mixed formulation [7] leading to a lagrangian formulation, which associated problem has been solved thanks to an Uzawa-like algorithm.
The laminate we have chosen for this comparison is assumed to admit a basic cell made up of two isotropic different materials, which strain energy densities are given by [2] (i_1, i_2, i_3 stand for the three principal invariants of the dilatation tensor $\mathbf{c}=\mathbf{f}^t\ \mathbf{f}$):

$$e(i_1,\ i_2,\ i_3) = \frac{E_1}{2}(i_1 - 3) + \frac{E_2}{2}(i_2 - 3) + \frac{E_3}{2}(i_3 - 1) - \frac{E_1 + 2E_2 + E_3}{2} Ln(i_3) \quad (4)$$

where the behavior coefficients of the layers have been chosen as follows (E, ν respectively stand for the Young's modulus and Poisson's ratio):

$$\left\{\begin{array}{l} \textbf{Layer 1 :} \quad (E = 1\ GPa,\ \nu = 0.3) \\ E_1 = 0.116\ GPa,\ E_2 = 0.268\ GPa,\ E_3 = 20\ MPa \\ \textbf{Layer 2 :} \quad (E = 1\ MPa,\ \nu = 0.45) \\ E_1 = 0.193\ MPa,\ E_2 = 0.152\ MPa,\ E_3 = 1.4\ MPa \end{array}\right. \quad (5)$$

Let us lastly precise that the volume fraction of layer 1 has been chosen equal to 20%. The finite element meshes we have used, have been constructed starting from a regular mesh of a period consisting of 310 Ruas-triangles and 1003 nodes.

CASE OF UNIAXIAL TENSION PARALLEL TO THE STACKING AXIS

Thanks to the symmetry of the problem to be solved in the case studied here, only a quarter of the entire laminate has been considered for the FEM solution. Figures 1 and 2 present the nominal homogenized and heterogenous stress induced at the boundary of the structure where a uniaxial tension displacement is prescribed, for different numbers of periods producing the laminate. One may first observe that the homogenized results do not agree with the heterogeneous ones when the number of periods is not sufficiently high. Next, it may be observed that far enough from the edges of the laminates, the homogenized and heterogeneous results agree very well, which proves the relevance of the homogenization technique proposed. The discrepancy found near the edges of the laminate stems from the fact that the homogenization process conducts to stresses which satisfy the boundary conditions only through their mean values. The homogenization process leads so to edges effects which may be corrected.

CASE OF SIMPLE SHEAR PERPENDICULAR TO THE STACKING AXIS

Another comparison between numerical and homogenized results have been carried out in the case of a simple shear loading, macroscopically prescribed to the considered laminate. The results presented in figure 3 concern the nominal stress induced at the upper boundary of the structure, where a shear displacement is prescribed. These results show first that the numerical solution obtained, leads to a stress vector which is fluctuating at this boundary. The reason of this phenomenon stems from the fact that the mesh considered is insufficiently fine because of the great deformation of the elastomer layers. Unfortunately no finer mesh may be considered because of the computers limitations. However the trends exhibited in the case of uniaxial traction are recovered. One may thus observe that homogenized and numerical-heterogeneous results well agree, except in the neighborhood of the laminate's free boundaries, where homogenized stresses do not satisfy the prescribed conditions of the heterogeneous problem.

CONCLUSIONS

The numerical-heterogeneous results from which the relevance of the homogenization technique, briefly presented in this paper, may be asserted, point out the limitations of the validity domain and accuracy of this technique. However, the homogenized results well agree with the numerical-heterogeneous ones, at least in the range of validity of the homogenization process.

Its use for the design of nonlinear elastic composite materials would allow to significantly reduce the CPU times required for the simulations. Moreover, as well as in the case of linear elastic behaviors [3], it allows to accurately compute the forces induced at the composite's heterogeneities level, which constitutes a powerful tool, when dealing, in a further step, with the study of damage in such composites.

On the other hand, this homogenization technique and its best solution's algorithm [1] require to solve, at each iteration and at both the microscopic and macroscopic scales, linear, yet highly-heterogeneous problems. Its application to realistic industrial cases (structures and loadings) will take benefit from the recent developments made inside the framework of parallelism applied to composite materials [5].

References

[1] Brieu M., Devries F. "Homogénéisation de composites élastomères. Méthode et algorithme." *Comptes Rendus Académie des Sciences, Paris*, to be published

(1998).

[2] Ciarlet P.G., Geymonat G. "Sur les lois de comportement en élasticité non linéaire compressible." *Comptes Rendus Académie des Sciences, Paris* **295-II**, pp. 423–426 (1982).

[3] Devries F. "A fatigue damage model by fibres breaks in unidirectional composites." *Proc. 14th ASME Energy Technology Conference and Exhibition, Composite Material Technology* **2**, pp. 137–144 (1991).

[4] Devries F. "Calcul du comportement homogénéisé de composites hyperélastiques." *Revue des Composites et des Matériaux Avancés* **2**, pp. 217–248 (1996).

[5] Devries F., Léné F., L'Hostis G., Soulat D. "Parallel computing and damage in composite materials." *Proc. 11th Int. Conf. Composite Materials* **2**, pp. 374–386 (1997).

[6] Geymonat G., Müller S., Triantafyllidis N. "Homogenization of nonlinearly elastic materials. Microscopic bifurcation and macroscopic loss of rank-one convexity." *Arch. Rational Mech. Anal.* **122**, pp. 231–290 (1993).

[7] Glowinski R., Le Tallec P. "Augmented lagrangian and operator-splitting methods in nonlinear mechanics." *SIAM Philadelphia* (1989).

[8] Müller S. "Homogenization of nonconvex integral functionals and cellular materials." *Arch. Rational Mech. Anal.* **99**, pp. 189–212 (1987).

[9] Ruas V. "A class of axisymmetric simplicial finite element method for solving incompressible elasticity." *Comp. Appl. Mech. Engng.* **27-3**, pp. 319–343 (1981).

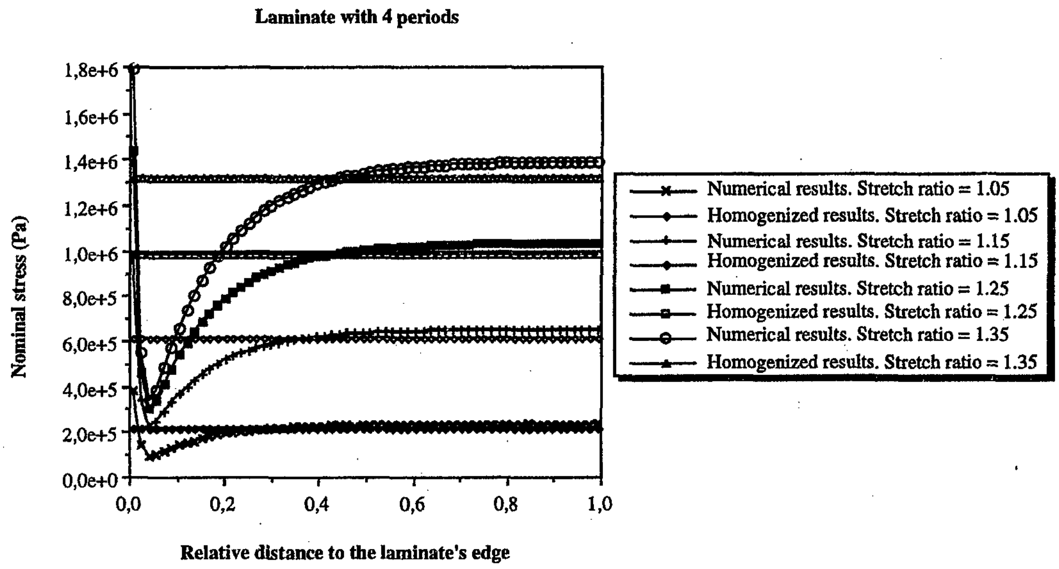

Figure 1: Homogenized and heterogeneous stretch/stress curves (Uniaxial tension parallel to the stacking axis (4 periods)).

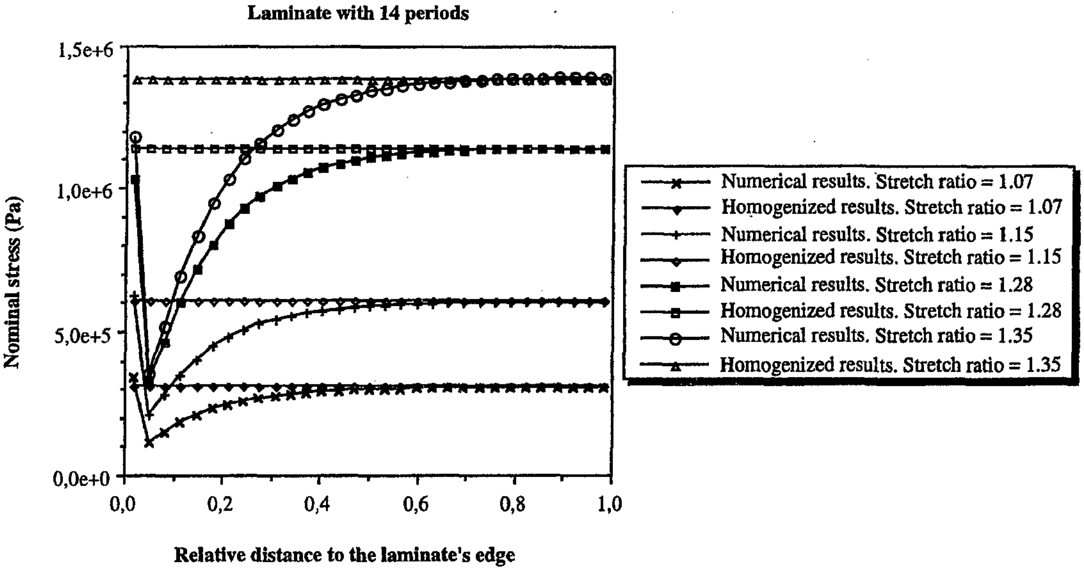

Figure 2: Homogenized and heterogeneous stretch/stress curves (Uniaxial tension parallel to the stacking axis (14 periods)).

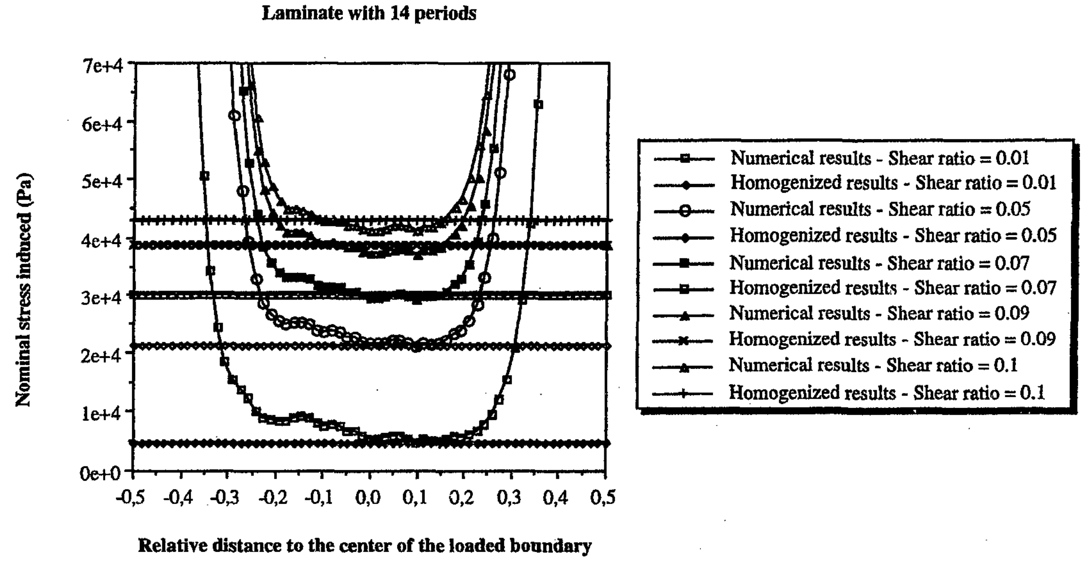

Figure 3: Homogenized and heterogeneous stretch/stress curves (Simple shear perpendicular to the stacking axis).

STUDY OF NEAR-SURFACE BUCKLING OF COMPOSITE MATERIALS IN ZONES OF COMPRESSION (MODEL OF A PIECEWISE-UNIFORM MEDIUM)

Yu. N. Lapusta

S.P. Timoshenko Institute of Mechanics, Nesterov Str.3, Kiev, 252057, Ukraine

INTRODUCTION

The problems on the near-surface buckling of composite materials in zones of compression are of great importance in modern technics since the buckling-like phenomena in compressed zones of products fabricated from composites can reduce significantly their load-carrying capacity. Such factors as the interaction between fibres and the effects of free boundaries are sufficiently characteristic of unidirectional composites, outer layers (faces) of composites and structure elements containing long fibre- like reinforcement. It should be noted that various simplified approaches, especially those based on smearing the internal structure of the composite (the model of a continual medium), do not always apply to the study of the problems mentionned above. Rigorously speaking, to obtain sufficiently satisfactory results on these problems, one should involve the appropriate three-dimensional equations of stability to describe the behaviour of each of the constituents of the internal structure and satisfy exactly all the boundary conditions resulting from such a problem statement. The purpose of the present paper is the study of the near-surface buckling of composite materials in zones of compression through employing such a rigorous solution technique based on the model of a piecewise-uniform medium.

PROBLEM STATEMENT

To model the near-surface behaviour of a fibre-reinforced composite material subjected to a compressive action of forces let us consider an infinite periodic series of fibres of a circular cross-section located in the vicinity of the free boundary of the composite. The axes of the fibres are parallel and located in a plane parallel to the free plane surface. We note that the results obtained within the framework of such a statement can be considered as upper bounds for the loads responsible for the near–surface instabilities in fibrous composites of regular structure.

In the study, Lagrangian coordinate systems (x, y, z) and (r_q, θ_q, z_q) coinciding in the undeformed state with rectangular and cylindrical coordinate systems, respectively, are associated with the matrix and each of the fibres. Relations between the coordinate systems introduced have the form

$$x = qD - r_q \sin\theta_q, \quad y = H - r_q \cos\theta_q \quad z = z_q \tag{1}$$

$$r_p \exp i\theta_p = \mid p - q \mid D \exp i\varphi_{pq} + r_q \exp i\theta_q, (p \neq q, p, q = 0, \pm 1, \pm 2, \pm 3, ...)$$

Here D is the distance between the axes of the neighbouring fibres, H is the distance between the axes of the fibres and the free surface, q takes all integer values from $-\infty$ to $+\infty$. The binder occupies the region $y \geq 0, r_q \geq R$, and the fibres are located in the regions $r_q \leq R$ where R is cross–sectional radius of each of the fibres. It is assumed that: the shortenings of the fibres and of the matrix along the fibres are equal; a continuous contact between the fibres and the matrix is realized, and the surface of the binder is not loaded. We describe the subcritical states in the matrix and in the fibres by the relations

$$\sigma_{zz}^{*0m} \neq 0, \quad \sigma_{zz,q}^{*0a} \neq 0, \quad \sigma_{zz,q}^{*0a} \neq \sigma_{zz}^{*0m} \tag{2}$$

$$\sigma_{xx}^{*0m} = 0, \quad \sigma_{yy}^{*0m} = 0, \quad \sigma_{rr,q}^{*0a} = 0, \quad \sigma_{\theta\theta,q}^{*0a} = 0$$

We note that up to the stage of numerical solution, we perform all the transformations for the general case of transversally isotropic compressible materials of the fibres and the matrix without employment of concrete material models.

We apply the general solutions of the three–dimensional linearized problems at homogeneous subcritical states [1] to each component of the composite and arrive to the following mathematical formulation of the problem: it is necessary to determine the minimal value of the loading parameter with which the equations

$$(\Delta_1 + \zeta_1^{a^2} \frac{\partial^2}{\partial z_q^2})\psi^{aq} = 0, \quad (\Delta_1 + \zeta_2^{a^2} \frac{\partial^2}{\partial z_q^2})(\Delta_1 + \zeta_3^{a^2} \frac{\partial^2}{\partial z_q^2})\chi^{aq} = 0, \tag{3}$$

for the fibres and similar equations for the matrix have nontrivial solutions satisfying the continuity conditions for the forces and displacements at the interfaces in the form

$$\vec{P}^{*aq} = \vec{P}^{*m}, \quad \vec{u}^{aq} = \vec{u}^{m}, \tag{4}$$

the conditions of zero forces at the free plane surface

$$\vec{P}^{*m} = 0, \quad (y = 0) \tag{5}$$

and the attenuation conditions for the displacements at $y \to \infty$. The components of the vectors $\vec{u}^{aq}, \vec{u}^{m}$ at the lateral cylindrical surfaces are determined by the formulas (superscripts "m" and "aq" have been omitted)

$$u_r = \frac{1}{r_q} \frac{\partial}{\partial \theta_q} \psi - \frac{\partial^2}{\partial r \partial z_q} \chi, \quad u_\theta = -\frac{\partial}{\partial r} \psi - \frac{1}{r_q} \frac{\partial^2}{\partial \theta_q \partial z_q} \chi,$$

$$u_3 = (\omega_{1133} + \omega_{1313})^{-1} (\omega_{1111} \Delta_1 + \omega_{3113} \frac{\partial^2}{\partial z_q^2}) \chi \tag{6}$$

SOLUTIONS OF THE PROBLEM

Usually, for elastic materials, $\zeta_2^{a2} \neq \zeta_3^{a2}$, $\zeta_2^{m2} \neq \zeta_3^{m2}$ and they are positive real numbers. In view of this, we search solutions of the equations for the matrix, satisfying the attenuation conditions at $y \to \infty$, in the form

$$\begin{aligned}
\psi^m = \gamma \sin \gamma z \sum_{p=-\infty}^{\infty} \{ & \sum_{n=1}^{\infty} A_{n,1}^{mp} K_n(\zeta_1^m \gamma r_p) \sin n\theta_p + \sum_{n=0}^{\infty} C_{n,1}^{mp} K_n(\zeta_1^m \gamma r_p) \cos n\theta_p + \\
& \sum_{n=1}^{\infty} A_{n,1}^{mp} \int_{-\infty}^{+\infty} L_{11n}(t) \exp(-\zeta_1^m \cosh(t)\gamma y) \sin[\zeta_1^m \sinh(t)\gamma(x-pD)]dt + \\
& \sum_{k=2}^{3} \sum_{n=0}^{\infty} A_{n,k}^{mp} \int_{-\infty}^{+\infty} L_{1kn}(t) \exp(-\sqrt{\zeta_1^{m2} + \zeta_k^{m2} \sinh^2 t}\gamma y) \sin[\zeta_k^m \sinh(t)\gamma(x-pD)]dt + \\
& \sum_{n=0}^{\infty} C_{n,1}^{mp} \int_{-\infty}^{+\infty} M_{11n}(t) \exp(-\zeta_1^m \cosh(t)\gamma y) \cos[\zeta_1^m \sinh(t)\gamma(x-pD)]dt + \\
& \sum_{k=2}^{3} \sum_{n=0}^{\infty} C_{n,k}^{mp} \int_{-\infty}^{+\infty} M_{1kn}(t) \exp(-\sqrt{\zeta_1^{m2} + \zeta_k^{m2} \sinh^2 t}\gamma y) \cos[\zeta_k^m \sinh(t)\gamma(x-pD)]dt \}
\end{aligned} \tag{7}$$

We utilize the same principle while constructing χ^m. In the solutions thus constructed we have unknown coefficients $A_{n,j}^{mp}, C_{n,j}^{mp}$ ($j = 1,2,3; n = 0,1,2,3,...;$ $p = 0, \pm 1, \pm 2, \pm 3, ...$) as well as unknown functions $L_{ijn}(t), M_{ijn}(t)$ to be determined from the conditions (5) at the free plane surface. $\gamma = \pi l^{-1}$, where l is the length of the halfwave of a stability loss mode. Solution for the fibre No.q is searched in the form

$$\psi^{ap} = \gamma \sin \gamma z \{ \sum_{n=1}^{\infty} A_{n,1}^{ap} I_n(\zeta_1^{ap} \gamma r_p) \sin n\theta_p + \sum_{n=0}^{\infty} C_{n,1}^{ap} I_n(\zeta_1^{ap} \gamma r_p) \cos n\theta_p \} \tag{8}$$

(χ^{ap} is represented analogously). In the solutions for the fibres $A_{n,j}^{aq}, C_{n,j}^{aq}$, ($j = 1,2,3$; $n = 0,1,2,3,...$; $q = 0, \pm 1, \pm 2, \pm 3, ...$) are unknown coefficients.

We represent solutions for the matrix in the rectangular coordinate system (x, y, z) in the form of improper integrals and introduce them into (5). As a result, after transformations, we obtain a system of equations permitting explicit determination of the unknown functions. When these functions are determined, the solutions constructed satisfy exactly the initial equations, the attenuation conditions at $y \to \infty$ and the conditions at the free plane surface. We note that these solutions describe all possible stability loss forms. By assigning specific relations between the unknown constants for the fibres and the matrix, one can obtain arbitrary combinations of forms of fibre stability loss. It follows, however, from the physical considerations that the most interesting are stability loss modes satisfying conditions of periodicity along the series of fibres when all fibres lose their stability by the same mode. Therefore we continue our consideration on the example of stability loss forms possessing the mentioned above property of periodicity. By virtue of the periodicity conditions accepted, we put

$$A_{n,j}^{mp} = A_{n,j}^{m}, \quad C_{n,j}^{mp} = C_{n,j}^{m}, \quad A_{n,j}^{ap} = A_{n,j}^{a}, \quad C_{n,j}^{ap} = C_{n,j}^{a},$$

Possible stability loss modes with a period equal to the period of the structure include: 1st - stability loss form for which the fibres axes remain in the planes perpendicular to the free plane surface of the binder and 2nd - stability loss form for which the fibre axes go out of these planes. All stability loss modes are studied in a similar manner. Henceforth we expose briefly the further solution techniques on the example of the stability loss mode, for which all the fibres become unstable in the phase and their axes remain in the planes perpendicular to the free surface of the binder. For the indicated stability loss form, by virtue of the periodicity conditions, it is sufficient to satisfy boundary conditions at the walls of one of the fibres, say with $q = 0$. Substituting solutions for the matrix represented in the coordinate system (r_0, θ_0, z_0) together with the solutions for the fibre No.0 into (4), after a change of variables, we obtain an infinite homogeneous system of algebraic equations

$$B_{\alpha k}^{m} X_k^{m} + B_{\alpha k}^{a} X_k^{a} + \sum_{n=0}^{\infty} Q_{\alpha k n} X_n^{m} = 0, \tag{9}$$

We derive a characteristic equation by means of equating to zero the determinant of the derived infinite system:

$$\Delta^1(\varepsilon, \kappa) = 0 \quad . \tag{10}$$

NUMERICAL INVESTIGATION

In the study we prove that the characteristic equations obtained can be resolved numerically using the truncation of the infinite determinants. For the calculations, it is necessary to specify the concrete model for the materials of the fibres and the matrix. We consider below the case of compressible isotropic linearly elastic materials of the fibres and the matrix and employ the second variant of the theory of small precritical deformations. Thus, we have

$$\sigma_{zz}^{0m} = -E_m \varepsilon_{zz}^{0m}; \quad \sigma_{zz}^{0a} = -E_a \varepsilon_{zz}^{0a}; \quad \varepsilon_{zz}^{0m} = \varepsilon_{zz}^{0a} = \varepsilon \tag{11}$$

Characteristic equations were solved on computer with the fixed values of the stiffness and geometrical parameters of the problem by means of the reduction method.

We obtained dependences $\varepsilon^1 = \varepsilon^1(\kappa)(\kappa = \gamma R)$ and $\varepsilon^2 = \varepsilon^2(\kappa)$ and determined the critical values of ε by means of comparing results for each of the stability loss forms considered.

As an illustration of the numerical results obtained, we present in Figure 1 the dependences of the critical values of ε with the rigidity ratio $E_aE_m^{-1}$. Curve 1 has been calculated with $HR^{-1} = 1.5$ and $DR^{-1} = 2.5$; curve 2 – with $HR^-1 \to \infty; DR^-1 \to \infty$ (limiting case corresponding to a single fibre located far from the boundary). Analysis of the results obtained affords a possibility of formulating the following main conclusions:

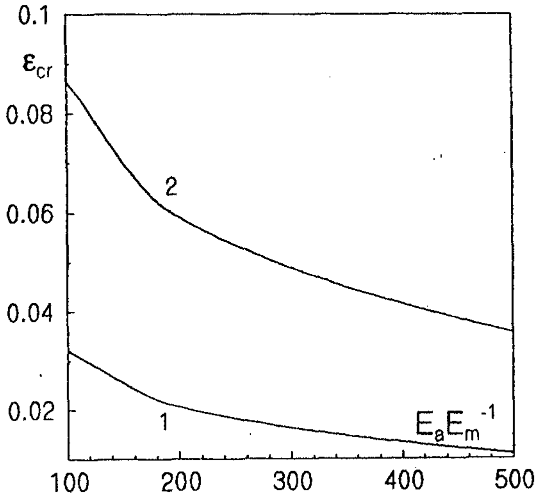

Fig.1. Dependence of ε_{cr} with rigidity ratio

For certain combinations of the problem parameters the free matrix boundary exercises a substantial effect on the stability of a series of fibres. Usually, this takes place when the fibre series approaches the free matrix boundary. The critical stability loss mode of fibres near the free boundary of a binder can differ from the critical stability loss mode for the same series of fibres located far from the boundary. Another factor, influencing significantly the critical stability loss form and the value of the critical load, is the mutual interaction of the fibres during stability loss. The mentioned two factors, coupled together, can reduce the critical load by several times (Fig. 1). Thus, the internal structure of fibre-reinforced composite materials can essentially influence their compressive strength and it is often necessary to simultaneously account for the effects of the matrix boundary and the mutual effects of the fibres.

REFERENCES

1. A.N.Guz', Chief Editor, "Mechanics of composite materials and structure elements", (in Russian), Naukova Dumka, Kiev, 1982–1983, in 3 volumes: Vol.1. "Mechanics of materials", Naukova Dumka, Kiev, 454 p. (1982)

EFFECT OF DRYING ON PROPERTIES OF CERAMIC COMPOSITE PRECURSORS: ANALYTICAL MODEL

I.B. Sevostianov [1], V.M. Levin [2], W. Pompe [3]

[1] Department of Mechanical Engineering, University of Natal, 4001 Durban, South Africa.
[2] Department of Mechanics, Petrozavodsk State University, Lenin Ave. 33,
185640 Petrozavodsk, Russia.
[3] Institut fuer Werkstoffwissenschaft, TU Dresden, D-01062 Dresden, Germany

INTRODUCTION

The method of suspension drying is used in modern ceramic composite technology in order to obtain materials with high strength, purity and homogeneity of phases [1-3]. Solid particles are crushed preliminary till nanometric size and then mixed with liquid. Initial concentration of solid particles usually account for 6-8 % in volume. The liquid phase should be able to prevent adhesion of the solid particles which can be associated with explosion due to Rebinder's effect. During drying of this mixture, called "sol", the solid skeleton is formed already when the solid phase concentration reaches 17% [4]. The following evaporation of liquid is connected with filtration through the porous skeleton to free surface. The wet gel being obtained by such a way is a porous viscoelastic body which contains few physically and chemically incoherent liquid. The final stage of the process consists of material aging and, sometimes, firing. Obviously the all stages of the process are associated with significant shrinkage of the material which leads to origination of cracks and can decrease the strength of the material being manufactured. One of the main problems in modeling of the process described above is change of mechanical properties of the material during manufacturing.

PROBLEM STATEMENT AND MODEL DESCRIPTION

The mechanical properties of compounds are defined mainly by their microstructure. The drying body is a good illustration to the above. We can observe the microstructure formation and mechanical properties evolution during such a process simultaneously. The relation between the volume concentration of the solid particles and liquid in unit volume varies during the process of drying. In Fig. 1 the real structure of the drying body and proposed computational model are presented. The situation is complicated by the fact that there is some kind of phase transition during process: in the first stage the material consists of the unconnected solid particles distributed in the liquid and exhibits the effective liquid-like behaviour. After the percolation limit is reached the average distance between the particles becomes comparatively small and the van der Waals' forces combine them in a network-like structure. From this moment the body exhibits the solid-like effective properties.

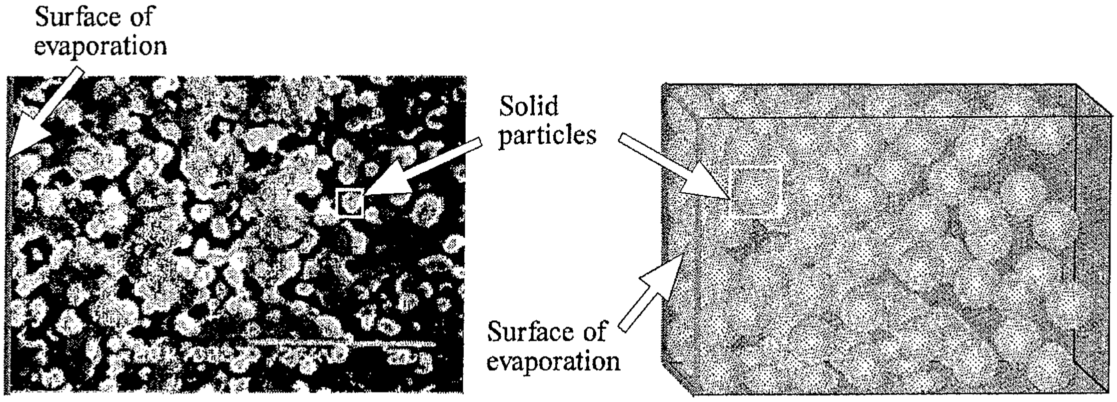

a) b)

Figure 1. Modelling of the microstructure formation in the drying ceramic:
a) SEM-micrograph of sol-gel derived $KTiOPO_4$ thin film [5]
b) Model for calculation of the average properties

According to this model of the process the following plan of the calculation of effective properties of drying bodies is proposed. Both solid and liquid materials are assumed to be viscoelastic having different properties. The infinite viscosity and infinite shear modulus give us limit cases of pure elastic solid and pure viscous liquid. The following assumptions are used in the subsequent analysis: the relaxation time is small comparing to the time of concentration variation, the dimensions of the body are always larger comparing to the mean particle diameter, and the concentration of the solid phase during the process is a known function of the time and the space coordinates (complete solution of this problem is discussed by Pompe *et al.* [6]. Macroscopic mechanical behaviour is defined as an average strain response of such a specimen to the boundary loading which would lead to uniform or polynomial states of stress in homogeneous medium. We describe here a wetted powder compact as a two-phase composite consisting of solid particles inside the viscoelastic gel in the first stage and liquid inclusions inside the solid network in the second stage (after the network formation).

EFFECTIVE FIELD METHOD OF AVERAGING

Firstly, let us consider an infinite linear-viscoelastic medium which satisfies the following constitutive law

$$\sigma_{ij}(t) = \int_0^t C^m_{ijkl}(t-\tau)\frac{d\varepsilon_{\mathrm{kl}}}{d\tau}d\tau, \tag{1}$$

where σ and ε are the stress and strain tensors, respectively and C^m is the forth rank tensor depended on time (function of relaxation). Let then a close compact region V of the medium be occupied by material which possesses different properties than those, described by the kernel C^i_{ijkl}. Using the Laplace's transformation which defined for an arbitrary function $f(t)$ as

$$\bar{f}(s) = \int_0^\infty f(t)e^{-st}dt \tag{2}$$

equation (1) can be rewritten in the follows form

$$\overline{\sigma}_{ij}(s)=\overline{C}^{m}_{ijkl}(s)\overline{\varepsilon}_{kl}(s) \qquad (3)$$

Hereafter, for simplicity, symbols which denote the Laplace-modes of the functions will be used without overline. Let us start with the equilibrium equation in displacement for the medium with a single inclusion in the Laplace-space

$$\nabla\cdot\left(\mathrm{C}(x,s):\nabla u(x,s)\right)=0, \qquad (4)$$

where colon denotes for the contraction of the tensors by two indices and u is displacement vector. Rewriting the tensor $C(x,s)$ in the form

$$\mathrm{C}(x,s)=\mathrm{C}^{m}(s)+\delta\mathrm{C}(s)V(x);\quad \delta\mathrm{C}(s)=\mathrm{C}^{i}(s)-\mathrm{C}^{m}(s), \qquad (5)$$

where $V(x)$ is the characteristic function of the domain V, the determination of field $u(x,s)$ can be reduced to the corresponding integral equation:

$$u(x,s)=u^{0}(x,s)+\int_{\mathrm{V}}\nabla\mathrm{G}(x-x',s):\delta\mathrm{C}(s):\varepsilon(x',s)dx', \qquad (6)$$

where G is the Laplace's transformation of the Green's tensor for viscoelastic media. For $x\in\mathrm{V}$ equation (6) defines the strain field $\varepsilon(x,s)=\left(\nabla u(x,s)+u(x,s)\nabla\right)/2$ inside the inclusion. Using this tensor the mechanical fields outside V can be determined relatively easy. If V has an ellipsoidal shape and ε^{0} does not depend on the coordinates, then the field ε is uniform inside V as well [7]. And for the deformation field in the inclusion one can get

$$\varepsilon(x,s)=\left(\mathrm{I}+\mathrm{P}(s):\delta\mathrm{C}(s)\right)^{-1}:\varepsilon^{0}(x,s)\equiv\mathrm{A}(s):\varepsilon^{0}(x,s) \qquad (7)$$

where $\mathrm{I}=\left(\mathrm{I}_{ijkl}\right)=\frac{1}{2}\left(\delta_{ik}\delta_{jl}+\delta_{il}\delta_{jk}\right)$ and P is integral over V for the second derivative of the Green's tensor.

$$\mathrm{P}_{ijkl}(x,s)=\int_{\mathrm{V}}\left.\frac{\partial^{2}\mathrm{G}_{ik}(x,s)}{\partial x_{j}\partial x_{l}}\right|_{(ij)(kl)}\mathrm{dV}. \qquad (8)$$

Next, let us consider an infinite viscoelastic body containing a spatial homogeneous random set of ellipsoidal inclusions, which occupy a system of compact regions $\{\mathrm{V}_{k}\}$ with characteristic functions $V_{k}(x)$. The equation for Laplace mode of the strain field can be written as

$$\varepsilon(x,s)=\varepsilon^{0}(x,s)+\sum_{k}\int_{\mathrm{V}_{k}}\mathrm{P}(x-x',s):\delta\mathrm{C}(x',s):\varepsilon(x',s)V_{k}(x')dx' \qquad (9)$$

To solve the homogenization problem and develop the macroscopic equation of equilibrium with help of (9), let us use the variant of the self consistent scheme [8], according to which

- every inclusion is considered as isolated one, 'sealed' into the homogeneous medium with the properties of the matrix;
- the presence of surrounding inclusions is taken into account by the introducing of effective strain field acting on the examined one.
- this strain field is uniform one.

RESULTS AND DISCUSSION

Let us consider the drying body as a two-phases viscoelastic medium, while both the phases are isotropic and one of them is a set of spheres (inclusions) distributed in other (matrix). In this case the Laplace mode of the relaxation kernel can be written as follows

$$C^{p}_{ijkl}(s) = K^{p}\mathrm{E}^{1}_{ijkl} + 2\mu^{p}(s)\mathrm{E}^{2}_{ijkl} \qquad (10)$$

where $p=i$ for the inclusions and $p=m$ for the matrix, μ and K are Laplace's images of the shear and bulk moduli of material, E^1 and E^2 are elements of the forth rank tensor basis [8]:

$$\mathrm{E}^{1}_{ijkl} = \delta_{ij}\delta_{kl}, \quad \mathrm{E}^{2}_{ijkl} = \mathrm{I}_{ijkl} - \frac{1}{3}\mathrm{E}^{1}_{ijkl} \qquad (11)$$

Since all inclusions have spherical shape of the same radius, tensor P(s) in (7) has the following form

$$\mathrm{P}_{ijkl}(s) = \frac{1}{9K_e(s)}\mathrm{E}^{1}_{ijkl} + \frac{1}{2\mu_e(s)}\mathrm{E}^{2}_{ijkl} \qquad (12)$$

where

$$K_e(s) = K_m + \frac{4}{3}\mu_m(s), \quad \mu_e(s) = \mu_m(s)\frac{5\big(3K_m + 4\mu_m(s)\big)}{6\big(K_m + 2\mu_m(s)\big)}.$$

If we assume that the inclusions have the isotropic distribution, then the macroscopic behavior of the body is isotropic and may be described by two functions:

$$\begin{aligned} K^{*}(s) &= K_m + c_i\left(\frac{1}{\delta K} + \frac{1-c_i}{K_e(s)}\right)^{-1} \\ \mu^{*}(s) &= \mu_m(s) + c_i\left(\frac{1}{\delta\mu(s)} + \frac{1-c_i}{\mu_e(s)}\right)^{-1} \end{aligned} \qquad (13)$$

where $\delta\mu$ and δK denote the differences between corresponding moduli of matrix and inclusions. Now the inverse Laplace's transformation should be made in (13). In order to obtain corresponding relations in the general case the numerical methods are more preferable since the final expressions are quite cumbersome.

To compare our approach with the real behavior of drying bodies, we use experimental data from [3,9] obtained for the acid catalyzed gel made by hydrolyzing distilled tetraethylorthosilicate (TEOS) with shear modulus $\mu_s = 1.6$ GPa and Poisson's ratio $\nu = 0.2$. The liquid is $\mathrm{H_2O / C_2H_5OH / HCl} = 16/4/0.01$, that is pure viscous mixture with viscosity $\eta_l = 0.82 \cdot 10^{-3}\,\mathrm{Pa \cdot s}$ and bulk modulus $K_l = 0.226$ GPa. It means that the solid phase of considered body is pure elastic and the liquid is viscous (without elastic part).

The effective properties of the body strongly depend on the distance from the surface of evaporation. However, the transversal shear modulus can be considered as a function of solid phase concentration only. Corresponding data are presented in Figure 2 for effective Young modulus and shear modulus of the material. Initial concentration of the solid phase is 0.06. The dotted curves correspond to a model for which the solid particles are distributed in the liquid. It is in a good agreement with experimental data unless 65% of liquid was evaporated and solid phase concentration reaches 17% (the concentration is assumed to get changed only due to the liquid evaporation). It is significant that the point of the model change corresponds to the solid phase concentration of 0.14. This point is in a good agreement with percolation limit discussed above.

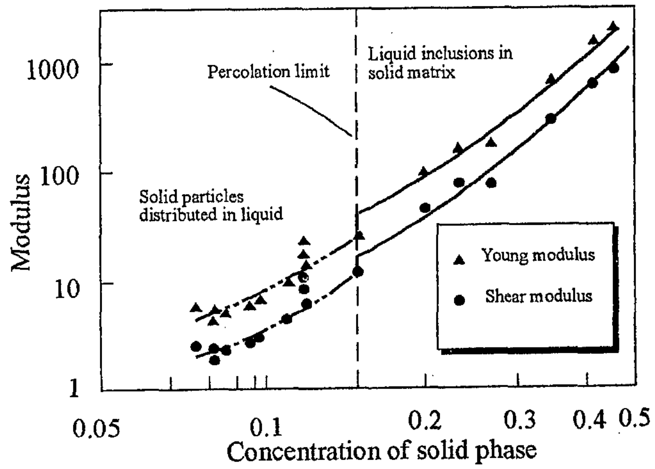

Figure 2. Comparison of the obtained results with experimental data.

In the case of cylindrical shape of the drying body the radial dependency of material parameters using the solution of the filtration problem can be used. Examples of such curves are shown in Figure 3. The radial dependency of solid phase concentration in arbitrary moment of the time (after the percolation limit is reached) is inserted . This solution is discussed in [5] and used here to obtain the radial dependency of effective momentary shear modulus μ and effective viscosity η.

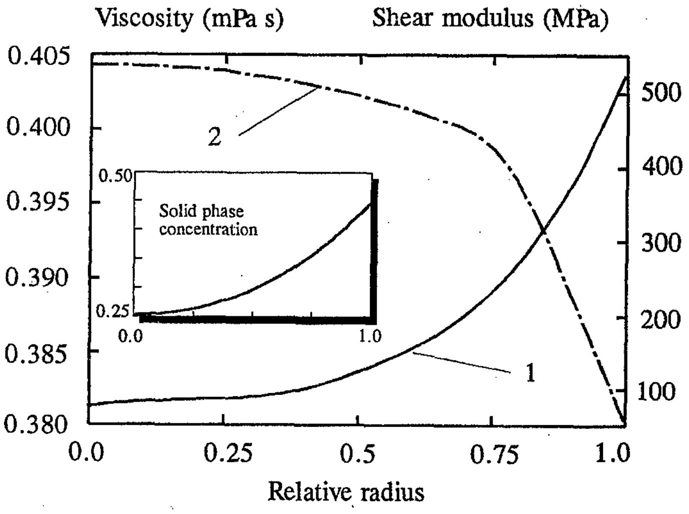

Figure 3. Evolution of mechanical properties of drying cylinder:
1 - effective shear modulus; 2 - effective viscosity

CONCLUSIONS

In the present study the drying derived material is designed as two-component composite with the variable volume concentration of the phases. The proposed approach allows to describe the drying materials when a large dissimilarity in mechanical properties of the solid particles and the humectant media takes place. The model is quite simple and at the same time reasonably accurate for the use in technological applications since the results obtained are in good agreement with experimental data available in the literature.

ACKNOWLEDGMENT

Partial financial assistance for this research was provided by INTAS-RFBR grant 95-481

REFERENCIES

1.Brinker, C.J. and Scherer, G.W. "*Sol-Gel Science*", Academic Press, San Diego (1990).

2.Hench, L.L. and West, J.K. "The sol-gel process." *Chemical Review* **90**, pp. 33-72 (1990).

3. Woigner, T., Phalippou, J., Hdach, H., Larnac, G., Pernot, F. and Scherer, G.W. "Evolution of the mechanical properties of ceramics during the alcogel-aerogel-glass process." *Journal of Non-Crystalline Solids* **147&148**, pp. 672-686 (1992).

4. Bouvard, D. and Lange, F.F. "Relation between percolation and particle coordination in binary powder mixtures." *Acta Metallurgica et Materialia* **39**, pp. 3083-3090 (1991).

5. Barbe, C.J., Harmer, M.A. and Scherer, G.W. "Microstructure, orientation and properties of sol-gel derived $KTiOPO_4$ thin films." *Journal of American Ceramic Society* **78**, pp.2033-2045 (1995).

6. Pompe, W., Lange, F.F. and Sevostianov, I.B., "Modelling of the fracture behaviour of drying ceramics." In: *Fracture mechanics of ceramics*, V.11/12, (ed. R.C.Bradt), Plenum Publ., New-York (1995).

7. Lyssiak, I.G. and Sevostianov, I.B. "Zur Frage der polinomialen Konservativitaet." *ZAMM* 77, pp.556-560 (1997).

8. Kanaun, S.K. and Levin, V.M. "The self-consistent field method in mechanics of matrix composite materials." In: *Advances in mathematical modelling of composite materials*, (ed. K.Z.Markov), World Scientific Publ., Singapoure (1994).

9. Scherer, G.W. "Effect of drying on properties of silica gel." *Journal of Non-Crystalline Solids* **215**, pp. 155-168 (1997).

PREDICTION OF RESIDUAL THERMAL STRESSES OF LAMINATED COMPOSITE TUBES

A. C. SEIBI[1], M. F. AMATEAU[2]

[1] Department of Mechanical Engineering, Sultan Qaboos University, P.O.Box33, Al Khod 123, Oman.

[2] Department of Engineering Science & Mechanics, Pennsylvania State University,
227 Hammond Bldg, PA, USA.

INTRODUCTION

The mechanical behavior of monolithic ceramics can be improved by incorporating reinforcements into ceramic matrices known as ceramic matrix composites. Ceramic composites offer greater advantage than monolithic ceramics for heat exchanger applications based upon higher temperature capability, higher toughness, lower density, and better corrosion resistance in a hostile environment [1-5]. Recently, multilayered composite (hybrid laminate) have been developed through the transformation process of the material microstructure [6] or through tailoring the thermoelastic properties of ceramic materials [7-8]. Designs based on classical laminate plate theory have been utilized recently to fabricate multilayered ceramic matrix composite plates by estimating the residual thermal stresses. This design method can be extended to design and fabricate composite tubes.

Estimation of the thermal residual stresses of laminated polymer-based composite tubes were based on the assumption that these tubes are long enough to consider the application of classical laminate plate theory (CLPT) within the gage length section [9-10]. This section is approximated to be within a distance of twice the radius of the tube from the edges for various loading conditions. In addition, trial and error procedures were routinely used in finalizing the design of ceramic composites based on the induced thermal residual stresses during cooling from processing temperature to room temperature. As yet, a design methodology has not been developed to optimize the parameters that influence the thermal residual stress profiles. Simultaneously, the effective thermal conductivity through the tube wall thickness is maximized. Layer thicknesses, t_k, volume fraction of the reinforcement, V_f, and stacking sequence are considered as design variables. In this paper, a design methodology based on sensitivity analysis to optimize the architecture of a laminated ceramic composite tube is developed.

DESIGN APPROACH

Structural components of monolithic ceramics under high temperature applications often exhibit catastrophic failure as a result of high thermal stresses. Such failure could be prevented by introducing favorable residual stresses in such components. This strengthening mechanism can be achieved by the incorporation of various types of reinforcements (particulates, platelets, whiskers) with ceramic matrix material, microstructural modification, and by the fabrication of laminated composites. The latter method can be achieved by tailoring the composite structure containing various laminae with different volume fractions. The design procedure of laminated composite tubes using CLPT starts with the elastic modulus of the fibers and matrix, E_f and E_m, respectively, the volume fraction of the fiber V_f, the fiber aspect ratio l/d, and the coefficients of thermal expansion for fiber and matrix, α_f and α_m followed by the use of the rule of mixture to determine the lamina elastic properties in the longitudinal and transverse directions. In addition, the design procedure involves the alteration of various laminae possessing different thermoelastic properties in the composite structure to induce favorable thermal residual stresses. Since tubular structures generate high hoop thermal stresses in the outer surface which may cause premature failure during fabrication, attention is focused on the minimization of the induced thermal residual tensile hoop stress as well as the maximization of the effective thermal conductivity, k_{eff}, through the tube wall thickness. Estimation of the induced thermal residual stresses is performed by means of a general purpose finite element program. The composite architecture considered in this study contains up to five layers consisting of 0, 10%, 20%, 30%, and 40% volume fractions of SiC_w/mullite.

FINITE ELEMENT MODELING

A two-dimensional axisymmetric element is used to model the composite laminate and the graphite mandrel as shown in Figure 1. This model initially represents both the graphite material at the inner section and the composite laminate, with altered volume fractions, at the outer section. Because of symmetry, only one half of the length is considered. It is assumed that each lamina with a prescribed volume fraction is transversely isotropic and that perfect bonding exists between the individual layers (no slippage). The Cartesian coordinates (r, z) represent the radial and axial coordinates for a tubular configuration, respectively. The graphite mandrel has an inner radius of 15.875 mm and the composite laminate is 3.175 mm thick. A two-dimensional interface element is employed at the graphite mandrel and the composite laminate interface to study the possibility of force transmission between both components. This element type allows both surfaces to maintain or break physical contact and also permits relative motion between both surfaces.

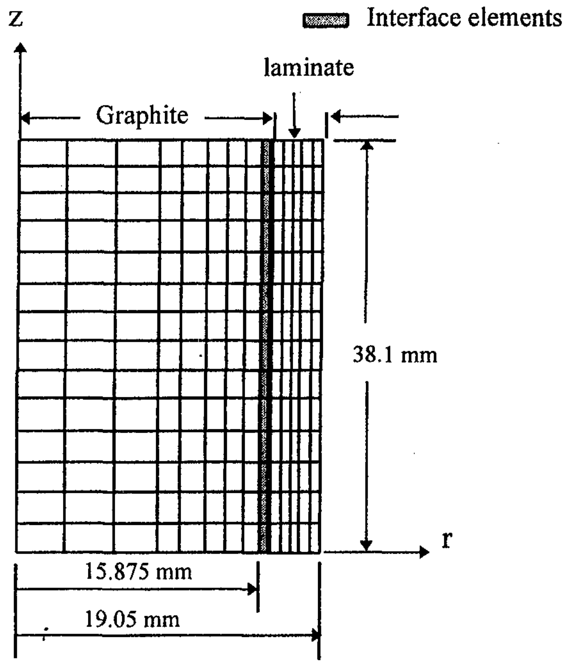

Figure 1 - Axisymmetric FE Model of Graphite/Laminate Composite Tube.

The boundary conditions requires a zero displacement in the direction normal to the plane of symmetry for all the nodes lying on that plane. All the nodes lying on the r axis of symmetry have zero displacement in the z direction. A preliminary study revealed that there is no contact between the graphite and the laminate for different friction coefficient values ($\mu_f = 0.01\text{-}0.05$) during the mesh refinement procedure for a temperature change of 1700 °C. This is mainly attributed to the thermal differential existing between the graphite and the composite laminate: the effective thermal expansion of the laminate is much lower than that of the graphite which causes it to shrink more, thus, creating a gap between both components. Therefore, the finite element analysis was proceeded for the composite tube only.

OPTIMIZATION PROCEDURE

In this analysis, the maximum nodal tensile hoop stress, σ_R, and the effective thermal conductivity, k_{eff}, represent the cost and constraint functions, respectively. The laminae thicknesses, t_i, and the stacking sequence of the volume fractions, V_f, are taken as the design variables. First-order Taylor series expansion of the cost function about t_i and V_f takes the following form

$$\sigma_R(\tilde{t},\tilde{V}_f)=\sigma_R(\tilde{t}_0,\tilde{V}_0)+\nabla\sigma_R(\tilde{t}_0,\tilde{V}_0)(\tilde{t}-\tilde{t}_0,\tilde{V}_f-\tilde{V}_0) \qquad (1)$$

where $\sigma_R(\tilde{t}_0,\tilde{V}_0)$ is the current value of the cost function. The constraint function is represented by the effective thermal conductivity, $k_{eff} = k_0$, where k_0 is obtained by substituting the initial design variable values in the following equation:

$$\mathrm{Re}\,s=\frac{1}{k_{eff}}=\frac{1}{t}\sum_{i=1}^{n-1}\frac{t_i}{k_i}-\frac{t_n}{t\,k_n} \qquad (2)$$

where k_{eff}, t, t_i, and k_i are the effective thermal conductivity through the tube wall thickness, the laminate thickness, lamina thickness, and the thermal conductivity of the individual lamina, respectively. The values of the thermal conductivity for the individual lamina were measured experimentally and presented in Table 1 [8]. Table 1 also includes the elastic properties of the different laminae used to design a hybrid composite tube with optimal characteristics.

Table 1 - Material Properties of Various SiC_w Reinforced Mullite Laminae With Different Volume Fractions, V_f.

V_f (%)	E_L (10^6 psi)	E_T (10^6 Psi)	α_L ($10^{-6}/^0C$)	α_T ($10^{-6}/^0C$)	ν	k (W/m.K)
0	32.66	32.66	5.2	5.2	0.22	5.20
10	37.44	36.57	4.9	4.9	0.22	6.93
20	41.21	40.05	4.8	4.8	0.21	9.10
30	45.0	43.54	4.76	4.8	0.21	11.88
40	51.67	49.92	4.7	4.76	0.21	15.60

The optimization design procedure is stated as follows:

min. max. value of $\sigma_R(\tilde{t})$ (linearized)

$$\text{Subject to} \quad \begin{Bmatrix} k_{eff} = k_0 \\ 0.0762 \le t_i \le 3.175\,\text{mm} \\ 0 \le V_f \le 0.50 \\ \Sigma t_i = 0.125 \end{Bmatrix} \qquad (3)$$

An independent variable defined by

$$t_n = t - \sum_{i=1}^{n-1} t_i$$

where t is the overall fixed thickness, gives the thickness of the remaining layer. The index n represents the number of laminae included in the laminated composite tube of wall thickness t. Each design variable is varied quantitatively by 10% to linearly approximate the cost function in the neighborhood of the initial values. Several computer runs using ANSYS are performed to evaluate the first derivative of the cost function with respect to each design variable, t_i and V_i at the current point. The material properties of the individual lamina used in the finite element model are listed in Table 1. Various designs consisting of combinations of at least two laminae with volume fractions ranging between 0 to 40% reinforcements are tested. It was found that two designs among others represent the best candidates for achieving favorable residual stresses. The first design consists of five laminae of [40/30/20/10/0] taken as design #1 and the second design (design #2) has four laminae of [40/30/20/10] volume fractions of SiC whiskers reinforced mullite. Since the tubes are intended for applications in aggressive chemical environments and because mullite exhibits better corrosion resistance than SiC_w, a corrosion resistant layer made of pure mullite or reinforced mullite at a low volume fraction of SiC_w at the outside surface is needed. Therefore, the outside layer must contain the lowest volume fraction such as pure matrix material and 10% for designs #1 and 2, respectively.

The values of the maximum hoop stress is obtained by performing several computer runs using ANSYS. Those values were then substituted into equation (1) to obtain an approximate first order explicit relationship for the hoop stress as a function of the design variables. An IMSL optimization subroutine is then used to minimize the approximated cost function; therefore, obtaining a better design. New design variable values are then obtained and implemented into the finite element model to estimate new values for the residual thermal stresses. Variation of each new design variable by 10% is repeated to linearly approximate the cost function which in turn is implemented into the linear optimization program. In this step, the effective thermal conductivity was increased by 10 to 20% and new values of t_i are obtained. This procedure is repeated several times until there is no change in the new values of the design variables which will be taken as the proper design values.

Stacking sequence is another design variable that was considered in the analysis. Combinations of altered volume fractions were performed to select the optimum stacking sequence which results in the lowest value of the tensile hoop stress. Optimum layer thicknesses were then obtained using the same procedure described above. The optimum stacking sequence, effective thermal conductivity, and layer thicknesses for designs # 1 and #2 are listed in Table 2. Table 2 presents the initial and final designs and the corresponding tensile hoop stresses at the outer layers. A reduction of 10% and approximately five times less in value of the residual tensile hoop stresses from the initial guesses at the outer layers were obtained for designs #1 and #2, respectively.

Table 2 - Initial and Optimum Laminated Composite Tube Architecture.

Composite Laminate Design	Stacking Sequence	Laminae Thickness (in)	Maximum Nodal Hoop Stress (Ksi)	% Reduction	Effective Thermal Conductivity
Design #1	Initial [40/30/20/10/0]	$t_{40} = 0.04$, $t_{30} = 0.03$ $t_{20} = 0.025$, $t_{10} = 0.015$ $t_0 = 0.015$	41.522	-------	
	Final [30/20/40/10/0]	$t_{40} = 0.006$, $t_{30} = 0.006$ $t_{20} = 0.006$, $t_{10} = 0.10$ $t_0 = 0.007$	37.42	10	9.7
Design #2	Initial [40/30/20/10]	$t_{30} = 0.03$, $t_{40} = 0.01$ $t_{20} = 0.04$, $t_{10} = 0.045$	10.766	------	
	Final [30/40/20/10]	$t_{30} = 0.006$, $t_{40} = 0.006$ $t_{20} = 0.013$, $t_{10} = 0.10$	2.142	500	7.5

A preliminary comparison between design #1 and #2 reveals that design #2 is less corrosion resistant than design #1 because of the 10% lamina as compared to pure mullite being at the outer surface. This is due to the existence of SiC whiskers in the 10% volume fraction which is less corrosion resistant than mullite. However, design #2 possess much lower tensile hoop stress in the outer lamina than that for design #1. This large reduction of the tensile hoop stress enhances the strength and the thermal degradation of the composite architecture made from design #2. Even though design #1 has better performance in severe chemical environment, its high induced thermal residual stresses may cause macrocracking of the outer lamina during cooling from the processing temperature. Figure 2 shows the initial and final residual hoop stress distribution through the tube thickness according to design #2. This improved composite architecture will eliminate the formation of microcracking as well as enhance the thermomechanical performance of the tube under severe loading conditions. Therefore, it is desirable to proceed with the fabrication of laminated composite tubes as outlined in design #2 for applications in less hostile chemical environments and severe thermal shock conditions.

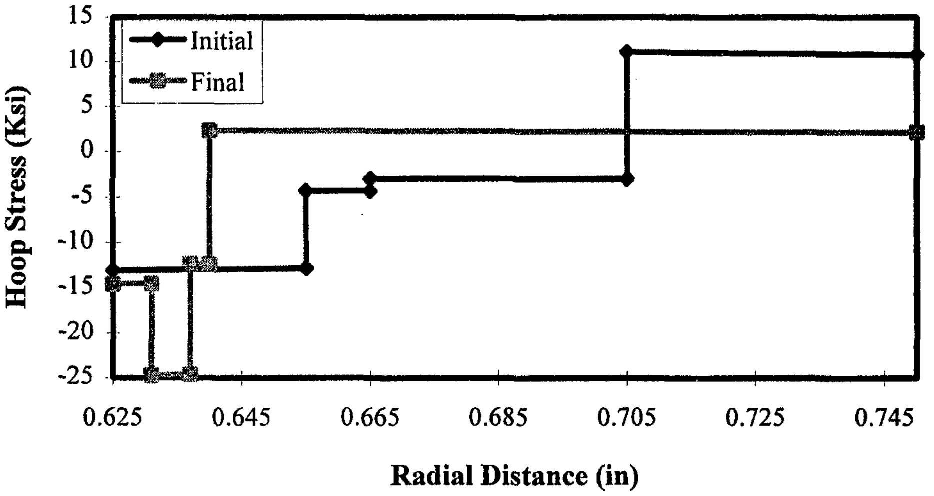

Figure 2 - Residual Hoop Stress of Laminated Composite Tube for Design #2.

CONCLUSIONS

The laminate plate theory was successfully used to predict the thermal residual stresses in laminated composite tubes. A finite element model of SiC_W/mullite laminated composite tubes was used in conjunction with a linear optimization program. An optimum tube design consisting of [30/40/20/10] stacking sequence was obtained. A reduction 51% of the thermal residual tensile stress for the selected design was achieved. It is concluded that design #2 is more favorable to utilize than design #1 for severe thermal loading conditions. It is worth to note that this methodology can be applicable to multilayered composites where the winding angle is of particular interest.

REFERENCES

[1] Liu H., et al, "Crack Deflection Process for Hot-Pressed Whisker-Reinforced Ceramic Composites," J. Am. Ceram. Soc., 72 [4] 559-563, (1988).

[2] Homeny J., Vaughn W. L., and Ferber M. K., "Processing and Mechanical Properties of Sic-Whisker-Al_2O_3-Matrix," Am. Ceram. Soc. Bull., 66 [2] 333-338, (1987).

[3] Hillig W. B., "Tailoring Multiphase and Composite Ceramics," Materials Science Research (Tressler, R. E., Messing, G. L, Pantano, G. C., eds), Vol. 20, pp 697-711, Plenum Press, New York, (1986).

[4] Ruh R., Majdiyasni K. S., and Mendiratta M. G., "Mechanical and Microstructural Characterization of Mullite and Mullite-SiC-Whisker and ZrO_2-Toughened-Mullite-SiC -Whisker Composites," J. Am. Ceram. Soc., 71 [6] 503-12, (1988):

[5] Wei G. C., and Becher P. F., "Development of SiC Whisker Reinforced Ceramics," Am. Ceram. Soc. Bull., 66 [2] 347-52, (1987).

[6] Huang J. L., and Cutler R. A., "Strengthening of Oxide Ceramics by Transformation -Induced Stresses," J. Am. Ceram. Soc., 70 [3] 164-70, (1987).

[7] Boch P., Chartier T., and Huttepain, "Tape Casting of Al_2O_3/ZrO_2 Laminated Composites," J. Am. Ceram. Soc., 69 [8] C191-C192, (1986).

[8] Kim T., "Fabrication and Design of Processing Silicon Carbide Whisker Reinforced Mullite Composites," Ph.D Thesis, The Pennsylvania State University, May (1990).

[9] Rizzo R. R., and Vicario A. A., "A Finite Element Analysis of Laminated Anisotropic Tubes," (Part I - A Characterization of the Off-Axis tensile Specimen), J. Comp. Mater., Vol.4, pp. 344-359, July (1970).

[10] Pagano N. J., "Geometric Design of Composite Cylindrical Characterization Specimen," J. Comp. Mater., Vol. 4, pp. 360-379, July (1970).

STRENGTH AND STIFFNESS OF BRAIDED FIBER COMPOSITES

STEPHEN R. SWANSON

Dept of Mechanical Engineering, 50 S. Central Campus Dr., Rm 2202 MEB
University of Utah, Salt Lake City, UT 84112-9208 USA

ABSTRACT

Advanced composite materials are being used in the form of textile preforms, with the typical advantage being lowered manufacturing costs. This paper summarizes some current work on predicting the stiffness properties of these materials, and also gives recent results on measured strength properties. The data show significant loss of strength in 2-D triaxial braid materials relative to tape laminates, which is believed to be due to the undulation of the fibers. Results of a model to help explain this strength loss associated with fiber undulation are presented.

INTRODUCTION

With the goal of reducing manufacturing costs, advanced fiber composites are being used or considered in the form of textile preforms in conjunction with resin transfer molding (RTM). The development of braiding as a technique for advanced fiber composite structures has been described in recent work [1,2]. Processing parameters have been considered by Popper [3] and Ko, Pastore, and Head [4]. The development of stiffness models for textile materials including braids has been considered by a number of authors, including [5-9]. Comparison of these models with experimental results for braids has been given in [10]. Information on the strength properties of textiles has been presented by Ishikawa and Chou [11], Ko [12], and by Crane and Camponeschi [13].

The present paper summarizes work on predicting stiffness of triaxial braids, reviews recent work on the strength properties, and presents new work on models for predicting the effects of fiber undulation characteristic of braids on the strength properties.

STIFFNESS OF 2-D TRIAXIAL BRAID COMPOSITES

Predictions of stiffness of 2-D triaxial braid materials have been based on the idea of a unit cell, that is representative of the fiber architecture. A schematic of the basic architecture of the 2-D triaxial braid is shown in Fig 1. A useful model for predicting stiffness has been termed the fiber inclination model. This model assumes the braid fiber path as a series of in-plane and through-the-thickness segments, and combines these segment properties to predict average braid stiffness as shown by Smith and Swanson [10,14].

As described in [14], the stiffness of the braid yarns can be described by a transformation T_2 through the crimp angle to the in-plane direction, and an in-plane transformation T_3 through the braid angle to the overall global coordinates. The three-dimensional braid material stiffness matrix is then given by

$$\overline{Q}_{XYZ} = T_3^{-1} T_2^{-1} [Q_{123}] T_2 T_3 \qquad (1)$$

In this model the path of the braid yarn within the unit cell is idealized as a series of straight segments. Following what has been entitled a "mechanics of materials" approach to stiffness, it was shown in [14] that both the E_{11} and E_{22} properties could be obtained by summations over the segments of the form

$$\frac{1}{E_s} = \sum \frac{v_f}{E} \qquad (2)$$

The results of computations of this kind are shown compared with measured stiffness properties in Fig 2.

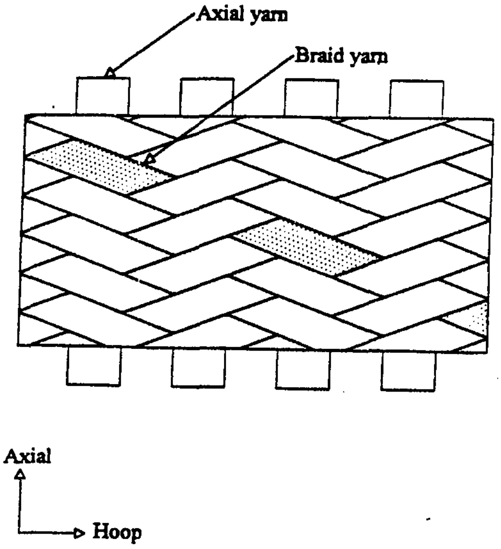

Fig 1. Illustration of 2-D triaxial braid architecture.

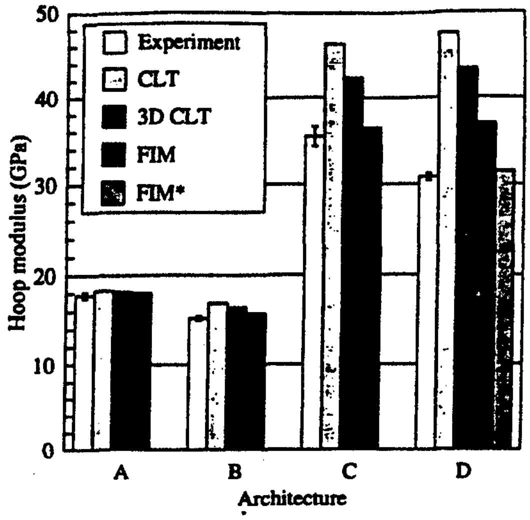

Fig 2. Comparison of models with experiment for hoop modulus of 2-D triaxial braid materials, from [14].

STRENGTH PROPERTIES OF 2-D TRIAXIAL BRAIDS

Experimental tests to determine the biaxial strength properties of 2-D triaxial braids have been carried out using tubular specimens, loaded by combinations of internal and external pressure, and axial tension and compression [15]. A typical failure envelope is shown in Fig 3. Also shown in this figure is a failure locus based on a maximum average in-plane strain in either the axial or braid direction fibers. This critical strain criterion has been shown in previous work to correlate ultimate failure in fiber dominated laminates and loadings [16]. As shown here, the application to braided materials seems to be useful as well. It should be noted that the strains used here are the in-plane, average, components, and thus differ from the actual strain, particularly in the braid fibers. The failed specimens exhibited a failure mode that could be readily identified as failure of either the axial fibers or the braid fibers, depending on the ratio of the applied stresses. Some specimens exhibited failure in both modes. These specimens had applied stresses that corresponded very closely to the "corner" of the failure locus where a change in failure mode is predicted.

A notable feature of the results is that a significant loss of strength occurs relative to pre-preg laminates made from the same or similar materials [17], in some cases on the order of 50%. This reduction in strength represents a reduction in ultimate strain capability, combined with the reduction in stiffness relative to the tape laminate. Clearly one of the factors in the loss of strength in the braid fibers is the stress concentration associated with the undulating path of the braid fibers. An additional mechanism was noted by Smith and Swanson [18], due to the variation of properties because of the discrete nature of the large yarn fiber bundles in braided materials. The region between the axial yarns has different transverse stiffness properties than the region where the braid yarns go over and under the axial yarns, because of the different Poisson ratio values for these regions. These variations of transverse strain were noted in Moire fringe surface strain measurements reported by Naik, Ifju, and Masters [19]. Thus the change of properties in the transverse direction gives a variation of the strain distribution, and thus a strain concentration in the braid fibers relative to the average strain.

Some limited work has been done to correlate the fiber undulation with strength properties and strength degradation. Much of this work has been associated with the effect of wavy fibers on compressive strength. Naik [20] has offered work based on strength of materials models intended to be applicable to braids.

ANALYSIS OF THE EFFECT OF FIBER WAVINESS ON STRENGTH

A new approach to estimating the effect of fiber undulation is presented here, that would seem to be applicable to the case of axial yarn undulation. This approach is based on an elasticity solution presented by Zhang and Latour [21], and was used by them as a model for compressive strength of fiber composites. However the elasticity solution can also be used as the basis for a model intended to show the effect of axial loads on wavy yarns. The basic geometry is a two dimensional array of wavy yarns, separated by resin rich areas. As shown by Zhang and Latour [21], the interaction between the axial load in the fibers and the stresses in the resin rich region can be determined by a straightforward elasticity solution. Finally, bending of the wavy yarn under the axial load can then be determined from the matrix stresses, using a beam-on-elastic-foundation model for the axial yarn. Obviously the model is highly idealized, but leads to a solution for the interaction between axial forces and bending effects in wavy yarns that would seem to give insight into the present case of a material with undulation of the axial yarns.

The basic model to be considered here consists of wavy fibers or yarns, interspersed with regions of lower stiffness, such as the matrix between fibers or the resin rich region between yarns or bundles of fibers. The model is two dimensional, and uses a slab to represent the fiber or yarn. The two-dimensional slabs representing the axial yarns or fibers are modeled by a simple beam-column on an elastic foundation, that interacts with the matrix or resin-rich region by means of the normal and shear stresses transmitted between the slab and material. If the slab (fiber or yarn) were initially straight, the equation of transverse equilibrium for the slab can be written as

$$EI\frac{d^4Y}{dx^4} - 2r\frac{d\tau_{xy}}{dx} + 2\sigma_y - T\frac{d^2Y}{dx^2} = 0 \tag{3}$$

where EI are the beam stiffness properties, Y is the transverse displacement, r is the half thickness of the beam, τ_{xy} and σ_y are the matrix stresses at the boundary with the beam, and T is a tensile force in the beam.

The initial wavy configuration of the axial yarns is taken as

$$Y_0 = A_0 \sin \lambda x \tag{4}$$

When the tensile force T acts on the fiber, it tends to straighten, producing bending in the fiber. Eqn 3 can be used to solve for the bending deformation in the fiber by considering that the force T acts through the wavy geometry, while the bending and matrix stress terms depend on the additional deformation from the initially wavy configuration. The equation of transverse equilibrium then becomes

$$EI\frac{d^4(Y-Y_0)}{dx^4} - 2r\frac{d\tau_{xy}}{dx} + 2\sigma_y - T\frac{d^2Y}{dx^2} = 0 \tag{5}$$

A beam on elastic foundation model has been used previously by Naik [20] to estimate the effects of fiber waviness on braid strength. A simplified treatment of the resin-rich region stresses was employed. However, it was pointed out by Zhang and Latour [21] that a straightforward elasticity solution can be obtained to determine the elastic stress distribution in the region between the fibers. This solution was used by Zhang and Latour to give insight into the fiber buckling problem in compressive loading of fiber composites. However it can also be used to investigate the effects of axial fiber waviness on fiber failure. Thus the solution will be shown to also give information about the effect of crimp of the axial yarns on axial failure in the present braided composites.

Zhang and Latour [21] show that the matrix stresses can be related to the bending deformation $Y\text{-}Y_0$ of the fiber by means of the Airy stress function

$$\phi(x,y) = \sin \lambda x \begin{bmatrix} c_1 \cosh \lambda y + c_2 \sinh \lambda y + \\ c_3 y \cosh \lambda y + c_4 y \sinh \lambda y \end{bmatrix} \tag{6}$$

The constants are then determined by obtaining stresses from this stress function, and then using the stress-strain and strain-displacement relations to obtain expressions for the displacements in terms of the above parameters and the constants. Finally, the expressions for the matrix stresses are substituted into Eqn 5 to determine the bending of the wavy yarn. The bending strain in the yarn is then obtained from

$$\varepsilon_b = r\frac{d^2(Y-Y_0)}{dx^2} \tag{7}$$

The total strain in the fiber or yarn is then the sum of the uniform axial strain plus the bending strain, or

$$\varepsilon_{tot} = \frac{T}{A_f E_f} + \varepsilon_b \tag{8}$$

Thus the additional strain produced in the fiber because of the axial force acting through the initially waviness can be obtained.

Results from this model are illustrated in Fig 4. It can be seen that the model predicts a significant reduction in strength with increasing crimp angle of the axial yarns. This would seem to reinforce the intuitive view that the undulation in the axial yarns leads to lower axial strength, and can thus be an explanation for the low axial strengths seen in the present material. The actual strength reduction seen in the experiments is quite consistent with that predicted by the model. This of course may be fortuitous, as the model is not a precise representation of the actual material. However the correlation of theory and experiment is encouraging.

SUMMARY AND CONCLUSIONS

The combination of 2-D triaxial braid preforms with advanced composite materials is being employed or considered in an effort to reduce manufacturing costs. Measured results of the material stiffness can be predicted by straightforward models that represent the fiber path in a unit cell. The strength properties of the braid materials can be significantly lower than those of comparable laminates, and this must be taken into account in design. The undulation of the fiber path introduces stress concentrations into the fibers. A model of the effect has been presented that gives insight into the loss of strength in braid specimens.

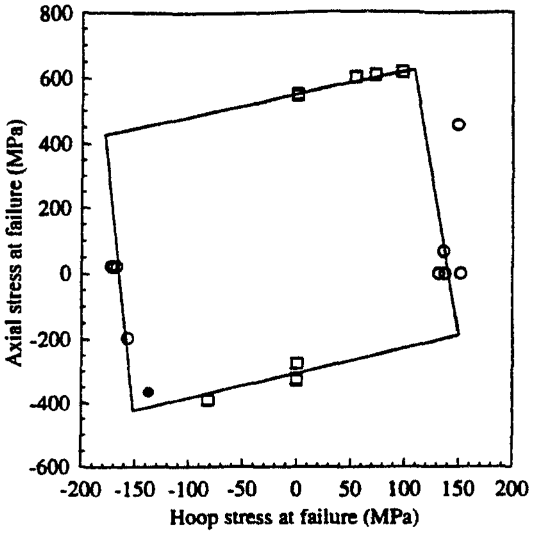

Fig 3. Biaxial stress failure envelope for 2-D triaxial braid, architecture B, from [15]. Line is prediction based on the maximum fiber direction strain failure criterion.

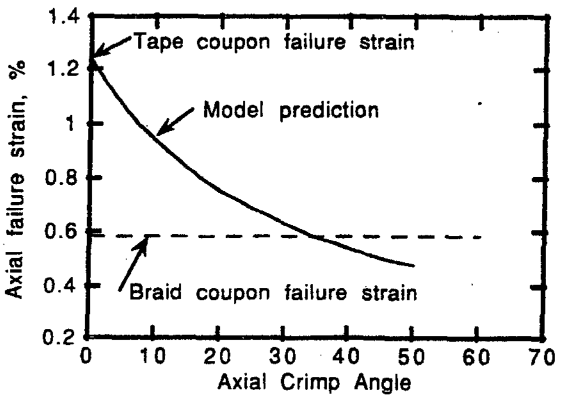

Fig 4. Predicted effect of crimp (undulation angle) in axial fibers on axial ultimate strain.

REFERENCES

1. Chou, T.W., and Ko, F.K., eds, Textile Structural Composites, 3, Elsevier (1989).
2. Soebroto, H. B. and Ko, F. K., "Composite Preform Fabrication by 2-D Braiding," Proceedings of the Fifth Annual ASM/ESD Advanced Composites Conference, 307-316 (1989).
3. Popper, P., "Braiding," Handbook of Composite Reinforcements, VCH Publishers, Inc., 24-41 (1993).
4. Ko, F. K., Pastore, C. M. and Head, A. A., "Handbook of Industrial Braiding", Atkins and Pearce (1993).
5. Ishikawa, T. and Chou, T. W., "One-Dimensional Micromechanical Analysis of Woven Fabric Composites," AIAA J., 21, 1714-1721 (1983).

is not a precise representation of the actual material. However the correlation of theory and experiment is encouraging.

SUMMARY AND CONCLUSIONS

The combination of 2-D triaxial braid preforms with advanced composite materials is being employed or considered in an effort to reduce manufacturing costs. Measured results of the material stiffness can be predicted by straightforward models that represent the fiber path in a unit cell. The strength properties of the braid materials can be significantly lower than those of comparable laminates, and this must be taken into account in design. The undulation of the fiber path introduces stress concentrations into the fibers. A model of the effect has been presented that gives insight into the loss of strength in braid specimens.

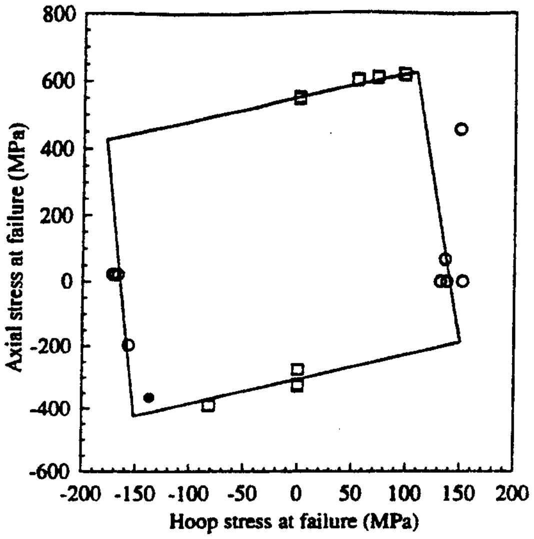

Fig 3. Biaxial stress failure envelope for 2-D triaxial braid, architecture B, from [15]. Line is prediction based on the maximum fiber direction strain failure criterion.

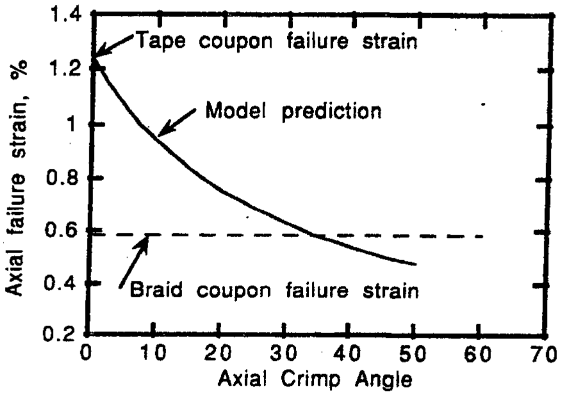

Fig 4. Predicted effect of crimp (undulation angle) in axial fibers on axial ultimate strain.

REFERENCES

1. Chou, T.W., and Ko, F.K., eds, Textile Structural Composites, 3, Elsevier (1989).
2. Soebroto, H. B. and Ko, F. K., "Composite Preform Fabrication by 2-D Braiding," Proceedings of the Fifth Annual ASM/ESD Advanced Composites Conference, 307-316 (1989).
3. Popper, P., "Braiding," Handbook of Composite Reinforcements, VCH Publishers, Inc., 24-41 (1993).
4. Ko, F. K., Pastore, C. M. and Head, A. A., "Handbook of Industrial Braiding", Atkins and Pearce (1993).
5. Ishikawa, T. and Chou, T. W., "One-Dimensional Micromechanical Analysis of Woven Fabric Composites," AIAA J., 21, 1714-1721 (1983).

PARTICULATE COMPOSITES WITH THE TZP MATRIX AND (Ti,W)C ADDITIVE

M. Faryna[1], Z. Pędzich[2], W. Pyda[2] , K. Haberko[2]

[1] Institute of Metallurgy and Materials Science, Polish Academy of Sciences, ul.Reymonta 25, 30-059 Kraków, Poland
[2] Department of Special Ceramics, University of Mining and Metallurgy, al.Mickiewicza 30, 30-059 Kraków, Poland

INTRODUCTION

Composites with the tetragonal zirconia polycrystals (TZP) matrix containing inclusions of hard and stiff carbides show better mechanical properties than the TZP matrix. Dense bodies with WC, SiC, TiC or Cr_xC_y additives were widely investigated during last few years [1-9]. These composite systems are harder and tougher than the TZP ceramics. Particularly, composites containing WC and TiC seem to be very perspective. Due to their very good wear resistance, they can be applied in the industry. In this paper we present the results of investigations on fabrication of the composites with another type of carbide additive. This is a TiC/WC solid solution of TiC type structure. Such carbide is applied in the cemented carbides technology.

EXPERIMENTAL

In the presented work an yttria stabilised zirconia solid solution (Y-TZP) of 2.9 mole %Y_2O_3 content, prepared by the coprecipitation-calcination method [10], was used as a matrix. A carbide phase applied as an additive was a commercially available titanium-tungsten carbide powder made by Baildon, Poland. The average Ti:W mole ratio was of 3:1.

Homogenisation of composite components was achieved by the rotation-vibration milling of the powder mixture in ethanol. Composite powders of the carbide content ranged from 10 to 50 vol.% were obtained. These powders were hot-pressed in a graphite die at 1400°C with 30 minute soaking time. The mixture containing 20 vol.% of the (Ti,W)C was similarly treated also at 1300, 1500 and 1600 °C. The applied pressure was 25 MPa.

Bulk densities of the samples were determined by the Archimedian method. Relative densities were estimated using densities of the composite components: 6.1 g/cm^3 for zirconia solid solution and 7.5 g/cm^3 for (Ti,W)C carbide.

X-ray diffraction was used to determine the phase composition of the samples. Young's modulus was calculated on the basis of ultrasonic measurement [11]. Vickers indentation technique was used for the hardness and fracture toughness measurements (Palmqvist's crack model and Niihara equation [12] were applied). Hardness was measured using 1.96 N loading. Palmqvist's cracks in the systems were caused applying the indent force of 49.05 N.

Wear resistance was tested according to the Dry Sand Test method. The abrasive powder (SiC of 0.4-0.5 mm grain size) was introduced between the rotating rubber wheel (of 50 mm diameter and 15 mm width) and the tested sample. The wheel load was of 44 N. The volume of the removed material resulting from the 5000 revolutions of the wheel was taken as a measure of material wear susceptibility.

For the microstructure investigations electron microscopy techniques were used. The SEM images were obtained at 20 kV accelerating voltage. Samples were previously coated with carbon film to eliminate the charging effect.

Thin foils for TEM investigations were prepared by mechanical polishing with the Gatan 656 Dimpler and final ion thinning with the Gatan DuoMill. The microstructure observations were performed with TEM Philips CM20 Twin (200 kV) equipped with Link eXL1 EDS attachment enabling chemical analyses. The local chemical composition was performed using 10 nm electron probe.

RESULTS AND DISCUSSION

X-ray diffraction shows (Fig.1) that tetragonal zirconia and (Ti,W)C are the only detected phases in all investigated material. Densities and mechanical properties of the composites and the matrix material are collected in Table I.. These data show that after heat treatment at 1400°C a sufficient (>98%) densification was achieved only in the systems with low (10 and 20%) volume of the added carbide. Fully dense composite samples reveal better mechanical properties than the zirconia matrix. They show 40% lower wear susceptibility than the TZP matrix, especially in the samples sintered at 1400°C. Composites containing 30% or more carbide additives show open porosity and have very poor wear resistance. Typical microstructures of the studied material are represented in Fig 2. The increase of the (Ti,W) carbide additive is manifested by a gradual deterioration of the structure. The bright particles embedded in the fine grain matrix correspond to the (Ti,W) carbides with an average grain size of 1 μm. However, one can observed a wide range of grain size distribution ranging from less than 1 μm and up to 5 μm. Such a distribution influences the fracture toughness of the system. The crack deflection process is a typical mechanism of fracture toughness increase in particulate composites. A crack deflection in the TZP-(Ti,W)C system occurs around smaller grains (Fig.3a), contrary to transgranular cracks observed in the case of the bigger ones (Fig.3b). The fracture toughness increase observed for dense composite bodies is about 15-20% compared to the matrix.

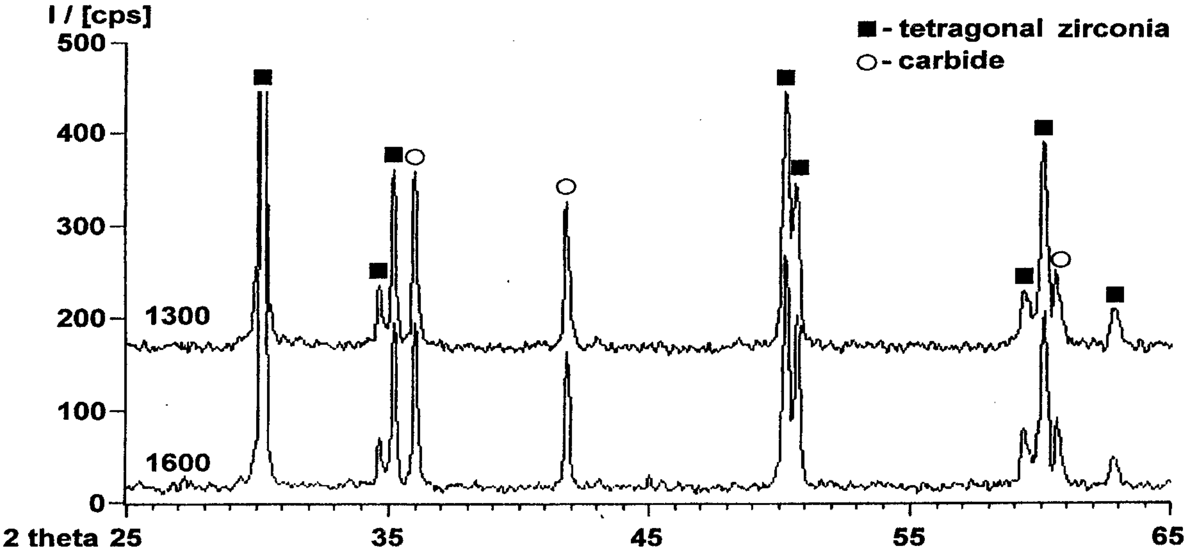

Fig.1. X-ray diffraction pattern of the composites containing 20 vol.% of carbide manufactured at 1300 and 1600°C.

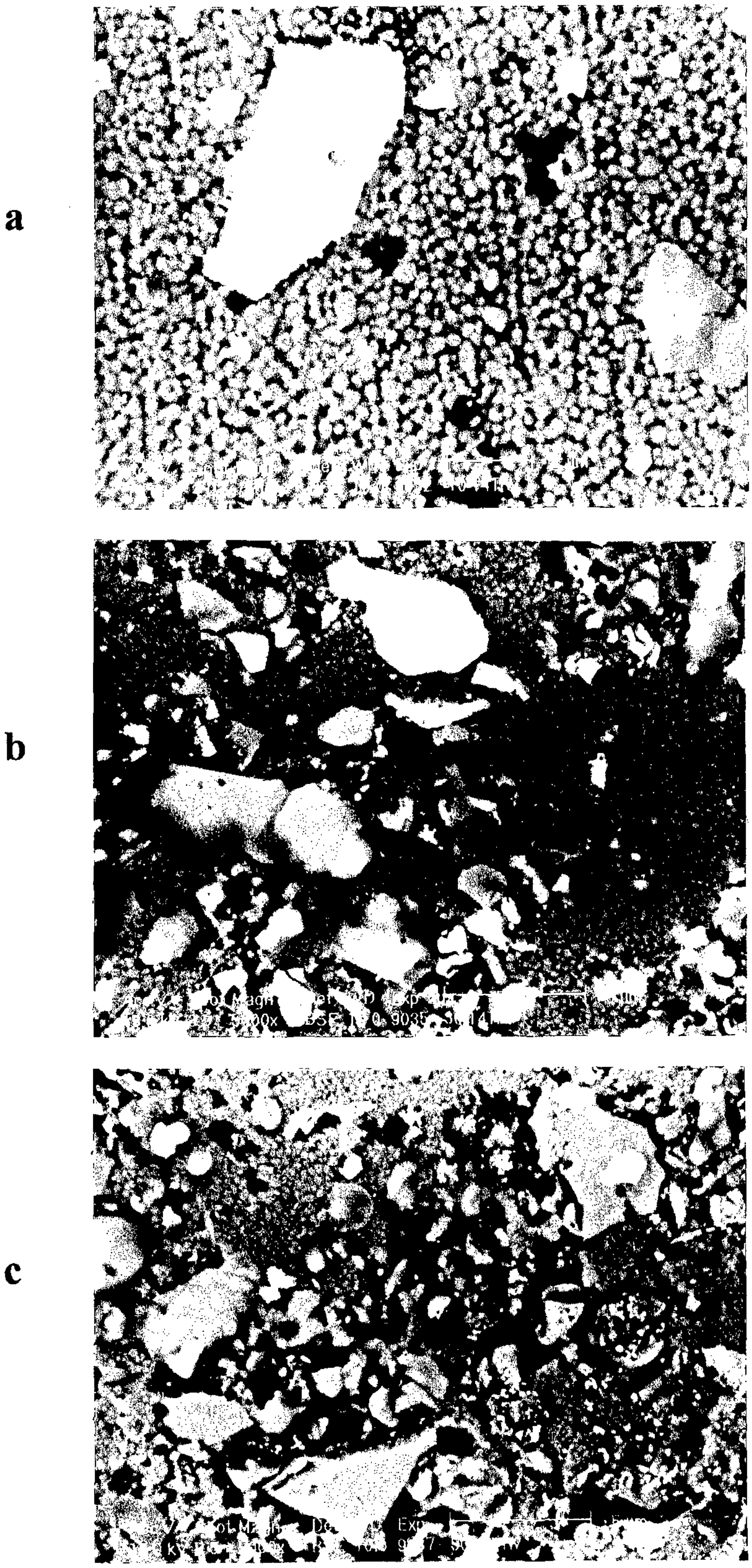

Fig.2. SEM micrographs of the TZP-(Ti,W)C composites microstructure. Samples hot-pressed at 1400°C. Carbide content: **a** - 10, **b** - 30, **c** -50 vol.%, respectively.

TABLE I.

Density, mechanical properties and wear test results.

System	HP Temp. [°C]	Bulk Density [g/cm^3] (±0.02)	Relative Density [%]	Open Porosity [%]	Young's Modulus E [GPa]	Vickers Hardness HV [GPa]	Fracture Toughness K_{Ic} [MPam$^{0.5}$]	Wear [mm^3] (±1.0)
Matrix	1300	6.05	99.2	-	206 ±4	13.0 ±0.4	4.3 ±0.1	13.2
	1400	6.06	99.3	-	210 ±3	14.2 ±0.4	4.7 ±0.1	12.5
	1500	6.07	99.5	-	206 ±6	12.8 ±0.3	5.1 ±0.4	12.9
	1600	6.08	99.7	-	209 ±8	12.8 ±0.5	4.2 ±0.1	12.9
10%(Ti,W)C	1400	6.18	99.0	-	221 ±6	13.6 ±0.5	5.0 ±0.1	7.4
20%(Ti,W)C	1300	6.21	97.3	-	214 ±14	14.0 ±0.9	5.2 ±0.2	9.9
	1400	6.27	98.3	-	236 ±13	14.7 ±1.4	6.2 ±0.9	7.4
	1500	6.34	99.4	-	235 ±20	14.8 ±0.3	5.7 ±0.3	9.6
	1600	6.37	99.8	-	250 ±21	15.6 ±1.4	6.0 ±0.6	9.2
30%(Ti,W)C	1400	6.11	93.7	2.8	224 ±24	15.7 ±1.4	5.2 ±1.0	25.1
40%(Ti,W)C	1400	6.07	91.1	6.8	222 ±15	10.0 ±1.5	5.7 ±0.7	42.1
50%(Ti,W)C	1400	5.96	87.0	12.1	200 ±16	8.9 ±0.7	4.6 ±0.4	89.0

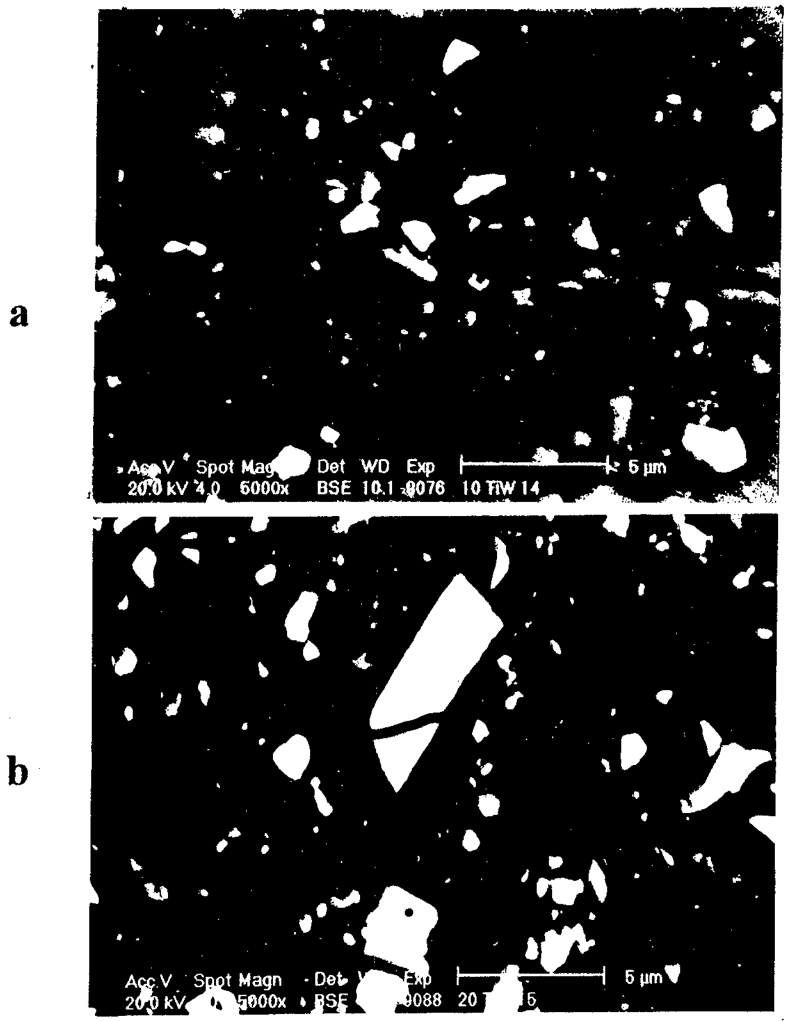
a
Acc.V Spot Mag Det WD Exp
20.0 kV 4.0 5000x BSE 10.1 0076 10 TiW 14
5 µm
b
Acc.V Spot Magn Det Exp
20.0 kV 5000x BSE 0088 20
5 µm

Fig.3. SEM micrographs of the crack path in the TZP-(Ti,W)C composite.

Figure 4 shows typical areas of the composite microstructure. Large grain of (Ti,W) carbide of 3.5 μm in diameter reveals a dislocation substructure in a strong diffraction contrast. The carbide grain is surrounded by the tetragonal zirconia crystals of a much smaller particle size (0.3-0.6 μm) showing, from grain to grain, a different diffraction contrast (Fig.4a). Though a predominant number of TZP grains has a tight contact with the carbide particles, there are, however, minor areas of worse adherence. The presence of extinction contours in the micrograph of the (Ti,W) carbide shown in the Figure 4b, indicates that the TZP grains interact with the former one by axial compression. It should be noted that the (Ti,W) carbide grains consist very often from smaller sub-grains separated by low-angle boundaries. In all observed cases the extinction contours were visible. It suggests that a deformation mechanism be involved. Most probably, these contours can be attributed to the compressive stresses which have been built up in the carbide grains due to the coefficient of thermal expansion mismatch in the system ($\alpha_{TZP}=11.0\cdot10^{-6}$ C^{-1}, $\alpha_{carbide}=8.0\cdot10^{-6}$ C^{-1}).

Observations of grain boundaries and their surroundings between zirconia and (Ti,W) carbide grains exclude the possibility of forming intermediate phases at the temperature of 1400°C.

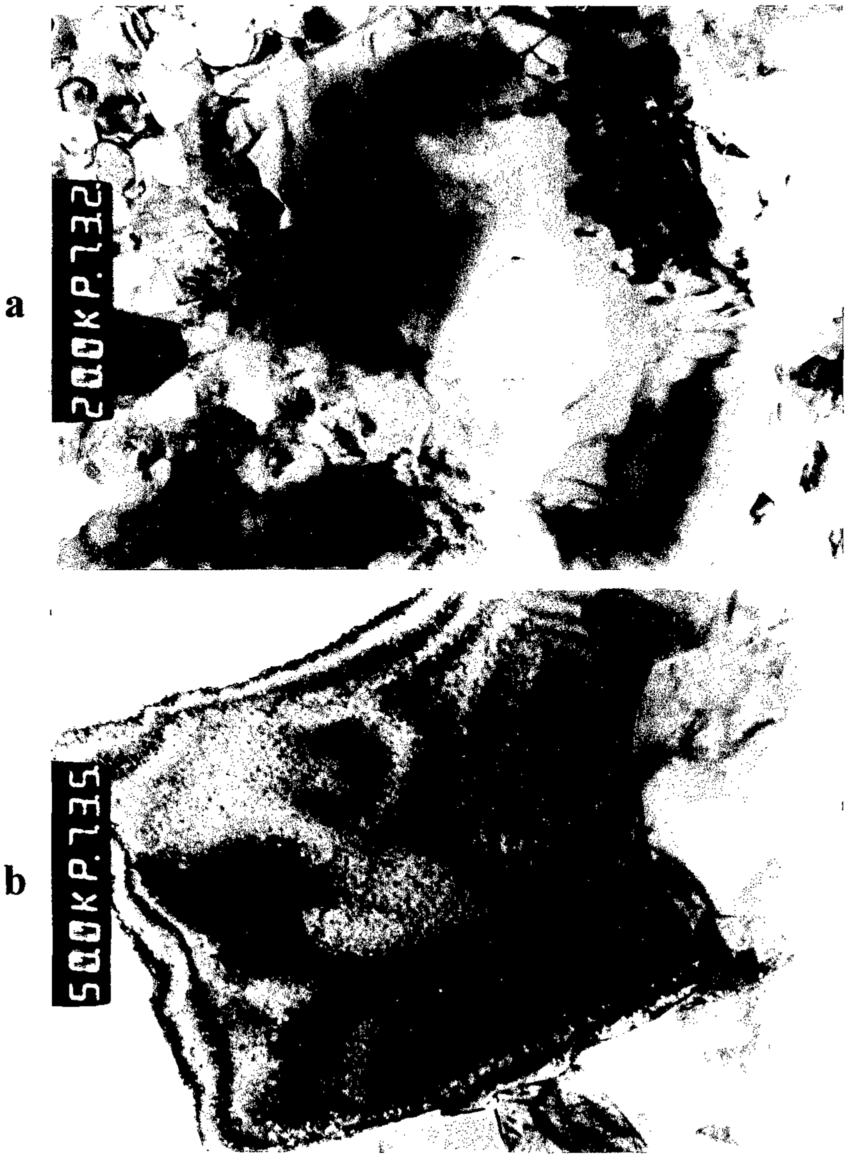

Fig.4. TEM micrographs of the composite with 20 vol.% of (Ti,W)C.

CONCLUSIONS

Hot pressing at 1400°C, which is the best temperature as far as the TZP matrix properties are concerned, allows achieving dense composite bodies in the TZP-(Ti,W)C system containing up to 20 vol.% of carbide. The increase of Young's modulus, hardness and fracture toughness for this composite is observed. Additionally, its wear susceptibility of the composite in the Dry Sand Test is significantly lower than in the case of the „pure" TZP matrix.

Microscopic investigations confirm a good adherence between zirconia and carbide phases. Stresses caused by the coefficient of thermal expansion mismatch do not evoke microcracks in the investigated system.

ACKNOWLEDGEMENT

This work was supported by the Polish State Committee for Scientific Research under grants 7 T08A 052 10 and 7 T08D 013 15.

REFERENCES

1. Haberko K., Pędzich Z., Piekarczyk J., Bućko M.M., Faryna M., in Eighth Cimtec - World Ceramics Congress Proceedings, *„Ceramics: Charting the Future", vol. 3*, Florence, Italy, 28 June - 4 July 1994, 2035-2044.
2. Haberko K., Pędzich Z., Róg G., Bućko M.M., Faryna M., *Eur. J. Solid State Inorg. Chem.*, **32** 1995, 593-601.
3. Pędzich Z., Haberko K., in *Key Engineering Materials Vols. 132-136,* Trans Tech Publications, Switzerland, 1997, 2076-79.
4. Claussen N., Weisskopf K.L., Rühle M., *J. Am. Ceram. Soc.,* **69** [3] 1986, 288-92.
5. Dingh Zh., Oberacker R., Frei H., Thümler F., *J.Europ.Ceram.Soc.,* **10** 1992, 255-261.
6. Dingh Zh., Oberacker R., Thümler F., *J.Europ.Ceram.Soc.,* **12** [5] 1993, 377-383.
7. Poorteman M., Descamps P., Cambier F., Leriche J., Thierry B., *J.Europ.Ceram.Soc.*, **12** 1993, 103-109.
8. Vleugeus J., Van der Biest O., in *Key Engineering Materials Vols. 132-136,* Trans Tech Publications, Switzerland, 1997, 2064-67.
9. Babiarz J., Haberko K., Pędzich Z., Piekarczyk J., in *Key Engineering Materials Vols. 132-136,* Trans Tech Publications, Switzerland, 1997, 2072-75.
10. Pędzich Z., Haberko K., *Ceramics International,* **20** [2] 1994, 85-89.
11. Piekarczyk J., Hennicke H.W., Pampuch R., *Ceramic Forum International /Ber. DKG,* **59** [4] 1982, 227-232.
12. Niihara K.A., *J. Mater. Sci. Lett.*, **2** 1983, 221-223.

MECHANICAL PROPERTIES AND EVALUATION OF MAGNESIUM MATRIX COMPOSITES

Quan Gaofeng[a], Song Yujiu[a], Tu Mingjing[b]
[a] School of Material Science & Engineering,
Xi'an Jiaotong University, Xi'an 710049, China
[b] Department of Metal Materials, Sichuan Union University, China

INTRODUCTION

Magnesium alloy matrix composites reinforced with both continuous fiber and discontinuous reinforcements (particulate, short fiber and whiskers) have stronger challenge in aviation and astroaviavion fields than aluminum and titanium matrix composites due to their lighter weight or specific properties [1, 2, 3]. There are some problems on material system design and preparation remained to solve for material workers in both discontinuously and continuously reinforced magnesium matrix composites. It appears that because of price and mechanical specific performance factor discontinuous reinforcements, especially particulate, are less selected to reinforce magnesium matrix composites [4, 5]. Even though continuous fiber reinforced magnesium matrix composites can obtain higher performance their price/property is not always exceeding that of discontinuously reinforced one. And the mechanical behaviors of the latter are likely to increase to higher level with relatively simple manufacture route. Silicon carbide particle is a very cheap industrial abrasive and provided with benign chemical and physical compatibility with most magnesium alloys, particularly in preparing with ordinary powder metallurgical routes. This type of composite materials also has moreover better machining characteristic [6], which is different from continuous fiber composites. Abachi et al studied fracture toughness of particulate reinforced magnesium composites [7], and they found that the fracture toughness decreases with the increase in SiC particle content, and the shapes of the ceramic particle show some effect on the fracture toughness. e. g., sharp irregular SiC particles reduce the fracture toughness of composites more than that of the blocky type. According to the investigation on ceramic particle size SiC particulate reinforced aluminum composites has effect on the mechanical performances of the composites, with the same preparing route the thinner the particle the higher the strength properties for the same content of composites as the particles are well-distributed. With powder metallurgical route there is a problem that the size match between ceramic particles and metal powders. If this ratio of both particle sizes is too large or small, the homogeneity of the ceramic particle distribution in composite must be poor so that the properties of the materials may be poor, too. In this paper the composite design, i. e., thickness of reinforcement and matrix materials, is discussed in the light of mechanical behaviors to provide some interaction of raw materials, preparation route and properties of ceramic particles reinforced magnesium composites.

EXPERIMENTATION AND RESULTS

Materials and Experimental Procedure

Silicon carbide particulate is used to act as the reinforcement of magnesium alloy MB15 (Mg-5Zn-0.6Zr). The composites were fabricated by P/M method. The silicon carbide particulate is industrial abrasives with two normal sizes of 5 and 20μm. The shape of the particles is angular. The volume fractions of ceramic particles are 10 and 20%. The matrix alloy is prepared with element mixture method. These metal powder's dimension is 250~200 mesh (50~74μm in diameter). The metal powder and ceramic particles are mixed in a nylon cylindrical tube at 24rpm for 4~6hours. After cold compacting of mixture in a vacuum mold the blanks then are heat-pressed and extruded into cylindrical sample with a diameter of ϕ16mm. After machining the T6 treatment is carried out on the specimens. The dimensions of the specimens are ϕ6×30mm, following grinding for precise dimension. The tensile test is conducted on

INSTRON1195 Universal Material Test System according to Chinese National Standard GB228-76. The displacement-load curves are recorded automatically and the proof stress, engineering proportional limits and elastic moduli of tested materials are measured and calculated in the light of the standard illustration. The microstructure of the extruded samples is analyzed on a microscope modeled Neophont21 and a scanning electronic microscope (SEM) modeled S-2700. The electron diffraction of thin-crystal analysis is conducted on JEM-200CX transmission electronic microscope.

Microstructure analysis

In Figs. 1 the micrographs show the microstructures of the composites in longitudinal sections. It is easy to find that the distribution of the ceramic particles for 5μm, 10% SiC_p is more homogeneous than that of 5μm, 20% SiC_p. In the latter ceramic particles in some zones are clustering heavily (Fig. 1 a, b), and more severely in very few zones there exists non-infiltrating cases. That inhomogeneous distribution has strong effect on the mechanical properties of the materials (see next section). This result is induced principally by the unappropriate size match of the metal powders and ceramic particles during blending the raw materials. i. e., the particle size ratio d_{Mg}/d_{SiCp} is as high as 12~15, when hot pressing the mixture the ceramic particles thoroughly surround the metal particle, and after extrusion the ceramic particle are striated and not well spread in metal matrix. As an alternative measure the coarser ceramic particles, normal diameter of 20μm, are taken. The ratio d_{Mg}/d_{SiCp} is decreased to about 3.5, thus the distribution of the reinforcing particles is on the whole going to more homogeneous (Fig.1 c, d). It is found that near interfaces there are some zigzag marks of chemical reaction (Fig. 2 a), at least in part of interfaces. The small amount of long-winded amorphous products near the interface may be formed at high fabricating temperature. Magnesium and the oxidized layer SiO2 outside the silicon carbide particles react at this temperature as following:

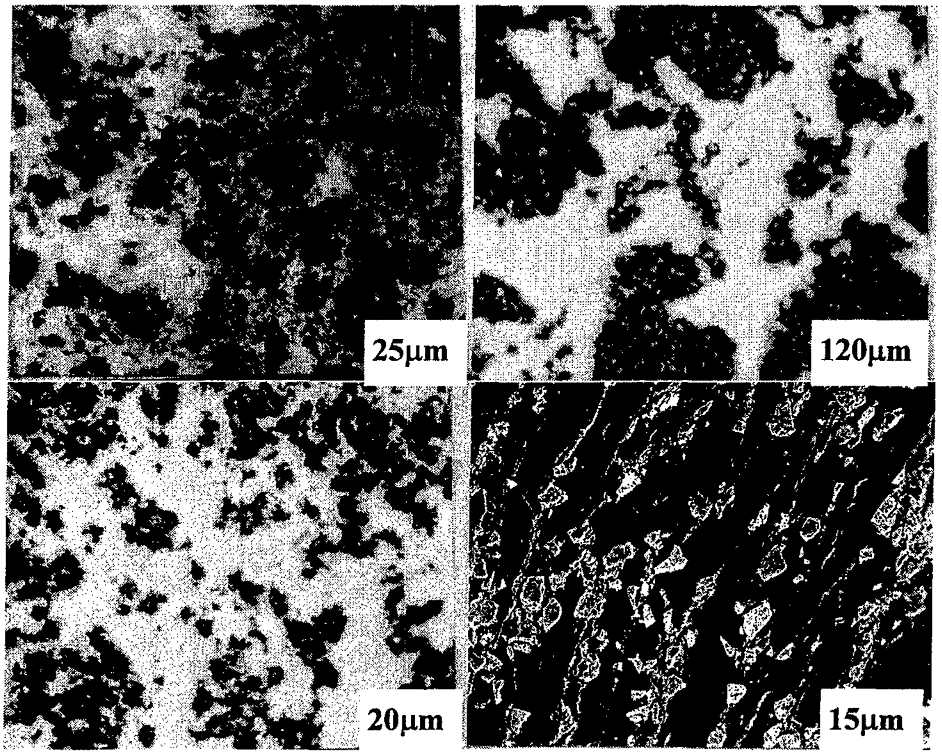

Fig. 1 Micrographs of the SiC_p/Mg composites

a) 10%, 5μm SiC_p, b) 20%, 5μm SiC_p, c) 20%, 10μm SiC_p, d) as the same to c)

$$2MgO + SiC \xleftrightarrow{H \cdot T} Mg_2Si + CO_2 \qquad (1)$$

$$4Mg + SiO_2 \xleftrightarrow{H \cdot T} 2MgO + Mg_2Si \qquad (2)$$

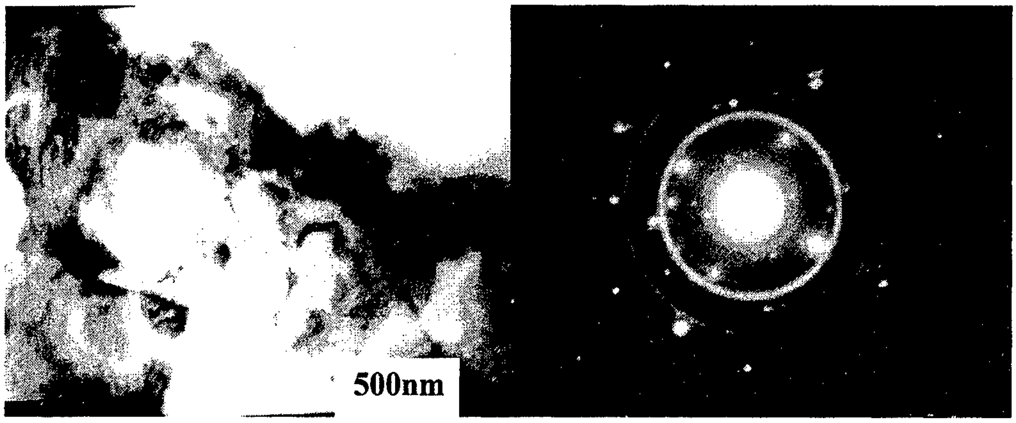

Fig. 2 Micrographs of TEM analysis

a) Micromorphology at interface (up-right) b)Electron diffration pattern

The reacted product MgO and Mg2Si are composed into compound, which is crystalline or amorphous state (the diffraction pattern is some unclear circle). In about 10 observed zones most interfaces are straight one and not found gradient evidence. Near minority interfaces there are small amount of lump products which is considered to be inclusion in the matrix alloy. The aging precipitates are needle-like and located in two orientations crossed about 90 degrees (Fig. 2 b). These precipitates near the interfaces are smaller than that far away to interfaces. And on some grainboundary there are also lump products which may be the undissolved metallic compound during heat treatment. It is seen that spherical aggregative particles are at few grainboundaries, which are considered to be magnesium oxide formed in sintering process. These oxides may be the main ringleader of low ductility for the composites.

MECHANICAL PROPERTIES AND ANALYSIS

Table 1 shows the mechanical properties measured of the materials. As a contrast the same data for aluminum matrix composites also cited in it. It is obvious that the reinforced materials have higher strength and modulus, especially greatly enhanced elastic deformation resistance， but lower ductility. In this table one also can find that this test obtained higher strength than that summarized in literature for the same materials [8]. According to the comparison of specific strength and absolute weight between magnesium and aluminum alloy matrix composites the former shows a little better application expectation.

Table 1. Comparison of Mechanical properties of magnesium and aluminum matrix composites

Materials	**Proportion limit** σ_p /MPa	**Proof strength** $\sigma_{0.2}$ /MPa	**Ultimate strength** σ_b /MPa	**Ductility** δ /%	**Modulus** E /GPa	**Density** ρ /g/cm	**Specific strength** σ_b/ρ $\times 10^3$m
MB15(Magnesium alloy)		250.0	320.0	6.0	45.0	1.76	18.55
10SiC$_p$(5μm)-MB15	266.0	336.3	366.7	1.53	67.0	1.904	19.65
20SiC$_p$(5μm)-MB15	271.5	339.0	386.5	<0.5	78.1	2.05	19.24
20SiC$_p$(20μm)-MB15	274.3	360.3	429.5	0.93	79.5	2.05	21.38

LY12(aluminum alloy)	196.0	285.0	450.0	12.0	70.0	2.76	16.64
20SiC$_p$(5μm)-LY12	318	426	598	2.5	112	2.89	21.11

The increase in ultimate strength of reinforced materials relies on the improvement of ceramic particle distribution and interfacial bonding state of them. At the same ceramic particle content the strength and ductility for 20μm composite is better than that for 5μm composite. In the latter the conglomerations of SiC particles is easy to look and this leads strain/stress concentration within the conglomerations and results in "hard zone" and "soft zone", both intensify the unhomogeneity in the composites. These unhomogeneous zones are the origin of fracture in them, cracks will nucleate at relative small strain level. According to the authors' opinion, the mechanics restrain effect within the particle densely distributed zones is higher than that of particle scarcely zones [9]. The increase with ceramic particle content in elastic modulus is apparent, too.

FRACTOGRAPGY

The observations of fracture surface appearance and sectional surface of the fractured tensile specimen are carried out on SEM. It is seen that although the appearances in matrix area all are ductile microscopically, the fractures show some brittle characteristic macroscopically exception to controlled alloy. The events of particle crack and interface failure both observed and the former is less happening. On the sectional surfaces (near fractured end) there are a few events of particle fracture and the breakdown may initiate in interfaces—debonding. This fact implies that the interfaces between ceramic particles and the matrix are far complete and the mechanical properties of the materials may increase further if more appropriate fabricating routes are adopted.

CONCLUSIONS

1. PM method may be good routine to fabricate magnesium alloy matrix composites with good properties. In this test the specific strength 20%, 10μm SiCp/Mg even exceed that of aluminum alloy matrix composite.
2. The limited data from the present test for magnesium matrix composites illustrate that the mechanical properties and the microstructure will be improved when the size ratio of metal powder and ceramic particle is small till to unity by PM route.
3. It is found from TEM analysis that there may exist marks of interfacial chemical reaction, and this reaction as well as lower ductility of the materials may be induced by exorbitant temperature during hot pressing.

ACKNOWLEDGEMENT

4. This work is carried out with kind help of Ms. HUANG Yinjue and Mr. LI Hao. The Science Foundation Committee of Xi'an Jiaotong University provided financial support.

REFERENCES

[1] O. Oettinger, W. Schaff, C. Hausmmann, T. Heyne and R. F. Singer, Mechanical properties of woven fabric carbon/magnesium-composites, Proc. ICCM-11, V2:804, Gold Coast, Australia, July 1997
[2] B. Sommer, K. U. Kainer, and H. Berek, Influence of the interface on the creep properties of carbon fibre reinforced magnesium alloy AS41, ibid, V3:221

[3] Suk-Won Lim, T. Imai, Y. Nishida and D. Jiang, Superplasticity of ceramic particulate reinforced magnesium alloy composites fabricated by a melt stirring method, ibid, V.3:486-494

[4] J. P. Lucas and J. K. Park, Assessment of microfracture mechanisms in Al2O3/6061 Al and SiC/6061 Al discontinuous reinforced composites, ibid, V3:337-347

[5] V. Laurent, P. Jarry, G. Regazzoni and D. Apelian, "Processing-Microstructure Relationships in Compocast Magnesium/SiC", J. Mater. Sci., Vol.27, No.16, 1992, pp.4447-4459

[6] K. Weinert, D. Biermann and M. Liedschulte , Machining of reinforced aluminum and magnesium, In: Proc. of ICCM-11, V3:205-214, Gold Coast, Australia, July 1997

[7] P. Abachi, B. L. Mordike and K. U. Kainer, Improving of the fracture toughness of mg-alloy composites produced by powder metallurgical technique, ibid, V2:424-430

[8] Cai Ye, Su Huaqin, Review and expectation of study on magnesium matrix composites, Special Foundry & Non-ferrous Metals (in Chinese), 1996, 3:17

[9] Quan Gaofeng, Chai Donglang, Song Yujiu and Tu Mingjing, Studies on the strengthening mechanisms of DRMMCs, Proc. ICCM-10, Ed. S.W.Tsai, Whistler, Vancouver, Canada, July, 1995, II. 521-525

INTERFACIAL STRESS AND STRENGTH ANALYSIS OF METAL MATRIX COMPOSITES IN THERMAL SHOCK PROCESS

Dong-Ying Ju

Department of Mechanical Engineering, Saitama Institute of Technology,
Fusaiji 1690, Okabe Saitama 369-02, Japan

INTRODUCTION

The metal matrix composites often be used in some harsh environments and working processes, for example, high temperature and high pressure, as well as thermal shock and so on. In these environment, it is important to predict themo-mechanical behavior and interfacial stress of the metal matrix composites. Because the rapid variation of temperature under a thermal shock process will tend to bring out phase transformation or microstructure change of the material, some complicated coupling effects of material behavior should be considered. On the other hand, the material strength effected by the jump behavior of stress and deformation on the interface boundary between the fiber and matrix should to be studied, especially.

Recently, the developments based on Metallo-thermo-mechanical theory[1-2] and some numerical method[3-4] are applied to simulate residual stresses of the metal matrix composites and to predict or control the physical and chemical properties at the fiber-matrix interface during quenching process[5]. If we see the thermal shock process to be similar a quenching process, as the development of above analysis above, it also can be to use to the thermal shock problem of composites which considered interaction of temperature, microstructure and the stress/strain fields. In this paper, the rapid variation of temperature in short time as thermal shock are loaded on the metal matrix composites with a short fiber. As an example of calculation, simulation of the thermal shock process associated with a Ti-Fe alloy reinforced unidrectionally by SiC fiber is engaged in this research. In results of this simulation, thermo-mechanical behavior and the residual stresses of the composites is evaluated, and the strength of the composites after the thermal shock are also predicted.

GOVERNING EQUATIONS

The detail of introducing the governing equations in the framework of thermodynamics capable of describing the governing equations for temperature and stress/strain fields incorporating metallic structures are already reported elsewhere[4-5]. Here, the fundamental equations are summarized in the following:

Heat Conduction Equations

The transient temperature field $T(x_i, t)$ at time t is governed by the equation:

$$\rho c\dot{T} - \frac{\partial}{\partial x_i}(k\frac{\partial T}{\partial x_i}) - \sigma_{ij}\dot{\varepsilon}^{p}{}_{ij} + \sum \rho_I l_I \dot{\xi}_I = 0 \ , \qquad (1)$$

where x_i is the coordination system of the body, k and l_I denote the coefficient of heat conduction and the latent heat produced by the progressive of volume fraction ξ_I as I-th phase transformation. $\sigma_{ij}\dot{\varepsilon}_{ij}$ is stress power associated with heat generation. Here, ρ and c are the density and the specific heat, respectively. And an assumption is made that a material parameters χ is described by the mixture law[6]

$$\chi = \sum_{I=1}^{N} \chi_I \xi_I ; \quad and \quad \sum_{I=1}^{N} \xi_I = 1, \qquad (2)$$

where χ_I denote the material parameter for the I-th phase.

The boundary conditions of heat transfer on the inner surface is assumed to be

$$-k\frac{\partial T}{\partial x_i}n_i = h(T - T_w) \ , \qquad (4)$$

where h and T_w are the heat transfer coefficient and the temperature of coolant on heat transfer boundary with unit normal n_I, respectively.

Constitutive Equation

Total strain rate $\dot{\varepsilon}_{ij}$ is assumed to be divided into elastic, plastic, thermal strain rates and those by structural dilatation due to phase transformation and creep such that

$$\dot{\varepsilon}_{ij} = \dot{\varepsilon}^{e}_{ij} + \dot{\varepsilon}^{p}_{ij} + \dot{\varepsilon}^{T}_{ij} + \dot{\varepsilon}^{m}_{ij} + \dot{\varepsilon}^{c}_{ij} \quad . \qquad (5)$$

Here, elastic and thermal strains are normally expressed as

$$\varepsilon^{e}_{ij} = \frac{1+\nu}{E}\sigma_{ij} - \frac{\nu}{E}\sigma_{kk}\delta_{ij} , \qquad (6)$$

and

$$\varepsilon^{T}_{ij} = \alpha(T - T_0)\delta_{ij} \ , \qquad (7)$$

with Young's modulus E, Poisson's ratio ν and thermal expansion coefficient α, respectively. Here, T_0 is the initial temperature of material.

Strain rates due to structural dilatation and transformation plasticity depending on the I-th constituent read

$$\varepsilon^{m}_{ij} = \sum_{I=1}^{N} \beta_I \xi_I \delta_{ij} \quad , \qquad (8)$$

where β stands for the dilatation due to structural change.

The plastic strain rate is reduced to the form when employing temperature dependent materials parameters

$$\dot{\varepsilon}^{p}_{ij} = \lambda\frac{\partial F}{\partial \sigma_{ij}} = \hat{G}(\frac{\partial F}{\partial \sigma_{kl}}\dot{\sigma}_{kl} + \frac{\partial F}{\partial T}\dot{T} + \sum_{I=1}^{N}\frac{\partial F}{\partial \xi_I}\dot{\xi}_I)\frac{\partial F}{\partial \sigma_{ij}} \ , \qquad (9)$$

with a temperature dependent yield function

$$F = F(\sigma_{ij}, \varepsilon^{p}, \kappa, T, \xi_I) \ , \qquad (10)$$

with hardening parameter κ, where

$$\frac{1}{\hat{G}} = -(\frac{\partial F}{\partial \varepsilon^{p}_{mn}} + \frac{\partial F}{\partial \kappa}\sigma_{mn})\frac{\partial F}{\partial \sigma_{mn}} \ , \tag{11}$$

Here, $\bar{\sigma}$ and $\bar{\varepsilon}$ are the equivalent stress and strain, respectively. Either isotropic or kinetic hardening type of yield function F is available to be used in the paper. Either isotropic or kinetic hardening type of yield function F is available to be used in this paper.

Kinetics of Quenching Process

The type of phase transformation during the heating and cooling is controlled by diffusion mechanism, and the volume fraction of developing phase such as pearlite may be expressed by modifying the Johnson-Mehl relation[11] as

$$\xi_p = 1 - \exp(-V_e) \ , \tag{12}$$

where V_e is defined by

$$V_e = \int_0^t \bar{f}(T,\sigma_{ij})(t-\tau)^3 d\tau \tag{13}$$

Here, we separate the function $\bar{f}(T,\sigma_{ij})$ into two independent function of temperature and stress as

$$\bar{f}(T,\sigma_{ij}) = f_1(T) f_2(\sigma_{ij}) \ . \tag{14}$$

Since the time-temperature-transformation *TTT* diagram under the applied stress σ_{ij} in logarithmic scale deviates from the one without stress which is represented by the function *f(T)*, the kinetic equation of diffusion type is often applied to the variations of pearlite or ferrite structure in quenching processes. An identification of the function *f(T)* can be made possible by the use of some experimental data of the structure change.

EVALUATION OF INTERFACIAL STRENGTH

Due to difference of materials behavior between the fiber and matrix composites, discontinuous phenomenon of thermo-mechanical fields on the interface of MMC materials during the thermal shock process will be presented. However, in order to describe the strength on the interface, real composite material are usually made up a gain-boundary sliding will occur during jump of deformation, especially at high temperature, which causes the development of local stress concentration[9].

Here, modification of the yield stress on the interface can be realized through Prager' s kinematic hardening law in following,

$$\sigma_y = \sigma_{y0}[1 - A\,exp(-C\bar{\varepsilon}^{p})] \ , \tag{15}$$

where A and C are parameters of the composites dependent on the plastic strain of interface. σ_{y0} and $^{-}{}_{p}$ denote the static yield stress and equivalent plastic strain. The advantage of equivalent of stress on the interface can be used to evaluate strength of the composite material.

SIMULATED RESULTS

Model of Simulation

The material for simulation of the thermal shock process was a metal matrix composite reinforced unidirection with short continuous fibers. The matrix material was a Ti-Fe alloy (β type) consisting of Ti-3.25Fe-2Cr-2Mo in weight percent. The reinforcing phase was continuous SiC fiber. The diameter of fibers is 100μm. It is assumed that the fiber is located periodically with the same interval and that each fiber is the same shape as shown in Fig.1(a). Then, the unit cell including a fiber depicted by broken line in Fig.1(a) is extracted from the bulk material. For the reason of simplification, a unit cell is considered as an axisymmertrical problem which is shown in Fig.1(b). The thermal shock process is loaded on the surface BC and CD which is shown in Fig.2. As for the finite element calculation of temperature and stress fields based on the obtained mixture rule of the phase transformations, the following material table are employed:

Table 1 Parameters for finite element analysis

	Matrix	Fiber
Heat conductivity [cal/mm · deg]	0.0216+0.0513T	0.0203+0.0498T
Density [g/mm]	7.9	8.1
Specific heat [cal/(g · deg)]	0.086	0.079
Young' s modulus [Gpa]	$220.0+0.054T-0.00032T^2$	$350.4+0.039T-0.00028T^2$
Poisson' s ratio	0.32	0.26
Thermalexpansion [1/deg]	0.218×10^{-5}	0.18×10^{-5}
Dilatation of phase transformation [%]	$\beta_M=-0.015$; $\beta_P=-0.011$	~
Yield stress [Mpa]	$526.5-0.12T-0.00045T^2$	$780.0-0.16T-0.00049T^2$
Hardening coefficient [Mpa]	238.2-0.225T	361.5-0.29T

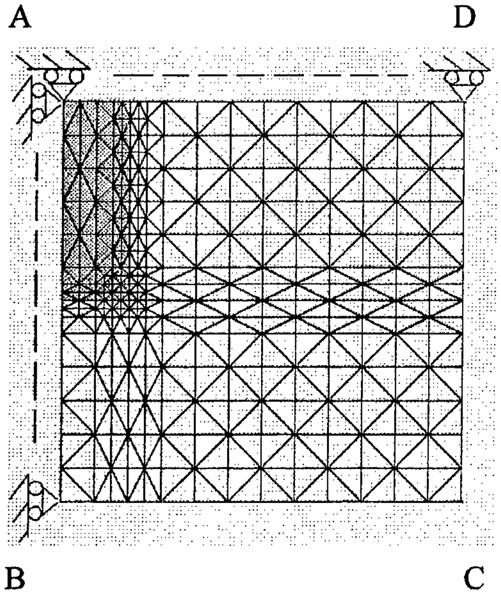

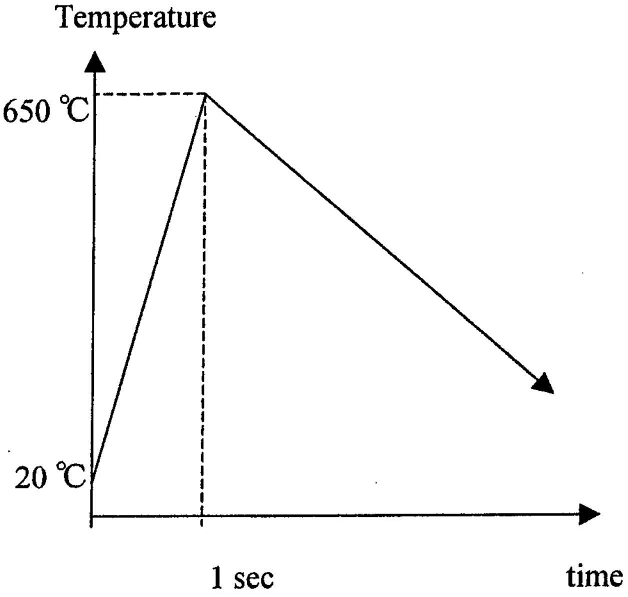

Fig. 1 Cross section of metal matrix on composite and unit cell model.

Fig.2 Thermal shock process loaded metal matrix composites

Results of Simulation

Figure 3 shows the variation of temperature distribution on the center of the fiber and the surface of the matrix corner. The volume fraction of the austenite and pearlite transformation at t=3.5(sec) in Fig.4. The residual stresses on the section AD shown in Fig.5. Figure 6 shows distribution of the residual equivalent stress in the model. From these results, we can observe that the temperature variation of composites of these two size ratio are nearly similar, but the distribution of pearlite transformation near the interface has different form. When pearlite transformation produced on the, i.e. t=3.5(sec), distribution of the equivalent stress which is shown in Fig.6 exhibits jump phenomenon. The jump of equivalent stress is remained until to finish of the thermal shock process.

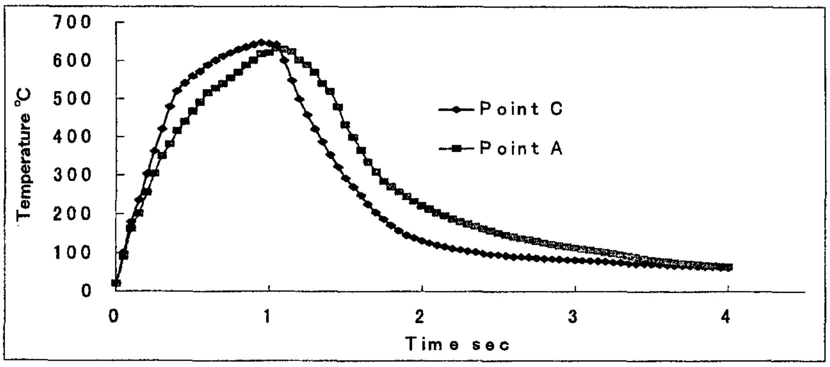

Fig.3 Temperature variation on point A of fiber and point C of matrix corner.

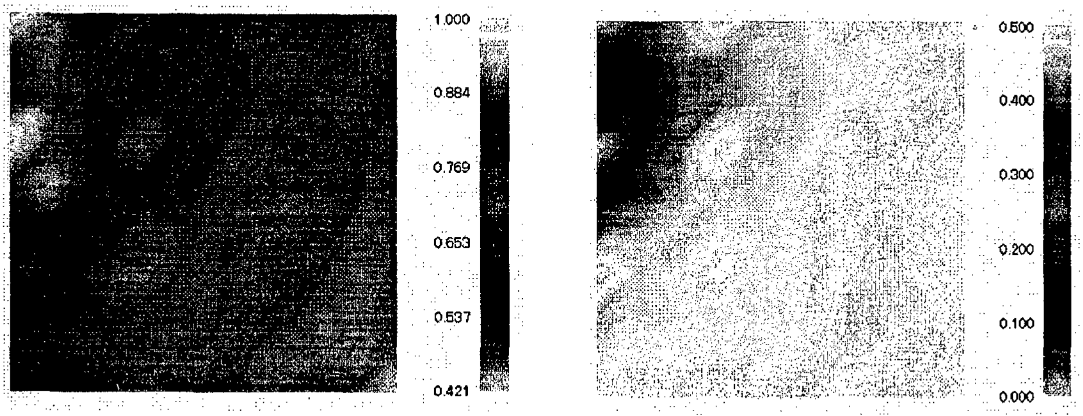

(a) Austenite (b) Pearlite

Fig.4 Distribution of austenite and pearlite transformation at t=3.5(sec).

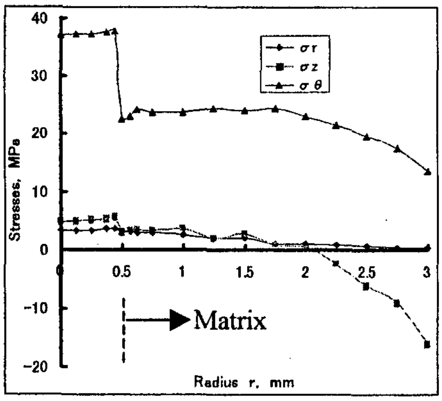

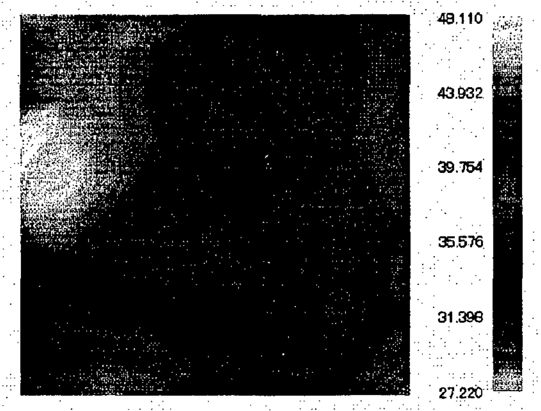

Fig.5 Distribution of stresses on section AD. Fig.6 Distribution of equivalent stress .

CONCLUDINGS

Metallo-thermo-mechanical theory previously developed is extended to simulated the interfacial stress and residual stress of MMC after a thermal shock process. By adopting this theory, finite element simulation of a unit cell of metal matrix composites is carried out, and some results of the calculated distribution of temperature and residual stress are discussed. From these results, we can obtain some useful conclusions:

(1) The simulated results of temperature and residual stresses based on the coupled analysis here describe the significant phenomena during phase transformation due to the thermal shock. Interfacial stress of MMC can be evaluated within an inhomogeneous structure.

(2) In this connection the rapid variation of temperature due to thermal shock are of great importance to predict the damage or fracture on the interface. The calculated interfacial stress can be used to evaluate the strength of the metal matrix composites, and to optimize the structure of the material.

REFERENCE

[1] Inoue, T. and Raniecki, B., "Determination of Thermal-hardening Stress in Steels by Use of Thermoplasticity", Journal of Mech. Phys. Solids, Vol.26, pp.87-212 (1978).

[2] Denis, S., Simon, A. and Beck, G., "Estimation of the Effect of Stress/Phase Transformation Interaction when Calculation Internal Stress During Martensitic Quenching of Steel", Trans. ISIJ, 22, pp.504-513(1982).

[3] Inoue, T., "Inelastic Constitutive Relationships and Applications to Some Thermo-mechanical Process Invoving Phase Transformations", Thermal Stresses, 3, (R.B. Hetnarski, ed.), Elsevier Science Publishers, B.V., pp.192-278(1989).

[4] Inoue, T., Ju, D.Y. and Arimoto, K. "Metallo-Thermo-Mechanical Simulation of Quenching Process --- Theory and Implementation of Computer Code Hearts", Proceeding of 1st International Conference on Quenching and Distortion Control, Chicago, September, pp.205-212(1992).

[5] D.Y. JU, "Simulation of Thermo-mechanical Behavior During Quenching Process of Metal Matrix Composites", Proc. of International Conference on Composite Materials, Gold Coast, Queensland Australia, July 14-18, Vol.1, pp.797-805(1997)

[6] Bowen, R.M., "Continuum Physics", Vol.3, (A.C. Eringen ed.), Academic Press, New York, pp.2-129(1976).

[7] Johnson, W.A. and Mehl, R.F., "Reaction Kinetics in Processes of Nucleation and Growth", Trans. AIME, 135, pp.416-458(1939).

[8] Chawla, K.K., Metal Matrix Composites, Materials Science and Technology, (Chahn, R.W. Haasen, P. and Kramer, E.J. eds.), Volume 13, pp.122-179(1991).

[9] Lim L.G. and Dunne E.P.E., "Modelling Void Nucleation and Growth Processes in a Particle-reinforced Metal Matrix Composite Material", J. of Computational Materials Science, 5, pp.177-186(1996).

INTERNAL STRESSES IN METAL MATRIX COMPOSITES REINFORCED BY PARTICLES

R Paskaramoorthy
Centre for Reinforced Plastics/Composites Facility
School of Mechanical Engineering
University of the Witwatersrand
South Africa

E-mail: moorthy@hertz.mech.wits.ac.za

ABSTRACT

In the design of advanced composite materials containing particulates, one important problem is the magnitude of the stress concentration in the matrix around the reinforcing elements. In this theoretical study, the steady-state stresses resulting from a dynamic loading in a particulate reinforced metal matrix composite are determined, and the stress concentration factors at the interface between the particle and the matrix are obtained in an effort to determine the parameters governing the dynamic response. Numerical results indicate that the dynamic stress concentrations are dependent on the frequency of excitation and elastic properties of the composite and, they can be larger than those encountered under static loading. It is also found that the dynamic stress concentration is significantly influenced by the interphase layer between the particle and the matrix. The results can be used to determine an optimal interphase to reduce the dynamic stress concentration.

INTRODUCTION

Particulate reinforced metal matrix composites (PRMMCs) are becoming important structural materials in the aerospace and automobile industries because of their high strength, excellent wear resistance and retention of strength at elevated temperatures. In spite of these desirable properties, the applications of PRMMCs and other forms of composites are generally limited by their poor fracture and fatigue properties.

Many experimental and theoretical studies have been conducted in order to gain a fundamental understanding of the influence of various parameters on the fracture and fatigue strength of PRMMCs. One important finding is the presence of microcracks at the ends of reinforcements. These microcracks eventually link up to form macrocracks [1]. The predominant factor that would aid in the formation of microcracks is stress concentration in the matrix around the reinforcements. The degree of this stress concentration depends on the shape, size and elastic modulus of the reinforcements.

The internal stresses in PRMMCs under static loads have been addressed in references [2,3,4]. Bogan and Hinders [5] considered dynamic loads and presented results for continuously reinforced fiber composites by using a two dimensional model. In three dimensions, the dynamic stress fields around rigid spherical inclusions have been determined [6]. When the inclusion is elastic, no numerical results for the dynamic stress field are, however, available even though some related problems have been studied by a number of investigators [6,7,8].

In this paper, the steady-state stresses resulting from a dynamic loading in a particulate reinforced metal matrix composite are determined, and the stress concentration factors in the matrix are obtained. The formulation includes interface layers between the fiber and matrix. The interface layers exist as a natural consequence of material processing or may be intentionally introduced to reduce the stress concentration and improve mechanical properties of the composite. For simplicity, the effect of interaction of neighboring particles are ignored. Therefore, the results are valid for low volume fraction of particles. Numerical results for a range of frequencies and material properties are presented. Due to lack of space, results showing the influence of interface layers could not be included here. Briefly, the dynamic stress concentrations are found to be dependent on the frequency of excitation and elastic properties of the composite and, they can be larger than those encountered under static loading.

BASIC EQUATIONS

The three dimensional model studied in this work is shown in Figure 1. The particulate reinforcement is represented by a solid spherical particle of radius a_0 and the interface layers are represented by concentric spheres. Owing to the geometry, the problem is best described by spherical coordinates (r, θ, ϕ). The particle, interface layers and matrix are assumed to be linearly elastic and isotropic, and the contact between them is assumed to be welded. The elastic property of each medium is given by Lamé constants λ_i and μ_i and the density is denoted by ρ_i.

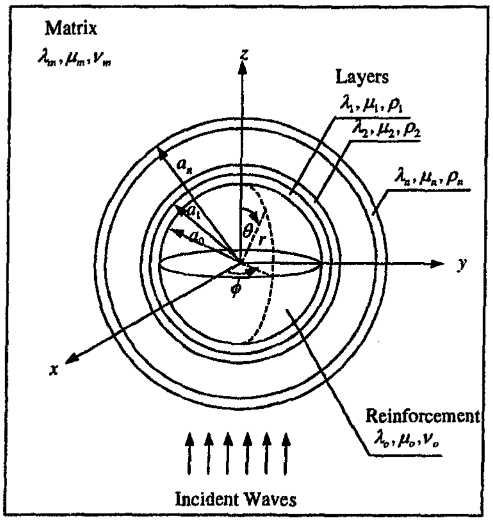
Matrix
λ_m, μ_m, ν_m
z
Layers
λ_1, μ_1, ρ_1
λ_2, μ_2, ρ_2
λ_n, μ_n, ρ_n
a_n
a_1
a_0
θ
r
ϕ
y
x
Reinforcement
λ_o, μ_o, ν_o
Incident Waves

Figure 1: Schematic of the problem

The dynamic excitation is provided by an incident plane compressional wave propagating in the positive direction of the z-axis. The problem is thus symmetric about the z axis and field quantities such as displacements and stresses are independent of the spherical coordinate ϕ.

The time variation is assumed to be of the form $e^{i\omega t}$, where ω is the circular frequency of excitation. Thus, all field quantities have the same time variation which is suppressed in all subsequent representations for notational convenience.

For each domain of the model the displacement vector, $\mathbf{U} = (U_r, U_\theta, U_\phi)$, satisfies Navier's equation of motion of dynamic elasticity with zero body forces:

$$(\lambda_i + 2\mu_i)\nabla(\nabla \cdot \mathbf{U}) - \mu_i \nabla \times \nabla \times \mathbf{U} + \rho_i \omega^2 \mathbf{U} = 0 \tag{1}$$

Following Helmholtz's decomposition of a vector field, the general solution of equation (1) can be written, taking symmetry into consideration, as

$$\mathbf{U} = \nabla\psi + \nabla \times \nabla \times (\mathbf{e}_r\, r\chi) \tag{2}$$

where $\mathbf{e}_r$ is a unit vector in the radial direction, and the potentials ψ and χ satisfy

$$(\nabla^2 + \alpha_i^2)\psi = 0 \tag{3}$$

$$(\nabla^2 + \beta_i^2)\chi = 0 \tag{4}$$

In the above, α_i and β_i are the compressional and equivoluminal wave numbers, respectively. They are defined by

$$\alpha_i^2 = \frac{\omega^2 \rho_i}{(\lambda_i + 2\mu_i)} \quad ; \quad \beta_i^2 = \frac{\omega^2 \rho_i}{\mu_i}. \tag{5}$$

INCIDENT, SCATTERED AND REFRACTED WAVE FIELDS

In the matrix, the wave field consists of incident and scattered waves. Let the incident plane compressional wave travelling in the positive z direction be represented by two potentials

$$\psi = e^{i(\alpha_2 z - \omega t)} \quad ; \quad \chi^i = 0 \tag{6}$$

In anticipation of writing the boundary conditions in spherical coordinates, the incident potential is expanded in terms of the spherical eigenfunctions as

$$\psi = \sum_{n=0}^{\infty} (2n+1) i^n j_n(\alpha_2 r) P_n(\cos\theta) \tag{7}$$

where j_n is the spherical Bessel function of the first kind and P_n is the Legendre polynomial.

Expressions for the scattered wave field in the matrix can be obtained from the solutions of the wave equations (3) and (4). In writing the expressions for the scattered field, only the waves propagating outward from the particle need to be considered. Thus the scattered waves are given by

$$\psi = \sum_{n=0}^{\infty} A_{1n} h_n(\alpha_2 r) P_n(\cos\theta) \tag{8}$$

$$\chi = \sum_{n=0}^{\infty} A_{2n} h_n(\beta_2 r) P_n(\cos\theta) \tag{9}$$

where h_n is the spherical Hankel function of the first kind. The total field in the matrix is obtained by the superposition of incident and scattered fields.

The wave field in the particulate reinforcement, being confined to a spherical volume, are standing waves. They can be represented by

$$\psi = \sum_{n=0}^{\infty} B_{1n} j_n(\alpha_1 r) P_n(\cos\theta) \tag{10}$$

$$\chi = \sum_{n=0}^{\infty} B_{2n} j_n(\beta_1 r) P_n(\cos\theta) \tag{11}$$

The wave field in the i-th layer can be written as

$$\psi^i = \sum_{n=0}^{\infty} C_{1n}^i j_n(\alpha_1 r) P_n(\cos\theta) + D_{1n}^i y_n(\alpha_1 r) P_n(\cos\theta) \tag{12}$$

$$\chi^i = \sum_{n=0}^{\infty} C_{2n}^i j_n(\beta_1 r) P_n(\cos\theta) + D_{2n}^i y_n(\beta_1 r) P_n(\cos\theta) \tag{13}$$

where y_n is the spherical Bessel function of the second kind.

By substituting equations (7–13) into equation (2), the displacement field in the media can be determined. The stress field is then obtained from the displacements by using the constitutive law of the media. The unknown constants $A_{1n}, A_{2n}, \ldots, D_{2n}$ in equations (8–13) can then be determined by imposing the continuity of displacements and stresses at the interfaces.

NUMERICAL RESULTS AND DISCUSSION

In this section results are presented to show the influence of the particulate reinforcement on the dynamic stresses in the matrix. Because of space constraints, results showing the influence of layers will only be presented at the conference.

The dynamic stresses in the matrix are expressed in dimensionless forms by normalizing with respect to the magnitude of the maximum incident stress, σ_o:

$$\sigma^*_{ij} = \frac{\sigma_{ij}}{\sigma_o} \qquad i, j = r, \theta, \phi \tag{14}$$

Thus the values of σ^*_{ij} can be considered as dynamic stress concentration factors. The dynamic stress concentration factors depend on the ratio of shear moduli $\mu^* = \mu_o/\mu_m$, Poisson's ratios ν_o and ν_m, ratio of mass densities $\rho^* = \rho_o/\rho_m$, and the frequency of excitation which is expressed in nondimensional form through

$$\omega^* = \omega a_o \sqrt{\frac{\rho_m}{(\lambda_m + 2\mu_m)}} \tag{15}$$

where a_o is the radius of the particle. The following values of the parameters have been chosen for the computations:

$$\begin{aligned} \mu^* &= 2, 8, 15, 25, 30 \\ \nu_o, \nu_m &= 0.20, 0.25, 0.30, 0.35, 0.40 \\ \rho^* &= 1, 2, 5 \end{aligned}$$

These values are sufficient to cover the range of parameters which might be encountered in practical applications and demonstrate the essential behavior of dynamic stress concentration.

The nature of the dynamic excitation is better appreciated by considering the limiting static case. When the frequency approaches zero, the applied stress field at infinity approaches

$$\sigma_{zz} = -\sigma_o \tag{16}$$

$$\sigma_{xx} = \sigma_{yy} = -\frac{\nu_m}{1 - \nu_m}\sigma_o \tag{17}$$

$$\sigma_{xy} = \sigma_{yz} = \sigma_{zx} = 0 \tag{18}$$

where σ_o is a constant and ν_m is the Poisson's ratio of the matrix. The stress field of equations (16–18) is triaxial. Thus, the results presented herein are for the dynamic counterpart of this triaxial load.

Figure 2 illustrates the angular distribution of σ^*_{rr} , $\sigma^*_{\theta\theta}$ and $\sigma^*_{\phi\phi}$ in the matrix at the interface for different values of the dimensionless frequency ω^*. In this case, it is to be noted that, when $\omega^* = 0.02$, stresses converge to the static solution corresponding to the loading given by the equations (16–18) and exhibit symmetry with respect to the $z = 0$ plane, as expected. At other frequencies, the applied stress field is not symmetric since the incident wave only illuminates the bottom half of the particle. The scattering phenomenon then dominates, considerably distorting the results from the static solution. It is apparent that the frequency has a strong influence on the stresses. Maximum values of σ^*_{rr} occur at $\theta = \pi$ for the five frequencies considered. A detailed calculation showed that maximum of σ^*_{rr} in the frequency range $0 \leq \omega^* \leq 3.0$ always occurred at $\theta = \pi$. At this location, all shear stresses vanish due to symmetry and, therefore, the normal stresses are principal stresses. Moreover, σ^*_{rr} is the major principal stress since it is greater than both $\sigma^*_{\theta\theta}$ and $\sigma^*_{\phi\phi}$. It can be seen from Figure 3a that maximum values of σ^*_{rr} are greater than unity. This would mean that the presence of a particle in the matrix amplifies this stress component under the given dynamic loading. For frequencies $\omega^* = 1.5$ and 2.0, the maximum values of σ^*_{rr} are also higher than the static value, suggesting the importance of dynamic loads in the design of composite materials. The stress components $\sigma^*_{\theta\theta}$ and $\sigma^*_{\phi\phi}$ are smaller than unity and therefore not critical.

Shown in Figure 3 are maximum values of σ^*_{rr} in the matrix around the interface as a function of the dimensionless frequency, ω^*, in the range $0 \leq \omega^* \leq 3.0$ for different values of μ^*. The stress components $\sigma^*_{\theta\theta}$ and $\sigma^*_{\phi\phi}$ were found to have values less than unity. Hence they are not critical and not presented here. However, the dynamic stress concentration factor for the stress component σ^*_{rr} reaches values over 2.0. The ensuing discussion therefore considers only this stress component. It is seen that the ratio of shear moduli, μ^*, strongly influences σ^*_{rr}. As μ^*increases, the maximum value of σ^*_{rr} increases and the location of the maximum stress tends to shift towards the high frequency end. The maximum dynamic stress concentration factor is 10 to 20 percent higher than the static values. In the case of $\mu^* = 8$, for example, the dynamic maximum value is about 15% higher than the static value.

Figure 4 shows the effect of density on σ^*_{rr} at $\theta = \pi$ as a function of the normalized frequency. All curves start off from the same point since the inertia has no effect when the frequency is very small. As ρ^*increases, the location of maximum σ^*_{rr} tends to shift towards the low frequency end. Increasing $\rho^*$from 1 to 2 does not seem to alter the maximum value of the stress. However, increasing $\rho^*$to 5 results in a significantly higher maximum occurring at a low nondimensional frequency around 0.5. In this case, the maximum dynamic stress concentration factor is about 58% higher than the static value.

CONCLUSION

The stress field at the interface between the particle and the matrix caused by a plane harmonic compressional wave has been studied. The results for the dynamic matrix stresses show that they are significantly different from the static stresses and, values above the static ones occur at various incident frequencies. The dynamic stresses also depend strongly on the elastic properties of the particle and the matrix. A significant mismatch of shear moduli and mass densities would result in large dynamic stresses. The largest stresses produced at the interface between the particle and the matrix are normal stresses which generally reach maximum values upto 58% greater than their corresponding static values.

REFERENCES

1 Davidson, D. L. The effect of particulate SiC on fatigue crack growth in a cast-extruded aluminium alloy composite, *Metall. Trans.*, **22** (1991), 97–112.

2 Tan, S. C. *Stress Concentrations Laminated Composites*, Technomic Publishing Co., 1994.

3 Wang, Z., Chen, T. K. and Lloyd, D. J. Stress distribution in particulate reinforced metal matrix composites subjected to external load, *Metall. Trans.*, **24A** (1993), 197–207.

4 Wu, Y. and Dong, Z. Three dimensional finite element analysis of composites with coated spherical inclusions, *Mater. Sci. Eng.*, **203** (1995), 314–323.

5 Bogan, S. D. and Hinders, M. K. Dynamic stress concentrations in fiber-reinforced composites with interface layers, *J. Comp. Materials*, **27** (1993), 1272–1240.

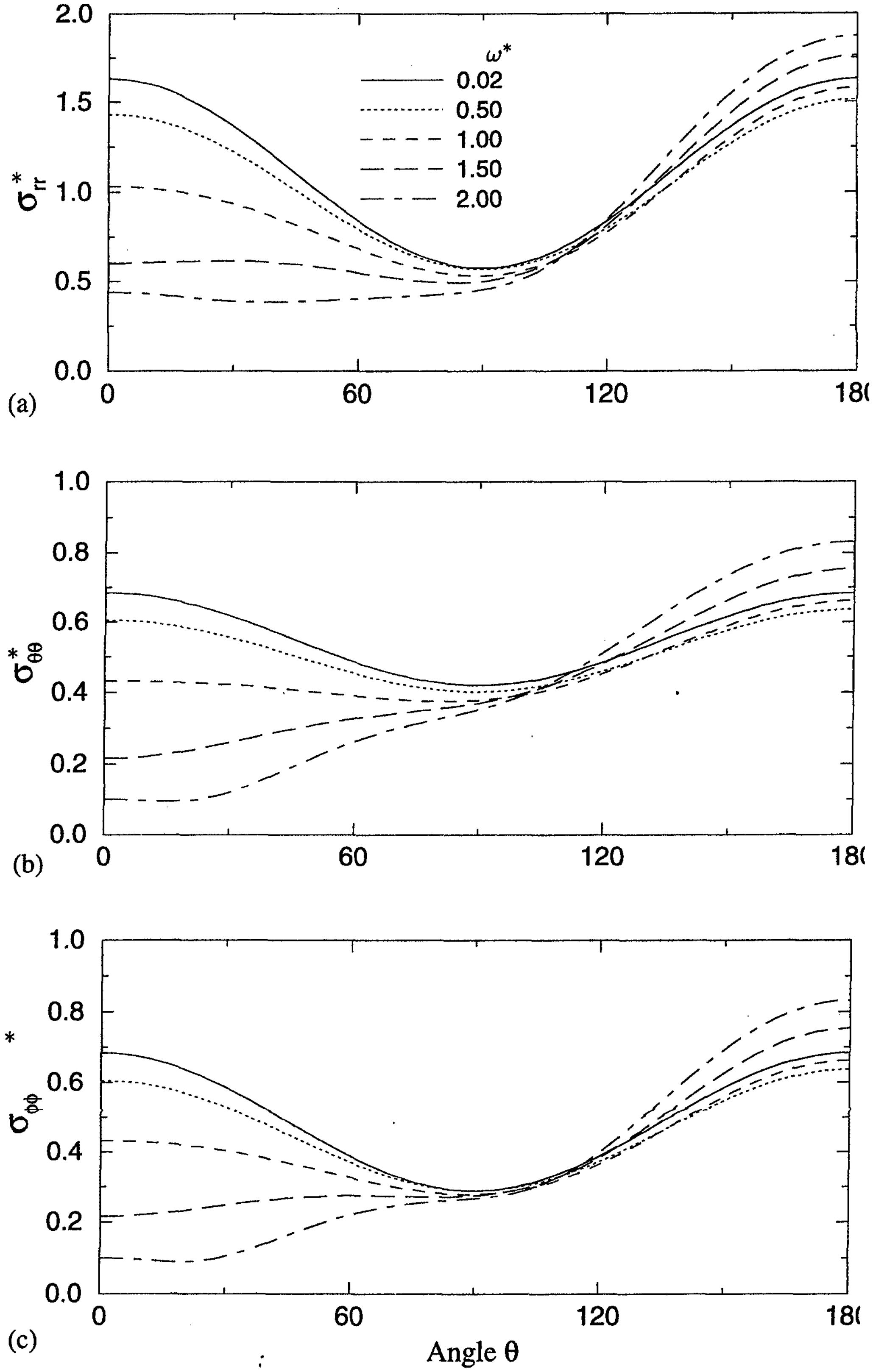

Figure 2: Angular distribution of stresses $(\rho^* = 1;\ \nu_o = \nu_m = 0.3)$

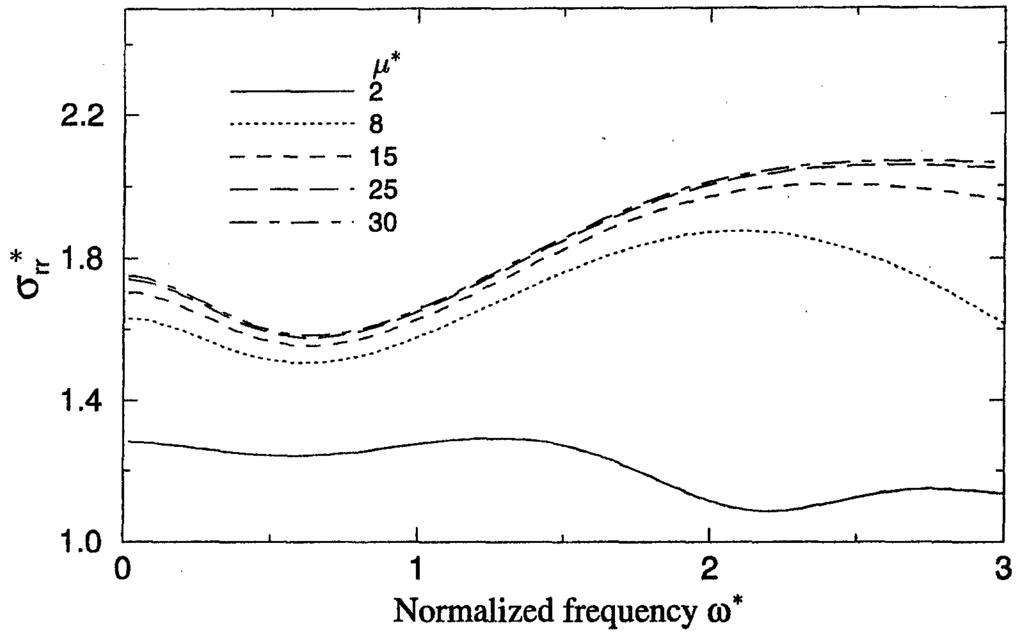

Figure 3: Effect of frequency and shear modulus on the stress ($\rho^* = 1$; $\nu_o = \nu_m = 0.3$)

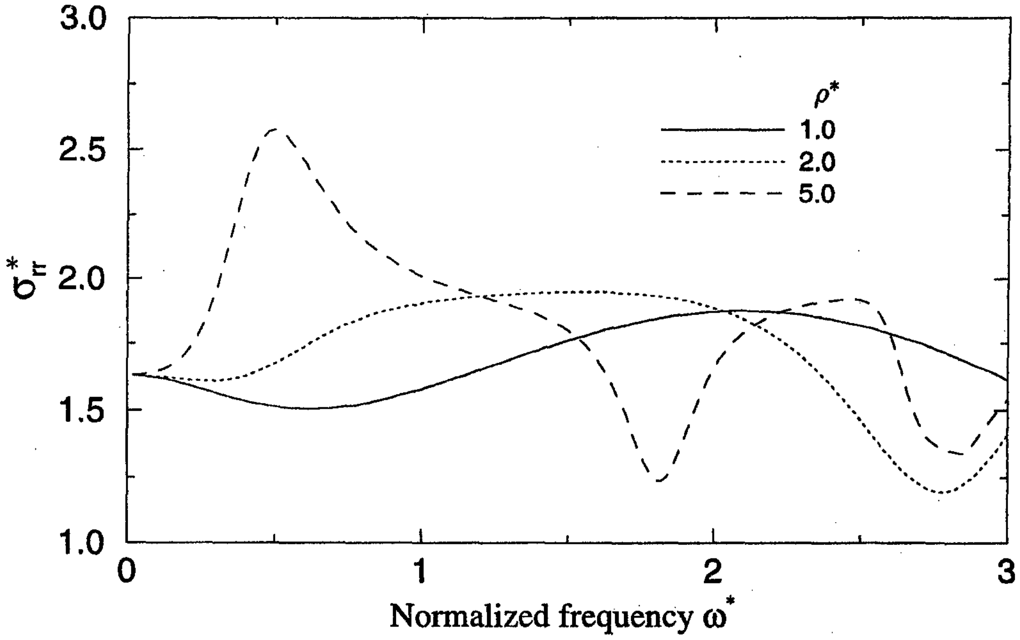

Figure 4: Effect of density and frequency on the stress ($\mu^* = 8$; $\nu_o = \nu_m = 0.3$)

6 Pao, Y. H. and Mow, C. C. *Diffraction of Elastic Waves and Dynamic Stress Concentrations*, Crane and Russak, New York, 1973.

7 Bostrom, A. Scattering by a smooth elastic obstacle, *J. Acoust. Soc. Am.*, **67** (1980), 1904–1913.

8 Paskaramoorthy, R., Datta, S. K. and Shah, A. H. Effect of interface layers on scattering of elastic waves, *J. App. Mech.*, **55** (1988), 871–878.

TiC INCLUSIONS SYNTHESISED IN SITU IN THE ZIRCONIA MATRIX

Waldemar Pyda

University of Mining and Metallurgy, Faculty of the Materials Science and Ceramics,
Department of Special Ceramics, al.Mickiewicza 30, 30-079 Cracow, Poland

ABSTRACT

The carbothermal reduction of titania originated from the zirconia s.s. was used to produce in situ the TiC phase. The carbothermally reduced zirconia powders and compacts were mainly composed of tetragonal and monoclinic phase. The samples heated at 1400°C contained TiC and some samples heated at 1500°C showed additionally the ZrC phase. The phase composition of the samples depended on carbon concentration, heating temperature and atmosphere. Gaseous products of the TiC and ZrC formation, (CO), suppressed densification of the compacts. At small carbon concentrations improved characteristics of the zirconia materials were obtained.

INTRODUCTION

Thermodynamic calculations[1] indicate that TiO_2 can react with carbon to produce titanium carbide at temperatures higher than 1280°C under a partial pressure of CO of 1atm. Lowering the partial pressure of CO falls the temperature of the reaction and presumably accelerates the reaction at a given temperature. The calculated range of temperatures which enables the synthesis of TiC covers the temperature rage of preparation of tetragonal zirconia polycrystals in the Y_2O_3- TiO_2- ZrO_2 system[2].

The aim of the presented work was to synthesise TiC in situ in the zirconia solid solution stabilised with Y_2O_3 and TiO_2 and to study an effect of the carbothermal reduction of TiO_2 originated from zirconia s.s. on properties of the tetragonal zirconia polycrystals.

EXPERIMENTAL

A co-precipitation and calcination method was used to prepare the powder of zirconia solid solution stabilised with 1.5 mole % Y_2O_3 and 18 mole % TiO_2 (sample P0). A zirconia-yttria-titania hydrogel was co-precipitated from an aqueous solution of appropriate chlorides with NH_4OH at a pH of 9. The gel was washed with distilled water, dried and calcined at a temperature of 700°C for 2h. In the same way the zirconia powder stabilised with 3 mole % Y_2O_3 (sample P3Y) was prepared. A calcination temperature of 950°C and a soaking time of 1h were applied.

Homogeneous mixtures of P0 and an ethanol solution of phenol - formaldehyde resin were prepared. The mixtures contained 33% (sample P6) and 200% (sample P36) of the carbon which was indicated by a stoichiometry of the reaction of TiO_2 and C. The mixture P36 was heated in an Ar atmosphere at 1500°C for 2h (sample P36w) to synthesise the TiC phase. This powder was used to prepare materials composed of 25 weight % of P36w and 75 weight % of P0 or P3Y. Isostatically pressed green bodies (P=350MPa) were sintered at 1400 and 1500°C for 2h in argon in a carbon bed. A furnace with Superkanthal 1900 heating elements was used. The mixtures P6 and P36 were also uniaxially pressed under a pressure of 5MPa and heat treated at 1400 and 1500°C for 2 hours in argon in a carbon bad. A furnace with tungsten heating elements was used.

X-ray analysis (CuKα radiation) was applied to characterise a phase composition of the powders and sintered bodies. The evaluation of phase contents was made by the following semi-quantitative formulas:

$$V_m = \frac{1.603 \cdot I(\bar{1}11)_m}{1.603 \cdot I(\bar{1}11)_m + I(111)_t + I(111)_{TiC}} \quad (1), \quad V_{TiC} = \frac{I(111)_{TiC}}{1.603 \cdot I(\bar{1}11)_m + I(111)_t + I(111)_{TiC}} \quad (2),$$

$$V_m + V_{TiC} + V_t = 1 \quad (3)$$

were: I denotes an integral intensity of an advisable peak of the monoclinic, m, tetragonal, t, and titanium carbide, TiC, phase. In the case of absence of TiC the equation (1) is reduced to the form given by Porter and Heuer for the quantitative determination of the monoclinic phase content in the system[3].

Transmission and scanning electron microscopy were applied to observe the morphology of the powders and the microstructure of the sintered bodies, respectively.

Fracture toughness, K_{Ic}, was determined on polished surfaces by Vickers' indentation using the Palmqvist crack model[4].

RESULTS AND DISCUSSION

Zirconia powders and composite materials with the TiC phase

The calcination of the zirconia-yttria-titania gel resulted in the powder of nano-crystalline sizes (~20nm) and isometric shapes (Fig.1a). The phase of tetragonal symmetry dominated in the powder (Fig.2). The second phase of monoclinic symmetry was found in the powder P0 in amount of 19.2±0.5 % (Tab.1).

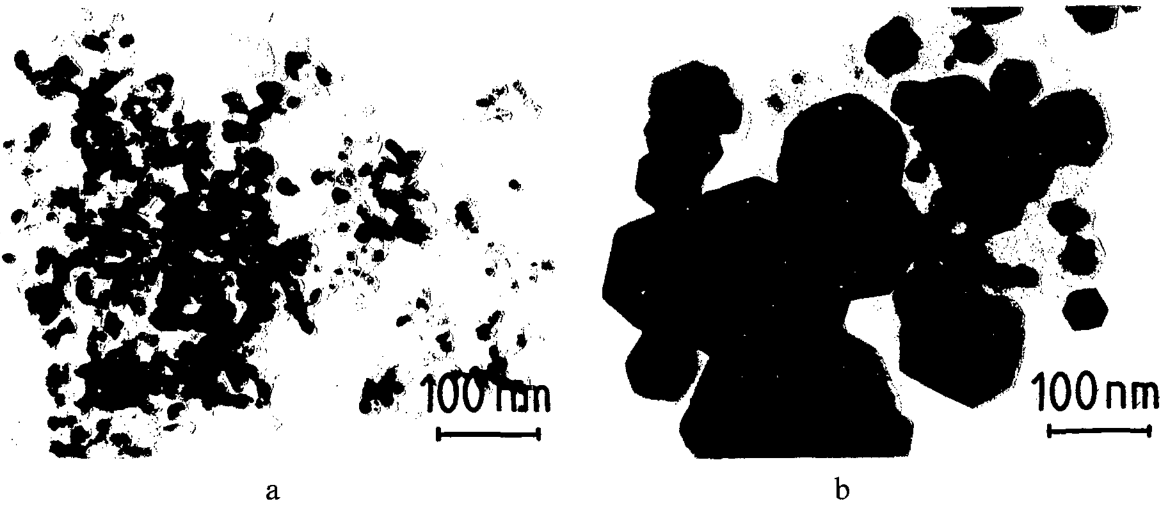

Fig.1. TEM microphotographs of the powders: a - original powder calcined at 700°C for 1 h in air, b - P36 mixture heat treated at 1500°C for 1h.

Table 1. Properties of the powders.

Property	P0	P36w as synthesised	P36w milled
Specific surface area, m^2/g	68.4	105.6	108.5
Monoclinic phase content, %	19.2±0.5	14.0	36.3
Tetragonal phase content, %	80.8±0.5	83.5	61.2
TiC content, %	0	2.5	2.5

The mixture of P0 and the carbon precursor heated at 1500°C for 2h in argon showed an increased crystallite size (~0.3µm, Fig.1b), decreased amount of the monoclinic phase (Tab.1) and detectable amount of TiC (Fig.2). An increased specific surface area of P36w can be attributed to remains of non-reacted carbon. This suggestion was confirmed by DTA-TG measurements (Fig. 3). The DTA curve in Fig. 3. shows two exothermic peaks at 511 and

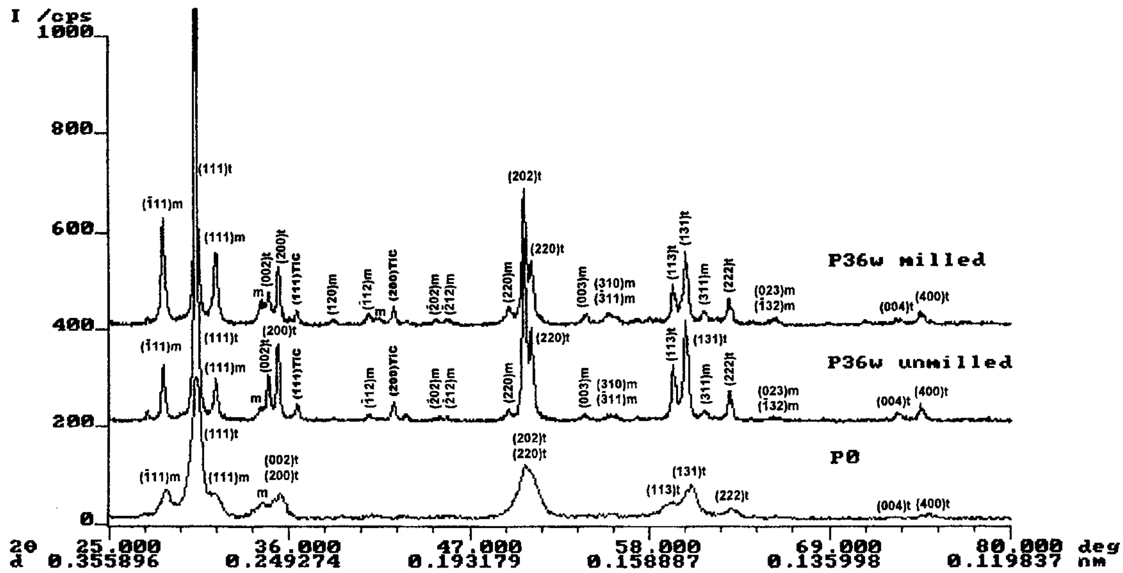

Fig.2. X-ray diffraction patterns of P0, P36w before and after attrition milling for 2h.

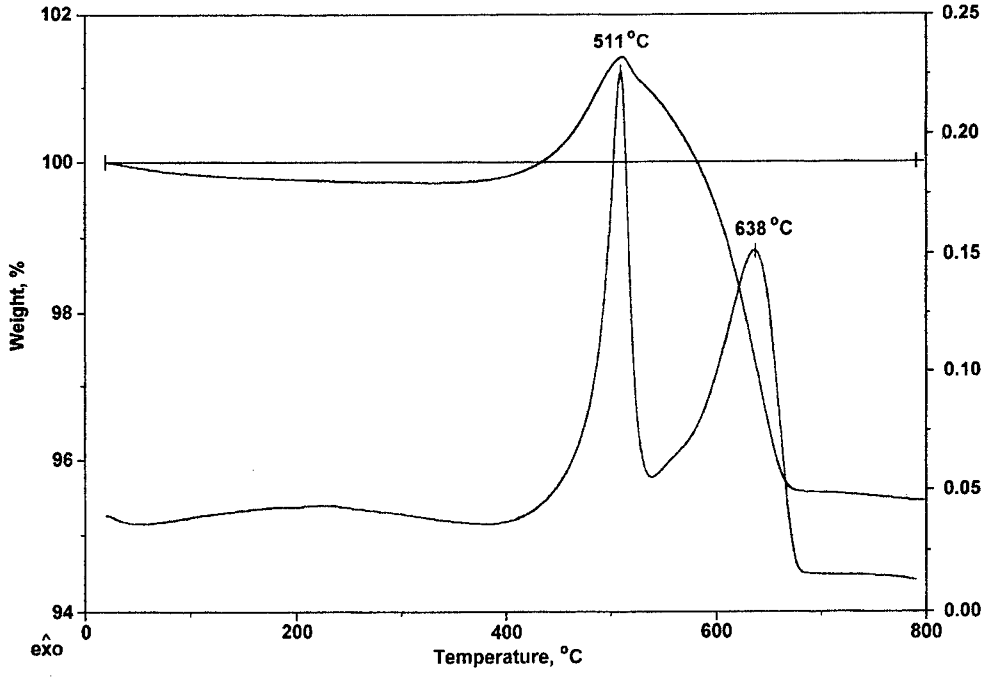

Fig.3. DTA and TG curves of the P36w powder (10°C/min, air).

638°C. A weight increase of the sample accompanies the first peak. This is due to the oxidation reaction of TiC. The minimal amount of TiC in the powder calculated on the basis of the sample weight increase was 5.5 weight %. This means that 59.5% of TiO_2 existing in the zirconia solid solution took part in the reaction with carbon. It caused a change of the zirconia s.s. composition to the probable following one: 1.7 mole % Y_2O_3 - 8.2 mole % TiO_2 - 90.1 mole % ZrO_2. A weight decrease accompanies the second peak. This can be attributed to the oxidation reaction of the non-reacted carbon. Its amount was estimated on about 6.3 weight % in relation to the starting sample. Attrition milling of P36w brought about an increased content of the monoclinic phase. This powder was used to prepare composites.

The data of Table 2 and 3 indicate that introducing P36w to the P3Y matrix caused a distinct decrease of the tetragonal phase content and apparent density of the composites

Table 2. Phase composition of the composites.

Sample	V_m, %	V_t, %	V_{TiC}, %
3Y-TZP, 1400°C	15.3	84.7	----
3Y-TZP, 1500°C	0	74 tetragonal+36 cubic	----
75%P3Y+25%P36w, 1400°C	47.3	52.7	----
75%P3Y+25%P36w, 1500°C	68.4	31.6	----
P0, 1400°C	51.7	48.3	----
75%P0+25%P36w, 1400°C	67.5	28.1	4.4
75%P0+25%P36w, 1500°C	43.2	53.2	3.6

Table 3. Properties of the composite materials sintered in argon in a carbon bad.

Sample	Sintering temperature, °C	Apparent density, g/cm^3	HV, GPa	K_{Ic}, MPam$^{0.5}$	Load, N
P3Y	1400	6.00±0.03	11.4±0.3	5.0±0.1	196
P3Y	1500	6.01±0.02	13.9±0.3	5.2±0.2	98.1
75%P3Y+25%P36w	1400	3.48±0.01	2.4±0.1	2.7±0.1	98.1
75%P3Y+25%P36w	1500	4.78±0.03	5.3±0.2	2.6±0.1	98.1
P0	1400	5.39±0.02	8.0±0.3	3.4±0.1	196
P0	1500	5.42±0.04	broken sample		----
75%P0+25%P36w	1400	4.09±0.31	4.8±0.2	3.0±0.1	196
75%P0+25%P36w	1500	5.64±0.05	11.2±0.6	4.6±0.1	196

when compared to the matrix and, as a result, deterioration of fracture toughness and hardness. There were no TiC observed. The combination of effects of the oxidation of the carbon remains and/or TiC which occurred in P36w could be responsible for this behaviour. The additional mechanism could be created by particles of the carbon remains which slowed down sintering processes when acted as inert inclusions.

The changes in the tetragonal phase content of the samples composed of P36w and the P0 matrix followed the density changes (Tab.2 and 3) similarly to those observed in the case of P36w-P3Y composites. The TiC content increased with the sintering temperature. This suggests the continuous reaction of the carbon remains with TiO_2 from the matrix zirconia s.s.. The additional carbon consumption resulted in an increased density of the bodies and improved mechanical properties (Tab.3).

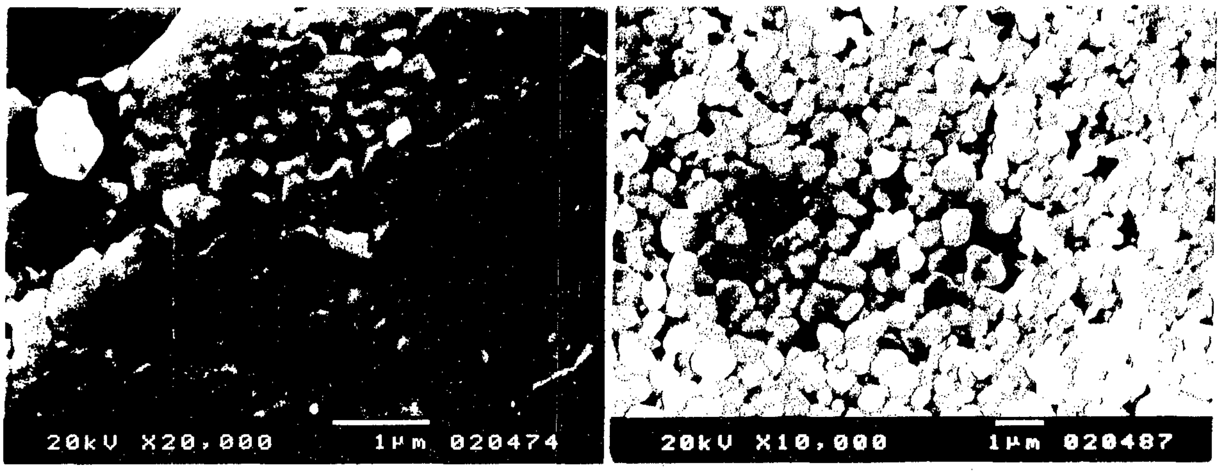

a b

Fig.4. SEM microphotographs of the composites sintered at 1500°C for 2h: a) 3Y+P36w, b) P0+P36w.

The destructive influence of the P36w with non-reacted carbon on the microstructure of P36w-P3Y composites is shown in Figure 4a. In contrast to that the microstructure of P36w-P0 composites was uniform, fine grained, free of cracks and large pores (Fig.4b).

Zirconia bodies with TiC synthesised during sintering

The materials derived from the original P0 powder showed the microstructure composed of the cubic zirconia s.s. (Fig.5) undoubtedly stabilised with vacancies that were formed during the deoxidation process[5]. The additives of carbon changed the phase composition of the P6 and P36 materials. The TiC and monoclinic phases appeared as a result of carbothermal reduction of TiO_2 and simultaneous destabilisation of zirconia s.s., respectively. The TiC content increased with an increase of carbon additive and the sintering temperature. At the highest temperature applied ZrC has been detected in P36. This fact indicates very low partial pressure of CO (< 0.17atm according to Ref.1) in the system and explains differences in the phase composition of the P0 and P36 samples heated in furnaces with the tungsten and Superkanthal 1900 elements (see Fig.2, Tab.2 and Fig.5).

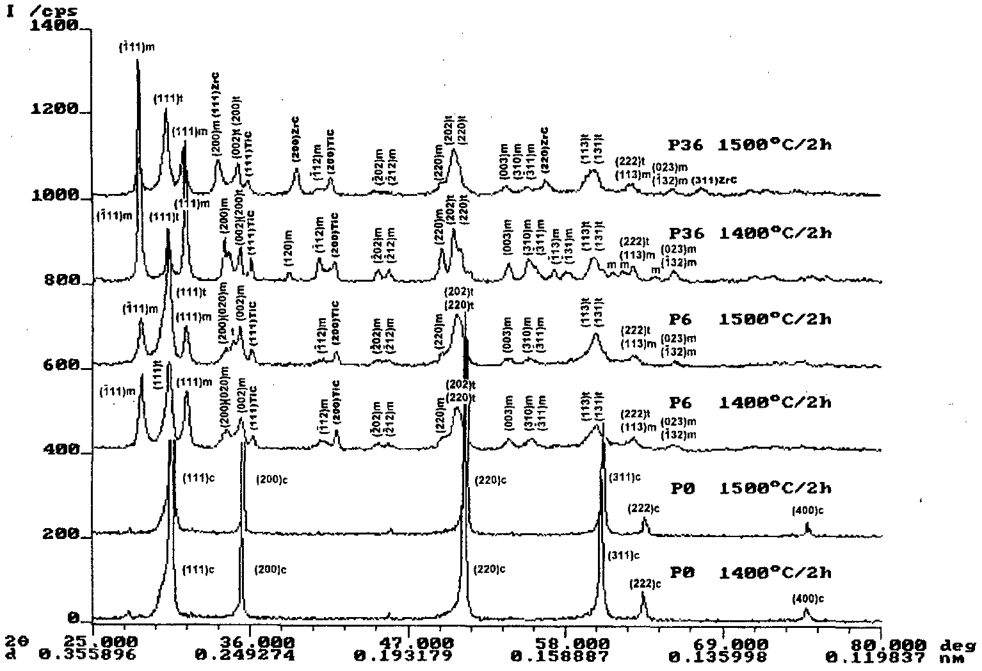

Fig.5. X-ray diffraction patterns of the samples sintered at 1400 and 1500°C for 2h.

Table 5. Apparent density and water absorption of the samples of P0, P6 and P36.

Sample	Apparent density, g/cm^3		Water absorption, %	
	1400C°/2h	1500C°/2h	1400C°/2h.	1500C°/2h
P0	5.66±0.02	5.48±0.01	0.14±0.03	0.22±0.03
P6	4.97±0.01	5.47±0.01	0.78±0.04	0.03±0.03
P36	2.35±0.03	4.08±0.01	14.08±0.07	5.90±0.06

Table 6. Hardness, HV, and fracture toughness, K_{Ic}, of P0 and P36 (F=49.05N, *F=98.1N).

Sample	HV, GPa		K_{Ic}, MPam$^{0.5}$	
	1400C°/2h	1500C°/2h	1400C°/2h.	1500C°/2h
P0	11.78±0.59	10.43 ±0.61	3.42±0.09	3.22±0.30
P6	8.02±0.55	10.35±0.79	7.06±0.68	4.49±2.19

The additive of carbon affected density and mechanical properties of the sintered materials as is shown in Table 5 and 6. Too high concentration of C in P36 caused degradation of the material due to gaseous products of the reaction of the TiC formation. However, the sample with lower additive of C (P6) sintered at 1400°C showed a great increase in fracture toughness. This can be attributed to the reduced grain size in P6 when compared with P0 (Fig.7), occurrence of the transformable tetragonal phase and some amount of porosity observed.

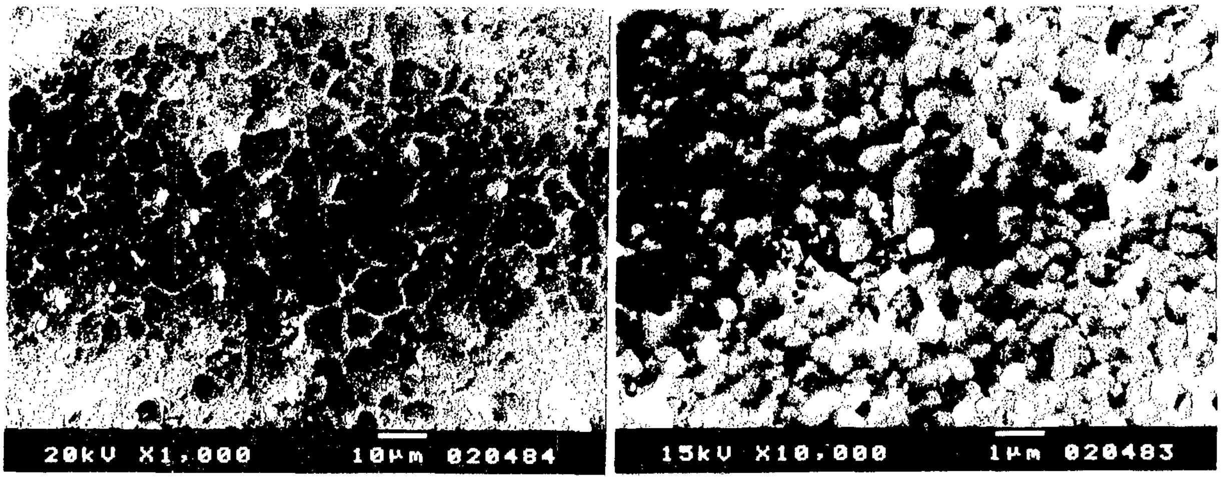

a b

Fig.7. SEM microphotographs of the samples sintered at 1400°C for 2h: a) P0 and b) P6.

TEM observations revealed the TiC inclusions of ~200nm in size in the sample of P6 sintered at 1400°C for 2h.

CONCLUSIONS

The presented work shows that TiC inclusions can be formed in situ in zirconia solid solutions which contained TiO_2 as a stabiliser. The carbothermal reduction of titania and TiC formation leads to the destabilisation of the zirconia solid solution and transformation of the deoxidised cubic phase to tetragonal or even monoclinic one. This can activate the toughening mechanism. The decreased titania concentration reduces the grain growth and also can lead to improved properties. Gaseous products of the formation of titanium carbide suppress densification of the materials. The phase composition of the materials depends on carbon concentration, heating temperature and CO concentration in an atmosphere.

ACKNOWLEDGEMENTS

This work was in part supported by the Polish State Committee for Scientific Research under grants 7 T08D 019 14.

REFERENCES

1. R.Róg, Thermodynamics of the reaction of the carbide and nitride formation in the ZrO_2 -Y_2O_3 -TiO_2 s.s. at different atmospheres, chapter II in Report PB/964/7/91, UMM, Cracow 1994.
2. Pyda, K. Haberko, M.M. Bućko, M. Faryna, A study on preparation of tetragonal zirconia polycrystals (TZP) in the TiO_2-Y_2O_3-ZrO_2 system, Ceramics Int. **18**(1992) 231-326
3. D.L. Porter, A.H. Heuer, Microstructural development in MgO-partially stabilised zirconia (Mg-PSZ), J.Am. Ceram. Soc., **62** [5-6](1979) 298-305
4. K.A. Niihara, A fracture mechanics analysis of indentation-induced Palmqvist crack in ceramics, J. Mater. Sci. Lett., **2** (1983) 221
5. K.Haberko, Z.Pędzich, J.Piekarczyk, M.M.Bućko, W.Suchanek, Tetragonal polycrystals under reducing conditions, Third Euro-Ceramics V.1, P.Duran, J.F.Fernandez Ed., Faenza Editrice Iberica S.L. 1993, pp. 967-971

CLOSED-FORM ANALYSIS OF THE THICKNESS EFFECT OF REGULAR HONEYCOMB CORE MATERIAL

W. Becker

Institute for Mechanics and Control, University of Siegen,
Paul-Bonatz-Str. 9-11, D-57068 Siegen, Germany

INTRODUCTION

Within sandwich structures for lightweight applications the use of regular honeycomb cores is very common [1]-[4]. Considering the structural behaviour of a sandwich the effect of the core is not only to maintain the distance between the faceskins, but it also contributes to the overall inplane stiffness of the entire sandwich [5].

Due to the coupling of the core displacements with those of the sandwich face sheets the stiffness contribution of the core is not simply proportional to its total thickness, as could be expected. As a consequence the effective core stiffness gets a nonlinear function of the total core thickness. This outcome is the well-observable so-called "core thickness effect" [7].

The objective of the present work is to give a closed-form description of the effective inplane core stiffnesses including the thickness effect.

CONSIDERED HONEYCOMB CORE STRUCTURE

The most common cellular honeycomb structure is periodically composed of perfectly regular hexagonal cells as it is shown in fig. 1. Within each hexagonal cell all six edges are of the same length l and all corner angles are equal to 120°. Correspondingly, the diameter of the hexagonal cells (distance of two opposite parallel edges) is $l\sqrt{3}$. Furtheron, the core structure is characterized by the cell wall thicknesses t and $2t$ for the diagonal and vertical cell walls, respectively (due to the fabrication process by an expansion method [2]), the core thickness h, and, of course, by the elastic properties of the employed cell wall material.

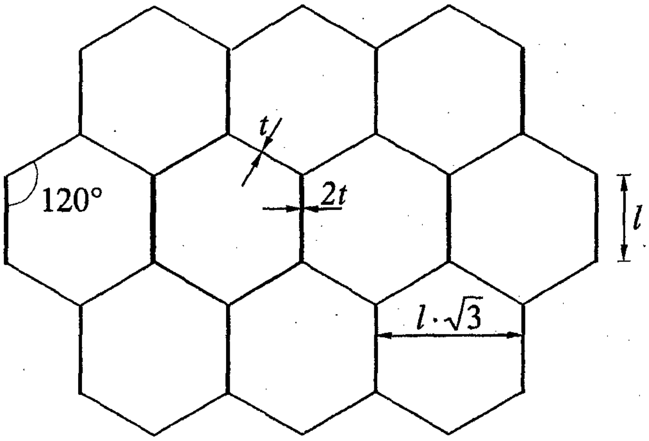

Figure 1: Regular hexagonal honeycomb

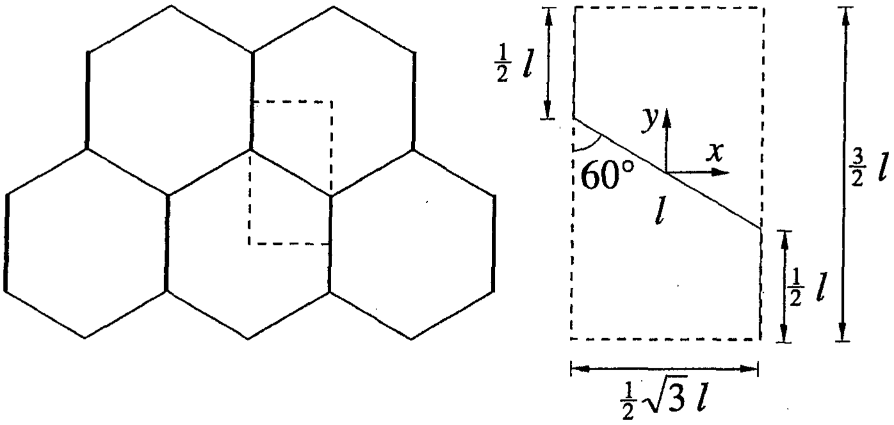

Figure 2: Representative unit cell

For the derivation of the effective overall core properties under a macroscopically homogeneous loading it is most convenient to follow the concept of a representative unit cell [5]. For the purposes here it is sufficient to consider the representative rectangular unit cell shown in fig. 2.

CLOSED-FORM APPROACH TO THE THICKNESS EFFECT

For the derivation of effective core stiffnesses the case is to be considered that the core is submitted to macroscopically homogeneous strains ε_x^0 and/or ε_y^0. On unit cell level the macroscopic strains go along with a corresponding displacement field within the cell walls.

For an appropriate displacement representation the local coordinates η_1, η_2, and ζ are introduced for the vertical and diagonal cell walls as it is indicated in fig. 3. For a clear distinction of local strains and displacements the vertical cell walls are

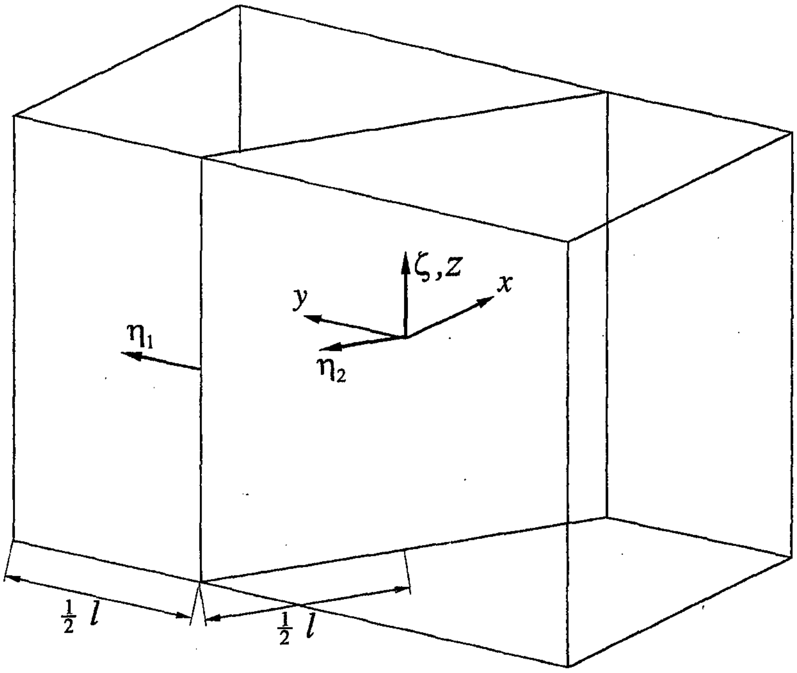

Figure 3: Employed coordinates

labelled by the index "1" and the diagonal cell wall by the index "2", respectively. Local strains and displacements are labelled in the same way.

In really many practical honeycomb cores the cell walls are rather thin. Then it is justified to assume that the cell walls predominantly transfer forces through membrane strains and that bending forces in the cell walls can be neglected. Correspondingly, the local displacements v^1 and v^2 in η^1- and η^2-direction respectively play the most important role. As a kind of compatibility condition along the cell wall interface $\eta_1 = 0$ or, equivalently, $\eta_2 = l/2$ due to the given geometrical situation the relation

$$v^1 = 2v^2 \tag{1}$$

has to be met.

The cell wall displacements can be described in a relatively easy way for two limiting cases, namely directly along the sandwich face skins and, on the other hand, sufficiently far away from the face skins within the core.

Assuming that the face skin laminate is sufficiently stiff the homogeneous face skin strains enforce the following cell wall deflections:

$$\left.\begin{aligned} v^1 &= \varepsilon_y^0 \cdot (\eta_1 + \tfrac{l}{4}) \\ v^2 &= (\tfrac{1}{4}\varepsilon_y^0 + \tfrac{3}{4}\varepsilon_x^0) \cdot \eta_2 \end{aligned}\right\} \qquad \text{for} \quad \zeta = \pm\frac{h}{2} \quad . \tag{2}$$

On the other hand, sufficiently far away from the face skins (for a sufficiently large total core thickness) force equilibrium between the respective cell walls leads to the following deflections:

$$\begin{aligned} v^1 &= (\frac{3}{10}\varepsilon_x^0 + \frac{3}{10}\varepsilon_y^0)\eta_1 + (-\frac{3}{20}\varepsilon_x^0 + \frac{3}{5}\varepsilon_y^0)l \quad , \\ v^2 &= (\frac{3}{5}\varepsilon_x^0 + \frac{3}{5}\varepsilon_y^0)\eta_2 \quad . \end{aligned} \tag{3}$$

On the background of the limiting cases (2) and (3) for the real case of a sandwich with a core of finite thickness h the following displacement representation is chosen as an approximation:

$$\begin{aligned} v^1(\eta_1, \zeta) &= \varepsilon_y^0(\eta_1 + \frac{l}{4}) + f(\zeta)\left[(\frac{3}{10}\varepsilon_x^0 - \frac{7}{10}\varepsilon_y^0)\eta_1 + (-\frac{3}{20}\varepsilon_x^0 + \frac{7}{20}\varepsilon_y^0)l\right] \\ v^2(\eta_2, \zeta) &= (\frac{3}{4}\varepsilon_x^0 + \frac{1}{4}\varepsilon_y^0)\eta_2 + f(\zeta)(-\frac{3}{20}\varepsilon_x^0 + \frac{7}{20}\varepsilon_y^0)\eta_2 \\ &\text{with} \qquad f(\zeta) = 1 - \frac{\cosh(\lambda\zeta)}{\cosh(\lambda h/2)} \quad . \end{aligned} \tag{4}$$

Herein, the function $f(\zeta)$ has been defined in such a way that it vanishes at the face skin interfaces $\zeta = \pm h/2$ and, on the other hand, becomes maximal in the thickness center $\zeta = 0$. The quantity λ is a free parameter that is still to be adjusted in such a way that the given approximation gets as good as possible. For this purpose the principle of minimum internal potential energy can be applied.

From the displacement representation (4) the accompanying strain components ε_η and $\gamma_{\eta\zeta}$ can be derived in a straightforward manner. Then in a subsequent step the strain energy can be calculated as

$$U = \int \frac{1}{2} E\varepsilon_\eta^2 dV + \int \frac{1}{2} G\gamma_{\eta\zeta}^2 dV \quad , \tag{5}$$

where E and G denote Young's modulus and the corresponding shear modulus and the integration is performed over the entire volume of the involved cell walls. Some tedious but straightforward calculation finally leads to

$$\begin{aligned} U &= 2Et\left[lh\frac{9}{80}(\varepsilon_x^0+\varepsilon_y^0)^2\right. \\ &\quad +\frac{l}{\lambda}\tanh\left(\lambda\frac{h}{2}\right)\frac{45\varepsilon_x^{02}-210\varepsilon_x^0\varepsilon_y^0+245\varepsilon_y^{02}}{1600} \\ &\quad \left.+\,lh\frac{1}{\cosh^2\left(\lambda\frac{h}{2}\right)}\frac{(3\varepsilon_x^0-7\varepsilon_y^0)^2}{640}\right] \\ &\quad +2Gt\left[2l^3\lambda\tanh\left(\lambda\frac{h}{2}\right)-l^3h\lambda^2\frac{1}{\cosh^2\left(\lambda\frac{h}{2}\right)}\right]\frac{(3\varepsilon_x^0-7\varepsilon_y^0)^2}{7680} \quad . \end{aligned} \tag{6}$$

When the strain energy U is divided by the volume of the considered representative unit cell the specific strain energy U^* per volume is obtained as

$$U^* = U\frac{4}{3\sqrt{3}l^2h} \quad . \tag{7}$$

Eventually, the effective core material stiffnesses

$$C_{xx}=\frac{\partial^2U^*}{\partial\varepsilon_x^{02}} \quad , \quad C_{yy}=\frac{\partial^2U^*}{\partial\varepsilon_y^{02}} \quad , \quad C_{xy}=\frac{\partial^2U^*}{\partial\varepsilon_x^0\partial\varepsilon_y^0} \tag{8}$$

can be calculated as

$$\begin{aligned} C_{xx} &= \frac{\sqrt{3}}{5}E\frac{t}{l}\left[1+\frac{1}{4\lambda h}\tanh\left(\lambda\frac{h}{2}\right)+\frac{1}{8\cosh^2\left(\lambda\frac{h}{2}\right)}\right] \\ &\quad +\frac{1}{160\sqrt{3}}Gt\lambda\frac{l}{h}\left[2\tanh\left(\lambda\frac{h}{2}\right)-\lambda h\frac{1}{\cosh^2\left(\lambda\frac{h}{2}\right)}\right] \quad , \\ C_{xy} &= \frac{\sqrt{3}}{5}E\frac{t}{l}\left[1-\frac{7}{12\lambda h}\tanh\left(\lambda\frac{h}{2}\right)-\frac{7}{24\cosh^2\left(\lambda\frac{h}{2}\right)}\right] \\ &\quad -\frac{7}{480\sqrt{3}}Gt\lambda\frac{l}{h}\left[2\tanh\left(\lambda\frac{h}{2}\right)-\lambda h\frac{1}{\cosh^2\left(\lambda\frac{h}{2}\right)}\right] \quad , \\ C_{yy} &= \frac{\sqrt{3}}{5}E\frac{t}{l}\left[1+\frac{49}{36\lambda h}\tanh\left(\lambda\frac{h}{2}\right)+\frac{49}{72\cosh^2\left(\lambda\frac{h}{2}\right)}\right] \\ &\quad +\frac{49}{1440\sqrt{3}}Gt\lambda\frac{l}{h}\left[2\tanh\left(\lambda\frac{h}{2}\right)-\lambda h\frac{1}{\cosh^2\left(\lambda\frac{h}{2}\right)}\right] \quad . \end{aligned} \tag{9}$$

These effective stiffnesses interrelate the homogeneized unit cell stresses $<\sigma_x>$, $<\sigma_y>$ (total forces per cross-sectional area A) with the macroscopic strains ε_x^0, ε_y^0 in the following way:

$$\begin{bmatrix} <\sigma_x> \\ <\sigma_y> \end{bmatrix} = \begin{bmatrix} C_{xx} & C_{xy} \\ C_{xy} & C_{yy} \end{bmatrix}\begin{bmatrix} \varepsilon_x^0 \\ \varepsilon_y^0 \end{bmatrix} \quad . \tag{10}$$

So far, there is still one degree of freedom within the derived results, namely the introduced parameter λ. Knowing that the real displacements minimize the resultant total strain energy the introduced quantity λ is determined by minimizing the strain energy of the considered representative unit cell. For the actual minimization a little FORTRAN programme has been implemented.

RESULTS AND THEIR COMPARISON WITH FINITE ELEMENT ANALYSES

In order to validate the derived closed-form results (9) some accompanying finite element analyses have been performed for the case of an aluminum core with a Young's modulus of $E = 72200.\text{MPa}$, the geometric dimensions $l = 4\text{mm}$ and $t = 0.05\text{mm}$ and a set of different core thickness values h. To this end the finite element code ABAQUS [6] has been employed, using 4-node shell elements of type S4R. A finite element mesh of the representative unit cell is shown in fig. 4. As "loading" on the cell surfaces and edges those displacements have been prescribed that correspond to the macroscopically homogeneous strain states ε_x^0, ε_y^0. Then the effective core cell stiffnesses can be identified either through the resultant reaction forces or through the respective total strain energy.

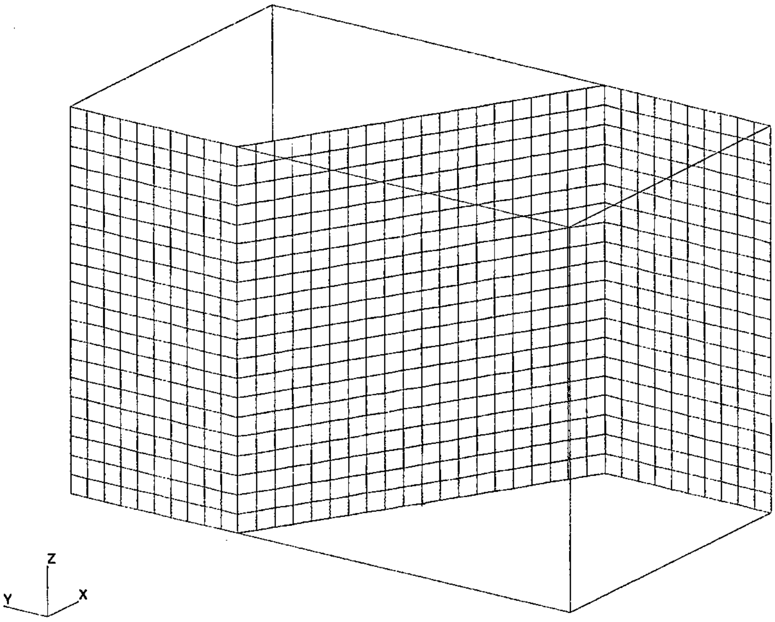

Figure 4: Representative unit cell finite element mesh

Fig. 5 shows the results for the effective core stiffnesses C_{xx}, C_{yy}, C_{xy} as functions of the total core thickness h within the range $h = 0...10\text{mm}$ according to the closed-form relations (9) and according to the performed finite element analyses. In this representation the solid line curves are the closed-form predictions whereas the isolated markers mean the obtained finite element results.

Obviously, the numerical finite element results validate the corresponding closed-form predictions — there is a satisfactory agreement between the respective results.

In comparison to the finite element modeling the presented closed-form approach is much more effective in regard of the involved numerical effort. With this advantage it is very useful for practical engineering applications and it enables an easier investigation of parameter sensitivities.

Considering the actual dependence of the effective core stiffnesses on the thickness h it has to be stated that the effective stiffness C_{yy} shows the most marked thickness

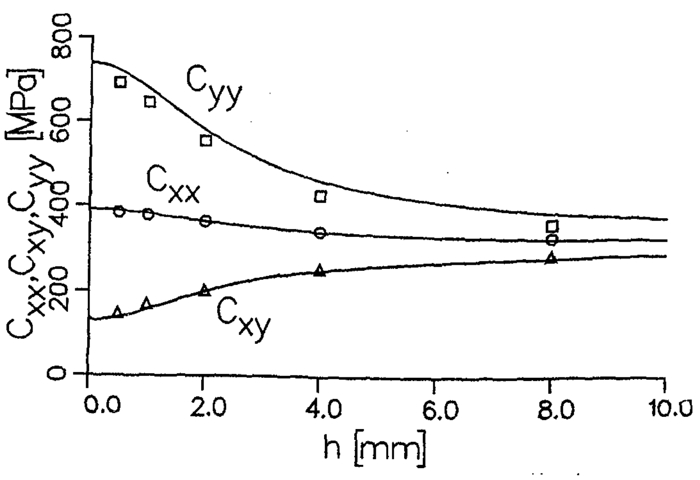

Figure 5: Effective core stiffnesses C_{xx}, C_{yy}, C_{xy} as functions of the core thickness h

effect. For a very thin core thickness, $h \to 0$, the amount of C_{yy} is about twice as large as for the case of a large core thickness, $h \to \infty$. The effective core stiffness C_{xy} also shows a marked thickness effect but with the opposite tendency. Eventually, the effective core stiffness C_{xx} shows the smallest thickness effect. For $h \to 0$ the stiffness increase is just in the order of about 30 percent. Of course, it is also important to have quantified this less pronounced thickness effect.

Another important aspect of the effective core stiffnesses is the symmetry of the properties. It is well-known that for $h \to \infty$ a hexagonal honeycomb core in regard of its inplane properties is isotropic [5]. In connection with the thickness effect, however, this property gets lost, as can be seen from the results in fig. 5. For the limiting case $h \to 0$ a marked degree of anisotropy has to be stated because C_{yy} gets almost twice as large as C_{xx}.

REFERENCES

[1] ESA "Structural Materials Handbook" ESA PSS-03-203. Noordwijk: ESTEC 1994.

[2] HEXCEL "Mechanical properties of Hexcel honeycomb materials" TSB 120, 1987.

[3] HEXCEL "The basics on bonded sandwich construction" TSB 124, 1987.

[4] Ehmann, D., Becker, W., Salmen, H. "Aspects of Structural Design Optimization for High Precision Reflectors and Mirrors". *Spacecraft Structures and Mechanical Testing*, pp. 263-272. Toulouse: CNES, Cepadues-Editions 1994.

[5] Gibson, L. J., Ashby, M. F. "Cellular Solids — Structure and Properties". Oxford: Pergamon 1988.

[6] ABAQUS Version 5.4. Hibbitt, Karlsson and Sorensen 1994.

[7] Becker, W. "The inplane stiffnesses of a honeycomb core including the thickness effect". Accepted for publication in *Archive of Applied Mechanics*.

HIGH-PRECISION MODELLING OF DEFORMATION OF SANDWICH STRUCTURES UNDER BILATERAL SYMMETRIC AND OBLIQUE-SYMMETRIC LOADING

O.G.Gurtovy

Departament of Strength of Materials and Structural Mechanics,
Ukrainian State Academy of Water Management, Soborna Street 11, Rivne, 266000,
Ukraine.

INTRODUCTION

Analysis of exact three-dimensional solutions of particular problems of elastic deformation sandwich plates [1,2] shows the principal difference of stress-strained state (SSS) under symmetric and oblique-symmetric loadings of front surfaces that cause unflexural and flexural deformation. Therefore, while constructing approximate SSS models it is necessary to introduce the approximations of SSS along the transverse coordinate for symmetric components of loadings that would add to the approximations of flexural models [3,4 and others]. Under unflexural deformation taking into consideration of cross compression is necessary, because under symmetric cross loading the purely shear models [3] lead to simply-zero solution. Specified continual models of deformation of layer plates, where the general order of differentiation of solution equations does not depend on the quantity of layers are given below.

PROBLEM STATEMENT

SSS of rectangular plate having thickness h is being modelled in orthogonal system of co-ordinates x_α ($\alpha=\overline{1,3}$; $x_3=z$). Orthotropic axes coincide with axes x_α in rigidly connected orthotropic layers of arbitrary $h^{(k)}$ $(k=\overline{1,n})$ thickness. Axes z is orthogonal to facial surfaces of the plate $z=a_0$, $z=a_n$. Let's introduce the components of vectors of mechanic loading $Y_{\alpha 0}$, $Y_{\alpha n}$ in the directions of axes x_α and temperature T_0, T_n on the facial surfaces as a sum of symmetric $p_{\alpha 0}$, $p_{\alpha n}$, T_p and oblique-symmetric $q_{\alpha 0}$, $q_{\alpha n}$, T_{q0}, T_{qn} components (concerning the middle surface $z=a_m$).

To postulate "rational" hypotheses for stress distributions across the thicness of transverse shear $\sigma_{i3}^{(k)}$ $(i=\overline{1,2})$ and cross compression $\sigma_{33}^{(k)}$ while modelling is the most rational. In these hypotheses, the approximations for the transverse co-ordinate z are given in such way thet the static conditions of contact of layers and the conditions on the facial surfaces are satisfied. Then it is possible to define approximately hypothetical components $u_\alpha^{(k)}$ of the displacement vector in the layer k from the equations [5]:

$$u_3^{(k)} = v_3 + \int_{\delta_i}^{z} a_{3333}^{(s)} \sigma_{33}^{(s)} dz; \qquad (1)$$

$$u_i^{(k)} = v_i - \int_{\delta_i}^{z} u_{3,i}^{(s)} dz + \int_{\delta_i}^{z} a_{i3j3}^{(s)} \sigma_{j3}^{(s)} dz; \quad i,j=\overline{1,2}$$

where $v_i(x_j)$ -unknown functions of tangential, and $v_3(x_j)$ -normal displacements on voluntary surfaces $z=\delta_\alpha$; $a_{\alpha\beta\gamma\delta}^{(k)}$ and $A_{\alpha\beta\gamma\delta}^{(k)}$ are coefficients of matrixes of pliability and rigidness of Hooke's law in axes x_α.

Here and further the particular derivatives are substituted by lower indexes after a comma. Summarizing of repeated lower indexes is introduced; at that $i,j=\overline{1,2}$; $\alpha=\overline{1,3}$. The sum of integrals in the quantity of z from the non-continuous function is marked as one integral of the given function [3-5]. The upper index in brackets is the number of the layer.

Let's introduce the hypotheses for the stresses $\sigma_{\alpha 3}^{(k)}$ in the symmetric structure looking like:

a) for oblique-symmetric normal loading $q_3 = 0,5(Y_{30} + Y_{3n})$:

$$\sigma_{i3}^{(k)} = f_{i1}^{(k)}(z^2)\beta_{i1} + f_{i2}^{(k)}(z^4)\beta_{i2}; \qquad \sigma_{33}^{(k)} = F_1^{(k)}(z^3)\,q_3 + F_2^{(k)}(z^5)\,\gamma_2; \tag{2}$$

b) for symmetric normal loading $p_{3n} = -p_{30} = Y_{3n} - q_3$:

$$\sigma_{i3}^{(k)} = f_{i3}^{(k)}(z^3)\beta_{i3}; \qquad \sigma_{33}^{(k)} = p_{3n} + F_3^{(k)}(z^4)\,\gamma_3; \tag{3}$$

c) for symmetric tangential loading $p_i = 0,5(Y_{i0} + Y_{in})$:

$$\sigma_{i3}^{(k)} = f_{i4}^{(k)}(z^1)\,p_i + f_{i3}^{(k)}(z^3)\beta_{i3}; \qquad \sigma_{33}^{(k)} = F_4^{(k)}(z^2)\,\gamma_4 + F_3^{(k)}(z^4)\,\gamma_3; \tag{4}$$

d) for oblique-symmetric tangential loading $q_{in} = -q_{i0} = Y_{in} - p_i$:

$$\sigma_{i3}^{(k)} = q_{in} + f_{i1}^{(k)}(z^2)\beta_{i1}; \qquad \sigma_{33}^{(k)} = F_5^{(k)}(z^3)\,\gamma_5. \tag{5}$$

In brackets under functions $f_{is}^{(k)}(z)$ and $F_s^{(k)}(z)$ the maximum stage of approximating grade polinom at z, and $\beta_{i\alpha}(x_j)$ and $\gamma_s(x_j)$ are unknown functions of transverse shear and compression.

In unsymmetric structure the unflexural and flexural deformations for tangential loading are interconnected. That is why the hypotheses (4) and (5) should not be separated. Symmetric tangential loading causes an essential flexural deformation in a non-symmetric package of layers.

Hypotheses (2)-(5) and the contents of the functions $f_{is}^{(k)}(z)$, $F_s^{(k)}(z)$ got as specifying of the next simpliest starting hypotheses for $\sigma_{\alpha 3}^{(k)}$: from the affect of loading q_3 - $\sigma_{i3} = \beta_{i\alpha}(x_j)$; $\sigma_{33} = f_0\, q_3$; from p_{3n}, p_{30} - $\sigma_{i3} = 0$; $\sigma_{33} = p_{3n}$; from q_{in}, q_{i0} - $\sigma_{i3} = q_{in}$; $\sigma_{33} = 0$; from the affect p_i -
$\sigma_{i3} = f_0\, p_i$; $\sigma_{33} = F_0\gamma_0(x_j)$, where $f_0 = 2(z - a_0)/h - 1$, $F_0 = (z - a_0)[(z - a_0)/h - 1]$.

In the procedure of the specifying the stresses $\sigma_{\alpha 3}$ were filled into (1) and got $u_\alpha^{(k)}$ - into Cauchy's correlations and the law of Hooke. Further the specified expressions $\sigma_{i3}^{(k)}$ were defined from the equations of steadiness $\sigma_{i\alpha,\alpha}=0$ by means of integrating (mind, as for two beams with elastic properties of the matter in the direction of axes x_i), and with $\sigma_{i3}^{(k)}$ were integrated with the new unknown functions $\beta_{i\alpha}$, γ_s (like in [4]) - derivatives from loading and from functions v_α , and also all static conditions were satisfied on the in-plane surfaces of the layers and of the plate. To decrease the quantity of approximating functions the hypothesis about the similarity of different degree functions $f_{is}^{(k)}(z)$, $F_s^{(k)}(z)$ with the same highest degree z is introduced, if during the transition to the homogeneous plate these functions are becoming linearly dependent.

As a result, the functions $f_{is}^{(k)}$, $F_s^{(k)}$ in expressions (2)-(5) look like:

$$f_{i1}^{(k)} = \int_{a_0}^{z} A_{iiii}^{(r)}(z-\zeta_i)dz \; ; \quad k,l=\overline{1,n}\, ; r=\overline{1,k}\, ; s=\overline{1,r}\, ; \quad p=\overline{1,l}\, ; \tag{6}$$

$$f_{i2}^{(k)} = \int_{a_0}^{z} A_{iiii}^{(r)} \int_{a_m}^{z} f_{i1}^{(s)} a_{i3i3}^{(s)} dz^2 - \varphi_i^{(k)} \int_{a_0}^{a_n} A_{iiii}^{(l)} \int_{a_m}^{z} f_{i1}^{(p)} a_{i3i3}^{(p)} dz^2 \; ;$$

$$f_{i3}^{(k)} = \theta_i^{(k)} - \theta_i^{(n)}(a_n)\varphi_i^{(k)} \; ; \quad f_{i4}^{(k)} = 2\varphi_i^{(k)} - 1 \; ;$$

$$F_1^{(k)} = 2\eta_1^{(k)} / \eta_1^{(n)}(a_n) - 1 \; ; \quad F_2^{(k)} = 0{,}5(F_1^{(k)}+1)\eta_2^{(n)}(a_n) - \eta_2^{(k)} \; ;$$

$$F_3^{(k)} = \eta_3^{(k)} \; ; F_4^{(k)} = \int_{a_0}^{z} \varphi_i^{(r)} dz - \int_{a_0}^{a_n} \varphi_i^{(l)} dz (z-a_0)/h \; ;$$

$$F_5^{(k)} = \eta_1^{(k)} - \eta_1^{(n)}(a_n)(z-a_0)/h \, ,$$

where

$$\zeta_i = \int_{a_0}^{a_n} A_{iiii}^{(l)} z dz \Big/ \int_{a_0}^{a_n} A_{iiii}^{(l)} dz \; ; \quad \varphi_i^{(k)} = \int_{a_0}^{z} A_{iiii}^{(r)} dz \Big/ \int_{a_0}^{a_n} A_{iiii}^{(l)} dz \; ;$$

$$\eta_\alpha^{(k)}(z) = \int_{a_0}^{z} (f_{1\alpha}^{(r)} + f_{2\alpha}^{(r)}) dz \; ; \quad \theta_i^{(k)} = \varphi_{3i}^{(k)} + \zeta_0 \varphi_{4i}^{(k)} \; ;$$

$$\varphi_{3i}^{(k)}(z) = \int_{a_0}^{z} A_{iiii}^{(r)} \varphi_0^{(r)} dz \; ; \quad \varphi_{4i}^{(k)}(z) = \int_{a_0}^{z} A_{iiii}^{(r)} \int_{a_m}^{z} dz^2 \; ;$$

$$\varphi_0^{(k)}(z) = \int_{a_m}^{z} \int_{a_0}^{z} a_{3333}^{(r)} dz^2 \; ; \quad \delta_{11} = \delta_{22} = 1 \; ;$$

$$\zeta_0 = [\delta_{ii} \int_{a_0}^{a_n} \varphi_{3i}^{(l)} dz - \delta_{ii} \varphi_{3i}^{(n)}(a_{n)} \int_{a_0}^{a_n} \varphi_i^{(l)} dz] / [\delta_{ii} \varphi_{4i}^{(n)}(a_{n)} \int_{a_0}^{a_n} \varphi_i^{(l)} dz - \delta_{ii} \int_{a_0}^{a_n} \varphi_{4i}^{(l)} dz] \; ;$$

On the facial surfaces $z=a_0$ and $z=a_n$ functions $f_{i\alpha}^{(k)}$, $F_s^{(k)}$ $(s=\overline{2,5})$ have zero meaning and the remaining ones are equal to 1 and -1. Functions $f_{i1}^{(k)}$, $F_1^{(k)}$ were used in [3-5 and others], while $f_{i2}^{(k)}$ are introduced in [3] and the remaining - are proposed here. Let's mark that introduced approximations $f_{i3}^{(k)}$, $F_3^{(k)}$ coincide in quality with the given in [1] exact solutions for $\sigma_{i3}^{(k)}$.

Functions $\beta_{i2}(x_j)$ and $\gamma_2(x_j)$ can be neglected. However, in the places of the localization of loading and also under relationship between coefficients of pliability of the material $a_{\alpha\beta\gamma\delta}^{(k)}$ in the layer, or in the different layers of more then 10^3 [3] they specify SSS essentially.

Under the arbitrary directed vector of loading $Y_{\alpha 0}$, $Y_{\alpha n}$ the hypotheses will look like:

$$\sigma_{i3}^{(k)} = f_{i\alpha}^{(k)} \beta_{i\alpha} + (\varphi_i^{(k)} - 1) Y_{i0} + \varphi_i^{(k)} Y_{in} \; ; \quad \alpha = \overline{1,3}\, ; \quad i = \overline{1,2}\, ; \tag{7}$$

$$\sigma_{33}^{(k)} = F_p^{(k)} \gamma_p + 0{,}5(F_1^{(k)} - 1) Y_{30} + 0{,}5(F_1^{(k)} + 1) Y_{3n} \; ; \quad p = \overline{2,5} \; ;$$

They contain six unknown functions of the transverse shear $\beta_{i\alpha}$ and four unknown functions of the cross compression γ_s. In the linear elastic problem instead of (7) it is possible to consider 4 simplier problems (2)-(5) under symmetric structure and 3 - under any structure of the package of layers.

In case of stationary facial thermal affect with the known temperature T_0 , T_n on the facial surfaces $z=a_0$, $z=a_n$ the distribution of the temperature along the thickness of the plate can be introduced as a piece-linear law [6] with approximating function $\psi_\lambda^{(k)}$. Using (2),(3) and dividing the temperature into constant in thickness symmetric $T_p(z)=(T_0+T_n)/2=t_p$ and obliquesymmetric $T_q(z)=(2\psi_\lambda^{(k)}-1)t_{qn}$, $t_{qn}=(T_n-T_0)/2$ components, let's take hypotheses in the form:

$$\sigma_{i3}^{(k)} = S_{i1}^{(k)}(z^1)t_{p},_i + S_{i2}^{(k)}(z^2)t_{qn},_i + f_{i\alpha}^{(k)}\beta_{i\alpha}\ ; \quad \sigma_{33}^{(k)} = F_p^{(k)}\gamma_p\ ; p=\overline{2,5}\ ; \qquad (8)$$

where the division into unflexural ($\beta_{ij}=\gamma_2=\gamma_4=0$ under $t_{qn}=0$) and flexural ($\beta_{i3}=\gamma_3=0$ under $t_{qn}=0$) deformation is possible only in the case of symmetry of the structure of the plate in its thickness.

Functions $S_{ij}^{(k)}$ look like:

$$S_{i1}^{(k)} = \int_{a_0}^{z} A_{iijj}^{(r)}\alpha_j^{(r)}dz - \overline{\alpha_j}\int_{a_0}^{z} A_{iijj}^{(r)}dz; \psi_\lambda^{(k)} = \int_{a_0}^{z}(\lambda_3^{(r)})^{-1}dz \Big/ \int_{a_0}^{a_n}(\lambda_3^{(l)})^{-1}dz;$$

$$S_{i2}^{(k)} = \int_{a_0}^{z} A_{iijj}^{(r)}\alpha_j^{(r)}(2\psi_\lambda^{(r)}-1)dz - (2\overline{\alpha_j}/h)\int_{a_0}^{z} A_{iijj}^{(r)}(z-\zeta_j^t)dz\ ,$$

where $\alpha_j^{(k)}$ are coefficients of the temperature widening of the layer in the directions x_j, and $\overline{\alpha_j}$ - average in the thickness of the plate; $\lambda_3^{(k)}$ is the coefficient of thermal conductivites in the direction of axes z.

The values of $\overline{\alpha_j}$ are defined from two equations $S_{i1}^{(n)}(a_n)=0$ and then ζ_j^t from $S_{i2}^{(n)}(a_n)=0$. They insure self-balance in the thickness of transverse shear stresses in the "free" plate with the linear depedence of $T(z)$ from z.

Let's introduce the kinematic model (1) corresponding to hypotheses (2)-(5) or (7), (8) in a summarized look (by analogy with [4,5]):

$$u_3^{(k)} = v_3 + \psi_{p,3}^{(k)}(z)\ \gamma_{p3} + U_3\ ;$$

$$u_i^{(k)} = v_i - \psi_0^{(k)}(z)\ v_{3,i} - \psi_p^{(k)}(z)\ \gamma_{p,i} - \psi_{i\alpha}^{(k)}(z)\ \beta_{i\alpha} + U_i \qquad (9)$$

where U_α are addings, containing components of facial loadings, temperatures and their derivatives.

The expressions for the SSS components may be obtained by filling (9) into the Cauchy's correlation and then into the law of Hooke. This leads to the unfulfilling in $\sigma_{33}^{(k)}$ of static conditions on the facial surfaces of layers , which in the problems of the curve has a little influence on the accuracy of computation. However, the definition $\sigma_{33}^{(k)}$ from the law of Hooke and not from the hypothes, allows to get a symmetric matrix of coefficients in the solutable system of differential equations of the linear elastic problem:

$$L_{\varepsilon\alpha}(v_\alpha) + L_{\varepsilon p}(\gamma_p) + L_{\varepsilon i\alpha}(\beta_{i\alpha}) = Z_\varepsilon\ ; \qquad \varepsilon=\overline{1,13}. \qquad (10)$$

Here $L_{\varepsilon s}$ (...) are differential operators of a not higher that the fourth level, and Z_ε are expressions for loading and temperature. System (10) with the correspondent boundary conditions is gotten according to the methodics [3-6] from the variational equation of Lagrange. The general order of differentiation (10) does not depend on the quantity of layers (continual model), and the part of each of the functions v_i , $\beta_{i\alpha}$ in it makes 2, and functions v_3 , γ_s - 4. That is why for each of the hypotheses separately (2)-(5) the general order of differentiation (10) will be given below.

Numerous solutions, obtained according to the proposed models for extreme meanings of stresses $\sigma_{i\alpha}^{\#}=10\sigma_{i\alpha}^{(k)}/g_0$ and of displacement $u_3^{\#}=10u_3^{(k)}\ G_{12}^{(k)}/(g_0 h)$ (in table meanings marked*) practically coincide for a square $b_1 \times b_2 \times h$, $b_i/h=3$ two-layer plate under boundary Navier-type with the exact three-dimensional solutions obtained according to methodics [1] (kindly given to the author by A.V.Marchuc). Loadings: $[q_3;p_{3n}] = g_0 sin(\pi x_1/b_1)\ sin(\pi x_2/b_2)$; $[q_{1n}+ q_{2n} ; p_1+ p_2] = g_0 cos(\pi x_i/b_i)\ sin(\pi x_j/b_j);\ i \neq j$. Characteristics of transversal-isotropic layers: $h^{(1)} = 2\ h/3;\ h^{(2)} = h/3;\ G_{12}{}^{(k)} = 10^4 MPa;$ $E_i{}^{(k)} = 2,6\ G_{12}{}^{(k)};\ E_3{}^{(1)} = 0,1\ E_i{}^{(k)};\ E_3{}^{(2)} = 0,5\ E_i{}^{(k)};\ G_{i3}{}^{(1)} = 0,5\ G_{12}{}^{(k)};\ G_{i3}{}^{(2)} = 0,2 G_{12}{}^{(k)};$ $\nu_{12}{}^{(k)} = \nu_{21}{}^{(k)} = \nu_{3i}{}^{(k)} = 0,3;\ \nu_{i3}{}^{(1)} = 0,03;\ \nu_{i3}{}^{(2)} = 0,15;\ i,k = \overline{1,2}$.

z/h	Y_α	$u_3{}^{\#}$	$\sigma_{13}{}^{\#}$	$\sigma_{33}{}^{\#}$	$\sigma_{11}{}^{\#}$	$\sigma_{12}{}^{\#}$
1	q_i	26,02	-10,00	0	46,71	-25,15
		*25,91	-10,00	0,02	46,80	-25,20
5/6		26,61	-0,90	1,72	23,10	-12,04
		*26,53	-0,88	1,69	23,14	-12,06
2/3		26,15	2,94	1,23	6,75	-3,35
		*26,08	2,91	1,20	6,80	-3,35
1/3		26,13	2,78	-1,17	-7,47	3,75
		*26,06	2,79	-1,19	-7,43	3,76
0		24,61	-10,00	0,00	-52,70	28,38
		*24,56	-10,00	0,01	-52,96	28,44
1	q_3	67,25	0,00	10,00	61,18	-30,64
		*66,94	0,00	9,96	60,86	-29,89
5/6		62,93	10,74	7,84	24,09	-11,16
		*62,65	10,81	7,83	23,97	-10,92
2/3		59,65	13,22	3,45	-3,00	2,41
		*59,30	13,19	3,45	-2,89	2,35
1/3		59,55	10,93	-5,09	-8,06	3,17
		*59,20	10,87	-5,07	-7,96	3,06
0		59,98	0,00	-10,00	-45,86	22,39
		*59,61	0,00	-10,02	-45,62	22,01
1	p_i	4,61	-10,00	0	-6,96	1,44
		*4,52	-10,00	0,03	-7,05	1,39
5/6		4,51	-4,58	2,45	-1,20	-1,63
		*4,46	-4,50	2,39	-1,22	-1,68
2/3		3,01	-1,49	3,47	0,28	-2,39
		*2,98	-1,42	3,40	0,19	-2,41
1/3		2,60	1,72	3,31	-0,95	-1,75
		*2,60	1,77	3,38	-1,03	-1,75
0		3,27	10,00	0,00	-4,22	-0,04
		*3,24	10,00	0,00	-4,33	0,02
1	p_3	-12,30	0,000	-10,00	-6,96	1,44
		*-12,22	0,000	-9,98	-6,84	1,44
5/6		-6,06	-0,587	-9,85	-1,20	-1,62
		*-6,04	-0,596	-9,88	-1,14	-1,63
2/3		0,19	-0,232	-9,70	0,28	-2,39
		*0,10	-0,244	-9,76	0,22	-2,41
1/3		2,65	0,358	-9,78	-0,95	-1,75
		*2,62	0,369	-9,80	-1,02	-1,80
0		5,03	0,000	-10,00	-4,22	-0,04
		*4,99	0,000	-9,98	-4,36	-0,12

The influence in symmetric components rises with the decrese of the relative transversal rigidness of the layer [1,2].

CONCLUSIONS

While building continual models of the deformation of layer plates, the specificiti of unflexural and flexural deformation from symmetric and oblique-symmetric components of bilateral loadings and temperature is considered. This made it possible to specify the known models.

The author thenks professor V.G.Piskunov and doctor A.V.Marchuc for assistance in the preparation of the report.

REFERENCES

[1] Piskunov, V.G., Sipetov, V.S., Tuimetov, Sh.Sh. "Solution of the problem of statics for laminated orthotropic plates in the space situation". Prikladnaia Mekhanika, Vol.26, N 2, pp. 41-49 (1990).

[2] Prusakov, A.P. "On the theory of bending of laminated plates". Prikladnaia Mekhanika, Vol.33, N 3, pp. 64-70 (1997).

[3] Rasskazov, A.O., Burygina, A.V. " To the specification of shift theory of orthotropic hoping shells". Prikladnaia Mekhanika, Vol.24, N 4, pp. 32-37 (1988).

[4] Piskunov, V.G., Verijenko, V.E. "Linear and non-linear problems of computation laminated constructions". Kiev: Budivelnik, 176 p. (1986).

[5] Gurtovy, O.G., Piskunov, V.G. " New account patterns and comparison of approximate specified with exact three-dimensional solutions problems of the flexure laminated anisotropic plates". Mechanics of Composite Materials, N 1, pp. 93-101 (1988).

[6] Piskunov, V.G., Sipetov, V.S. "Calculation of laminated hoping shells of anisotropic composits for static and themperature action". Problemy Prochnosti, N 10, pp. 79-82 (1987).

BUCKLING AND FAILURE ANALYSIS OF FRP FACED SANDWICH PLATES

A. MUC and P. ZUCHARA

Institute of Mechanics & Machine Design,Cracow University of Technology,ul. Warszawska 24,31-155 Kraków, Poland

INTRODUCTION

Failure analysis of plated and shell sandwich structures having FRP faces is a complex problem especially due to variety of global (overall) and local instabilities encountered in such constructions in practice. It is known that the mechanical characterisation of FRP faced sandwich construction is generally orthotropic. In addition, due to the low core shear moduli (in-plane and transverse shear) the evaluation of theoretical failure loads is strongly dependent on the used approximations understood in the sense of 2-D and (or) 3-D formulations of plate or shell theories.
A considerable body of literature exists on the modelling, analysis and design of sandwich plates and shells. Lists and reviews of the contributions are given in the review papers [1,2,3]. The cited survey papers demonstrate the variety of trends in modelling sandwich structures as well as point out the diversity of the recent progress in this area.

Sandwich construction analysed herein consists of two faces made of multilayered FRP (fibre reinforced plastic) and separated by an isotropic core – Fig. 1.

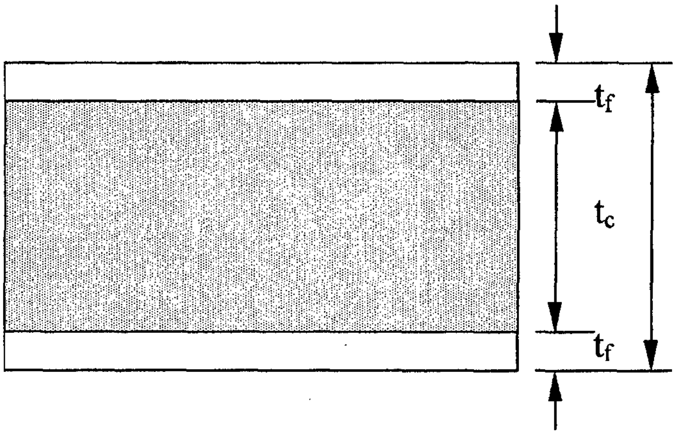

Figure 1. Geometry of sandwich structures having multilayered composite face sheets.

The objectives of the present work are following: (i) to discuss the effects of used 2-D formulations (kinematical hypotheses) on values of global buckling loads and on the prediction of natural frequencies and (ii) to model stress distributions and concentrations with the use of 3-D FE approach. The attention is mainly focused on one particular construction,i.e. rectangular plates subjected to axial compression. The theoretical analysis have been conducted for simply supported sandwich plates in order to be in an agreement with the experiments. Therefore, the overall buckling loads have been determined with the use of the classical Rayleigh-Ritz method. In addition the assumed type of boundary conditions allows us to model easily the local failure modes connected with the local instabilities.

2-D FORMULATIONS OF GOVERNING EQUATIONS

For sandwich structures the formulations of governing equations are based on the variety of assumptions dealing mainly with: (1) kinematical hypotheses,i.e. the form of series representations of 3-D displacements with respect to the thickness z coordinate, (2) the assumed form of geometrical relations, (3) statical hypotheses and (4) the assumed material models of the faces and (or) particularly of the sandwich core (e.g.corrugated). The first part of our investigations is devoted to the discussion of kinematical assumptions effects on overall buckling and natural frequencies. In particular, we adopt herein three different sandwich plate theories (so-called global laminatewise formulation), based on : a) the HSDT theory suggested by Reddy, b) the FSDT and c) the Love-Kirchhoff classical theory. The normal deflection w is the same for the core and composite faces. In addition, let the core material sustains only transverse shear stresses.

For simply-supported boundary conditions with the use of the standard procedures, the Hamiltonian principle (for free vibrations problems) and the Lagrangian principle (overall buckling), finally one can find the required solutions in the closed analytical form. For higher ordered plate theories the computations are associated with a great number of algebraic relations and transformations. To simplify it one can apply the symbolic packages , e.g. *Maple* or *Mathematica*.

FREE VIBRATIONS AND OVERALL BUCKLING (2-D)

The correctness of the evaluated relations have been verified with the use of the NISA II finite element program [4]. The plate have been discretized with the use of 64 eight noded quadrilateral sandwich elements (NKTP 33). The results of analytical and numerical calculations are shown in Tables 1 and 2.

Eigenmodes (m,n)	**L-K**	**FSDT**	**HSDT**	**NISA II**
(1,0)	11.76	8.77	8.05	7.60
(1,1)	29.85	15.80	14.13	13.95
(2,0)	47.05	22.98	18.23	17.79
(1,2) or (2,1)	69.35	26.88	21.84	21.09

Table 1. Comparison of dimensionless natural frequencies [$\Omega = (\omega b^2/t)(\rho/E_2)^{0.5}$] for sandwich plates ($a/b = 1$, $t/b = 0.1$, $t^c/t = 0.8$, $\rho^c / \rho^f = 0.8$, $\theta = 45$ deg).

Computations have been carried out for sandwiches having graphite/epoxy resin faces and isotropic cores. The mechanical properties of materials used are given below:

Faces:
$E_1 = 125.79$ GPa, $E_2 = 13.03$ GPa, $G_{12} = 6.41$ GPa, $G_{13} = G_{32} = 3.21$ GPa, $\nu_{12} = 1/3$,
$\rho = 2800$ kg/m^3

Core: $G_{13} = G_{32} = 1.603$ GPa

As it may be seen the agreement of pure numerical results and analytical ones seems to be very good and increases as the order of the applied theory increases. However, it should be noticed that the good results have been obtained with the use of the global (laminatewise) theory. This is possible since we intend to describe an overall behaviour of the structures. Local effects understood in the sense of local instabilities require more precisely defined kinematical effects and it leads to the increase of the number of independent kinematical variables in 2-D approach or to 3-D analysis. Let us note that the discrepancy between HSDT and FSDT is rather small so that from practical point of view FSDT may be used even for considered moderately thick sandwich plates.
With the use of the closed analytical form of final relations for natural frequencies or buckling loads it is possible to solve optimization problems. Some results in that area are presented by Muc,Zuchara [5].

Eigenmodes (m,n)	**L-K**	**FSDT**	**HSDT**	**NISA II**
(1,0)	60.17	64.11	69.04	71.15
(1,1)	72.81	78.03	79.28	85.14
(2,0)	91.43	95.4	98.78	103.6
(1,2) or (2,1)	108.32	117.11	121.32	128.4

Table 2. Comparison of dimensionless buckling load factor $\lambda = N_{calc} / N_x$ for sandwich plates ($a/b = 1$, $t/b = 0.1$, $t^c/t = 0.8$, $\rho^c / \rho^f = 0.8$, $\theta = 45$ deg).

Numerical eigenvalue extraction methods for buckling and free vibration problems are identical. However,the differences of the eigenvalues determined with the use of various methods not exceeded 1 %.

FE MODELLING OF FAILURE

In addition to classical overall (global) buckling sandwich constructions can undergo several local failure modes commonly associated with local buckling instabilities. In order to model them in a consistent manner it is necessary to take into account not only transverse shear stress components but also the normal stress component denoted herein as σ_{zz} (σ_{33}). For plated or shell structures it is possible to introduce it as additional parameter (kinematical or statical variable) or to model the problem in a pure numerical way with the use of FE. Due to the complexity of the problem for arbitrary loading and boundary conditions our attention is mainly focused on FE modelling of sandwich structures in 3-D approach. Similarly as previously we consider sandwich plate with FRP faces subjected to in-plane compressive loads. To compare the results various types of FE have been used:

A. 3-D solid hexahedron (brick) 20 nodes elements (NKTP 4)– they possess extra shape functions enable the element to model pure bending problems exactly.
B. 3-D solid hexahedron (brick) 20 nodes laminated composite elements (NKTP 7) – the elements are suited for modelling various stacking sequences of FRP faces and have all capabilities of the previous elements (model A).
C. The interface between FRP faces and the core is described by 3-D gap-friction elements (NKTP 50) having high stiffness in order to determine more exactly the mechanical characteristics of bonding – the FRP faces and core deformations are discretized with the use of 3-D (NKTP 4) elements.
D. The same as previously but NKTP 4 elements have been replaced by NKTP 7 elements.

The results of the comparative studies are presented in Table 3 and in Fig.2. A quarter of a simply supported plated have been divided in the z – direction into 5 layers having the identical thicknesses. Each layer is divided into 100 elements (equal division in x and y directions). Two external layers have characterized the FRP faces behaviour, whereas 3 internal - the sandwich core. The material and geometrical parameters of the plate are identical as those discussed in the previous section. There is only one difference in the thickness ratio since now $t^c/t = 0.6$.

Maximal stresses in [MPa]	**Model A**	**Model B**	**Model C**	**Model D**
σ_{zz}	0.061	0.059	0.0505	0.0495
σ_{zx}	0.032	0.03	0.024	0.024
σ_{zy}	0.034	0.0305	0.0243	0.024
σ_{yy}	0.31	0.295	0.277	0.265

Table 3. Comparison of maximal (absolute) values of stress tensor components – the faces are made of FRP oriented at 90 deg.

As it may be noticed the highest difference between models occurs for geometrically nonlinear contact elements (C and D) and linear (A and B). There is no visible differences between solid (classical) elements and composite elements – e.g. the results for models A and B. However, it is worth to note a great influence of normal and transverse shear stresses – their magnitudes are of the same order as the magnitudes of the stresses in the direction y of the compressive external forces having the intensity 0.05 [MPa].

The highest compression is always observed in the interface region and may result in the local loss of stability of faces or of the core. Therefore, for sandwich structures all failure criteria should take into account all 3-D components of the stress tensor.

Figure 2 gives also the indication on the effects of orthotropy. The increase of the faces strength in the compression direction reduces the maximal values of the normal stresses. For isotropic structures the normal shear stress effects may be completely neglected.

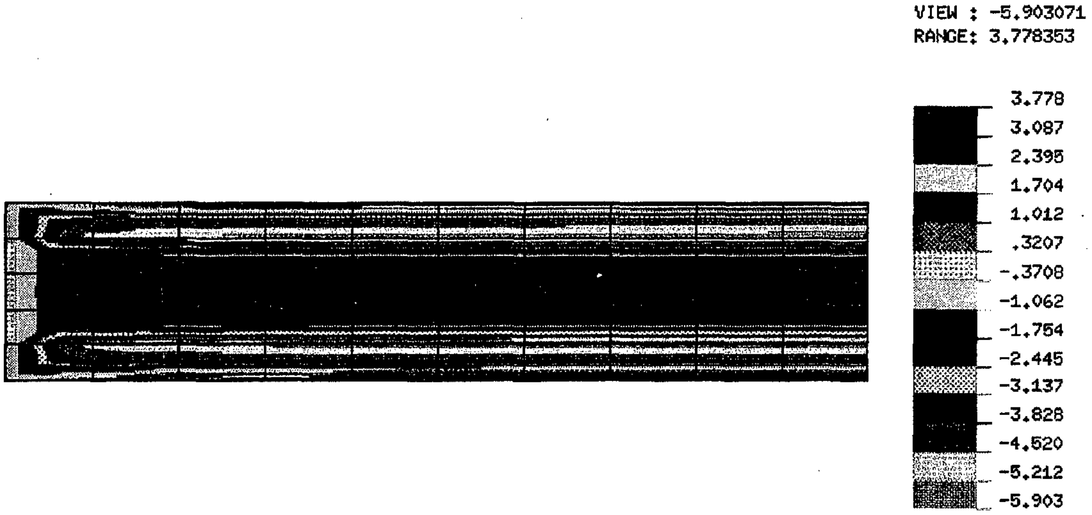

a) FRP faces oriented at 0 ^{0}

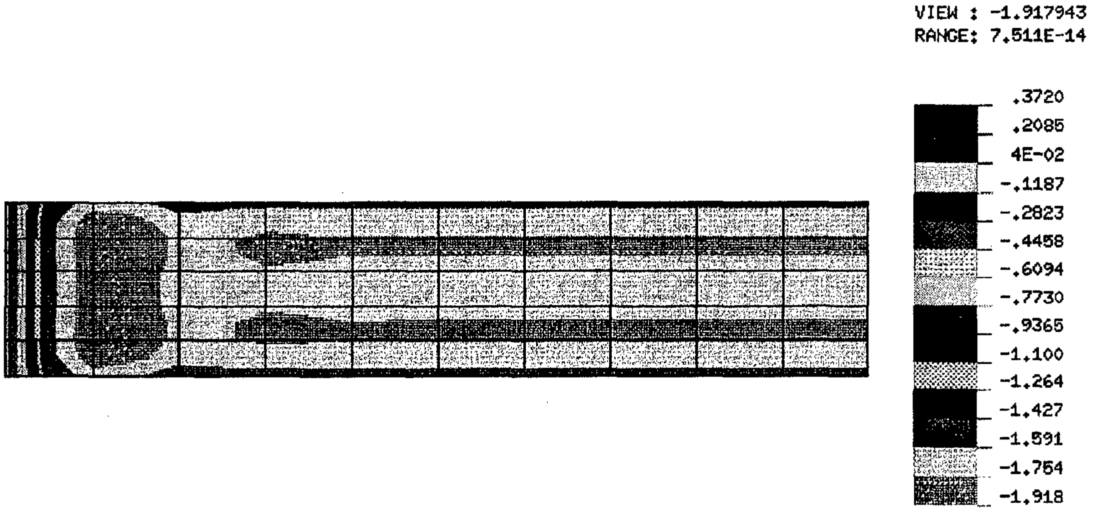

b) isotropic plate

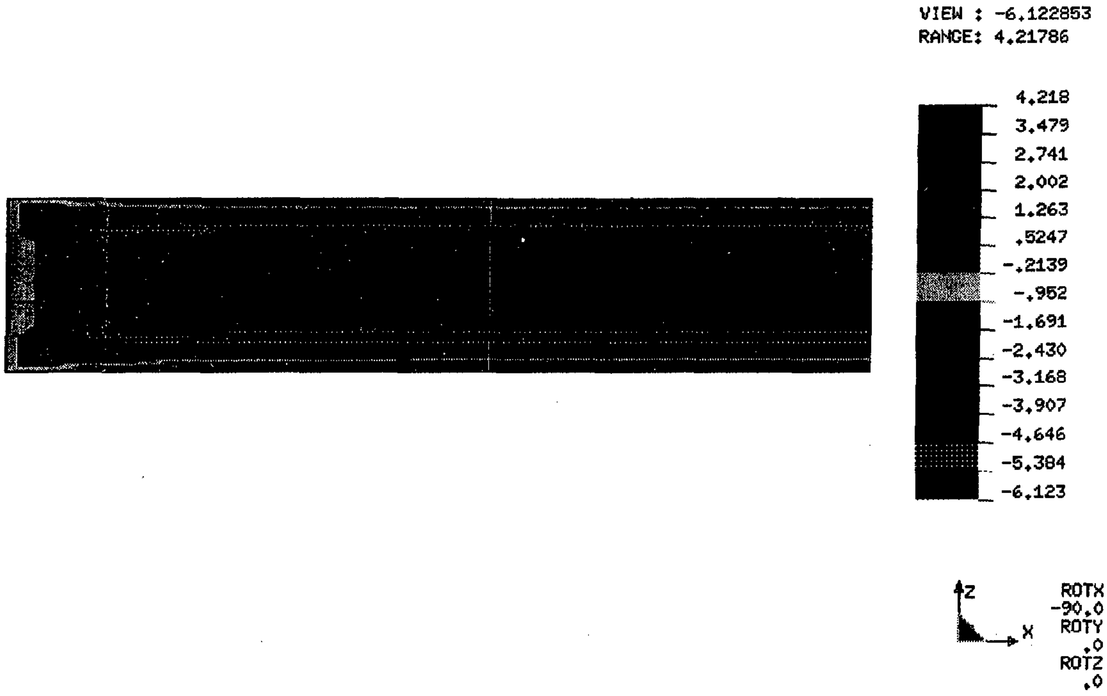

c) FRP faces oriented at 90 ^{0}

Fig.2. Distributions of normal stresses σ_{zz}.

REFERENCES

[1] Noor,K.A.,Burton,W. S., Bert C.W., Computational models for sandwich panels and shells, *Appl. Mech. Rev.*, **49**,pp. 115-199 (1996).

[2] Rao, K.M., Buckling analysis of FRP faced anisotropic sandwich plates , *AIAA J.*, **23,** pp.1247-53 (1985).

[3] Noor, K.A.,Burton, W.S., Assesment of computational models for multilayered composite plates,*Composite Str.*,**14**,pp. 233-265 (1990).

[4] NISA II, User's Manual, EMRC Troy (1996).

[5] Muc,A.,Zuchara,P., Sandwich plates – free vibrations and damping analysis, *Mech. Kompozitn. Mater.* , 1998 (in print).

STRESS CONCENTRATION IN BENDING OF SANDWICH PANELS UNDER POINT FORCES

V. POLYAKOV

Institute for Polymer Mechanics, Latvian Academy of Sciences
23 Aizkraukles St., LV-1006, Riga, Latvia

INTRODUCTION

The growing use of sandwich and laminated plates requires a theoretical based prediction of the mechanical behaviour of such structural elements. Starting with a pioneering papers of E. Reissner, W. Allen there are developed a great number of theories for engineering calculations. The classification of theories and the discussion some of them in detail was given in [1].The expanding range of investigations is motivated by the need for the consideration of physical features in behavior of structural sandwich elements under different loading conditions, thermal and dynamic loads included. Integral characteristics of a structure at the loss of stability and the fundamental vibrations have been studied first. Qualities of the local behavior of a layered model were examined in the general context of a stability problem in [2]. Nevertheless, the local stress fields in the vicinity of point forces and/or fixing points of a sandwich still remain not clearly understood. The general method of calculation of local characteristics based on the solutions in boundary functions for the semi-infinite layered models was given in [3]. The solution of boundary-value problem for the finite length panel [4] was proposed by the method incommensurably more complex relative to a design procedure needed in an engineering practice. The guideline in selection of the particular version of theory is the opportunity to give the clear-cut physical interpretation of all final and intermediate results of its application and the scope for going from a complex structural geometry to that ordinary (e.g. from layered structure to that uniform).

PROBLEM STATEMENT

For the purpose to derive the analytical solution version, considering a local load factor in the work the discrete model is used, which consider the Kirchhoff-Love kinematics of deformation of face layers and the transversal compression combined with shear of a midlayer. Under these assumptions the mechanism of traction transfer between the layers, based on energy estimates, is not considerably simplified, however it can be analyzed more easily than with the use of numerical solutions.

Cylindrical bending by point forces, each of them being invariable along the panel width, is considered using the refined applied method [5]. The method is based on the analytical solution of the variational problem for sandwich plates.

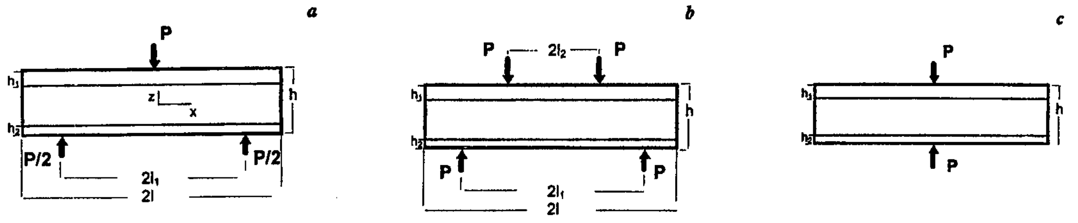

Fig.1 Point-force loading chart of a sandwich panel

In the present statement the longitudinal and transverse displacements of the midplane of the outer sandwich layers are representative of the four degrees of displacement freedom of the model. The set of the Euler equations of the variational problem $\delta V = 0$ for the functional of the total energy V, obtained for the independent displacements has the following form

$$\frac{d^2u_i}{d\xi^2} \pm \frac{k_1}{n_i\chi_i}\left[u_2 - u_1 + \frac{1}{2}\left(\frac{dw_1}{d\xi} + \chi_0\frac{dw_2}{d\xi}\right)\right] = 0$$

$$i = 1, 2 \qquad (1)$$

$$\frac{d^4w_i}{d\xi^4} \pm \frac{6}{\mu_i^2\chi_i^2}\cdot\frac{d^3u_i}{d\xi^3} \mp \frac{12k_2}{n_i\chi_i^3}\left(w_2 - w_1\right) = q_i$$

where assumed that if $i = 1$ then $\mu_1 = \mu$, $\chi_1 = n_1 = 1$ and the upper sign is taken, but if $i = 2$ then alongside with the lower sign the parameters $\mu_2 = \mu/\sqrt{\chi_0}$, $\chi_2 = \chi$, $n_2 = n_x$ are taken. In Eqs. (1) the following nondimensional variable and parameters are introduced:

$$\xi = \frac{x}{h_1 + h_0}, \qquad q_0 = \frac{6P(1-\nu_1^2)}{E_x^{(1)}b(h_1 + h_0)\mu^3}, \qquad n_x = \frac{E_x^{(2)}(1-\nu_1^2)}{E_x^{(1)}(1-\nu_2^2)}$$

$$\mu = \frac{h_1}{h_1 + h_0}, \quad \chi = \frac{h_2}{h_1}, \quad \chi_0 = \frac{h_2 + h_0}{h_1 + h_0}, \qquad (2)$$

$$n_z = \frac{E_z}{E_x^{(1)}}(1-\nu_1^2), \quad m_z = \frac{G_{xz}}{E_x^{(1)}}(1-\nu_1^2), \quad k_1 = \frac{m_z}{\mu(1-\mu)}, \quad k_2 = \frac{n_z}{\mu^3(1-\mu)}$$

The displacements w_i and u_i in Eqs. (1) are also dimensionless (related to $h_0 + h_1$) and E_z, G_{xz} are respectively the shear and compression elastic moduli of the midlayer (core). For the point loading the right-hand sides of Eqs. (1) are given in terms of the Dirac function $\delta(\xi)$ and for the three-point bending, see Fig. 1 *a*, they are:

$$q_1 = 2q_0\delta(\xi), \qquad q_2 = -\frac{q_0}{n_x\chi^3}\delta(|\xi| - \xi_1) \qquad (3)$$

In the case of a uniform load, see Fig. 2 *a*, equal to *P/2bl* (*b* - panel width) the function $\delta(\xi)$ in the relation (3) when $i = 1$ is replaced with the unit function divided by $2\xi_l$. Boundary conditions at the free panel end $\xi = \xi_l$ are the natural boundary conditions determined upon variation of the total energy functional V:

$$w_i'''(\pm\xi_l) - \frac{3k_1}{n_i\mu_i^2\chi_i^3}[w_1' + \chi_0 w_2' + 2(u_2 - u_1)]_{\pm\xi_l} = 0$$

$$w_i''(\pm\xi_l) = u_i'(\pm\xi_l) = 0, \qquad i = 1,2 \tag{4}$$

Due to the application of the Dirac $\delta(\xi)$-function in light of the local nature of the load under the action of point forces the Laplace integral transformation was used in solving the set of equations of the twelfth order. The solution method allows us to pass to the limit in the sought-for function instead of the calculation leading to the solution in the case of expansions into the Fourier series. On the other hand the fundamental functions available from this method give us a convenient way to define the kinematics characteristics at the panel central section in terms of the unknown constants in the Cauchy problem. Laborious calculations by this method were presented in [5]. In the work [6], that follows, the general solution was obtained for bending of an asymmetric structure panel under uniform piecewise continuous load.

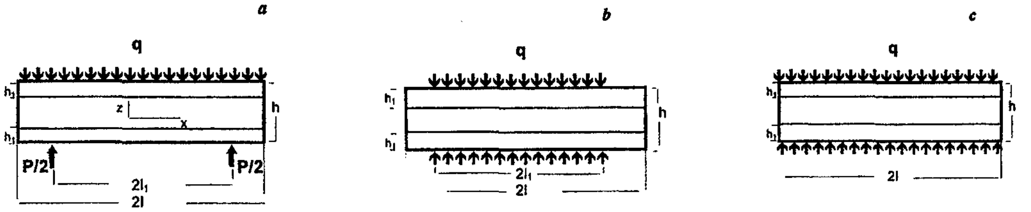

Fig. 2. Piecewise uniform load chart of a sandwich panel

Presented here are the cases of the loading of a symmetric structure panel ($E_x^{(1)} = E_x^{(2)}$, $h_1 = h_2$) at the different disposition of point forces and piecewise constant load, along with the cases of the limiting process in the physical and geometric parameters of the sandwich model.

RESULTS AND DISCUSSION

An analysis of the solutions obtained in [5], [6] has shown, that all design characteristics of the problem considered in the case of asymmetric sandwich structure are dependent on both transverse rigidities of the core - in shear and compression, as their coupling occurs at the stage of eigenvalues derivation of the boundary-value problem. However with a symmetric sandwich structure the core transversal stresses in shear τ_{xz}^0 and compression σ_z^0 are dependent respectively on nothing but relative physical parameters G_{xz} / E_x^{out} and E_z / E_x^{out}. Because of this the symmetric parts of deflections and longitudinal displacements *(w₁ - w₂)/2* and *(u₁ + u₂)/2* like their antisymmetric component *(w₁ + w₂)/2* and *(u₁ - u₂)/2* are liable to be of specific interest in the analysis of the results depending on physical parameters of the model. As for the stresses and displacements of face layers, they are the functions of both physical parameters mentioned, however we have succeeded in separating the contribution of these parameters in the form of individual solution summands.

The key characteristics, defining local deformation in bending of a sandwich panel are the relative transverse compression of a central section $\hat{w}_\Delta = [w_1(0) - w_2(0)]/q_0$ and the relative increment of a local curvature at the panel center κ_α. For a symmetric structure both of these parameters are dependent on merely the relative rigidity in compression $\alpha = (6k_2)^{1/4}$, whereas the relative values of face layer curvatures $w_1''(0) = -q_0(\hat{\xi}_1/2 + \kappa_\alpha)$ and $w_2''(0) = -q_0(\hat{\xi}_1/2 - \kappa_\alpha)$ are also the functions of the shear parameter $a_1 = [2\mu^2 k_1/(3+\mu^2)]^{1/2}$ entering in the expression for a double value of the mean curvature:

$$\hat{\xi}_1 = \frac{\xi_1}{1+3/\mu^2} + \frac{sh a_1\xi_l - sh[a_1(\xi_l - \xi_1)]}{a_1(1+\mu^2/3) ch a_1 \xi} \tag{5}$$

For the above-mentioned local parameters the following formulae can be found for the case of loading by three point forces (Fig. 1 *a*):

$$\hat{w}_\Delta = \frac{s''(\alpha\xi_l) + s''[\alpha(\xi_l - \xi_1)] - 2\kappa_\alpha s'''(\alpha\xi_l)}{4\alpha^4 s'(\alpha\xi_l)} \tag{6}$$

$$\kappa_\alpha = \frac{2}{\alpha} \cdot \frac{s'(\alpha\xi_l)[s'(\alpha\xi_l) + s'[\alpha(\xi_l - \xi_1)]] - s(\alpha\xi_l)[s''(\alpha\xi_l) + s''[\alpha(\xi_l - \xi_1)]]}{s'^2(2\alpha\xi_l) - s(2\alpha\xi_l)s''(2\alpha\xi_l)} \tag{7}$$

where $s(\alpha\xi) = sh\,\alpha\xi \sin\alpha\xi$, and by a prime the operation of derivation with respect to relative variable ξ is designated. In the case of distributed bilateral pressure at the section *2l₁* , that is less than *2l*, see Fig. 2 *b*, the formulae take the form:

$$\hat{w}_\Delta = \frac{s'(\alpha\xi_l) - s'[\alpha(\xi_l - \xi_1)] - \kappa_\alpha \xi_1 s'''(\alpha\xi_l)}{2\alpha^4 \xi_1 s'(\alpha\xi_l)} \tag{8}$$

$$\kappa_\alpha = \frac{sh\,\alpha\xi_l\, sh\,\alpha(\xi_l - \xi_1)\sin\alpha\xi_1 + sh\,\alpha\xi_1 \sin\alpha\xi_l \sin\alpha(\xi_l - \xi_1)}{\alpha^2\xi_1(sh\,2\alpha\xi_l + \sin 2\alpha\xi_l)} \tag{9}$$

The asymptotic formulae for $l \to \infty$ (an infinite strip) in the above two cases are found as:

$$\text{Fig. 1 } a\text{: } \lim_{\xi_l \to \infty} \hat{w}_\Delta = \frac{1 + e^{-\alpha\xi_1}(\cos\alpha\xi_1 + \sin\alpha\xi_1)}{4\alpha^3}, \quad \text{Fig. 2 } b\text{: } \lim_{\xi_l \to \infty} \hat{w}_\Delta = \frac{1 - e^{-\alpha\xi_1}\cos\alpha\xi_1}{2\alpha^4\xi_1}$$

$$\lim_{\xi_l \to \infty} \kappa_\alpha = \frac{1 + e^{-\alpha\xi_1}(\cos\alpha\xi_1 - \sin\alpha\xi_1)}{4\alpha}, \quad \lim_{\xi_l \to \infty} \kappa_\alpha = \frac{e^{-\alpha\xi_1}\sin\alpha\xi_1}{2\alpha^2\xi_1} \tag{10}$$

In the remaining cases of loading shown in Fig. 1 *b*, *c* and Fig. 2 *a*, *c* the corresponding expressions of all design values can be found by the superposition of solutions for the two already solved cases at $\xi_1 \to 0$ or $\xi_1 = \xi_l$. It is notable that in the case of loading shown in Fig. 2 *c* for a finite length panel $\xi_l = \xi_1$ we found $\sigma_z(\xi) = const = q$ and $\kappa_\alpha = 0$.

The moment stresses in the face layers at $\xi = 0$, depending on the relative parameter κ_α, contribute to an overload from three-point bending of the upper face layer. The load factor of mere moment stresses increases infinitely at $\kappa_\alpha \to \hat{\xi}_1 / 2$, i.e., when the local bending of the lower face layer is absent $\left(w_2''(0) = 0 \right)$. This situation is possible for a panel with elastic characteristics of such materials as HEXCEL/Al with $\mu_V = 2h_1 / h = 1/6$, $E_x^{out} = 40\ GPa$, $E_z^{core} = 0.31\ GPa$, $G_{xz}^{core} = 0.138\ GPa$, see Fig. 3. Then the maximum value of moment stresses in the central section at point reaching the outer surface of the upper face layer equals $\sigma_x^{mom}(0) = -E_x q_0 \mu(\hat{\xi}_1/2 + \kappa_\alpha) / \left[2(1-\nu_1^2)\right]$, that differs from the membrane stress $\sigma_x^{memb}(0) = -E_x q_0 \mu^2 (\xi_1 - \hat{\xi}_1) / \left[12(1-\nu_1^2)\right]$ approximately by two times. The latter stress, defined as the average stress throughout the face layer thickness, is comparable to the value of flexural stress σ_x^{cl}, determined according to the classical Kirchhoff-Love hypotheses for the whole stack of layers [7].

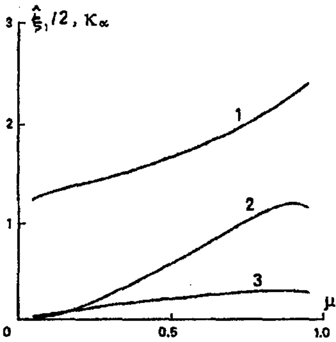

Fig. 3. Summands of relative curvature at the central section versus face layers fraction: *2l/h = 5*, curves *1, 2* - $\hat{\xi}_1 / 2$ at $G_{xz} = 0$ and at $G_{xz} = 0.138\ GPa$, *3* - κ_α at $E_z = 0.31\ GPa$.

Notice that for $G_{xz} = 0$ the doubled value of the relative mean curvature equals $\hat{\xi}_1 = \xi_1$, while in the case of $G_{xz} = \infty$ (the bending of a uniform panel according to Kirchhoff-Love) and for a thin filling interlayer, when $\mu_V \to 1$, we have $\hat{\xi}_1 = \xi_1 / 4$. This is also evident from a comparison of the sum of two cylindrical rigidities of plates with a cylindrical rigidity of one plate, which is twice as thick as each of them.

The transversal stresses σ_z in the midlayer are identical both for bending combined with slippage *(G_{xz} = 0)* and for bending without one. At the center of the panel loaded according to three charts shown in Fig. 1 *a, b, c* the stresses $\sigma_z(0)$ are evaluated respectively by the formulae:

$$\sigma_z(0) = (-1/4)\sigma_z^*, \quad \sigma_z(0) = -e^{-\alpha\xi_1}(\cos\alpha\xi_1 + \sin\alpha\xi_1)\sigma_z^*, \quad \sigma_z(0) = (-1/2)\sigma_z^* \quad (11)$$

where $\sigma_z^* = \frac{P}{bh_0}\sqrt[4]{\frac{6(1-\nu_1^2)E_z h_0^3}{E_x h_1^3}}$, and in the case Fig. 1 *b* the span length l_1 is assumed equal to l_2. For the support section $\xi = \xi_1$ the asymptotic formulae were deduced when $\xi_1 >> 1$. In view of the charts Fig. 1 *a, b* the following estimates were found respectively as $\sigma_z(\xi_1) = -(1/8)\sigma_z^*$, $\sigma_z(\xi_1) = -(1/4)\sigma_z^*$. The same condition was also considered for the end section $\xi = \xi_l$ however the cases $\xi_1 \neq \xi_l$ and $\xi_1 = \xi_l$ have called for careful analysis. Fundamental change in the transfer mechanism of pressure on a midlayer occurs when the overhang of panel length beyond the supports is varied between 0 and *(1/4)h,* see Fig. 4, The distribution of $\sigma_z(\xi)$ with superposition of local effects caused by point forces at the support and the center of a panel is shown for the moderate panel length *2l = 5h.*

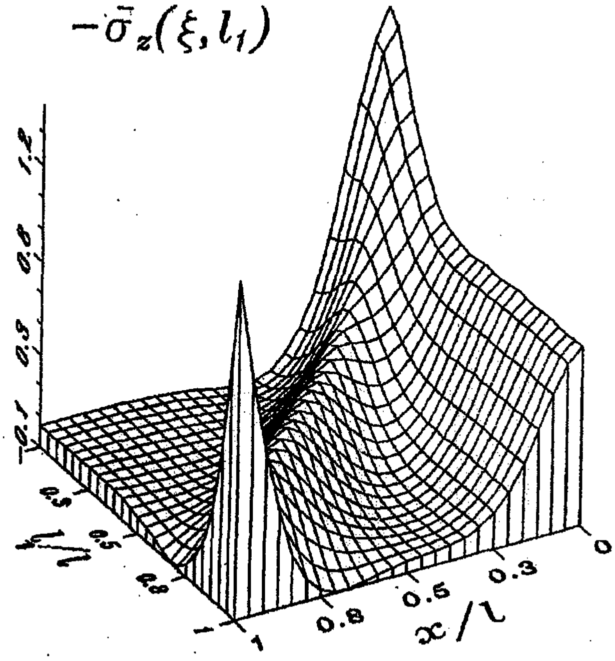

Fig. 4 Transverse normal stress diagrams along the panel length and against the extent of a span between the supports, $(\bar{\sigma}_z = \sigma_z / \sigma_0,\ \sigma_0 = P / bh)$

At the end section $\xi = \xi_l$ of the panel loaded as shown in Fig. 1 *a, b, c* the relative value of stresses $\sigma_z(\xi_l)/\sigma_z^*$ can respectively be found as $-(1/2)e^{-\alpha(\xi_l - \xi_1)}\cos\alpha(\xi_l - \xi_1)$, $-e^{-\alpha(\xi_l - \xi_1)}\cos\alpha(\xi_l - \xi_1)$ and $-e^{-\alpha\xi_l}\cos\alpha\xi_l$. In the case of loading chart shown in Fig. *2 b* the normal transversal stress on the interval $\xi_1 \le \xi \le \xi_l$ may be calculated from the following asymptotic formula

$$\sigma_z(\xi) = -(q/2)e^{-\alpha(\xi - \xi_1)}\cos\alpha(\xi - \xi_1) \qquad (12)$$

In both cases the maximum *positive* value of transversal stress σ_z at the end section $\xi=\xi_l$ occurs when $\xi_l-\xi_1=3\pi/4\alpha$.

CONCLUSIONS

An analytical method devised for analysis of the sandwich panel in bending allows us to obtain refined characteristics for the inplane and transverse normal stresses. Taking into account the important aspects neglected in the classical theory the following conclusions were made:

- For the panel of symmetric structure with respect to middle plane was shown that the local curvatures of layers and the bending stresses can be determined in terms of the mean curvature depending from transverse shear and the additional curvature from transverse compression. The final formulae allows us to analyze the stresses over the whole range of shear rigidity of the midlayer including $G_{xz}\to 0$ (the case of slippage over the interlayer surface).
- The panel parts extending beyond the supports may be the cause of the advent of positive value $\sigma_z(l)$ at the free end, which by an order of magnitude less than the value $\sigma_z(0)$ at the panel center.
- Local bending characteristics amplify the applied theory of layered plates by the analytical description of local effects, and in the special cases of boundary conditions.

REFERENCES

[1] Noor, A. K., Burton, W. S. and Bert, Ch. W. "Computational models for sandwich panels and shells." *Appl. Mech. Rev.* **49**, pp. 155-199 (1996).

[2] Bolotin, V. V. **Stability problems in fracture mechanics.** John Wiley and Sons, inc., New York p. 188 (1996).

[3] Bolotin, V. V. and Yu. N. Novichkov **Mechanics of multilayered structures**. [in Russian], Mashinostroenie, Moscow, 375 (1980).

[4] Frostig, Y. "On the stress concentration in the bending of sandwich beams with transversely flexible core." *Composite Structures* **24**, pp. 161-169 (1993).

[5] Polyakov, V. A. "Deformation of sandwich panels in cylindrical bending by point forces. 1. Analytical construction." *Mechanics of Composite Materials* **32,** pp. 588-611 (1996).

[6] Polyakov, V. A., Zhigun, I. G., Shlitsa, R. P. and Khitrov, V. V. "Deformation of sandwich panels cylindrically bent by point forces. 2. Development of procedure." *Mechanics of Composite Materials* **33**, 23-45 (1997).

[7] Vasil'ev, V. V. **Mechanics of composite structures**, Transl. from the 1988 Russian ed., Taylor and Francis, Basingstoke, Hampshire, (1993).

OPTIMIZATION OF ANGLE–PLY LAMINATES FOR MINMAX DEFLECTION UNDER IMPRECISELY SPECIFIED DYNAMIC LOADS

J C Bruch, Jr.[1], S Adali[2], J M Sloss[3] and I S Sadek[4]
[1]Dept of Mechanical & Environmental Eng., UCSB, Santa Barbara, CA, USA
[2]Department of Mechanical Eng., University of Natal, Durban, South Africa
[3]Department of Mathematics, UCSB, Santa Barbara, CA, USA
[4]Dept of Mathematical Sciences, Univ of North Carolina, Wilmington, NC, USA

Abstract–*Design optimization of angle–ply plates is studied under imprecisely specified dynamic loads using a non–probabilistic model. The optimal design is obtained such that the maximum deflection of the plate is minimized using the ply angles as design variables. In computing the deflection the least favorable response of the laminate is determined under uncertain dynamic loads.*

INTRODUCTION

Dynamic loads acting on a structure are usually of an uncertain nature due to the difficulty of predicting the magnitudes of such loads. It is important to determine the response of a structure under uncertainty, and in particular its least favourable response, to be able to assess the reliability of its performance. One approach in evaluating the structural reliability is to use a probabilistic model. However, in many cases complete probabilistic information may not be available.

In the present study, the deflection of an angle ply rectangular plate is minimized under uncertain dynamic loads using the fibre orientations as the design variables. A non–probabilistic approach is employed to determine the dynamic response of a laminated plate under loads the precise forms of which are not known *a priori*. The uncertain dynamic loads producing the least favourable response are computed by convex modelling. This technique has been applied to a number of problems and the reader is referred to [1–3] for extensive literature surveys. The application of convex modelling to optimal design problems are given in Refs. [4–7].

The specific problem involves the computation of optimal ply angles a symmetrically laminated angle–ply plate subject to uncertain excitations to minimize its deflection. This in turn requires the computation of the least favourable dynamic response of the plate to the uncertain excitation which may be in the form of a forcing function and/or initial disturbances. The least favourable response of the plate is determined by analyzing the convex sets associated with the uncertainties in the input.

OPTIMAL DESIGN FORMULATION

We consider a simply supported rectangular laminate of length a, width b and thickness H in the x, y, and z directions, respectively. The laminate is composed of an even number of orthotropic layers with the fibers oriented alternatively at $+\theta$ and $-\theta$ degrees. The layer thicknesses and fiber orientations are symmetrically placed with respect to the middle surface. Plates with these characteristics are commonly known as symmetric angle–ply laminates. The laminate is subjected to a forcing function $F(x, y, t) = \tilde{F}(x, y)\, G(t)$ in the z direction and the initial conditions

$$w(x, y, 0) = \tilde{\phi}(x, y)\,, \qquad w_t(x, y, 0) = \tilde{\Psi}(x, y) \tag{1}$$

where $w = w(x, y, t)$ denotes the deflection in the z–direction and the symbol "~" indicates that the functions $\tilde{F}(x, y)$, $\tilde{\phi}(x, y)$ and $\tilde{\Psi}(x, y)$ are specified imprecisely and contain uncertain data in the sense that the information on these functions are incomplete. The time component of the forcing function, i.e., $G(t)$, is a specified quantity. The plate is also subjected to in–plane forces N_1 and N_2 in the x and y directions, respectively, with N_1 and N_2 satisfying the constraint that their magnitudes are less than the buckling load.

The design problem involves computation of the optimal fibre orientation which minimizes the maximum deflection. The deflection under uncertain forcing function and/or initial conditions correspond to the least favourable response of the laminate. The least favourable response is defined as the response producing the maximum possible deflection at a given point. The computation of this response and the corresponding forms of the uncertain functions are given as part of the solution. Let $w(x_0, y_0, t)$ be the least favourable deflection at a point $P(x_0, y_0)$ obtained by maximizing the deflection w over the uncertain functions $\tilde{F}(x, y)$, $\tilde{\phi}(x, y)$ and $\tilde{\Psi}(x, y)$. Then the maximum deflection w_{max} is given by

$$w_{max} = \max_{P,t} w(x, y, t)\,, \qquad t \leq T \tag{2}$$

where T is a specified time. Optimal design problem can be stated as

$$w_{min} = \min_{\theta} w_{max}\,, \qquad t \leq T \tag{3}$$

subject to $0^\circ \leq \theta \leq 90^\circ$.

EQUATION OF MOTION AND UNCERTAINTY MODELLING

The equation governing the transient vibrations of the laminate under in–plane loads is given by

$$D_{11}\, w_{xxxx} + 2\,(D_{12} + 2\,D_{66})\, w_{xxyy} + D_{22}\, w_{yyyy} + \rho\, H\, w_{tt}$$

$$+ N_1\, w_{xx} + N_2\, w_{yy} = \tilde{F}\,(x,\, y)\; G(t) \tag{4}$$

where ρ is the mass density, and D_{ij} are the bending stiffnesses given by

$$D_{ij} = \int_{-H/2}^{H/2} \bar{Q}_{ij}^{(k)}(\theta)\;\; z^2\, dz \tag{5}$$

where $\bar{Q}_{ij}^{(k)}$ is the transformed plane stress reduced stiffness component of the kth layer which can be computed as a function of the ply angles using standard transformation relations.

The simply supported boundary conditions on the laminate are

$$w = 0,\; D_{11}\, w_{xx} + D_{12}\, w_{yy} = 0 \;\text{ for }\; x = 0,\, a,\; t \geq 0 \tag{6a}$$

$$w = 0,\; D_{12}\, w_{xx} + D_{22}\, w_{yy} = 0 \;\text{ for }\; y = 0,\, b,\; t \geq 0 \tag{6b}$$

The uncertainties in the forcing function and the initial disturbances are modelled by expressing these quantities as the sum of deterministic and uncertain parts, viz.

$$\tilde{F}(x,\, y) = F_0(x,\, y) + \tilde{f}(x,\, y) \tag{7}$$

$$\tilde{\Phi}(x,\, y) = \Phi_0(x,\, y) + \tilde{\phi}(x,\, y),\quad \tilde{\Psi}(x,\, y) = \Psi_0(x,\, y) + \tilde{\psi}(x,\, y) \tag{8}$$

where the subscript "o" denotes the known deterministic part. The only condition imposed on the uncertain quantities is that they will be bounded in the L_2 norm with the exception of the uncertainty in the displacement initial condition. For the uncertain vibration problem to be well–defined, the gradient of the uncertain displacement function needs to be bounded in the L_2 norm. Thus the conditions on $\tilde{f}$, $\nabla\tilde{\phi}$ and $\tilde{\psi}$ can be expressed as

$$\|\, \tilde{f}\, \|_2^2 \leq \varepsilon_1^2\, , \qquad \|\, \nabla\tilde{\phi}\, \|_2^2 \leq \varepsilon_2^2\, , \qquad \|\, \tilde{\psi}\, \|_2^2 \leq \varepsilon_3^2 \tag{9}$$

where ε_1, ε_2 and ε_3 are prescribed measures of maximum allowable uncertainties.

METHOD OF SOLUTION

The solution of the differential equation (4) is obtained by eigenfunction expansion of the displacement, viz.

$$w(x, y, t) = \sum_{m=1}^{\infty} \sum_{n=1}^{\infty} z_{mn}(t)\, v_{mn}(x, y) \tag{10}$$

where $v_{mn}(x, y) = sin(m\pi x/a)\, sin(n\pi y/b)$ are the eigenmodes of the freely vibrating plate with simply supported boundary conditions. The forcing functions and the initial conditions are expanded in terms of the eigenmodes, viz.

$$(F_0(x, y), \phi_0(x, y), \Psi_0(x, y)) = \sum_{m=1}^{\infty} \sum_{n=1}^{\infty} (a_{mn}, b_{mn}, c_{mn})\, v_{mn}(x, y) \tag{11}$$

$$(\tilde{f}(x, y), \tilde{\phi}(x, y), \tilde{\psi}(x, y)) = \sum_{m=1}^{\infty} \sum_{n=1}^{\infty} (\tilde{a}_{mn}, \tilde{b}_{mn}, \tilde{c}_{mn})\, v_{mn}(x, y) \tag{12}$$

where the coefficients a_{mn}, b_{mn} and c_{mn} are determined from

$$(a_{mn}, b_{mn}, c_{mn}) = (4/ab) \int_0^b \int_0^a (F_0, \phi_0, \Psi_0)\, v_{mn}(x, y)\, dx\, dy \tag{13}$$

The coefficients $\tilde{a}_{mn}$, $\tilde{b}_{mn}$ and $\tilde{c}_{mn}$ of the uncertain components are not known *a priori*. However, it is assumed that $\tilde{a}_{mn} = \tilde{b}_{mn} = \tilde{c}_{mn} = 0$ for $m > M$ and $n > N$ where M and N are positive numbers.

SOLUTION FOR LEAST FAVORABLE RESPONSE

The values of the uncertainty parameters $\tilde{a}_{mn}$, $\tilde{b}_{mn}$ and $\tilde{c}_{mn}$ are unknown subject to the requirement that they satisfy the inequalities (9). The uncertainty problem consists of determining these values such that they produce the least favourable response of the structure. In the present problem, the deflection at a specified time $t = t_0$ and location $(x, y) = (x_0, y_0)$ is specified as the response to be studied. In the coordinates $(\tilde{a}_{mn}, \tilde{b}_{mn}, \tilde{c}_{mn})$, the domains defined by inequalities (9) are convex regions. In fact, these regions correspond to $M \times N$ dimensional elliptical cylinders in the $3MN$ dimensional Euclidean space. The constants M and N denote the number of terms in the truncated series. To obtain the least favourable response, $\{\tilde{a}_{mn}\}$, $\{\tilde{b}_{mn}\}$ and $\{\tilde{c}_{mn}\}$ must satisfy the equality constraints

$$\sum_{m=1}^{M} \sum_{n=1}^{N} \tilde{a}_{mn}^2 = 4\, \varepsilon_1^2/(ab)\,, \qquad \sum_{m=1}^{M} \sum_{n=1}^{N} (m^2/a^2 + n^2/b^2)\, \tilde{b}_{mn}^2 = 4\, \varepsilon_2^2/(\pi^2 ab)$$

$$\sum_{m=1}^{M} \sum_{n=1}^{N} \tilde{c}_{mn}^2 = 4\, \varepsilon_3^2/(ab) \tag{14}$$

This observation enables us to employ the method of Lagrange multipliers to compute the optimal values of the uncertainty coefficients causing the least favourable response of the plate. This problem is an equality constrained optimization problem and can be stated as: *Maximize* $w(x_0, y_0, t_0)$ *over the uncertainty parameters* $\tilde{a}_{mn}, \tilde{b}_{mn}, \tilde{c}_{mn}$ *subject to the constraints* (14).

OPTIMAL DESIGN EXAMPLES

The solution procedure and the design optimization of the laminate subject to uncertain excitations and in–plane loads are illustrated with a numerical example. The example involves optimization under an uncertain forcing function.

Optimal design under a distributed transient force

The transient force acting on the laminate is taken as

$$\tilde{F}(x, y)\, G(t) = pxy/(ab) + \tilde{f}(x)\, H(t) \tag{15}$$

where p is the magnitude of the deterministic force at $x = a$, $y = b$ and $H(t)$ is the Heaviside function given by $H(t) = 0$ for $t < 0$ and $H(t) = 1$ for $t \geq 0$. Initially the plate is at rest so that $\phi(x, y) = \tilde{\Psi}(x, y) = 0$. From equation (11), with $F_0(x, y) = pxy/(ab)$, it follows that

$$a_{mn} = (-1)^{m+n}\, 4\, p\, /(\pi^2\, m\, n) \tag{16}$$

Zero initial conditions yield $b_{mn} = \tilde{b}_{mn} = c_{mn} = \tilde{c}_{mn} = 0$. The solution is given by

$$w(x, y, t) = w_0(x, y, t) + \tilde{w}(x, y, t) \tag{17}$$

where

$$w_0(x, y, t) = \sum_{m=1}^{\infty} \sum_{n=1}^{\infty} (\rho\, H\, \Omega_{mn}^2)^{-1}\, (-1)^{m+n} (4p/\pi^2 m\, n)\, (1 - \cos\Omega_{mn} t)\, v_{mn}(x, y) \tag{18}$$

$$\tilde{w}(x, y, t) = \sum_{m=1}^{M} \sum_{n=1}^{N} (\rho\, H\, \Omega_{mn}^2)^{-1}\, \tilde{a}_{mn}\, (1 - \cos\Omega_{mn} t)\, v_{mn}(x, y) \tag{19}$$

The values of the elastic constants are taken as $E_1/E_2 = 25$, $G_{12}/E_2 = 0.5$, $\nu_{12} = 0.25$ which are typical of an advanced fiber–reinforced composite material. The plate is taken as a multi–layered laminate with a stacking sequence $(\theta/-\theta/\theta/-\theta/\ldots)_s$ with equal layer thicknesses. Large number of layers ensures that the bending stiffnesses D_{16} and D_{26} are negligible.

The optimization results are given in the following table:

a/b	$N_1 = N_2 = 0$	θ_{opt}	$N_1 = N_2 = 5$	θ_{opt}
0.5		4.9		10.6
0.75		42.3		41.4
1.0		44.6		44.8
1.5		69.6		70.0
2.0		90.0		90.0

CONCLUDING REMARKS

The optimal design of angle–ply laminates under uncertain loads is determined by convex analysis. In the present approach, a non–probabilistic model of the uncertainty is employed in which the uncertain components of the dynamic loads are taken to be arbitrary but bounded in the L_2 norm.

The solution procedure is outlined and the optimal fibre orientations are computed for an example involving an uncertain forcing function.

REFERENCES

1 I S Sadek, J M Sloss, S Adali & J C Bruch Jr, Non–probabilistic modelling of dynamically loaded beams under uncertain excitations. *Mathematical and Computer Modelling*, V 18, 59–67, 1993.

2 S Adali, J C Bruch Jr, I S Sadek & J M Sloss, Transient vibrations of cross–ply plates subject to uncertain excitations. *Appl Math Modelling* V 19, 56–63, 1995.

3 Y Ben–Haim, *Robust Reliability in the Mechanical Sciences.* Springer–Verlag, Heidelberg, Germany, 1996.

4 S Adali, Convex and fuzzy modelling of uncertainties in the optimal design of composite structures. *Proceedings of IUTAM Symposium on Optimal Design with Advanced Materials*, Lyngby, Denmark, 1992.

5 S Adali, A Richter & V E Verijenko, Non–probabilistic modelling and design of sandwich plates subject to uncertain loads and initial deflections. *Int. J. of Engineering Sciences*, V. 33, 855–866, 1995.

6 S Adali, A Richter & V E Verijenko, Minimum weight design of symmetric angle–ply laminates under multiple uncertain loads. *Structural Optimization*, V. 9, 89–95, 1995.

7 S Adali, A Richter & V E Verijenko, Minimum weight design of symmetric angle–ply laminates with incomplete information on initial imperfections. *ASME J. of Applied Mechanics*, V. 64, 90–96, 1997.

OPTIMISATION OF FIBER REINFORCED COMPOSITES

Georges DUVAUT and Ghislaine TERREL

1. INTRODUCTION

Long fibers are currently used to reinforce composite structures, but one main difficulty is to determine the optimal amont and directions of fibers at each point of the structure ; very often it is the intuition of the engineers that gives the anser; this one is certainly good if the man has a long experience of the behaviour of composite structures, which is not necessarly realised and not easily transmitted.

The method which is proposed here is systematic and can be operated by low experienced engineers. It consist of minimizing a functional which includes the flexibility of the structure, the price of the material, and the weight of the structure. Depending of the case, it can also include other parameters. It works here for elastic and elastoplastic structures, and can be extended to other types of materials.

The algorithm consists of two alternating minimisations: a global one and a local one: the first one is for solving an homogenized structure problem when the homogenized constitutive relations are knowned; the second one is two improve, at each point, the amont and direction of fibers. The type of fibers is given but the fiber proportion is to be determined. The algorithm is convergent because, at each step, the functional is decreasing. The method leads quickly to an optimal composite structure; the resulting stress field is also obtained. Several examples are given, including plate and shell structures. The method has a very wide field of applications: aeronautics, naval , cars, civil engineering ...

2. Some results

Up to now, several computations have been performed concerning rectangular plates, some including holes. The computations have been realised using finite element method ; on each element we get the optimal direction of the fibers according to the loads which have been applied, in order to minimise the displacements, that is to say the flexibility of the structure.

Following the same kind of idea, we can take into account the optimal rate of fibers at each element of the structure.

We give some of our results in the following pictures.

Pictures N°1 :. Perforated plate in traction.

Initial state: fibers at 0 degree angle: $U_x initial = 1.105.10^{-3}$.

Final state after optimisation : $U_x = 0.701.10^{-3}$.

Initial map of Von Mises stresses.

Final map of Von Mises stresses.

Pictures N°2 :. Two holes perforated plate in traction and shear : $F_x = 100$, $F_y = -100$.

Initial state : fibers at 0 degree angle : $U_x initial = 2.08.10^{-3}$, $U_y initial = -7.42.10^{-2}$.

Final state after optimisation : $U_x final = 0.745.10^{-3}$, $U_y final = -1.58.10^{-2}$.

(A. One) Lab. de Modélisation et Mécanique des Structures (LM2S), URA 1776 du CNRS, Univ. P. et M. Curie, tour 66, 4 Place Jussieu, 75005 PARIS, France.
URL: `<duvaut@ccr.jussieu.fr>`

(A. Two) ONERA / IMFL / DMSE, 5 Brd Paul Painlevé, 59045 LILLE, France.

Picture N° 1 : Traction -

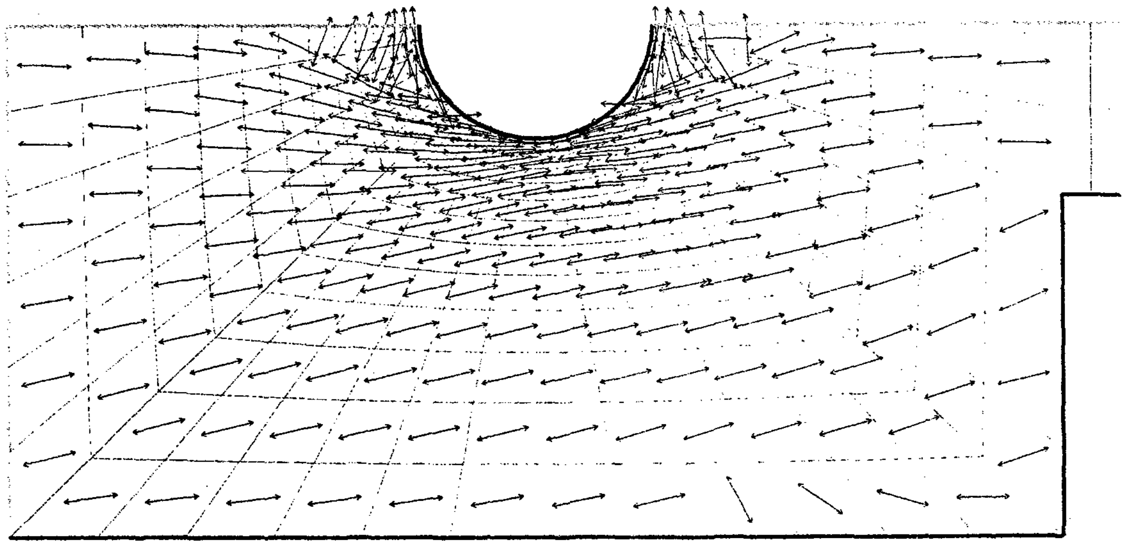

PLAQUE :

FORCE DE TRACTION

356 POINTS
356 NOEUDS
316 ELEMENTS
316 QUADRANGLES

RIGIDITES LOCALES :
E1 = 80000 MPa
E2 = 5600 MPa
MU12 = 0.34
G12 = 2100 MPa

DIRECTIONS DES FIBRES

ONERA-Lille / LM2S-Univ. Paris 6.

Picture N°21 = Von Mises Stress (Final State)

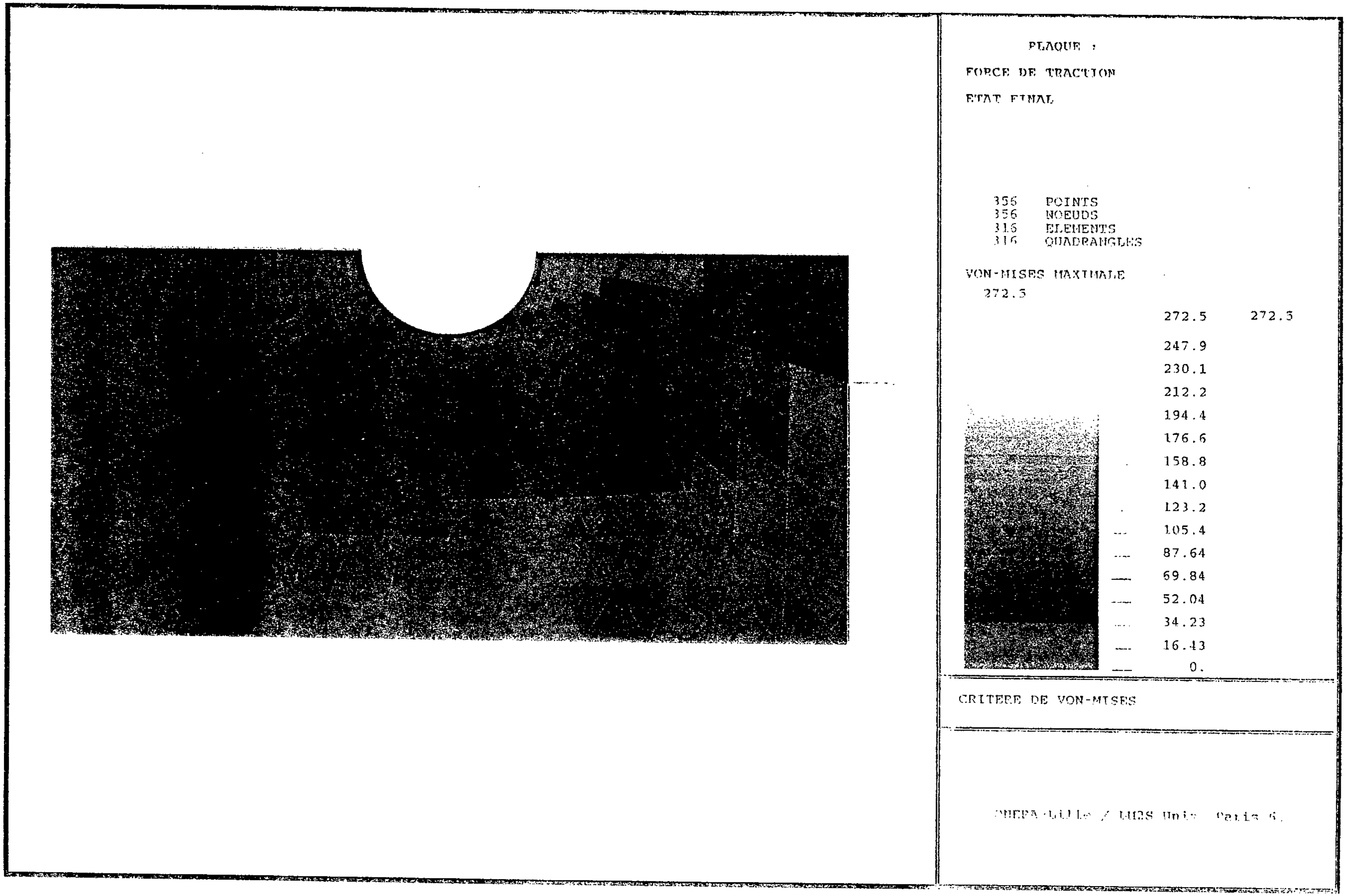

Picture N° 2 . Final state

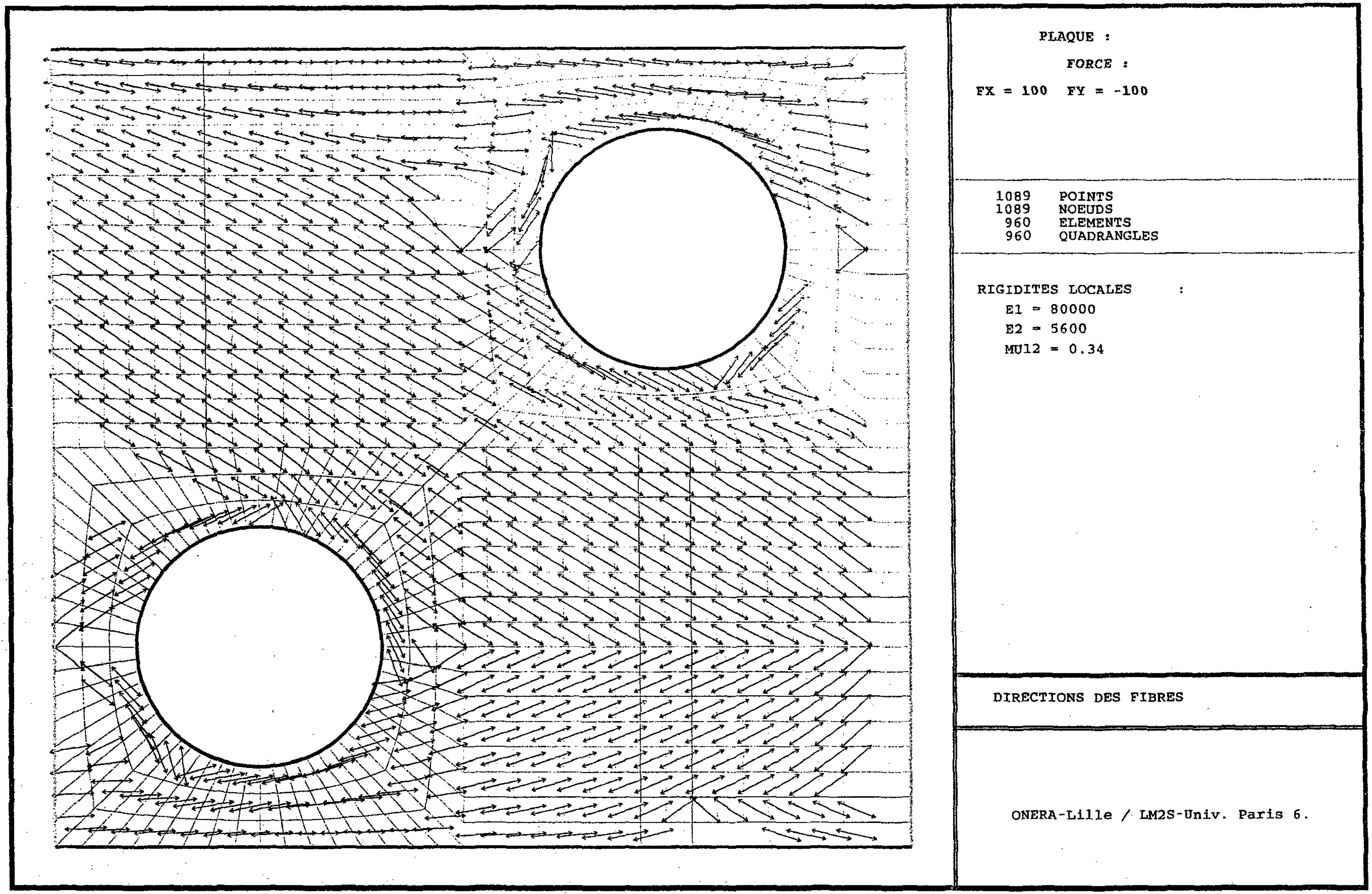
PLAQUE :
FORCE :
FX = 100 FY = -100
1089 POINTS
1089 NOEUDS
960 ELEMENTS
960 QUADRANGLES
RIGIDITES LOCALES :
E1 = 80000
E2 = 5600
MU12 = 0.34
DIRECTIONS DES FIBRES
ONERA-Lille / LM2S-Univ. Paris 6.

ANALYSIS AND DESIGN OF REINFORCED COMPOSITE STRUCTURES

A. L. KALAMKAROV
Department of Mechanical Engineering
Dalhousie University
P.O. Box 1000, Halifax, Nova Scotia
B3J 2X4 CANADA

ABSTRACT

In the present paper, the solution of the modeling and design problems for the composite structures is based on the application of the general asymptotic homogenization model for the composite shells. This theory enables the prediction of both the local and effective properties of the composite structure. The design algorithm for the fiber-reinforced shells with a prescribed set of effective stiffnesses is developed. The set of prescribed effective stiffness values for which the design problem is solvable, is described, and the effective method of the design parameters calculation is developed. In particular, the minimal number of reinforcing layers required for the design of the composite laminate with the prescribed effective stiffnesses is determined. The design problem is generalized on account of minimization of the fiber volume content.

GENERAL HOMOGENIZATION COMPOSITE SHELL MODEL

Consider a three-dimensional composite layer of a periodic structure with the unit cell Ω_δ. Thickness of this layer, δ, and scale of the composite material inhomogeneity are assumed to be small as compared with the dimensions of the structure as whole. It is common practice in performing the stress analysis of a composite structural member that the inhomogeneous medium being studied is replaced with a homogeneous anisotropic medium whose response is believed to be equivalent to that of the actual composite in a certain average sense. If the composite material has a periodic structure, the averaged (or effective) properties of the equivalent anisotropic homogeneous material can be estimated by means of the asymptotic homogenization method, which also gives asymptotically correct results for the local stress field in the bulk of the composite solid. In the previous studies by the author [1], this approach was adopted in the analysis of composite and reinforced thin-walled structural members. As a result, the general composite shell model was developed. It was shown that it is possible to calculate both the effective and local properties of this composite layer by first solving appropriate three-dimensional local problems set on the unit cell, and subsequently solving a two-dimensional boundary-value problem for a homogeneous (or quasi-homogeneous) anisotropic shell with the effective stiffness moduli obtained at the first step.

The constitutive relations for the anisotropic homogeneous shell, that is those between the stress resultants N_1, N_2, N_{12} and moment resultants M_1, M_2, M_{12} on the one hand, and the mid-surface strains ε_{11}, ε_{22} (elongations), $\varepsilon_{12}=\varepsilon_{21}=\omega/2$ (shear), τ_{11}, τ_{22} (bending), $\tau_{12}=\tau_{21}=\tau$ (torsion) on the other, can be represented as follows [1, 2]:

$$N_\beta = \delta\langle b_{\beta\beta}{}^{\lambda\mu}\rangle\varepsilon_{\lambda\mu} + \delta^2\langle c_{\beta\beta}{}^{\lambda\mu}\rangle\tau_{\lambda\mu}, \qquad N_{12} = \delta\langle b_{12}{}^{\lambda\mu}\rangle\varepsilon_{\lambda\mu} + \delta^2\langle c_{12}{}^{\lambda\mu}\rangle\tau_{\lambda\mu} \tag{1}$$

$$M_\beta = \delta^2\langle zb_{\beta\beta}{}^{\lambda\mu}\rangle\varepsilon_{\lambda\mu} + \delta^3\langle zc_{\beta\beta}{}^{\lambda\mu}\rangle\tau_{\lambda\mu}, \quad M_{12} = \delta^2\langle zb_{12}{}^{\lambda\mu}\rangle\varepsilon_{\lambda\mu} + \delta^3\langle zc_{12}{}^{\lambda\mu}\rangle\tau_{\lambda\mu} \tag{2}$$

where β assumes the values 1 and 2, and is not summed here; $\lambda,\mu = 1,2$ and are summed. The functions $b_{kl}{}^{mn}(\xi_1,\xi_2,z)$ and $c_{kl}{}^{mn}(\xi_1,\xi_2,z)$, $k,l,m,n,=1,2,3$ can be calculated from the solution of local problems on the unit cell [1]. They are periodic in variables $\xi_1=\alpha_1 A_1/(\delta h_1)$ and $\xi_2=\alpha_2 A_2/(\delta h_2)$ with periods A_1 and A_2 correspondingly; α_1, α_2 and γ are the orthogonal curvilinear coordinates, such that the coordinate lines α_1 and α_2 coincide with the curvature lines of the mid-surface of the shell and coordinate lines γ are normal to the mid-surface ($\gamma=0$), and $z=\gamma/\delta$. Functions $A_1(\alpha_1,\alpha_2)$ and $A_2(\alpha_1,\alpha_2)$ are the coefficients of the first quadratic form of the mid-surface of the layer, and δh_1, δh_2 are tangential dimensions of the periodicity cell Ω_δ. The averaging symbol <...> denotes the integration over the three-dimensional unit cell of composite layer, as follows:

$$\langle F(\xi_1,\xi_2,z)\rangle = \int_\Omega F(\xi_1,\xi_2,z)\,d\xi_1 d\xi_2 dz \tag{3}$$

Local problems having been solved, the functions $b_{kl}{}^{mn}(\xi_1,\xi_2,z)$ and $c_{kl}{}^{mn}(\xi_1,\xi_2,z)$ are averaged by application of Eq. (3), giving the effective stiffnesses of the anisotropic homogeneous shell, $\langle b_{\alpha\beta}{}^{\lambda\mu}\rangle$, $\langle zb_{\alpha\beta}{}^{\lambda\mu}\rangle=\langle c_{\lambda\mu}{}^{\alpha\beta}\rangle$, and $\langle zc_{\alpha\beta}{}^{\lambda\mu}\rangle$. One may proceed then to solution of the boundary-value problem for the homogeneous shell [1], to calculate the mid-surface strains $\varepsilon_{\lambda\mu}(\alpha_1,\alpha_2)$ and $\tau_{\lambda\mu}(\alpha_1,\alpha_2)$.

The notation for the effective stiffnesses used in Eqs. (1) and (2) is naturally related to the local problem formulation in the general homogenization composite shell model. There is the following simple correspondence between this notation and the conventional notation of classical laminated plate theory (see e.g., [3]) for the effective stiffnesses:

$$\begin{array}{lll}
A_{11} = \delta\langle b_{11}{}^{11}\rangle, & B_{11} = \delta^2\langle zb_{11}{}^{11}\rangle = \delta^2\langle c_{11}{}^{11}\rangle, & D_{11} = \delta^3\langle zc_{11}{}^{11}\rangle \\
A_{12} = \delta\langle b_{11}{}^{22}\rangle, & B_{12} = \delta^2\langle zb_{11}{}^{22}\rangle = \delta^2\langle c_{11}{}^{22}\rangle, & D_{12} = \delta^3\langle zc_{11}{}^{22}\rangle \\
A_{16} = \delta\langle b_{11}{}^{12}\rangle, & B_{16} = \delta^2\langle zb_{11}{}^{12}\rangle = \delta^2\langle c_{11}{}^{12}\rangle, & D_{16} = \delta^3\langle zc_{11}{}^{12}\rangle \\
A_{22} = \delta\langle b_{22}{}^{22}\rangle, & B_{22} = \delta^2\langle zb_{22}{}^{22}\rangle = \delta^2\langle c_{22}{}^{22}\rangle, & D_{22} = \delta^3\langle zc_{22}{}^{22}\rangle \\
A_{26} = \delta\langle b_{22}{}^{12}\rangle, & B_{26} = \delta^2\langle zb_{22}{}^{12}\rangle = \delta^2\langle c_{22}{}^{12}\rangle, & D_{26} = \delta^3\langle zc_{22}{}^{12}\rangle \\
A_{66} = \delta\langle b_{12}{}^{12}\rangle, & B_{66} = \delta^2\langle zb_{12}{}^{12}\rangle = \delta^2\langle c_{12}{}^{12}\rangle, & D_{66} = \delta^3\langle zc_{12}{}^{12}\rangle
\end{array} \tag{4}$$

DESIGN OF THE FIBER-REINFORCED COMPOSITE LAMINATE

The composite laminate is formed by N layers reinforced by parallel fibers. The fiber within a jth layer, $j=1,2,\ldots,N$, makes an angle φ_j with the coordinate line α_1. The thickness of laminate is δ, and the departure of the axis of the fiber of the jth ply from the mid-surface

(γ=0) is equal to δa_j, where a_j is a dimensionless quantity equal to a departure of the axis of the fiber normalized by δ. The application of the general homogenization composite shell model to the analysis of the fiber-reinforced laminate provides the accurate calculation of its effective stiffnesses [1, 4]. These results are used in this section for the design of a composite laminate with the required set of effective stiffnesses.

Suppose it is required to design the fiber-reinforced angle-ply laminate with the prescribed set of effective stiffnesses. The application of the general homogenization composite shell model provides formulas for the effective moduli of the high-stiffness fiber-reinforced laminate in terms of fiber placement angles φ_j, fiber volume content θ_j, where j is a number of the layer and some other material properties and geometrical dimensions of the laminate [1]. Let us assume that all fibers are of a circular cross-section, and that they are made of a similar material with Young's modulus E. We also assume that $A_1=A_2=1$, which is possible for the cylindrical shells or plates, in particular. The set of effective stiffnesses in the tangential directions to the shell surface can be then expressed as follows:

$$\begin{aligned} &A_{11} = \delta\langle b_{11}{}^{11}\rangle = E\omega Y_1(\gamma,\varphi), \qquad A_{22} = \delta\langle b_{22}{}^{22}\rangle = E\omega Y_2(\gamma,\varphi) \\ &A_{16} = \delta\langle b_{11}{}^{12}\rangle = E\omega Y_3(\gamma,\varphi), \qquad A_{26} = \delta\langle b_{12}{}^{22}\rangle = E\omega Y_4(\gamma,\varphi) \\ &A_{66} = A_{12} = \delta\langle b_{12}{}^{12}\rangle = \delta\langle b_{11}{}^{22}\rangle = 0.5\, E\omega\, [1 - Y_1(\gamma,\varphi) - Y_2(\gamma,\varphi)] \end{aligned} \tag{5}$$

where

$$\begin{aligned} &Y_1(\gamma,\varphi) = \sum_{j=1}^{N} \gamma_j \cos^4\varphi_j, \qquad Y_2(\gamma,\varphi) = \sum_{j=1}^{N} \gamma_j \sin^4\varphi_j \\ &Y_3(\gamma,\varphi) = \sum_{j=1}^{N} \gamma_j \sin\varphi_j \cos^3\varphi_j, \qquad Y_4(\gamma,\varphi) = \sum_{j=1}^{N} \gamma_j \sin^3\varphi_j \cos\varphi_j \end{aligned} \tag{6}$$

Here $\omega = \sum_{j=1}^{N} \theta_j$, $\gamma = (\gamma_1,\gamma_2,\dots,\gamma_N)$, and $\gamma_j = \theta_j/\omega$ is the proportion of fiber content within the jth layer, and $\varphi = (\varphi_1,\varphi_2,\dots,\varphi_N)$. By replacing functionals $Y_1(\gamma,\varphi)$, $Y_2(\gamma,\varphi)$, $Y_3(\gamma,\varphi)$, and $Y_4(\gamma,\varphi)$ by the variables y_1, y_2, y_3, and y_4, and using the conventional notation for the effective stiffnesses, see Eq.(5), we obtain the following algebraic system:

$$A_{11} = E\omega y_1,\ \ A_{22} = E\omega y_2,\ \ A_{16} = E\omega y_3,\ \ A_{26} = E\omega y_4,\ \ A_{66} = A_{12} = 0.5\, E\omega(1 - y_1 - y_2) \tag{7}$$

If we prescribe values of the effective stiffnesses A_{11}, A_{22}, A_{16}, A_{26}, and $A_{66} = A_{12}$, then Eq. (7) will represent the system for determining $y = (y_1, y_2, y_3, y_4)$. Since the number of equations in the system (7) exceeds a number of unknowns, the following condition (it is natural to call it a solvability condition) should be fulfilled:

$$A_{66} = A_{12} = 0.5\,(E\omega - A_{11} - A_{22}) \tag{8}$$

The system (7) can be resolved explicitly, so that

$$y_1 = A_{11}(E\omega)^{-1}, \quad y_2 = A_{22}(E\omega)^{-1}, \quad y_3 = A_{16}(E\omega)^{-1}, \quad y_4 = A_{26}(E\omega)^{-1} \tag{9}$$

The next and major step in the design problem is to determine the fiber volume fractions $\gamma = (\gamma_1, \gamma_2, \ldots, \gamma_N)$ and the fiber placement angles $\varphi = (\varphi_1, \varphi_2, \ldots, \varphi_N)$, such that satisfy equations:

$$Y_1(\gamma,\varphi) = y_1, \qquad Y_2(\gamma,\varphi) = y_2, \qquad Y_3(\gamma,\varphi) = y_3, \qquad Y_4(\gamma,\varphi) = y_4 \tag{10}$$

The following natural limitations are imposed on the design parameters:

$$\sum_{j=1}^{N} \gamma_j = 1, \qquad \gamma_j \geq 0,\ j=1,2,\ldots,N \tag{11}$$

$$\varphi_j \in [0, \pi],\ j=1,2,\ldots,N \tag{12}$$

The question of a great practical importance here is the determining the minimum number of layers, N_{min}, that is required to design the fiber-reinforced shell with the prescribed set of effective stiffnesses.

Design Problem Formulation:

(1) determine if the system (10) is solvable in the set of variables satisfying conditions (11) and (12), and

(2) if the answer on the first question is affirmative, then find the set of solutions of the system (10) under the conditions (11) and (12).

Design Problem Solution:

To solve the design problem, we first define a following set of intervals within $[0, \pi]$ that impose the limitations on fiber placement angles φ_j: $\Phi^N = \sum_{i=1}^{N} [a_i, b_i] \subset [0, \pi]$, and consider a set

$$U_\Phi^N = \{\varphi \in \Phi^N, \gamma \in R^N, \gamma \textit{ satisfies conditions (11)}\} \tag{13}$$

Problem (10) and (11) is solvable in the set of variables U_Φ^N if and only if the right-hand sides of equations (10), (y_1, y_2, y_3, y_4) belong to an image of the set U_Φ^N under the mapping **Y**, given by equations (6),

$$\mathbf{Y}: (\gamma,\varphi) \in U_\Phi^N \rightarrow (Y_1(\gamma,\varphi), Y_2(\gamma,\varphi), Y_3(\gamma,\varphi), Y_4(\gamma,\varphi)) \in R^4 \tag{14}$$

Statement 1:

(a) If $N \geq 5$, then image of the set U_Φ^N under the mapping **Y**, given by equations (6), represents a convex hull [5] of the following curve Γ:

$$\Gamma = \{\mathbf{y} \in R^4: \mathbf{y} = (\cos^4\varphi, \sin^4\varphi, \sin\varphi \cos^3\varphi, \sin^3\varphi \cos\varphi),\ \varphi \in \Phi^N\} \tag{15}$$

(b) Any point that belongs to the image of the set U_Φ^N under the mapping **Y** can be obtained as a value of the function **Y** on a vector $(\gamma,\varphi) \in R^5 \times \Phi^5$.

According to the above Statement, a fiber-reinforced angle-ply laminate with any prescribed effective stiffness moduli $\{A_{\alpha\beta}\}$ satisfying the solvability condition (8), can be designed by using not more than five plies of reinforcing fibers.

BALANCED FIBER-REINFORCED LAMINATES

Let us consider now a practically important type of a laminate with the balanced placement of fibers about the mid-surface of a laminate. In this case, for any ply with the fiber placement angle + φ_j, there is a symmetric ply with the fiber placement angle - φ_j, and the fiber volume fraction γ_j is similar in these two layers. In the case of balanced reinforcement, the two last functionals in Eqs. (6) are identically equal to zero. It is also sufficient in this case to limit the fiber placement angles by the interval $[0, \pi/2]$.

Design Problem Formulation:

(1) determine if the following equations, cf. Eq. (10):

$$Y_1(\gamma,\varphi) = y_1, \qquad Y_2(\gamma,\varphi) = y_2 \tag{16}$$

are solvable in the set of variables, cf. Eq. (13),

$$V_\Phi^N = \{(\gamma,\varphi) \in U_\Phi^N, \gamma_j = \gamma_{N-j}, -\varphi_j = \varphi_{N-j} \in [0, \pi/2], j=1,2,...,N/2\} \tag{17}$$

(2) if the answer on the first question is affirmative, then find the set of solutions of the system (16) under the conditions (11).

Statement 2:

(a) If $N \geq 6$, then image of the set V_Φ^N under the mapping $\{Y_1(\gamma,\varphi), Y_2(\gamma,\varphi)\}$, given by two first equations (6), represents a convex hull of a curve

$$\Gamma = \{y\in R^2: y=(\cos^4\varphi, \sin^4\varphi), \varphi\in\Phi^N\} = \{y\in R^2: y=(\eta, (1-\sqrt{\eta})^2), \eta\in\cos^4\Phi^N\} \tag{18}$$

where $\cos^4\Phi$ denotes the image of the set Φ under the mapping $(\cos)^4$.

(b) Any point that belongs to image of the set V_Φ^N under the mapping $\{Y_1(\gamma,\varphi),Y_2(\gamma,\varphi)\}$ can be obtained as a value of the function $\{Y_1(\gamma,\varphi),Y_2(\gamma,\varphi)\}$ on a vector $(\gamma,\varphi)\in U_\Phi^6$.

According to the above Statement, a balanced fiber-reinforced composite shell with any prescribed effective stiffnesses $\{A_{\alpha\beta}\}$, satisfying the solvability condition (8), can be designed by using not more than three pairs of plies with fiber placement angles $+\varphi_j$ and - φ_j.

MINIMIZATION OF FIBER VOLUME CONTENT

Let us consider now an optimization of the design problem concerning the minimization of the fiber volume content, ω. We include now the variable ω into the set of independent variables of the system (9), and consider the problem of minimization of ω on account the condition that the laminate has the prescribed set of effective stiffnesses. Suppose, we already solved the above design problem for some fixed ω value, e.g., $\omega = \omega_0$, so that, cf. Eq. (10),

$$Y_i(\gamma,\varphi) = y_i^0, \ i = 1,2,3,4 \tag{19}$$

where $\mathbf{y^0} = (y_1{}^0, y_2{}^0, y_3{}^0, y_4{}^0)$ is determined from expressions (9) with $\omega = \omega_0$. It follows from the formulas (9) that $\mathbf{y} = (\omega_0/\omega)\mathbf{y^0}$ will represent a solution for a given ω value. Moreover, fiber volume fractions γ_i satisfy conditions (11). As a result, we arrive to a problem to find a minimum ω value, such that the point $\mathbf{y}(\omega) = (\omega_0/\omega)\mathbf{y^0}$ belongs to convex set, *conv* Γ. Curve Γ has been described in Statements 1 and 2. The set

$$L = \{\mathbf{y}(\omega) = (\omega_0/\omega)\mathbf{y^0},\ \omega \in (0, \omega_0)\} \tag{20}$$

represents a ray having an origin in the point $\mathbf{y^0} \in$ *conv* Γ, and tending to infinity when $\omega \rightarrow 0$. Since the set *conv* Γ is compact (because Γ is compact), the ray L will intersect the boundary of the convex compact set *conv* Γ when ω equals some certain value, $\omega = \omega^*$, and they will have no other intersections when $\omega < \omega^*$. We formulate this result in form of the following Statement 3.

Statement 3:
The above formulated problem of the fiber volume content minimization is solvable if the design problem with the required set of effective stiffnesses and some prescribed ω_0 value is solvable. The ω minimum value is equal to ω^* that corresponds to an intersection of the ray L with the boundary of the set *conv* Γ. A design project for the composite shell with a minimum fiber content ω^* can be found by solving problem (10), (11) or the problem (16), (11) with a right-hand side equal to $\mathbf{y} = (\omega_0/\omega^*)\mathbf{y^0}$.

ACKNOWLEDGMENT

This work has been supported by the Natural Sciences and Engineering Research Council of Canada (NSERC).

REFERENCES

[1] Kalamkarov, A.L. *Composite and Reinforced Elements of Construction.* Wiley, Chichester, New York (1992).

[2] Kalamkarov, A.L. and Kolpakov, A.G. *Analysis, Design and Optimization of Composite Structures.* Wiley, Chichester, New-York (1997).

[3] Vinson, J.R. *The Behavior of Shells Composed of Isotropic and Composite Materials.* Kluwer, Dordrecht (1993).

[4] Kalamkarov, A. L. "On the Determination of Effective Characteristics of Cellular Plates and Shells of Periodic Structure." *Mechanics of Solids*, **22**, pp. 175-179 (1987).

[5] Rockafellar, R. T. *Convex Analysis.* Princeton University Press, Princeton, NJ (1970).

OPTIMUM DOME CONTOUR OF COMPOSITE SHELL WOUND WITH A ROVING OF FINITE WIDTH

Aleksey A. Krikanov
MATI-Russian State University of Technology
19-3-255, Shosseinaya Str., Moscow, 109548, Russia
Tel:(095)-915-2127, E-mail:akrikan @ openmail.irex.ru

Abstract– Composite shell of revolution formed by winding is considered. A new thickness formula for the shell wound with a roving of a finite width has been derived. Using equilibrium equations and Clairaut's equation for the geodetic winding an optimum dome contour of the shell is obtained with a uniform stress state over the shell. The numerical results and graphics are given to show the real shell thickness and optimum dome contour depending on the roving width.

1. INTRODUCTION

Composite shells of revolution formed by filament winding (Fig 1) have a wide application as pressure vessels and as bearing structures for a solid rocket motor case. In this paper a new thickness formula for a such shell is proposed. The traditional one was suggested for a winding with a roving of an infinitesimal width. Real shells are wound with a roving of finite width to accelerate the winding process. The suggested formula substantially differs from the previous one in the polar opening range, where shell radius is comparable with a roving width. An optimum dome contour is defined using the new formulas. Comparison of the new meridian shape is done with the previous one.

2. SHELL THICKNESS

A thickness distribution is the important variable for design and analysis of composite shells of revolution produced by filament winding. Obviously, the thickness h of the shell is a variable quantity because during continuous winding the same number of rovings passing through cross section is located along the parallels of different radii. Usually the next formula is used [1]

$$h = \frac{nf}{2\pi r \cos\varphi} \tag{1}$$

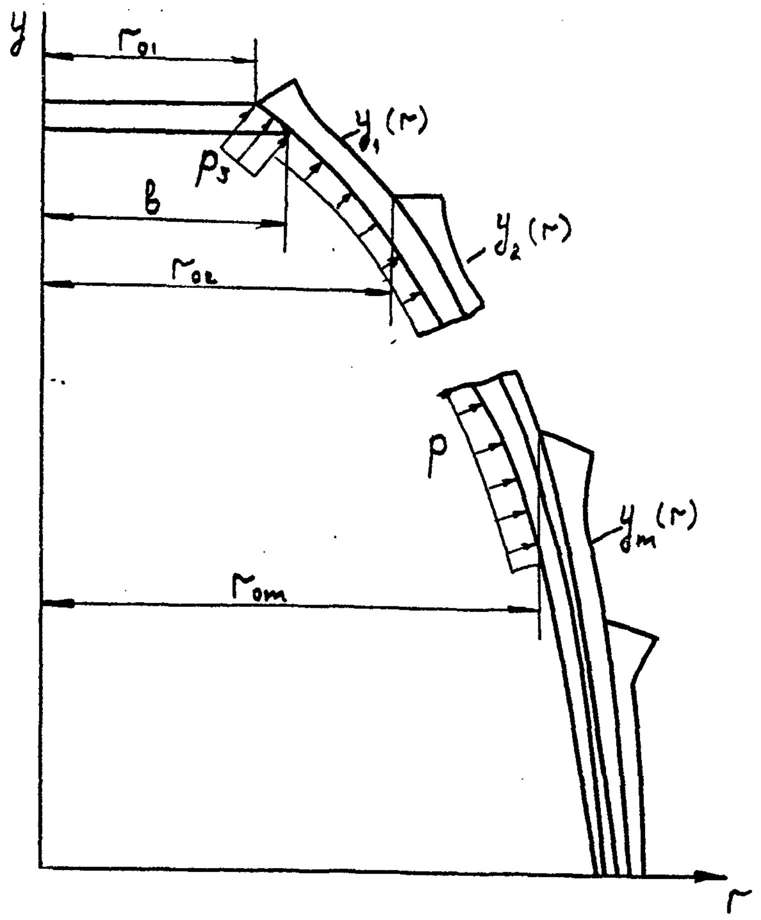
y
r_{01}
$y_1(r)$
p_3
b
$y_2(r)$
r_{02}
p
$y_m(r)$
r_{0m}
r

Fig 1: Cross section of laminate composite shell of revolution

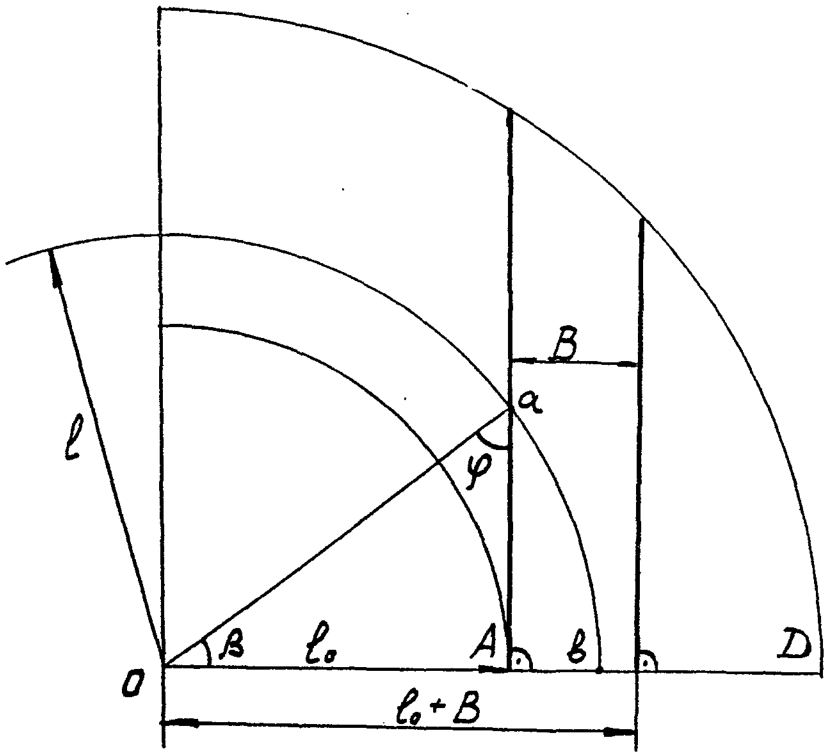
l
B
a
φ
β
l_0
A
b
D
0
l_0+B

Fig 2: Development of the shell surface, cut near the shell polar opening

where n — number of rovings passing through a cross section; $f = B\delta$ — cross section of the roving; B, δ — roving width and thickness respectively; r — shell radius; φ — angle between a fiber and the meridian. The Eqn (1) can be obtained in the following manner. Let set aside a cross section shell element and approximate it by cylinder and unfold it on a plane. In so doing n rovings with cross section f pass through n arbitrary cross section r=const. Then, taking into account that rovings intersect parallels at an angle of $\pi/2 - \varphi$, we can write the formula (1) for the area of the shell cross section. This formula is suitable for a gently sloping surface and in the case when a roving width is significantly less than shell radius ($B/r \longrightarrow 0$). However this formula is not correct near polar opening range ($h \longrightarrow \infty$ at $\varphi \longrightarrow \pi/2$), when in fact thickness goes to zero at $\varphi \longrightarrow \pi/2$. This can be avoided if the shell cross section element is unfolded as a taper surface. Let set aside a cross section element near the shell polar opening and approximate it with a taper element and unfold it on a plane (Fig 2). At a point A the roving is a tangent to the polar opening, so all its fibers are perpendicular to the taper meridian OD. The roving cross section is represented as an arc $\overset{\smile}{ab}= l \cdot \beta$, where $l = r\sqrt{1+z^2}$ — the meridian length, $z = y'(r)$ - derivative of the shell meridian $y(r)$. The angle β can be expressed through the wound angle φ. Considering a triangle OaA we have $\beta = \pi/2 - \varphi$. Then $\overset{\smile}{ab}= r\sqrt{1+z^2}(\pi/2 - \varphi)$. Multiplying $\overset{\smile}{ab}$ by the roving thickness δ and number of rovings n and dividing by $2\pi r$ we'll get the shell thickness

$$h(r) = \frac{n\delta}{2\pi}\sqrt{1+z^2}(\pi/2 - \varphi).$$

Taking into account that a geodetic winding takes place, i.e.

$$\sin\varphi = r_0/r, \tag{2}$$

we obtain

$$h(r) = \frac{n\delta}{2\pi}\sqrt{1+z^2}\left(\frac{\pi}{2} - \arcsin\frac{r_0}{r}\right), \qquad r_0 \le r \le r_0^*, \tag{3}$$

where radius r_0^* approximately can be defined as follows

$$r_0^* = r_0 + \frac{B}{\sqrt{1+z^2(r_0^*)}}. \tag{4}$$

Now set aside an infinitesimal cross section shell element at the central part of the dome $l_0 + B \leq l$, approximate it with a taper element and unfold it on a plane (Fig 3). The roving cross section is represented as an arc $\overset{\smile}{ab}= l(\beta_1 - \beta_2)$, where $l = r\sqrt{1+z^2}$. Roving fibers are parallel to each other, so $\beta_1 - \beta_2 = \varphi_2 - \varphi_1$, where φ_1, φ_2 — wound angles of the extreme left and right roving fibers respectively. As is well known, a flexible fiber wound over the surface of revolution without friction tends to align along the geodetic line of the surface obeying the Clairaut's equation (2) whence we have

$$\varphi_1 = \arcsin r_0/r, \qquad \varphi_2 = \arcsin(r_0 + B/\sqrt{1+z^2})/r.$$

and thickness formula is reduced to the following

$$h(r) = \frac{n\delta}{2\pi}\sqrt{1+z^2}\left(\arcsin\frac{r_0 + B/\sqrt{1+z^2}}{r} - \arcsin\frac{r_0}{r}\right), \qquad r_0^* \leq r. \tag{5}$$

We can expanse Eqn (5) in Taylor series using Eqn (2)

$$h(r) = \frac{nf}{2\pi r\cos\varphi}\left(1 + \frac{\sin\varphi}{\cos^2\varphi}\cdot\frac{\Delta}{2!} + \frac{1+2\sin^2\varphi}{\cos^4\varphi}\cdot\frac{\Delta^2}{3!} + \ldots\right), \tag{6}$$

where $\Delta = B/r\,\sqrt{1+z^2(r)}$. Eqn (6) is true for $r_0^* \leq r$ and turns into Eqn(1) when $(B/r \longrightarrow 0)$. At a point3 $r = r_0^*$ Eqn (3) coincides with Eqn (4). Three curves of shell thickness at various roving widths are given in Fig 4, from which follows that the more a roving width than the less a peak height of the curve.

3. OPTIMUM DOME CONTOUR

Derivation of the optimum dome contour of filament wound shells was done in [1] and based on the thickness formula (1). In this work the refined optimum dome contour based on the new formulas (3,5) have done. Equilibrium equations can be written as

$$(rN_\alpha)' - N_\beta = 0; \tag{7}$$

$$\frac{z'}{(1+z^2)^{3/2}}N_\alpha + \frac{z}{r\sqrt{1+z^2}}N_\beta = -p, \tag{8}$$

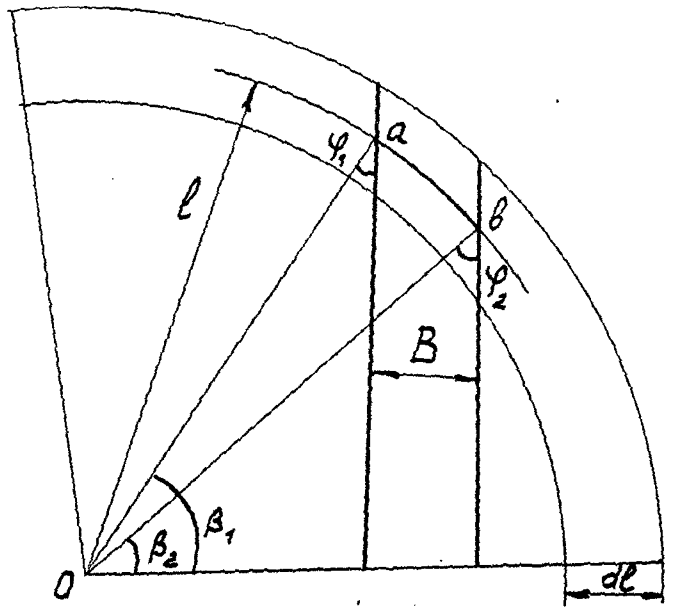

Fig 3: Development of the shell surface, cut in the central part of the shell

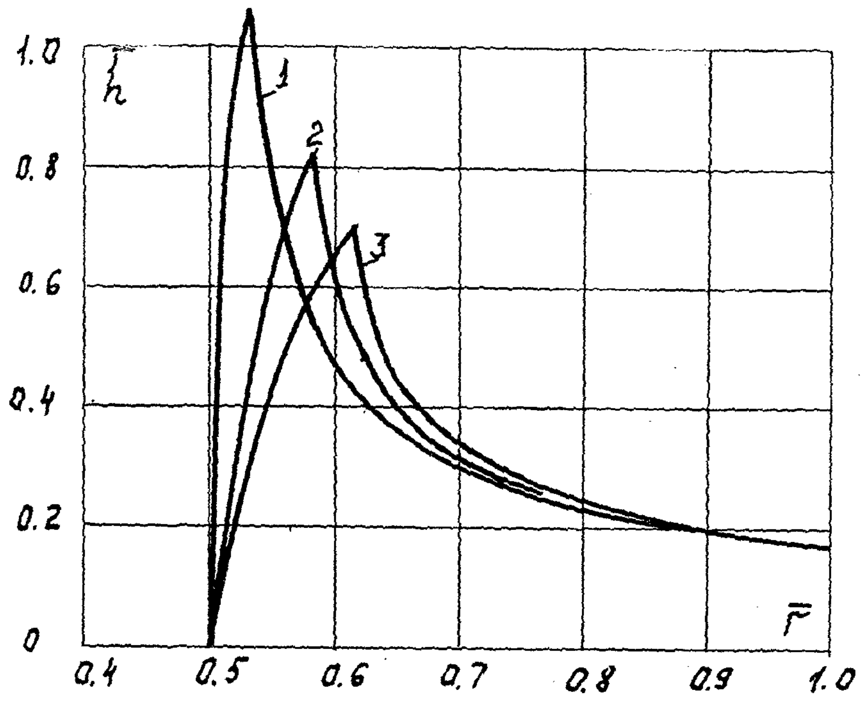

Fig 4: Variation of shell thickness as a function of dome radius at various roving widths: 1 — $\bar{B} = 0.04$, 2 — $\bar{B} = 0.10$, 3 — $\bar{B} = 0.14$, $\bar{B} = B/R$

where N_α and N_β — stress resultants acting in the shell along and across the meridian; the prime denotes the derivative with respect to r. Substituting N_β from (7) to (8), taking into considering the equality $(z/\sqrt{1+z^2})' = z'/(1+z^2)^{3/2}$ and integrating the obtained one with due regard for the condition $1/z(a) = 0$ (which requires that for $r = a$ the tangent to the meridian be parallel to y-axis) we have

$$\frac{\sqrt{1+z^2}}{z} = -\frac{2N_\alpha}{pr}. \tag{9}$$

Further a netting analysis is used, i.e. we assume that stresses σ_2 and τ_{12} borne by matrix are negligible in comparison with stresses σ_1 acting along the fibers. The stress resultants are expressed through stresses σ_1 in the following manner

$$N_\alpha = \sigma \int_0^B \cos^2\varphi \, dh; \qquad N_\beta = \sigma \int_0^B \sin^2\varphi \, dh, \tag{10}$$

where dh — thickness of the shell, formed by roving with dx width, where $x \in [0, B]$ — current coordinate along the roving width. Using Eqn (5) we derive

$$dh = \frac{n\delta}{2\pi}\sqrt{1+z^2}\,\frac{du^*}{\sqrt{1-u^{*2}}}; \qquad u^* = \frac{r_0 + x/\sqrt{1+z^2}}{r}; \tag{11}$$

Substituting (11) to (10) and supposing $z(r)$ =const along the width we obtain

$$\begin{aligned} N_\alpha &= 0,5A\left(\frac{\pi}{2} - \arcsin u - u\sqrt{1-u^2}\right), && r_0 \le r \le r_0^*, \\ N_\alpha &= A\int_{u_0}^{u_1}\sqrt{1-u^2}\,du = 0,5A\left(\arcsin u + u\sqrt{1-u^2}\right)\Big|_{u_0}^{u_1}, && r_0^* \le r, \end{aligned} \tag{12}$$

where $A = 0,5n\delta\sigma\sqrt{1+z^2/\pi}$; $u_0 = r_0/r$; $u_1 = u_0 + \Delta$; $\Delta = B/r\sqrt{1+z^2}$. Eqn (10) with Eqs (12) is used to determine the equilibrium shapes of shells of revolution in which loading is sustained by a system of fibers. Expanding Eqn (12) in Taylor series we have

$$\frac{\sqrt{1+z^2}}{z} = \frac{u^2\sqrt{1-u^2}}{\alpha \bar{r}_0^2}\left(1 - \frac{u}{1-u^2}\frac{\Delta}{2!} - \frac{1}{(1-u^2)^2}\frac{\Delta^2}{3!} - \ldots\right); \tag{13}$$

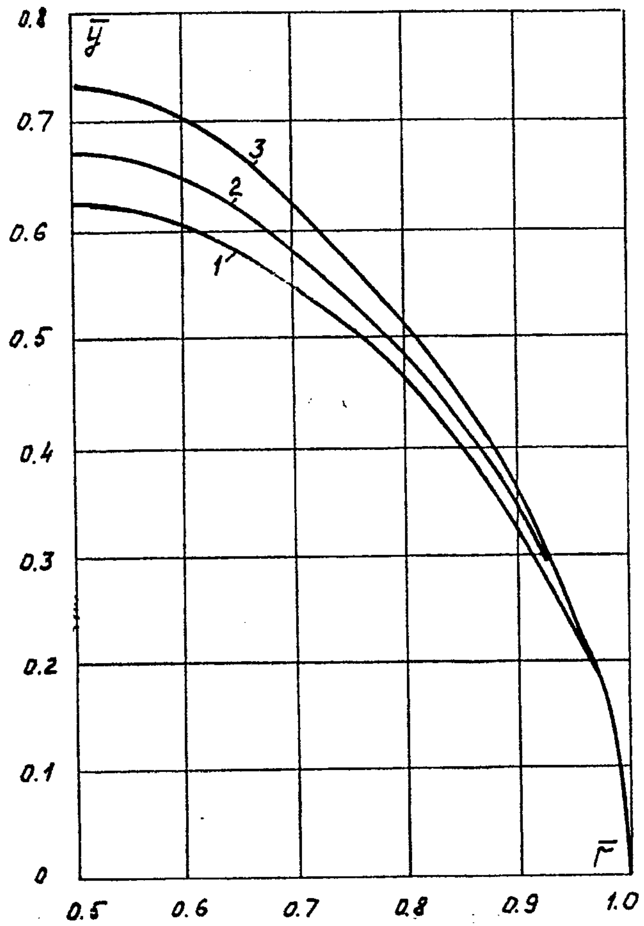

Fig 5: Meridian shape of a shell with polar opening $\bar{r}_0 = 0.5$ as a function of radius at different roving widths: $1 — \bar{B} \longrightarrow 0$, $2 — \bar{B} = 0.10$, $3 — \bar{B} = 0.20$

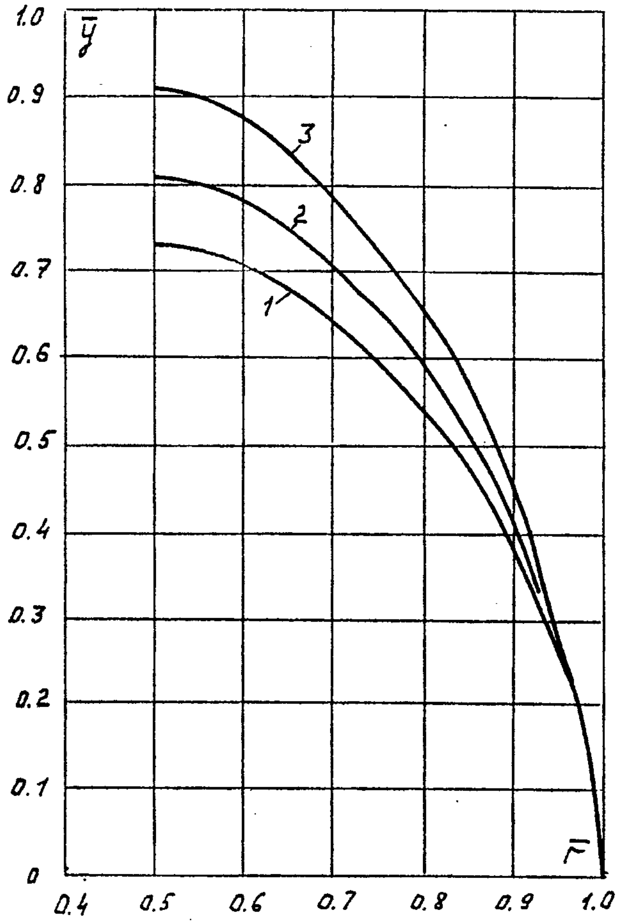

Fig 6: Meridian shape of a two laminate shell with $\bar{r}_{01} = 0.5$; $\bar{r}_{02} = 0.9$; $\beta = 0.16$ as a function of radius at various roving widths: $1 — \bar{B} \longrightarrow 0$, $2 — \bar{B} = 0.10$, $3 — \bar{B} = 0.20$

where $\alpha = \sqrt{1-\bar{r}_0^2}$ and $r_0^* \leq r \leq a$. Function $z = y'(r)$ is determined as a solution of nonlinear Eqn (13) written in unopened form. The dome contour equation $y(r)$ is defined by numerical integration z with respect to r. The Fig 5 shows contours of shells with polar opening radius $\bar{r}_0 = 0,5$, produced by roving of an infinitesimal width (curve 1) and rovings of various finite widths: $\bar{B} = 0,10$ (curve 2) and $\bar{B} = 0,20$ (curve 3). For the laminate shell we have a similar expression

$$\frac{\sqrt{1+z^2}}{z} = \frac{1}{\alpha\bar{r}^2}\left[\sum_{i=1}^{m-1}\beta_i\sqrt{1-u_i^2}\left(1-\frac{u_i}{1-u_i^2}\frac{\Delta}{2!}-\frac{1}{(1-u_i^2)^2}\frac{\Delta^2}{3!}-\ldots\right)+\right.$$

$$\left.+\frac{\beta_m}{2\Delta}\left(\frac{\pi}{2}-\arcsin u_m-u_m\sqrt{1-u_m^2}\right)\right], \qquad r_{0m}\leq r\leq r_{0m}^*; \tag{14}$$

$$\frac{\sqrt{1+z^2}}{z}=\frac{1}{\alpha\bar{r}^2}\sum_{i=1}^{m-1}\beta_i\sqrt{1-u_i^2}\left(1-\frac{u_i}{1-u_i^2}\frac{\Delta}{2!}-\frac{1}{(1-u_i^2)^2}\frac{\Delta^2}{3!}-\ldots\right), \quad r_{0m}^*\leq r\leq r_{0m+1}, \tag{15}$$

where $\beta_i = n_i f_i \sigma_i/(n_1 f_1 \sigma_1)$, $\alpha = \sum_{i=1}^{k}\beta_i\sqrt{1-\bar{r}_{0i}^2}$, $u_i = r_{0i}/r$. Eqn (13) is used to determine optimum contour at $r_{01}^* \leq r \leq r_{02}$. Fig 6 shows the contours of two laminate shells ($\bar{r}_{01} = 0,5$; $\bar{r}_{02} = 0,9$; $\beta = 0,16$;) based on Eqs (14),(15) and (13) at different roving widths; curve 1 — $\bar{B} \longrightarrow 0$; curve 2 — $\bar{B} = 0,10$; curve 3 — $\bar{B} = 0,20$.

4. CONCLUSIONS

1. Thickness formulas for the shell produced by roving winding (3,5) has been derived that permit to specify Eqn (1) near polar opening range.
2. Optimum dome contour has been obtained based on Eqs (3,5) formed by rovings which are slightly stretched in an axial direction of the shell with comparison to contour formed by rovings of infinitesimal width.

REFERENCE

1. Valery V.Vasiliev *Mechanics of Composite Structures*, Taylor & Francis, 1993.

DESIGN AND ANALYSIS OF A LIGHTWEIGHT FRIGORIFIC SEMITRAILER BY MEANS OF A NUMERICAL SIMULATION PROCEDURE

E. LARRODÉ, L. CASTEJÓN, M.A. JIMENEZ y R. CLEMENTE

Department of Transportation Engineering
University of Zaragoza
c/ María de Luna, 3 - 50.015 Zaragoza (Spain) Tel: (+34) 76 761888, Fax: (+34) 76 761861

ABSTRACT

Self portable trailers are different from usual portable trailer structures since it is the structure by itself which support all load requirements. A new design and optimization of the structure of a self portable frigorific trailer is presented. The weight optimization of the frigorific self portable trailer can be achieved due to the great number of possible combinations which are feasible to be done with different kinds of materials and their corresponding geometric configurations, this involved a redesign of the initial structure as well as the ultimate calculation, obtaining 30% weight saving[17] [20] [19].

Keywords: self portable frigorific trailer, composite materials, substructures, finite element method.

1. INTRODUCTION

Low fuel consumption and higher velocities are some of the benefits that can be achieved as a consequence of this weight reduction. An important design parameter that can be kept in mind is the specific strength of composite materials[11] because the most of uses of composite materials in the automotive industry are due to this characteristic. Nowadays, safety requirements and vehicle stability as well as fuel consumption are important design parameters of transportation vehicles and composite materials offers alluring solutions for all these requirements.

2. DESIGN OF THE SUPERSTRUCTURE

Frigorific vehicles are widely manufactured all over the world and due to the ability to introduce new materials makes this type of structure feasible to be redesigned and optimized for weight and cost. A self portable frigorific trailer is a new design which is different with respect to last designs because of the proper definition. Usual portable trailers are supported in a metallic frame, as shown in figure 2.1, that takes the task of bearing reaction forces and stresses caused by the structure and the load in static and dynamic situations. So, this portable trailer it is usually an unloaded and over dimensioned structure. Self portable trailer (see figure 2.3) are designed to substitute frame tasks; that is, it is the same box structure which has the role to bear reaction forces and stresses. So, metallic frame is removed (see figure 2.4) and a replacing carbon grid is fitted in this place.

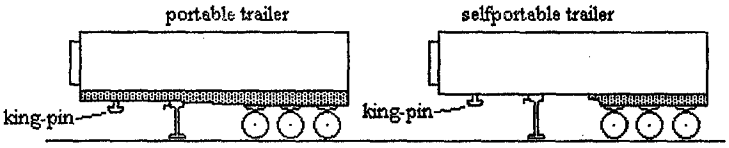

Figure 2.1. Self portable trailer definition.

This grid is introduced inside the sandwich panel of the floor structure, as well as the grid which is attached to the parking device. Only a little metallic frame is maintained in the rear axes group because of the standardization of this part. A light structure is achieved this way and weight saving can be obtained, gaining more load capability and reducing fuel consumption. Global dimensions of the structure are given below and they must be kept invariable because of the standards of the European Community. Only internal dimensions as well as material composition are suitable to be varied. (Trailer length: 13500 mm ; Trailer width: 2590 mm ; Trailer height: 2800 mm). Main structure is basically composed of five substructures, namely; front, which has to bear cool equipment; floor, which has the task to bear all the stresses due to the carried load and the rest of the structure as well as to transfer loads to head truck by means the fifth wheel (king-pin) and to the rear axis group; laterals and roof making a close box structure[30]. Once all substructures are assembled, the result it is a close structure with a good flexural and torsion behavior resembling a hollow box beam as shown in figure 2.2.

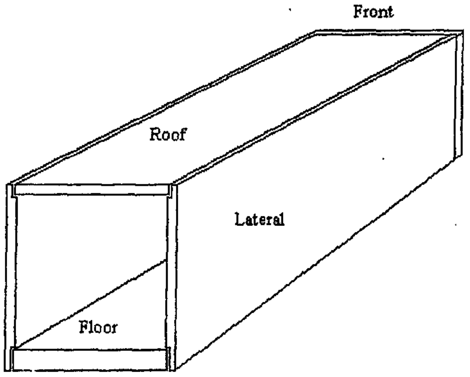

Figure 2.2. ***Substructures assembling***

Taking a look at the micro-composition of the self portable trailer, it can be considered composing of different parts depending on the substructure. All substructures are composed by stiffened sandwich panels[29] but the stiffeners of laterals and roof are light beams made of glass fiber laminates.

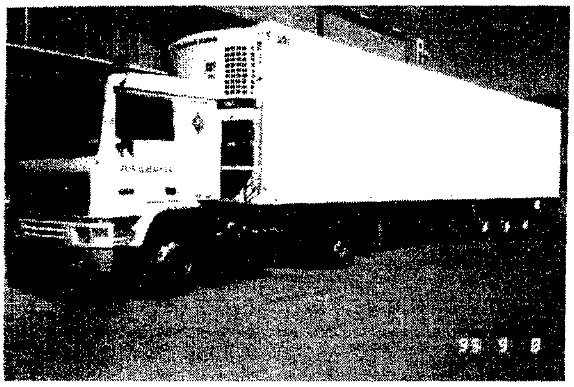

Figure 2.3. Self portable frigorific semitrailer view

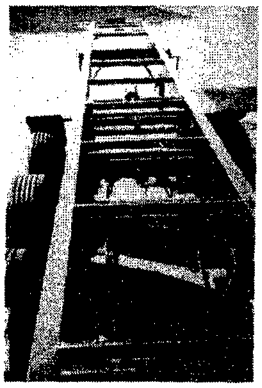

Figure 2.4. King-pin structure

3. FINITE ELEMENT MODEL AND CALCULATION

3.1. Model Creation

Finite element analysis[3] has been carried out on the whole structure. A Silicon Graphics Workstation and IDEAS program was used to do the modelization.(see figures 3.1 to 3.3) [18]. The modelization was done bearing in mind two basic ideas: introduce all the components of the structure (stiffeners, laminates, cores, etc.) and obtain the maximum discretization (refined meshing) to analyze singular areas.

Table 3.1. Number of nodes and elements in the modelization

Zone	n° Nodes	n° Elements
Floor		
- king-pin zone	3.993	2.626
- rest zone	2.226	1.672
Left Lateral	4.078	2.532
Right Lateral	4.078	2.532
Front	665	450
Roof	883	572
TOTAL	15.923	10.384

Frigorific trailer is considered as a superstructure[12] [25] not only due to dimensions but also to the number of different materials forming the structure. Manufacturing process makes the substructures composition totally heterogeneous. Modelization was made by means substructures technique, this way we could follow the same order than the manufacture process, joining different parts as in the real case. The number of elements and nodes per substructure are shown in Table 3.1.

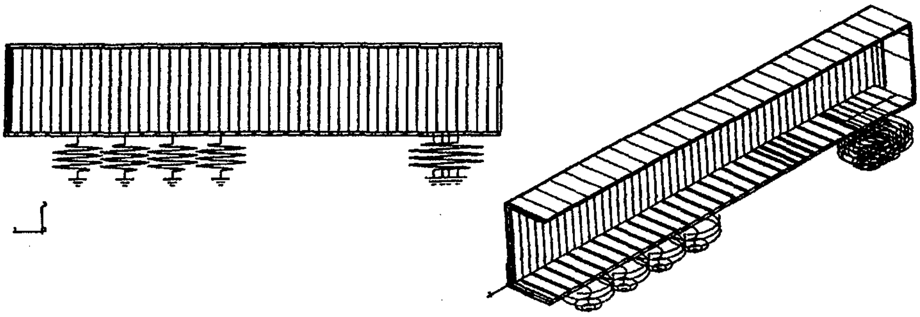

Figure 3.1. Half model discretization

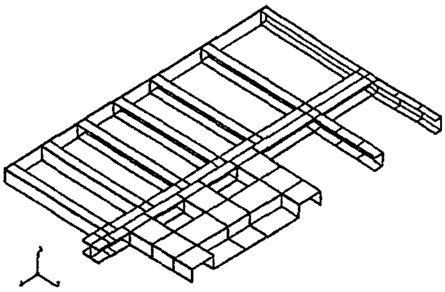

Figure 3.2. Half king-pin grid detail.

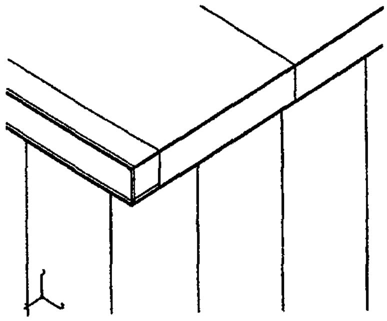

Figure 3.3. Roof and floor details.

3.2. Load Hypothesis and Boundary Conditions

The analysis of different external loads over the structure has resulted in obtaining several basic load conditions. These basic load conditions have been subdivided in four groups; vertical loads, longitudinal loads, transversal loads and the corresponding loads for specific testing to carry out the quality control. Description of basic load conditions as well as the basic boundary conditions are as follow[22]:

1) Basic load conditions.
- Vertical loads:
1.1. Gravity load of the trailer.
1.2. Maximum distributed load in the trailer.
- Longitudinal loads:
1.3. Trailer with maximum load accelerating with maximum acceleration.
1.4. Trailer with maximum load decelerating with maximum deceleration.
- Transversal loads:
1.5. Trailer swerving with minimum swerve radius.
- Statutory testing loads:
    1.6. Trailer in testing over lateral.
    1.7. Trailer in testing over front.
    1.8. Trailer in testing over floor (fork-lift).
    1.9. Trailer in testing over roof.

2) Basic support states.
2.1. Support over suspension in rear axes and suspension in tractor head.
2.2. Support over suspension in rear axes and parking supports.
2.3. Specific supports when statutory testing.

3.3. Results

Calculations were done using ABAQUS/standard[1] as a finite elements code in a CONVEX computer. A security coefficient of three was taken for the calculations. Results for every load case are showed in figures 3.4 to 3.12, where deformed shapes and contour of principal stresses[23] are presented (being the upper figure the deformed shape and the second figure the stress profile for each case). In figure 3.13 the deformed shapes of the three principal frequencies are shown for loaded and unloaded trailer[9] [13].

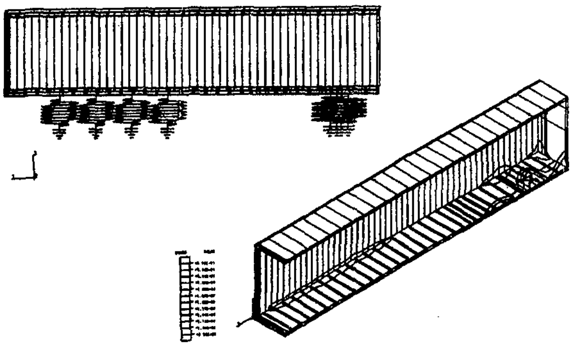

Figure 3.4. Gravity load.

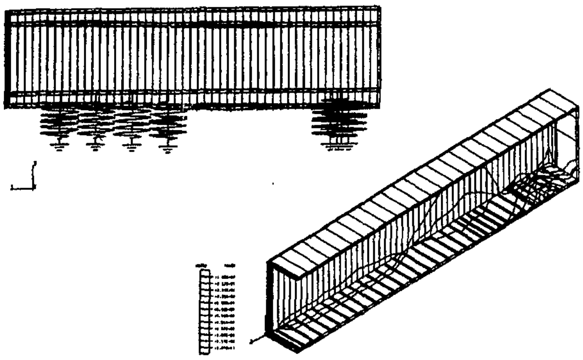

Figure 3.5. Maximum distributed load.

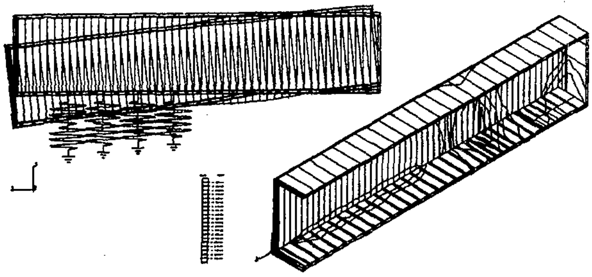

Figure 3.6. Parking state with maximum load.

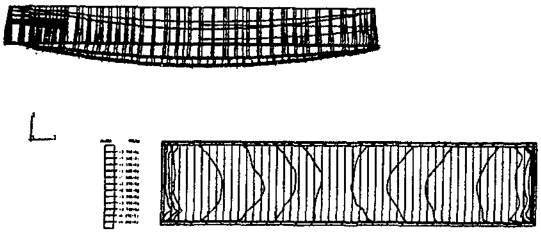

Figure 3.7. Lateral testing.

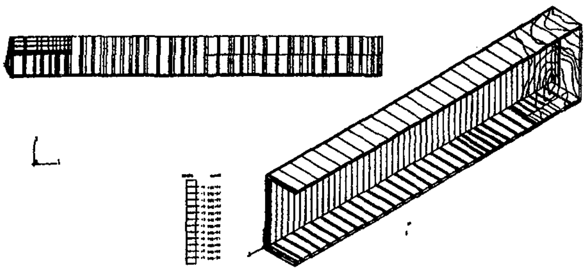

Figure 3.8. Front testing.

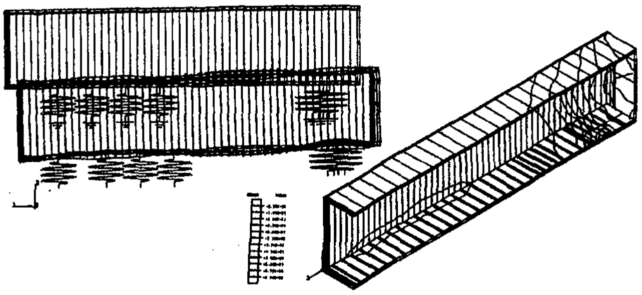

Figure 3.9. Sudden braking with maximum load.

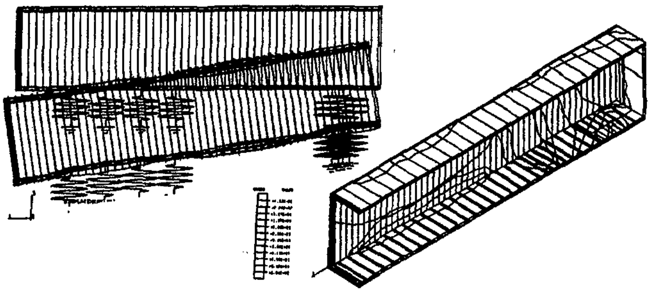

Figure 3.10. Strong swerving with maximum load.

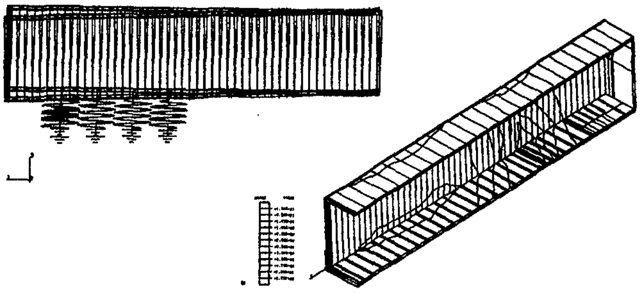

Figure 3.11. Lift-fork during parking state.

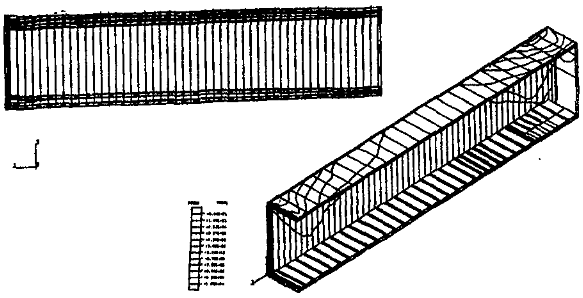

Figure 3.12. Roof testing.

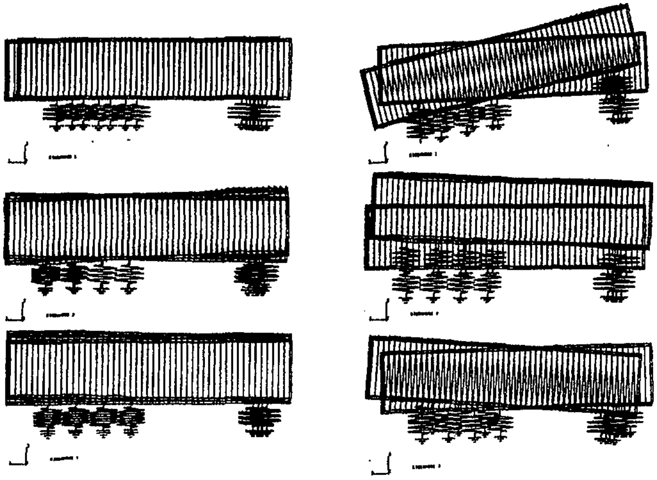

(I) (II)

Figure 3.13. Principal frequencies
I) Empty trailer. II) Loaded trailer.

4. WEIGHT OPTIMIZATION

The aim of this study is intended to optimize the weight of the present portable trailer (see figure 4.1) without an increase of cost. So, new raw materials as well as new configuration of present materials will be used in order to get high strength and rigidity and light structures at low cost. Numerical analysis will be used to notice weak areas and no-loaded zones which will be feasible to be respectively reinforced or lightened. The following tables and figures show how materials can be modified in order to achieve weight savings and maintaining design conditions as stiffness-strength and inertia-weight ratios.

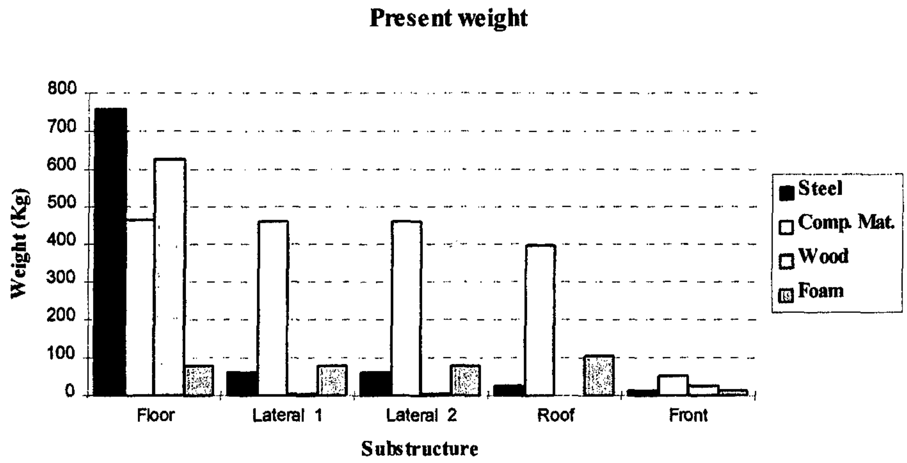

Figure 4.1. Present substructures weight

Present skin configurations belonging to sandwich panels of all substructures (lateral, floor, roof and front) used to be composed by mat or mat and woven laminates. An adequate change of the percentage of fiber in volume content, and modifying weight content in order to maintain inertia and strength conditions, weight saving percentage can be obtained.

5. CONCLUSIONS

The philosophy followed to perform the optimization study has been to replace present configurations by new ones which satisfy all stiffness and strength requirements but taking a substantial weight saving. Due to the impossibility to modify some manufacturing process, the basic design has been maintained and therefore material configurations have been optimized mainly. The most important changes were :

- appropriate design of laminates (introducing non-balanced woven).
- increasing of laminate properties (increasing the percentage of fiber in volume content)
- replacement of reinforcement beams by pultruded beams
- replacement of the steel grid at the fifth wheel zone by other made of carbon

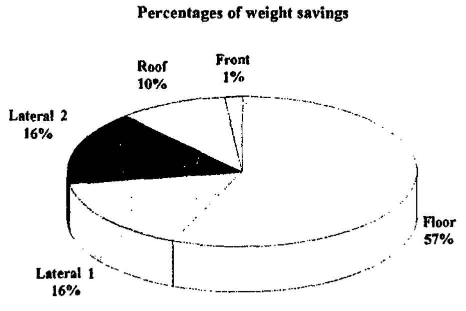

Figure 5.1. Weight saving percentage obtained

Therefore a weight saving of about 30% has been achieved and this makes this new design more competitive because of its lightness. The entire model has been designed in composite materials, calculated by means the most advanced methods of calculation, and offers the advantage to have one ton of weight saving which implies increasing of load capacity and reducing of fuel consumption.

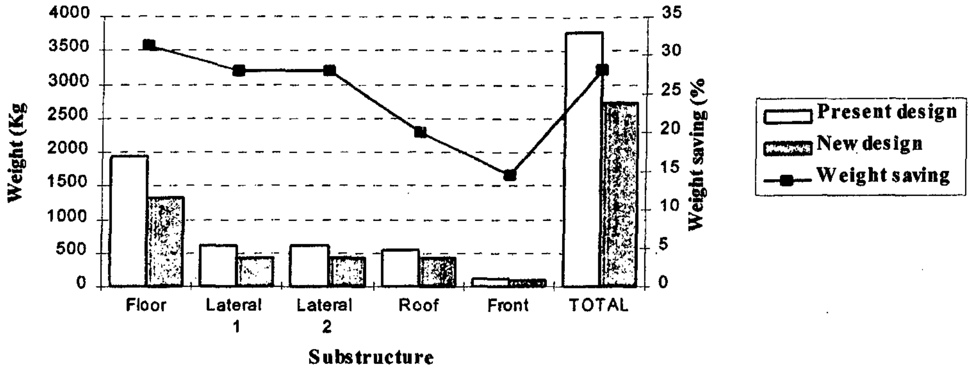

Figure 5.2. Weight comparison

6. REFERENCES

1. ABAQUS, version 5.3, Hibbitt, Karlsson and Sorensen, Inc.
2. AUBRY M. Suspensions de Vehicules Automobiles a base de Materiaux Composites. Int. Ingenieurs de l'automobile.
3. BATHE, K.J. and WILSON, E.L. *Numerical methods in finite element analysis.* Prentice-Hall, 1976
4. BENJAMIN B.S.. Structural Design with Plastics. New York, 1982
5. BRAVO P., LARRODÉ E., MIRAVETE A. Crash Absorbing Elements for Automotive Aplications. (ICCM IX), Madrid, España. Julio 1993.
6. BRAVO P., LARRODÉ E., MIRAVETE A., TAMPARILLAS S. Analysis of a Crash Absorbing Elements for Automotive Aplications. (ICCS VIII), Paisley, Escocia (U.K.). Julio 1993.
7. FRAEIJS DE VEUBEKE, B., SANDER, G., BECKERS, P., Dual Analysis by Finite Elements: Linear and Nonlinear Applications. TR 72-93, Air Force Flight Dynamics Laboratory, Fairborn, Ohio, EE.UU., (1972).
8. HERTZBERG R.W., MANSON J.A. Fatige of Engineering Plastics. Ac. Press, Inc. London, 1980
9. HUNCKLER, C. J., YANG, T. Y., AND SOEDEL, W., A Geometrically Nonlinear Shell Finite Element for Tire Vibration Analysis. Computers and Structures, Vol. 17, No.2, pp. 217-226, (1983).
10. JAMES M.P. Les Composites dans l'automobile. Perspectives a Moyer Terme. Int. Ingenieurs de l'automobile.
11. JONES R. M. *Mechanics of composite materials.* Hemisphere Publishing Corporation, 1975.
12. JONES R. CALLINAN R., TEH T.K. and BROWN K.C., Analysis of multy-layer laminates using three dimensional super-elements. Int. J. Numer. Meth. Engng. 20, 583-587 (1984).
13. KAPANIA, R. K., AND YANG T. Y., Time Domain Random Wind Response of Cooling Towers. Journal of Engineering Mechanics, ASCE, Vol 110, No. 10, pp. 1524-1543, (1984).
14. LANFRANCHINI M.J.J. Sythèse sur l'industrialisation des Composites dans l'automobile. Int. Ingenieurs de l'automobile.
15. LARGUIER M.P. Les Composites et la Mecanique. Int. Ingenieurs de l'automobile, 3-83, pp. 21-25
16. LARRODÉ E. Determination of interlaminar shear stresses by means of the double notch testing. (SAMPE), Maastrich, Holanda. May 1991.
17. LARRODÉ E., CASAMAYOR M.J., MIRAVETA A., ULLOD J. Design and Optimisation of a full Composite Isotherm Structure. COMPOSITE & STRUCTURES International Journal, Paisley, U.K.. Mayo 1994.
18. LARRODÉ E., MIRAVETE A. Finite Element Analysis of a Bus Structure Using Subestructure Technique. INTERNATIONAL CONGRESS ON COMPOSITE STRUCTURES (ICCS VIII), Paisley, Escocia (U.K.). Julio 1993.
19. LARRODÉ E., MIRAVETE A., ALBA J.J. Analysis of composite structures using the substructures technique. INTERNATIONAL CONGRESS ON COMPOSITE MATERIALS (ICCM-IX), Madrid, España. Julio 1993.
20. LARRODÉ E., MIRAVETE A., CASAMAYOR M.J. Optimización de un Semirremolque Isotermo. I CONGRESO IBEROAMERICANO DE INGENIERIA MECANICA. Madrid. España. Sept. 1993.
21. MARTELET M.C. Les Materiaux Composites et l'automobile. Compatibilité entre Fibres et Matrice. Int. Ingenieurs de l'automobile, 3-83, pp. 50-54
22. MIRAVETE A., BRAVO P., LARRODÉ E. F.E.M. applied to a truck frame made of hybrid composites. Finite element methods for composite materials. A workshop held at imperial college. London, U.K. 5-6 Septiembre 1991.
23. MIRAVETE A., LARRODÉ E., CASAMAYOR M.J. .Design and Manufacturing of 3-D continuous composite structures. CONGRESO INTERNACIONAL DE MATERIALES COMPUESTOS (ICCM VIII), Hawaii (U.S.A.). Julio 1991
24. PAGANO N.J. and PIPES R.B., Some observations on the interlaminar strength of composite laminates. Int. J. Mech. Sci. 15 (1973).
25. PETERSSON H. and POPOV E.P., Substructuring and equation system solutions in finite element analysis. Comput. Struct. 7, (1977).
26. REYMAN MM.J.J., RUSSIER R., SIDOROFF F., VINCENT L. Les Composites et la Mecanique: le Ressort de Suspension. Int. Ingenieurs de l'automobile.
27. REDDY, J.N., "A review of refined theories of laminated composite plates", Shock & Vibration Digest, 22 (7), (1990).
28. TSAI S. W. *Theory of Composite Design.* Think Composites, 1992.
29. VENG C.E.S., UNDERWOOD E.E., LIU T.L. Shear Modulus of New Sandwich Cores Made of Superplastic Sheet. AIAA Journal, vol. 18, 1980 pp. 721-725
30. VIEGAS H.K., PEDERSON D.L. A Structural Analysis Design Procedure for Truck Mounted Refrigeration unit Frame Assemblies. 4th International Conference on Vehicle Structural Mechanism, Detroit, 1981.

STANDARDS: U.N.E., D.I.N., I.S.O., A.S.T.M.

DESIGN OF COMPOSITE PLATES UNDER CYCLIC LOADING

A. MUC and Z. KRAWIEC

Institute of Mechanics & Machine Design,Cracow University of Technology,ul. Warszawska 24,31-155
Kraków, Poland

INTRODUCTION

In order to utilize completely the potential of composite materials as advanced materials it is also necessary to propose a methodology for assesment of their long term properties. Development of such a methodology requires analysis of the basic mechanisms of degradation of properties and then the application of the knowledge into modelling of the structural response due to fatigue loads.

Now a great number of monographs and review papers present the actual state-of-the-art understanding of damage mechanisms in composite fatigue. However, in this work we do not intend to dwell on it. It is worth to emhasize only that the conducted analysis of fatigue damage may be classified in the following way:

- the parametrical description of fatigue process, employing also the statistical distributions – see e.g. Yang *et al.* [1],
- the progressive damage analysis with the use of the fracture mechanics techniques – possible cracks and their progression are treated as delaminations in composite materials – see e.g. O'Brien *et al.* [2].

Generally, the fatigue damage mechanisms results in the reduction of the strength, stiffnesses and other material properties. The amount of the stiffness loss depends on the fibre orientations of the cracked ply, stacking sequences,the relative moduli of the fibre and the matrix and the density of cracks in the individual ply.

The aim of the present work is twofold:

i. to propose and discuss methods of numerical analysis of composite structures, such as plates and shells, and subjected to fatigue loads, mainly with the use of the commercial FEM package NISA II [3],
ii. to demonstrate the results of numerical studies on the example of plates made of aramid/epoxy resin and subjected to cyclic shear loads.

The present work is an extension of methods and results discussed by Muc & Krawiec [4].

At the end of our considerations we present an experimental model which have been used to the critical verification of numerical modelling. However, the results of the fatigue tests have not been completed yet.

OPEN PROBLEMS IN MODELLING OF FATIGUE FAILURE PROCESS

Fatigue damage in composite laminates or structures (fibre reinforced plastics/ polymeric resin) is a phenomenon involving various failure mechanisms that are typically preceeded by an accumulation of matrix cracks. The consistent and correct description of progressive failure behaviour due to fatigue load is a complex and difficult task taking in addition into account possible statistical distributions of material constants. However, even in the pure deterministic approach to the problem one can encounter a variety of problems that cannot be uniquely solved. Therefore, at the beginning we intend to point out the basic areas of difficulties and then in the next paragraph to propose and present our choice – they are listed below:

1. Geometric nonlinearities – the development of the material degradation during the fatigue process results in the increase of deformations, so that a consistent geometrically nonlinear approach including even large strain analysis is required in numerical modelling of fatigue problems. It is especially important as bending is a dominant failure mode.
2. 3-D vs. 2-D approach – delamination failure is one of possible modes of failure of composite structures and as it is well-known the correct description utilizes σ_{zz} components of the stress tensor. In this sense plate or shell theories should incorporate normal deformations into kinematic variables or it is necessary to use the full 3-D approach what is equivalent to the application of numerical analysis only due to the variety of boundary and loading conditions.
3. Material nonlinearities - static deformations of composite materials have a great influence on the fatigue behaviour. For instance, Yang *et al.* [1] distinguish linear (fibre dominated) static stress-strain diagrams and nonlinear ones (so-called matrix dominated). It proves evidently that material nonlinearities should be taken into account.
4. Failure criteria – there is lack of generally acceptable failure criteria for composite materials. In view of that a lot of authors emphasize that effect on fatigue modelling
5. Progression of fatigue failure – in general, it requires nonlinear approach since possible openning or closure of cracks is a typical contact,i.e. nonlinear problem. Our proposals of solving it are disccussed further.

In summary, one can notice immediately that a consistent approch to the fatigue problem is associated with nonlinearities of various types joined commonly with the 3-D analysis. Thus, the modelling requires a strict FE approach but associated with the understanding of the theoretical background of problems.

FATIGUE DAMAGE ANALYSIS

The mechanisms developed for polymeric composites are complex and quite different from those for metals. In contrast to them the fracture of composite laminates is induced by the initiation and progression of four failure modes such as matrix cracks, fibre breaks, delamination between adjacent plies of the laminate and interfacial debonds. Despite of the local damage the first three types of failure modes may be described sufficiently well (see Tsai and Hahn [5]) and analysed with the use of the lamination (homogenized) theory.

The matrix failure is determined with the use of the Tsai- Wu criterion:

$$F_{01}\sigma_{11} + F_{11}\sigma_{11}^2 + F_{12}\sigma_{11}\sigma_{22} + F_{02}\sigma_{22} + F_{22}\sigma_{22}^2 + F_{44}\sigma_{12}^2 \leq 1 \qquad (1)$$

since it predicts the layer strength for stress states with relatively large transverse stresses that affects much more the matrix than fibres. Thus, for an individual ply in the laminate its post-cracking stiffness is is changed (the matrix stiffness is removed).
The experiments demonstrate that for unidirectional composites the Tsai-Wu criterion overestimates the strength in the fibre direction. Therefore, for the analysis of fibre cracking the use of the simplest maximum stress criterion is proposed:

$$\sigma_{ij}^C \leq \sigma_{ij} \leq \sigma_{ij}^T \qquad i,\ j = 1,2,3 \qquad (2)$$

Finally,in the post-cracking stiffness matrix of an individual layer the fibre stiffness is eliminated.
As it is reported in the literature (see e.g. Talreja [6]) delamination damage is caused and treated as the mode I and II of crack growth. The interlayer separation is an equivalent to a macro-crack in metals. In the present work, the initiation of delaminations is investigated with the use of the quadratic delamination criterion (Lagace and Brewer [7]):

$$\frac{\sigma_{13}^2}{X_{13}^2} + \frac{\sigma_{23}^2}{X_{23}^2} + \frac{\sigma_{33}^2}{X_{33}^2} \leq 1 \qquad (3)$$

As it was mentioned previously the definition of the crack initiation is still a subject of controversy. However, for our purposes we use the definitions given by Eqns (1) – (3). Crack propagation will be examined in pure numerical way using NISA II package. The crack growth is determined by the classical ratio dc/dN, where a denotes a crack length whereas N is a number of cycles. The fatigue crack growth life estimations are carried out with the use of the following criteria (Broek [8]):

- Paris law
- Forman law – it includes the stress ratio as a parameter
- Elber's law – the first crack closure model
- Collipriest law
- Walker's law
-

The applicability of the above relations depends entirely on materials used in the analysis. Therefore, we intend to examine more criteria in order to find the most suitable for our analysis, taking also into account that the above laws have been evaluated for isotropic materials. Finally, with the use of the above relations it is possible to estimate fatigue life of the structure and (or) the stiffness degradation.

SQUARE PLATE UNDER SHEAR CYCLIC LOADS

Let us consider the example of a square plate (250 x 250 x 1.5 mm) subjected to cyclic shear loads. The plate is made of aramid/epoxy resin and consists of four layers having the same thickness. The numerical analysis of plate deformations have been performed with the use of 3-D nonlinear wedge elements (NKTP 4) having 6 or 15 nodes (NORDR = 10 and 11, respectively). The aim of the study was to study the crack initiation and then to compare the fatigue life of the structure.The numerical model of the structure (deformed and undeformed) is presented in Fig. 1a. As it may be noticed the deformations of the structure are large, so that in the numerical analysis it is necessary to take into account not only geometrical nonlinearity option but also large strains. In addition, due to the change of the deformed shape we utilize deformation dependent forces (non-conservative) – their direction depends on the deformation. A full Newton-Raphson procedure was used to solve the nonlinear equations. The fundamental loading path is demonstrated in Fig.2, the increase of the loading parameter up to the average value and then repeated loading and unloading.

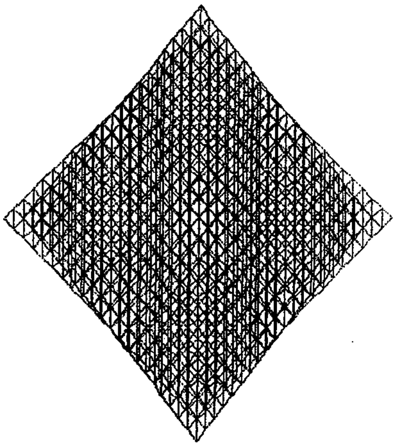

Fig. 1a Deformed and undeformed shapes of plate (not to scale).

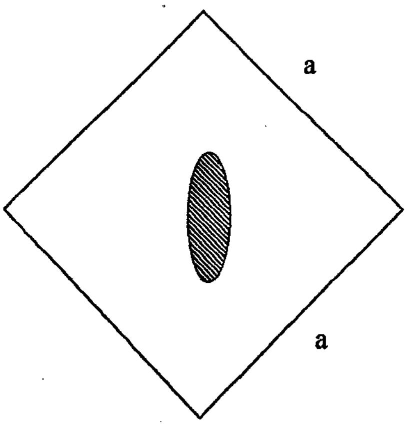

Fig. 1b The initiation and the form of a crack (not to scale).

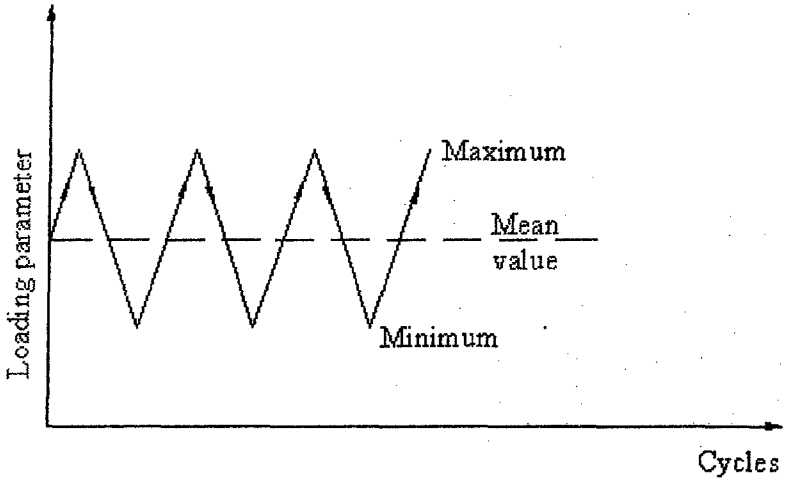

Fig. 2 Loading trajectory.

No	Propagation law	Life (cycles N)
1	Paris	0.423E05
2	Forman	0.211E05
3	Elber	0.178E05
4	Collipriest	0.314E07
5	Walker	0.189E05

Table 1. Comparison of fatigue life estimations.

Using the symmetry of the problem (see Fig. 1) with the increasing load parameter an initial crack have been detected in the form of an ellipse at the plate center – Fig.1b. It turns out that the delamination between third and fourth plies is a dominant failure mode. The delamination arises due to the significant bending effects. It is worth to emphasize that the classical geometrically linear analysis leads to the classical plane effects. Bending of the plate under shear loading (before buckling) can be obtained only with the use of large strains option associated with the deformation deoendent forces. As the initial failure have been observed the initial numerical problem have been remodelled in order to analyse the crack propagation. Then, with the use of ENDURE (fatigue and fracture in the NISA II program) the crack propagation have been investigated. Table 1 gives the crack propagation lives corresponding to an initial and final crack length of 0.1 and 0.3 mm at R=0.1 obtained by various propagation laws.

The differences between the examined propagation laws are very high , even in the order of the magnitude. In general, the Collipriest law gives the worst estimations. On the other hand , the predictions of fatigue lives is very close to each other for three laws, i.e. proposed by Forman, Elber and Walker .

EXPERIMENTAL STUDIES

To evaluate the correct values of the fatigue life (understood as the number of cycles), the initiation of the crack and the final failure modes of structures an experimental rig have been prepared – Fig. 3. Up to now the static failure modes have been studied. As it may be noticed in the photograph a typical buckling failure is a dominant static failure mode. However, during the experiments a single delamination have been observed that arised close to the plate center under the top ply, particularly due to the increase of deformations in that region. It confirms entirely the numerically evaluated mode of failure – Fig. 1b.

The fatigue experimental analysis of plates is carried out in our laboratory and the results will be reported later.

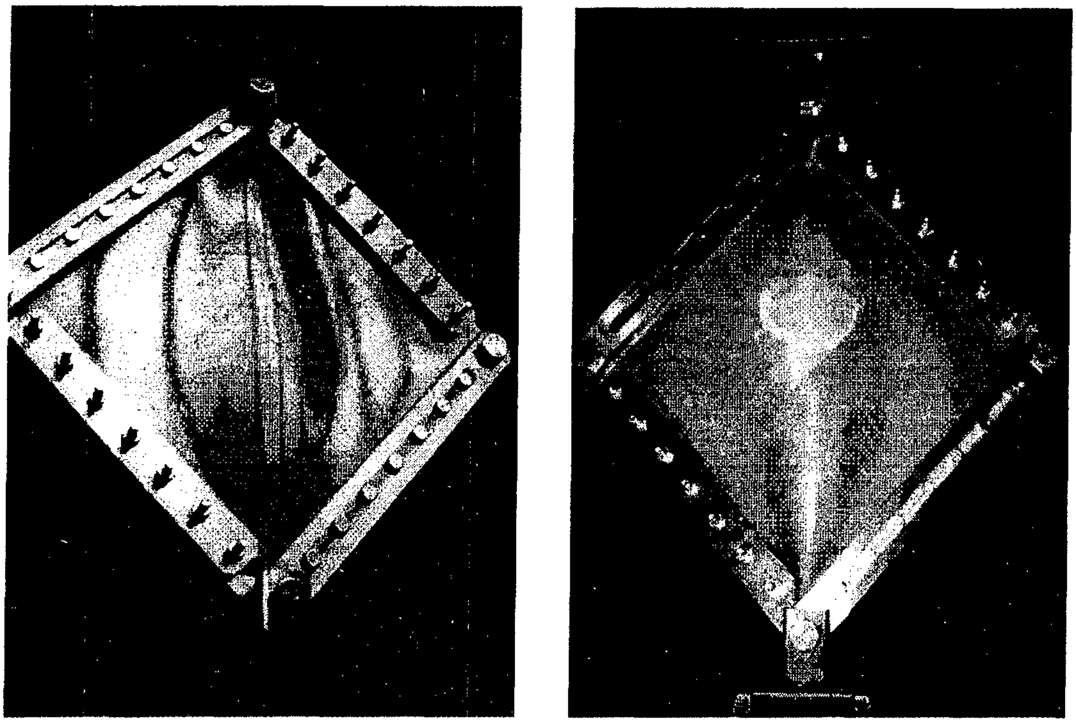

Fig. 3 Photographs of a damaged plate subjected to shear loads.

REFERENCES

[1] Yang,J.N,Lee,L.J.,Sheu,D.Y.,Modulus reduction and fatigue damage of matrix dominated composites laminates,*Composite Str.* **21**,pp.91-100 (1992)

[2] Caslini,M,Zenotti,C.,O'Brien,T.K., Study of matrix cracking and delamination in glass/epoxy laminates,*J.Composites Techn. Res.* **9**,pp.121-130 (1987).

[3] NISA II, *User's Manual*, EMRC Troy (1996).

[4] Muc,A.,Krawiec,Z., FE modelling of laminates degradation in thinwalled structures due to fatigue loads, Proceedings IV – WCCM ,(1998 – in print).

[5] Tsai, S.W.,Hahn H.T., Introduction to Composite Materials, Technomic Publishing, Lancaster (1980).

[6] Tarleja,R.,Fatigue of composite materials, Technomic Publishing, Lancaster (1990).

[7] Lagace,P.A., Brewer,J.C., Studies of delamination growth and final failure under tension loading, Proc.ICCM/6,Vol.5,pp.262-273, Elsevier, London (1987).

[8] Broek,D.,The practical use of fracture mechanics, Kluwer Academic Publishers, Dordrecht (1989).

DESIGN/OPTIMISATION OF ISOGRID CYLINDRICAL STRUCTURES

D. Slinchenko, V. E. Verijenko, S. Adali and I. B. Sevostianov.
Department of Mechanical Engineering, University of Natal, Durban 4041,
South Africa

ABSTRACT

Stress analysis of isogrid cylindrical shell has been performed using exact finite element model and integrated equivalent stiffness model. The integrated equivalent stiffness model was used to homogenise grid structure with laminated skin and thus simplify the use of optimization subroutines available in the software package. Comparison of the results obtained on the basis of exact and equivalent stiffness models using two different FEM codes has been performed and conclusions on the efficiency and accuracy of equivalent stiffness model are made.

INTRODUCTION

Composite grid structure represents the lattice of interconnected ribs made from continuous very strong, stiff and tough fibres. Unidirectional arrangement of ribs possesses good impact damage tolerance, resistance to delimitation and crack propagation across the grid. This structural concept also has great potential for automation of manufacturing process including continuous filament winding and resin transfer moulding. Only within the recent time the concept of the grid made of unidirectional continuous fibres was introduced and it is predominantly applied in aerospace industry [8-10]. This new concept possesses a lot of advantages compared to aluminium isogrid structures. Due to the geometric constrains of composite filament wound isogrid the optimization tool is required when the design of the structure with different loading conditions is undertaken.

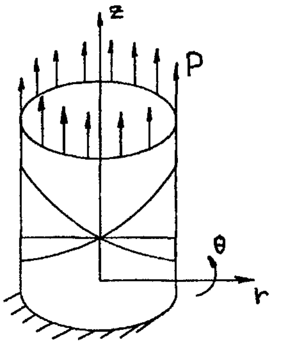

Figure 1. Loading and boundary conditions.

PROBLEM FORMULATION

In the present study the structure under consideration has the shape of circular cylinder (Figure 1) which is fixed at one side and free at the opposite side. The system is subjected to different loading conditions which are applied on the free edge of the cylinder. The material of the cylinder is a grid (Figure 2) consisted of interconnected composite shrouds covered with outer and inner layers of composite skin.

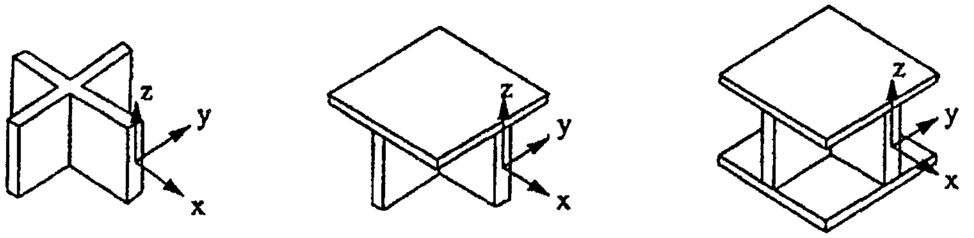

Figure 2. Grid structure.

Exact Model

Exact FEM model has been created using FEM package COSMOS/M. Triangular laminate composite shell elements and 3D beam elements representing top and the bottom layers of skin and lattice respectively (Figure 3) were used. Both elements were assigned orthotropic material properties with the corresponding material directions given on the Figure 4. Laminated shell element SHELL3L used in the model takes into account transverse shear stress. The total number of finite elements required for precise modelling of the isogrid structure is quite large. In the case of cylindrical shell 2775 elements were used (see Figure 3). As it could be seen the large number of finite elements required for exact modelling of the isogrid structure is determined by the need of FEM mesh (beam and shell elements) to be coincident with the real geometry of the isogrid. Creation of complex models like this will make stress analysis extensive and could pose difficulties in further optimisation calculations which usually require many iterations and in the case of exact model constant remeshing of the structure. The above-mentioned difficulties could be avoided by incorporating homogenized model with the stiffness equivalent to the exact modal.

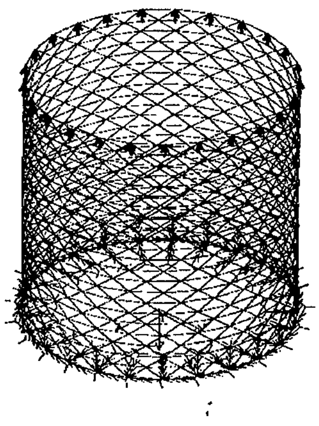

Figure 3. Exact model.

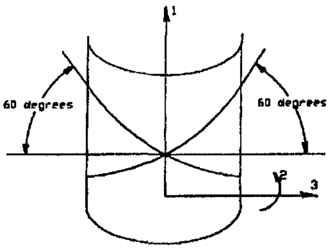

Figure 4. Orientation of material axes.

Equivalent stiffness model (ESM)

Several attempts were made to represent the complex non-uniform structure as a uniform homogeneous structure with the same stiffness properties as the original one. Some of the approaches [3-7] were undertaken for the creation of Equivalent Stiffness Model (ESM) models suitable for the particular applications, i.e. certain type of loading conditions, rib's orientation, etc. In these models assumptions were made regarding stress distribution and in some models in-plane bending and shear of ribs are not taking into account. The most complete transition from the exact model to the equivalent stiffness model has been performed by Chen, H.-J. and S. Tsai [1] for arbitrary rib configuration. Their model takes into account in-plane bending and shear of ribs as well as local buckling. Under this approach a lattice panel is characterised by a regular plate theory. The stiffnesses of each unidirectional set of parallel ribs are derived and calculated separately and then the total stiffness of the whole grid panel is obtained by the principle of superposition for all individual sets. The resultant equivalent stiffness matrices for the orthotropic grid with outer skins then can be written as:

$$
\begin{aligned}
[A] &= [A]^{skin} + [A]^{rib} \\
[B] &= [B]^{skin} + [B]^{rib} \\
[D] &= [D]^{skin} + [D]^{rib} \\
[H] &= [H]^{skin} + [H]^{rib}
\end{aligned}
\qquad (1)
$$

Where $[A]$, $[B]$, $[D]$ and $[H]$ are correspondingly extension, coupling, flexural and transverse shear stiffness matrices of the structure. Notations with indices *skin* and *rib* are the stiffness matrices corresponding separately to the ribs and outer skins:

$$
\begin{aligned}
[A]^{skin} &= \int [Q] dz \\
[B]^{skin} &= \int [Q] z dz \\
[D]^{skin} &= \int [Q] z^2 dz \\
[H]^{skin} &= \chi \int \begin{bmatrix} C_{55} & C_{45} \\ C_{45} & C_{44} \end{bmatrix} dz
\end{aligned}
\qquad (2)
$$

$$
[A]^{rib} = \begin{bmatrix}
\dfrac{E_x A_0}{d_0} + 2\dfrac{E_x A_\theta}{d_\theta} m^4 & 2\dfrac{E_x A_\theta}{d_\theta} m^2 n^2 & 0 \\
2\dfrac{E_x A_\theta}{d_\theta} m^2 n^2 & \dfrac{E_x A_{90}}{d_{90}} + 2\dfrac{E_x A_\theta}{d_\theta} n^4 & 0 \\
0 & 0 & 2\dfrac{E_x A_\theta}{d_\theta} m^2 n^2
\end{bmatrix}
\qquad (3)
$$

$$[D]^{rib} = \begin{bmatrix} D_{11}^{rib} & D_{12}^{rib} & 0 \\ D_{21}^{rib} & D_{22}^{rib} & 0 \\ 0 & 0 & D_{66}^{rib} \end{bmatrix}$$

$$[H]^{rib} = \begin{bmatrix} \frac{E_s A_0}{d_0} + 2\chi \frac{E_s A_\theta}{d_\theta} m^2 & 0 \\ 0 & \frac{E_s A_{90}}{d_{90}} + 2\chi \frac{E_s A_\theta}{d_\theta} n^2 \end{bmatrix}$$

$$\begin{aligned} D_{11}^{rib} &= \frac{E_x I_0}{d_0} + 2\frac{E_x I_\theta}{d_\theta} m^4 + 2\frac{E_x J_\theta}{d_\theta} m^2 n^2 \\ D_{22}^{rib} &= \frac{E_x I_{90}}{d_{90}} + 2\frac{E_x I_\theta}{d_\theta} m^4 + 2\frac{E_x J_\theta}{d_\theta} m^2 n^2 \\ D_{12}^{rib} &= D_{21}^{rib} = 2\frac{E_x I_\theta}{d_\theta} m^2 n^2 - 2\frac{E_x J_\theta}{d_\theta} m^2 n^2 \\ D_{66}^{rib} &= 2\frac{E_x J_\theta}{d_\theta} m^2 n^2 + \frac{E_s J_0}{4d_0} + \frac{E_s J_{90}}{4d_{90}} + \frac{E_s J_\theta}{2d_\theta}\left(m^2 - n^2\right)^2 \end{aligned} \tag{4}$$

where $m = \cos\theta, n = \sin\theta$; E_s, E_x are longitudinal and shear moduli; d - spacing for each set of ribs; J's, A's and I are torsion constant, area and second moment of inertia of ribs respectively; χ is shear correction factor. Subscripts *0, 90* and θ indicate differently oriented sets of ribs.

In the present study the equivalent stiffness model has been created on the basis of orthotropic shell elements with non-homogeneous material properties described by $[A]$, $[B]$, $[D]$ and $[H]$ matrices using FEM code Pro/Mechanica and was implemented in the analysis of the isogrid structure described in the following section.

STRUCTURAL ANALYSIS AND RESULTS

For the given circular cylindrical shell (Figure 1) equivalent stiffness matrices were first calculated and then used as an input data for the shell elements in the ESM model. The same problem was modelled using shell and beam elements with material characteristics given in the Table 1 and cross-section geometry shown on Figure 4. In this case COSMOS/M FEM package was used. Linear static analysis have been performed for the following loading conditions: tension and bending in the form of prescribed displacements uniformly applied to the free end of the cylindrical shell. Obtained results presented in the Table 2.

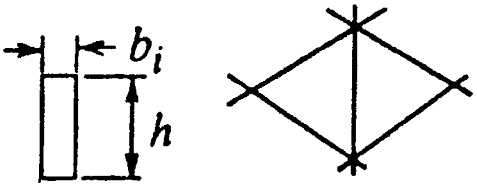

Figure 4. Cross-section and arrangement of the ribs in isogrid structure.

Table 1. Material properties of the ribs and skins.

Material	E_1, Pa	E_2, Pa	ν_{12}	G_{12}, Pa
T300/5208	$1.81\ 10^{11}$	$1.03\ 10^{10}$	0.28	$7.17\ 10^{9}$

Geometric parameters of the structure:
Ribs: b=0.003 m; h=0.005 m; d_{90}=0.0025 m; d_θ=0.0025 m;
Skin thickness: h_{sk}=0.0025 m
Angle of isogrid rib's orientation: θ=30 degrees.

Table 2. Comparison of obtained results.

Load case	COSMOS/M			Pro/Mechanica	
	Applied displ. m.	Max VM stress, Pa	Applied displ. m.	Max VM stress, Pa	Differences, %
Bending	0.003	7.74E+08	0.003	8.55E+08	10.49
Tension	0.003	1.39E+09	0.003	1.28E+09	7.63

CONCLUSIONS

Linear static analysis of both models shows a good correlation in the obtained results. It also shows the possibility to substitute complex and extensive stress analysis of exact FEM model with analysis on the basis of equivalent stiffness model within very reasonable range of accuracy. This makes further optimisation process of complex grid structures less complicated and time-consuming. Equivalent stiffness model is currently being implemented into optimization routine.

REFERENCES

1. Chen, H.-J., S. Tsai "Analysis and Optimum Design of Composite Grid Structures", Journal of Composite Materials, vol. 30, NO 4/1996:503-532.
2. Huybrechts, S. M., Tsai S. "Analysis and Behaviour of Grid Structures" , Composite Science and Technology 56/1996:1001-1015.
3. Thompson, P. A., Bettess P. and Caldwell J. B. 1988. "An Isoparametric Eccentrically Stiffened Plate Bending Element", Engineering Computation, 5:110-116.
4. Deb, A. and M. Booton. 1988 "Finite Element Models for Stiffened Plates under Transverse Loading", Computers and Structures, 28(3):361-372
5. Mukherjee, A. and Mukhopadhyay. 1988 "Finite Element Free Vibration of Eccentrically Stiffened Plates", Computers and Structures, 30(6):1303-1317.
6. Palani, G. S., N. R. Iyer and T. V. S. R. Appa Rao. 1992. "An Efficient Finite Element Model for Static and Vibration Analysis of Eccentrically Stiffened Plates/Shells", Computers and Structures, 43(4):651-661

7. Rao, D. V., A. H. Sheikh and M. Mukopadhyay. 1993. "A Finite Element Large Displacement Analysis of Stiffened Plates", Computers and Structures, 47(6):987-993.
8. Reddy, A. D., L. W. Rehfield, R. S. Haag and C. G. Wildman, "Compressive Buckling Behaviour of Grifite/Epoxy Isogrid Wide Column with Progressive Damage", ASTM Symposium on Compression Testing of Homogeneous Materials and Composites. ASTM-STP 808, pp. 187-199, 1983.
9. Rehfield, L. W. and A. D. Reddy, "Damage Tolerance of Continuous Filament Composite Isogrid Structures: A Preliminary Assessment", Composite Materials: Mechanics, Mechanical Properties and Fabrication, Japan - U.S. Conference, Tokyo, pp. 545-553, 1982.
10. Reddy, A. D., R. R. Vasiletty and L. W. Rehfield, "Contineous Filament Wound Composite Concepts for Aircraft Fuselage Structures", Journal of Aircraft, Vol. 22, 3, pp. 249-255, 1985.

FIBRE COMPOSITE INTRA-MEDULLARY NAILS: DESIGN CONSIDERATIONS

CJ von Klemperer and R Bodger

Department of Mechanical Engineering, University of Natal, Durban 4041, South Africa

ABSTRACT

Although fibre composite materials have shown great promise in many engineering applications, the medical community has been slow to accept and research their possibilities. The suitability of fibre composites as an alternative to the current titanium and stainless steel alloys used for the manufacture of intra-medullary nails has been investigated. These nails are used to pin serious femoral fractures. Biomechanical loading and stresses as well as current metallic nail designs were studied, and a new design in carbon fibre has been proposed. This design has been modelled using various Finite Element packages.

INTRODUCTION

Fibre composite materials are not new to engineering applications, and have been available since the Second World War. Although they were initially championed as the new generation of materials, which would replace metals, it wasn't until the 1970's and 80's that they gained acceptance. This change was mainly as a result of the leisure industry, which was quick to exploit the simple manufacturing processes, and good corrosion resistance, which these materials offered.

The high strength to weight ratio, coupled with the good corrosion resistance of high performance fibre reinforced polymers, has led biomechanics researchers to study the possibility and advisability of using them in biomechanic applications and especially in the area of surgical implants. The biggest single issue facing designers of these devices and implants, is the cost. This is especially important in a third world country such as South Africa, where the government is often forced to pick up the tab on any expensive medical procedure.

Intra-medullary nails are an internal fixation device used to support unstable fractures of the femur or thighbone. The intra-medullary canal in the centre of the bone is reamed and a shaped column of metal is inserted. These nails have usually been made from Titanium or stainless steel, and come in a wide variety of cross sections; from simple circles, to octagons and even complicated cloverleaf designs, with hollow and solid designs. The nail may be fastened to the bone using locking screws, or be of an expanding design. The nail has to be able to support the forces on the femur as a result of the patients body weight, and kinematic forces resulting from every day activities.

The current nail designs have often proven to be too weak to perform this task, especially if the fracture is severely comminuted, such as in an injury caused by a gun shot. (See Fig. 1) The nails are then prone to fatigue failure as a result of the cyclical nature of the loading. This coupled with the very high cost of the imported nails has prompted the University of Natal into extensive research in the viability of producing a local nail based on the titanium Huckstep design. At present, a hollow octagonal design, in Stainless steel is undergoing final testing.

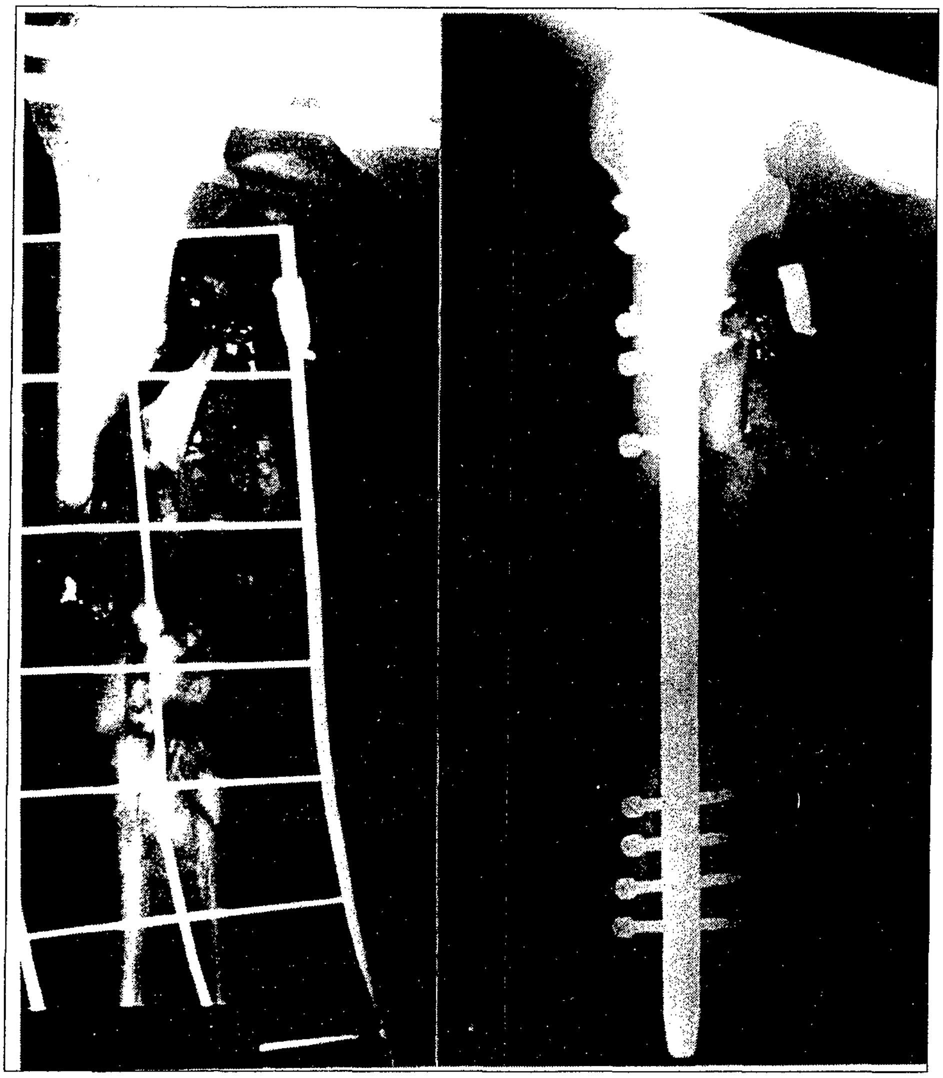

Figure 1 X-Ray of Intra-Medullary nail inserted to support the femur of a gunshot victim.

A drawback of using stainless steel is that the elastic modulus is nearly four times that of natural bone, this difference in the "stiffness" between bone and the implant are undesirable. The problem is that any bending of the femur will cause micro-motion between the bone and implant this damages the bone and leads to the development of scar tissue. The bone being living will tend to reabsorb around the implant, as it "detects" a region of high strength. This makes the use of glass or carbon fibre polymer composites suitable for the intra-medullary nail, as their elastic moduli are similar to those of the natural bone. As carbon can be absorbed by the body it may be possible to develop a nail, which can be reabsorbed by the body over time (Assuming the matrix material is biodegradable as well). This would save the patient from a second operation to remove the nail after the bone has healed

The loading on the femur is an area of great study and debate, as a result, a decision was made to reverse engineer the current designs, thus the proposed design can be optimised to be stronger than the current nails. Two finite element packages were used to study firstly the current design and in particular the stainless steel design developed at the University of Natal and secondly the proposed Carbon composite design. The results from the first FE analysis were then compared to the physical testing performed on the stainless steel design, this allowed a check to be performed on the FE packages.

LOADING AND BIOMECHANICS

The most critical part of any engineering design is determining the forces, which the design must withstand. If the component to be designed is an orthotic or surgical implant, the forces will predominately be biomechanical. Unfortunately, the biomechaical forces on a human's legs are not fully understood, and there is a wide range of opinion, and argument. In studying the feasibility of using fibre composites in biomechanical applications, another method, which may be used, is to reverse engineer the current designs. The proposed component can then be designed to be as strong or stronger than the existing part.

Investigation revealed that there are two main approaches to the force question. Firstly there is the biomechanics approach; this deals with the specific strength and forces on the human body. Secondly there is the biokinetistist approach. This deals with the relationship between forces and stresses and the corresponding specific motion. These two methods often vary significantly both in the methods used as well as the results obtained. A third method known as in vivo measuring produces the most useful results. Implants such as intra-medullary nails or hip replacements are fitted with some form of strain or load measuring devices. Michel et al (1995) used an intra-medullary nail to study internal loads on the femur. GN Duda (1996) comments that the results obtained are questionable, as they are not the results, which may have been obtained from a healthy individual. (Michel et al implanted the nail in thirty-three year old male, with a mid-shaft fracture of his left femur) The results obtained are as follows.

Loading.	**During healing.**	**After the fracture had healed.**
Torsional	2 - 5 Nm	2 – 5 Nm
Bending Moments	18 – 22 Nm	4 Nm
Axial Force		Up to 300 N
Shear Forces		60 – 80 Nm

Table 1 Internal Loads on the Femur (Duda 1996)

There is considerable debate, as to whether an intra-medullary nail experiences higher forces as a result of the reduced load carrying capacity of the femur, or whether this is compensated for by the injured leg bearing less of the body weight. Although their accuracy may be questioned these results are however very useful for the design of an intra-medullary nail, as they represent a true case.

BIO-COMPATIBILITY AND CORROSION RESISTANCE

For an implant to be bio-compatible, it must contain no materials, which are toxic, carcinogenic, or could cause an allergic reaction. Furthermore in order for a material to be considered as a biomedical implant material, certain criteria must be satisfied, including chemical, biological, and mechanical. It would be preferable to use a material whose bio-compatibility has already been determined, as this will save on the expense and time required for full bio-compatibility testing. Furthermore the human body is an exceptionally corrosive environment; various solution testing is performed, often at increased temperatures. In addition stress corrosion testing is vital, as all orthopaedic implants are susceptible to SCC. Corrosion control is usually attained by one or more of three methods, modification of the corrosive medium, and electrical protective method or a surface coating / pre-treatment of the material. The first two are not possible or practical in the case of a medical implant, this leaves the surface finish and or treatment. Treatments can be applied to the surface to "coat" the nail, but can be easily damaged during the insertion of the nail. The surface finish is very important, as imperfections can allow "starting points" for corrosive attack. It is important to note that although corrosion is usually something to be avoided, there are advantages in that intra-medullary nails could be manufactured to be biodegradable. A nail could thus be inserted and after the bone has fully healed, slowly dissolve.

ANALYSIS OF NAIL DESIGNS

The current metallic intra-medullary nail consists of a hollow parallel sided octagonal cross-sectioned nail with locking screw holes drilled through it. The nail design was modelled using Pro-Mechanica, (see Fig. 2) the results showed that the maximum stress was found at the locking screw holes. This is consistent with studies of failed nails and with fatigue tests of the nail design. On the basis of these results, and discussions with doctors, the decision was made to change the design to one which did not require locking screws. The hollow octagonal cross-section was kept, as it allowed a high moment of inertia, while ensuring that there are still spaces between the bone and the nail for fluid to flow. By choosing this design, the operation is simplified as additional incisions and drilling of the bone is not necessary. If a "biodegradable" nail is used, the nail could be anchored in place using a similar bone cement to that used to fasten artificial hips in place. A hollow octagonal cross-sectioned nail without locking screw holes was modelled on COSMOS/M. the nail was assumed to be constructed from unidirectional carbon (as if manufactured by pultrusion). The maximum stress found was to be nearly 30 times lower than that of the stainless steel design. This suggests that the nail could be further reduced in thickness, and / or a lower grade of carbon fibre used. Figures 3 and 4 show the stresses calculated by finite element analyses of the current and proposed design.

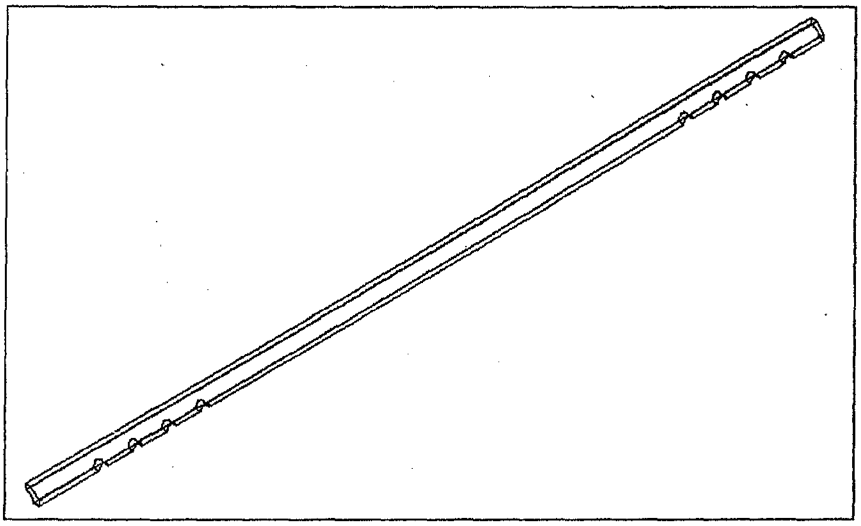

Figure 2 Pro-Mechanica quarter model of existing stainless steel Intra-medullary nail.

CONCLUSIONS

The intra-medullary nail is a very complex device, the effect of being inserted into a human body, produce a number of constraints, including size, bio-compatibility, and corrosion resistance. The current metal nail cannot be simply constructed out of carbon fibre, but rather a complete redesign is required. By designing a nail, which uses carbon fibre as its reinforcement and a biodegradable matrix it would not need to be removed; rather it would slowly be absorbed by the body, at a similar rate to the re-growth of bone. This design also saves the patient and surgeon from a second operation. This design would allow the use of nail without locking screws of any type, but rather would be bonded into the medullary canal using an orthopaedic cement similar to those used to bond artificial hips to bone. This approach offers the most significant advantages, as the nail could be stronger than current metallic designs, however extensive research will be necessary to determine the required rate of decomposition of the nail. Various matrix materials should be studied and tested, both for bio-compatibility and decomposition rate. Work is also needed to accurately determine the short- and long-term effects of Carbon on the human body.

This study tends to suggest that the complexities involved with the current locking screw intra-medullary nail, would not make a fibre-composite design more feasible than the current metallic designs. The costs involved in overcoming problems such as damage due to drilling, and manufacture of hollow nail with locking screw holes, outweigh the advantage of using a material with properties similar to those of human bone. A biodegradable approach shows far more promise, as it avoids most of the problems inherent with the locking screw design. The simplified geometry, could be manufactured by pultrusion, which would allow mass production and lower costs than many other methods. Further testing and analysis will need to be performed however, to confirm this result.

REFERENCES

Agarwal BD and Broutman LJ, “Analysis and Performance of Fibre Composites”, John Wiley and Sons, 1990.

Apley AG and Solomon L, “Concise system of orthopaedics and fractures”, Butterworth-Heinemann, 1991.

Bonfield W, “Composites for Bone replacement”, Journal of Biomedical Engineering, vol. 10, p. 522-526, 1988.

Duda GN, “Influence of Muscle Forces on the internal loads on the femur during Gait”, Shaker Verlag, 1996.

Hotter DS, “Band-Aids for Broken Bones”, Journal of Machine Design, vol. 68, no. 7, p.39-44, 1996.

Hunt MS, “Introduction to the use of Carbon Fibre reinforced Composite Materials for surgical implants”, CSIR, 1980.

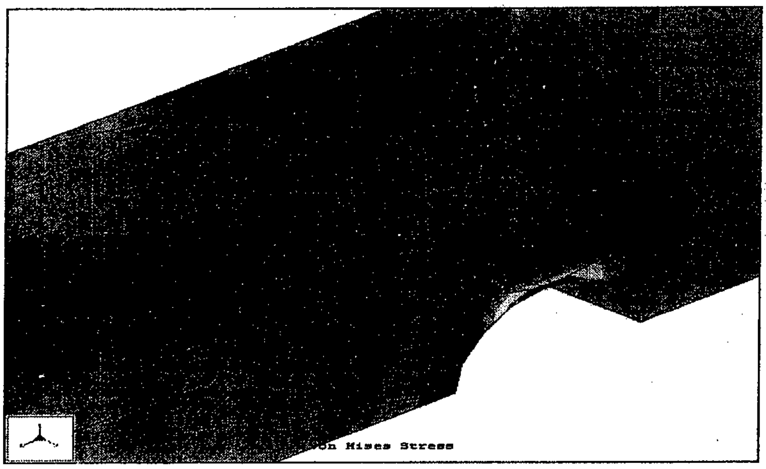
n Mises Stress

Figure 3 Close up of stress on locking screw hole (current stainless steel design)

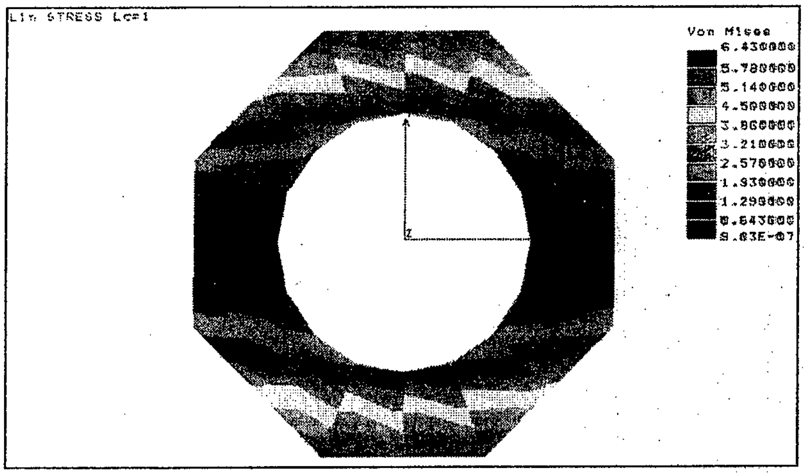
LIN STRESS LC=1
Von Mises
6.430000
5.780000
5.140000
4.500000
3.860000
3.210000
2.570000
1.930000
1.290000
0.643000
9.83E-07
Z

Figure 4 Section-Plot of stresses in proposed Carbon Epoxy nail

DESIGN FOR MANUFACTURE AND OPTIMISATION OF LAMINATES USING GENETIC ALGORITHMS AND FINITE ELEMENT ANALYSIS

M. Walker
CADENCE[*] *Technikon Natal, Durban, South Africa*

April 16, 1998

ABSTRACT

A method of using genetic algorithms linked to finite element analysis for fitness testing to design for manufacture and optimise composite laminates with several design variables is described. The plates used as examples of the method have eight layers, and are symmetric about the midplane. Thus, the four fiber orientations and laminae thicknesses are to be determined optimally. In addition, the fiber orientations and layer thicknesses must be selected from a set of discrete (and easy to construct) values. The method determines global optima, and has proven to be reliable and accurate.

INTRODUCTION

It is well known that designs for structures to be constructed of fiber-reinforced laminated composites can be tailored for additional advantage. Thus, for example, by using the ply angles as design variables, and determining the optimal values to maximise or minimise criterion like strength or mass, the most benefit can be obtained from these materials. Due to manufacturing constraints, the sets of values from which the ply angles and layer thicknesses can be selected are generally discrete, and in such cases, the optimisation problem becomes one of finding the best combination of these.

An important failure mode for laminated structures is bending under transverse loading. By selecting the layup configuration (ie. stacking sequence) optimally, the deflection and mass of a structure can be minimised for a given design strength constraint.

A common type of composite layup is the symmetrically laminated angle ply configuration which avoids bending-stretching effects by virtue of mid-plane symmetry. One phenomenon associated with symmetric angle-ply configurations is the occurrence of bending-twisting coupling which may cause significantly different results as compared to cases in which this coupling is exactly zero [1]. The effect of bending-twisting coupling becomes even more pronounced for few layers. Due to this coupling, closed-form solutions cannot be obtained even for simple laminated plates, and thus many studies involving design optimisation of composite structures have neglected the effect. The present study adopts a numerical approach to include the effect of bending-twisting coupling, and determine the fitness of a candidate design which is produced using a genetic algorithm.

---

[*] Centre for Advanced Materials, Design & Manufacture Research

Walker *et al* [2] carried out an optimisation design study of laminated plates with the objective of minimising the deflection and weight, using finite element analysis and the *Golden Section* method, but this was limited to only two design variables, viz. fiber orientation and layer thickness. In addition, several reports have been published which deal with optimisation of laminates for minimum deflection, or minimum weight. For example, angle-ply laminates subjected to uncertain loads were considered by Adali *et al* [3] who used a convex modelling approach in their analysis. The optimal design of symmetrically laminated plates under transverse loads was given by Tauchert & Adibhatla [4] using the minimum strain energy criterion, and by Quian *et al* [5] and Kengtung [6] using the minimum structural compliance criterion. A maximum stiffness design for both symmetric and antisymmetric laminates was considered by Kam & Chang [7]. Adali *et al* [8] investigated the minimum weight and deflection design of thick sandwich laminates via symbolic computation.

Phillips & Gürdal [9] and Triantafillou *et al* [10] detailed the optimal design of composite panels and hybrid box beams, respectively. The former used analysis routines in conjunction with, an optimisation package to provide design schemes for geodesically stiffened minimum weight aircraft wing rib panels. Optimal weight design of shells is considered by Min & de Charantency [11], who investigated sandwich cylinders under combined loadings. A study by Ostwald [12] considered the combined loading cases of external pressure and axial compression in the optimisation of thin walled shells. The Bubnov-Galerkin method was used to solve the stability problem.

Genetic algorithms, which can be used to find the global solution of discrete optimisation problems, simulate the mechanics of natural genetics for artificial systems based on operations which are the counterparts of the natural type [13]. They use techniques derived from nature, and rely on Darwin's principle of survival of the fittest. When a population of biological species evolves over generations, characteristics that are useful for survival tend to be passed on to future generations, because individuals carrying them get more chances to breed. Individual characteristics in biological populations are stored in chromosomal strings. The mechanics of natural genetics are based on operations that results in structural yet randomised exchange of genetic information (ie. useful traits) between the chromosomal strings of reproducing parents, and consist of crossover and occasional mutation of the chromosomal strings. The reader is referred to Ref. 13 for further discussion of the standard genetic operators and theoretical properties of GAs.

In order to demonstrate the use of GAs in the optimisation of laminated structures, the design of fibre-reinforced plates are chosen here as examples. To determine the best configuration, optimal ply angles for each layer are selected from amongst a predefined set of fiber orientations, commonly used in industry. This approach leads to cost-effective (and easy to construct) designs by virtue of allowing the use standard composite plies. The most common orientations are 0°, $\pm 45^o$ and 90° which are the ones used in the present study. Previous work on discrete optimisation of composite laminates include Refs 14 - 16.

This study considers the optimal design of symmetrically laminated plates for minimum deflection (viz. maximum rigidity) and minimum weight.. The ply angles are taken as the optimising variables for the minimum deflection design and the minimum weight is then obtained using the Tsai-Wu failure criterion with the optimising variables then becoming the individual layer thicknesses. Results are presented for different loadings both symmetrical and unsymmetrical, and various combinations of clamped, simply supported and free boundary conditions are considered. The effect of aspect ratio on the minimum deflection and weight is also investigated.

BENDING OF RECTANGULAR LAMINATES

Consider a symmetrically laminated rectangular plate of length a, width b and thickness h under a transverse bending load $q(x,y)$, as shown in Fig. 1. The plate is located in the x, y, z plane and constructed of an arbitrary number K of orthotropic layers of thickness h_k and fibre orientation θ_k where $k = 1, 2, ..., K$. The displacement of a point (x^0, y^0, z^0) on the reference surface is denoted by (u^0, v^0, w^0).

The governing equation for the deflection w in the z direction under a transverse load q is given by [17]:

$$D_{11}w_{,xxxx} + 4D_{16}w_{,xxxy} + 2(D_{12} + 2D_{66})w_{,xxyy} + 4D_{26}w_{,xyyy} + D_{22}w_{,yyyy} = q \quad (1)$$

where variables after the comma denote differentiation with respect to that variable, and

$$D_{ij} = \int_{-h/2}^{h/2} \bar{Q}_{ij}^{(k)}\ z^2 dz \quad (2)$$

are the bending stiffnesses and $\bar{Q}_{ij}^{(k)}$ are components of the transformed reduced stiffness matrix for the k-th layer.

As no simplifications are assumed on the elements of the $[D]$ matrix, equation (1) includes bending-twisting coupling as exhibited by virtue of $D_{16} \neq 0$, $D_{26} \neq 0$.

FINITE ELEMENT FORMULATION

We now consider the finite element formulation of the problem [18]. Let the region S of the plate be divided into n sub-regions S_r ($S_r \in S; r = 1, 2, ..., n$) such that

$$\Pi(u) = \sum_{r=1}^{n} \Pi^{Sr}(u) \quad (3)$$

where Π and Π^{Sr} are potential energies of the plate and the element, respectively, and u is the displacement vector. Using the same shape functions associated with node j ($j = 1, 2, ..., n$), $S_j(x,y)$, for interpolating the variables in each element, we can write

$$u = \sum_{j=1}^{n} S_j(x,y) u_j \quad (4)$$

where u_j is the value of the displacement vector corresponding to node j, and is given by

$$u = \{u^{(j)}, v^{(j)}, w^{(j)}, \phi_1^{(j)}, \phi_2^{(j)}\}^T \quad (5)$$

The displacements $\{u, v, w, \phi_1, \phi_2\}$ are approximated as

$$\begin{aligned} u &= \sum_{j=1}^{n} u_j \psi_j(x,y), \; v = \sum_{j=1}^{n} v_j \psi_j(x,y), \; w = \sum_{j=1}^{n} w_j \psi_j(x,y) \\ \phi_1 &= \sum_{j=1}^{n} S_j^1 \psi_j(x,y), \; \phi_2 = \sum_{j=1}^{n} S_j^2 \psi_j(x,y) \end{aligned} \tag{6}$$

where ψ_j are Lagrange family of interpolation functions. From the equilibrium equations of the first order theory, and equations (6), we obtain the finite element model of the first-order theory,

$$\sum_{\beta=1}^{5} \sum_{j=1}^{n} K_{ij}^{\alpha\beta} \Delta_j^{\beta} - F_i^{\alpha} = 0, \;\; (\alpha = 1, 2, ..., 5) \tag{7}$$

or

$$[K]\{\Delta\} - \{F\} = \{0\} \tag{8}$$

where K and F are the stiffness and force coefficients respectively, and the variable Δ denotes the nodal values of w and its derivatives.

STACKING SEQUENCE CODING FOR GENETIC ALGORITHMS

In its standard form, application of the operators of the GA to a search problem requires the representation of design variables in terms of bit strings that are counterparts of the natural chromosomes. In specialising genetic algorithms for laminate stacking sequence design, the first departure from the classical problem formulation is in design variable coding. Since laminates are generally built from 0°, $\pm 45^o$ and 90° plies, it is convenient to replace the binary coding with a higher alphabet. In addition, for balanced laminates we require a $+45^o$ ply to be paired a -45° ply, therefore, the coding can be simplified by rising stacks of two plies each as the basic building blocks. Thus, the four possible stacks are: 0° coded as the integer 0, $-45^z o$ coded as 1 with $+45^o$ as 2, and 90° coded as 3. For example, the symmetric laminate $[90_2^o/+45_2^o/90_2^o/0_2^o/-45_2^o/0_2^o]$ is coded as 3 2 3 0 1 0. The rightmost character corresponds to the layer closest to the plane of symmetry.

Genetic Operators

Basic operators used to create successive improved populatioris include selection, crossover, mutation, and interchange. Typically, two designs selected from a population are mated to create child design(s). In order to ensure that good designs propagate to the child populations, a higher chance to be selected as parents is given to those designs that are better than the rest of the population. Selection is the part of the algorithm that provides better opportunity to good designs by implementing a roulette wheel which is divided into slices representing different designs. Those designs with better characteristics are given a proportionally larger slice of the wheel. When the wheel is spun (simulated by using a random number generator between 0 and 1, where the circumference of the wheel is normalized to be 1), those designs that occupy larger slices of the wheel have a better chance to be chosen as parent designs.

When maximizing some value this is ideal but minimization requires an inversion function of some sort. The following was used for an inversion function:

Let F_i = Fitness for individual i, where $i = 1, 2, 3, ..I$

Let $F_{i\,\max} = \max F_i$ where $F_{i\,\max}$ is constant

Then $F_{i\ \text{new}} = F_i(S/R)$

where

$S = \sum_{i=1}^{I} F_i$ and $R = \sum_{i=1}^{I} (F_{i\,\max}/F_i)$ where $i = 1, 2, 3, \ldots\ I$

Crossover operator: Once a pair of parents are selected, the mating of the pair also involves a random process called crossover. This is achieved by generating a random integer k between 1 and $L-1$, where L is the string length. This number defines a cutoff point in each of the two strings, and separates each into two substrings. By splicing together the left part of the string of one parent with the right part of the string of the other parent a child string is generated. Consider, for example, two symmetric laminates coded in a string of length $L = 9$, and a crossover point $k = 5$

parent 1: 0 0 1 2 1||3 1 1 $[0^o/0^o/\text{-}45^o/45^o/\text{-}45^o/90^o/\text{-}45^o/\text{-}45^o]_s$,

parent 2: 0 2 0 2 1||2 3 2 $[0^o/45^o/0^o/45^o/\text{-}45^o/45^o/90^o/45^o]_s$.

The two possible child designs are

child 1: 0 0 1 2 1 2 3 2 $[0^o/0^o/\text{-}45^o/45^o/\text{-}45^o/45^o/90^o/45^o]_s$,

child 2: 0 2 0 2 1 3 1 1 $[0^o/45^o/0^o/45^o/\text{-}45^o/90^o/\text{-}45^o/\text{-}45^o]_s$.

One or both of the child designs are then selected for the next generation.

Mutation operator: Mutation is implemented by changing, at random, the value of a digit in the string with small probability, and served for the purposes of avoiding premature loss of diversity in the designs. Since inferior designs may have some good traits that can get lost in the gene pool when these designs are not selected as parents, by introducing occasional mutations, different portions of the design space can be investigated for valuable information.

Consider this example:

Suppose a representation

Individual 1: 0 0 1 2 1||3 1 1 - is found to yield a better value when a 3 is introduced in position 8, but no genes in the population exist with a 3 in position 8, then mutation may lead to an introduction of this particular kind.

OPTIMAL DESIGN PROBLEM

The objective of example design problem is to minimise the maximum deflection $w_{\max}(x, y)$ and then the weight W of the laminated plate. The minimum deflection is achieved by optimally determining the fibre orientations, given by $[\theta_1/\theta_2/\ldots\ /\theta_i]_{sym}$. The first part of the design problem may thus be stated as:

$$w_{\min} \overset{\Delta}{\equiv} \min_{\theta} \left[w_{\max}(\theta) \right], \qquad \theta \in 0^\circ, \pm 45^\circ, 90^\circ \tag{9}$$

where

$$w_{\max}(\theta) = \max_{x,y} w(x, y; \theta) \tag{10}$$

Here, the maximum deflection $w_{\max}$ is determined from the finite element solution of the problem given by (8).

The second part of the design problem involves minimising the laminate thickness H subject to a failure criterion. In this study, the Tsai-Wu failure criterion [19] is used which stipulates that the condition for non-failure for any particular ply is

$$F(\theta) = F_{11}\sigma_1^{(k)}\sigma_1^{(k)} + F_{22}\sigma_2^{(k)}\sigma_2^{(k)} + F_{66}\tau_{12}^{(k)}\tau_{12}^{(k)} + 2F_{12}\sigma_1^{(k)}\sigma_2^{(k)} + F_1\sigma_1^{(k)} + F_2\sigma_2^{(k)} \leq 1 \tag{11}$$

where the strength parameters F_{11}, F_{22}, F_{66}, F_{12}, F_1 and F_2 are given by

$$F_{11} = 1/(X_tX_c);\; F_{22} = 1/(Y_tY_c);\; F_{66} = 1/G^2 \tag{12}$$

$$F_1 = 1/X_t - 1/X_c;\; F_2 = 1/Y_t - 1/Y_c;\; F_{12} = -\frac{1}{2}\sqrt{F_{11}F_{22}} \tag{13}$$

and X_t, X_c, Y_t, Y_c are the tensile and compressive strengths of the composite material in the fibre and transverse directions, and G is the in-plane shear strength.

The second part of the problem may thus be stated as

$$W_{\min} = \min_{H} W(\theta_{opt}) \tag{14}$$

subject to constraint (11), which is evaluated for all plies.

In addition, a further constraint is added: the thickness of each layer must be a multiple of a minimum feasible dimension. For example, if a standard ply thickness is $0.001m$, then each individual layer should have thickness $0.001k$, where $k \in Z$ (and $Z \neq 0$). Thus, the second part of the optimisation is then also reduced to a discrete value problem, and solved using a GA.

In summary, the first optimisation procedure involves the stages of determining the maximum deflection $w_{\max}(x, y)$ for a given configuration and improving the fibre orientations to minimise $w_{\max}$, while the second optimisation stage involves evaluating $F(\theta)$ using eqn. (11), with the various stresses required in calculating $F(\theta)$ determined using the finite element method for a given H, and improving the laminate thickness to minimise the weight.

This step may be described explicitly as

$$\min_{H} |F(\theta_{opt}) - 1| \tag{15}$$

in order to minimise thickness.

Thus the computational solution consists of successive stages of analysis and optimisation until a convergence is obtained and the optimal configuration and then $H_{\min}$ is determined.

RESULTS

Preliminary numerical results are given for a typical T300/5208 graphite/epoxy material with E_1 = 181 GPa, E_2= 10.3 GPa, G_{12}= 7.17 GPa and ν_{12}= 0.28. The symmetric plate is constructed of eight layers with $[\theta_1/\theta_2/\theta_3/\theta_4]_{sym}$. Different combinations of free four edges of the plate. In particular, four different combinations are studied, namely, (F,S,F,S), (F,S,C,S), (S,S,S,S) and (C,S,C,S), where the first letter refers to the first plate edge, and the others follow in the anti-clockwise direction as shown in Fig. 1.

The results presented in this section are obtained for rectangular plates with aspect ratios varying between 0.5 and 2.

Table 1 shows the influence of the boundary conditions on the optimal design of a plate with $a/b = 1$ (viz. each side is $1m$ long) and with a uniformly distributed load covering the entire plate surface, of magnitude $2.5\times10^5 Pa$. The table shows the optimal layup which maximises the stiffness in column 2 for each plate, and the optimal layer thickness in column 3 (where, for example, 1,2,1,3 means layer 1 has thickness 1mm etc). As the number of degrees of freedom decreases, so the plate becomes stiffer and the maximum deflection and the optimum weight decrease. Thus, the (F,S,F,S) plate has a total thickness of 14mm, while the (C,S,C,S) plate has a thickness of 12mm.

Table 2 shows the influence of the aspect ratio on the optimal layup and thickness for (S,S,S,S) plates with the same loading as before. It can be seen that as the aspect ratio increases, so the plates become less stiff, and thus the total thickness increases. In addition, as a/b increases, so the optimal layup changes from $(0^\circ/0^\circ/0^\circ/0^\circ)_s$ to $(90^\circ/90^\circ/90^\circ/90^\circ)_s$.

CONCLUSIONS

A method of using genetic algorithms linked to finite element analysis for fitness testing to design for manufacture and optimise composite laminates with several design variables is described. The objective is to maximise the structural rigidity, and minimise the mass, within the bounds of the Tsai-Wu Failure criterion. The plates used as examples of the method have eight layers, and are symmetric about the midplane. Thus, the four fiber orientations and laminae thicknesses are determined optimally. In addition, the fiber orientations and layer thicknesses are selected from a set of discrete design problem ideal for the application of GAs. The method determines global optima, and has proven to be reliable and accurate.

REFERENCES

1. Jones, R.M., (1975), *Mechanics of Composite Materials,* Chap. 4, 166, McGraw Hill.

2. Walker, M., Adali, S. and Verijenko, V. E., (1995), 'Optimisation of symmetrically laminates for maximum buckling load including the effects of bending-twisting coupling', *Computers & Structures,* 58, pp. 313 - 319.

3. Adali, S., (1992) 'Convex and fuzzy modelling of uncertainties in the optimal design of composite structures', Proceedings of the *IUTAM Symposium on Optimal Design with Advanced Materials,* Denmark, pp. 1-21.

4. Tauchert, T. R., and Adibhatla, A., (1984), 'Design of laminated plates for maximum stiffness', *Journal of Composite Materials,* Vol. 18, pp. 58 - 69.

5. Quian, B., Reiss, R., and Aung, W., (1990), 'The maximum stiffness design of rectangular symmetric angle-ply laminates', *Proceedings of the 2nd Int. Conf. on Computer Aided Design in Composite Material Technology* , Free University of Brussels / Wessex Institute of Technology, Computational Mechanics Publications, Southampton, pp. 451 - 464.

6. Kengtung, C., (1986), 'Sensitivity analysis and a mixed approach to the optimization of symmetric layered composite plates', *Engineering Optimization*, Vol. 9, pp. 233 - 248.

7. Kam, T.Y., and Chang, R. R., (1992), 'Optimum layup of thick laminated composite plates for maximum stiffness', *Engineering Optimization*, Vol. 19, pp. 237 - 249.

8. Adali, S., Summers, E. B., and Verijenko, V. E., (1994), 'Minimum weight and deflection design of thick sandwich laminates via symbolic computation', *Composite Structures*, Vol. 29, pp. 145 - 160.

9. Phillips, J. L., and Gurdal, Z., (1990), 'Analysis and Optimal Design of Geodesically Stiffened Composite Panels', *Proceedings of the 2nd Int. Conf. on Computer Aided Design in Composite Material Technology*, Free University of Brussels / Wessex Institute of Technology, Computational Mechanics Publications, Southampton, pp. 509 - 520.

10. Triantafillou, T. C., Kim, P., and Meier, U., (1991), 'Optimisation of hybrid aluminium / c.f.r.p. box beams', *International Journal of Mechanical Sciences*, Vol. 33, No. 9, pp. 729 - 739.

11. Min, K.T., and de Charenteney, F.X., (1986), 'Optimum Weight Design of Sandwich Cylinders with Orthotropic Facings and Core under Combined Loads', *Computers and Structures*, Vol. 24, No. 2, pp. 313 - 322.

12. Ostwald, M., (1990), 'Optimum Weight Design of Sandwich Cylindrical Shells under Combined Loads', *Computers and Structures*, Vol. 11, pp. 247.

13. Goldberg, D. E., , (1989), *Genetic algorithms in search optimisation and machine learning*, Addison-Wesley Publishing Company, Inc., New York.

14. Haftka, R. & Walsh, J, (1992), 'Stacking sequence optimization for buckling of laminated plates by integer programming', *AIAA*, 30, pp. 814-819.

15. Nagendra, S, Haftka, R. & Gürdal, Z, (1992), 'Stacking sequence optimization of simply supported laminates with stability and strain constraints' *AIAA* , 30, pp. 2132-2137.

16. Kogiso, N, Watson, L. T, Gürdal, Z. & Haftka, R. T, (1994), 'Genetic algorithms with local improvement for composite laminate design', *Structural Optimization*, 7, pp. 207-218.

17. Gibson, R. F., (1994), *Principles of Composite Material Mechanics*, McGraw Hill, New York.

18. Ochoa, O. O, and Reddy, J. N., (1992), *Finite Element Analysis of Composite Laminates*, Solid Mechanics and its Applications, Kluwer Academic Publishers, Dordrecht.

19. Tsai, S.W., and Wu, E. M., (1971), 'A general theory of strength for anisotropic materials', *Journal of Composite Materials*, Vol. 5, pp. 58 - 80.

20. Tsai, S.W., (1987), *Composites Design*, 3rd edition, Think Composites, Dayton, Ohio.

Boundary Conditions	Layup $(\theta_1/\theta_2/\theta_3/\theta_4)_s$	Layer Thickness (x 10^{-3}m) $(t_1/t_2/t_3/t_4)_s$
(F,S,F,S)	-45° 45° 45° 45°	1,2,1,3
(F,S,C,S)	90° 90° 90° 90°	1,2,1,3
(S,S,S,S)	-45° 45° 45° 45°	1,1,4,1
(C,S,C,S)	90° 90° 90° 90°	2,1,2,1

Table 1. Results for plate with a/b = 1.0 and UDL = 2.5 x 10^5 Pa.

Aspect ratio (a/b)	Layup $(\theta_1/\theta_2/\theta_3/\theta_4)_s$	Layer Thickness (x 10^{-3}m) $(t_1/t_2/t_3/t_4)_s$
0.50	0° 0° 0° 0°	1,2,1,1
0.75	-45° 45° 45° 45°	1,3,1,1
1.0	-45° 45° 45° 45°	1,1,4,1
1.50	90° 90° 90° 90°	1,3,4,1
2.0	90° 90° 90° 90°	2,2,1,4

Table 2. Results for (S,S,S,S) plates with various aspect ratios and UDL = 2.5 x 10^5 Pa.

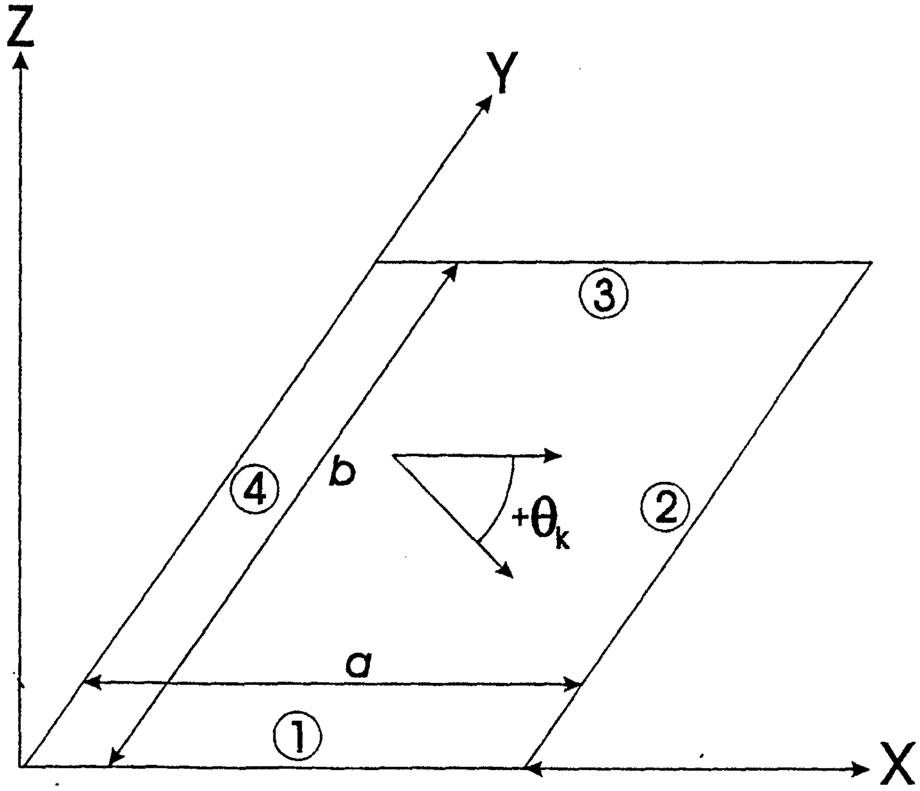

Fig 1. Configuration of the laminated plate.

MINIMUM WEIGHT DESIGN OF LAMINATED PLATES SUBJECTED TO FATIGUE LOADS USING A CUMULATIVE DAMAGE RULE CONSTRAINT

M. Walker & D. Jonson
CADENCE[*] *Technikon Natal, Durban, South Africa*

April 22, 1998

ABSTRACT

A procedure to optimally design laminated plates for a specific cyclic life using a cumulative damage rule constraint is described. The objective is minimum weight, and the design variables are the fiber orientation, and the plate thickness. The plates are subjected to cyclic bending loads, and the finite element method, in conjunction with the Golden Section routine, is used to determine the design variables optimally. The FE formulation is based on Mindlin theory for thin laminated plates and shells, and the formulation includes bending-twisting coupling. In order to demonstrate the procedure, several plates with differing events, aspect ratios and boundary conditions are optimised, and compared.

INTRODUCTION

The use of laminated composite materials in structural applications has increased dramatically in the last quarter of the twentieth century, particularly in the marine and aerospace industries (Jones - 1975). This is mainly due to the high strength-to-weight and stiffness-to-weight ratios these materials afford. Many composite structures are routinely subjected to cyclic loading regimes, and though the applied stresses may be low, failure can occur due to fatigue.

Damage occurs during each cycle of fatigue loading, and worsens as the number of cycles increases, because it is cumulative. Eventually the damage may exceed the limit a material can handle. At this point, fatiguing, one of the most common forms of failure, takes place.

Various researchers have investigated the behaviour of laminated composites under static and dynamic loads (eg. Refs 1 & 2), and cyclic loads (eg. Refs 4, 6, 8 & 12). Most of these fatigue studies are experimental, and have added to the understanding of the mechanisms involved in the fatiguing of composites. Some have even developed design methodologies, and an extensive list of these can be found in a paper by Nyman (1996) which also describes a simplified fatigue design approach. None the less the amount of work reported in the literature concerning procedures for *optimally* designing laminated composite structures under fatigue loads is small.

---

[*] Centre for Advanced Materials, Design & Manufacture Research

In terms of design optimisation, Adali (1985) used an approach described by Rotem and Hashin (1976) to optimally design laminated plates subjected to cyclic in-plane loads, with the objective of minimising the weight. The formulation used is analytical, and thus limited in its application.

One phenomenon associated with symmetric angle-ply configurations is the occurrence of bending-twisting coupling which may cause significantly different results as compared to cases in which this coupling is exactly zero (Walker *et al* - 1995). The effect of bending-twisting coupling becomes even more pronounced for laminates with few layers. Due to this coupling, closed-form solutions cannot be obtained for any of the boundary conditions and this situation led to neglecting bending-twisting coupling in design studies. In actual fact, closed-form solutions for symmetric laminates are not available even for the simplified models where this coupling is neglected except if the boundary conditions are simply supported all around. The present study adopts a numerical approach to include the effect of bending-twisting coupling and to obtain the optimal design solutions for a variety of boundary conditions.

Optimisation of composite plates for a given fatigue life is necessary to realise the full potential of fiber-reinforced materials. The procedure described here is used to optimally design laminated plates which are subjected to fatigue loading for a specific cyclic life using a damage rule constraint. The objective is minimum weight, and the design variables are the fiber orientation, and the plate thickness. The plates are subjected to cyclic bending loads, and the finite element method, in conjunction with the *Golden Section* routine (Haftka and Gürdal - 1992), is used to determine the design variables optimally. The finite element formulation is based on Mindlin theory for thin laminated plates and shells, and the formulation includes bending-twisting coupling. In order to demonstrate the procedure, several plates with differing events, load magnitudes and type, aspect ratios, boundary conditions and cyclic lives are optimised, and compared.

CUMULATIVE DAMAGE THEORY

Service operation at any given cyclic stress amplitude produces fatigue damage (which is assumed to be permanent), the seriousness of which will be related to the total number of cycles that would be required to produce failure of an undamaged component at that stress amplitude. The method adopted in this study is a linear cumulative damage method based on Miner's rule. To have a better understanding of the general theory, first consider the following example:

Assume that operation at several different stress amplitudes S_1, S_2, ..., S_t in sequence for a number of cycles n_1, n_2, ..., n_t will result in an accumulation of total damage equal to the sum of the damage increments accrued at each individual stress level. Then if operation at a stress amplitude S_1 produces complete damage (or failure) in N_1 cycles, operation at stress amplitude S_1 (event 1 - in the following development each one of the different load level operations, which may consist of a number of cycles, is called an event) for a number of cycles n_1 smaller than N_1 will produce a smaller fraction of damage, say D_1. Factor D_1 is termed a damage fraction (or *usage factor*). Operation over a spectrum of different stress levels results in a usage factor D_i for each of the different stress levels S_i in the spectrum. When these factors sum to unity, failure is predicted; viz:

$$D_1 + D_2 + \ldots + D_i \geq 1 \tag{1}$$

The linear damage rule states that the damage fraction, D_i, at stress level S_i is equal to the cycle ratio n_i/N_i. Thus, the damage fraction D due to one cycle of loading is $1/N$. In other words, the application of one cycle of loading consumes $1/N$ of the fatigue life. The failure criterion for variable amplitude loading can now be stated as

$$\frac{n_1}{N_1} + \frac{n_2}{N_2} + \ldots + \frac{n_i}{N_i} \geq 1 \tag{2}$$

ANALYSIS PROCEDURE FOR CYCLIC LOADING

After defining a design fatigue curve (S-N curve), the stresses at the nodes throughout the FE plate model are determined. Next, the partial usage factor D_i for the i-th alternating stress intensity is evaluated in that list by evaluating the cycle ratio n_i/N_i (as its equivalence). The i-th alternating stress intensity is formed by the combination of loadings A_E and B_F, where E and F are the corresponding events. Here, n_i corresponds to the lower number of cycles interpolated from the design fatigue curve (S-N curve).

After evaluating the partial usage factor D_i, the updates are made to the alternating stress intensity list by reducing the number of cycles of both events E and F by n_i. Consequently, one of the two events E or F will be eliminated (or both if E and F have the same number of cycles) and the other event will have n_i cycles less in the later calculations. Elimination of an event results in elimination of the corresponding loadings. Once a loading is eliminated the corresponding stress intensities (formed by combination of that loading with other loadings) will also be eliminated from the list. After updating the list, the next alternating stress intensity in the list is checked and the corresponding partial usage factor evaluated, added that to the cumulative one and the list updated. This procedure is repeated for the next alternating stress intensity in the list and continues until all stress intensities are considered.

For any alternating stress within the stress range S_1 and S_2 (the first and last points) of an S-N curve log-log interpolation is used to find the corresponding cycles.

OPTIMAL DESIGN PROBLEM

The objective of the design problem is, *for a given specific fatigue life* (consisting of several events), to minimise the maximum damage $D_{\max}(x, y)$ and then the weight W of the plate by minimising the thickness h subject to a cumulative damage law constraint. Minimising $D_{\max}(x, y)$ is achieved by optimally determining the fiber orientations given by $\theta_k = (-1)^{k+1}\theta$ for $k \leq K/2$ and $\theta_k = (-1)^k\theta$ for $k \geq K/2 + 1$ in order to minimise the maximum cumulative stresses (and thus damage) which occur during loading events.

Thus, the first part is stated as

$$D_{\min} \triangleq \min_{\theta} \; [D_{\max}(\theta)], \; 0^o \leq \theta \leq 90^o \tag{3}$$

where

$$D_{\max}(\theta) = \max_{x,y} \; D(x, y; \theta) \tag{4}$$

The second part of the design problem involves minimising the laminate thickness h within the constraints of the a damage rule, and may be stated as

$$h_{\min} = \min_{h} \; h(\theta_{opt}) \tag{5}$$

The nodal stresses and subsequently the remaining life n_i (which is interpolated from the S-N curve) and thus the maximum damage $D_{\max}$ are determined from the finite element solution of the problem. The first optimisation procedure involves the stages of determining the maximum damage $D_{\max}(x, y)$ for a given θ and improving the fiber angle to minimise $D_{\max}$. The second optimisation stage involves evaluating $D(\theta_{opt})$ for a given h and improving the laminate thickness to minimise the weight. This step may be described explicitly as

$$\min_{h} \; |D(\theta_{opt}) - 1| \tag{6}$$

in order to minimise the thickness. Thus the computational solution consists of successive stages of analysis and optimisation until a convergence is obtained and the optimal fibre angle θ_{opt} and then $h_{\min}$ is determined within a specified accuracy. In both optimisation stages, the *Golden Section* method is employed firstly to determine θ_{opt} and then $h_{\min}$.

NUMERICAL EXAMPLES

For the purpose of illustrating the method described, numerical results are given for a typical T300/5208 graphite/epoxy material with $E_1 = 181$ GPa, $E_2 = 10.3$ GPa, $G_{12} = 7.17$ GPa and $\nu_{12} = 0.28$ (Tsai - 1987). The symmetric plates studied here are constructed of four equal thickness layers with $\theta_1 = -\theta_2 = -\theta_3 = \theta_4 = \theta$ and for design purposes, the S-N curve of Fig. 2 is specified (Dorey - 1990). Different combinations of free (F), simply supported (S) and clamped (C) boundary conditions are implemented at the four edges of the plates. In particular, the different combinations studied are (F,S,C,S), (S,S,S,S) and (C,C,C,C), where the first letter refers to the first plate edge, and the others follow in an anti-clockwise direction as shown in Fig. 1. Also, the plates are subjected to uniformly distributed transverse bending loads of magnitude P Pa, which are applied cyclically (and fully reversed).

The dependence of stresses and thus the damage D on the fibre angle θ is illustrated in Fig. 3, for a (F,S,C,S) plate and (C,C,C,C) plate, both having $a/b = 1$. The plates are subjected to the first loading regime or event shown in Table 1 below (viz. the load of 100 000 Pa is applied and then removed 50 000 times). The (F,S,C,S) plate has $h/b = 0.0074$, while the other has $h/b = 0.0042$. This demonstrates that the damage is indeed dependant on the fiber orientation, and it is clear that the minimum damage for a laminate can be several times lower than the damage at other fibre angles. In addition, the plate thickness can be determined optimally, such that the plate is designed for a particular cyclic life. This fact emphasises the importance of carrying out optimization in design work of this nature to obtain the best performance of fibre composite plates.

Event	Load (Pa)	Cyclic Life
1	100 000	50 000
2	200 000	25 000

Table 1. Loading vs. life for the two events

Example 1: Plates with differing events

Consider a (C,C,C,C) plate with $a/b = 2$. The plate is subjected to the first loading regime or event shown in Table 1 , and should fail at the end of the last cycle of that event. Thus, the plate must be designed such that θ and h are selected optimally to ensure minimum weight and sufficient life.

The result is compared to that for a similar plate (plate no. 2) which is subjected to both events shown in Table 1.

Plate	θ_{opt}	$h_{\min}/b \times 10^{-3}$
1	90°	4.50
2	45°	7.69

Table 2. Optimal designs for plates subjected to differing events

As expected, the plate which is subjected to both events has a minimum thickness which is approximately 40% more than the plate which is designed optimally to endure the first event only.

Example 2: Plates with differing aspect ratios

In order to demonstrate the effect of a/b on the results, two plates with different aspect ratios were optimally designed. The boundary conditions implemented along the edges of each plate is (C,C,C,C), with the first having $a/b = 1.25$, and the second $a/b = 2$ (the standard plate of example 1). The plates are subject to both events.

a/b	θ_{opt}	$h_{\min}/b \times 10^{-3}$
1.25	90°	6.15
2	45°	7.69

Table 3. Optimal designs for plates with differing aspect ratios

The plate with the larger aspect ratio ends up with a minimum thickness which is approximately 20% greater than the smaller plate after the process of optimally designing is completed. This is expected, since the smaller plate is stiffer.

Example 3: Plates with differing boundary conditions

In order to demonstrate the effect of the boundary conditions on the results, three plates, each of aspect ratio $a/b = 1.75$ but with differing boundary conditions were optimally designed. The first is clamped along all four edges, while the second is simply supported along all four edges. The third plate has a combination of free, simply supported and clamped boundary conditions, viz.(F,S,C,S), and all are subjected to the first event only.

Boundary Conditions	θ_{opt}	$h_{\min}/b \times 10^{-3}$
(C,C,C,C)	90°	4.48
(S,S,S,S)	87.7^o	6.02
(F,S,C,S)	26.9^o	9.93

Table 4. Optimal designs for plates with differing boundary conditions

As the number of degrees of freedom of a plate is curtailed along the boundary, so it becomes stiffer. For this reason, the (F,S,C,S) plate is 26% thicker than the (S,S,S,S) plate, and 55% thicker than the (C,C,C,C) plate, as can be seen from the results in Table 4.

CONCLUSIONS

A procedure for optimally designing laminated plates for a specific cyclic life using a damage rule constraint is described. The objective is minimum weight, and the design variables are the fiber orientation, and the plate thickness. The plates are subjected to cyclic bending loads, and the finite element method, in conjunction with a search routine is used to determine the design variables optimally. The FEM formulation is based on Mindlin-type laminated plate theory. The numerical approach employed in the present study is necessitated by the fact that the inclusion of the bending-twisting coupling effect and the consideration of various combinations of free, clamped and simply supported boundary conditions, rule out an analytical approach. It must be emphasised that different damage rules may be used, and that the one chosen in this study is used merely to demonstrate the procedure.

The effect of partial optimisation on the damage was investigated by plotting D against the first design variable θ for a given plate thickness (Figure 3). The results show that the difference in the damage of optimal and non-optimal plates could be quite substantial, emphasising the importance of optimisation for fiber composite structures.

In order to demonstrate the complete procedure described in this paper, several plates are then completely optimised, such that both the fiber angle and plate thickness are determined optimally. The plates have differing events, aspect ratios and boundary conditions, and the optimal design of each is compared to the others. Such differences result in differing optimal designs, thus emphesising the importance of optimisation in every case.

CLOSURE

When the plates described by the results depicted in Fig. 3 are fully optimised, the results are as follows:

Boundary Condition	θ_{opt}	$h_{\min}/b \times 10^{-3}$
(F,S,C,S)	0°	6.62
(C,C,C,C)	45°	4.15

REFERENCES

1. Adali, S., 1983, 'Multiobjective design of an anti-symmetric angle-ply laminate by non-linear programming', *ASME J. Mechs, Trans., Automation in Design*, **105**, pp. 214 - 219.

2. Adali, S., 1984, 'Design of shear deformable antisymmetric angle-ply laminates to maximise the fundamental frequency and frequency separation', *Composite Structures*, **2**, pp. 349 - 369.

3. Adali, S., 1985, 'Optimisation of fiber reinforced composite laminates subject to fatigue loading', *Composite Structures*, **3**, pp. 43 - 55.

4. Buggy, M. and Dillion, G., 1991, 'Flexural fatigue of carbon fiber-reinforced p.e.e.k. laminates', *Composites*, **22**, pp. 191 - 198.

5. Dorey, G., 1990, 'The fiber-matrix interface and composite strength', *Composite Materials in Aircraft Structures*, Edited by D. H. Middleton, Longman Scientific and Technical, Essex, England, pp. 50 - 68.

6. El Kadi, H. and Ellyin, F., 1994, 'Effect of stress ratio on the fatigue of unidirectional glass fiber/epoxy composite laminates', *Composites*, **25**, pp. 917 - 924.

7. Haftka, R. T., and Gürdal, Z., 1992, *Elements of Structural Optimisation*, 3rd Edition, Kluwer Academic Publishers, Dordrecht.

8. Harris, B., Reiter, H., Adam, T., Dickson, R. F. and Fernando, G., 1990, 'Fatigue behaviour of carbon reinforced plastics', *Composites*, **21**, pp. 232 - 242.

9. Jones, R. M., 1975, *Mechanics of Composite Materials*, Chap. 4, pp.166, McGraw Hill, New York

10. Nyman, T., 1996, 'Composite fatigue design methodology: a simplified approach', *Composite Structures*, **35**, pp. 183 - 194.

11. Rotem, A. and Hashin, Z., 1976, 'Fatigue of angle-ply laminates', *AIAA*, **14**, pp. 868 - 872.

12. Rotem, A., 1979, 'Fatigue failure of multidirectional laminate', *AIAA*, **17**, pp. 271 - 277.

13. Tsai, S. W., 1987, *Composites Design*, 3rd Edition, Think Composites, Dayton, Ohio.

14. Walker, M., Adali, S. and Verijenko, V. E., 1995, 'Optimisation of symmetrically laminates for maximum buckling load including the effects of bending-twisting coupling', *Computers & Structures*, **58**, pp. 313 - 319.

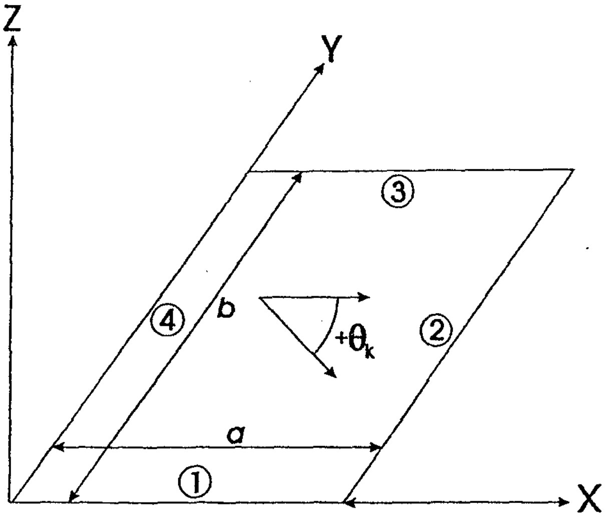

Fig 1. Configuration of the laminated plate.

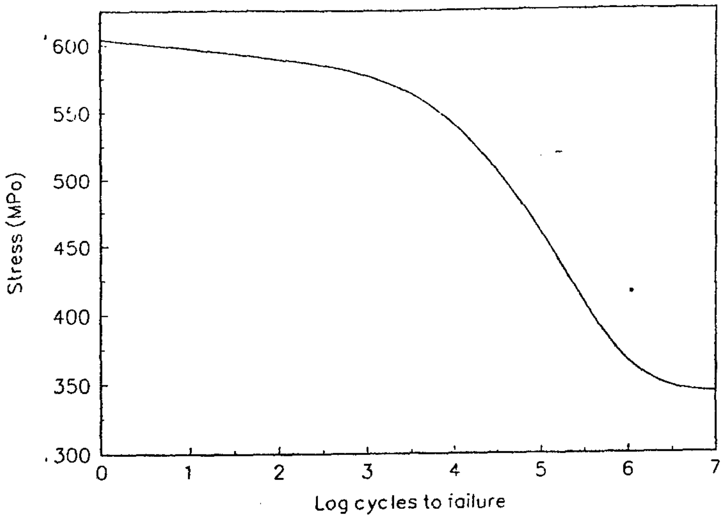

Figure 2. S-N curve for T300/5208 material

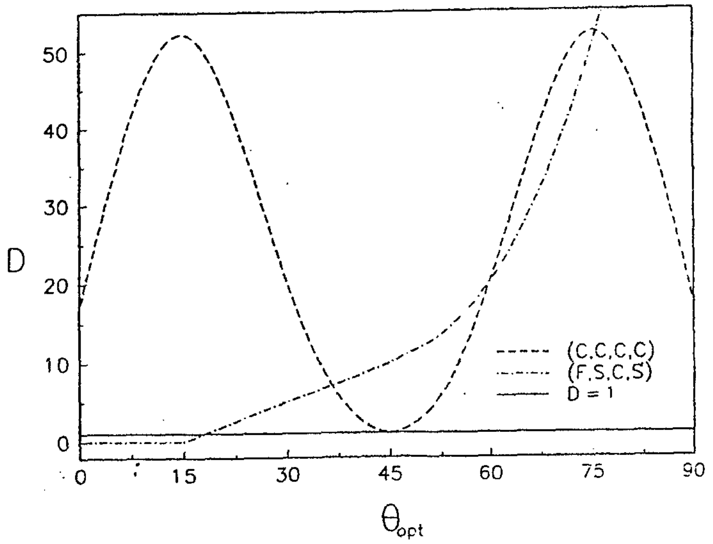

Figure 3. Dependence of damage D on the fibre angle

ASPECTS OF STRUCTURAL DESIGN AND MANUFACTURE OF AN ALL COMPOSITE MOTORGLIDER WING

W. M. Banks and J. A. Russell

Dept of Mechanical Engineering
University of Strathclyde
Montrose Street
Glasgow G1 1XJ Scotland UK

ABSTRACT

There is currently a widespread demand for a personal light aircraft. This demand has been partially met by the Europa Aircraft Company Ltd in the supply of what is called 'The Europa'. This aircraft is a low wing monoplane of composite construction. The aircraft has been designed to meet the Joint Airworthiness Requirements (JAR) for very light aircraft. The requirements have had to be met in respect of stability, handling and overall structural integrity. In the case of "The Europa", the primary composite structures are manufactured by the company. However the aircraft is supplied as a series of kits to be assembled by the customer.

The paper covers some aspects of the structural design and manufacture of an all composite retrofit motor glider wing. This wing has to accommodate the current structural make-up of the light aircraft air frame. Particular attention is paid to designing for the most unfavourable aerodynamic loads acting on the glider wing. A review of these loads has led to a more detailed examination of the wing profile and make-up and, in particular, an analysis of the wing skin, the rib and the overall spar. In the latter case the spar strength is of particular concern and importance.

The analysis thus undertaken ultimately leads to a material selection process for the appropriate parts of the wing details including the skin, ribs and spar. It involves 'composite superfactoring'. This is reviewed in detail. Attention is paid to its overall influence on the final material choice.

INTRODUCTION

The purpose of the work presented in this paper was to design a prototype glider wing as a direct replacement for the standard wing employed by "The Europa" light aircraft. Although not a fully certified aircraft component, the proof of concept glider wing structure was designed to meet the utility category requirements of JAR-22. Planform geometry was defined by Europa Aircraft's aerodynamicist. The following engineering constraints had to be met.

- minimum changes to the existing Europa light aircraft fuselage
- commonality of airframe coupling mechanism
- commonality of materials and construction techniques
- glider wing must be capable of being assembled within a standard car garage by the non-specialist

- glider wing must be capable of being shipped in component form within a six metre container

The main factors which govern the choice of materials and structural design is the ratio of the applied loads to the dimensions of the structure. In order to determine the applied loads, it is necessary to examine the nature of the aerodynamic loads acting on the glider wing.

AERODYNAMIC LOADS

The greatest aerodynamic loads on any aircraft come from the generation of lift during high-g manoeuvres. The aircraft load factor (n) expresses the manoeuvering envelope of an aircraft as a multiple of the acceleration due to gravity. At lower airspeeds the highest load factor an aircraft will experience is limited by the maximum lift available from the main wing, which in turn is a function of wing area and profile shape. At higher airspeeds the maximum value of load factor is limited to a value based upon the expected use of the aircraft during normal operations. This load factor is defined as the limit load factor. For "The Europa" glider aircraft, the limit load factors for both low and high speed cases is defined within the relevant standards. "The Europa" glider aircraft was sized to meet the utility category of the standard JAR-22. This resulted in the limit load factors of +5.3g and -2.65g for the low speed case, with +4.0g and -1.5g being the limited load factors for the high speed case. These values can be plotted on a chart known as the V-N diagram.

Conditions A and D

The V-N diagram depicts the aircraft limit load factor as a function of airspeed and defines the 'flight envelope' for the aircraft. In order to determine the strength of any wing structure, two critical conditions on the flight envelope require considerable investigation. The first condition exists at V_A, the aircraft manoeuvring speed. This condition represents the slowest speed at which the maximum limit load factor can be reached without stalling the wing. This part of the flight envelope requires investigation because the load on the wing is approximately perpendicular to the flight direction; not as might be thought, perpendicular to the fuselage horizontal datum. At this condition (*Condition A*) the wing presents a very high angle of attack to the airflow. The load direction will be forward of the aircraft fuselage vertical datum, causing a forward load component on the wing structure. If the wing was not stressed to meet this condition, the wings could fail by shedding forward in flight. The combination of high angle of attack and maximum load factor results in the wing skins experiencing the highest torsional load within the aircraft flight envelope.

The second critical condition requiring investigation occurs at V_D, the aircraft dive speed. This condition (*Condition D*) at the extreme right hand side of the aircraft flight envelope, represents the point where maximum dynamic pressure and maximum limit load factor coincide. This condition is important for structural sizing of the wing spar. At *Condition D* the wing is at a low angle of attack because of the high dynamic pressure, so the load is approximately perpendicular to the fuselage horizontal datum. The combination of dynamic pressure and maximum load factor results in the wing spar experiencing the highest bending load within the aircraft flight envelope.

Conditions A and *D* above ignore the effect of very strong gusts acting on the aircraft. It is true that the loads experienced when an aircraft encounters a strong gust can exceed the limit manoeuvring loads evaluated at *Conditions A* and *D*. However the load experienced by the gust depends on the gust penetration speed location on the V-N diagram. By reducing the aircraft gust penetration speed the gust g load can be tailored to coincide with the limit manoeuvring factor load of +5.3g. By making the gust factor coincident with the manoeuvring limit load factor there is also the added benefit of reduced aircraft weight as less substructure is required to resist transient peak bending loads experienced during the gust. These loads would have been greater than those experienced at V_A or V_D. With the V-N diagram for "The Europa" glider aircraft defined, the actual loads and load distributions acting on the wing surface can be determined. For the glider wing aircraft this only needs to be done at *Conditions A* and *D*. It is therefore necessary to conduct two separate static strength tests in order to fully represent the loads acting on the glider wing at *Conditions A* and *D*.

Stability and control calculations

Initially stability and control calculations are conducted to determine the required lift on the horizontal tailplane to balance the wing pitching moment at V_A and V_D. The stability calculations are approximated by summation of the wing and tailplane moments about the most forward position of the aircraft centre of gravity. A simple approximation made within JAR-22 is to assume that 5% of the lift produced by the main wing can be generated as a balance load by the horizontal tailplane. The horizontal tailplane load is then added to the main wing lift to give the balance lifting load acting on the wing.

With the balanced lifting load known, the spanwise and chordwise lift distributions can be determined. From classical wing theory, on an elliptical planform wing the spanwise lift distribution is of an elliptical shape. A semi-empirical method for determining the spanwise lift load is known as Shrenk's approximation. This method assumes that the load distribution on an un-twisted, non-elleptical planform such as "The Europa" glider wing, has a shape that is the average of the actual planform shape and an elliptical shape of the same span and area. The total area under the Shrenk lift load curve then must be equal to the balance lifting load. With the spanwise load distribution defined, the main wing shear and bending stresses can be determined at both *Conditions A* and *D*.

Torsional stresses

To determine the wing torsional stresses, in particular those at *Condition A* on the flight envelope the airfoil moment coefficient is applied to spanwise strips and the total torsional moment is summed from the wing tip to the wing root. The torsional stresses experienced by the wing depend heavily on the chordwise position of the wing centre of pressure, and the location of the wing flexural centre. On the Europa glider wing aircraft the wing flexural centre was assumed to act at the spar location which is approximately 40% chord.

The chordwise position of the centre of pressure varies with angle of attack. This results in the necessity to examine the chordwise distributions at both *Conditions A* and *D* on the flight envelope.

COMPOSITE SUPER FACTORING

A safety factor of 1.5 is always used when sizing any aircraft structural component. This factor defines ultimate load, where ultimate load = limit load * 1.5. The aircraft structure must be able to support ultimate load for three seconds without failure. The use of composite materials means the use of additional factors of safety to account for the effects of moisture, temperature, and manufacturing variability. Multiplying these factors together results in a *'composite super factor'* of 1.5. For "The Europa" glider wing, sized to meet the utility category of JAR-22, the resulting limit load of 5.3g becomes:

+5.3*(*composite super factor*)* 1.5(factor of safety) = 12g.

This approach accounts for degradation of the composite material over the lifespan of the aircraft. It does not mean that "The Europa" glider wing is fully aerobatic, because the placarded maximum permissible limit g loading is still +5.3g. This approach equates to an equivalent aluminium glider wing with a resulting ultimate g load of

$$+5.3*1.5 \text{ (factor of safety)} = 7.95g.$$

Even with extensive material testing of moisture conditioned pre-preg composite specimens at elevated temperature, the composite super factor would only reduce from 1.5 to 1.2. Unfortunately superfactoring can lead to heavier wing structures, or in some cases failures in metallic components not strength checked to meet the super factored loads.

DETAILED STRUCTURAL CONSTRAINTS

With the wing spanwise and chordwise load distributions defined, the wing spar bending stresses, and the skin torsional stresses can be determined. By choosing composite materials common with the Europa light aircraft wing, these stresses are then factored with the composite super factors, and the safety factor of 1.5.

Aspects of the detailed structural design of the standard light aircraft that are common with the glider wing can now be investigated in more detail. Three key areas of the glider wing design must maintain commonality with the light aircraft wing. These structural constraints are now considered in detail.

The wing spar housing cross sectional geometry within the Europa fuselage

The proximity of the seatback bulkhead in relation to the main fuel tank and aileron coupling mechanism restricts wing spar width. The spar depth is restricted by the location of the wing on the fuselage side. This limits the depth of the spars at the point of maximum bending loads at the outer most spar pin. Analysis of the bending stresses developed by the wing at both *Conditions A* and *D* on the flight envelope yield the peak values of load at the point of maximum bending. The cross sectional area of the spar boom at this point drives the spar material choice. The upper spar boom is particularly critical as it supports compressive loads due to spar bending. Unidirectional CFRP rovings with a compressive failure strength of $900MN/m^2$ was eventually chosen for the upper and lower spar boom. The shear stresses experienced by the spar are also a maximum at the spar pin location. Satin weave bi-directional GRP shear webs, oriented at ±45 degrees to the spar, were used to transmit shear from one spar cap to the other. This was achieved in practice by staggering the number of shear web plies to match the shear stress gradient developed along the span of the wing spar. The excellent drapability of this cloth is used to dimensionally control the cross section of the spar.

The wing spar coupling mechanism

The wing spar coupling mechanism design employs two 10mm pins which locate within both wing spars through the cockpit seatback. Analysis of the wing spar coupling by hand calculation, in conjunction with previous static strength tests conducted on the light aircraft wings revealed that the failure mode of the wing spars is by spar buckling between the two spar pins. This mode of failure was aggravated by the single shear overlapping nature of the coupling mechanism. The spar pins were restricted from being put into double shear due to the spar housing cross sectional geometry constraint. An initial solution employed to prevent the onset of buckling was to tie both spars together with a 'composite buckling prevention strap'. Further development led to a final design which employed threaded spar pin bushes.

Analysis of the wing spar in bending revealed shear loads at the spar pins, which at ultimate load, were approximately 35% higher than those experienced by the light aircraft spar pins. These shear loads resulted from the combined effects of a higher g loading specified in JAR-22, and the 42% increase in wing span of the glider wing. These loads were combated by the use of 12.5mm pins with threaded bushes.

The wing torque housing located on the fuselage sides
To maintain commonality with the light aircraft wing, the housing located on the fuselage side which diffuses torsion from the main wing as shear, had to remain unchanged. The glider wing torque pins should also locate within these housings on the fuselage sides with the minimum of changes.

Previously the standard light aircraft wing employed rigid stainless steel pins within a rigid housing on the fuselage side. This arrangement was inexpensive and relied on the inherent flexibility of the fuselage sides to relieve any offset bending loads which would occur from wing torque and wing bending. However the larger span of the glider wing, with its more outboard spanwise centre of pressure, develops a very forward chordwise bending load at high angles of attack. In addition, with airbrakes deployed the glider wing develops a very aft chordwise bending load. These extreme cases can lead to the sandwich panels which make up the fuselage sides experiencing high bending stresses in the region of the fuselage adjacent to the wing torque housing. To compensate for the lack of stiffness of the fuselage sides, a steel tie bar was used to join both torque housings across the inside of the aircraft fuselage. The increase in rigidity of the fuselage sides resulting from this arrangement could lead to the rigid torque pins which locate within the torque housing, experiencing high bending loads. There could also be a fatigue problem. To prevent extreme damage to the fuselage sides which might result from both extreme chordwise and spanwise bending loads, articulating sockets were employed on the side of the fuselage. These sockets prevent the rigid torque pins and the adjacent wing root inserts experiencing any offset bending load.

BENEFITS OF THE USE OF COMPOSITE MATERIALS FOR PROTOTYPE CONSTRUCTION

The most efficient means of reducing structural mass is to reduce the density of the material, rather than increase the overall strength or stiffness of the material. The use of composites for rapid prototyping, particularly in the case of the glider wing, allows both to be done. Another reason for adopting composite materials is their excellent fatigue resistance. GRP, particularly when used as a wing skin material, provides an efficient means of tailoring the skin thickness to prevent buckling. The spanwise decrease in the number of wing spar shear webs, and the spanwise decrease in spar boom area is tailored to coincide with the spanwise decrease in span bending stiffness. In addition to the strength and stiffness benefits, GRP skins result in a surface finish that is free from surface irregularities therefore have the benefit of low drag.

"The Europa" prototype glider wing has a CFRP spar that is approximately 12 times stiffer than the wing skins. The spar was specifically designed to take all the bending loads. This results in the GRP wing skins only experiencing about 4% of the bending stress. The skin structure is designed to feed the aerodynamic load back to the wing spar via the wing ribs and Styrofoam reinforcement. The Styrofoam mouldless construction of the prototype Europa glider wing structure does not suffer from conventional skin panel buckling. Skin fibre alignment is employed to transmit torque efficiently from the wing skins to the wing spar. The GRP wing skins were constructed from wet lay up glass at ±45 degrees to the wing spar.

AEROELASTIC EFFECTS

Unfortunately composites, specifically unbalanced GRP laminates, can experience high strain under load. Wing flexibility can cause distortions which can in the case of a high aspect ratio wing, such as "The Europa" glider wing, have an adverse effect on lateral stability. Wing twisting in response to aileron deflection decreases the available rolling moment of the wing as a function of the dynamic pressure, which is proportional to speed squared, because as speed doubles the loads on the wing defined for *Condition D* on the flight envelope quadruples. In extreme cases aileron reversal can occur. This is where the aileron load deflects the adjacent wing structure rather than deflecting the air passing over the control surface. It is necessary to ensure that the aileron reversal speed is outwith the maximum operating speed of the flight envelope. Specifically aileron reversal should not occur at an airspeed 20% greater than the speed V_D on the flight envelope.

One benefit of both GRP and CFRP is the ability to tailor wing skin orientation and thickness therefore increasing the torsional stiffness of the wing skins to correct flutter or resonant vibration problems. Additional plies of GRP were added to the Europa glider wing for that reason.

PRODUCTION GLIDER WING

The wet lay up mouldless construction of the prototype glider wing will give way to low temperature pre-preg sandwich panel construction for the production Europa glider wing structure. There is no difficulty for a skin membrane to take tension. The problem lies with the skin taking compression without buckling. Work is ongoing at Europa Aircraft to select the optimum sandwich thickness, and rib pitch for a production pre-moulded glider wing. The aim is to reduce the customer build time for a set of these wings to 50 hours.

INFLUENCE OF PLASTIC COATING OF RADIAL PLAIN BEARINGS ON CONTACT STRESS

Chigarev A.V. and Kravchuk A.S.
Belarussian State Polytechnic Academy, Dept. of Theoretical Mechanics
Minsk, 220027, Belarus

INTRODUCTION

The thin metal coating are widly used in a mechanical engineering. They improve work of machine parts with lubrication and in conditions of dry friction [1]. An appropriate selection of metal of a covering and its thickness it is allowed to supply serviceability of bearings of dry friction in deep vacuum, with high temperatures and large pressure [1-3].

In this paper we will describe an explicit approximate solution of the contact problem for rough rigid disk and isotropy plate with plastic coating on the smooth cylindrical hole. It will allowed to receive an analytical expression for principal tangential stress along axis of force action.

CONTACT PROBLEM FOR ROUGH RIGID DISK AND ISOTROPY PLATE WITH PLASTIC COATING ON THE SMOOTH CYLINDRIC HOLE

Consider an elastic isotropy plate with a composite cylindric hole of radius R with thickness of coating h. The rigid rough disk of radius r is put in it. It will be assumed that ε^2, ε/R $(\varepsilon = R - r > 0)$ are low reject values. Force P acts along the y-axis (Fig. 1).

In the area of contact L we have

$$(x+u^{**})^2 + (y+v^{**})^2 = (r\sin(\zeta) - (\varepsilon+\delta))^2 + r^2\cos(\zeta)^2,$$

here

$$x = R\cos(\zeta),\ y = R\sin(\zeta),$$

u^{**}, v^{**} are components of the displacemets of the plate with the coating, δ is the displacement of the disk center. It's easy to see that on L we receive that

$$\varepsilon + u^{**}\cos(\zeta) + v^{**}\sin(\zeta) = -2(\varepsilon+\delta)\sin(\zeta)$$

Let

$$u^{**} = u^{*} + u,\ v^{**} = v^{*} + v,$$

where u, v, u^{*}, v^{*} are displacements of the basic material and the of disk roughness in plastic coating accordingly.

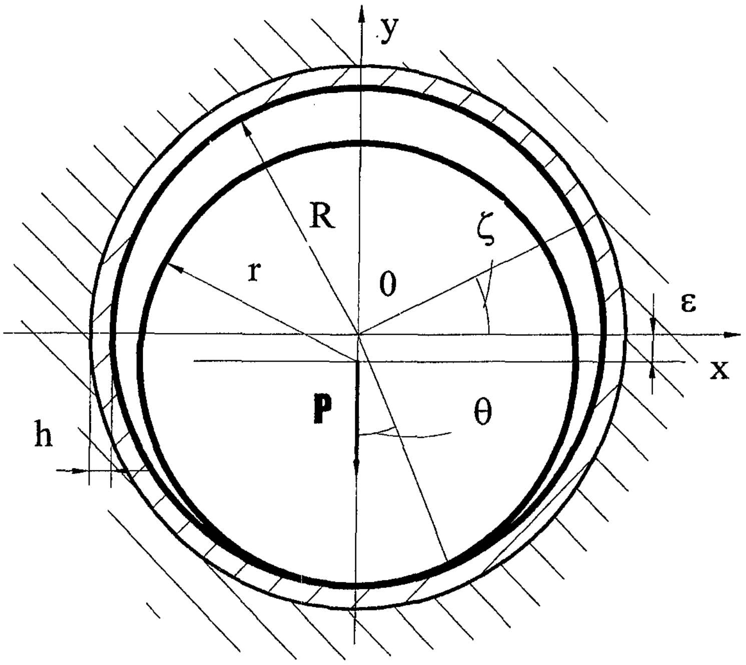

Fig.1. Geometry of disk and coating.

We shall assume, that the elastic radial displacement in the area of the contact being determined by the introduction of the micro-irregularity in layer is fixed and proportional to average contact stress σ. Then, taking into account the accepted suppositions, after elementary transformations is obtained:

$$(\varepsilon-\Delta)+\frac{R}{E}\left(G_1\sigma_\zeta-\nu G_2\sigma_r\right)+\frac{\partial}{\partial\zeta}\left(\frac{\partial u}{\partial\zeta}\cos(\zeta)+\frac{\partial v}{\partial\zeta}\sin(\zeta)\right)=0 \qquad (1)$$

where $G_1=(1-\nu^2)$, $G_2=(1+\nu)$ – for state of plane deformation; $G_1=G_2=1$ - for state of plane stress; ν is Poisson's ratio of the basic material; E is Young's modulus of the basic material; σ_ζ, σ_r is normal components of the stress.

It's known that [4]

$$\begin{aligned}
&\sigma_\zeta+\sigma_r=2\left[\Phi(z)+\overline{\Phi(z)}\right],\\
&\sigma_\zeta-\sigma_r+2i\tau_{r\zeta}=2e^{2i\zeta}\left[\bar{z}\Phi'(z)+\Psi(z)\right],\\
&2\mu(u+iv)=\kappa\varphi(z)-z\overline{\Phi(z)}-\overline{\psi(z)}
\end{aligned} \qquad (2)$$

here μ is Lame's coefficient; $i=\sqrt{-1}$; $\varphi(z)$, $\psi(z)$ are Kolosov-Mushelishvily complex potentials; $\varphi'(z)=\Phi(z)$, $\psi'(z)=\Psi(z)$, $z=x+iy$; $\kappa=3-4\nu$ – for state of plane deformation; $\kappa=(3-\nu)/(1+\nu)$ – for state of plane stress.

Applying (1) and (2) we receive that

$$\varepsilon-\Delta+\frac{R}{E}\left(2G_1\left[\Phi(t)+\overline{\Phi(t)}\right]-\left(G_1+\nu G_2\right)\sigma_r\right)+$$

$$+R\frac{\partial}{\partial\zeta}\left(\frac{(\kappa+1)}{4\mu}i\left[\Phi(t)-\overline{\Phi(t)}\right]\right)=0,\quad t\in L \tag{3}$$

Then using equals [4]

$$\Phi(z)=\frac{\kappa}{2\pi(1+\kappa)}\frac{iP}{z}-\frac{1}{2\pi i}\int_L\frac{\sigma_r(\tau)d\tau}{\tau-z}, \tag{4}$$

and (3), we arrive the integral equation:

$$\frac{t}{\pi i}\int_L\frac{\sigma_r'(\tau)d\tau}{\tau-t}=\gamma_1\sigma_r(\tau)-\frac{iP}{\pi}\gamma_2\left(\frac{1}{t}-\frac{t}{R^2}\right)-\frac{b}{R^2}-\gamma_3(\varepsilon-\Delta), \tag{5}$$

where

$$\gamma_1=\frac{-(G_1-\nu G_2)}{2G_1},\quad \gamma_2=\frac{\kappa(1+\nu)}{4G_1},$$

$$\gamma_3=\frac{E}{2RG_1},\quad \frac{\mathrm{b}}{\mathrm{R}^2}=-\frac{1}{2\pi i}\int_L\frac{\sigma_r}{\tau}d\tau,\quad \mathrm{t}=\mathrm{Re}^{\mathrm{i}\zeta},$$

The parameter Δ is defined from equations [1]:

- when $\Delta>h^2/2r_1$:

$$\Delta^\lambda+(\Delta-\frac{h^2}{2r_1})^\lambda\sqrt{\frac{\Delta}{r_1}}\left(0.2\frac{r_1}{h}+0.1\frac{h}{\Delta}-0.14\right)=\frac{H_{\max}^\lambda\,P}{6.8\,\sin(\alpha_0)\,R\,\sigma_s b}$$

- and $\Delta\le h^2/2r_1$:

$$\Delta=H_{\max}\left(\frac{P}{6.8\,\sin(\alpha_0)\,R\,\sigma_s b}\right)^{\frac{1}{\lambda}}$$

$r_1, H_{\max}$ are parameters of microdeviations of disk; λ, b are parameters of bearing area curve of disk [2]; α_0 is a contact half-angle; σ_s yield pressure of coating.

Results of investigations show that the approximate solution of (5) can be assumed in the following form [4]:

$$\sigma_r(\theta) = -P\frac{\sqrt{2}}{R}\left[\gamma_2\frac{2}{\pi} + \frac{\gamma_1}{\alpha_0 + \cos(\alpha_0)\sin(\alpha_0)}\right]\times$$
$$\times\sqrt{\cos(\theta) - \cos(\alpha_0)}\cos(\theta/2) + \tag{6}$$
$$+2\left[\frac{b}{R^2} + \gamma_3(\varepsilon - \Delta)\right]\ln\left[\frac{\sqrt{1+\cos(\theta)} - \sqrt{\cos(\theta) - \cos(\alpha_0)}}{\sqrt{1+\cos(\alpha_0)}}\right]$$

Suppose that the α_0 is known. Then the values P and b are defined from following equals:

$$P = -2R\int_0^{\alpha_0}\sigma_r(\theta)\cos(\theta)d\theta, \quad b = -\frac{R^2}{\pi}\int_0^{\alpha_0}\sigma_r(\theta)d\theta.$$

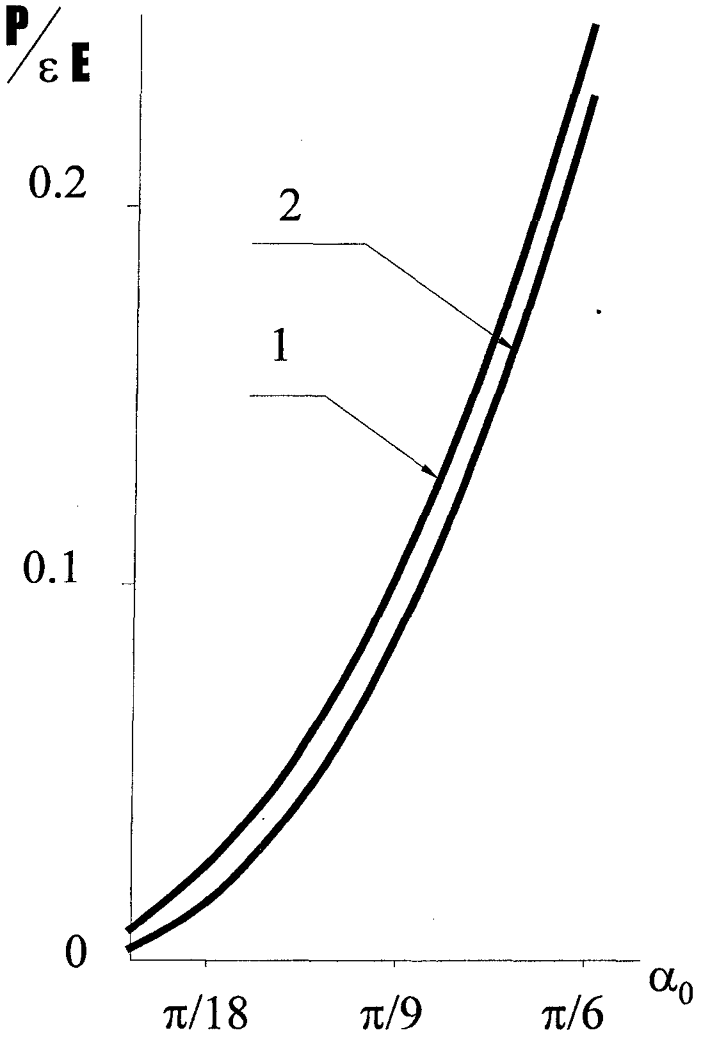

Fig. 2. The relation between α_0 and parameter $P/\varepsilon E$:
1 - for a smooth hole;

2 - for rough hole with silver coating;

The carried out accounts show, that in case of rough hole contact half-angle increased on a comparison with a half-angle for smooth hole (Fig. 2) and the greatest contact stress decreased.

We receive from (2):

$$\frac{\sigma_\zeta - \sigma_r}{2} + i\tau_{r\zeta} = e^{2i\zeta}\left[\left(\bar{z} - \frac{R^2}{z}\right)\Phi'(z) - \frac{iP\kappa}{2\pi(1+\kappa)}\left(\frac{1}{z} - \frac{R^2}{z^3}\right) + \frac{b}{z^2}\right] \tag{7}$$

Substituting (4) in (7) we obtain expression for principal tangential stress along axis of force action ($h \geq R$):

$$\begin{aligned}\tau_{\max}(h) = \left(h - \frac{R^2}{h}\right)\Bigg\{ & -\frac{P}{2}\left[\frac{\gamma_2}{\pi} + \frac{\gamma_1}{2\left(\alpha_0 + \cos(\alpha_0)\sin(\alpha_0)\right)}\right] \times \\ & \times \left[\left(\frac{1}{h^2} + \frac{1}{R^2}\right) - \frac{1}{\sqrt{h^2 + R^2 - 2Rh\cos(\alpha_0)}} \times \right. \\ & \left. \times \left(\frac{-R}{h^2} - \frac{\cos(\alpha_0)}{h} + \frac{\cos(\alpha_0)}{R} + \frac{h}{R^2}\right)\right] + \\ & + \frac{1}{2}\left(\frac{b}{R^2} + \gamma_3(\varepsilon - \Delta)\right)\left(\frac{1}{h} - \frac{1}{\sqrt{h^2 + R^2 - 2Rh\cos(\alpha_0)}}\left(1 - \frac{R}{h}\right)\right)\Bigg\} + \\ & + \frac{\kappa P}{2\pi(1+\kappa)}\left(\frac{1}{h} + \frac{R^2}{h^3}\right) + \frac{b}{h^2}\end{aligned}$$

It's impotent to point out that the tangential stress $\tau_{r\zeta}$ is absent for all point of y-axis. Therefore σ_r, σ_ζ are normal principal stresses in this case. It's necessary to note that the value of principal tangent stress $\tau_{\max}$ depends on α_0 and covering.

CONCLUSIONS

The contact problem for smooth rigid disk and isotropy plate with coating on the cylindrical hole was considered with help of method of complex potentials. The special explicit approximate solution, of integral equation is presented in the paper. The analytical expression for principal tangential stress along axis of force action is received on this base.

The investigations considerably facilitate application of the theoretical results in practice. It can be expanded to the case of two elastic cylinders.

REFERENCES

1. Alekseev N., *Metal coverings of plain bearings*, [In Russian], Moskow, 1973.
2. Demkin N., Ruzov B., *Quality of a surface and contact of details of machines*, [in Russian], Moskow, 1981.
3. Vineshtane V., Troyahovskaya G., *Dry greasings and self-greased materials*, [In Russian], Leningrad, 1968.
4. Chigarev A., Kravchuk A., *Contact problem for rigid disc and isotropy plate with cylindrical hole,* Mechanika, 4 (11), 17-19, 1997.

ON RESPONSE OF FUNCTIONALLY GRADED CYLINDRICAL PANELS TO THERMAL LOADING

E. Feldman and I. Belostotsky

Dept. of Solid Mechanics, Materials and Structures, Tel-Aviv University
Ramat-Aviv 69978, Israel

INTRODUCTION

The traditional approach to fabricating composite materials implies that the reinforcement phase is distributed either uniformly or randomly, such that the resulting properties of a composite do not vary spatially at the macroscopic level. Recently, a new concept based on tailoring the microstructure of a composite material to specific applications has taken root. This idea has given rise to the term "functionally graded materials", or FGMs. FGMs are a relatively new generation of composite materials in which the microstructural details are varied spatially. The result is a microstructure that produces gradient of mechanical properties at a continuum level. Such an approach offers a number of potential benefits over the more traditional methods; it brings the entire structural design process to the material level, thereby increasing the number of possible material configurations for specific design applications.

In order to develop a structural element made of FGM, it is necessary to model such an element and investigate its required properties. There are presently two approaches for the modeling of functionally graded materials. The first is based on a homogenization of the FGM in which the microstructural effects are decoupled from the global response by calculating pointwise effective thermoelastic properties without regard as to whether the actual microstructure admits the presence of a representative volume element (RVE). In the second approach the coupling between the microstructural and the global macrostructural effects is accounted for.

The concept of stiffness tailoring for improved buckling resistance of functionally graded plates under compressive loading was investigated in [1-3]. The present study addresses the idea of tailoring the microstructure of a composite material for the purpose of improving the thermal non-bifurcational response of a cylindrical panel. It is supposed that the gradients of material properties throughout the structure are produced by changing the local reinforcement volume fraction v_f.

GOVERNING EQUATIONS

Consider an elastic functionally graded rectangular cylindrical panel of a length a in the longitudinal x-direction, width b in the circumferential y-direction, thickness h in the normal z-direction, and radius of curvature R. The structure is reinforced by either long fibers or discontinuous ones, with the reinforcements volume fraction v_f being a function of the spatial coordinates x, y, z. It is supposed that the reinforcements are oriented either in x- or in y-direction.

It is assumed that thickness temperature gradient is negligible, and a quasi-static temperature field T the panel is exposed to is a function of the in-plane coordinates x, y and the time t. The geometrically non-linear response of the non-homogeneous panel to thermal loading may be described (in the framework of the classical shells theory) in terms of the stress function Φ and the out-of-plane displacement w, in much the same way as it is done in [4]:

$$\begin{aligned}&\left(D_{11}^{*} w_{,\xi\xi} + \lambda^{2} D_{12}^{*} w_{,\eta\eta} + \lambda^{2} B_{11}^{*} \Phi_{,\eta\eta} + B_{21}^{*} \Phi_{,\xi\xi}\right)_{,\xi\xi} \\ &\quad + \lambda^{2}\left(D_{12}^{*} w_{,\xi\xi} + \lambda^{2} D_{22}^{*} w_{,\eta\eta} + \lambda^{2} B_{12}^{*} \Phi_{,\eta\eta} + B_{22}^{*} \Phi_{,\xi\xi}\right)_{,\eta\eta} + a^{2}\left(G_{\xi\xi,\xi\xi}^{T} + 2\lambda G_{\xi\eta,\xi\eta}^{T}\right. \\ &\quad \left. + \lambda^{2} G_{\eta\eta,\eta\eta}^{T}\right) - \frac{a^{2}}{R}\Phi_{,\xi\xi} + \lambda^{2}\left(-\Phi_{,\eta\eta} w_{,\xi\xi} + 2\Phi_{,\xi\eta} w_{,\xi\eta} - \Phi_{,\xi\xi} w_{,\eta\eta}\right) = 0 \qquad (1)\end{aligned}$$

$$\begin{aligned}&\lambda^{2}\left(\lambda^{2} A_{11}^{*} \Phi_{,\eta\eta} + A_{12}^{*} \Phi_{,\xi\xi} - B_{11}^{*} w_{,\xi\xi} - \lambda^{2} B_{12}^{*} w_{,\eta\eta}\right)_{,\eta\eta} \\ &\quad + \left(\lambda^{2} A_{12}^{*} \Phi_{,\eta\eta} + A_{22}^{*} \Phi_{,\xi\xi} - B_{21}^{*} w_{,\xi\xi} - \lambda^{2} B_{22}^{*} w_{,\eta\eta}\right)_{,\xi\xi} + \lambda^{2}\left(A_{66}^{*} \Phi_{,\xi\eta} - 2B_{66}^{*} w_{,\xi\eta}\right)_{,\xi\eta} \\ &\quad = -\frac{a^{2}}{R} w_{,\xi\xi} + \lambda^{2}\left(w_{,\xi\eta}^{2} - w_{,\xi\xi} w_{,\eta\eta}\right) + a^{2}\left(\lambda \gamma_{\xi\eta,\xi\eta}^{T} - \lambda^{2} \gamma_{\xi\xi,\eta\eta}^{T} - \gamma_{\eta\eta,\xi\xi}^{T}\right) \qquad (2)\end{aligned}$$

Here the nondimensional coordinates $\xi = x/a, \eta = y/b, \zeta = z/h$, and the panel aspect ratio $\lambda = a/b$ are introduced. Due to the effects of temperature-dependent material properties, non-uniform distribution of the reinforcement phase, and, possibly, non-uniform heating, the stiffness matrices $\boldsymbol{A}^{*}, \boldsymbol{B}^{*}$ and $\boldsymbol{D}^{*}$ are functions of the spatial coordinates and the time t. The expressions for the thermal functions $G_{\alpha\beta}^{T}, \gamma_{\alpha\beta}^{T}, (\alpha, \beta = \xi, \eta)$ may be found in [5].

Further, simply-supported and clamped panels will be considered. To obtain a solution to the problem at hand, a method based on a combination of micromechanical and structural approaches is employed. The method, which is described in more detail in [4, 5], allows to establish the effective constitutive behavior of a non-homogeneous composite panel and provides the response of the structure to non-uniform temperature loading.

The micromechanical analysis performed relies on the RVE-based version of the method of cells [6]. It enables one to obtain the effective constitutive law at every point of a functionally graded composite structure in the form

$$\boldsymbol{\sigma}(x, y, z, t) = \boldsymbol{C}(x, y, z, t)\boldsymbol{\varepsilon}(x, y, z, t) - \boldsymbol{U}(x, y, z, t)\Delta T(x, y, t)$$

where $\boldsymbol{\sigma}$ and $\boldsymbol{\varepsilon}$ are stress and strain tensors, $\boldsymbol{C}$ and $\boldsymbol{U}$ are effective stiffness and effective thermal stress tensors, respectively, and ΔT denotes the deviation of the temperature from a reference value T_{ref}. As a result of a structural analysis, the behavior of a functionally graded panel, subjected to a given temperature field $T(x, y, t)$, is obtained for a given reinforcement volume fraction $v_f(x, y, z)$. In particular, the transverse deflection $w(x, y, t)$ may be calculated.

OPTIMAL REINFORCEMENT DISTRIBUTIONS

In the present study, the response of a FGM panel to a given temperature field $T =$

$T(\xi,\eta,t)$ is characterized by the maximum value of the out-of-plane displacement W_{max} that is achieved during the thermal loading:

$$W_{max} = \max|w(\xi,\eta,t)|, \quad \xi \in [0,1], \eta \in [0,1], t \in [t_{min}, t_{max}] \tag{3}$$

For greater resistance of a FGM panel to temperature loading, the functional $W_{max}(v_f)$ is minimized. This is performed as follows. Function v_f is expended into the Legendre polynomials

$$v_f(\xi,\eta,\zeta) = \sum_{i=0}^{I}\sum_{j=0}^{J}\sum_{k=0}^{K} V_{ijk}P_i(\xi)P_j(\eta)P_k(\zeta) \tag{4}$$

with V_{ijk} being unknown coefficients to be determined. This allows to introduce an objective function $W_{max} = W_{max}(V_{ijk})$.

It is required that the total amount of reinforcements (namely the panel weight) remains a given constant

$$\int_{\xi=0}^{1}\int_{\eta=0}^{1}\int_{\zeta=-1/2}^{1/2} v_f d\xi d\eta d\zeta = v_f^* = const \tag{5}$$

Two additional constraints stem from the following requirements: $v_f \geq 0, v_f \leq 1$. The objective function $W_{max}(V_{ijk})$ is minimized, with V_{ijk} being a set of design variables subject to the above constraints.

RESULTS AND DISCUSSION

To illustrate the proposed approach, consider SiC/Al unidirectional panels subjected to a non-uniform temperature field $T = T(x,t)$. It is assumed that the reinforcements are oriented in the x-direction and that v_f^*=0.3. Two types of non-uniform temperature distributions are considered. A symmetric (with respect to the centerline $\xi = 1/2$) heating is taken to be of the form

$$T(\xi,t) = T_{ref} + T_0(t)\sin^n \pi\xi \tag{6}$$

while its asymmetric counterpart is

$$T(\xi,t) = T_{ref} + T_0(t)\sin^n \pi\xi/2 \tag{7}$$

The value n=0 in (6),(7) corresponds to a uniform temperature change; as n increases, the heating becomes more and more localized. Note, that, for a given n, both temperature distributions have the same average value $T_{av}(t)$.

For the purpose of estimation the effect of a functionally graded panel, introduce a ratio $W_{max}^{opt}/W_{max}^{hom}$, where W_{max}^{opt} and W_{max}^{hom} denote the maximum deflections for a functionally graded panel with optimal distribution $v_f^{opt}(\xi,\eta,\zeta)$ and for its homogeneous counterpart. Furthermore, two examples of tailoring the distribution of reinforcement phase are considered.

Short-fiber panel with reinforcements non-uniformly distributed in the x-direction. Consider an aluminum matrix panel reinforced by SiC particles, whose distribution is non-uniform only in the x-direction, such that $v_f = v_f(x)$.

In Fig. 1, optimal distributions v_f^{opt} of a SiC phase along the x-axis are shown for simply-supported panels subjected to symmetric (6) and asymmetric (7) heating. Corresponding response curves, both for the functionally graded panels with optimal distribution $v_f^{opt}(x)$ and for its uniformly reinforced counterparts with $v_f = v_f^*$, are presented in Fig. 2.

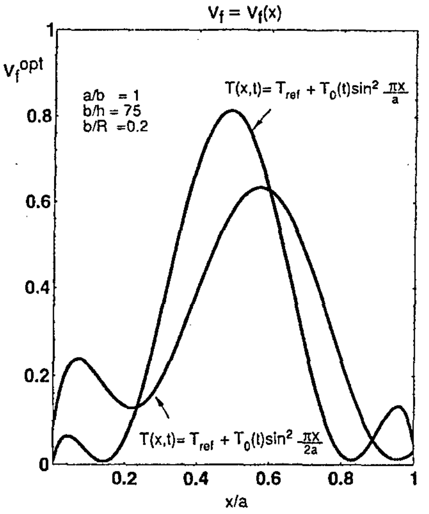

Fig.1. Optimal reinforcement volume fraction distribution along the x-axis for particle-reinforced functionally graded panel, for different types of thermal loading.

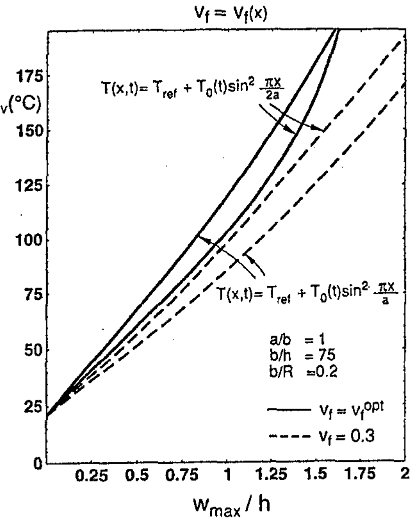

Fig.2. Response curves for functionally graded and uniformly reinforced panels, for different types of thermal loading.

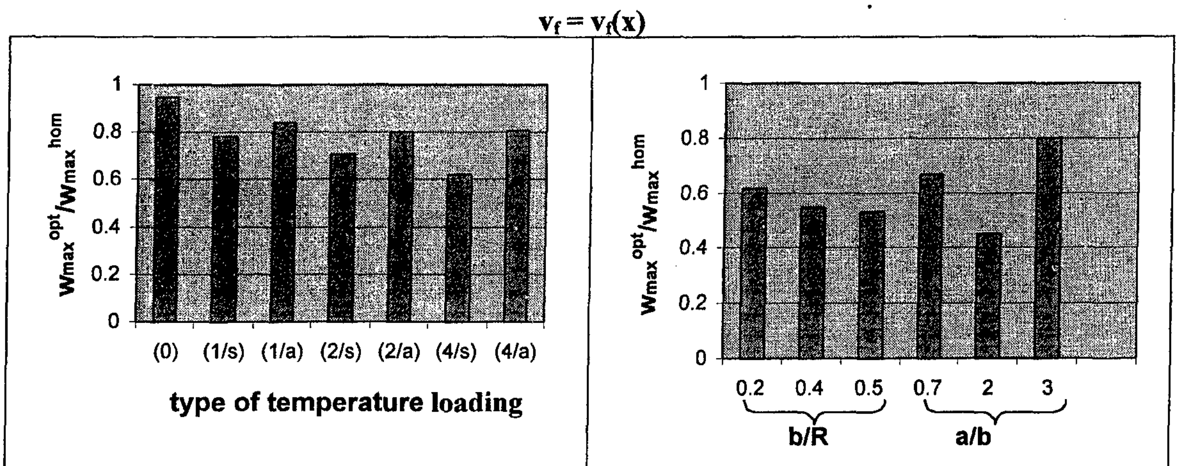

(a) a/b=1; b/h=75; b/R=0.2

(b) b/h=75; $T(x,t) = T_{ref} + T_0(t)\sin^4 \pi x/a$

Fig.3. Maximum deflection improvements for particle-reinforced functionally graded panels.

A beneficial effect of a non-homogeneous reinforcement for different types of thermal loading is illustrated in Fig. 3a. To present different types of temperature change, the following notation is used: the first number stands for the value of n in (6),(7); the second letter indicates whether the distribution of T is symmetric or asymmetric with respect to ξ=1/2. Thus, "2/a" stands for $T(\xi, t) = T_{ref} + T_0(t)\sin^2(\pi\xi/2)$. In Fig. 3b, the histograms $W_{max}^{opt}/W_{max}^{hom}$ are presented for non-uniformly heated panel for several values of the panel curvature b/R (for a/b=1) and aspect ratio a/b (for b/R=0.2). As can be seen from the figure, the maximum deflection improvements that may be attained are quite small for the case of uniform heating; the values $W^{opt}_{max}/W^{hom}_{max}$ go down as thermal loading becomes more localized.

Long-fiber panel with fibers non-uniformly distributed through the thickness. Consider an long-fiber SiC/Al panel such that the fibers are non-uniformly distributed in the z-direction, *i.e.* $v_f = v_f(z)$.

For the case of uniform heating, the effects of panel's curvature and width-to-thickness ratio on the optimal volume fraction distribution is illustrated in Fig. 4. Maximum deflection improvements are presented in Fig. 5; it may be seen that the beneficial effect of grading the material's microstructure is significant.

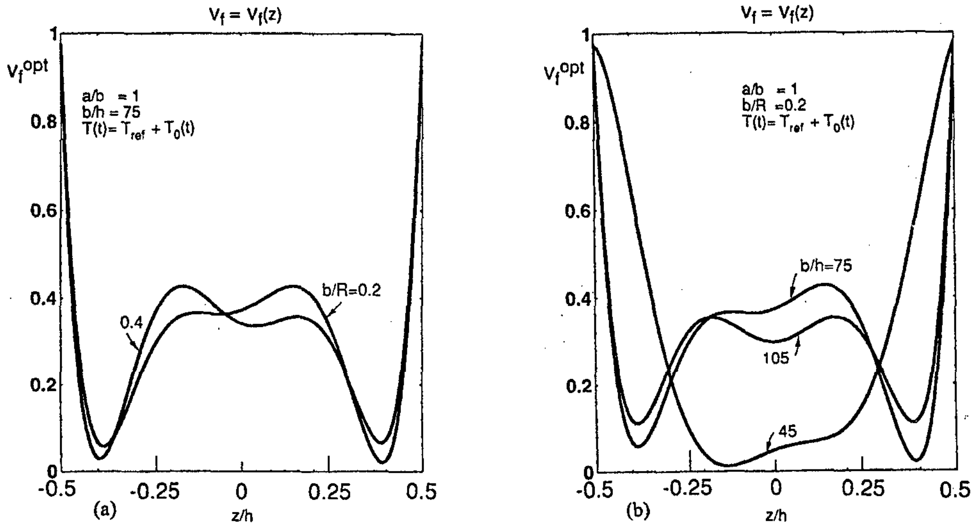

Fig.4. Optimal reinforcement volume fraction distribution through the thickness for long-fiber functionally graded panels (in the case of uniform heating); (a) the effect of panel's curvature, (b) the effect of width-to-thickness ratio.

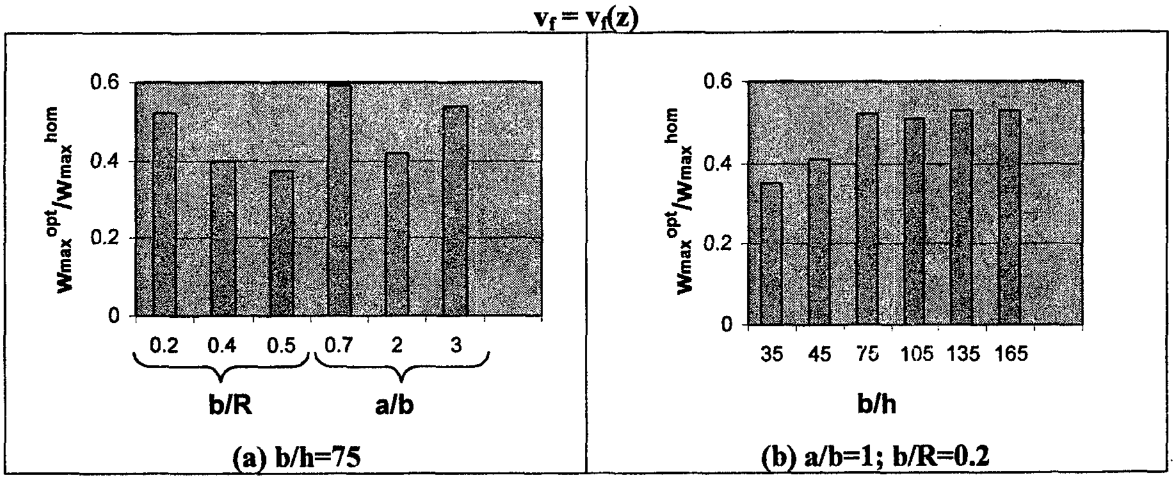

Fig.5. Maximum deflection improvements for uniformly heated functionally graded panels; (a) the effects of panel's curvature and aspect ratio, (b) the effect of width-to-thickness ratio.

The beneficial effect of the optimal reinforcement $v_f^{opt}(z)$ in the case of non-uniform heating is illustrated in Fig. 6 (light-colored bars) for several types of thermal loading (Fig. 6a) and for different values of the panel curvature and width-to-thickness ratio (Fig. 6b). To attain an additional insight into the sensitivity of the results obtained to the specific type of temperature distribution $T(x,t)$, the following simplified analysis was performed. For a given panel, an optimal volume fraction distribution $v_f^{opt(u)}(\zeta)$ for the case of uniform thermal loading $T = T(t)$ was calculated. Then the function $v_f = v_f^{opt(u)}(\zeta)$ was used to solve (without further optimization) the system of governing equations and obtain the response of the panel to the actual non-uniform temperature field. The corresponding results are presented in Fig. 6 by dark-colored bars. As is apparent from the histograms, the proposed simplified approach may by useful, since it yields actually the same maximum deflection improvements (as compared to the values $W_{max}^{opt}/W_{max}^{hom}$).

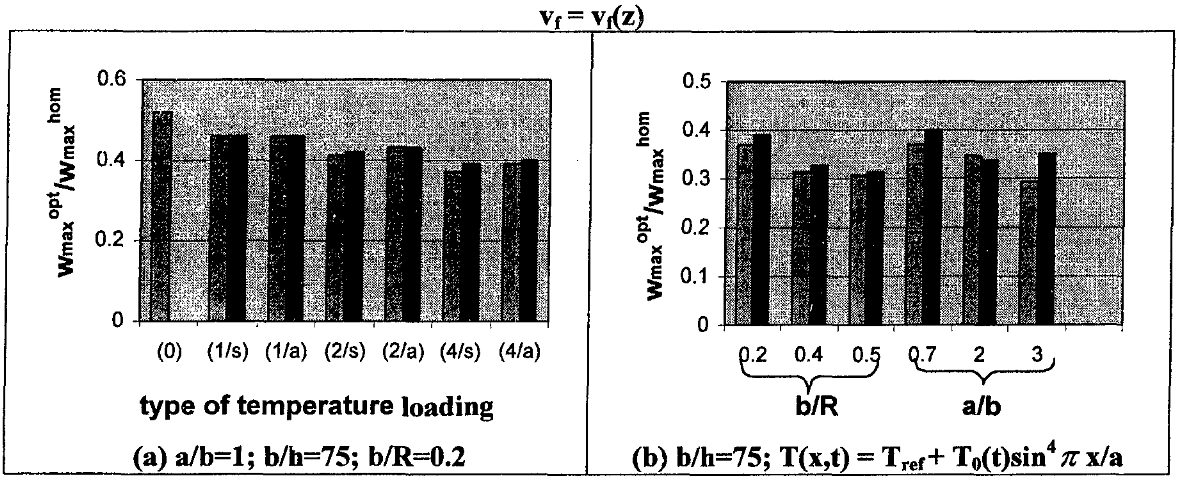

(a) a/b=1; b/h=75; b/R=0.2

(b) b/h=75; $T(x,t) = T_{ref} + T_0(t)\sin^4 \pi x/a$

Fig.6. Maximum deflection improvements for non-uniformly heated functionally graded panels and comparison with the results obtained using a simplified approach (dark-colored bars). (a) the effect of different types of temperature distribution, (b) the effects of panel's curvature and aspect ratio.

REFERENCES

1. Biggers, S.B., Browder, T.M. "Buckling-load interaction in tailored composite plates". *Composites Engineering* **4**, pp. 745-761 (1994).

2. Birman, V. "Stability of functionally graded hybrid composite plates". *Composites Engineering* **5**, pp. 913-921 (1995).

3. Feldman, E., Aboudi, J, "Buckling analysis of functionally graded plates subjected to uniaxial loading". *Composite Structures* **38**, pp. 29-36 (1997).

4. Feldman, E., Belostotsky, I. "On the response of MMC laminated plates to non-uniform temperature loading: the effect of temperature-dependent material properties". *Composite Structures* **38**, pp. 83-89 (1997).

5. Feldman, E. "The effect of temperature-dependent material properties on elasto-viscoplastic buckling behaviour of non-uniformly heated MMC plates". *Composite Structures* **35**, pp. 65-74 (1996).

6. Aboudi, J. *"Mechanics of Composite Materials – A Unified Micromechanical Approach"*. Elsevier, Amsterdam, 1991.

SEMI-ANALYTICAL STUDY OF COMPOSITE CONTAINERS UNDER INTERNAL AND EXTERNAL PRESSURE

N. LE BRIS, H. DUMONTET and F. LENE

Laboratoire de Modélisation et Mécanique des Structures (LM2S),
U.R.A. C.N.R.S.1776, Université Paris VI - E.N.S.A.M. - E.N.S. Cachan,
Tour 66 5ème étage, 4 place Jussieu 75252 Paris cedex 05, France.

INTRODUCTION

A research program, developed by IFREMER (Institut Français de Recherche et d'Exploitation de la Mer), is concerning with the study of cylindrical containers used to immerse electronic equipment. Recently, these containers are realized in filament winding of E-glass fibers and epoxy resin, protected by a waterproof gel. Standard qualifications being established for metallic containers, excessive safety factors are used for the structural design of these composite containers. To reduce long and expensive experiments, we propose a simplified semi-analytical model to determine the distribution of displacements, stresses and strains in the thickness and along the length of the structure.
Most of publications on composite cylindrical containers are based on classical shell theory [2]. Three-dimensional analytical solution [5] have been developed far from the plugs, but in the region near the ends it is insuffisant to take account the curvation of the structure.
In this paper, the semi-analytical model presented gives a refined three-dimensional solution inside cylindrical containers under general mechanical loading of internal and external uniform pressure taking into account plug effects. This solution is approached by Fourier-series [1], [3], [4], [6]. It gives more accurate results than classical shell theory approximations and requires less computational time and effort than a numerical calculation. Also, confrontation with experimental results shows a good agreement.

BASIC EQUATIONS

The behavior of an unidirectional fiber-reinforced ply is experimentally characterized and the equivalent behavior of the composite structure is obtained by a homogenization process. So, we consider an homogeneous orthotropic elastic container represented by a closed tubular domain where plug actions are modelized by adequate boundary conditions. Because of symmetric properties of the geometry and the mechanical load, we solve an axisymmetric problem on the half of the structure (fig.1). Stresses and strains are varying in both axial and radial directions.

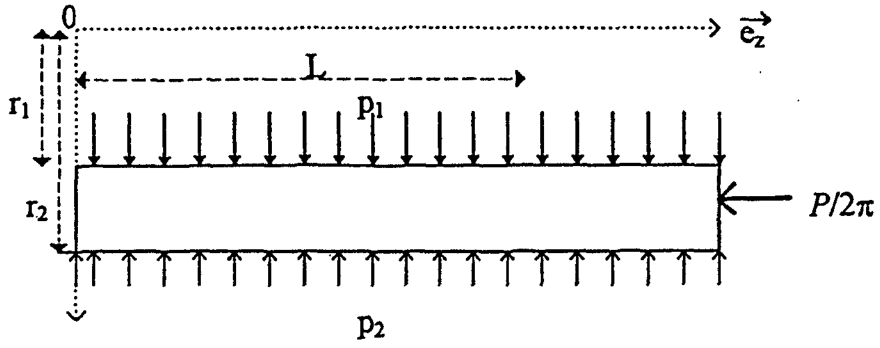

Figure 1 : Cylinder geometry and loading

The generalized Hooke's law for a orthotropic homogeneous material is given by :

$$\begin{pmatrix} \sigma_{rr} \\ \sigma_{\theta\theta} \\ \sigma_{zz} \\ \sigma_{rz} \end{pmatrix} = \begin{pmatrix} a_{11} & a_{12} & a_{13} & 0 \\ a_{21} & a_{22} & a_{23} & 0 \\ a_{31} & a_{32} & a_{33} & 0 \\ 0 & 0 & 0 & a_{44} \end{pmatrix} \begin{pmatrix} \varepsilon_{rr} \\ \varepsilon_{\theta\theta} \\ \varepsilon_{zz} \\ 2\varepsilon_{rz} \end{pmatrix} \tag{1}$$

in which the $a_{ij} = a_{ji}$ $(i,j) = (1, ..., 4)$ are the stiffness constants of the material. In the absence of body forces, the elastic response of the axisymmetic cylinder must satisfy the equilibrium equations :

$$\frac{\partial \sigma_{rr}}{\partial r} + \frac{\partial \sigma_{rz}}{\partial z} + \frac{1}{r}(\sigma_{rr} - \sigma_{\theta\theta}) = 0; \qquad \frac{\partial \sigma_{rz}}{\partial r} + \frac{\partial \sigma_{zz}}{\partial z} + \frac{\sigma_{rz}}{r} = 0 \tag{2}$$

where σ is the Cauchy tensor and r, θ and z are the radial, circumferential and axial coordinates.

The strain-displacement relations are given by :

$$\varepsilon_{rr} = \frac{\partial u}{\partial r}; \quad \varepsilon_{\theta\theta} = \frac{u}{r}; \quad \varepsilon_{zz} = \frac{\partial w}{\partial z} \quad 2\varepsilon_{rz} = \frac{\partial u}{\partial z} + \frac{\partial w}{\partial r} \tag{3}$$

where u and w are the r, z displacement components respectively, ε being the linear strain tensor.

BOUNDARY CONDITIONS

The loading on the outer surface ($r = r_2$) is described by the boundary conditions $\sigma.\vec{n} = -p_2\,\vec{n}$ and on the inner surface ($r = r_1$) by $\sigma.\vec{n} = -p_1\,\vec{n}$, where $\vec{n} = \vec{e}_r$. The plug can be supposed rigid and in a perfect bonding with the tubular part of the container. Then, the plug actions are modelized by an axial global force along the z-axis :

$$\int_{r1}^{r2} \sigma_{zz}(r, z = L)\, r\, dr = \frac{P}{2\pi} = \frac{(p_1 r_1^2 - p_2 r_2^2)}{2} \tag{4}$$

and by conditions on the displacement weakly imposed on the terminal section :

$$\int_{r1}^{r2} u(r, z = L)\, r dr = 0 \qquad \int_{r1}^{r2} w(r, z = L)\, r dr = \text{Cste unknown} \tag{5}$$

Then, we add symmetric conditions on $z=0$: $\sigma_{rz}(r,z=0)=0$, $w(r,z=0)=0$.

CONSTRUCTION OF THE SOLUTION

First, we propose a solution of this problem where P is equal to zero in (4) ; the container being only loaded on the lateral surfaces by the internal and external pressure (fig.2).

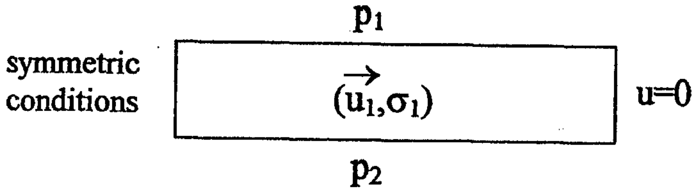

Figure 2 : Problem P_1

For solving this first problem, denoted P_1, we assume that the displacement is in the form of Fourier series :

$$u_r(r,z)=\sum_{n=1,3,5,..} u_n(r)\cos\left(\frac{n\pi z}{2L}\right);\quad w(r,z)=\sum_{n=1,3,5,..} w_n(r)\sin\left(\frac{n\pi z}{2L}\right). \qquad (6)$$

Under this form, the boundary conditions at $z=0$ and the boundary conditions on the displacement at $z=L$ are satisfied. The serie coefficients $u_n(r), w_n(r)$ are determined by the equilibrium equations and the loading boundary conditions. Combining equations (1)-(3) and (6), equilibrium equations are satisfied if the fonctions $u_n(r)$ and $w_n(r)$ are solutions, for all n=1,3,5..., of the following system :

$$\left[\left(\frac{n\pi}{2L}\right)^2[A]+\frac{n\pi}{2L}\left(\frac{1}{r}[B]+\frac{d}{dr}[D]\right)+\frac{1}{r^2}[C]+\frac{1}{r}\frac{d}{dr}[E]+\frac{d^2}{dr^2}[E]\right]\begin{pmatrix} w_n(r)\\ u_n(r)\end{pmatrix}=0 \qquad (7)$$

where the matrix $[A]$, $[B]$, $[C]$, $[D]$ and $[E]$ are given by :

$$[A]=\begin{pmatrix} -a_{33} & 0\\ 0 & -a_{44}\end{pmatrix}\qquad [C]=\begin{pmatrix} 0 & 0\\ 0 & -a_{22}\end{pmatrix}\qquad [E]=\begin{pmatrix} a_{44} & 0\\ 0 & a_{11}\end{pmatrix}$$

$$[B]=\begin{pmatrix} 0 & -(a_{44}+a_{23})\\ -a_{23}+a_{13} & 0\end{pmatrix}\qquad [D]=\begin{pmatrix} 0 & -(a_{13}+a_{44})\\ a_{13}+a_{44} & 0\end{pmatrix}$$

This system is a four-order ordinary differential system with r dependent coefficients and is solved by a simplified approach searched in terms of the following expansion :

$$u_n(r)=\sum_{j=1}^{4} C_j\, u_{nj}(r);\quad w(r,z)=\sum_{j=1}^{4} C_j\, w_{nj}(r)$$

where C_j (j=1,...,4) are unknown constants and where the functions u_{nj} et w_{nj} are written :

$$\begin{pmatrix} w_{nj}(r)\\ u_{nj}(r)\end{pmatrix}=\exp\left(\lambda^j\left(\frac{r}{R}-1\right)\right)\begin{pmatrix} d^w_{nj}\\ d^u_{nj}\end{pmatrix}=exp\left(\lambda^j\left(\frac{r}{R}-1\right)\right)\mathrm{d}_{nj}.$$

R is the radius of the midsurface : $R = (r_1 + r_2)/2$. Vectors d_{nj} and scalar λ^j are solutions of the generalized eigenvalue problem :

$$\{\, [H_1] + \lambda\, [H_2] + \lambda^2\, [H_3] \,\}\, \mathrm{d}_{nj} = 0 \tag{8}$$

with :

$$[H_1] = \left(\frac{Rn\pi}{2L}\right)^2 [A] + \frac{Rn\pi}{2L}[B] + [C]; \quad [H_2] = \frac{Rn\pi}{2L}[D] + [E]; \quad [H_3] = [E].$$

Equation (8) is solved with a symbolic code. Constants C_j (j=1,...,4) are determined from loading boundary conditions. Then, the uniform pressure p is developed in the form of cosine series Fourier :

$$p = p \sum_{n=1,3,5,..} \frac{4}{n\pi} \sin\left(\frac{n\pi}{2}\right) \cos\left(\frac{n\pi z}{2L}\right),$$

and C_j (j=1,...4) are solution of the system :

$$\begin{pmatrix} a_1 & \dots & a_4 \\ b_1 & \dots & b_4 \\ c_1 & \dots & c_4 \\ d_1 & \dots & d_4 \end{pmatrix} \begin{pmatrix} C_1 \\ C_2 \\ C_3 \\ C_4 \end{pmatrix} = \frac{4}{n\pi} \begin{pmatrix} -p_1 \sin(n\pi/2) \\ -p_2 \sin(n\pi/2) \\ 0 \\ 0 \end{pmatrix}$$

$$\begin{aligned} \text{with : } \quad a_j &= \left[a_{13} d^w_{nj} \frac{n\pi}{2L} + \frac{a_{12}}{r_1} d^u_{nj} + a_{11} \frac{\lambda_j}{R} d^u_{nj} \right] \exp\left(\lambda_j \left(\frac{r_1}{R} - 1\right)\right) \\ b_j &= \left[a_{13} d^w_{nj} \frac{n\pi}{2L} + \frac{a_{12}}{r_2} d^u_{nj} + a_{11} \frac{\lambda_j}{R} d^u_{nj} \right] \exp\left(\lambda_j \left(\frac{r_2}{R} - 1\right)\right) \\ c_j &= \left[a_{55} \left(-\frac{n\pi}{2L} d^u_{nj} + \frac{\lambda_j}{R} d^w_{nj} \right) \right] \exp\left(\lambda_j \left(\frac{r_1}{R} - 1\right)\right) \\ d_j &= \left[a_{55} \left(-\frac{n\pi}{2L} d^u_{nj} + \frac{\lambda_j}{R} d^w_{nj} \right) \right] \exp\left(\lambda_j \left(\frac{r_2}{R} - 1\right)\right) \qquad j = 1,\, 2,\, 3,\, 4. \end{aligned}$$

To these problem we superpose another one where the lateral pressures are taken equal to zero and the global force in (4) is now equal to $P/2\pi$. This second problem, denoted P_2, is obtained by a linear combination (fig. 3) of the solution of the problem P_1 and the classical solution without plug effects where stress are supposed fonction of r only, [5].

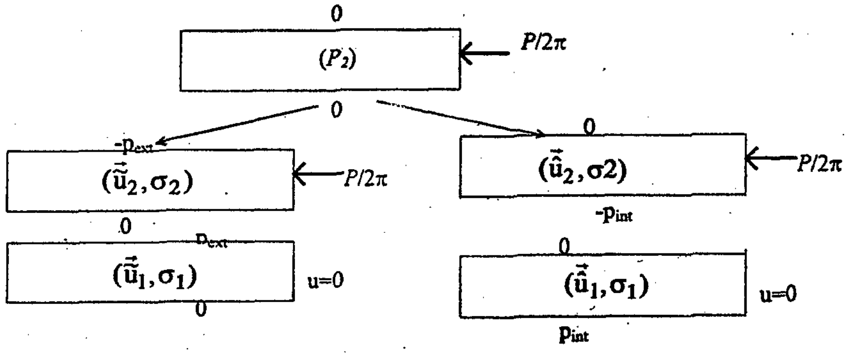

Figure 3 : Decomposition of the problem P_2

Notice $(\vec{\tilde{u}},\tilde{\sigma}) = (\vec{\tilde{u}}_1,\tilde{\sigma}_1) + (\vec{\tilde{u}}_2,\tilde{\sigma}_2)$ and $(\vec{\hat{u}},\hat{\sigma}) = (\vec{\hat{u}}_1,\hat{\sigma}_1) + (\vec{\hat{u}}_2,\hat{\sigma}_2)$ the solutions of the elementary problems described at the figure 3.
Finally, the global solution of the initial problem is given by :

$$(\vec{u},\sigma) = (\vec{u}_1,\sigma_1) + D_1\,(\vec{\hat{u}},\hat{\sigma}) + D_2\,(\vec{\tilde{u}},\tilde{\sigma})$$

where D_1 et D_2 are given by :

$$D_1 \int_{r_1}^{r_2} \hat{u}(r,z=L)\,r dr + D_2 \int_{r_1}^{r_2} \tilde{u}(r,z=L)\,r dr = 0; \qquad D_1 + D_2 = 1.$$

The equilibrium equations are satisfied only on the middle radius, so this solution is more accurate for thin container. For very thick containers, an accurate solution is obtained by the same method by considering a several ply laminate cylinder where continuity conditions are used at each interface.

RESULTS AND COMPARAISONS

This semi-analytical approached resolution has been compared with a numerical solution computed on the finite elements code Modulef, included the mesh of plugs. The composite container is a ±55° filament winding submitted to the pressures $p_1 = 1\,\mathrm{Atm}$ and $p_2 = 300\,\mathrm{Bars}$. The geometric and elastic constants of the homogeneous material in the (r,θ,z) directions are :

$$r_1 = 0.0875\,\mathrm{m}; \quad r_2 = 0.1065\,\mathrm{m}; \quad L = 0.175\,\mathrm{m}$$
$$E_1 = 17\,\mathrm{GPa}; \quad E_2 = 22.7\,\mathrm{GPa}; \quad E_3 = 14.8\,\mathrm{GPa};$$
$$G_{32} = 12.6\,\mathrm{GPa}; \quad G_{31} = 5.69\,\mathrm{GPa}; \quad G_{31} = 5.59\,\mathrm{GPa}$$
$$\nu_{32} = 0.39; \quad \nu_{31} = 0.26; \quad \nu_{21} = 0.15$$

Figures 4 and 5 present the evolution of the $\varepsilon_{\theta\theta}$ and ε_{zz} strain components along the z-axis on $r = R$.

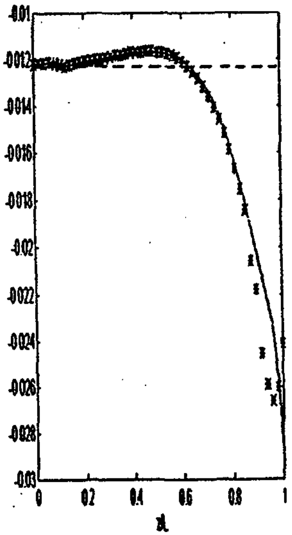

Figure 4 : $\varepsilon_{\theta\theta}(R,z)$

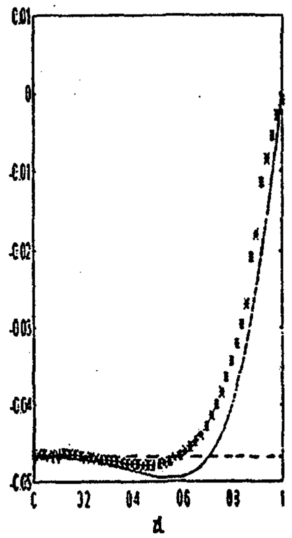

Figure 5 :$\varepsilon_{zz}(R,z)$

$*$: numerical solution; – : approched model ; – – : solution whitout plug effects [5]

Comparisons with experimental measurements (in μdef) are given in table 1 for a oceanographic container where geometric constants are r_1=0.05 m, r_2=0.0685 m, L=0.3 m.

	$\varepsilon_{\theta\theta}^{\text{anal.}}$	$\varepsilon_{\theta\theta}^{\text{exp.}}$	$\varepsilon_{zz}^{\text{anal.}}$	$\varepsilon_{zz}^{\text{exp.}}$	$\varepsilon_{\theta\theta}^{\text{clas.}}$	$\varepsilon_{zz}^{\text{clas.}}$
$z/L = 0.9$	-2165	-2290	-1812	-1565	-2580	-1061
$z/L = 0.66$	-2901	-3434	-1017	-1087	-2580	-1061
$z/L = 0$	-2580	-2536	-1061	-1260	-2580	-1061

Far from the ends, the refined solution joins, of course, the solution in which plug effects are not taking into account. Near the plug, the refined analytical approach gives a good approximation of the the strain compared to the classical model without plug effects. It is interesting to notice that from about 25 terms in the series, this semi-analytical resolution gives good results and beyond 1200 terms, there is no any improvements in the solution and time resolution is about 3 minutes.

ACKNOWLEDGMENT

This work has been received supported by IFREMER. We would like to thank them for their collaboration.

REFERENCES

[1] Chandrashekhara, K., Gopalakrishnan, P. "Elasticity Solution for a Multilayered Transversely Isotropic Circular Cylindrical Shell." *J. appl. Mech.*, 49, pp. 108-114, (1982).
[2] Gay, D. "Matériaux composites." *Hermès* (1991).
[3] Kardomateas, G.A. "Bifurcation of equilibrium in thick orthotropic cylindrical sells under axial compression." *J. appl. Mech.* 62, pp. 43-52, (1995).
[4] Kollar L.P. "Three-dimensional analysis of composite cylinders under axially varying hygrothermal and mechanical loads.", *Comp. and Struct.*, 50, No. 4, pp. 525-540, (1994).
[5] Leikhnitski, S.G. "Theory of elasticity of an anisotropic elastic body." *Holden-Day, Inc.*, San Francisco, (1963).
[6] Misovec, A.P., Kempner, J. "Approximate elasticity solution for orthotropic cylinder under hydrostatic pressure and band loads.", *J. of Applied Mech.*, pp. 101-108, (1970).

PERFORMANCE EVALUATION OF COMPOSITE TUBE REINFORCED CONCRETE COLUMNS

Zongjin Li[1], Ricky Lee[2], Ming Chen [3], and Pin Tong [2]

[1] Department of Civil and Structural Engineering, The Hong Kong University of Science and Technology, Clear Water Bay, Kowloon, Hong Kong, China
[2] Department of Mechanical Engineering, The Hong Kong University of Science and Technology, Hong Kong, China
[3] Department of Civil Engineering, Zhejiang University, China

ABSTRACT

Rapid deteriorations of structural concrete caused by corrosion of reinforcing steel is becoming a serious problem faced by construction industries world wide. The extent of the problem caused by corrosion is so serious that concrete durability has been recently described as a "multimillion dollar opportunity". One way to eliminate corrosion problem is to use composite (or fiber reinforced plastics) as reinforcing materials. As a pioneer work along this line, this paper presents the experimental results of concrete columns reinforced by composite members.

The column size was 150 mm in inner-diameter and 450 mm in length. Three types of columns were prepared using different composite materials. They are: filament-wound fiber glass composite tube, with a wall thickness of 14 mm, reinforced column, carbon fiber strand. reinforced column, and glass fiber strand. reinforced column. The fiber strand.s were pre-wound with different spacing on a PVC tube (8 mm wall-thickness) and then concrete was filled in the tube to cast the specimens. In this way, PVC tube acted as a mold and formwork was saved. In addition, plain concrete columns and steel tube reinforced columns were also prepared for the purpose of comparison. The compressive tests were conducted using 450 metric ton MTS machine. For tube reinforced columns, the load was applied to concrete only through a circular steel plate. On the outside surface of the tube, strain gauges were used to measure both axial and lateral strain during loading.

The experimental results show that the strength of concrete columns reinforced with fiber strand. increases with decrease of spacing of the strand.s. For a spacing of 25.5 mm, the strengths of the specimens reinforced with either carbon or glass fiber strand.s are twice as much as the plain concrete column. The ductility of concrete columns reinforced with fiber strand. can also be significantly improved, especially for glass fiber strand. reinforced specimen. The filament-wound composite tube reinforced concrete columns can significantly increase both strength and toughness of concrete through strong confinement. A three time increase in strength and a five time increase in strain capability have been achieved. A big potential exists for the application of this kind of hybrid structure in the field construction.

INTRODUCTION

The beneficial effect of confine stress on strength and ductility improvement of concrete has been long recognized. When a concrete specimen under compression is restrained from dilating laterally, its behavior is quite different from the case of uniaxial compression. The restraint to lateral dilation can be provided by lateral steel stirrups in the form of spirals or rectangular ties. Alternatively, lateral pressure can be achieved by a steel tube. It has been shown that for equal weights of lateral reinforcement, spirals are more than twice as effective, in terms of strength enhancement, as rectangular ties. An extensive investigations has been conducted to evaluate the confining effect of different lateral reinforcement. Since the steel tube reinforced concrete showed the advantages of stronger, more ductile, and tougher performance, this kind of structural form has been widely utilized in tall buildings, long span structures, and earthquake proof constructions. However, due to the nature of steel, steel member reinforced concrete frequently encountered a serious corrosion problem.

There are two kinds of steel corrosion in steel member reinforced concrete structures, chloride-induced corrosion and carbonation-induced corrosion. The chloride-induced corrosion is more dangerous because of its localized nature which can substantially reduce the effective area of steel and lead to a sudden failure of a structure. It is well known that under the normal conditions, steel inside concrete is prevented by the strong alkaline nature of $Ca(OH)_2$ (pH of about 13) through a formation of a thin protective film of iron oxide. The steel corrosion in structural concrete is primarily caused by the presence of free chloride ions in the matrix. The chloride in the atmosphere can penetrate into the concrete. The penetrated chloride ions diffuse through a concrete cover to steel surface first. Then a sufficient quantities of chloride ions have to be accumulated. Next, when the concentration of chloride ion in concrete reaches a certain level for a certain value of pH, it dissolves the protective oxidized film. Thus a localized breakdown of the passive film on the steel is formed by the action of these accumulated chloride ions and then a galvanic cell is created. The process becomes autocatalytic and proceeds with the deepening of corrosion pits rather than the spreading corrosion laterally along the steel. As the steel increases its state of oxidation, the volume of the corrosion products expands. These expansion creates cracking and spalling inside concrete, and finally destroy the integrity of the structural concrete and cause the failure of buildings and infrastructures.

To solve the corrosion problem of reinforcing steel in concrete, composites or fiber reinforced plastics (FRP) are being seriously considered as the replacement for steel rebars in some structural concrete members. In the past few years, some research and development work was devoted to assess the strength, durability characteristics, and design of composite materials as well as the structural members reinforced with composites. Nanni et al.[1] studied the bond anchorage of fiber-reinforced plastics acting as tendons. They concluded that the FRP tendons might experience slit cracks which could not be accepted because of the durability issue. Nanni[2] also investigated the flexural behavior of FRP rod reinforced concrete beams. He put his emphases on the design guidelines for the structural member reinforced by FRP. Because FRP is linear elastic up to failure, he concluded that the working stress method was more suitable for FRP reinforced concrete. Saadatmanesh et al[3] investigated the strength and ductility of concrete columns externally reinforced with fiber composite straps. The parametric study of their analytical model indicated that the strengthening method with composite straps could effectively increase the strength and durability of concrete columns degraded by seismic loading.

In this study, the effectiveness of using composite members to reinforce the concrete columns has been investigated. It has been demonstrated that confine pressure can be established through the properly utilized composite members. With these confinement, both strength and ductility of concrete column can be significantly improved.

EXPERIMENTAL PROCEDURES

Total five groups of specimens were for compression tests. The specimens include plain concrete columns, steel tube reinforced columns, composite tube reinforced columns, carbon fiber strand reinforced columns and glass fiber strand reinforced columns. The fiber strand reinforcement was made possible by pre-wound the fiber strand on the surface of PVC tube. During casting stage, the PVC tube acted as the mold for filling the concrete. All the specimens are 150 mm in diameter and 450 mm in length. The test program is summarized in Table I.

Table I Specimen Details

Specimen Identification	Reinforcement form	Spacing (mm)
P-C-C	----	----
S-T-RC	Steel tube	----
C-T-RC	Composite tube	----
C-F-S-RC-1	Carbon fiber strand	51
C-F-S-RC-2	Carbon fiber strand	38
C-F-S-RC-3	Carbon fiber strand	25.5
G-F-S-RC-1	Glass fiber strand	51
G-F-S-RC-2	Glass fiber strand	38
G-F-S-RC-3	Glass fiber strand	25.5

The concrete was prepared by using Type I ordinary Portland cement, river sand, and crushed limestone. The mix ratio is 1:0.55:1.8:2.5 (Cement : water : sand: aggregate by weight). The column specimens were cured under the conditions of 23°C and 100% relative humidity before test.

The column specimens were tested using a digital closed loop controlled 450 ton MTS machine. The compression tests were conducted using a stroke control under a rate of 0.1 mm /min. Four strain gauges were glued onto the surface of the specimens, two in axial direction and two in lateral direction in order to measure the axial and circumferential strain. The load was applied to the column through two circular steel plates. The test data were acquired using a computer and the data were recorded every two seconds.

TEST RESULTS

Fig. 1 shows the stress-strain curves for a plain concrete column, a steel tube reinforced column, and a composite tube reinforced columns. The compressive strength of plain concrete column, 38.5 MPa, was smaller than that of standard cylinder specimen, 46 MPa, although they were made from the same batch of concrete. This phenomenon can be attributed to the size effect. On the other hand, tube reinforced concrete showed a significant increase in both strength and ductility. As shown in the Figure, the steel tube reinforced concrete column reached 130 MPa with a very long plateau. After deducting the contribution from steel tube, the net strength of concrete was 94 MPa which was 2.4 times as high as that of plain concrete column. As for toughness, more than 100 times increase was observed. Similar phenomenon was observed for composite tube reinforced concrete column. As shown in the figure, the strength of composite tube concrete reached 250 MPa. The strength of concrete can be estimated by using a parallel model. After deducting the failure load of composite tube from the maximum load carried by composite tube reinforced concrete column, the value turned out to be 125 MPa which is 3 times of the plain concrete specimen's strength. Moreover, a significant increase in toughness was achieved by composite tube reinforced concrete column. It should be indicated that the visual inspection on the concrete inside the tube after removing either steel or composite jacket did not find any obvious damage. It seemed that the concrete

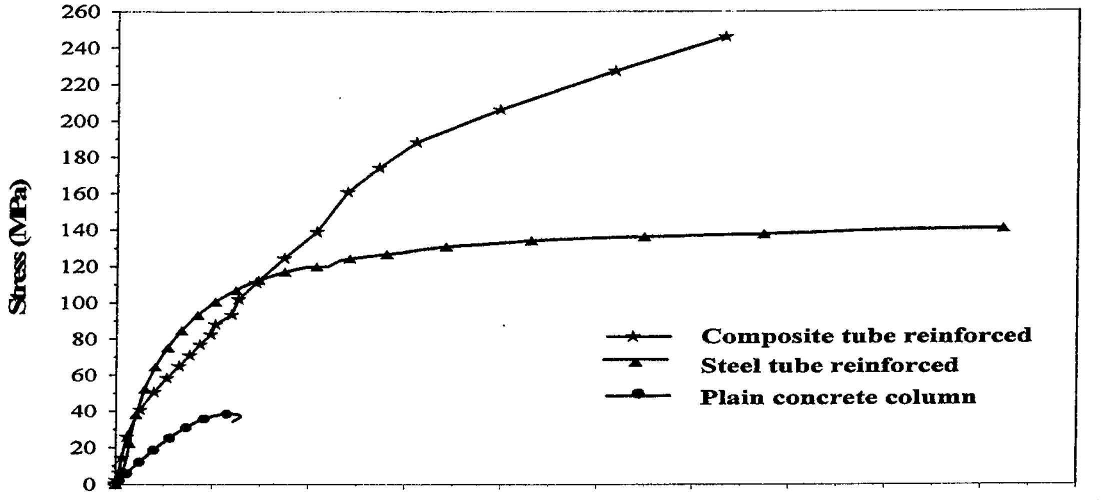

Figure 1 Stress-strain curve comparison for tube reinforced concrete columns

was still in a fairly good condition even after carrying such a heavy load.

Fig. 2 shows the stress-strain curves for a plain concrete specimen and three carbon fiber strand reinforced concrete columns with different spacings. It can be seen from the figure that there are a substantial increase in strength for all fiber strand reinforced columns. The degree of strength increase of these columns depends on the fiber strand spacing. For the columns with a spacing of 51 mm, the strength only increases by 39%. For those with a pacing of 38 mm, the strength increases by 79%, while for those with a spacing of 25.5 mm, the strength is almost doubled. In additional to the strength increase, the strain capability of the columns with fiber strand is also enhanced significantly. Comparing with the plain concrete columns, whose strain capacity only reached 0.002, the strain capacity of carbon fiber strand reinforced columns are 3.5 times, 4 times, and 5 times of that of plain columns for the spacings of 51 mm, 38 mm and 25.5 mm, respectively.

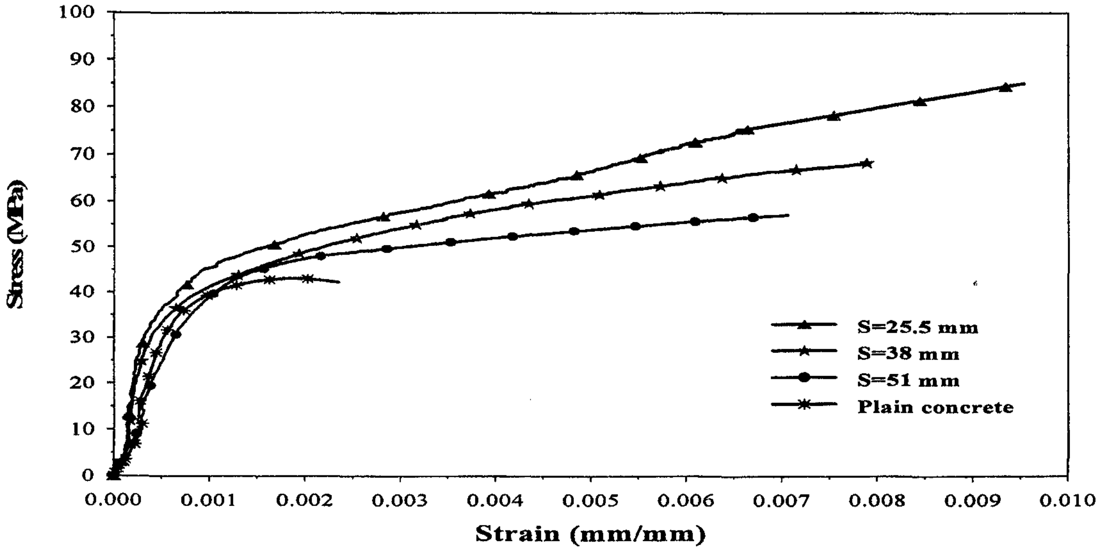

Figure 2 Stress-strain curve comparison for carbon fiber strand reinforced concrete columns

Fig. 3 plots the stress-strain curves for three glass fiber reinforced concrete columns and compares them to the curve of a plain concrete column. The spacing among the glass fiber strands for three columns is 51 mm, 38 mm, and 25.5 mm, respectively. The corresponding strength increases of three columns with glass fiber strand reinforcement are 28%, 57%, and 94%. These values, slightly smaller than those achieved by carbon fiber strand reinforcement. However, if we take a look about the strain capability, we will find that the glass fiber reinforced concrete columns are superior to carbon fiber reinforced concrete column. The ultimate axial strain of the glass fiber reinforced concrete columns reached the values of 1.1 percent, 1.22 percent, and 1.5 percent, respectively, while the corresponding carbon fiber reinforced concrete columns only 0.7

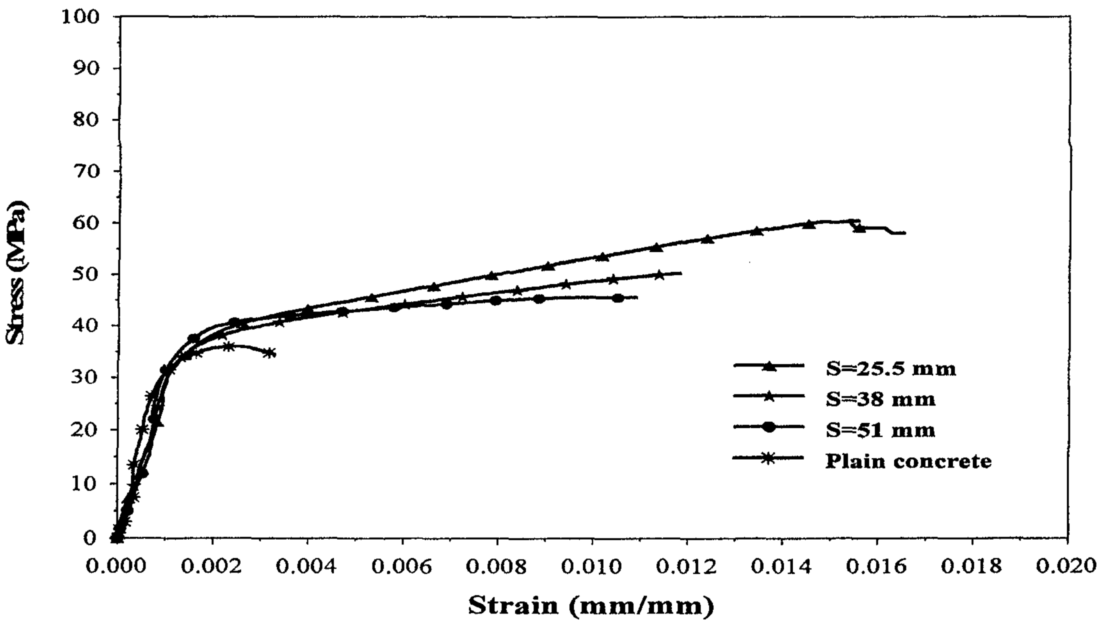

Figure 3 Stress-strain curve comparison for glass fiber strand reinforced concrete columns

percent, 0.83 percent, and 0.95 percent. In other words, there is about 50% increase in strain capability for glass fiber reinforced concrete columns. .

CONCLUSIONS

(1) Fiber glass composite tube with continuous filament winding can provide a strong confinement to inner concrete. With such a confinement, the strength of concrete can increase by four times. In addition, fiber glass composite tube can also increase the strain capability of concrete as high as five times.

(2) The carbon fiber strand reinforced columns can provide a reasonable confinement to inner concrete. A strength increases of 39%, 79%, and 114% were observed for the strand spacing of 51 mm, 38 mm, and 25.5 mm.

(3) The glass fiber strand reinforced columns showed a smaller increase in strength but a lager increase in strain capability as compared with carbon fiber reinforced columns.

REFERENCES

1. Nanni, A., Tanigaki, M., and Hasuo, K. (1992), "Bond anchorage of pretensioned FRP tendon at force release", J. of Structural Engineering, V 118, No. 10, pp 2837-53.

2. Nanni, A. (1993), "Flexural behavior and design of RC members using FRP reinforcement", J. of Structural Engineering, V 119, No. 10, pp 3344-59.

3. Saadatmanesh, H., Ehsani, M. R., and Li, M. W. (1994), "Strength and durability of concrete columns externally reinforced with fiber composite straps", ACI Structural Journal, V. 91, No. 4, pp 434-47.

Response of Composite Isogrid Cylinders Under Axial Compression

H. Mahfuz, M. Rahman, E. Foster, P. S. Das,
and S. Jeelani

Tuskegee University's Center for Advanced Materials (T-CAM)
Tuskegee University, Tuskegee, Alabama 36088, USA.

ABSTRACT

Filament wound composite isogrid is a structural concept that utilizes the use of repetitive equilateral pattern of stiffening ribs. The name isogrid is used because the triangular grid exhibits isotropic properties. The ability of isogrid structure to withstand compressive, bending and combined loads makes this structure attractive to the designers for spacecraft applications. Composite isogrid structures by virtue of their lighter weight, superior mechanical and thermal properties, further enhance these characteristics. However, the fabrication of these composite isogrid structures, especially the cylindrical ones, possesses a major challenge to the manufacturers. One of the methods that is being pursued by NASA and Air Force's Phillips Lab to manufacture composite isogrid is through the use of thermally stable foam mandrels. During the cure process, low coefficient of thermal expansion of the foam causes less compaction of the rib extremities. Lesser compaction of the ribs initiate delamination at the earlier stage of the loading and eventually affect the ultimate load carrying capacity of the isogrid structures.

A comprehensive finite element analysis (FEA) has been performed in this study to investigate composite isogrid cylinders representing the intertank of the space shuttle. The intertank is the structural connection that joins the liquid oxygen and liquid nitrogen tanks to provide structural continuity between the assemblies on the external tank (ET). A two stage approach has been adopted for the development of the FEA model of the composite isogrid cylinder. In the first stage a unit cell representative of the cylindrical structure has been modeled and subjected to in-plane compression to have a first-hand estimate of the stress and compact force distributions. In the second stage, unit cells have been generated in multiples to form into a complete cylinder. Axial loads are then applied on the cylinder, and parametric studies are conducted with various rib geometry. In each case, stress distribution and the distribution of compact force have been analyzed. Details of the finite element modeling and the analysis of the parametric studies are presented in this paper

INTRODUCTION

The investigation of efficient, lightweight, cost-effective aerospace vehicle is a major goal of the aerospace industry. Structural efficiency is an important aspect of the design of cost-effective aircraft structures and this can be achieved by using Isogrids into the main structure of the spacecraft. The selection of lightweight, high-strength materials have been narrowed down to the isogrid structure. A few of the characteristics of isogrids that make this structure attractive to designers are, 1) they behave isotropically, which means that the properties are uniformly distributed throughout the entire framework, 2) It has the ability to withstand both compression and bending, which is an important factor for spacecraft design. The isotropic property and effective Poisson's ratio of 5/3, enables the isogrid to be mathematically transformed to an equivalent homogeneous material layer. This transformed expression can be substituted into shell equations to analyze the overall behavior of isogrid structures. Further optimization of these characteristics are being investigated and the primary focus is now on composite materials. This isogrid - stiffened structure when formed into a cylindrical form, becomes a useful part for aerospace structures. This structure shows its effectiveness for space - craft tankage, interstages and in the skylab crew quaters. It also functions as a protective compartment housing for the operational instruments and range safety components.

It is observed that the former studies were performed most frequently with aluminum alloy specimens. However, the composite isogrid structure by various buckling and compression test, shows the characteristics that are necessary to optimize and achieve the goal of the aerospace industry, which is primarily to lower the weight of the aircraft while maintaining the high strength that is required.

One of the first projects to employ the isogrid structure was the Delta Launch Vehicle project which began in 1959. This design was incorporated into the external skin structure of the booster and was machined from flat 5.27cm (5/2 in) thick 54ST6 free machining aluminum alloy plate, brake-formed into curved shapes and finally welded into 2.44m (4ft) diameter tank shells. The evaluation of isogrid structures indicated that they possessed advantages that were critical to the improvement of aircraft structures. This reinforced the decision to design the interstage and the fairing for new model Deltas, using isogrid structures. Likewise, one of the earliest analysis was performed using finite element program NASTRAN [3] . The importance of this analysis, was to determine the general instability, theoretical allowable for compression loading, which includes axial compression, equivalent axial compression due to bending as well as offsetting axial tension forces due to internal pressure. The earliest detailed usage of composite material found in this investigation was performed by McDonnell Douglas Astronautics Company in 1972, where three composite cylinders were designed with the isogrid patterns on the external surface of the cylinder. Each cylinder experienced one of the mode of buckling behavior of isogrid stiffened structure which was either general - instability buckling, skin buckling or rib crippling.

The first continuous filament isogrid stiffened structure was produced in 1976. Again, compression buckling and dynamic behavior of the structure was tested [5-6]. One study on a Lockheed C-530 transport aircraft center fuselage using the continuous filament winding structure, showed a weight savings of 20-30 percent over metallic design. As recent as 1992 and 1993, more studies were done on these structures, such as, the use of the COSMOS/M finite element analysis program, which was used to determine the buckling load for a composite isogrid flat panel, as well as work done to verify the feasibility of using acoustic barrier vibration control (ABVC) system with the isogrid structure. As part of very recent works, the effect of stiffness discontinuities and selected structural parameters on the behavior of grid stiffened panels, specifically the effects of both manufacturing introduced stiffness discontinuities and induced damage on grid stiffened panels were also performed by Reddy and Rehfield[8-10]. The studies were performed on both isogrid and orthogrid panels.

FINITE ELEMENT MODEL DEVELOPMENT

A nonlinear Finite Element Analysis (FEA) using ANSYS is conducted to study the compaction of the rib extremities for the different rib geometry of the composite structures. The isogrid composite cylinders are modeled with 8 - noded structural solid, solid46. The formulation of the solid element used in this investigation is based on the lamination theory that the strain distribution in the thickness direction remains constant. This layered version of the 8 noded structural solid element allows up to 100 different material layers and has three degrees of freedom at each node: translations in the nodal x, y and z directions.

A two stage approach has been adopted to develop the complete FEA model of the isogrid cylinder. At the first stage, a unit cell representing the isogrid structure has been developed. The rib to skin thickness ratio i.e. d/t has been used as 3.5, as found in some early work. and kept constant throughout the analysis, for unit cell as well as for the complete cylinder. The geometric dimension of the unit cell is shown in Figure 1(a).

In the second stage, a flat model using 40 unit cells (4 along Y- direction & 5 along X-direction) is developed. This flat model, then, converted to a complete cylinder through suitable cylindrical coordinate system to conform the shape of the isogrid stiffened cylinder. This general procedure is adopted for all the three cylinders. The three different rib geometry are shown in Fig. 2(b). The skin section of all the cylinders have been configured with four identical layers & their rib sections have been generated with 12 identical layers. The lay up sequence for the skin is $[0^0/45^0/-45^0/90^0]$ & it is an alternative arrangement of 60^0 & -60^0 for the rib. Carbon composite is used as the material for this isogrid structures and the properties as used in the FEA model are as follows: $E_x = 20.44\text{x}10^6$ psi, $E_y = 3.70\text{x}10^6$ psi, $G_{xy} = 1.04\text{x}10^9$6psi & $\nu_{xy} = 0.32$

. The applied compressive load was computed according to the conventions used in the "Isogrid Design Hand Book", [1]. This value has been obtained as 650 Mpa from equation (2).

$$N_C = 10.87E\,\bar{t}\left(\frac{t}{h}\right)^2 \tag{1}$$

$$f_C = \frac{N_C}{\bar{t}} \tag{2}$$

Where, N_C = critical load for skin buckling in compression, lb/in.
E = Young's modulas of elasticity, psi
t = skin thickness, in.
h = height of isogrid triangle

$\bar{t}$ = equivalent skin thickness, in.
f_c = allowable compression stress, psi

Here $\bar{t}$ can be defined by the following equations (3) & (4)

$$\bar{t} = \alpha(t+1) \tag{3}$$

And $$\alpha = \frac{bd}{th} \tag{4}$$

Where, b = width of the isogrid rib, in.
d = rib thickness, in.

RESULTS AND DISCUSSIONS

It has been stated earlier that for simplifying the modeling effort, unit cells were developed at the initial stage of this investigation to represent an ideal repetitive structural unit of the isogrid cylinder. Although the response of the unit cell cannot be directly linked with those of the cylinders, it was of particular interest in this study to investigate the unit cell response. This importance was due to the fact that unit cells were also fabricated and tested in the lab during the earlier part of this investigation. Unit cells were tested under axial compression and correspondingly compressive loads were applied in the Y-direction in the FEM model as indicated in Fig. 1(b). The following discussions are therefore, presented in two categories, namely, (1) Unit cell Response, and (2) Response of the isogrid cylinders

Unit Cell Response

Three different stress distributions, namely, σ_x, σ_y and σ_z along the thickness of the unit cell arrangement is shown in figure 3(a). These stress distributions have been plotted in the locations of their maximum values. The region inside the small circle as shown in figure 1(b) corresponds to these locations. The distribution of σ_x dominates the other stress distributions. However, each of these stress distributions follows the same pattern, starting with a minimum value and then keeps increasing until it attains its maximum value at the rib-skin interface and then it keeps decreasing up to the total thickness. These large stress values at the rib-skin interface are due to the stress concentration at that location. The abrupt change in cross-sectional area from the skin to the rib is mostly responsible for this stress concentration. These large stress values cause fiber rupture, matrix crack and delamination. The clear separation between skin and rib as has been observed from different stress contour plots supports this fact.

Figure 3(b) shows the distribution of the compaction force (F_Z) along the thickness of the unit cell. But much lower value is noted from this distribution. However, this distribution cannot reflect the importance of study of the compaction force for the isogrid structures. This can only indicate that the rib-skin interface is the location where an abrupt change in values of the compaction forces is taking place.

Response of the Isogrid Cylinders

Owing to the importance of axial, radial and interlaminar shear stress for determining the failure mechanism of isogrid cylinders, their distributions have been analyzed in the present investigation. The current investigation has been focused on three different isogrid cylinders with three different rib geometry under same loading and boundary conditions. These are rectangular, triangular and taper rib geometry. Since both D/L and d/t ratios have been kept constant for these three different cylinders, it is possible to pursue a comparative study between them. The through thickness distributions of axial, radial and interlaminar shear stress for three different rib geometry are shown in figure 4(a), 4(b) and 5(a) respectively. These distributions have been plotted in the locations of maximum stress thru the thickness. For three different rib geometry, maximum axial stress occurs near the points of loading. The maximum radial stress attains in the region, which is about from 0.5L to 0.7L away from the fixed end of different cylinders. But the maximum interlaminar shear stress occurs near the fixed end.

From the axial stress distribution, isogrid cylinders with triangular rib geometry shows a peak of 1250 Mpa at the rib-skin interface. These values are obtained as 1100 Mpa and 940 Mpa for the isogrid cylinders with taper and rectangular rib sections respectively. These axial stress values are much higher than the compressive strength of any matrix material that we usually encounter in the standard composite material system. Therefore, matrix crack will take place at the locations of maximum axial stress. This will lead to delamination of corresponding layers. Triangular and taper rib geometry are most susceptible for this crack phenomenon compared to rectangular rib geometry. This observation can recommend isogrid cylinder with rectangular ribs as a suitable one for axial compressive loading situation.

The through thickness distributions of radial stress for three different rib geometry is plotted in figure 4(b). The isogrid cylinder with triangular rib geometry presents maximum radial stress. Large radial stress (tensile) at the rib-skin interface for the triangular rib geometry suggests the possibilities of tensile rupture of fibers at those locations. Besides this, large radial stress in tension in the neighborhood of inner radius may cause local buckling of the wall at that location. This is not the case with other two rib geometry. Although the rectangular rib geometry has a tensile peak at the rib-skin interface, its smaller value can't dictate any failure mechanism. The radial stress distribution for the taper geometry is entirely compressive in nature. This suggests the tendency of fibers to be contracted under axial loading situation. This can eventually restrain isogrid cylinder with taper ribs from fiber pullout. The tangential stress distribution which has not been presented here shows very good correlation with their corresponding radial stress distribution.

Interlaminar shear stress distributions are presented in figure 5(a). Interlaminar shear stress distributions attain their maximum value close to the outer surface of skin. For taper and rectangular rib geometry, these values are very large compared to the interlaminar shear strength of any composite material. This fact alone can predict delamination as a viable failure mode for the isogrid cylinder under compression, specially for rectangular and taper rib geometry. For triangular rib geometry, the contribution towards delamination is very negligible from interlaminar shear stress. In this case high radial stress is responsible for fiber pull out and ultimate delamination to occur.

The compaction force distribution for three rib geometry is shown in Fig. 5(b). The nodal forces in the radial direction have been taken as compaction forces. The isogrid cylinder with triangular ribs exhibits comparatively higher compaction force than the other two cylinders. However, much smaller compaction force indicate its insignificance related with the present study.

Although the stresses are found to be lowest in isogrid cylinders with rectangular rib section, the axial displacement of the cylinder with the rectangular rib is 65% more than that of cylinder with triangular rib and it is 24% more than that of cylinder with tapered rib. This is because of more stiffening capabilities of triangular rib section over the other two types.

CONCLUSIONS

A composite unit cell representative of cylindrical isogrid structure for finite element analysis has been successfully developed. The unit cell has been extended to a complete cylinder consisting of equilateral lattice of composite isogrids. Finite element analysis on these cylinders reveals that higher stresses are observed due to the stress concentration effect at the rib-skin interface, suggesting that the interface is most vulnerable for any kind of rib geometry. This stress behavior for the isogrid cylinders is found similar to the unit cells response. The lower value of compaction force in both the unit cell as well as in the isogrid cylinders suggests that future investigation is necessary and the residual stresses introduced in the cylinders during curing of the manufacturing process needs to be considered. Out of the three geometry, the isogrid cylinder with rectangular rib-section shows the lowest stress values at the rib-skin interface compared to cylinders with tapered and triangular rib-sections, indicating the better geometry for the manufacturing of composite isogrid cylinders.

ACKNOWLEDGMENT

The financial support for this work provided by NASA Marshall Space Flight Center, Huntsville, AL, is gratefully, acknowledged.

REFERENCES

1. "Isogrid Design Hand Book", prepared by Macdonnell Douglas Astronautics Company, February 1973.
2. Slysh, Paul, '*Picking The Best High - Strength, Lightweight Structures,*' Machine Design, October 11, 1990.
3. Knighton, D. J., '*Delta Launch Vehicle Isogrid Structure NASTRAN Analysis,*' Sept. 11-12, 1972.
4. Finckenor, Jeffery L., '*Isogrid Design Handbook,*' MDC G4225A, McDonnell Douglas Astronautics Company, February, 1970.
5. Slysh, Paul, '*Isogrid Structural Tests and Stability Analyses,*' Journal Aircraft, Vol. 10, No. 10, October 1976.
6. Jenkins W. C., '*Determination of Critical Buckling Loads for Isogrid Stiffened Cylinders,*' MDC Report No. G2722, Feb. 1972.
7. '*Forming The Limits set for Isogrid Plates,*' American Machinist & Automated Manufacturing, August, 1987.
8. Reddy, Ambur D., '*Continuous Filament Wound Composite Concepts for Aircraft Fuselage Structures,*' Journal of Aircraft, Vol. 22, No. 0, March 1985.
9. Rehfield, Lawrence W., '*Buckling of Continuous Filament Composite Isogrid Panels: Theory and Experiment,*' Progress in Science and Engineering of Composites ICCM-IV, 1992.
10. Reddy, Ambur D., '*Effect of Stiffness Characteristics on the Response of Composite Grid-Stiffened Structures,*' Journal of Aircraft, Vol. 00, No. 4, July-Aug., 1990
11. Atluri, Satya N., '*Innovative Methods in the Dynamics of Large Space Structures,*' AFOSR/NA Boiling AFB, DC 20002, July 1992.
12. Robinson, Micheal J., '*Advanced Composite Structures for Launch Vehicles,*' SAMPE Quarterly, January 1991.

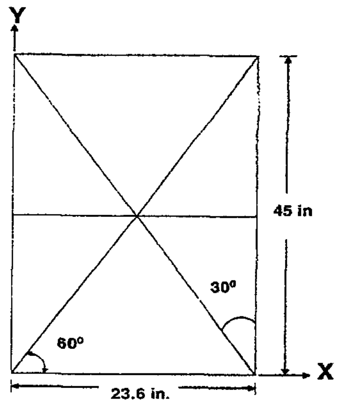

Fig 1(a). Unit Cell of Isogrid

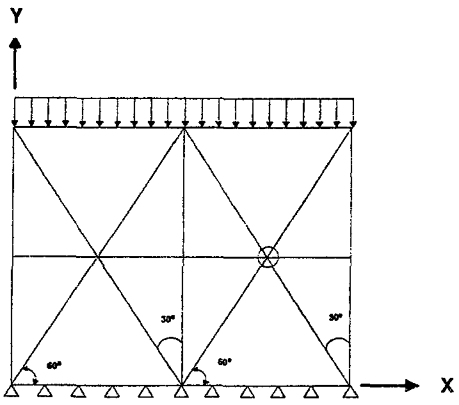

Fig 1(b). Unit Cells With its Loading

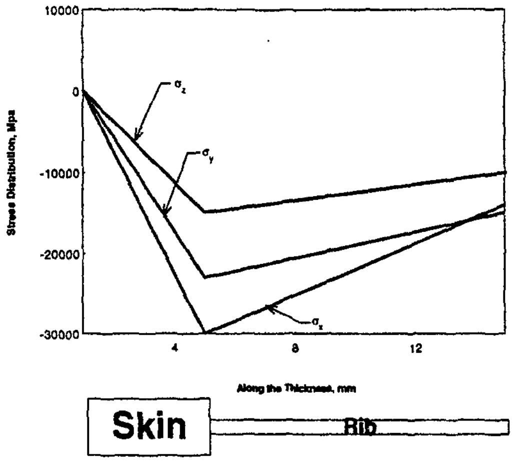

Fig 3(a). Stress Distribution Along Thickness of the Unit Cell for Y direction Loading.

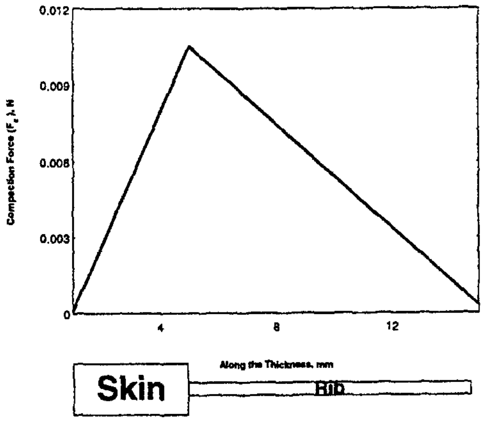

Fig 3(b). Variation of Compaction force along the Thickness of Unit-Cell.

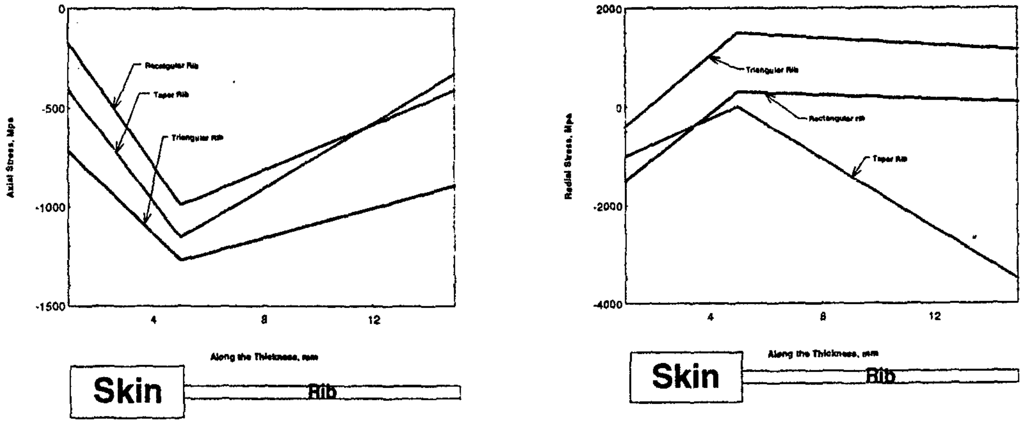

(a) Axial Stress (b) Radial Stress

Fig 4. Stress Distribution Along the Thickness of Isogrid Cylinders

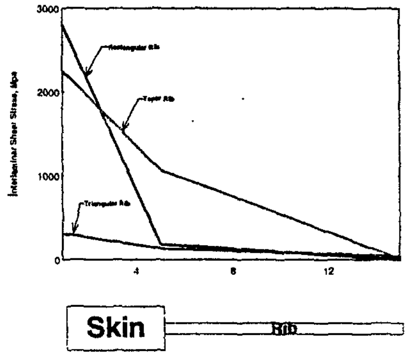

Fig 5(a). Interlaminar Shear Stress distribution along the thickness of the three different cylinders

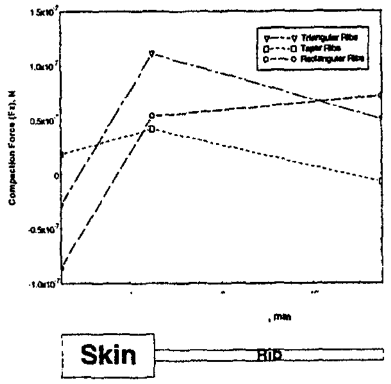

Fig 5(b). Variation of Compaction Forces Along the Thickness of Three Cylinders

HIGHER-ORDER MODEL FOR THE STRESS-STRAIN STATE OF COMPOSITE BEAMS

V. G. Piskunov[1], A. V. Goryk[2] and A. L. Lyakhov[2].

[1]Ukrainian Transport University,
Kiev-252010, Suvorova St., No 1, Ukraine
[2]Poltava State Technical University,
Poltava-314601, Pershotravnevy Av., No 24, Ukraine

INTRODUCTION

Method of analysis of a bending composite beams of a piece-homogeneous structure, taking with account deplanation of the cross sections, give the possibility to investigate features of a stressed-strained state (SSS) in zones of boundary effects is developed. Such theory of the flat bending of layered constructions is resulted in [1]. The expansion of this theory to constructions of a more general structure is connected to large difficulties as at formation of initial settlement hypothesizes, as at its realization. It requires a effective mathematical apparatus and approach's to programming of calculations. The mathematical formulation of the theory is given in the terms of the theory of generalized functions. It enables to create the effective software by methods of computer algebra, expanding, thus, area of application of the developed theory.

PROBLEM STATEMENT

All transformations are executed with use of mixed designations: the expressions have the integrated form, the displacements and stresses are designated as “classical” functions, simultaneously at expressions there are generalized Heaviside step function and “ simple layer”. It does not result in misunderstanding. From finitely valued of energy of deformations follows local integrable of functions, which describing SSS of the body [2]. By Dyu'Buà-Raymîde lemma [3] one-to-one correspondence between of sets of local integrable functions and sets of regular generalized functions exists. At the same time, application of the generalized functions is expedient for the realization of the theory:

Firstly, the Heaviside step functions and “ simple layer” are, de-facto, of the logical predicates, that enables to receive expressions for parameters SSS as piece-homogeneous area uniform expression. Secondly, they are generalized functions, that enables to remove all necessary expressions by analytical transformations on the basis of properties these functions. In third, these functions and their properties by the terms of algorithm language of a system of computer algebra ANALYTIC [4] are expressed. It enables all necessary transformations and calculations, including symbolical, to make automatically with the help of a computer.

MAIN EXPRESSIONS

We shall consider a piece-homogeneous body in the form of a beam in Cartesian system of coordinates *XYZ*. Cross section A has a border Γ_A of any form, not varying along a longitudinal axis (Fig.1). The cross section of the beam consists areas A_k ($k=0,1,2,\ldots N$) of various material phases ($A = \bigcup_{k=0}^{N} A_k$). The elastic characteristics, Yunge module and share module, various material phases we shall designate accordingly E_k and G_k. On borders of section of various material phases rigid contact takes place. Along each direct, parallel of the beam axis, SSS is superposition of independent SSS in planes, taking place through this direct, in parallel to the coordinate planes *XCZ* and *XCY* [1]. The equations of equilibrium of section *A* of composite beam for normal stresses $\sigma_x(x,y,z)$ can be written as

$$\begin{aligned} &\sigma^1_{x,x}(x,z) + \tau_{zx,z}(x,z) = 0 \\ &\sigma^2_{x,x}(x,y) + \tau_{yx,y}(x,y) = 0\,, \qquad (x,y,z) \in A, \qquad 0 \le x \le l \qquad (1) \\ &\sigma_x(x,y,z) = \sigma^1_x(x,z) + \sigma^2_x(x,y) \end{aligned}$$

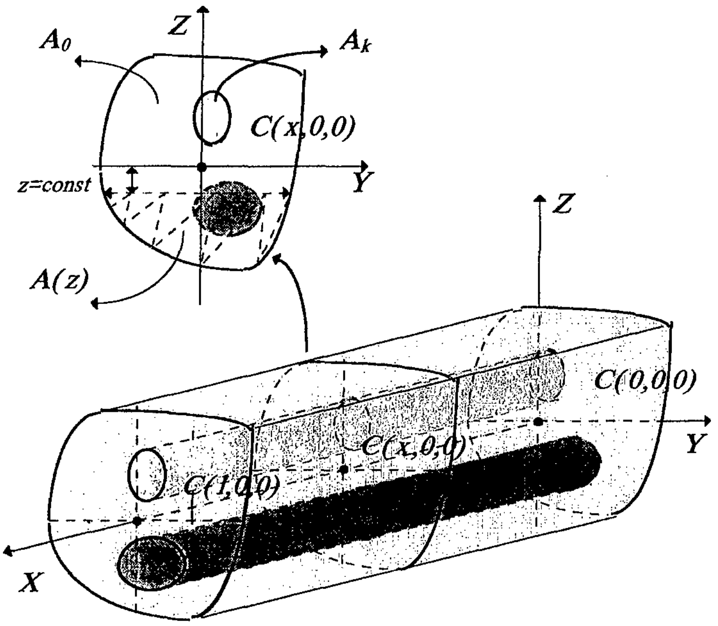

Figure 1 Piece-homogeneous beam.

A feature SSS of the piece-homogeneous body is that the components of SSS can be not enough smooth functions of coordinates, since the their borders derivative at crossing of section of various phases of materials will can to have a jumps. It results jumps a component tensor of stresses.

The differential equations of equilibrium (1) has only the local classical decision inside each homogeneous area A_k . It has not decision in a classical sense for the whole piece-homogeneous area *A*. At the same time, the rigid contact of various phases of materials means a continuity of displacement of points whole bodies. From finitely valued of energy of deformations follows, that the stresses in composite beam should be local integrable functions [2]. Thus, the equation (1) can be considered as the equation containing the regular generalized functions.

We shall define generalized Heaviside step function as

$$\theta(y,z)=\begin{cases}0, & (y,z)\notin A\\ 1/2, & (y,z)\in\Gamma_A\\ 1, & (y,z)\in A\end{cases} \tag{2}$$

We shall consider first equation(second similarly) from in (1), designating of stress by the symbol σ_x without the top index. The equilibrium of the area about $A(z)\subseteq A$, lying below to direct $z=const$ (Fig.1), is described by a local element of a equation (1)

$$\int_{R^2}(\sigma_{x,x}+\tau_{zx,x})\theta_{A(z)}dA=0 \tag{3}$$

R^2 - is the plane, which belongs section A; $\theta_{A(z)}$ - characteristic function of area $A\ (z)$.

The elastic characteristics of materials, from which produced the piece-homogeneous area A, present uniform expressions for whole area as

$$\begin{aligned}E&=\left(E_k-E_0\right)\theta_k+E_0\theta\\ G&=\left(G_k-G_0\right)\theta_k+G_0\theta\end{aligned} \tag{4}$$

θ, θ_k - characteristic functions of areas A, A_k accordingly. The representation (4) permits to avoid at numerical realization of the theory to integrate on the multispanned area A_0.

We accept as hypothesizes [1], that displacement along the axis CX is $u=u(x,z)$, along the axis CZ is $w=w\ (x)$, and tangential stresses are distributed under the law

$$\tau_{zx}(z,x)=-\frac{d\chi(x)}{dx}f(z) \tag{5}$$

$\chi(x)$ - unknown, so named function of shift, and $f(z)$ - function of distribution of tangential stresses [1]. This function, according to [1] and (4), has a kind

$$f(z)=-\frac{1}{b(z)}\int_{R^2}E\theta_{A(z)}zdA \tag{6}$$

$b\ (z)$ - size of the area A along direct $z=const$.

After transformations of a equation (2), in view of properties of generalized functions and known rules of the theory of elasticity, we receive

$$b(z)\tau(x,z)=-\int_{R^2}\tau_{zx}\delta_{\Gamma'A(z)}n_z dydz-\int_{R^2}E\theta_{A(z)}\frac{\partial^2 u}{\partial x^2}dydz \tag{7}$$

$$
\begin{aligned}
b(z)u(x,z) = -\int_{R^2} u\delta_{\Gamma' A(z)} n_z dydz - \\
- w_{,x} \int_{R^2} \theta_{A(z)} dydz - \chi_{,x} \int_{R^2} \theta_{A(z)} G^{-1} f(z) dydz
\end{aligned} \tag{8}
$$

$$
\sigma_x = E\frac{\partial u}{\partial x}
$$

$\delta_{\Gamma' A(z)}$ - generalized function "a simple layer" with the carrier $\Gamma^1{}_{A(z)}$ - part of a border of the area $A(z)$, lying below to direct $z=const$; n_z - projection of the unit external normal to $\Gamma^1{}_{A(z)}$ to the axis CZ.

Augends in (7) and (8) contain boundary values accordingly tangential stresses τ_{xz} and displacements u on the border $\Gamma^1{}_{A(z)}$, which is determined by a type of a boundary problem.

DEFINITION OF UNKNOWN FUNCTIONS

The necessary condition for a minimum of potential energy of a considered body can be written as :

$$
\int_0^l \int_{R^2} \left[\sigma_x \delta\varepsilon_x + \tau_{xz}\delta\gamma_{xz}\right] dxdA - \int_0^l q\delta w dx = 0 \tag{9}
$$

In (9) $q(x)$ - density of the bending load . The variations of deformations $\delta\varepsilon_x$, $\delta\gamma_{xz}$ and displacement δw are independent. The expression (9), pursuant to these condition and (4)-(5), acquires the kind of the system of differential equations

$$
\begin{aligned}
D_{11} w_{,xxxx}(x) + D_{12}\chi_{,xxxx}(x) = q(x) \\
D_{21} w_{,xxxx}(x) + D_{22}\chi_{,xxxx}(x) - D_{23}\chi_{,xx}(x) = 0
\end{aligned} \tag{10}
$$

The system (10) is supplemented by equations

$$
\delta w_{,x}(x)\left\{B_{12}(z)N(x) - M(x)\right\}\Big|_0^l = 0
$$

$$
\delta w(x)\left\{B_{12}(z)N_{,x}(x) - M_{,x}(x)\right\}\Big|_0^l = 0
$$

$$\begin{aligned}&\delta\chi_{,x}(x)\{B_{13}(z)N(x)-\overline{M}(x)\}\Big|_0^l=0\\&\delta\chi(x)\{B_{13}(z)N_{,x}(x)-(\overline{M}_{,x}(x)+\overline{Q}_{,x}(x)\}\Big|_0^l=0\end{aligned}\qquad(11)$$

depending on a kind of a boundary problem for the beam.

In expressions (10) and (11) D_{11}, , D_{12}, , D_{21} , D_{22} , D_{23} , - are constants and B_{12} , B_{13} - are functions, determined by boundary, geometrical and mechanical properties of beam. N - a force, M - a bending moment, $\overline{M},\overline{Q}$ - a high-order moments [1]. In general case forms of expressions for these quantities are a bulky kinds and are not here resulted.

REALIZATION BY METHODS OF COMPUTER ALGEBRA

The realizations of the theory are distinctions:
- obvious kind of the used analytical expressions depends from particular problem (system of coordinates *XYZ*, in which is calculated SSS, is determined by properties of a particular researched body; - the characteristics SSS are calculated as integrals on the area *A (z)*, the structure and form of a border of which is determined significance's *z*; - SSS is defined predicative relationships owing to piece-homogeneity of a structure of a beam, the form of which depends on geometrical properties of areas A_k and etc.). The well-known programming systems are oriented to processing of numerical models. The form used thus analytical expressions should be static. In this connection, for realization of the theory a system of computer algebra ANALYTIC [4] and principles of programming, described in [5] are used. The set of expressions of the theory is considered as object with a hierarchical structure, which is ordered by a substituting operation. By initial objects for formation of a obvious kind of expressions at each level is a obvious kind of expressions at the previous levels. On such structure the ANALYTIC does not impose any semantic restrictions and it correctness is completely determined by initial data and program. Initial data for problems, within the framework of the described theory, is reasonably the complete information about geometric properties of areas A_k and elastic constants. On the basis of this information analytical equations of areas Ak, then obvious kind of expressions (4), then (6) and etc. are formed. The last level of this structure is expressions (7-8). Their obvious kinds are the output information of the programs. A high level of intelligence of means of a system the ANALYTIC for recognition of properties and transformation of objects, as well as representation predicate expressions by generalized function, permits to create effective algorithms for automatic realization of all calculations, including symbolical. Dialogue mode of operations is if necessary possible.

For demonstration of application of such technique we put example:
Consider piece-homogeneous beam (fig.2) of rectangular section $A\ (E_0 = 13,\ G_0 = 5)$ with two rectangular inclusions A_1 and A_2 $(E_1 = E_2 = 140,\ G_1 = G_2 = 50)$. The sizes and elastic constant are given in conditional units. The results are shown on Fig.3.

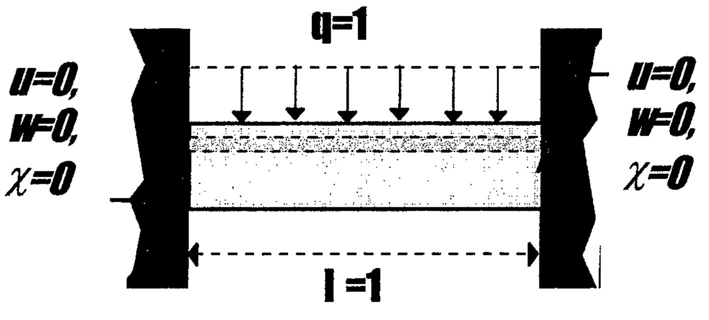

a)

Figure 2. Beam under in a regular intervals distributed load:
a)- general kind; b) - cross section.

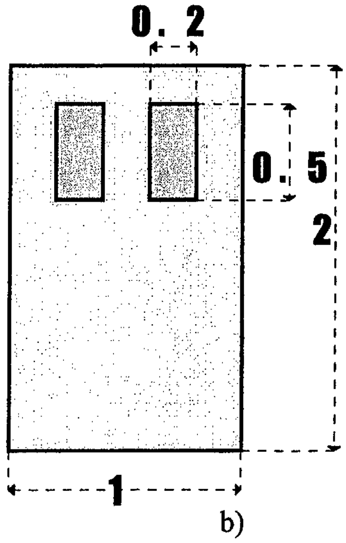

b)

Figure 3. Space distribution of longitudinal stresses σ_x in section of the beam (Fig.2) near the clamp

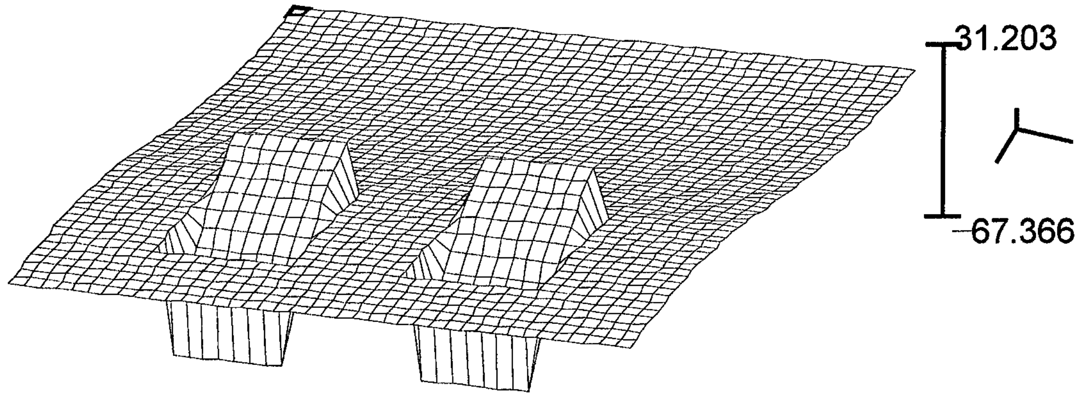

REFERENCES

[1] Piskunov V.G., Verijenko V.Å. Linear and nonlinear problems in the analysis of laminated structures. Kiev, Budivelnyk, 1986, 176 p., (in Russian).

[2] Parton V.Z., Perlyn P.I. Methods of the mathematical theory of elasticity. Moscow, Science, 1981, 688 p., (in Russian).

[3] Vladimirov V.S. Equations of mathematical physics. Moscow, Science, 1971, 512 p., (in Russian).

[4] Morozov A.A., Klimenko V.P., Fishman J.C., Bublic B.A., Gorovoy V.D.,Kalyna E.A. ANALYTIC-93. Cybernetics and system analysis, Kiev, No 5, 1995, p.127-156, (in Russian).

[5] Lyakhov A.L. Synthesis of a equation a piece-smooth flat line by methods of computer algebra. - Problems of mathematical machines and systems, Kiev, 1997, No 2, (in Russian).

SOLUTION OF DYNAMIC BOUNDARY PROBLEMS IN A CONTINUOUS ELASTIC CURVILINEAR ANISOTROPIC MEDIUM WITH A SPHERICAL CAVITY

Yuriy A. Rossikhin and Marina V. Shitikova

Department of Theoretical Mechanics,
Voronezh State Academy of Construction and Architecture,
ul.Kirova 3-75, Voronezh 394018, Russia
Tel/Fax: +7-0732-773992, E-mail: MVS@vgasa.voronezh.su

Summary. The ray method for solving boundary problems involving the propagation of surfaces of strong discontinuity in curvilinear anisotropic media is developed. The method employs the solution behind the surface of strong discontinuity whcih is constructed in terms of power series (ray series). Shock subjections to boundaries of cavities in transversely isotropic bodies having spherical anisotropy are investigated.

1 Introduction

The definition of the curvilinear anisotropic material, i.e., the material whose anisotropy conforms to the shape of the body, is given in Love (1927), where it is demonstrated that curvilinear anisotropic bodies have the same types of symmetry as common anisotropic bodies.

Curvilinear anisotropy is introduced by artificial means as a result of the design of elastic objects from various laminated composites (Jones,1975; Chou and Ko, 1989).

Static problems for bodies with curvilinear anisotropy were studied by Lekhnitsky (1963) and Conway et al (1967). Dynamic problems concerning harmonic vibration and wave propagation were examined in Mitra (1959), Ohnabe and Nowinski (1971), and Toshiaki (1990), where as curvilinear anisotropic bodies were used plates, cylindrical bars with cylindrical anisotropy, and thickwalled spherical shells with spherical anisotropy, respectively.

In the present paper, boundary value problems concerning the propagation of nonstationary volume waves in curvilinear anisotropic media with spherical anisotropy are studied by applying the ray method (Rossikhin and Shitikova, 1995) based on the theory of singular surfaces (Thomas, 1961).

2 Governing equations

Consider orthogonal system of curvilinear coordinates $x_\alpha = \alpha, x_\beta = \beta, x_\gamma = \gamma$. With reference to these coordinates the motion of an elastic body is described by the following system of equations:

$$\frac{\partial}{\partial\alpha}(H_2H_3\sigma_{\alpha\alpha}) + \frac{\partial}{\partial\beta}(H_1H_3\sigma_{\alpha\beta}) + \frac{\partial}{\partial\gamma}(H_1H_2\sigma_{\alpha\gamma}) - \sigma_{\beta\beta}H_3\frac{\partial H_2}{\partial\alpha} - \sigma_{\gamma\gamma}H_2\frac{\partial H_3}{\partial\alpha}$$

$$+\sigma_{\beta\alpha}H_3\frac{\partial H_1}{\partial\beta} + \sigma_{\gamma\alpha}H_2\frac{\partial H_1}{\partial\gamma} = \rho\frac{\partial v_\alpha}{\partial t}H_1H_2H_3. \qquad \begin{pmatrix} \alpha & \beta & \gamma \\ 1 & 2 & 3 \end{pmatrix} \tag{2.1}$$

Hereafter the symbols (α, β, γ) and (1, 2, 3) denote that the remaining dependences are obtained by the circular repositioning of the indices, $H_1 = H_1(\alpha, \beta, \gamma)$, $H_2 = H_2((\alpha, \beta, \gamma)$, and $H_3 = H_3(\alpha, \beta, \gamma)$ are Lamé constants, σ_{ij} and $v_i\,(i, j = (\alpha, \beta, \gamma)$ are the components of the stress and velocity, respectively, ρ is the density, t denotes time.

Assuming the coordinate γ to be perpendicular to the plane of isotropy at every point in the curvilinear body (transversely isotropic body), we ibtain the generalized Hooke's law

$$\begin{aligned} e_{\alpha\alpha} &= \frac{1}{E}(\sigma_{\alpha\alpha} - \nu\sigma_{\beta\beta}) - \frac{\nu'}{E'}\sigma_{\gamma\gamma}, & e_{\beta\gamma} &= \frac{1}{\mu'}\sigma_{\beta\gamma}, \\ e_{\beta\beta} &= \frac{1}{E}(\sigma_{\beta\beta} - \nu\sigma_{\alpha\alpha}) - \frac{\nu'}{E'}\sigma_{\gamma\gamma}, & e_{\gamma\alpha} &= \frac{1}{\mu'}\sigma_{\gamma\alpha}, \\ e_{\gamma\gamma} &= -\frac{\nu'}{E'}(\sigma_{\alpha\alpha} + \sigma_{\beta\beta}) + \frac{1}{E'}\sigma_{\gamma\gamma}, & e_{\alpha\beta} &= \frac{1}{\mu}\sigma_{\alpha\beta}, \end{aligned} \tag{2.2}$$

where $e_{ij}\,(i, j = \alpha, \beta, \gamma)$ are the components of the strain; E, E' and μ, μ' are Young's moduli and shear moduli in the planes which are parallel and perpendicular to the isotropy plane, respectively; ν and ν' Poisson's coefficients characterizing the contraction in the plane of isotropy under tension in the plane of isotropy and in the directions normal to this plane, respectively.

The components of the strain are related to the displacement components $u_i\,(i = \alpha, \beta, \gamma)$ by the relations

$$\begin{aligned} e_{\alpha\alpha} &= \frac{1}{H_1}\frac{\partial u_\alpha}{\partial \alpha} + \frac{1}{H_1 H_2}\frac{\partial H_1}{\partial \beta}u_\beta + \frac{1}{H_1 H_3}\frac{\partial H_1}{\partial \gamma}u_\gamma, \\ e_{\alpha\beta} &= \frac{H_1}{H_2}\frac{\partial}{\partial \beta}\left(\frac{1}{H_1}u_\alpha\right) + \frac{H_2}{H_1}\frac{\partial}{\partial \alpha}\left(\frac{1}{H_2}u_\beta\right), \qquad \begin{pmatrix} \alpha & \beta & \gamma \\ 1 & 2 & 3 \end{pmatrix}. \end{aligned} \tag{2.3}$$

3 Wave surface geometry

Suppose that as a result of some shock exposure to a medium having curvilinear anisotropy, a surface of a strong discontinuity Σ propagating with the constant normal velocity G is generated.

Let the unit normal vector to the wave surface be aligned with the tangent to the coordinate line x_α and, moreover, $H_1 = 1$ (this assumption is justified by the fact that the coordinate lines x_α are the straight lines for the most important practical applications). Then from the relations given in Thomas (1967, sec.2.7), it follows that the normal trajectories to the wave surface Σ (normal trajectory is the line in the space $x_i\,(i = \alpha, \beta, \gamma)$ at every point of which the tangent unit vector coincides with the normal unit vector to Σ at the instant when the wave surface arrives at this point) are the straight lines ($\nu_\alpha = 1, \nu_\beta = \nu_\gamma = 0$) along which $x_\alpha = Gt + x_\alpha^0$ (x_α^0 is the initial magnitude of the value x_α) but x_β and x_γ remain constant and can be used as curvilinear coordinates on Σ (Ivlev and Bykovtsev, 1971).

Hence, the condition of compatibility on the wave surface for the desired value Z, which denotes one of the displacement velocity or stress components, reads

$$G[\partial Z_{,(k)}/\partial \alpha] = -[Z_{,(k+1)}] + \delta[Z_{,(k)}]/\delta t, \tag{3.1}$$

where the sign [...] denotes a difference in magnitudes of a certain value on different sides of the discontinuity surface, $[Z_{,(k)}]$ are the jumps of kth derivatives of the function Z with respect to time t, and $\delta/\delta t$ is the Thomas (1967) derivative.

To ascertain the validity of the formula (3.1), it is sufficient to check it for the jumps of derivatives of the components of a certain vector or tensor, e.g., of the displacement velocity, with respect to x_α. There is not need to use the compatibility condition for the jumps of derivatives of the same values with respect to x_β and x_γ, since these spatial coordinates are concurrently the curvilinear coordinates on the wave surface. Using tensor relations in curvilinear spatial coordinates [9]

$$\begin{aligned} [\partial v_j/\partial x^i] &= \lambda_j \nu_i + \Gamma_{ji}^m[v_m] + g^{\alpha\beta}g_{ik}[v_{j,\alpha}]x_\beta^k, \\ G\lambda_j &= -[\partial v_j/\partial t] + \delta[v_j]/\delta t - G\Gamma_{ji}^m[v_m]\nu^i, \end{aligned} \tag{3.2}$$

and eliminating the values λ_j from (3.2), we obtain

$$G[\partial v_j/\partial x^i] = -[\partial v_j/\partial t]\nu_i + \nu_i \delta[v_j]/\delta t - G\Gamma^m_{jn}[v_m]\nu^n\nu_i + G\Gamma^m_{ji}[v_m] + Gg^{\alpha\beta}g_{ik}[v_{j,\alpha}]x^k_\beta, \quad (3.3)$$

where v_j are covariant components of the velocity vector, $\lambda_j = [v_{j,k}]\nu^k$, ν_i and ν^i are the covariant and contravariant components of the normal unit vector tothe wave surface, respectively, g_{ij} and $g_{\alpha\beta}$ are the covariant components of the metric tensors in the space and on the wave surface, respectively, Γ^m_{ij} are Christoffel's symbols in the space, an index after a comma denotes the covariant derivative with respect to a corresponding spatial or surface coordinate, Latin indices take the values 1, 2, 3, Greek indices take the values 1, 2, the summation is performed over two repeated indices, x^i and u^β are curvilinear coordinates in the space and on the wave surface respectively, and $x^i_\beta = \partial x^i/\partial u^\beta$.

Setting $x^1 = x_\alpha = \alpha$ in Eq. (3.3) and invoking the above assumptions, Eq. (3.3) takes the form

$$G[\partial v_j/\partial\alpha] = -[\partial v_j/\partial t] + \delta[v_j]/\delta t. \quad (3.4)$$

Consider

$$v_j = v_j^{\text{phys}} H_j \text{ and } \delta H_j/\delta t = G\partial H_j/\partial\alpha.$$

where $v_1^{\text{phys}} = v_\alpha$, $v_2^{\text{phys}} = v_\beta$, and $v_3^{\text{phys}} = v_\gamma$, and on replacing v_j by $v_{j,(k)}$ in (3.4), we obtained the condition of compatibility (3.1) for $v^{\text{phys}}_{j,(k)}$.

Note that the compatibility condition (3.1) for the components of the desired values on the curvilinear surface Σ in the curvilinear coordinates is coincident with the compatibility condition for the corresponding values on a plane wave in Cartesian coordinates as the plane wave propagates along one of the coordinate axes.

4 Recurrent relations of the ray method

The solution for the desired function Z behind the wave surface Σ is constructed in terms of the ray series

$$Z = \sum_{k=0}^{\infty}(t - t_\alpha)^k[Z_{,(k)}]|_{t=t_\alpha}H(t - t_\alpha), \quad t_\alpha = \frac{x_\alpha - x^0_\alpha}{G}, \quad (4.1)$$

where $H(t)$ is the unit Heaviside function.

To determine the coefficients of the ray series for the desired functions v_i, σ_{ij} $(i, j = \alpha, \beta, \gamma)$, we differentiate Eqs.(2.1) k times and Eqs.(2.2) and (2.3) $(k + 1)$ times with respect to t, take their difference on the different sides of the wave surface and apply the conditions of compatibility (3.1). As a result we obtain

$$(\rho G^2 - c_1)[v_{\alpha,(k+1)}] = -2c_1 L[v_{\alpha,(k)}] + f_{\alpha,(k)} + F_{\alpha,(k-1)} \quad (4.2)$$

$$(\rho G^2 - \mu)[v_{\beta,(k+1)}] = -2\mu L[v_{\beta,(k)}] + f_{\beta,(k)} + F_{\beta,(k-1)} \quad (4.3)$$

$$(\rho G^2 - \mu')[v_{\gamma,(k+1)}] = -2\mu' L[v_{\gamma,(k)}] + f_{\gamma,(k)} + F_{\gamma,(k-1)} \quad (4.4)$$

where $Lu = \delta u/\delta t + 1/2\, Gu\partial \ln(H_2H_3)/\partial\alpha$, $c_1 = 1/2b + \mu$, $b = (1 - \nu)/E - 2\nu'^2/E'$, the functions $f_{i(k)}$ and $F_{i(k-1)}$ are dependent on the discontinuities of the kth and $(k - 1)$ order, respectively.

At $k = -1$ the recurrent Eqs.(4.2)-(4.4) govern the three types of nonstationary waves: one quasi-longitudinal and two quasi-transverse waves propagating with the respective velocities

$$G^{(1)} = (c_1/\rho)^{1/2}, \quad G^{(2)} = (\mu/\rho)^{1/2}, \quad G^{(3)} = (\mu'/\rho)^{1/2}, \quad (4.5)$$

where an upper index in brackets pertains to an ordinal number of the wave.

It follows from (4.5) that in curvilinear anisotropic body only those waves, whose symmetry conforms to a symmetry of the considering body, propagate with constant velocities.

To apply the obtained formulas of the ray method to pseudo-isotropic bodies having spherical anisotropy, we set $\alpha = r$, $\beta = \theta$, $\gamma = \varphi$, $H_2 = r$, and $H_3 = r\sin\theta$. Then Eqs.(4.2)-(4.4) take the following form:

$$\begin{aligned}\left(\rho G^2 - c_1\right)[v_{r,(k+1)}] &= -2c_1\frac{\delta[v_{r,(k)}]}{\delta t} - 2\frac{Gc_1}{r}[v_{r,(k)}] - \frac{G}{r}(\mu + c_3)\cot\theta[v_{\theta,(k)}] \\ &\quad -\frac{G}{r}\left((\mu + c_2)\frac{\partial[v_{\theta,(k)}]}{\partial\theta} + \frac{\mu' + c_3}{\sin\theta}\frac{\partial[v_{\varphi,(k)}]}{\partial\varphi}\right) + F_{r(k-1)}\end{aligned} \tag{4.6}$$

$$\begin{aligned}\left(\rho G^2 - \mu\right)[v_{\theta,(k+1)}] &= -2\mu\frac{\delta[v_{\theta,(k)}]}{\delta t} - 2\frac{G\mu}{r}[v_{\theta,(k)}] + \frac{G}{r}\biggl((c_3 - c_2)\cot\theta[v_{r,(k)}] \\ &\quad -(c_2 + \mu)\frac{\partial[v_{r,(k)}]}{\partial\theta}\biggr) + F_{\theta(k-1)}\end{aligned} \tag{4.7}$$

$$\left(\rho G^2 - \mu'\right)[v_{\varphi,(k+1)}] = -2\mu'\frac{\delta[v_{\varphi,(k)}]}{\delta t} - 2\frac{G\mu'}{r}[v_{\varphi,(k)}] - \frac{G}{r}\frac{c_3 + \mu'}{\sin\theta}\frac{\partial[v_{r,(k)}]}{\partial\varphi} + F_{\varphi(k-1)} \tag{4.8}$$

where

$$\begin{aligned}F_{r(k-1)} &= c_1\frac{\delta^2[v_{r,(k-1)}]}{\delta t^2} + \frac{G}{r}\biggl(2c_1\frac{\delta[v_{r,(k-1)}]}{\delta t} + (\mu + c_3)\cot\theta\frac{\delta[v_{\theta,(k-1)}]}{\delta t}\ (\mu + c_2)\frac{\partial}{\partial\theta}\frac{\delta[v_{\theta,(k-1)}]}{\delta t} \\ &\quad +\frac{\mu' + c_3}{\sin\theta}\frac{\partial}{\partial\varphi}\frac{\delta[v_{\varphi,(k-1)}]}{\delta t}\biggr) + \frac{G^2}{r^2}\biggl(-c_5[v_{r,(k-1)}] + \mu\cot\theta\frac{\partial[v_{r,(k-1)}]}{\partial\theta} + \mu\frac{\partial^2[v_{r,(k-1)}]}{\partial\theta^2} \\ &\quad +\frac{\mu'}{\sin^2\theta}\frac{\partial^2[v_{r,(k-1)}]}{\partial\varphi^2} - (\mu + c_4)\cot\theta[v_{\theta,(k-1)}] - (3\mu + c_3)\frac{\partial[v_{\theta,(k-1)}]}{\partial\theta} - \frac{c_4 + \mu'}{\sin\theta}\frac{\partial[v_{\varphi,(k-1)}]}{\partial\varphi}\biggr),\end{aligned}$$

$$\begin{aligned}F_{\theta(k-1)} &= \mu\frac{\delta^2[v_{\theta,(k-1)}]}{\delta t^2} + \frac{G}{r}\left(2\mu\frac{\delta[v_{\theta,(k-1)}]}{\delta t} + (c_2 - c_3)\cot\theta\frac{\delta[v_{r,(k-1)}]}{\delta t} + (\mu + c_2)\frac{\partial}{\partial\theta}\frac{\delta[v_{r,(k-1)}]}{\delta t}\right) \\ &\quad +\frac{G^2}{r^2}\biggl(-(c_3 + 2\mu + c_4\cot^2\theta)[v_{\theta,(k-1)}] + c_1\cot\theta\frac{\partial[v_{\theta,(k-1)}]}{\partial\theta} + c_1\frac{\partial^2[v_{\theta,(k-1)}]}{\partial\theta^2} \\ &\quad +\frac{\mu'}{\sin^2\theta}\frac{\partial^2[v_{\theta,(k-1)}]}{\partial\varphi^2} + (c_1 - c_4)\cot\theta[v_{r,(k-1)}] + (c_1 + c_3 + 2\mu)\frac{\partial[v_{r,(k-1)}]}{\partial\theta} \\ &\quad -(c_4 + \mu')\frac{\cot\theta}{\sin\theta}\frac{\partial[v_{\varphi,(k-1)}]}{\partial\varphi} + \frac{c_3 + \mu'}{\sin\theta}\frac{\partial^2[v_{\varphi,(k-1)}]}{\partial\theta\partial\varphi}\biggr),\end{aligned}$$

$$\begin{aligned}F_{\varphi(k-1)} &= \mu'\frac{\delta^2[v_{\varphi,(k-1)}]}{\delta t^2} + \frac{G}{r}\left(2\mu'\frac{\delta[v_{\varphi,(k-1)}]}{\delta t} + \frac{\mu' + c_3}{\sin\theta}\frac{\partial}{\partial\varphi}\frac{\delta[v_{r,(k-1)}]}{\delta t}\right) \\ &\quad +\frac{G^2}{r^2}\biggl(-\frac{\mu'}{\sin^2\theta}[v_{\varphi,(k-1)}] + \frac{c_4}{\sin^2\theta}\frac{\partial^2[v_{\varphi,(k-1)}]}{\partial^2\varphi} + \mu'\cot\theta\frac{\partial[v_{\varphi,(k-1)}]}{\partial\theta} + \mu'\frac{\partial^2[v_{\varphi,(k-1)}]}{\partial\theta^2} \\ &\quad +\frac{c_3 + c_4 + 2\mu'}{\sin\theta}\frac{\partial[v_{r,(k-1)}]}{\partial\varphi} + (c_4 + \mu')\frac{\cot\theta}{\sin\theta}\frac{\partial[v_{\theta,(k-1)}]}{\partial\varphi} + \frac{c_3 + \mu'}{\sin\theta}\frac{\partial^2[v_{\theta,(k-1)}]}{\partial\theta\partial\varphi}\biggr).\end{aligned}$$

where $c_2 = c_1 - 2\mu$, $c_3 = \nu'/b$, $c_4 = E' + 2\nu' c_3$, and $c_5 = 2\mu + c_3 + c_4$.

Putting $k = 0, 1$ in Eqs.(4.6)-(4.8) yields
on the first wave

$$[v_{r,(0)}] = c_{(0)}(\theta, \varphi)r^{-1}, \quad [v_{\theta,(0)}] = [v_{\varphi,(0)}] = 0$$

$$[v_{\theta,(1)}] = \frac{G}{r^2}\left(-c_{(0),\theta} + \frac{c_3 - c_2}{c_1 - \mu}\cot\theta\ c_{(0)}\right), \quad [v_{\varphi,(1)}] = -\frac{G}{r^2}\frac{c_3 + \mu'}{c_1 - \mu'}\frac{1}{\sin\theta}c_{(0),\varphi}$$

$$[v_{r,(1)}] = c_{(1)}(\theta,\varphi)r^{-1} - \frac{1}{2}\frac{G}{r^2}\left\{c_{(0),\theta\theta} + \cot\theta\, c_{(0),\theta} + \frac{1}{\sin^2\theta}\frac{c_6}{c_1(c_1 - mu')}c_{(0),\varphi\varphi}\right.$$
$$\left. - \left(\cot^2\theta\,\frac{(c_3 - c_2)^2}{c_1(c_1-\mu)} + \frac{c_1 + c_4}{c_1}\right)c_{(0)}\right\}; \tag{4.9}$$

on the second wave

$$[v_{\theta,(0)}] = g_{(0)}(\theta,\varphi)r^{-1}, \quad [v_{r,(0)}] = [v_{\varphi,(0)}] = 0$$
$$[v_{r,(1)}] = \frac{G}{r^2}\left(g_{(0),\theta} + \frac{c_3+\mu}{c_1-\mu}\cot\theta\, g_{(0)}\right), \quad [v_{\varphi,(1)}] = 0$$
$$[v_{\theta,(1)}] = g_{(1)}(\theta,\varphi)r^{-1} - \frac{1}{2}\frac{G}{r^2}\left\{\left[\cot\theta\left(\frac{(\mu+c_3)(c_3-c_2)}{(c_1-\mu)\mu} + \frac{\mu+c_3-c_4}{\mu}\right) - 1\right]g_{(0)}\right.$$
$$\left. + \cot\theta\, g_{(0),\theta} + g_{(0),\theta\theta} + \frac{1}{\sin^2\theta}\,\frac{\mu'}{\mu}g_{(0),\varphi\varphi}\right\}; \tag{4.10}$$

on the third wave

$$[v_{\varphi,(0)}] = h_{(0)}(\theta,\varphi)r^{-1}, \quad [v_{r,(0)}] = [v_{\theta,(0)}] = 0$$
$$[v_{r,(1)}] = \frac{G}{r^2}\frac{c_3+\mu'}{c_1-\mu'}\frac{1}{\sin\theta}h_{(0),\varphi}, \quad [v_{\theta,(1)}] = 0$$
$$[v_{\varphi,(1)}] = h_{(1)}(\theta,\varphi)r^{-1} - \frac{1}{2}\frac{G}{r^2}\left\{-\frac{1}{\sin^2\theta}h_{(0)} + \cot\theta\, h_{(0),\theta} + h_{(0),\theta\theta}\right.$$
$$\left. + \frac{1}{\sin^2\theta}\left(\frac{c_4}{\mu'} - \frac{(c_3+\mu')^2}{\mu'(c_1-\mu')}\right)h_{(0),\varphi\varphi}\right\}; \tag{4.11}$$

Substituting the known jumps (4.9)-(4.11) into the ray series (4.1), we determine the relations for velocities behind each front of the three waves and their superposition gives the solution we are looking for

$$V_r = \frac{c_{(0)}}{r}H\left(t - \frac{r-a}{G^{(1)}}\right) + \left\{\frac{c_{(1)}}{r} - \frac{1}{2}\frac{G^{(1)}}{r^2}\left(c_{(0),\theta\theta} + \cot\theta\, c_{(0),\theta} + \frac{1}{\sin^2\theta}\frac{c_6}{c_1(c_1-\mu')}c_{(0),\varphi\varphi}\right.\right.$$
$$\left.\left. - \left(\cot^2\theta\,\frac{(c_3-c_2)^2}{c_1(c_1-\mu)} + \frac{c_1+c_4}{c_1}\right)c_{(0)}\right)\right\}\left(t - \frac{r-a}{G^{(1)}}\right)H\left(t - \frac{r-a}{G^{(1)}}\right)$$
$$+\frac{G^{(2)}}{r^2}\left(g_{(0),\theta} + \frac{c_3+\mu}{c_1-\mu}\cot\theta\, g_{(0)}\right)\left(t - \frac{r-a}{G^{(2)}}\right)H\left(t - \frac{r-a}{G^{(2)}}\right)$$
$$\frac{G^{(3)}}{r^2}\frac{c_3+\mu'}{c_1-\mu'}\frac{1}{\sin\theta}h_{(0),\varphi}\left(t - \frac{r-a}{G^{(3)}}\right)H\left(t - \frac{r-a}{G^{(3)}}\right) \tag{4.12}$$

$$V_\theta = \frac{g_{(0)}}{r}H\left(t - \frac{r-a}{G^{(2)}}\right) + \left\{\frac{g_{(1)}}{r} - \frac{1}{2}\frac{G^{(2)}}{r^2}\left(\cot\theta\left(\frac{(\mu+c_3)(c_3-c_2)}{(c_1-\mu)\mu} + \frac{\mu+c_3-c_4}{\mu}\right) - 1\right)g_{(0)}\right.$$
$$\left. + \cot\theta\, g_{(0),\theta} + g_{(0),\theta\theta} + \frac{1}{\sin^2\theta}\,\frac{\mu'}{\mu}g_{(0),\varphi\varphi}\Big)\right\}\left(t - \frac{r-a}{G^{(2)}}\right)H\left(t - \frac{r-a}{G^{(2)}}\right)$$
$$+\frac{G^{(1)}}{r^2}\left(-c_{(0),\theta} + \frac{c_3-c_2}{c_1-\mu}\cot\theta\, c_{(0)}\right)\left(t - \frac{r-a}{G^{(1)}}\right)H\left(t - \frac{r-a}{G^{(1)}}\right) \tag{4.13}$$

$$V_\varphi = \frac{h_{(0)}}{r}H\left(t - \frac{r-a}{G^{(3)}}\right) + \left\{\frac{h_{(1)}}{r} - \frac{1}{2}\frac{G^{(3)}}{r^2}\left(-\frac{1}{\sin^2\theta}h_{(0)} + \cot\theta\, h_{(0),\theta} + h_{(0),\theta\theta}\right.\right.$$

$$+\frac{1}{\sin^2\theta}\left(\frac{c_4}{\mu'}-\frac{(c_3+\mu')^2}{\mu'(c_1-\mu')}\right)h_{(0),\varphi\varphi}\Bigg)\Bigg\}\left(t-\frac{r-a}{G^{(3)}}\right)H\left(t-\frac{r-a}{G^{(3)}}\right)$$

$$-\frac{G}{r^2}\frac{c_3+\mu'}{c_1-\mu'}\frac{1}{\sin\theta}c_{(0),\varphi}\left(t-\frac{r-a}{G^{(1)}}\right)H\left(t-\frac{r-a}{G^{(1)}}\right) \tag{4.14}$$

Three sets of the arbitrary functions $c_{(k)}(\theta,\varphi)$, $g_{(k)}(\theta,\varphi)$, and $h_{(k)}(\theta,\varphi)$ must satisfy either of two types of the boundary conditions

$$V_i|_{r=a} = V_i^0(\theta,\varphi)H(t) \tag{4.15}$$

or

$$\sigma_{ri}|_{r=a} = \sigma_{ri}^0(\theta,\varphi)H(t) \tag{4.16}$$

where $V_i^0(\theta,\varphi)$ and $\sigma_{ri}^0(\theta,\varphi)$ are given functions.

Substituting the arbitrary functions found from the boundary conditions (4.15) or (4.16) into superposition of the ray series behind the fronts of three waves (4.12)-(4.14), we obtain the final expressions for the solution of the boundary problems.

Acknowledgements

The research described in this publication has been made possible in part by Grant No.97-01-0651 from the Russian Foundation for Basic Research.

REFERENCES

Chou T.-W., Ko, F.K. (eds.): Textile structural composites. Amsterdam: Elsevier 1989.

Conway, H.D., Farnham, K.A., Ku, T.C.: The indentation of a transversely isotropic half space by a rigid shere. Trans. ASME. J. Appl. Mech. **34**, 491-492 (1967).

Ivlev, D.D., Bykovtsev, G.I.: Theory of a strengthening elastic body. Moscow: Nauka 1971.

Jones R.M.: Mechanics of composite materials. Washington: Scripta Book 1975.

Lekhnitsky, S.G.: Theory of elasticity of an anisotropic elastic body. San-Francicko: Holden-Day 1963.

Love, A.E.H.: A treatise on the mathematical theory of elasticity. Cambridge: University Press 1927.

Mitra, M.: Propagation of elastic waves in an infinite plate of cilindrically aelotropic material. ZAMP **10**, 579-583 (1959).

Ohnabe, H., Nowinski, J. L.: On the propagation of flexural waves in anisotropic bars. Ing. Arch. **40.** 327-338 (1971).

Rossikhin, Yu.A., Shitikova, M.V.: Ray method for solving dynamic problems connected with propagation of wave surfaces of strong and weak discontinuities. Appl. Mechanics Reviews **48**(1), 1-39 (1995).

Toshiaki, H.: Determination of transient thermoelastic responses of a thick-walled transversely isotropic spherical shell by the ray theory. Trans. JSME.A. **56**,2130-2136 (1990).

Thomas, T.Y.: Plastic flow and fracture in solids. New York: Academic Press 1961.

EXACT ELASTICITY SOLUTION FOR INVESTIGATION PECULIARITIES IN DEFORMATIONS OF THICK PLATES AND SHELLS IN COMPOSITE MATERIALS

S. M. Galileev, A. V. Matrosov
State University for Water Communications, 7 Admiralteiskii Canal, Apt. 5, St.Petersburg,
190000, Russia, e-mail: galiley@pop3.rcom.ru

N. N. Gubin
Scientific and Manufacturing Firm "Sigma-ST", Moscow, Russia

I. N. Miroshnichenko
Central Research Institute of Design Materials "Prometey", St.Petersburg, Russia

1 INTRODUCTION

Many models of structures in composite materials are based on the notions of the linearly elastic theory of anisotropic solids. Using three dimensional models allows to reveal peculiarities in the stress and strain state which couldn't be detected by numerical methods and approximate nonclassical (refined) theories. This is concerned with the existence of great gradients of stresses and displacements, substantial anisotropic elastic features of materials, local concentrated loads and also dynamic character of problems. For analysis of such complicated models analytical methods are the most effective ones, e.g. such that the method of initial functions (MIF).

MIF was proposed by A.S. Maliev [1] in 1951 and then it was developed and applied in studies by his pupils and followers. One can find the most complete survey in [2].

The MIF is based on representation of displacements and stresses in a solid body in terms of initial functions which are displacements and stresses determined on one of coordinate surface (initial surface). Such a representation is realized by operators which are power series on one of coordinate variables with coefficients in form of differential operators. As a rule not all of the initial functions are known. They can be found satisfying the boundary conditions on the surface which is equidistant to the initial surface. The differential equations for finding the unknown initial functions can be solved by various methods. Finding the solution in trigonometric series is the most popular one. In this case the problem is reduced to determining three unknown Fourie coefficients (for every m and n in expansion). Such an approach is very convenient for investigation of layered structures, because a number of unknown coefficients is equal to three and does not depend on a number of layers in the structure.

2 BASIC EQUATIONS

The basic equations of the elasticity theory of anisotropic bodies in curvilinear orthogonal coordinate system α,β,γ may be expressed in matrix operator form as

equations of motion

$$\mathbf{a}\mathbf{s}_1+\mathbf{b}_1\mathbf{s}_1+\mathbf{c}_1\mathbf{s}_2+\mathbf{d}\mathbf{W}=\mathbf{0}, \tag{1}$$

Cauchy's relations

$$\begin{aligned}\boldsymbol{\varepsilon}_1&=\frac{1}{H_1H_2H_3}(\mathbf{a}\mathbf{W}+\mathbf{b}\mathbf{W}),\\ \boldsymbol{\varepsilon}_2&=\frac{1}{H_1H_2H_3}\mathbf{c}\mathbf{W},\end{aligned} \tag{2}$$

generalised Hook's law

$$\begin{aligned}\boldsymbol{\sigma}_1&=\mathbf{P}\boldsymbol{\varepsilon}_1+\mathbf{Q}\boldsymbol{\varepsilon}_2,\\ \boldsymbol{\sigma}_2&=\mathbf{S}\boldsymbol{\varepsilon}_1+\mathbf{T}\boldsymbol{\varepsilon}_2.\end{aligned} \tag{3}$$

Here $\boldsymbol{\sigma}_1=\{\tau_{\gamma\alpha}\ \tau_{\gamma\beta}\ \sigma_\gamma\}$, $\boldsymbol{\sigma}_2=\{\sigma_\alpha\ \sigma_\beta\ \tau_{\alpha\beta}\}$, $\boldsymbol{\varepsilon}_1=\{\varepsilon_{\gamma\alpha}\ \varepsilon_{\gamma\beta}\ \varepsilon_\gamma\}$, $\boldsymbol{\varepsilon}_2=\{\varepsilon_\alpha\ \varepsilon_\beta\ \varepsilon_{\alpha\beta}\}$, $\mathbf{W}=\{u_\alpha\ v_\beta\ w_\gamma\}$.

Matrices $\mathbf{a},\mathbf{b}_1,\mathbf{c}_1,\mathbf{c},\mathbf{d}$ — operator matrices which entries consist of the differential operators $\partial_\alpha,\partial_\beta,\partial_\gamma$, Lame's coefficients H_1,H_2,H_3; $\mathbf{P},\mathbf{Q},\mathbf{S},\mathbf{T}$ — matrices of the elastic constants A_{ij}.

Using these relations the equations of the mixed method are derived as

$$\partial_\gamma\mathbf{U}_0=\mathbf{D}\mathbf{U}_0,$$

$$\mathbf{D}=\begin{bmatrix}-\dfrac{1}{H_1H_2}\left(\mathbf{b}+\mathbf{P}^{-1}\mathbf{Q}\mathbf{c}\right) & H_3\mathbf{P}^{-1}\\ \dfrac{1}{H_1H_2}\mathbf{c}_1\left(\dfrac{\mathbf{S}\mathbf{P}^{-1}\mathbf{Q}+\mathbf{T}}{H_1H_2H_3}\mathbf{c}\right)-\mathbf{d} & -\dfrac{1}{H_1H_2}\left(\mathbf{b}_1+\mathbf{S}\mathbf{P}^{-1}\mathbf{c}_1\right)\end{bmatrix} \tag{4}$$

$$s_2 = \mathbf{BU_0},$$

$$\mathbf{B} = \left[-\frac{1}{H_1 H_2 H_3}\left(\mathbf{SP^{-1}Q - T}\right)\mathbf{c} \quad \mathbf{SP^{-1}} \right]. \qquad (5)$$

Here $\mathbf{U_0} = \left\{ u_\alpha \; u_\beta \; u_\gamma \; \tau_{\gamma\alpha} \; \tau_{\gamma\beta} \; \sigma_\gamma \right\}$.

The methods of computational algebra enables the equations of the method of initial functions to be derived as

$$\mathbf{U} = \mathbf{LU^0}, \qquad (6)$$

where $\mathbf{L} = \left[L_{ij} \right]$, $i = 1,2,K,9$, $j = 1,2,K,6$ - the matrix of the differential operators of the method, $\mathbf{U^0} = \left\{ u_\alpha^0 \; u_\beta^0 \; u_\gamma^0 \; \tau_{\gamma\beta}^0 \; \tau_{\gamma\alpha}^0 \; \sigma_\gamma^0 \right\}$, $\mathbf{U} = \left\{ u_\alpha \; u_\beta \; u_\gamma \; \tau_{\gamma\alpha} \; \tau_{\gamma\beta} \; \sigma_\gamma \; \sigma_\alpha \; \sigma_\beta \; \tau_{\alpha\beta} \right\}$.

The basic equations of the MIF for cylindrical shells or thick rectangular plates can be written also in the form (6) but with other entries.

For circular cylindrical shells: $\mathbf{U} = \left\{ u, v, w, \tau_{rz}, \sigma_r, \tau_{r\theta}, \sigma_z, \sigma_\theta, \tau_{z\theta} \right\}$, $\mathbf{U^0} = \left\{ u^0, v^0, w^0, \sigma_r^0, \tau_{rz}^0, \tau_{r\theta}^0 \right\}$, $\mathbf{L} = \left[L_{ij} \right]$, L_{ij} are operator-functions which are power series in terms of the variable r; the entries of the vectors $\mathbf{U} = \left\{ u_\alpha \; u_\beta \; u_\gamma \; \tau_{\gamma\alpha} \; \tau_{\gamma\beta} \; \sigma_\gamma \; \sigma_\alpha \; \sigma_\beta \; \tau_{\alpha\beta} \right\}$ and $\mathbf{U^0} = \left\{ u_\alpha^0 \; u_\beta^0 \; u_\gamma^0 \; \tau_{\gamma\beta}^0 \; \tau_{\gamma\alpha}^0 \; \sigma_\gamma^0 \right\}$ are functions of the variables r, θ, z, t. The main equations for spherical shells and shells with boundaries are derived.

For anisotropic plates: $\mathbf{U} = \left\{ u, v, w, \sigma_z, \tau_{yz}, \tau_{xz}, \sigma_x, \sigma_y, \tau_{xy} \right\}$, $\mathbf{U^0} = \left\{ \tau_{xz}^0, \tau_{yz}^0, \sigma_z^0, w^0, v^0, u^0 \right\}$, $\mathbf{L} = \left[L_{ij} \right]$, $i = 1,2,K,9$, $j = 1,2,K,6$ are operator-functions which are power series in terms of the variable z.

A consideration of bound problems for plates and shells including layered ones allow to state and solve the problems from a common position and, it is extremely important, to estimate for sure the accuracy of solutions. For a large class of problems this method enables exact solutions to be derived without employing any hypotheses about the character of the stress and strain state of the structures.

For example, exact governing equations of the bending problem of an anisotropic plate subjected to the load on the top surface $\mathbf{U}_\sigma^\mathbf{0} = \left\{\tau_{xz}^0, \tau_{yz}^0, \sigma_z^0\right\}$ and on the bottom one $\mathbf{U}_\sigma^+ = \left\{\sigma_z^+, \tau_{yz}^+, \tau_{xz}^+\right\}$ may be found in the form

$$\mathbf{L}_\mathbf{w}^+ \mathbf{U}_\mathbf{w}^\mathbf{0} = \mathbf{U}^+ - \mathbf{L}_\sigma^+ \mathbf{U}_\sigma^\mathbf{0} , \tag{7}$$

ãäå $\mathbf{U}_\mathbf{w}^\mathbf{0} = \left\{w^0, v^0, u^0\right\}, \mathbf{L}_\mathbf{w}^+ = \left[L_{ij}\right]_h, i, j = 4{,}5{,}6; \mathbf{L}_\sigma^+ = \left[L_{ij}\right]_h, i = 4{,}5{,}6, j = 1{,}2{,}3$ are the matrices of operator functions L_{ij} determined when $z = h$.

Expanding the initial functions $\mathbf{U}^\mathbf{0}$ and the load functions $\mathbf{U}^+$ into the trigonometric series, the system of differential equations (7) becomes the system of the three linear algebraic equations for finding the unknown coefficients in the expanding of unknown functions $\mathbf{U}_\mathbf{w}^\mathbf{0}$.

Using (6), main equations of the MIF for analysis of laminated composite plates and shells may be derived. The layers are assumed to be perfectly bonded such that the interface conditions at any surface are expressed as

$$\left\{\tau_{xz}^k, \tau_{yz}^k, \sigma_z^k, w^k, v^k, u^k\right\} = \left\{\tau_{xz}^{k+1}, \tau_{yz}^{k+1}, \sigma_z^{k+1}, w^{k+1}, v^{k+1}, u^{k+1}\right\},$$

where the superscript k refers to the k-th layer. No one restriction on the thickness of layers, the number and sequence of layers, elastic constants and densities of layers is imposed.

The basic equations of this method for analysis of multy layered plates in composite materials are

$$\mathbf{U}^{\mathrm{k}}=\mathbf{L}^{\mathrm{k}}\mathbf{L}_0^{\mathrm{k-1}}\cdots\mathbf{L}_0^2\mathbf{L}_0^1\mathbf{U}^{\mathbf{0}}, \tag{8}$$

where $\mathbf{U}^0=\left\{\tau_{xz}^0,\tau_{yz}^o,\sigma_y^0,w^o,v^0,u^0\right\}$ — a vector of initial functions determined on the coordinate plane $z=0$, $\mathrm{U}=\left\{u,v,w,\sigma_z,\tau_{xz},\tau_{yz},\sigma_x,\sigma_y,\tau_{xy}\right\}$ — a vector of displacements and stresses, in the matrix $\mathbf{L}^{\mathrm{k}}$ the operator-functions L_{ij} are calculated for $z\in\left[0,h_k\right]$ and with elastic constants and density of the k-th layer: A_{ij}^k,ρ_k (for static problems $\partial_t=0$ or $\rho_k=0$); $\mathbf{L}_0^{\mathrm{n}}=\left[L_{ij}^n\right]$, $n=(k-1)K1$, $i=6K1$, $j=1K6$ — the matrices of the operator-functions when $z=h_m$, $m=(k-1)K1$ [3].

3 NUMERICAL RESULTS

Using the main equations two programs were designed: *MIFTP* for plate analysis, *MIFTP* for shell analysis. As an example consider a square plate with dimensions $a\times a$ and a thickness $h/a=1/3$. The plate consists of ten layers: ***layer 1***, isotropic, $E=0.315\cdot 10^5$, $\nu=0.2$, $\rho=2500$; ***layer 2*** , transversaly isotropic, $E=10^5$, E/E' = 5, E/G'=20 $\nu=\nu'=0.1$, $\rho=2000$; ***layer3,*** isotropic, $E=0.72\cdot 10^5$, $\nu=0.33$, $\rho=2800$; ***layer 4***, orthotropic, $E_x=0.46\cdot 10^5$, $E_y=0.16\cdot 10^5$, $E_Z=0.112\cdot 10^5$, $G_{xy}=0.056\cdot 10^5$, ν_{xy}=0,27, $\nu_{xz}=0.07$, $\nu_{yz}=0.3$, $\rho=1600$; ***layer 5*** , as a layer 3; ***layer 6***, transversaly isotropic, Å=10^4, Å/Å'=3, E/G'=5, $\nu=\nu'$=0,1 , $\rho=2000$; ***layer 7***, isotropic, Å=$2.1\cdot 10^5$, $\nu=0.3$, $\rho=7800$; ***layer 8***, continuously nonhomogeneous, Å = Å$_0$å^{0,5ÿ}, $\rho=\rho_0$å^{0,05z}, ν=0,2, $E_0=10^4$, $\rho_0=2000$; ***layer 9***, isotropic, Å=$0.008\cdot 10^5$, $\nu=0.47$, $\rho=1200$; ***layer 10***, as a layer 1. The dimension of Young's modulus is MPa, densities – kg/m^3. The layer thicknesses: $h_1/h=0.146$, $h_2/h=h_{10}/h=0.0976$, $h_3/h=h_5/h=h_7/h=0.0244$, $h_4/h=h_9/h=0.0488$, $h_6/h=0.195$, $h_8/h=0.293$.

The load in a static problem is $q=q_0\sin(\alpha_{\mathrm{m}}x)\sin(\beta_{\mathrm{n}}y)$, in dynamic one - $q=q_0\sin(\alpha_{\mathrm{m}}x)\sin(\beta_{\mathrm{n}}y)\mathrm{e}^{\mathrm{i}\omega t}$, $\omega=3000s^{-1}$, $\alpha_m=m\pi/a$, $\beta_n=n\pi/a$, $m=n=1$.

Some graph results are presented: Fig 1. (static), Fig. 4 (dynamic) displacements u in the section $x = 0, y = a/2$; Fig. 2 (static), Fig. 5 (dynamic) σ_x when $x = y = a/2$ (the center of the plate); Fig. 3 (static), Fig. 6 (dynamic) τ_{xz} when $x = 0, y = a/2$.

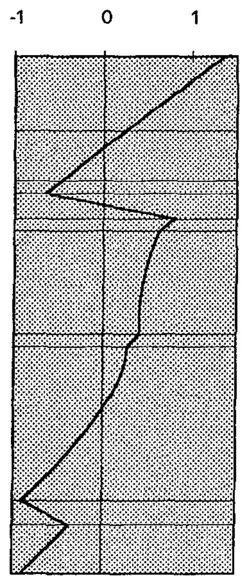

Fig. 1

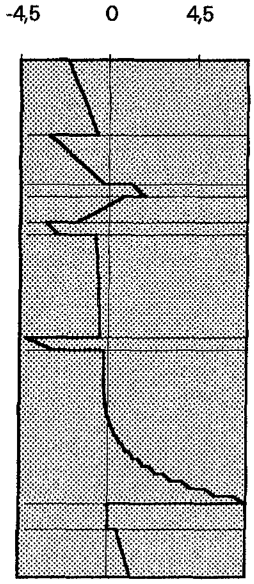

Fig. 2

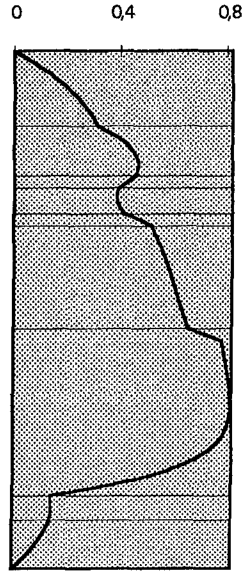

Fig. 3

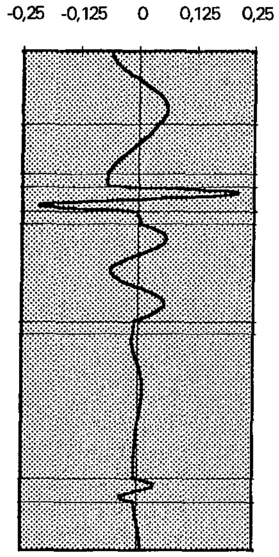

Fig. 4

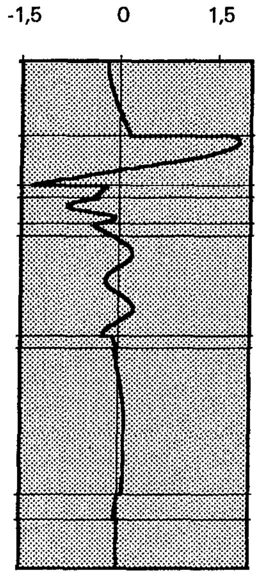

Fig. 5

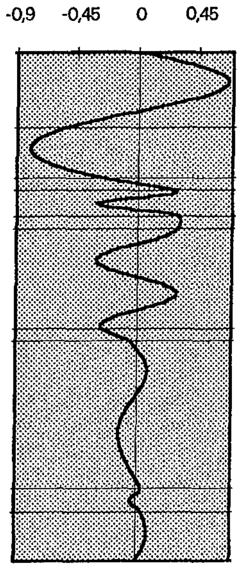

Fig. 6

The proper frequencies of the ten layered plate are presented in the Table 1 $(\omega^* = \omega a / \sqrt{E_1 / 2\rho_1 (1 + \nu'_1)})$.

Table 1

m,n	1,1	1,2	2,1	2,2	5,5	15,15	27,27	38,38
ω^*	1,8733	6,0821	6,1006	4,7793	20,4711	60,5255	84,1127	85,6951

The equations (6) allow to solve problems of investigation of the SSS of circular and spherical thick composite shells under static and dynamic loads. For example, consider the problem of the analysis of 10-layered circular shell under moving inner exponential load (Fig. 7). The character of the strain state of the wall of the shell when the wave velocity is equal to 1000m/s is shown on Fig. 8.

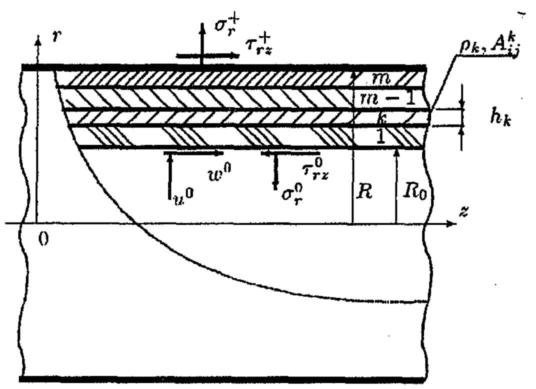

Fig. 7

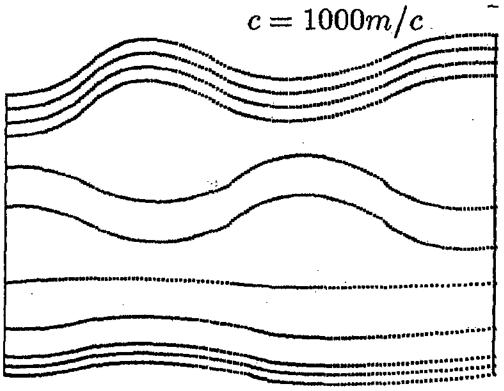

Fig. 8

REFERENCES

[1] A.S. Maliev, On Choosing Functions for General Solutions of Equilibrium Problems of an Isotropic Elastic Body. *Bulletin of Leningrad Electrotechnical Institute of Railway Transport Engineers*, **4** (1952), pp. 180-244 (in Russian)

[2] S.M. Galileev, Thesis for Doctor of Science Degree. St-Petersburg, 1992.

[3] S.M. Galileev, A.V. Matrosov, Stable Algorithms of the Method of Initial Functions in the Analysis of Thick Laminated Composite Plates. *Proc. Of First Int. Conf. On Composite Science and Technology (ICCST/1)*. Durban, South Africa, 1996, pp. 149-158.

COMPOSITE PLATES WITH UNDULATING SURFACES

MARIA KASHTALYAN

Timoshenko Institute of Mechanics, Nesterov str. 3, 252057 Kiev, Ukraine

ABSTRACT

Three-dimensional stress-strain analysis of laminated plates with interfaces, the shape of which is slightly perturbed and may be described by sufficiently smooth function of two variables and small dimensionless parameter, has been fulfilled. Using the method of perturbation of boundary shape based on representing of stresses and displacements as series in respect to the small parameter which describes the shape of interfaces, the initial three-dimensional problem of theory of elasticity has been reduced to the sequence of problems for the plate with perfectly flat interfaces. The influence of the interface shape (amplitude of waving and value of the wave-forming parameter) on stresses and deflection of isotropic two-layered plates under bending with periodically waved in one direction interfaces has been examined. To obtain the numerical results with sufficient accuracy first three approximations for stresses and displacements have been proved to be enough.

INTRODUCTION

Mechanical failure of composites often results from stress concentration at the interfaces due to the interface defects, imperfections and inhomogeneities inherited from the manufacturing process [1]. Imperfections of many varieties such as layers of uneven thickness, wavy layers or undulated interfaces in which nominally flat surfaces of the layers are developing during manufacturing, are present in laminated composite structures. The adhesion between the layers at the interfaces is not usually broken by the above-mentioned imperfections, and therefore, they may be considered as geometrical anomalies but not serious technological defects to be necessarily to avoid.

The nature of these imperfections reflects the nature of surface evolution dictated by the competition between surface and elastic energies. The nominally flat surface of an elastically stressed body is unstable with respect to the formation of surface undulations of wavelengths greater than some critical value

[2]. The amplitude of these perturbations is sufficiently small in comparison with structure length scales of the composite material structure. However, they could be so important in determining the response of composite materials that steps must be undertaken to understand their role.

For analytical description of deformation of macroscopically inhomogeneous solids like composite materials various kinds of continual theories have been developed and used in mechanics of composites, in which inhomogeneous material is modelled by the homogeneous anisotropic medium. Another approach to investigation of mechanical behaviour of composites is based on the structural model, i.e. the model of piecewise-homogeneous medium.

The first attempts to examine the role which play geometrical imperfections in the failure of composite material have been already undertaken within the both approaches [3]. They were concentrated on determination of self-equilibrated stresses in bulk composite material acting at the parts of the interfaces the size of which is comparable with or less than length scale of material structure. At this point the second approach is more advantageous, since structural model allows to determine the above stresses more precisely. However, no investigations of composite structures like plates or shells with geometrical interfacial imperfections has not yet been made.

The present paper is focused on investigation of stress distribution in laminated plates with perturbed interfaces and on examination of stress redistribution effects due to this kind of geometrical imperfections.

PROBLEM STATEMENT

The problem statement is as follows. Laminated plate of finite dimensions $0 \leq x \leq a$, $0 \leq y \leq b$ with surfaces and interfaces S_i $(i = 0, N)$ has been considered. External surfaces and interfaces are being treated as slightly perturbed from reference state in which they would be perfectly flat. Their geometry is assumed to allow description by sufficiently smooth function of two variables which characterises the shape, and a small dimensionless parameter ϵ which characterise the magnitude of deviation from the appropriate reference plate $z = h_i$. The interface shape equations are then:

$$S_i : z = h_i + \epsilon f(x, y), \qquad (h_0 = 0, h_N = h) \tag{1}$$

Suppose the bonding between the layers is perfect, and continuity conditions for stresses and displacements are fulfilled at the interfaces:

$$S_k \quad : \quad (\sigma_{xt,k+1} - \sigma_{xt,k})n_{x,k} + (\sigma_{yt,k+1} - \sigma_{yt,k})n_{y,k} +$$

$$+(\sigma_{zt,k+1} - \sigma_{zt,k})n_{z,k} = 0 \qquad (2)$$

$$S_k \ : \ u_{t,k} - u_{t,k+1} = 0, \qquad (t = x, y, z) \qquad (3)$$

where $\sigma_{jt,k}, u_{t,k}$ are stresses and displacements in the k-th layer $k = 1...N$; $n_{t,i}$ are direction cosines for S_i. Suppose plate is loaded by transversal load $Q(x, y)$ at the top surface with bottom surface free; boundary conditions at S_N, S_0 are:

$$S_N \ : \ \sigma_{xt,N}n_{x,N} + \sigma_{yt,N}n_{y,N} + \sigma_{zt,N}n_{z,N} = Q(x, y)n_{t,N}; \qquad (4)$$

$$S_0 \ : \ \sigma_{xt,1}n_{x,0} + \sigma_{yt,1}n_{y,0} + \sigma_{zt,1}n_{z,0} = 0; \qquad (5)$$

On the edge planes the boundary conditions of Navier type are assumed to be fulfilled for each layer.

Due to the complexity of the geometrical shape of the interfaces the stated three-dimensional boundary-value problem (1)-(2) cannot be solved directly, and the method of perturbation of boundary shape [4] has been applied. According to it, stresses and displacements as well as components of load and direct cosines in boundary conditions are to be presented as series in respect to the small parameter ϵ , i.e.

$$[\sigma_{jt,k}, u_{t,k}, Q_t, n_{t,i}] = \sum_{p=0}^{\infty} \epsilon^p [\sigma_{jt,k}^{(p)}, u_{t,k}^{(p)}, Q_t^{(p)}, n_{t,i}^{(p)}] \qquad (6)$$

and $\sigma_{jt,k}^{(p)}$ and $u_{t,k}^{(p)}$ are supposed to be expanded in Taylor series in vicinity of $z = h_i$, so that on S_i

$$[\sigma_{jt,k}, u_{t,k}]|_{S_i} = \sum_{p=0}^{\infty} \epsilon^p \sum_{q=0}^{p} \frac{f^q}{q!} \frac{\partial^q}{\partial z^q} [\sigma_{jt,k}^{(p-q)}, u_{t,k}^{(p-q)}]|_{z=h_i} \qquad (7)$$

By means of this approach the initial boundary-value problem for the plate with perturbed interfaces may be reduced to the sequence of recurrent boundary-value problems for plate with interfaces $z = h_i$.

NUMERICAL RESULTS

The analysis of stress distribution in two-layered free-supported plate under bending with periodically waved in one direction interfaces based on the above approach has been carried out. The load and shape functions were taken as follows:

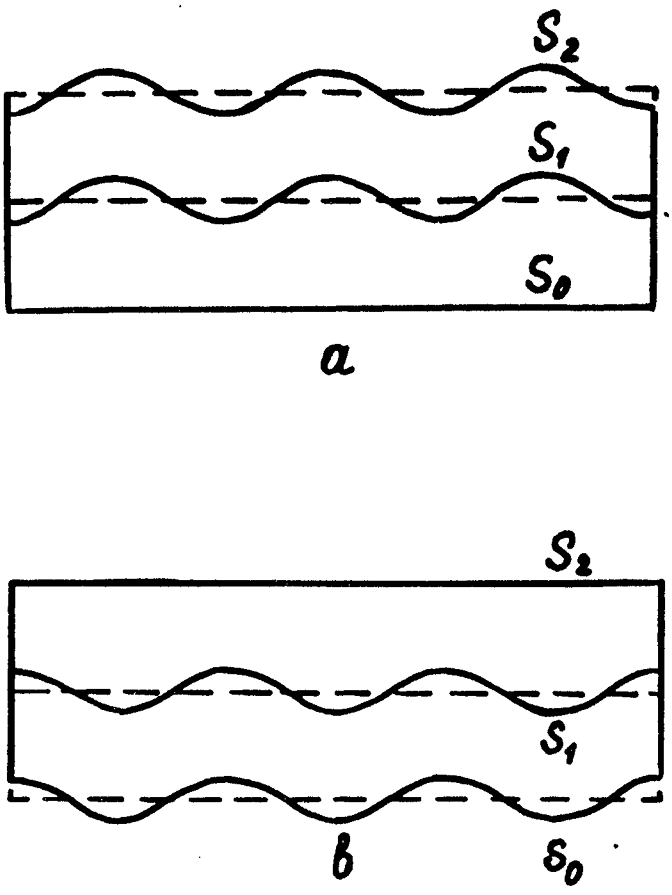

Figure 1: Types of plate geometry: a (at the top), b (at the bottom)

$$\begin{aligned} Q(x,y) &= -q\sin\frac{\pi x}{a}\sin\frac{\pi y}{b} \\ f(x,y) &= f(y) = \pm h\cos\frac{\pi\omega y}{b} \end{aligned} \tag{8}$$

where ω is a parameter of wave foundation. The layers were considered to be isotropic with shear moduli G_k and Poisson ratios $\nu_1 = \nu_2 = 0.3$. For solving of the obtained recurrent boundary-value problems Youngdahl's general solution of equilibrium equations [5] has been used.

Numerical results for the values of $\sigma_{xx,1}/q$ at the middle of perturbed interface S_1 ($\epsilon = 0.1$) in comparison with the appropriate data for the plate of the same dimensions ($h/a = 3$, $h/b = 18$, $h_1/h = 0.5$) but with perfectly flat interface $z = h_1$ are given in Table 1. These data, i.e. $\sigma_{xx,1}/q|_{z=h_1}$, are being the approximation of the 0-th order in the considered problem; the other results have been obtained using approximations up to the third orded and, hence, have the accuracy of $O(\epsilon^3)$. Stress analysis has been made for two types of plates, the profiles of which are shown on Figure 1 (for $\omega = 2$).

Table 1.

ω	$\frac{\sigma_{xx,1}}{q}\|_{z=h_1}$	a		b		$\frac{G_1}{G_2}$
		$\frac{\sigma_{xx,1}}{q}\|_{S_1}$	$\delta, \%$	$\frac{\sigma_{xx,1}}{q}\|_{S_1}$	$\delta, \%$	
2	-8.085	-7.099	-12.2	-6.620	-18.1	10
6	-8.085	-8.716	7.8	-6.204	-22.2	
10	-8.085	-9.641	19.3	-5.340	-33.8	
2	0.820	0.660	-19.5	0.737	-10.2	0.1
6	0.820	0.630	-23.2	0.900	9.7	
10	0.820	0.540	-34.1	0.993	21.1	

From the obtained results the conclusion about strong influence of the parameter of wave foundation and geometrical type of the plate on values of stresses at the perturbed interface can be made. Increasing of wave foundation parameter may increase as well as decrease the value of stresses depending on geometry of interface and shear moduli ratio.

REFERENCES

[1] Piatti, G. (ed.) Advances in Composite Materials. Applied Science Publishers, London (1978).

[2] Srolovitz, D.J. "On the stability of surfaces of stressed solids". *Acta Metallurgica* **37**, pp.621-625 (1989).

[3] Guz, A.N. (ed.) Mechanics of Composites. Vol. 4: Guz, A.N., Akbarov, S.D. (eds.) Mechanics of Materials with Curved Structures [in Russian]. Naukova Dumka, Kiev (1995).

[4] Nemish, Yu.N. Elements of the Mechanics of Piecewise-Homogeneous Bod-

ies with Non-Canonical Boundary Surfaces [in Russian]. Naukova Dumka, Kiev (1989).

[5] Youngdahl, C.K. "On the completeness of a set of stress functions appropriate to the solution of elasticity problems in general cylindrical coordinates". *International Journal of Engineering Sciences* **7**, pp.61-69 (1969).

THERMOELASTICITY OF SPATIALLY REINFORCED COMPOSITE PLATES

E.V. Morozov

Department of Mechanical Engineering, University of Natal, 4041 Durban, South Africa

INTRODUCTION

Implementation of composites with spatial orientation of reinforcement has necessitated and resulted in the formulation and analytical use of new theoretical models suitable for the analysis and design of composite structural components. The main objective of this paper is the development of a thermoelastic plate theory, which could be applied to the analysis of spatially reinforced thin-walled composite structures. The governing equations of such a theory should take into account the basic features of material structure and the number of effects such as transversal shear deformability and general anisotropy of physical and mechanical characteristics. This is achieved by introducing special averaging procedures for mechanical parameters such as transverse stresses and strains as well as for physical characteristics of thermal conductivity and heat transfer. As a result the system of equations produced on the basis of the proposed formulation provides the possibility to analyse the stress-strain state of spatially-reinforced composite plates subjected to mechanical and thermal loads.

MATERIAL STRUCTURE

Consider a spatially-reinforced element of the composite plate of thickness *h*. The coordinate axes are x_1, x_2 and x_3, where x_3 is perpendicular to the plate, with the original lying in the reference surface of the plate as shown in Figure 1.

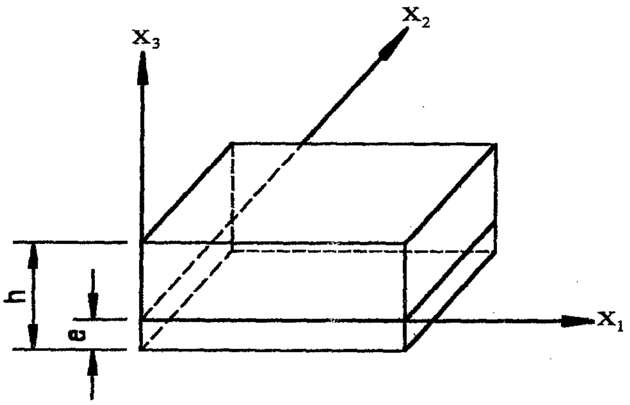

Figure 1. An element of a plate in an orthogonal reference system

The bottom plane of the plate is situated at the distance *e* from the reference surface. The plate consists of a spatially oriented orthotropic layers. The material coordinate system is represented by axes x_1', x_2', x_3', where x_1' direction coincides with the fibre orientation for unidirectional orthotropic layer or with the basic fibre orientation for fabric reinforcement. As shown in Figure 2 the orientation of the orthotropic elementary layer is characterized by three angles of reinforcement orientation ϕ, ψ, η [1]. Apparently the material with this sort of reinforcement orientation exposes a general type of anisotropy of physical and mechanical properties with respect to the x_1, x_2 and x_3 system of coordinates. The variant of applied theory of spatially reinforced shells has been obtained in Reference [1] by reducing the three-dimensional elasticity theory equations to the two-dimensional system. The hypothesis of free thermal expansion in the direction orthogonal to the reference surface has been introduced. In this work the similar approach is used to reduce three-dimensional equations of thermal conductivity to the two-dimensional ones and obtain the specific coefficients of the thermoelastic theory of spatially reinforced anisotropic plates..

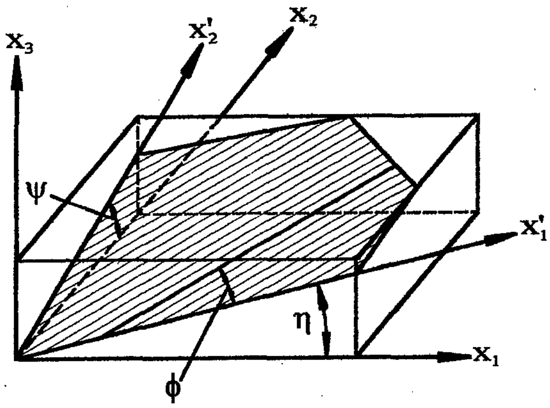

Figure 2. Spatial orientation of the composite reinforcement

THERMAL CONDUCTIVITY ANALYSIS

The equations of thermoelasticity for the composite plate considered in this paper can be derived on the basis of the approach implemented in References [1, 2]. Three-dimensional coupled heat equation of thermal conductivity may be written in the following form [3]

$$\left(\lambda_{ij}t_{,i}\right)_{j} - t\beta_{ij}\dot{e}_{ij} = c_v\dot{\theta} - w_t \qquad (1)$$

where λ_{ij} are the coefficients of thermal conductivity; *t* is the temperature; β_{ij} are the thermal physical coefficients of the material; e_{ij} are the components of the strain tensor; c_v is the volumetric specific heat; θ is the local temperature change ; w_t is the density of internal heat sources. For given system of coordinate x_1, x_2 and x_3, related to the reference surface, the Fourier law of heat conduction is presented as follows

$$q_{ij} = -\lambda_{ij} \frac{\partial t}{\partial x_j} \qquad (2)$$

where q_{ij} are the components of the heat flux vectors. According to Onsager's reciprocal hypothesis the symmetry conditions should be satisfied, i.e. $\lambda_{ij} = \lambda_{ji}$ [4]. The coefficients of thermal conductivity λ_{ij} may be expressed in terms of the coefficients of thermal conductivity of the elementary layers λ'_{ij} in the following form

$$\lambda_{ij} = \lambda'_{ij} l_{ij} l_{ji}$$

where the coefficients l_{ij} may be calculated as follows [1]

$$\begin{gathered}
l_{11} = \cos\chi\cos\zeta; \quad l_{12} = -\sin\chi\cos\zeta; \quad l_{13} = -\sin\zeta; \\
l_{21} = \sin\chi\cos\psi - \sin\psi\sin\zeta\cos\chi; \\
l_{22} = \cos\chi\cos\psi + \sin\psi\sin\chi\sin\zeta; \quad l_{23} = -\sin\psi\cos\zeta; \\
l_{31} = \sin\psi\sin\chi + \cos\psi\cos\chi\sin\zeta; \\
l_{32} = \sin\psi\cos\chi - \cos\psi\sin\chi\sin\zeta; \quad l_{33} = \cos\psi\cos\zeta; \\
\zeta = \tan^{-1}(\tan\eta\cos\psi); \quad \chi = \phi + \tan^{-1}(\sin\zeta\tan\psi);
\end{gathered}$$

Substituting for λ_{ij} from (2) in the equations (1) gives

$$\begin{gathered}
\frac{\partial}{\partial x_1}\left[q_{11} + q_{12} + q_{13}\right] + \frac{\partial}{\partial x_2}\left[q_{21} + q_{22} + q_{33}\right] + \\
+ \frac{\partial}{\partial x_3}\left[q_{31} + q_{32} + q_{33}\right] = t\beta_{ij}\dot{e}_{ij} - c_v\dot{\theta} + w_t
\end{gathered} \qquad (3)$$

Assume that the boundary conditions at the surfaces $x_3 = -e$ and $x_3 = h - e$ are given in Newton's form

$$\left[\lambda_{33}\frac{\partial t}{\partial x_3} + \lambda_{32}\frac{\partial t}{\partial x_2} + \lambda_{31}\frac{\partial t}{\partial x_1}\right] \pm \alpha^{\pm}(x_1, x_2)\left[t - t_e^{\pm}(x_1, x_2, \tau)\right] = 0 \qquad (4)$$

where $\alpha^{\pm}$ are the coefficients of the heat transfer at the top and bottom surfaces of the plate; $t_e^{\pm}$ are the environment temperatures at the top and bottom surfaces respectively; τ is the time parameter.

The equation (3) and boundary conditions (4) together with the constitutive equations from Reference [1] compose the corresponding initial-boundary value problem [5]. Since we consider the material with general type of anisotropy the flux component q_{ij} $(i \neq j)$ represents the heat flow which is directed along the axis x_i and caused by the change of the temperature in the axis x_j direction.

AVERAGING OPERATIONS

Introducing the averaging operations for the fluxes q_{13} and q_{23} along the thickness of the plate gives

$$R_{13}^{e} = \int_{-e}^{h-e} q_{13} dx_3 , \qquad R_{23}^{e} = \int_{-e}^{h-e} q_{23} dx_3 \tag{5}$$

or, correspondingly

$$q_{13} = \frac{R_{13}^{e}}{h}, \qquad q_{23} = \frac{R_{23}^{e}}{h}. \tag{6}$$

The similar procedure can be used with respect to the average temperature change along the thickness. As a result the following equation can be obtained

$$\xi = \frac{1}{h} \int_{-e}^{h-e} \frac{\partial t}{\partial x_3} dx_3 \qquad . \tag{7}$$

where ξ is the average temperature change. Substituting for $\frac{\partial t}{\partial x_3}$ from equation (2) into (7) and accounting for the relationships (6) yields

$$R_{13} = \overline{\Lambda}_{13} \xi , \qquad R_{23} = \overline{\Lambda}_{23} \xi \tag{8}$$

where $R_{13} = -R_{13}^{e}$, $R_{23} = -R_{23}^{e}$, and

$$\overline{\Lambda}_{13} = \left(\frac{1}{h^2} \int_{-e}^{h-e} \frac{1}{\lambda_{13}} dx_3 \right)^{-1} , \qquad \overline{\Lambda}_{23} = \left(\frac{1}{h^2} \int_{-e}^{h-e} \frac{1}{\lambda_{23}} dx_3 \right)^{-1}$$

Assume the following temperature distribution in the direction of x_3

$$t = T + \frac{x_3}{h} T_0$$

where T_0 is the temperature at the reference surface. After integrating the equation (3) with the boundary conditions (4) the following relationships may be obtained

$$
\begin{gathered}
\frac{\partial}{\partial x_1}\left[\Lambda_{11}\frac{\partial T}{\partial x_1}+\Lambda_{11}^{*}\frac{\partial T_0}{\partial x_1}+\Lambda_{12}\frac{\partial T}{\partial x_2}+\Lambda_{12}^{*}\frac{\partial T_0}{\partial x_2}+\overline{\Lambda}_{13}\xi\right]+\\
+\frac{\partial}{\partial x_2}\left[\Lambda_{12}\frac{\partial T}{\partial x_1}+\Lambda_{12}^{*}\frac{\partial T_0}{\partial x_1}+\Lambda_{22}\frac{\partial T}{\partial x_2}+\Lambda_{22}^{*}\frac{\partial T_0}{\partial x_2}+\overline{\Lambda}_{23}\xi\right]-\\
-\alpha_{+}(x_1,x_2)\left[T-t_{+}(x_1,x_2,\tau)\right]-\alpha_{-}(x_1,x_2)\left[T_0-t_{-}(x_1,x_2,\tau)\right]=\\
=B_{ij}+C(x_1,x_2)\dot{T}+C^{*}(x_1,x_2)\dot{T}_0-W_t(x_1,x_2,\tau)\\
\\
\frac{\partial}{\partial x_1}\left[3\Lambda^{*}{}_{11}\frac{\partial T}{\partial x_1}+\Lambda_{11}^{**}\frac{\partial T_0}{\partial x_1}+3\Lambda_{12}^{*}\frac{\partial T}{\partial x_2}+\Lambda_{12}^{**}\frac{\partial T_0}{\partial x_2}+\overline{\Lambda}_{13}^{*}\xi\right]+\\
+\frac{\partial}{\partial x_2}\left[3\Lambda^{*}{}_{12}\frac{\partial T}{\partial x_1}+\Lambda_{12}^{**}\frac{\partial T_0}{\partial x_1}+3\Lambda_{22}^{*}\frac{\partial T}{\partial x_2}+\Lambda_{22}^{**}\frac{\partial T_0}{\partial x_2}+\overline{\Lambda}_{23}^{*}\xi\right]-\\
-3\Big\{\alpha_{-}(x_1,x_2)\left[T-t_{+}(x_1,x_2,\tau)\right]-\alpha_{+}(x_1,x_2)\left[T_0-t_{-}(x_1,x_2,\tau)\right]+\\
+\frac{4T_0}{h^2}\left[\Lambda_{13}^{*}+\Lambda_{23}^{*}+\Lambda_{33}^{*}\right]\Big\}=B_{ij}^{*}+3C^{*}(x_1,x_2)\dot{T}+C^{**}(x_1,x_2)\dot{T}_0-W_t^{*}(x_1,x_2,\tau)
\end{gathered}
\tag{9}
$$

where

$$\alpha_{\pm}(x_1,x_2)=\alpha^{+}(x_1,x_2)\pm\alpha^{-}(x_1,x_2);$$

$$t_{\pm}(x_1,x_2,\tau)=\frac{1}{2}\left[t_e^{+}(x_1,x_2,\tau)\pm t_e^{-}(x_1,x_2,\tau)\right];$$

$$\Lambda_{ij}=\int_{-e}^{h-e}\lambda_{ij}dx_3;\quad \overline{\Lambda}_{ij}=\left(\frac{1}{h^2}\int_{-e}^{h-e}\frac{1}{\lambda_{ij}}dx_2\right)^{-1};\quad \Lambda_{ij}^{*}=\frac{2}{h}\int_{-e}^{h-e}\lambda_{ij}x_3dx_3;$$

$$\overline{\Lambda}_{ij}^{*}=\left(\frac{1}{h^2}\int_{-e}^{h-e}\frac{1}{\lambda_{ij}x_3}dx_3\right)^{-1};\quad \Lambda_{ij}^{**}=\frac{12}{h^2}\int_{-e}^{h-e}\lambda_{ij}x_3^2dx_3;$$

$$C=\int_{-e}^{h-e}c_v(x_1,x_2,x_3)\rho(x_1,x_2,x_3)dx_3;\quad C^{*}=\frac{2}{h}\int_{-e}^{h-e}c_v(x_1,x_2,x_3)\rho(x_1,x_2,x_3)x_3dx_3;$$

$$C = \int_{-e}^{h-e} c_v(x_1,x_2,x_3)\rho(x_1,x_2,x_3)dx_3\ ; \quad C^* = \frac{2}{h}\int_{-e}^{h-e} c_v(x_1,x_2,x_3)\rho(x_1,x_2,x_3)x_3 dx_3\ ;$$

$$C^{**} = \frac{12}{h^2}\int_{-e}^{h-e} c_v(x_1,x_2,x_3)\rho(x_1,x_2,x_3)x_3^2 dx_3\ ;$$

$$W_t = \int_{-e}^{h-e} w_t(x_1,x_2,x_3,\tau)dx_3; \quad W_t^* = \frac{6}{h}\int_{-e}^{h-e} w_t(x_1,x_2,x_3,\tau)x_3 dx_3;$$

$$B_{ij} = \int_{-e}^{h-e} \beta_{ij}\dot{e}_{ij} t dx_3\ ; \qquad B_{ij}^* = \int_{-e}^{h-e} \beta_{ij}\dot{e}_{ij} t x_3 dx_3\ ;$$

The number of variants of the coupled thermoelasticity theory may be formulated for thin-walled composite structures. The set of equilibrium equations, stress-strain relations, and strain-displacement relations should be combined with the equations presented above, including the mathematical formulation of the boundary conditions corresponding to different physical situations. Specifically, the equations (9) together with the basic set of the relationships of thermoelastisity, presented in References [1,2], can be used for the thermo-mechanical analysis of thin-walled spatially reinforced composite components operating under thermo-mechanical loading conditions.

ACKNOWLEDGEMENT

The financial support of the South African Foundation for Research Development (GUN 2034618) is gratefully acknowledged.

REFERENCES

[1] Vasiliev, V.V., Morozov, E.V. "Applied theory of spatially reinforced composite shells." *Mechanics of Composite Materials*, **24**, No.3, pp.393-400 (1988).

[2] Vorobey, V.V., Morozov, E.V., Tatarnikov, O.V. *Analysis of Termoloaded Composite Structures.* Moscow, Mashinostroenie, 236 p. (1992).

[3] Novacky, V. *Theory of elasticity.* Mir, 872 p. (1975)

[4] Boley, B.A., Weiner, J.H. *Theory of thermal stresses.* Jonn Wiley & Sons (1967).

[5] Morozov, E.V., Pashkov, A.V. "Thermoelasticity of spatially-reinforced composite plates", *Statics and Dynamics of Nonhomogeneous Structures,* MGATY, Moscow, pp. 82-87 (1994).

ANALYSIS OF STRESS-STRAIN STATE OF COMPOSITE LAMINATED SHELLS AND PLATES BY THE SECOND ORDER SHEAR THEORY

V.G.Piskunov, A.A.Rasskazov and S.G.Burihyn

Ukrainian Transport University, Kiev 252010, Suvorova Street 1, Ukraine

1. INTRODUCTION

Design of composite laminated shallow shells and plates is considered. This problem requires special study because the effect of transverse shear have to be taken into account for this design. It is known that the null-order theories are based on the linear principle for the tangential displacements through the thickness and the first-order shear theories are based on the cube law for these displacements [1,3,4]. These theories do not give the possibility to take into account the inhomogeneouse of the shear deformations through the thickness of the laminated composite structure (M0) and establish the linear principle for the tangential displacement through the thickness of the laminated system. The additions of the third component to the first-order model (M1) with the cube law for these displacements are taking place. The full form of the equation (1.3) corresponds with the second-order model and establishes the fifth degree of the distribution function.

The equations (1.1), (1.2), (1.3) and the corresponding tangential strains e_{ij} and stresses σ_{ij} form the shear second-order model of the stressed-strained state of the composite laminated orthotropic shallow shell.

The Reissner's variational principle is used for the construction of the equations of the equilibrium which takes into account the shear strains with the definite accuracy.

The refined shear second-order theory for the composite laminated shells and plates is presented in this paper. In this theory the tangential displacements through the thickness are based as law of the fifth degree.

2. PROBLEM STATEMENT

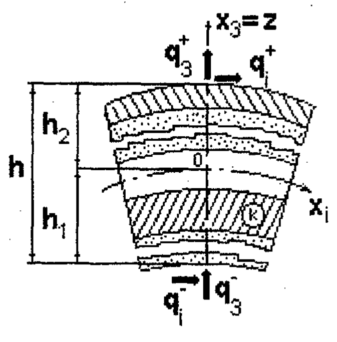

Fig. 1. Layered shell fragment.

A laminated shell of constant thickness and consisting of n homogeneous orthotropic layers is considered. The shell is referred to an orthogonal curvilinear coordinate system (Fig.1). The model of the second order [3] is the base of an iteration step for the construction of the proposed theory. The three-dimentional equations of the equilibrium with taking into account of the tangential stresses σ_{ij}, (i,j =1,2), of the first-order model are integrated.

As the result of this integration the transverse shear stresses are obtained in the following form:

$$\sigma_{i3} = F_{1i}^{(1)}(z)\psi_{1i}^{(1)}(x_1,x_2) + F_{2i}^{(1)}(z)q_i^+ + F_{3i}^{(1)}(z)q_i^- +$$
$$+F_{1i}^{(2)}(z)\psi_{1i}^{(2)}(x_1,x_2) + F_{2i}^{(2)}(z)(q_{1,1}^+ + q_{2,2}^+)_{,i} + F_{3i}^{(2)}(z)(q_{1,1}^- + q_{2,2}^-)_{,i}; \qquad (1.1)$$
$$i = 1,2.$$

These expressions are used as hypotheses for the derivation of the second-order theory. Here $F_{pi}^{(1)}(z)$ and $F_{pi}^{(2)}(z)$, (p=1,2,3) are the known nonlinear distribution functions of the stresses σ_{i3} for the null- and first-order accordingly; $\psi_{1i}^{(1)}(x_1,x_2)$ and $\psi_{1i}^{(2)}(x_1,x_2)$ are the unknown functions of the shear for these orders.

The hypotheses

$$e_{33} = 0; \sigma_{33} = 0. \qquad (1.2)$$

are taken into account too.

By the using of the hypotheses (1.1) and the Hook's law the transversal shear strains are obtained. Then by the integration of the Caushy's equations the tangential displacements were obtained as

$$u_i = v_i - zw_{,i} - f_{pi}^{(1)}(z)\psi_{pi}^{(1)} - f_{pi}^{(2)}(z)\psi_{pi}^{(2)}; \qquad (1.3)$$
$$i = 1,2; p = 1,2,3.$$

The summation is assumed over subscript p.

The equation (1.3) includes the unknown displacements v_i, w and function of shear $\psi_{1i}^{(s)}$, (s=1,2) and the known functions of the loading too:

$$\psi_{2i}^{(1)} = q_i^+; \psi_{3i}^{(1)} = q_i^-;$$
$$\psi_{2i}^{(2)} = (q_{1,1}^+ + q_{2,2}^+)_{,i}; \psi_{3i}^{(2)} = (q_{1,1}^- + q_{2,2}^-)_{,i}; \qquad (1.4)$$

The distribution functions for the displacements (1.3) are given by

$$f_{2i}^{(s)}(z) = -\int_0^z G_{i3}^{-1} F_{pi}^{(s)}(z)dz; s = 1,2. \qquad (1.5)$$

The first and second components of the equations (1.3) are corresponding to the null-order model equilibrium and boundary conditions.

The equations of equilibrium are given by

$$N_{rt,t} + q_r^- + q_r^+ = 0;$$
$$M_{rt,rt} - k_{rt}N_{rt} - \left(q_r^- h_1 - q_r^+ h_1\right)_{,r} + q_3 = 0; \qquad (1.6)$$
$$M_{rt,t}^{(s)} + Q_r^{(s)} + q_r^- f_{1g}^{(s)}(h_1) + q_r^+ f_{1g}^{(s)}(h_2) = 0;$$
$$r,t = 1,2; g = r; s = 1,2.$$

and boundary conditions are written as

$$N_{nn}\delta v_n = N_{nl}\delta v_l = 0; M_{nn}\delta w_{,n} = 0;$$
$$[(M_{nn,n} + 2M_{nl,l}) - (q_n^- h_1 - q_n^+ h_2)]\delta w = 0; \qquad (1.7)$$
$$M_{nn}^{(s)}\delta\psi_{1n}^{(s)} = 0; M_{nl}^{(s)}\delta\psi_{1l}^{(s)} = 0; s = 1,2.$$

Here n and l are the normal and tangential directions to the boundary.

The equations (1.6) and conditions (1.7) with the index s=1 are corresponding to the first-order model and with index s=1,2 - to the second order model.

The system of the governing differential equations is received from equations (1.6) by using of the relations of elasticity. These relations are expressed in terms of functions of the unknown functions of displacement and shear. The system of the equations is given in the matrix form as

$$L_{kp}\vec{v} = R_{kf}\vec{q}; k, p = 1,\dots,7; f = 1,\dots,5. \tag{1.8}$$

Here L_{kp} is the matrix of the differential operators of the vector of unknown functions

$$\vec{v} = \{ v_1, v_2, w, \psi_{11}^{(1)}, \psi_{12}^{(1)}, \psi_{11}^{(2)}, \psi_{12}^{(2)} \}^T; \tag{1.9}$$

R_{kf} is the matrix of the operators of the vector of given loads

$$\vec{q} = \{ q_1^+, q_2^+, q_1^-, q_2^-, q_3 \}^T. \tag{1.10}$$

The general order of the system of differential equations (1.8) equals 16. Therefore, 8 boundary conditions (1.7) have to be satisfied on each edge of the shell or plate. In the case M1 the order is 12, and for M0 the order equals 8.

The second-order model of the stress-strain state and corresponding equations of equilibrium, the boundary conditions and the system of the governing equations form the second-order shear theory of laminated composite shells and plates.

3. NUMERICAL RESULTS AND ANALYSIS

The analytical solution of the system of differential equations (1.8) is possible for the case of a supported shell or plate with a rectangular plan view. The solution is given by the trigonometric series. On the base of this solution the stress-strain state of some type of the laminated structure is performed.

The sinusoidal load is implemented. In this case the exact solution basing on the three-dimentional model (MT) is known.

The transversal-isotropic and orthotropic three-layered plates and shells are examined. The most essential refinement into the stress-strain state is received for the three-layered structure with a thin light layer. The diagrams of the transversal shear stresses and tangential normal stresses for three types of models - M0, M1, M2 are given in Fig.2. These diagrams have the essential refinement and only the results obtained by M2 are corresponding with the three-dimentional solution - MT.

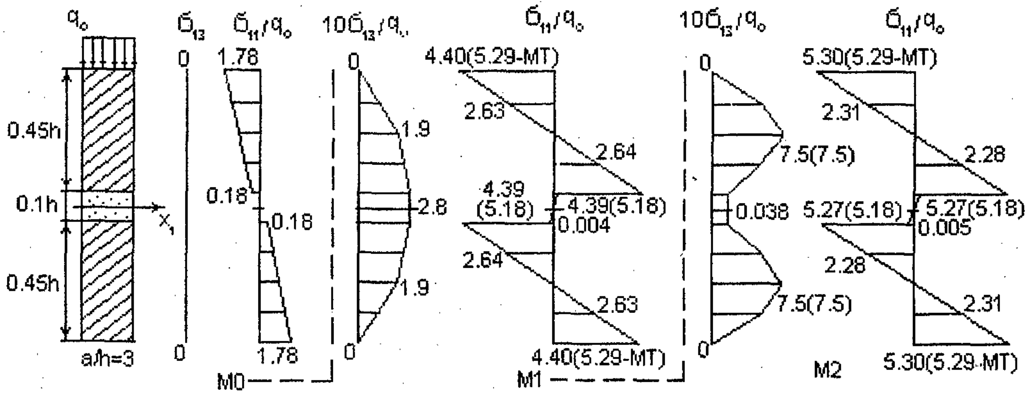

q₀
σ₁₃
σ₁₁/q₀
10σ₁₃/q₀
σ₁₁/q₀
10σ₁₃/q₀
σ₁₁/q₀
0.45h
0.1h
0.45h
x₁
a/h=3
0
0
1.78
0.18
0.18
1.78
M0
0
1.9
2.8
1.9
0
4.40(5.29-MT)
2.63
2.64
4.39
(5.18)
4.39(5.18)
0.004
2.64
2.63
4.40(5.29-MT)
M1
0
7.5(7.5)
0.038
7.5(7.5)
0
5.30(5.29-MT)
2.31
2.28
5.27(5.18)
5.27(5.18)
0.005
2.28
2.31
M2
5.30(5.29-MT)

Fig.2. Stress in the three-layered transversal-isotropic plate.

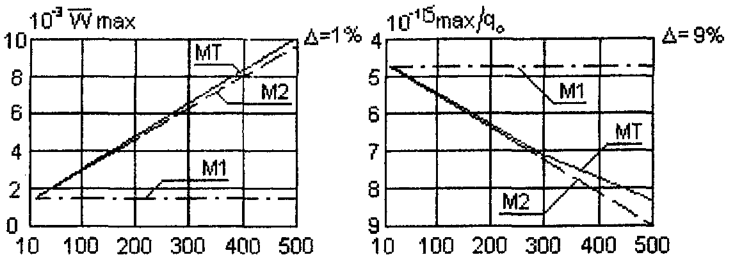

Fig.3. Results comparison for three-layered plate according to the different models.

This correspondance have place for a wide range of the shear modules tangential/normal ratio (G/G’ = 10 ... 500).

The comparison of the limits for M1 and M2 is given in Table 1.

Table 1

	G/G’	
a/h≥	M1	M2
	homogeneous plate	
3	≤10	50
5	≤20	100
10	≤50	500
20	≤100	1000
	three-layered plate with interlayer	
3	-	50
5	-	100
10	≤10	500 ·
20	≤100	1000

The comparison of the results M1 and M2 for the orthotropic three-layered (0°/90°/0°) plates is presented in Fig.4. Only M2 have the correspondance with the three-dimentional solution - MT.

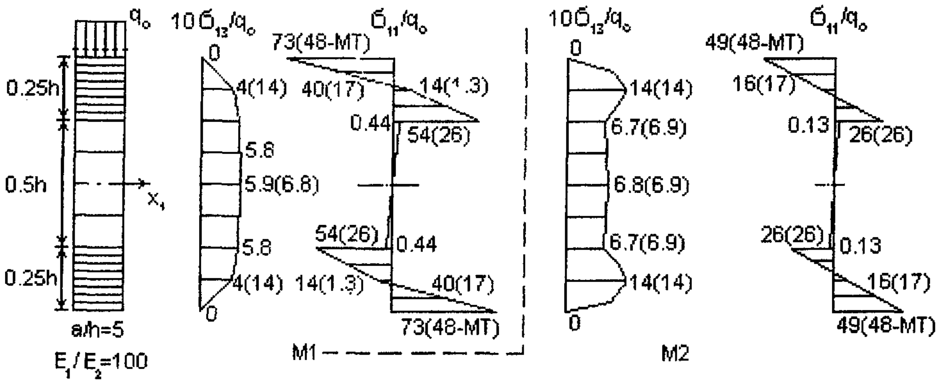

q_o
0.25h
0.5h
0.25h
x_1
a/h=5
E_1/E_2=100
10$σ_{13}/q_o$
0
4(14)
5.8
5.9(6.8)
5.8
4(14)
0
$σ_{11}/q_o$
73(48-MT)
40(17)
14(1.3)
0.44
54(26)
54(26)
0.44
14(1.3)
40(17)
73(48-MT)
M1
10$σ_{13}/q_o$
0
14(14)
6.7(6.9)
6.8(6.9)
6.7(6.9)
14(14)
0
$σ_{11}/q_o$
49(48-MT)
16(17)
0.13
26(26)
26(26)
0.13
16(17)
49(48-MT)
M2

Fig.4. Stress in the three-layered orthotropic plate.

Series of the problems for orthotropic composite shallow shells is solved. The results for the five-layerer (0°/90°/0°/90°/0°) system are given in Fig.5 and Table 2.

As for the preceding cases only M2 gives the correspondance with MT.

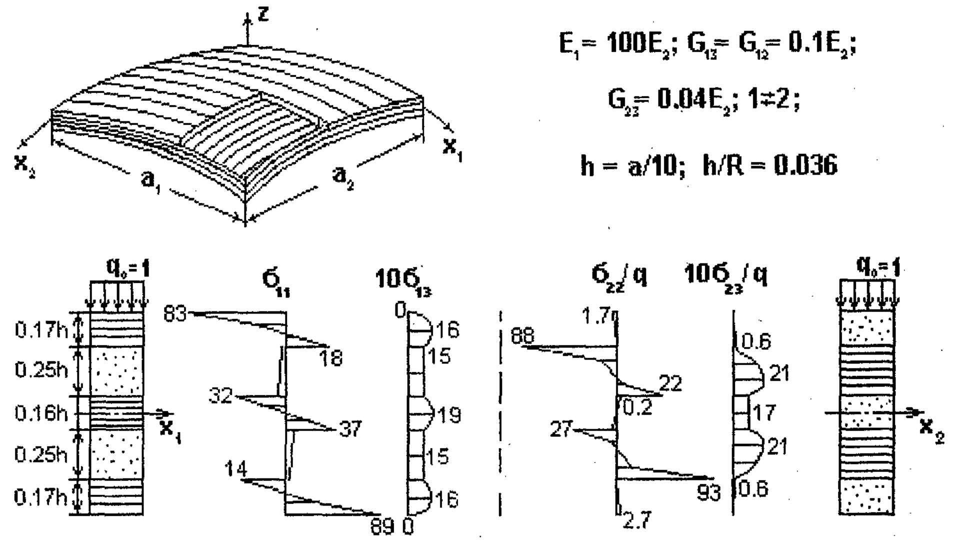
z
x_2
a_1
a_2
x_1
$E_1 = 100E_2$; $G_{13} = G_{12} = 0.1E_2$;
$G_{23} = 0.04E_2$; 1÷2;
h = a/10; h/R = 0.036
$q_0 = 1$
0.17h
0.25h
0.16h
0.25h
0.17h
σ_{11}
83
18
32
37
14
89
$10\sigma_{13}$
0
16
15
19
15
16
0
σ_{22}/q
88
1.7
22
0.2
27
93
2.7
$10\sigma_{23}/q$
0.6
21
17
21
0.6
$q_0 = 1$
x_2

Fig.5. Stress in the orthotropic shallow shell.

Table 2. The comparison of the results for five-layerer plates (r=∞) and shells (r=4 and r=2) with thickness h=a/5

r	Model	Wmax	σ_{11}	σ_{22}
∞ plate	M0	0.76	15.0	10.0
∞ plate	M1	19.1	55.6	65.5
∞ plate	M2,MT	25.0	48.0	47.0
4	M1	18.4	54.1	63.7
4	M2	23.8	46.5	46.4
2	M1	16.7	49.2	57.9
2	M2	20.8	41.3	41.2

The numerical results and their analysis show the high exactitude of the second-order theory for pliable to the transversal shear composite laminated plates and shells.

REFERENCES

1. *Ambartsumyan S.A.*. General Theory of Anisotropic Shells. - Moscow, Nauka, 1974, 488p. (in Russian).

2. *Grigorenko Ya.M., Vasilenko A.T. and Pankratova N.D.* Static of the Anisotropic Thick Shells. - Kiev, High School, 1985, 189p. (in Russian).

3. *Rasskazov A.O., Sokolovskaya I.I. and Shulga N.A.* Theory and Analysis of Layered Orthotropic Plates and Shells. - Kiev, High School, 1986, 191p. (in Russian).

4. *Piskunov V.G. and Verijenko V.E.* Linear and Nonlinear Problems in the Analysis of Laminated Structures.- Kiev, Budivelnyk, 1986, 176p. (in Russian).

BUCKLING BEHAVIOUR OF LAMINATED COMPOSITE PLATES UNDER THERMAL LOADING

PS SIMELANE and B SUN

Centre for Research in Applied Technology
And Department of Mechanical Engineering
Peninsula Technikon, P.O. Box 1906, Bellville, 7535, South Africa

ABSTRACT

A thermal buckling analysis of composite laminated plate is studied using the Finite Element Method. The effects of transverse shear deformation are accounted for by the use of the Mindlin first-order shear deformation (FSDT) theory on a plate of rectangular construction. The plate has antisymmetric lamination with respect to the middle plane. The intermediate class of deformation is employed for this non-linear analysis. The first variation of the total potential energy establishes the equilibrium equation and the second variation analyses the stability of the laminated composite. A displacement-based finite element with five degrees of freedom in each node is used. The effects of lamination angle, modulus ratio, plate aspect ratio, and boundary constrains upon the critical buckling temperature are investigated.

INTRODUCTION

Fiber-reinforced composites have found wider applications in recent years and this has resulted in renewed interest in their study under elevated temperatures. Studies have been conducted of the laminated composites under inplane mechanical loading and to a certain extent thermal loading has been investigated, but thermal buckling remains one of the challenges facing the aerospace and other industries. Shaikh *et al* [1] proposed a higher-order theory of laminated composite plates and shells under thermal and static loading. Zeggane and Sridharan [2] used the Reissner-Mindlin 'infinite strip' to study the stability of long laminated composite plates. Chandrashekhara [3] investigated thermal buckling of laminated plates using a shear flexible finite element. Chen *et al* [4] used the eight-noded Serendipity finite element to study thermal buckling under uniform and nonuniform temperature distribution. Mathew *et al* [5] analysed an antisymmetric cross-ply composite laminate using a one-dimensional finite element having two nodes and six-degrees of freedom.

PROBLEM STATEMENT

As in metallic structures, changes in temperatures are commonplace in composite structures during fabrication and structural usage. Changes in temperature results in expansion when the material is heated, and contracts when cooled, and in most cases this expansion is proportional to the temperature change. The equation governing the behaviour of a laminated composite under thermal loading is given by

$$\begin{pmatrix} \{N\} \\ \{M\} \\ \{Q\} \end{pmatrix} = \begin{pmatrix} [A] & [B] & 0 \\ [B] & [D] & 0 \\ 0 & 0 & [\bar{A}] \end{pmatrix} \begin{pmatrix} \{\bar{\varepsilon}\} \\ \{\kappa\} \\ \{\bar{\gamma}\} \end{pmatrix} - \begin{pmatrix} [N_t] \\ [M_t] \\ 0 \end{pmatrix} \qquad (1)$$

where extensional stiffness A_{ij}, flexural-extensional coupling stiffness B_{ij}, and flexural stiffness D_{ij} of the plate are defined as

$$\left(A_{ij}, B_{ij}, D_{ij}\right) = \sum_{k=1}^{N} \int_{h_{k-1}}^{h_k} \left(\bar{Q}_{ij}\right)_k \left(1, z, z^2\right) dz \qquad (i,j, = 1,2,6)$$

$$\left(\bar{A}_{ij}\right) = \beta \sum_{k=1}^{N} \int_{h_{k-1}}^{h_k} \left(\bar{Q}_{ij}\right)_k dz \qquad (i,j = 4,5)$$

β is the shear correction factor [8].

MATHEMATICAL MODEL

Based on the Mindlin plate theory, the deformation field can be written in the following form

$$u(x, y, z) = u_0(x, y) + z\theta_x(x, y) \quad v(x, y, z) = v_0(x, y) + z\theta_y(x, y)$$
$$w(x, y, z) = w(x, y) \qquad (2)$$

where v_0, v_0 and w_0 are the displacements of the reference surface in the x, y and z direction, respectively, and θ_x, θ_y are the rotations of the transverse normal about the x- and y-axes. The intermediate class of deformation is defined by the limitations that the strains be small compared with unity, the rotations relative to the x and y directions moderately small, and that the $\bar{\varepsilon}_x$, $\bar{\varepsilon}_y$, $\bar{\gamma}_{xy}$, $\bar{\gamma}_{yz}$ and $\bar{\gamma}_{xz}$ components of the strain-displacement relations for a three-dimensional medium, including thermal strains are

$$\{\varepsilon\} = \left(\bar{\varepsilon}_x \quad \bar{\varepsilon}_y \quad \bar{\gamma}_{xy}\right)^T + \left(\bar{\kappa}_x \quad \bar{\kappa}_y \quad \bar{\kappa}_{xy}\right)^T - \left(\alpha_x \quad \alpha_y \quad \alpha_{xy}\right)^T \Delta T$$
$$\{\gamma\} = \left(\bar{\gamma}_{yz} \quad \bar{\gamma}_{xz}\right)^T = \left(w_{,y} + \theta_y \quad w_{,x} + \theta_x\right)^T \qquad (3)$$

where

$$\left(\bar{\varepsilon}_x \quad \bar{\varepsilon}_y \quad \bar{\gamma}_{xy}\right)^T = \left(u_{,x} \quad v_{,y} \quad u_{,y} + v_{,x}\right)^T + \tfrac{1}{2}\left(\varphi_x^2 \quad \varphi_y^2 \quad 2\varphi_x\varphi_y\right)^T$$

$$\left(\bar{\kappa}_x \quad \bar{\kappa}_y \quad \bar{\kappa}_{xy}\right) = \left(\theta_{x,x} \quad \theta_{y,y} \quad \theta_{x,y} + \theta_{y,x}\right) \tag{4}$$

$\bar{\varepsilon}_x, \bar{\varepsilon}_y, \bar{\gamma}_{xy}, \bar{\gamma}_{yz}$ and $\bar{\gamma}_{xz}$ are extensional and shearing strains at any point through the plate thickness and ε_x, ε_y and γ_{xy} denote the corresponding quantities at points on the plate middle plane only. We note that

$$\varphi_x = w_{,x} \qquad \varphi_y = w_{,y}$$

where "$_{,x}$" and "$_{,y}$" represent partial differentiation with respect to x and y. The stress-strain relation of the k-th layer of a laminated composite plate is given by

$$\begin{Bmatrix} \sigma_x \\ \sigma_y \\ \tau_{xy} \end{Bmatrix} = \begin{bmatrix} \bar{Q}_{11} & \bar{Q}_{12} & \bar{Q}_{16} \\ \bar{Q}_{12} & \bar{Q}_{22} & \bar{Q}_{26} \\ \bar{Q}_{16} & \bar{Q}_{26} & \bar{Q}_{66} \end{bmatrix} \left(\begin{Bmatrix} \varepsilon_x \\ \varepsilon_y \\ \gamma_{xy} \end{Bmatrix} + z \begin{Bmatrix} \theta_{x,x} \\ \theta_{y,y} \\ \theta_{x,y} + \theta_{y,x} \end{Bmatrix} \right) - \begin{bmatrix} \bar{Q}_{t11} & \bar{Q}_{t12} & \bar{Q}_{t13} \\ \bar{Q}_{t12} & \bar{Q}_{t22} & \bar{Q}_{t23} \\ \bar{Q}_{t13} & \bar{Q}_{t23} & \bar{Q}_{t33} \end{bmatrix} \begin{Bmatrix} \alpha_x \\ \alpha_y \\ 2\alpha_{xy} \end{Bmatrix} \Delta T$$

$$\begin{pmatrix} \tau_{xz} \\ \tau_{yz} \end{pmatrix} = \begin{pmatrix} \bar{Q}_{44} & \bar{Q}_{45} \\ \bar{Q}_{45} & \bar{Q}_{55} \end{pmatrix} \begin{pmatrix} \gamma_{xz} \\ \gamma_{yz} \end{pmatrix} \tag{5}$$

where α_i, are thermal expansion coefficients in the principal material directions. ΔT is the temperature rise. In the derivation of the above equations, the stresses and strains were transformed from the principal material directions of the orthotropic lamina to the x,y co-ordinate system according to

$$T_{ij} = a_{ik} a_{jl} T_{kl} \tag{6}$$

From the general plate theory we know that

$$\{N\}^T = \left(N_x, N_y, N_{xy}\right) = \int_{\frac{h}{2}}^{\frac{h}{2}} \left(\sigma_x, \sigma_y, \tau_{xy}\right) dz$$

$$\{M\}^T = \left(M_x, M_y, M_{xy}\right) = \int_{-\frac{h}{2}}^{\frac{h}{2}} \left(\sigma_x, \sigma_y, \tau_{xy}\right) z\,dz$$

$$\{Q\}^T = \left(Q_x, Q_y\right) = \int_{\frac{h}{2}}^{\frac{h}{2}} \left(\tau_{xz}, \tau_{yz}\right) dz \tag{7}$$

where N, M, and Q are the inplane, bending and shear stress resultants over the thickness of the plate. The use of Mindlin plate theory together with the intermediate class of deformation and the general plate theory results in the stress-strain relation of the form of equation (1). The stress state developed in the plate very much depends on the lay-up and boundary conditions, and it is this stress state that is responsible for plate buckling rather than the applied one. The loss of stability is analysed by setting $u = u_0 +$

u_1, $v = v_0 + v_1$, $w = w_0 + w_1$, $\theta_x = \theta_{x0} + \theta_{x1}$, and $\theta_y = \theta_{y0} + \theta_{y1}$, where the subscript "$_1$" denotes the incremental displacement on the primary path of equation (1)

FINITE ELEMENT MODEL

For a conservative structural system, the total potential energy Π of a loaded structure is defined as the sum of the strain energy of the structure itself and the potential energy of the applied load.

$$\Pi = \Pi_m + \Pi_b + \Pi_s \tag{8}$$

where m, b, and s are the membrane, bending and shear strain energies, respectively. The problem is solved by dividing the region Ω of the plate into n-noded quadrilateral finite elements, each with five degrees of freedom per node, such that

$$\Pi(\mathbf{a}) = \sum_{i=1}^{n} \Pi^e(\mathbf{a}) \tag{9}$$

where Π and $\Pi^{(e)}$ are potential energies of the plate and element, respectively, $\mathbf{a}$ is the displacement vector $\{u_1, v_1, w_1, \theta_{x1}, \theta_{y1}$. The variation in each element can be interpolated, for node i (i = 1,2, ...n), as

$$u_1 = \sum_{i=1}^{n} N_i u_1^i \quad v_1 = \sum_{i=1}^{n} N_i v_1^i \quad w_1 = \sum_{i=1}^{n} N_i w_1^i \quad \theta_{x1} = \sum_{i=1}^{n} N_i \theta_{x1}^i \quad \theta_{y_1} = \sum_{i=1}^{n} N_i \theta_{y1}^i \tag{10}$$

where N_i are the interpolation functions. Using the same shape function associated with node i, we can write

$$\mathbf{u}_1 = \sum_{i=1}^{4} \mathbf{N}_i \mathbf{a}_1^i \tag{11}$$

where $\mathbf{N}_i$ are the interpolation functions and are used to interpolate both the nodal in-plane displacements u, v, the lateral displacement w as well as the normal rotation θ_x, θ_y. The shape functions are expressed in terms of the natural (local) element co-ordinate system (ξ, η). $\mathbf{u}_1$ is the element displacement vector and $\mathbf{a}_1^i$ is the vector of variables for node i in the element e. The normal and shear strain matrices and the curvature matrix are given by

$$\varepsilon_{1t} = \sum_{i=1}^{n} \mathbf{B}_{ti} \mathbf{a}_1^i \qquad \varepsilon_{1b} = \sum_{i=1}^{n} \mathbf{B}_{bi} \mathbf{a}_1^i \qquad \varepsilon_{1s} = \sum_{i=1}^{n} \mathbf{B}_i \mathbf{a}_1^i \tag{12}$$

where $\mathbf{B}_{ti}$, $\mathbf{B}_{bi}$, and $\mathbf{B}_{si}$ are, respectively, the normal-, shear- and curvature-displacement matrix associated with element e. The bending stresses and the shear stresses are defined as

$$\sigma = \sum_{i=1}^{4}\left(\mathbf{A}\mathbf{B}_{ti} + \mathbf{B}_{d}\mathbf{B}_{bi}\right)\mathbf{a}_{1}^{i} \qquad \tau = \sum_{i=1}^{4}\overline{\mathbf{A}}\mathbf{B}_{si}\mathbf{a}_{1}^{i} \tag{13}$$

where $\mathbf{A}$, $\mathbf{B}_d$ and $\overline{\mathbf{A}}$ are material property matrices of the laminated composite as defined in equation (1). Using the constitutive equations, we have

$$\{\mathbf{N}_1\} = \left[[\mathbf{A}][\mathbf{B}_{ti}] + [\mathbf{B}_d][\mathbf{B}_{bi}]\right]\{\mathbf{a}_1^i\} \qquad \{\mathbf{M}_1\} = \left[[\mathbf{B}_d][\mathbf{B}_{ti}] + [\mathbf{D}][\mathbf{B}_{bi}]\right]\{\mathbf{a}_1^i\}$$

$$\{\mathbf{Q}_1\} = [\overline{\mathbf{A}}][\mathbf{B}_{si}]\{\mathbf{a}_1^i\} \tag{14}$$

Substituting into the second variation of equation (9), and for arbitrary $\delta\mathbf{u}_1$ $\delta\mathbf{v}_1$ $\delta\mathbf{w}_1$ $\delta\theta_1$ $\delta\theta_1$, we have

$$[\mathbf{K}_1]\{\mathbf{a}_1^i\} + [\mathbf{K}_2]\{\mathbf{a}_1^i\} + [\mathbf{K}_3]\{\mathbf{a}_1^i\} + [\mathbf{K}_4]\{\mathbf{a}_1^i\} + [\mathbf{K}_5]\{\mathbf{a}_1^i\} + [\mathbf{K}_g]\{\mathbf{a}_1^i\} = \mathbf{0}$$

and
$$\left([\mathbf{K}] + [\mathbf{K}_g]\right)\{\mathbf{a}_1^i\} = \mathbf{0} \tag{15}$$

where $[\mathbf{K}]$ is the structural stiffness matrix and $[\mathbf{K}_g]$ is the geometric stiffness matrix. Due to space limitations the full form of $[\mathbf{K}]$ and $[\mathbf{K}_g]$ cannot be given in this paper.

Classical eigenvalue buckling analysis is often used to estimate the critical (buckling) load of "stiff" structures such as the laminated composite. "Stiff" structures are those that carry design loads primarily by axial or membrane action, rather than by bending action. Their response usually involves very little deformation prior to buckling. In the finite element context, the classical eigenvalue-buckling problem may be stated as follows. Given a structure with an elastic stiffness matrix, K_b^{ij}, a loading pattern defined by the vector $\{N_t\}$, and an initial stress and loading stiffness matrix, K_g^{ij}, find load multipliers (eigenvalues), λ_i, and buckling mode shapes (eigenvectors), a_i^j, which satisfy equation (15). The critical buckling loads are then given by $\lambda_i N^j$. In this study only the smallest load multiplier and its associated mode shape are of interest. The eigenvector a_i^j associated with λ_{cr} defines the buckling mode.

CONCLUSION

The performance of laminated composites under adverse temperature variation dictates that careful analysis be made to determine the optimum configuration of the composite structures. The combination of numerical/mechanical aspects is essential for the accurate prediction of the non-linear structural behaviour of composites (where instead of secant stiffness matrix, we use tangent stiffness matrix) in the prebuckling, buckling and postbuckling regime. The effects of lamination angle, aspect ratio, and material parameter, etc have a significant influence on the critical buckling temperature of laminated plates.

ACKNOWLEDGEMENT

The authors would like to thank the Foundation for Research Development for its financial assistance. The technical support of Peninsula Technikon and the support from the Centre for Research in Applied Mechanics is acknowledged.

REFERENCES

1. Shaikh, C., Verijenko, V.E., Tabakov, P.Y., Adali, S., Higher-Order Theory of Laminated Composites under Thermal and Static Loading, *Proc. of the 2nd South African Conference on Applied Mechanics*. Vol. 2, pp. 913-924, 1998.
2. Zeggane, M., Sridharan, S., Stability Analysis of Long Laminated Composite Plates using Reissner-Mindlin 'Infinite' Strips, *Computers and Structures*, Vol. 40, No. 4, pp. 1033 - 1042, 1991.
3. Chandrashekhara, K., Thermal Buckling of Laminated Plates using a Shear Flexibility Finite Element, *Finite Elements in Analysis and Design*, Vol. 12, pp. 51-61, 1992.
4. Chen, W.J., Lin, P.D., Chen, L.W., Thermal Buckling Behaviour of Thick Composite Laminated Plates under Non-uniform Temperature Distribution, *Computers and Structures*, Vol. 41, No. 4, pp. 637-645, 1991.
5. Mathew, T.C., Singh, G., Rao, G.V., Thermal Buckling of Cross-Ply Composite Laminates, *Computers and Structures*, Vol. 42, No. 2, pp. 281-287, 1992.
6. Mindlin, R.D., Influence of Rotatory Inertia and Shear on Flexural Motions of Isotropic, Elastic Plates, *J. Appl. Mech.* 31-38, 1954.
7. Reissner, E., The Effect of Transverse Shear Deformation on the Bending of Elastic Plates, *J. Appl. Mech.* Vol. 12, 1945.
8. Bath, K., *Finite Element Procedures*, Prentice-Hall, Englewood, New Jersey, 1996.

LINEAR ANALYSIS OF LAMINATED COMPOSITE PLATES USING SINGLE LAYER HIGHER ORDER DISCRETE MODELS

Dj.Vuksanovic

Faculty of Civil Engineering, University of Belgrade,
Bulevar revolucije 73, 11000 Belgrade, Yugoslavia

INTRODUCTION

The transverse shear effects are strongly pronounced in filamentary composite plates owing to the low transverse shear modulus relative to the in-plane Young's moduli. The classical plate theory underpredicts deflections and overpredicts natural frequencies and buckling loads due to the neglection of transverse shear strains. Although, the first order shear deformation theory could overcome this problem, recently many higher order shear deformation theories have been proposed for the enhancement of solutions in orthotropic and anisotropic laminates. In an attempt to obtain the nonstraight deformation of normals to the plate midplane and to model the warping of cross sections, which is quite strong for thick laminates, Reddy [1] presented a simple higher order theory for laminated composite plates. This theory accounts for the cubic variation of the in-plane displacements through the plate thickness and for the quadratic variation of transverse shear strains which vanish on the top and bottom faces of the plate. The objective of this paper is to present the development of a simple C^0 isoparametric single layered finite element model based on higher order theory and its application to dynamic analysis and free vibrations of symmetric cross-ply and angle-ply laminated composite and sandwich plates.

KINEMATICS

Consider a plate of sides *a* and *b* and of total thickness *h* laminated of a finite number of orthotropic layers of thickness h_i with the material axes of each layer being arbitrarily oriented with the respect to the midplane of the plate. A Cartesian coordinate system is chosen in such a way that the *x-y* plane coincides with the midplane of the plate. The displacement field in the plate is assumed to be of the form:

$$\begin{aligned} u(x,y,z,t) &= z\psi_x(x,y,t) + z^3\zeta_x(x,y,t) \\ v(x,y,z,t) &= z\psi_y(x,y,t) + z^3\zeta_y(x,y,t) \\ w(x,y,z,t) &= w^*(x,y,t) \end{aligned} \tag{1}$$

where *t* is the time, *u*, *v*, *w* are the displacements in the *x*, *y*, *z* directions respectively, w^* denotes the transverse displacements of the midplane, ψ_x and ψ_y are the middle-surface slopes in the *xz* and *yz* planes respectively. The parameters ζ_x and ζ_y are the higher order terms in the Taylor's series expansion defining the warping of cross sections which is important in case of thick laminates. The strains associated with displacements in equation (1) are:

$$\varepsilon = \begin{Bmatrix} \varepsilon_b \\ \varepsilon_s \end{Bmatrix} = \begin{Bmatrix} z\begin{Bmatrix} \psi_{x,x} \\ \psi_{y,y} \\ \psi_{x,y}+\psi_{y,x} \end{Bmatrix} \\ w_{,x}+\psi_x \\ w_{,y}+\psi_y \end{Bmatrix} + \begin{Bmatrix} z^3\begin{Bmatrix} \zeta_{x,x} \\ \zeta_{y,y} \\ \zeta_{x,y}+\zeta_{y,x} \end{Bmatrix} \\ 3z^2\begin{Bmatrix} \zeta_x \\ \zeta_y \end{Bmatrix} \end{Bmatrix} \qquad (2)$$

where subscripts *b* and *s* stand for bending and shear respectively.

CONSTITUTIVE EQUATIONS

The constitutive equations for the kth layer of the laminate can be written as:

$$\bar{\sigma} = \begin{Bmatrix} \sigma_1 \\ \sigma_2 \\ \sigma_6 \\ \sigma_4 \\ \sigma_5 \end{Bmatrix} = \begin{bmatrix} C_{11} & C_{12} & 0 & 0 & 0 \\ C_{12} & C_{22} & 0 & 0 & 0 \\ 0 & 0 & C_{66} & 0 & 0 \\ 0 & 0 & 0 & C_{44} & 0 \\ 0 & 0 & 0 & 0 & C_{55} \end{bmatrix}^{(k)} \begin{Bmatrix} \varepsilon_1 \\ \varepsilon_2 \\ \varepsilon_6 \\ \varepsilon_4 \\ \varepsilon_5 \end{Bmatrix} = \mathbf{C}\bar{\varepsilon} \qquad (3)$$

where C_{ij} are the reduced stiffness components in the material axes of the layer, as follows:

$$C_{11} = \frac{E_1}{1-\nu_{12}\nu_{21}} \quad C_{22} = \frac{E_2}{1-\nu_{12}\nu_{21}} \quad C_{12} = \frac{\nu_{12}E_2}{1-\nu_{12}\nu_{21}} = \frac{\nu_{21}E_1}{1-\nu_{12}\nu_{21}}$$
$$C_{66} = G_{12} \quad C_{44} = G_{13} \quad C_{55} = G_{23} \qquad (4)$$

The relationships used to transform stress and strain vectors from one coordinate system to another are:

$$\bar{\sigma} = \mathbf{T}\sigma \qquad \bar{\varepsilon} = \mathbf{T}\varepsilon \qquad (5)$$

where **σ** and **ε** are the stress and strain components in the *x-y* coordinate system and **T** is the transformation matrix of the form:

$$\mathbf{T} = \begin{bmatrix} \cos^2\theta & \sin^2\theta & 2\sin\theta\cos\theta & 0 & 0 \\ \sin^2\theta & \cos^2\theta & -2\sin\theta\cos\theta & 0 & 0 \\ -\sin\theta\cos\theta & \sin\theta\cos\theta & \cos^2\theta-\sin^2\theta & 0 & 0 \\ 0 & 0 & 0 & \cos\theta & -\sin\theta \\ 0 & 0 & 0 & \sin\theta & \cos\theta \end{bmatrix}^{(k)} \qquad (6)$$

where θ is the layer angle. The reduced stiffness matrix, **Q**, from the material coordinates to the global plate coordinates, can be calculated as:

$$\mathbf{Q} = \mathbf{T}^{-1}\mathbf{C}\mathbf{T} \qquad (7)$$

Therefore, the constitutive relations for k^{th} layer in the *x-y* system are of the form:

$$\sigma=\begin{Bmatrix}\sigma_x\\ \sigma_y\\ \tau_{xy}\\ \tau_{xz}\\ \tau_{yz}\end{Bmatrix}=\left[\begin{array}{ccc|cc} Q_{11} & Q_{12} & Q_{13} & 0 & 0\\ Q_{12} & Q_{22} & Q_{23} & 0 & 0\\ Q_{13} & Q_{23} & Q_{33} & 0 & 0\\ \hline 0 & 0 & 0 & Q_{44} & Q_{45}\\ 0 & 0 & 0 & Q_{45} & Q_{55}\end{array}\right]^{(k)}\begin{Bmatrix}\varepsilon_x\\ \varepsilon_y\\ \gamma_{xy}\\ \gamma_{xz}\\ \gamma_{yz}\end{Bmatrix}=\begin{Bmatrix}Q_b\varepsilon_b\\ -\\ Q_s\varepsilon_s\end{Bmatrix} \tag{8}$$

FINITE ELEMENT MODEL

In C^0 finite element theory, the continuum displacement vector within the single layered finite element is discretized such that:

$$\mathbf{u}=\sum_{i=1}^{n}\mathbf{N}_i\,\mathbf{u}_i \tag{9}$$

in which *n* is the number of nodes in an element, $\mathbf{N}_i$ is the isoparametric shape function associated with node *i* in terms of the normalised coordinates ξ and η, $\mathbf{u}_i$ is the generalised displacement vector corresponding to the ith node of an element. Vectors **u** and $\mathbf{u}_i$ may be written as:

$$\mathbf{u}=\begin{Bmatrix}w(x,y,t)\\ \psi_x(x,y,t)\\ \psi_y(x,y,t)\\ -----\\ \zeta_x(x,y,t)\\ \zeta_y(x,y,t)\end{Bmatrix}=\begin{Bmatrix}\mathbf{u}_m\\ ---\\ \mathbf{u}_\omega\end{Bmatrix}\qquad \mathbf{u}_i=\begin{Bmatrix}w_i\\ \psi_{xi}\\ \psi_{yi}\\ ---\\ \zeta_{xi}\\ \zeta_{yi}\end{Bmatrix}=\begin{Bmatrix}\mathbf{u}_{m_i}\\ ---\\ \mathbf{u}_{\omega_i}\end{Bmatrix} \tag{10}$$

where subscripts *m* and ω imply Mindlin plate theory terms and additional terms due to the warping of cross sections, respectively. Relationships between curvature and displacement vectors are of the form:

$$\mathbf{k}_{bm}=\begin{Bmatrix}\psi_{x,x}\\ \psi_{y,y}\\ \psi_{x,y}+\psi_{y,x}\end{Bmatrix}=\sum_{i=1}^{n}\mathbf{B}_{bmi}\mathbf{u}_{mi}\qquad \mathbf{k}_{sm}=\begin{Bmatrix}w_{,x}+\psi_x\\ w_{,y}+\psi_y\end{Bmatrix}=\sum_{i=1}^{n}\mathbf{B}_{smi}\mathbf{u}_{mi}$$

$$\mathbf{k}_{b\omega}=\begin{Bmatrix}\zeta_{x,x}\\ \zeta_{y,y}\\ \zeta_{x,y}+\zeta_{y,x}\end{Bmatrix}=\sum_{i=1}^{n}\mathbf{B}_{b\omega i}\mathbf{u}_{\omega i}\qquad \mathbf{k}_{s\omega}=\begin{Bmatrix}\zeta_x\\ \zeta_y\end{Bmatrix}=\sum_{i=1}^{n}\mathbf{B}_{s\omega i}\mathbf{u}_{\omega i} \tag{11}$$

where:

$$\mathbf{B}_{bmi}=\begin{bmatrix}0 & N_{i,x} & 0\\ 0 & 0 & N_{i,y}\\ 0 & N_{i,y} & N_{i,x}\end{bmatrix} \qquad \mathbf{B}_{smi}=\begin{bmatrix}N_{i,x} & N_i & 0\\ N_{i,y} & 0 & N_i\end{bmatrix}$$

$$\mathbf{B}_{b\omega i}=\begin{bmatrix}N_{i,x} & 0\\ 0 & N_{i,y}\\ N_{i,y} & N_{i,x}\end{bmatrix} \qquad \mathbf{B}_{s\omega i}=\begin{bmatrix}N_i & 0\\ 0 & N_i\end{bmatrix} \tag{12}$$

Upon evaluating the matrices **Q** and **B** as given by equations (8) and (12), respectively, the element stiffness matrix can be readily computed using the standard procedure of minimisation of the total potentional energy with respect to the nodal variables:

$$\mathbf{K}_{ij}^{e}=\int_{A_e}\begin{bmatrix}\mathbf{B}_{bmi}^{T}\mathbf{D}_{bmm}\mathbf{B}_{bmj}+\mathbf{B}_{smi}^{T}\mathbf{D}_{smm}\mathbf{B}_{smj} & \mathbf{B}_{bmi}^{T}\mathbf{D}_{bm\omega}\mathbf{B}_{b\omega j}+\mathbf{B}_{smi}^{T}\mathbf{D}_{sm\omega}\mathbf{B}_{s\omega j}\\ \mathbf{B}_{b\omega i}^{T}\mathbf{D}_{b\omega m}\mathbf{B}_{bmj}+\mathbf{B}_{s\omega i}^{T}\mathbf{D}_{s\omega m}\mathbf{B}_{smj} & \mathbf{B}_{b\omega i}^{T}\mathbf{D}_{b\omega\omega}\mathbf{B}_{b\omega j}+\mathbf{B}_{s\omega i}^{T}\mathbf{D}_{s\omega\omega}\mathbf{B}_{s\omega j}\end{bmatrix}dA_e \tag{13}$$

where:

$$\mathbf{D}_{bmm}=\int_{-h/2}^{+h/2}z^2\mathbf{Q}_b dz \qquad \mathbf{D}_{smm}=\int_{-h/2}^{+h/2}\mathbf{Q}_s dz \qquad \mathbf{D}_{bm\omega}=\mathbf{D}_{b\omega m}=\int_{-h/2}^{+h/2}z^4\mathbf{Q}_b dz$$

$$\mathbf{D}_{sm\omega}=\mathbf{D}_{s\omega m}=3\int_{-h/2}^{+h/2}z^2\mathbf{Q}_s dz \quad \mathbf{D}_{b\omega\omega}=\int_{-h/2}^{+h/2}z^6\mathbf{Q}_b dz \quad \mathbf{D}_{s\omega\omega}=9\int_{-h/2}^{+h/2}z^4\mathbf{Q}_s dz$$

The moment and force stress-resultants per unit length are introduced in the present shear deformation theory in the following way:

$$(M_x,M_y,M_{xy})=\int_{-h/2}^{+h/2}(\sigma_x,\sigma_y,\tau_{xy})z\,dz \qquad (P_x,P_y,P_{xy})=\int_{-h/2}^{+h/2}(\sigma_x,\sigma_y,\tau_{xy})z^3dz$$

$$(T_x,T_y)=\int_{-h/2}^{+h/2}(\tau_{xz},\tau_{yz})dz \qquad (R_x,R_y)=\int_{-h/2}^{+h/2}(\tau_{xz},\tau_{yz})z^2dz \tag{14}$$

In finite element formulation [2] we adopted a hierarchical concept to represent all degrees of freedom (Serendipity shape functions plus a bubble function). Therefore, we easily obtained enhanced 8-node Serendipity element, 9-node Lagrangian element and Heterosis element following the same formulation. Using selective integration all major properties of the previous finite elements (number of zero energy modes, ability to pass patch and locking tests and to overcome the formation of mesh mechanisms and overall accuracy) have been preserved in the new developed elements. New plate elements have been implemented in a computer code for dynamic and eigenvalue analyses of laminated plates.

NUMERICAL RESULTS AND DISCUSSION

To emphasise the capability of the proposed finite element model some numerical results will be presented herein. First we have three-ply orthotropic laminates with identical top and bottom plies, $h_1/h=0.1$ and $h_2/h=0.8$; the relative values of the moduli are the same in all the plies:

$E_2/E_1 = 0.5252$	$G_{12}/E_1 = 0.2928$
$\nu_{12}=0.44$	$G_{23}/E_1 = 0.2972$
$\nu_{21}=0.23$	$G_{13}/E_1 = 0.1781$

Orthotropic properties assumed in the following numerical example correspond to Aragonite crystals. We considered dynamic response of a simply-supported plate, $b/a=\sqrt{2}$, $h/a=0.1$, with modular ratio between outer and middle plies, $\beta=E_1^{(1)}/E_1^{(2)}=15$ and mass density ratio $\rho_1/\rho_2=5$, subjected to a step pulse acting as uniformly distributed load p over the top surface. The values of central deflection w and bending moment M_x in dimensionless form for different plate theories respectively are given in Table 1.

Table 1.

T_0	Classical theory		Mindlin's theory		Present model	
	w_0	M_{x0}	w_0	M_{x0}	w_0	M_{x0}
1.	1.640	205.5	1.801	194.4	2.174	192.2
2.	3.764	377.8	4.171	391.7	4.685	333.8
3.	5.828	613.4	6.331	551.3	6.978	492.7
4.	4.763	501.4	6.406	568.0	8.258	574.8
5.	2.709	324.2	3.957	382.5	6.335	463.1
6.	0.352	88.4	1.768	207.3	3.107	224.0
7.	0.859	163.0	0.086	16.0	1.325	119.9
8.	2.735	314.0	1.853	195.3	0.647	75.4

$T_0=T\sqrt{\left(E_1^{(2)}/\rho_2\right)}/a$

$w_0=wE_1^{(2)}h/p$

$M_{x0}=12M_x/pa^2h^2$

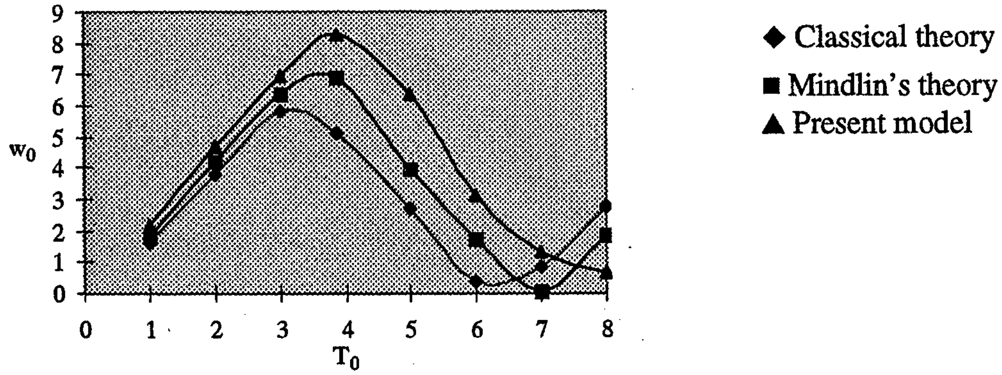

Figure 1. Centre deflection versus time

From Figure 1 it is obvious that both plate theories, classical and Mindlin underestimate deflection w compared to higher order theory.

The eigenvalue problems for free vibrations and buckling of laminated plates are of the standard form:

$$\left(\mathbf{K}-\omega^2\mathbf{M}\right)\mathbf{u}=0 \qquad \left(\mathbf{K}-\lambda\mathbf{K}_\sigma\right)\mathbf{u}=0 \qquad (15)$$

where $\mathbf{K}$, $\mathbf{M}$ and $\mathbf{K}_\sigma$ are the global stiffness, mass and geometric stiffness matrices respectively and $\mathbf{u}$ is the generalised displacements vector. The parameters ω and λ are the circular natural frequency and the in-plane load factor, respectively. To obtain the eigenvalues and associated eigenvectors subspace iteration method has been used. For element mass matrix we performed the special mass lumping scheme in which mass is lumped in the proportion of the diagonal entries of the consistent mass matrix while the total mass of the element has been preserved.

In the following problems, simply supported square plate made up of layers of equal thickness, symmetric cross-ply ($0^0/90^0/0^0$...) laminae, are considered. Each layer is a unidirectional fibre reinforced composite possessing the following engineering elastic constants:

$E_1/E_2=3,10,20,30$ $\quad G_{12}/E_2=0.6$ $\quad G_{23}/E_{23}=0.5$
$\nu_{12}=0.25$ $\quad \rho=1.0$ $\quad G_{13}=G_{23}$

The effect of orthotropy of individual layers on the fundamental frequency of simply supported square multilayered composite plate with *h/a=0.2* is presented in Table 2. The results presented in Table 2 compare well with 3-D elasticity solutions [3] and other solutions available in the open literature [4].

Table 2.
Nondimensional fundamental frequencies $\varpi = (\omega a^2/h)(\rho/E_2)^{1/2}$

Source	N. of layers	E_1/E_2			
		3	10	20	30
Noor	3	0.26474	0.32841	0.38241	0.41089
Owen and Li		0.26948	0.33917	0.38979	0.41941
Present		0.26733	0.33175	0.37491	0.40149
Class. Pl. Theory		0.29198	0.41264	0.54043	0.64336
Noor	5	0.26587	0.34089	0.39792	0.43140
Owen and Li		0.26988	0.34534	0.40297	0.43704
Present		0.26841	0.34419	0.39390	0.42685
Class. Pl. Theory		0.29198	0.41264	0.54043	0.64336

CONCLUSIONS

Numerical results obtained using this refined finite element analysis and their comparison with exact three dimensional analysis pointed out that the higher order theory and the present single layered model provide results which are accurate and acceptable for all ranges of thickness and modular ratio. This approach provides more accurate results than conventional thin or thick plate theory and has advantages over a full three-dimensional continuum analysis in terms of simplicity and economy.

REFERENCES

[1] Reddy, J. N. "A simple higher-order theory for laminated composite plates." *Journal of Applied Mechanics* **51**, pp. 745-752 (1984).

[2] Vuksanovic, Dj. and Perisic, Z. "Free vibrations and buckling of laminated plates using finite element technique." *Proceedings ICCE/4,* pp.1023-1024 (1997).

[3] Noor, A. K. "Free vibrations of multilayered composite plates." *AIAA J.*, **11**, 1038-39 (1973)

[4] Owen, D.R.J. and Li, Z. H. "A refined analysis of laminated plates by finite element displacement methods - II. Vibration and stability." *Comput. Struct.* **26**, 915 - 923 (1987)

VIBRATION CONTROL OF THERMALLY LOADED ORTHOTROPIC PLATES WITH PIEZOELECTRIC STIFFENERS

S Adali[1], T R Tauchert[2] & V E Verijenko[1]
[1]Department of Mechanical Engineering, Univ of Natal, Durban, South Africa
[2]Department of Mechanical Engineering, Univ of Kentucky, Lexington, KY, USA

ABSTRACT – *Converse piezoelectric effect is used to suppress the vibrations of a thermally loaded orthotropic plate stiffened with piezoelectric actuators. The control problem involves the minimization of the dynamic response of the plate by using the voltage applied to the piezoelectric stiffeners as a control variable. The piezoelectric stiffeners are bonded on the opposite surfaces of the plate and placed symmetrically with respect to the middle plane. The control moments are activated by applying out-of phase voltages. The active control takes the form of a piecewise constant alternating voltage with varying switch-over intervals to achieve optimum effect. The specific thermal loading is taken as step temperature rise on one surface with the other surface insulated.*

INTRODUCTION

One of the new directions in the active control of structures involves the application of piezoelectric actuators using the converse piezoelectric effect to induce control forces and moments. These actuators can be implemented in the form of additional layers, patches or stiffeners (see [1] for references). Excessive vibrations may arise as a result of external factors and need to be damped out actively for improved service performance.

The present study is concerned with the active control of an orthotropic plate subjected to thermally induced vibrations using piezoelectric actuator–stiffeners. Structural vibrations due to thermal effects such as rapid heating may arise in aerospace and nuclear reactor applications and has been analysed in [2]. Control of a thermoelastic beam using mechanical actuators has been studied in [3].

The present study takes advantage of the fact that the electric field can be employed as a time–dependent, control variable in suppressing the excessive vibrations. Structural control of an orthotropic plate is achieved by employing the piezoelectric material as actuator–stiffeners. The objective of the control is expressed as a quadratic cost functional involving the deflection and the velocity. The equations are derived for the case of a plate subject to out–of–phase voltage. Vibration control is achieved by applying positive and negative voltages alternatively and determining optimal switch–over times.

BASIC EQUATIONS

We consider a specially orthotropic plate of length a and width b which is reinforced with equally spaced strip–stiffeners as shown in Figure 1. The piezoelectric stiffeners are placed parallel to the geometric coordinates x and y, and are of identical size. The governing equations for the above structure are derived on the basis of the simplifying assumptions discussed in Ref. 1.

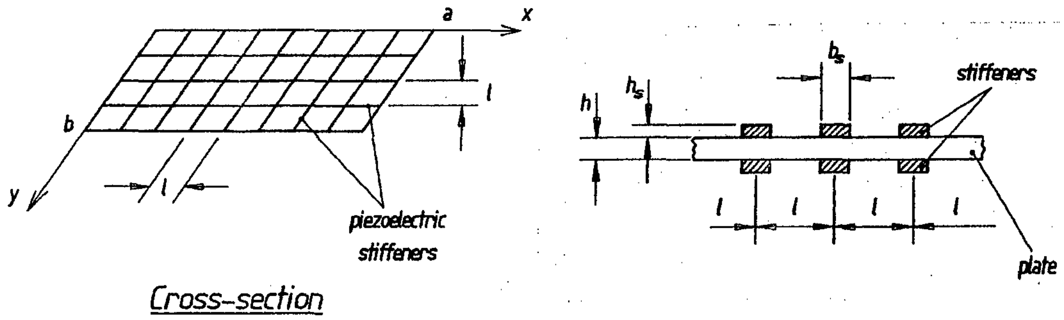

Figure 1. Geometry of the stiffened plate

The equations of motion for the reinforced plate are given by

$$N_{1,x} + N_{6,y} = 0, \quad N_{6,x} + N_{2,y} = 0 \tag{1}$$

$$M_{1,xx} + 2M_{6,xy} + M_{2,yy} + = \rho\, w_{,tt} \tag{2}$$

In eqns. (1) and (2), N_i and M_i are stress resultants and stress couples, respectively, $w(x,y,t)$ is the transverse deflection, ρ is the mass per unit area, and t is time. In the present study, only piezoelectrically induced components of stress resultants are retained. Stress couples and stress resultants can be expressed as a sum of the contributions of the plate and the stiffeners. The plate contributions are given by

$$N_1' = A_{11}\, u_{,x} + A_{12}\, v_{,y}, \qquad N_2' = A_{12}\, u_{,x} + A_{22}\, v_{,y} \tag{3}$$

$$N_6' = A_{66}\,(u_{,y} + v_{,x}), \quad M_1' = -(D_{11}\, w_{,xx} + D_{12}\, w_{,yy}) - M_1^T \tag{4}$$

$$M_2' = -\,(D_{12}\, w_{,xx} + D_{22}\, w_{,yy}) - M_2^T, \quad M_6' = -\,2\, D_{66}\, w_{,xy} \tag{5}$$

where A_{ij} and D_{ij} are extensional and bending stiffnesses of the plate, and u and v are in–plane displacements in the x and y directions. Thermal moments are given by

$$(M_1^T, M_2^T) = \int_{-h/2}^{h/2} (\lambda_1\, , \lambda_2)\; T\, z\, dz \tag{6}$$

where λ_i are stress–temperature coefficients.

The constitutive relation for a slender piezoelectric stiffener, polarized in the z direction and oriented in the x direction is given by

$$\sigma_{xp} = E_p\,(u_{,x} - z\,w_{,xx} - d_{31}\,V_c\,/\,h_s - \alpha_p\,T) \tag{7}$$

where E_p, d_{31} and h_s denote the modulus of elasticity, the piezoelectric constant and the thickness of the stiffeners, respectively. $V_c(x,y,t)$ is the applied voltage and serves as the a control variable and α_p is thermal expansion coefficient of the piezoelectric stiffeners.

The stress resultant and the stress couple induced by the stiffener–actuators oriented in the x direction are obtained from

$$(N_1'', M_1'') = (b_s/l) \int_z \sigma_{xp}\,(1, z)\,dz \tag{8}$$

where b_s is the width of a stiffener and l is the spacing between the stiffeners.

In the present study an electric field of opposite orientation is considered which corresponds to the out–of–phase voltage. In this case, the signs of the piezoelectric strains are opposite leading to a piezoelectric stress couple but no stress resultant. Consequently the control is exercised by bending moments.

PIEZOELECTRIC STRESS RESULTANTS AND COUPLES

The voltage $V_c = V_c(x,y,t)$ has the opposite sign in the stiffeners which are symmetrical about the middle plane. The integration of eqn. (8) yields

$$N_1'' = 2\,E_p\,(b_s\,h_s/l)\,u_{,x} \tag{9}$$

$$M_1'' = -\,2(E_p/l)\,(I\,w_{,xx} + d_{31}\,V_c\,F/h_s + \alpha_p\,(T_2 - T_1)\,(F/2)) \tag{10}$$

where it is assumed that the temperatures of the stiffeners are equal to the corresponding surface temperatures of the plate, viz.

$$T_1(x, y, t) = T(x, y, -h/2, t),\ T_2(x, y, t) = T(x, y, h/2, t) \tag{11}$$

and

$$F = (b_s/\,2)\,[(h/2 + h_s)^2 - (h/2)^2], \quad I = (b_s/3)\,[(h/2 + h_s)^3 - (h/2)^3] \tag{12}$$

are the first and second moments of a stiffener about the middle plane. For the stiffeners along the y direction the corresponding expressions are

$$N_2'' = 2\,E_p\,(b_s\,h_s/l)\,v_{,y} \tag{13}$$

$$M_2'' = -2(E_p/l)\,(I\,w_{,yy} + d_{31}\,V_c\,F/h_s + \alpha_p\,(T_2 - T_1)\,(F/2)) \tag{14}$$

EQUATIONS OF MOTION

The summation of forces and moments contributed by the plate and the stiffeners give the total stress resultants and couples, viz.

$$N_i = N_i' + N_i'' , \qquad M_i = M_i' + M_i'' , \quad i = 1, 2, 6 \tag{15}$$

Substitution of eqns. (15) into the linearized equations of motion (1) and (2) yields the uncoupled equations of motion:

$$\begin{aligned} \bar{D}_{11}\, w_{,xxxx} + 2\,(D_{12} + 2\,D_{66})\, w_{,xxyy} + \bar{D}_{22}\, w_{,yyyy} + \bar{M}^T_{1,xx} + \bar{M}^T_{2,yy} \\ + 2\,E_p\,(h\,F\,/\,l\,h_s)\,(V_{,xx} + V_{,yy}) + \bar{\rho}\, w_{,tt} = 0 \end{aligned} \tag{16}$$

where

$$\bar{M}^T_i = M^T_i + (E_p\,\alpha_p /\, l)\, F\,(T_2 - T_1) \tag{17}$$

$$\bar{M}^T_i = \int_{-h/2}^{h/2} \lambda_i\, T\, z\, dz + (E_p\,\alpha_p /\, l)\, F\,(T_2 - T_1) \tag{18}$$

In eqn. (17) $\bar{D}_{ii} = D_{ii} + 2\,E_p\,I\,/\,l$ are modified bending stiffnesses of a reinforced plate,

$$V = d_{31}\,V_c\,/\,h \tag{19}$$

is the nondimensional control voltage, and

$$\bar{\rho} = \rho_{pl}\,h + \rho_{pz}\,b_s\,h_s\,/\,l \tag{20}$$

is the "smeared" mass per unit area of the structure with ρ_{pl} denoting the mass density of the plate and ρ_{pz} that of the stiffeners. The boundary conditions are also uncoupled and are given by

$$w = 0,\ \bar{D}_{11}\, w_{,xx} + D_{12}\, w_{,yy} + \bar{M}^T_1 + 2\,E_p\,(h\,F/\,l\,h_s)\,V = 0 \quad \text{for } x = 0, a \tag{21}$$

$$w = 0,\ D_{12}\, w_{,xx} + \bar{D}_{22}\, w_{,yy} + \bar{M}^T_2 + 2\,E_p\,(h\,F/\,l\,h_s)\,V = 0 \quad \text{for } y = 0, b \tag{22}$$

The initial conditions of the problem are specified as

$$w(x, y, 0) = \Phi(x, y) , \qquad w_{,t}(x, y, 0) = \Psi(x, y) \tag{23}$$

ACTIVE CONTROL PROBLEM

The control problem is concerned with minimizing the dynamic response of the plate subject to a bound on the maximum value of the voltage that can be applied to the piezoelectric stiffeners which creates a control force on the plate. The control force is in the form of a stress couple.

The minimization is achieved by applying the voltage $V_c(x,y,t)$ in such a manner that the dynamic response of the plate is reduced with time. It was found that a uniform voltage reduces the dynamic response for a certain time duration, but starts to increase it again unless the direction of voltage is reversed at the end of this duration. Thus the application of positive or negative voltage achieves a reduction in the dynamic response in a time interval, and thereafter the sign of the voltage needs to be reversed to continue with the control process. In practice this means that the voltage changes sign at the end of each time interval while the switch–over time for that interval is determined so as to achieve the fastest decrease in the dynamic response.

Let the switch–over times be denoted as t_i, $i = 1, 2, \dots$ and the uniform voltage in the interval $t_i \leq t \leq t_{i+1}$ as $V(t_i)$. It is noted that in a given interval of time the voltage is constant and its sign could be positive or negative. Furthermore, this sign changes alternatively in each consecutive interval. Let the voltage applied in the initial interval $0 \leq t \leq t_1$ be V_0 the sign of which is to be determined so as to reduce the dynamic response at $t = t_1$. Then $V(t_i) = (-1)^i \, V_0$ for $i = 1, 2, \dots$

The objective function describing the dynamic response of the plate is chosen as

$$J_r(t;\, V) = \mu_1 \int_0^a \int_0^b w^2 \, dx \, dy + \mu_2 \int_0^a \int_0^b w_{,t}^2 \, dx \, dy \tag{24}$$

where $\mu_1, \mu_2 > 0$ are weighting factors. The applied voltage satisfies the constraint

$$| V(t_i) | \leq V_{max} \tag{25}$$

where V_{max} is the maximum voltage that can be applied to the plate.

Thus the active control problem studied in this work can be stated as follows:

> Determine the voltage $V(t_i)$ and the switch–over times t_i for each i such that the objective function given by eqn. (24) is reduced as time goes subject to the constraint (25) on the voltage.

METHOD OF SOLUTION FOR RAPID TEMPERATURE RISE

Consider the thermal loading case of suddenly applied uniform temperature $T_o(t)$ acting on the plate surface and zero temperature on the insulated surface $z = -h/2$, ie, $T(x,\, y,\, -h/2,\, t) = 0$. Then (see Ref. 2)

$$T(z,\, t) = T_o \left\{ 1 + \sum_{m=1}^{\infty} \frac{2}{j \pi} (-1)^m \, e^{-j^2 \psi t} \cos\left(\frac{j \pi}{h} (z + h/2) \right) \right\} \tag{26}$$

where $j = m - 1/2$, $\psi = \pi^2 \kappa/h^2$ and κ is the thermal diffusivity [2]. A solution of the problem is sought in the form

$$\{w,\ V,\ \overline{M}_1^T,\ \overline{M}_2^T(x,y,t)\} = \sum_m \sum_n \{z_{mn},\ V_{mn},\ G_{mn},\ H_{mn}(t)\}\ sin(m\pi x/a)\ sin(n\pi y/b) \tag{27}$$

which satisfies the boundary conditions identically. The expressions for M_1^T and M_2^T in eqns (17) and (18) are given in [2]. We define the nondimensional quantities

$$Z_{mn} = z_{mn}/a\ , \qquad \tau = \Omega_{11}\ t, \qquad \omega_{mn} = \Omega_{mn}/\ \Omega_{11} \tag{28}$$

with Ω_{mn} denoting the vibration frequency. The frequencies Ω_{mn} are given by

$$\Omega_{mn} = \{(1/\bar{\rho})\ [\overline{D}_{11}(m\pi/a)^4 + 2(D_{12} + 2D_{66})\ (m\pi/a)^2\ (n\pi/b)^2 + \overline{D}_{22}(n\pi/b)^4]\}^{1/2} \tag{29}$$

The differential equation satisfied by $Z_{mn}^{(i)}(\tau)$ is given by

$$\ddot{Z}_{mn}^{(i)} + \omega_{mn}^2\ Z_{mn}^{(i)} = [(m\pi/a)^2/(\Omega_{11}^2 a\bar{\rho})]\ G_{mn} + [(n\pi/b)^2/(\Omega_{11}^2 a\bar{\rho})]\ H_{mn} + \eta_{mn}\ V_{mn} \tag{30}$$

in the interval for $\tau_i \leq \tau \leq \tau_{i+1}$ where $(\dot{\ \ }) = \partial(\ \ )/\partial\tau$ and

$$\eta_{mn} = (h\ /\ 2\ a)\ (1 + h_s/\ h)\ \kappa_{mn} \tag{31}$$

$$\kappa_{mn} = 2\ E_p\ h\ b_s\ [(m\pi/a)^2 + (n\pi/b)^2]\ /\ (\bar{\rho}\ \Omega_{11}^2\ l) \tag{32}$$

The solution of eqn. (30) can be obtained using standard techniques.

CONCLUSIONS

The problem of actively controlling the thermally induced vibrations of a plate reinforced with piezoceramic stiffener–actuators has been formulated. The control is applied by adopting a time–dependent out–of–phase voltage for optimum vibration damping with the voltage assuming alternatively positive and negative bounds. The switch–over times are determined at every step optimally.

ACKNOWLEDGEMENT

This material is based upon work supported by the Division of International Programs of the National Science Foundation under Grant No. INT–9515326.

REFERENCES

1. V Birman & S Adali, Vibration damping using piezoelectric stiffener–actuators with application to orthotropic plates. *Composite Structs*, V. 35, 251–261, 1996.

2. N N Huang & T R Tauchert, Thermally induced vibration of doubly curved cross–ply laminated plates. *J of Sound and Vibration*, V. 154, 485–494, 1992.

3. J C Bruch Jr, S Adali, IS Sadek & J M Sloss, Structural control of thermoelastic beams for vibration suppression. *J of Thermal Stresses*, V. 16, 249–263, 1993.

MINIMIZATION OF DEFLECTION USING PIEZO EFFECT AND PLY ANGLES FOR THICK LAMINATED PLATES

S. ADALI[1] V.E. VERIJENKO[1] T.R. TAUCHERT[2] A. RICHTER[3]

[1] Department of Mechanical Engineering, University of Natal, South Africa
[2] Department of Mechanical Engineering, University of Kentucky, USA
[3] Department of Mechanical Engineering, University of Siegen, Germany

ABSTRACT

The converse piezo effect is used to minimize the deflection at a given point for antisymmetrically laminated thick rectangular plates. The piezoelectric layers are bonded to the top and bottom surfaces of the laminate and are subjected to an electrical field. The deformation generated by the piezo effect counteracts the deflections induced by mechanical and/or thermal loads. In the numerical examples, the mid-point of the plate is specified as the point deflection of which is to be minimized.

INTRODUCTION

Adaptive materials technology provides a highly effective tool for the static and dynamic control of structural systems. In particular piezoelectric materials may be used as sensors and/or actuators by employing direct or converse piezoelectric effects.

It is quite common for structural systems to work under mechanical and thermal loads leading to the coupling of these fields with the electrical field when piezoelectric materials are part of the structure. Piezothermoelastic response of composite structures has been studied in order to incorporate the advanced materials technology with smart materials technology in the presence of thermal effects [1]. The particular application of piezothermal materials as sensors have been proposed by Ashida and Tauchert [2].

In the present study, the objective is to investigate the use of piezoelectric materials in the static control of laminated structures. Both the electric field and the ply angles can be employed as design variables in reducing the deflection of a laminate. The particular problem solved in this study involves the minimization of the deflection of a given point of an antisymmetric thick laminate using the voltage and ply angles as design variables. It is shown that the converse piezo effect and the material directions can be used effectively to counter the deformation induced by mechanical and/or thermal loads.

BASIC EQUATIONS

Consider a multilayered rectangular laminate of length a, width b and thickness

h in the x, y and z directions. The laminate is composed of N number of generally orthotropic layers and layers of a piezoelastic material. The laminate may be subjected to mechanical, thermal and electrical loads leading to static deformation.

A general higher–order theory is employed to compute the displacement components u, v and w in the x, y and z directions, respectively. In particular choosing a third–order theory in the thickness direction, these components can be expressed as

$$(u, v, w) = (u^\circ, v^\circ, w^\circ) + z(\psi_x, \psi_y, \psi_z) + z^2(\xi_x, \xi_y, \xi_z) + z^3(\varphi_x, \varphi_y, \varphi_z) \qquad (1)$$

where the superscript "o" denotes mid–plane displacements and the variables ψ, ξ and φ are functions of x and y coordinates only. Imposing the condition of zero transverse shear at $z = \pm h/2$, ξ_x, ξ_y, φ_x and φ_y can be expressed in terms of other variables.

The stress–strain equations for structural and piezoelectric layers ($k = 1, 2, \ldots, N$) are given by

$$\begin{bmatrix}\sigma_x\\ \sigma_y\\ \sigma_z\\ \tau_{yz}\\ \tau_{xz}\\ \tau_{xy}\end{bmatrix} = \begin{bmatrix} \overline{Q}_{11} & \overline{Q}_{12} & \overline{Q}_{13} & 0 & 0 & \overline{Q}_{16}\\ & \overline{Q}_{22} & \overline{Q}_{23} & 0 & 0 & \overline{Q}_{26}\\ & & \overline{Q}_{33} & 0 & 0 & \overline{Q}_{36}\\ & & & \overline{Q}_{44} & \overline{Q}_{45} & 0\\ & & & & \overline{Q}_{55} & 0\\ & & & & & \overline{Q}_{66} \end{bmatrix}$$

$$\times \begin{bmatrix}\varepsilon_x\\ \varepsilon_y\\ \varepsilon_z\\ \gamma_{yz}\\ \gamma_{xz}\\ \gamma_{xy}\end{bmatrix}_k - \begin{bmatrix}\overline{e}_{31}\\ \overline{e}_{32}\\ \overline{e}_{33}\\ 0\\ 0\\ \overline{e}_{36}\end{bmatrix} [E_z]_k - \begin{bmatrix}\overline{\lambda}_1\\ \overline{\lambda}_2\\ \overline{\lambda}_3\\ 0\\ 0\\ \overline{\lambda}_6\end{bmatrix} t \qquad (2)$$

where $\overline{Q}_{ij}$ are the transformed elastic coefficients, $\overline{e}_{ij}$ are the transformed piezoelectric coefficients, $\overline{\lambda}_i$ are transformed stress–temperature coefficients, E_z is the applied electric field and t is a temperature rise from a stress–free equilibrium. Note that $\overline{e}_{ij}$ are zero for the structural material.

Using the principle of virtual displacements the governing equations and the boundary conditions of the problem can be obtained. The principal of virtual displacements can be expressed as

$$\int_{-h/2}^{h/2}\int_A (\sigma_x\delta\varepsilon_x + \sigma_y\delta\varepsilon_y + \sigma_z\delta\varepsilon_z + \tau_{xy}\delta\gamma_{xy} + \tau_{yz}\delta\gamma_{yz} + \tau_{xz}\delta\gamma_{xz})dAdz = \int_A q\delta w^\circ dA \qquad (3)$$

where q is the transverse load acting on the plate.

The equations of equilibrium can be derived using eq. (3) by substituting the stresses and strains expressed in terms of stress resultants and deformation variables. These results are given in [3], and are not included here for brevity.

THE DESIGN PROBLEM

The design problem investigated in the present study refers to the problem of minimizing the transverse deflection $|w(x,y,z)|$ at a given point (x_0, y_0, z_0) using the ply angles and the electric field as design variables. The loading on the plate could be mechanical, thermal or a combination of both. Thus, the deflection w is a function of the transverse load q, temperature variation t as well as the design variables θ_k and E_z, viz.

$$w = w(x,y,z,q,t;\theta_k,E_z) \tag{4}$$

where, in general, $q = q(x,y)$ and $t = t(x,y,z)$. Let S_0 denote the given set of values of location and loading, i.e.,

$$S_0 = \{x_0,y_0,z_0,q,t\} \tag{5}$$

and $w_0 = w_0(S_0;\ \theta_k,\ E_z)$ denotes the deflection evaluated at s_0. The optimal design problem can be stated as

Determine the optimal values of θ_k and E_z for a laminate subject to the mechanical and thermal loads q and t such that the transverse deflection at (x_0, y_0, z_0) is minimized, viz,

$$\min_{\theta_k,E_z} |w_0(S_0;\ \theta_k,\ E_z)| \tag{6}$$

Note that the minimum value could be zero, however, in general $|w_0| > 0$.

ANTISYMMETRIC PIEZOELASTIC LAMINATE

The specific laminate to be studied in the present work is chosen as an antisymmetric one with fiber orientations $\pm\theta$ with respect to the x-axis so that $\theta_k = (-1)^{k+1}\theta$, $k = 1,2,\ldots,N$ where N is an even number. The piezoelastic layers are required to have principal material directions coinciding with the geometric coordinates. This configuration leads to a number of simplifications and some of the stiffnesses become zero (see Ref. [3]).

For a simply supported laminate, Navier-type solutions could be expressed in terms of trigonometric series for the variables u°, v°, w°, ψ_x, ψ_y, ψ_z, ξ_z and φ_z. The stress resultants due to electric field and thermal loading can be expressed using Fourier series. Finally employing the equations of equilibrium, a linear system of equations is obtained to compute the unknown Fourier coefficients. The details of these calculations are given in [3] and are not shown here.

NUMERICAL RESULTS

The results are given for a laminate with graphite/epoxy structural layers PZT-5A piezoelectric layers. The material properties of the graphite/epoxy (T300/5208) material are taken as

$$E_1 = 181GPa,\ E_2 = E_3 = 10.3GPa,\ G_{12} = G_{13} = 7.17GPa,\quad G_{23} = 2.87GPa$$

$$\nu_{12} = \nu_{13} = 0.28,\ \nu_{23} = 0.33,\ \alpha_1 = 0.02\cdot 10^{-6}/C,\ \alpha_2 = \alpha_3 = 22.5\cdot 10^{-6}/C$$

The properties of the PZT-5A material are

$$E_1 = E_2 = 61GPa,\ E_3 = 53.2GPa,\ G_{12} = 22.6GPa$$

$$G_{13} = G_{23} = 21.1GPa,\ \nu_{12} = 0.35,\ \nu_{13} = \nu_{23} = 0.38$$

$$\alpha_1 = \alpha_2 = 1.5 \cdot 10^{-6}/C, \quad \alpha_3 = 2.0 \cdot 10^{-6}/C,$$

$$d_{31} = d_{32} = -171 \cdot 10^{-12} m/v,\ d_{33} = 374 \cdot 10^{-12} m/v$$

where α_i and d_{ij} denote the thermal expansion and piezoelectric compliance coefficients, respectively. The results are obtained for a twelve–layer laminate of configuration $(p/p/(\theta/-\theta)_4/p/p)$ where p denotes the piezoelastic layers.

The mechanical loading is specified as a uniformly distributed load of q and the thermal load as $t(z) = 2zT/h$, where T indicates the temperature.

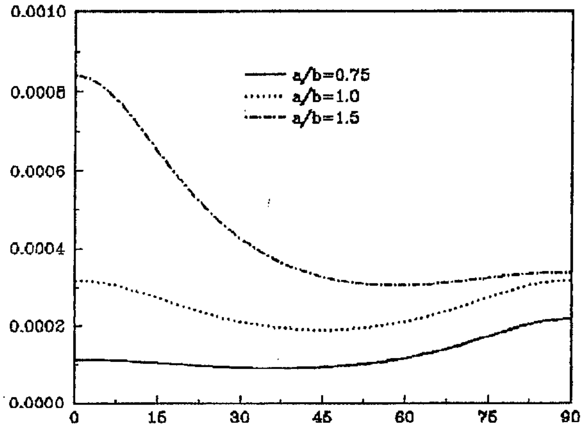

Figure 1. Mid–point deflection versus ply angle ($q = 100Pa, T = E_z = 0$).

In the present study, the location of the displacement to be minimized is chosen as the mid-point of the plate, i.e., $x_0 = 0.5a$, $y_0 = 0.5b$ and $z_0 = 0$. The thickness ratio in all the calculations is taken as $h/b = 0.1$. Figures 1 and 2 show the curves of w_0/b versus θ for various aspect ratios under mechanical ($q = 100Pa$) and thermal ($T = 40°C$) loading only, i.e. $E_z = 0$. The curves indicate the optimum values of θ for minimum deflection at different aspect ratios. Thus, for $a/b = 1.0$ $\theta_{opt} = 45°$. For $a/b > 1$, $\theta_{opt} > 45°$ and for $a/b < 1$, $\theta_{opt} > 45°$.

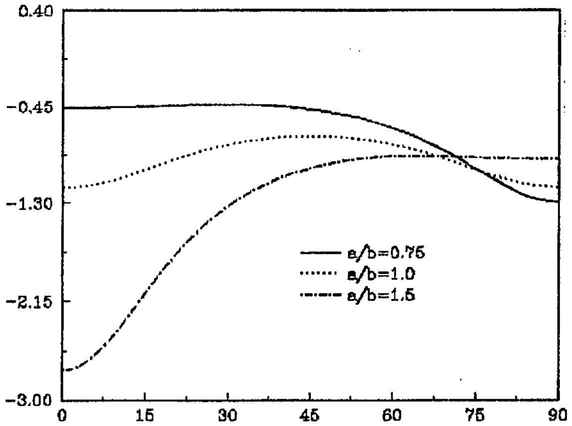

Figure 2. Mid–point deflection versus ply angle ($T = 40°C, q = E_z = 0$).

Figure 3 shows the curves of w_0/b versus θ for various aspect ratios with the electric field specified as $E_z = -/+30 \cdot 10^6 v/m$, and $q = t = 0$, i.e., deflections due to piezoelectric effect only. It is observed that the deflection depends on the fiber angle, aspect ratio and the magnitude of the electric field. Clearly, the piezo effect can be used to suppress the deflections due to mechanical and thermal loading by adjusting the direction and magnitude of the electrical field.

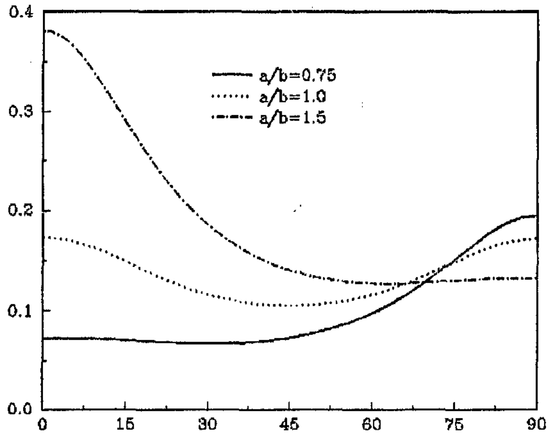

Figure 3. Mid–point deflection versus ply angle ($E_z = 30 \cdot 10^6 v/m, q = T = 0$).

Figure 4 shows the graph of w_0/b plotted against E_z and θ for a plate with $a/b = 2.0$, $q = 100Pa$ and $t = 0$. It is clear that $w_0 = 0$ at certain values of E_z and θ.

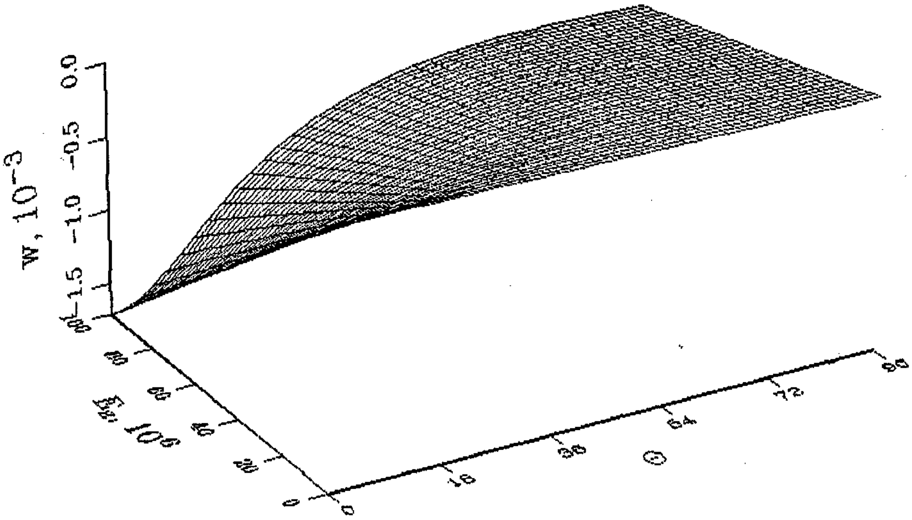

Figure 4. Mid–point deflection versus E_z and ply angle
($q = 100Pa, T = 0, a/b = 2$).

The corresponding results for a laminate under thermal loading are given in Fig. 5. Figure 5 shows the graph of w_0/b versus E_z and θ for a plate with $a/b = 2.0$, $T = 10°C$ and $q = 0$.

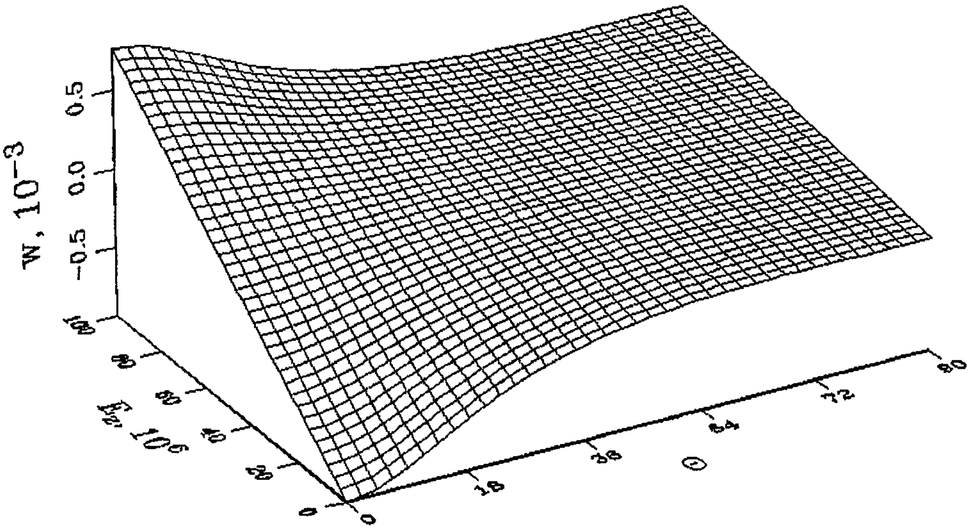

Figure 5. Mid–point deflection versus E_z and ply angle ($T = 10°C, q = 0, a/b = 2$).

CONCLUSIONS

The piezoelectric effect has been used to minimize the deflection at a given point of an antisymmetric laminate under mechanical and/or thermal loads. It was shown that it is possible to compute the right combination of the electrical field and the fiber orientation to reduce the deflection of a point. In the calculations the mid-point deflection of the laminate was chosen to be minimized and the results were obtained to suppress this deflection by applying a certain electrical field at a given fiber orientation.

The use of converse piezo effect for deformation control appears to be an effective way of suppressing excessive deflection of laminates under given mechanical or thermal loads. As the electric field could be adjusted for any loading conditions, the resulting structure is adaptive with respect to deformations and its in-service performance will be superior to that of a non-adaptive structure.

ACKNOWLEDGEMENT

This material is based upon work supported by the Division of International Programs of the National Science Foundation under Grant No. INT–9515326

REFERENCES

[1] Tauchert, T. R., 1992, “Piezothermoelastic Behaviour of a Laminate.” *Journal of Thermal Stresses,* **15**, pp. 25–37.

[2] Ashida, F., and Tauchert, T. R., 1997, “An Inverse Problem for Determination of Transient Surface Temperature from Piezoelectric Sensor Measurement.” *In Review.*

[3] Xu, Y., Tauchert, T. R., and Blandorf, G. E., 1993, “Piezothermoelastic Analysis of an Antisymmetric, Angle-Ply Laminate Using a High–Order Displacement Formulation.” AD – **37**/AMD – **179**, *Composite Materials and Structures, ASME,* 1993, pp. 89–102.

VIBRATION ANALYSIS OF LAMINATED COMPOSITE BEAMS WITH PIEZOELECTRIC LAYERS USING A HIGHER ORDER THEORY

D. HUANG and B. SUN

Centre for Research in Applied Technology and Dept. Mechanical Engineering, Peninsula
Technikon, P.O. Box 1906, Bellville 7535, Cape Town, South Africa
E-mail: huangd@mecheng.pentech.ac.za

Abstract In this paper, a model to demonstrate the dynamic analysis of composite beams with bonded or embedded piezoelectric sensors and actuators is presented. A theory of laminated composite beams with piezoelectric laminae is developed. The higher order shear deformation theory of Reddy is used in formulating the model. The method of exact solutions for the frequencies of free vibration for simply supported composite beams with piezoelectric layers is also presented.

INTRODUCTION

The intelligent/smart structures featuring a network of integrated sensors and actuators within a host material will have a tremendous effect upon numerous industrial fields. The idea of applying "smart" materials to mechanical and structural systems has been studied by researchers in various disciplines. Among the promising materials with adaptable properties such as piezoelectric polymers and ceramics, shape memory alloys, electrorheological fluids and optical fibers, piezoelectric materials can be used both as sensors and actuators because of their high direct and converse piezoelectric effects. Especially piezoelectric materials, which exhibit mechanical deformation when an electric field is applied and conversely, generate a change in response to mechanical deformation, is very good smart materials. By employing piezoelectric materials, it is feasible to achieve accurate response monitoring and effective control of flexible structures. This advantage is especially apparent for structures that are deployed in aerospace and civil engineering.

In order to utilise the strain-sensing and actuating properties of piezoelectric materials, the interaction between the structure and SSA (strain sensing and actuating) material must be well understood. Mechanical model for studying the interaction of piezoelectric patches surface-mounted to beams have been developed by Crawley and de Luis (1987), Im and Atluri (1989), and Chandra and Chopra (1993). The present paper is different from these in that we study laminated beams containing piezoelectric laminae. The modeling aspects of laminated plates incorporating the piezoelectric property of materials have been reported in Lee (1990), Crawley and Lazarus (1991), and Wang and Rogers (1991). And Lee (1990) derived a theory for laminated piezoelectric plates, where the linear piezoelectric constitutive equations were the only source of coupling between the electric field and the mechanical displacement field. However, these models are based on classical laminated plate theory, which neglects the transverse shear effects. But the effects of transverse shear stresses are important in composite materials because the interlaminar shear module are usually much smaller than the inplane Young's module. An overview of recent developments in the area of sensing and control of structures by piezoelectric materials has been reported in Rao and Sunar (1994). Recently G. Mei and Y. Shen (1997) used optical fiber sensors to measure transient impact induced strain.

There are two essential ideas in this paper. Firstly, the purpose of present study is to derive a set of approximate governing equations for laminated beams with piezoelectric laminae using Hamilton's principle based on a higher order shear deformation theory, which does not require shear correction factors. Secondly, the objective of the present study is to develop exact solutions for the frequencies of free vibration for simply supported, laminated beams composed in part of piezoelectric layers. The simply supported beam is one of the few geometries for which the in-plane function can be selected to exactly satisfy the governing equations and boundary conditions. The arbitrary transformations of constitutive equations for smart composite structures are also presented.

DISPLACEMENT FIELD

In this paper, the model of beam comes from the plate. It is a specific plate. The assumption to the point where exist theories can be utilised. In the higher order shear deformation theory of Reddy (1984), the displacement field chosen is of a special form. The form is dictated by the satisfaction of the conditions that the transverse shear stresses vanish on the plate surfaces and be nonzero elsewhere. This requires the use of a displacement field in which the inplane displacements are expanded as cubic functions of thickness co-ordinate and the transverse deflection is constant through plate thickness. The displacement field in Ref.[10] can be written as:

$$
\begin{aligned}
u_1(x,y,z,t) &= u(x,y,t) + z\left[\psi_x - \frac{4}{3}\left(\frac{z}{h}\right)^2\left(\psi_x + \frac{\partial w}{\partial x}\right)\right] \\
u_2(x,y,z,t) &= v(x,y,t) + z\left[\psi_y - \frac{4}{3}\left(\frac{z}{h}\right)^2\left(\psi_y + \frac{\partial w}{\partial y}\right)\right] \qquad (1) \\
u_3(x,y,z,t) &= w(x,y,t)
\end{aligned}
$$

The salient feature of this particular theory is that it allows for cubic distortion of the normals to the midplane while at same time eliminating the need for shear correction factors normally used in the first order shear deformation theory.

Using the above definitions, the displacement field for beam can be expressed as:

$$
\begin{aligned}
u_1(x,y,z,t) &= u(x,t) + z\left[\psi - \frac{4}{3}\left(\frac{z}{h}\right)^2\left(\psi + \frac{\partial w}{\partial x}\right)\right]. \\
u_2(x,y,z,t) &= 0 \qquad (2) \\
u_3(x,y,z,t) &= w(x,t)
\end{aligned}
$$

where $u(x,t)$ and $w(x,t)$ in Eq.(6) are the mid-plane displacements and $\psi(x,t)$ is the rotation of a transverse normal to mid-plane about y-axis. The displacement for y-axis is neglected and u, w and ψ are only function of x-axis and time (t) in the present model of the beam.

CONSTITUTIVE RELATIONSHIP

The laminae constitutive equation accounting for piezoelectric effect for the kth layer in the material axes can be written as

$$
\begin{Bmatrix} \sigma_1 \\ \sigma_2 \\ \tau_{23} \\ \tau_{13} \\ \tau_{12} \end{Bmatrix}_k = \begin{bmatrix} Q_{11} & Q_{12} & 0 & 0 & 0 \\ Q_{12} & Q_{22} & 0 & 0 & 0 \\ 0 & 0 & Q_{44} & 0 & 0 \\ 0 & 0 & 0 & Q_{55} & 0 \\ 0 & 0 & 0 & 0 & Q_{66} \end{bmatrix}_k \begin{Bmatrix} \varepsilon_1 \\ \varepsilon_2 \\ \gamma_{23} \\ \gamma_{13} \\ \gamma_{12} \end{Bmatrix}_k - \begin{bmatrix} 0 & 0 & e_{31} \\ 0 & 0 & e_{32} \\ 0 & e_{24} & 0 \\ e_{15} & 0 & 0 \\ 0 & 0 & 0 \end{bmatrix}_k \begin{Bmatrix} E_1 \\ E_2 \\ E_3 \end{Bmatrix}_k \qquad (3)
$$

$$
\begin{Bmatrix} D_1 \\ D_2 \\ D_3 \end{Bmatrix}_k = \begin{bmatrix} 0 & 0 & 0 & e_{15} & 0 \\ 0 & 0 & e_{24} & 0 & 0 \\ e_{31} & e_{32} & 0 & 0 & 0 \end{bmatrix}_k \begin{Bmatrix} \varepsilon_1 \\ \varepsilon_2 \\ \gamma_{23} \\ \gamma_{13} \\ \gamma_{12} \end{Bmatrix}_k + \begin{bmatrix} g_{11} & 0 & 0 \\ 0 & g_{22} & 0 \\ 0 & 0 & g_{33} \end{bmatrix}_k \begin{Bmatrix} E_1 \\ E_2 \\ E_3 \end{Bmatrix}_k \qquad (4)
$$

However, the material axes of laminae often do not coincide with the plate co-ordinate directions. Then, transforming constitutive relations from the principal material directions to the laminate co-ordinate directions is needed (Ref. [7]). Upon transformation for using transformed matrix $[T]$ and $[T_0]$ (see Appendix), the lamina constitutive equations can be expressed in term of stresses and strains in the laminae co-ordinates (x, y, z) as

$$\begin{Bmatrix} \sigma_x \\ \sigma_y \\ \tau_{yz} \\ \tau_{xz} \\ \tau_{xy} \end{Bmatrix}_k = \begin{bmatrix} \overline{Q}_{11} & \overline{Q}_{12} & 0 & 0 & \overline{Q}_{16} \\ \overline{Q}_{12} & \overline{Q}_{22} & 0 & 0 & \overline{Q}_{26} \\ 0 & 0 & \overline{Q}_{44} & \overline{Q}_{45} & 0 \\ 0 & 0 & \overline{Q}_{45} & \overline{Q}_{55} & 0 \\ \overline{Q}_{16} & \overline{Q}_{26} & 0 & 0 & \overline{Q}_{66} \end{bmatrix}_k \begin{Bmatrix} \varepsilon_x \\ \varepsilon_y \\ \gamma_{yz} \\ \gamma_{xz} \\ \gamma_{xy} \end{Bmatrix}_k - \begin{bmatrix} 0 & 0 & \overline{e}_{31} \\ 0 & 0 & \overline{e}_{32} \\ \overline{e}_{14} & \overline{e}_{24} & 0 \\ \overline{e}_{15} & \overline{e}_{25} & 0 \\ 0 & 0 & \overline{e}_{36} \end{bmatrix}_k \begin{Bmatrix} E_x \\ E_y \\ E_z \end{Bmatrix}_k \tag{5}$$

$$\begin{Bmatrix} D_x \\ D_y \\ D_z \end{Bmatrix}_k = \begin{bmatrix} 0 & 0 & \overline{e}_{14} & \overline{e}_{15} & 0 \\ 0 & 0 & \overline{e}_{24} & \overline{e}_{25} & 0 \\ \overline{e}_{31} & \overline{e}_{32} & 0 & 0 & \overline{e}_{36} \end{bmatrix}_k \begin{Bmatrix} \varepsilon_x \\ \varepsilon_y \\ \gamma_{yz} \\ \gamma_{xz} \\ \gamma_{xy} \end{Bmatrix}_k + \begin{bmatrix} \overline{g}_{11} & \overline{g}_{12} & 0 \\ \overline{g}_{12} & \overline{g}_{22} & 0 \\ 0 & 0 & \overline{g}_{33} \end{bmatrix}_k \begin{Bmatrix} E_x \\ E_y \\ E_z \end{Bmatrix}_k \tag{6}$$

The constitutive relationship for the kth laminae can be simply expressed by using matrix expression as

$$\{\sigma\}_k = [\overline{Q}]_k \{\varepsilon\}_k - [\overline{e}]_k^T \{E\}_k \tag{7}$$

$$\{D\}_k = [\overline{e}]_k \{\varepsilon\}_k + [\overline{g}]_k \{E\}_k \tag{8}$$

where $\{\varepsilon\}$ is the strain, $\{\sigma\}$ is the stress, $\{D\}$ is the electric displacement, $\{E\}$ is the electric field intensity, $[\overline{Q}]$ is the elastic stiffness matrix, $[\overline{e}]$ is the piezoelectric stress coefficient matrix, and $[\overline{g}]$ is the permitivity matrix (for more details, see Appendix). For non-piezoelectric laminae, it can be modelled by simply setting the piezoelectric constants to zero.

Piezoelectric materials possess anisotropic properties. PVDF (polyvinylidene fluoride) and PZT (lead zirconate-titanate) are excellent candidates for the role of sensors and actuators. Piezoelectric material layers are polarised in the thickness direction and exhibit transversely isotropic properties in the xy-plane. Considering piezoelectric materials while retaining the anisotropic behaviour of the master structure, Eq. (5) can be written as

$$\begin{Bmatrix} \sigma_x \\ \sigma_y \\ \tau_{yz} \\ \tau_{xz} \\ \tau_{xy} \end{Bmatrix}_k = \begin{bmatrix} \overline{Q}_{11} & \overline{Q}_{12} & 0 & 0 & \overline{Q}_{16} \\ \overline{Q}_{12} & \overline{Q}_{22} & 0 & 0 & \overline{Q}_{26} \\ 0 & 0 & \overline{Q}_{44} & \overline{Q}_{45} & 0 \\ 0 & 0 & \overline{Q}_{45} & \overline{Q}_{55} & 0 \\ \overline{Q}_{16} & \overline{Q}_{26} & 0 & 0 & \overline{Q}_{66} \end{bmatrix}_k \begin{Bmatrix} \varepsilon_x \\ \varepsilon_y \\ \gamma_{yz} \\ \gamma_{xz} \\ \gamma_{xy} \end{Bmatrix}_k - \begin{bmatrix} 0 & 0 & \overline{e}_{31} \\ 0 & 0 & \overline{e}_{31} \\ \overline{e}_{25} & \overline{e}_{15} & 0 \\ \overline{e}_{15} & \overline{e}_{25} & 0 \\ 0 & 0 & 0 \end{bmatrix}_k \begin{Bmatrix} 0 \\ 0 \\ E_z \end{Bmatrix}_k \tag{9}$$

For a beam problem, we can use $\sigma_y = \tau_{yz} = \tau_{xy} = 0$ while assuming the $\varepsilon_y \neq \gamma_{yz} \neq \gamma_{xy} \neq 0$, to obtain the following reduced constitutive equations

$$\begin{Bmatrix} \sigma_x \\ \tau_{xz} \end{Bmatrix}_k = \begin{bmatrix} \widetilde{Q}_{11} & 0 \\ 0 & \widetilde{Q}_{55} \end{bmatrix}_k \begin{Bmatrix} \varepsilon_x \\ \gamma_{xz} \end{Bmatrix}_k - \begin{bmatrix} \widetilde{e}_{31} \\ 0 \end{bmatrix}_k E_z^k \tag{10}$$

where

$$\widetilde{Q}_{11} = \overline{Q}_{11} + \left(\frac{\overline{Q}_{16}\overline{Q}_{26} - \overline{Q}_{12}\overline{Q}_{66}}{\overline{Q}_{22}\overline{Q}_{66} - \overline{Q}_{26}^2} \right) \overline{Q}_{12} + \left(\frac{\overline{Q}_{12}\overline{Q}_{26} - \overline{Q}_{22}\overline{Q}_{16}}{\overline{Q}_{22}\overline{Q}_{66} - \overline{Q}_{26}^2} \right) \overline{Q}_{16}$$

$$\widetilde{Q}_{55} = \overline{Q}_{55} - \frac{\overline{Q}_{45}^2}{\overline{Q}_{44}}, \quad \widetilde{e}_{31} = \left(1 - \frac{\overline{Q}_{12}\overline{Q}_{66} - \overline{Q}_{16}\overline{Q}_{26}}{\overline{Q}_{22}\overline{Q}_{66} - \overline{Q}_{26}^2} \right) \overline{e}_{31}$$

The strain displacement relations for a laminated beam based on a higher order shear deformation theory can be expressed as (Ref.[2])

$$\begin{cases} \varepsilon_x = \varepsilon_x^0 + z\kappa_x^1 + z^3\kappa_x^2 \\ \gamma_{xz} = \gamma_{xz}^0 + z^2\kappa_{xz} \end{cases} \tag{11}$$

where

$$\begin{cases} \varepsilon_x^0 = \dfrac{\partial u}{\partial x}; \quad \kappa_x^1 = \dfrac{\partial \psi}{\partial x}; \quad \kappa_x^2 = -\dfrac{4}{3h^2}\left(\dfrac{\partial \psi}{\partial x} + \dfrac{\partial^2 w}{\partial x^2}\right) \\ \gamma_{xz}^0 = \psi + \dfrac{\partial w}{\partial x}; \quad \kappa_{xz} = -\dfrac{4}{h^2}\left(\psi + \dfrac{\partial w}{\partial x}\right) \end{cases} \tag{12}$$

In this paper, the laminated beam having length *l*, width *b*, and thickness *h*. We assume that the top and bottom layers of the present beam model are sensor and actuator layers. Using Eq.(11) in Eq.(10) and integrating through the thickness, the laminated beam constitutive equation can be written as:

$$\begin{Bmatrix} N_x \\ M_x \\ P_x \end{Bmatrix} = \begin{bmatrix} \overline{A}_{11} & \overline{B}_{11} & \overline{E}_{11} \\ \overline{B}_{11} & \overline{D}_{11} & \overline{F}_{11} \\ \overline{E}_{11} & \overline{F}_{11} & \overline{H}_{11} \end{bmatrix} \begin{Bmatrix} \varepsilon_x^0 \\ k_x^1 \\ k_x^2 \end{Bmatrix} - \begin{Bmatrix} N_x^p \\ M_x^p \\ P_x^p \end{Bmatrix} \tag{13a}$$

$$\begin{Bmatrix} Q_{xz} \\ R_{xz} \end{Bmatrix} = \begin{bmatrix} \overline{A}_{55} & \overline{D}_{55} \\ \overline{D}_{55} & \overline{F}_{55} \end{bmatrix} \begin{Bmatrix} \gamma_x^0 \\ k_{xz} \end{Bmatrix} \tag{13b}$$

where

$$\{N_x, M_x, P_x\} = \int_{-\frac{h}{2}}^{\frac{h}{2}} \sigma_x\left(1, z, z^3\right)dz, \quad \{Q_{xz}, R_{xz}\} = \int_{-\frac{h}{2}}^{\frac{h}{2}} \tau_{xz}\left(1, z^2\right)dz$$

$$\{\overline{A}_{11}, \overline{B}_{11}, \overline{D}_{11}, \overline{E}_{11}, \overline{F}_{11}, \overline{H}_{11}\} = \sum_{k=1}^{n}\int_{z_{k-1}}^{z_k} \widetilde{Q}_{11}\left(1, z, z^2, z^3, z^4, z^6\right)dz$$

$$\{\overline{A}_{55}, \overline{D}_{55}, \overline{F}_{55}\} = \sum_{k=1}^{n}\int_{z_{k-1}}^{z_k} \widetilde{Q}_{55}\left(1, z^2, z^4\right)dz$$

$$\{N_x^p, M_x^p, P_x^p\} = \int_{z_{n-1}}^{z_n} \widetilde{e}_{31}E_z^k\left(1, z, z^3\right)dz + \int_{z_0}^{z_1} \widetilde{e}_{31}E_z^k\left(1, z, z^3\right)dz$$

Where the $\widetilde{Q}_{ij}$ are the kth material constants. For non-piezoelectric layers $\widetilde{Q}_{ij} = \widetilde{Q}_{ij}^b$, and for piezoelectric layers $\widetilde{Q}_{ij} = \widetilde{Q}_{ij}^p$.

SENSOR EQUATION

The Eq.(6) is used to calculate the output charge created by the strains in the beam. Since no external electric field is applied to the sensor layer, the electric displacement developed on the sensor surface is directly proportional to the strain acting on the sensor. If the z-axis is the poling axis, the charge is collected only in the z-direction. Hence, only D_z^k is considered. For a PVDF layer acting as a sensor $E_z = 0$ and (Ref.[6])

$$D_z^k = \widetilde{e}_{31}\left(\varepsilon_x^0 + z\kappa_x^1 + z^3\kappa_x^2\right) \tag{14}$$

The total charge measured through sensor layer is given by (Ref.[8])

$$q(t) = \frac{1}{2}\left[\left(\int_R D_z^k dA\right)_{z=z_1} + \left(\int_R D_z^k dA\right)_{z=z_0}\right] \tag{15}$$

where *R* is the effective surface electrode of the piezoelectric layer. Substitution of Eq.(14) in Eq.(15) results in

$$q(t) = \int_0^l \widetilde{e}_{31}\left(\varepsilon_x^0 + z_k^1\kappa_x^1 + z_k^3\kappa_x^2\right)b\,dx \tag{16}$$

where

$$z_k^1 = \frac{1}{2}\left(z_1 + z_0\right), \quad z_k^3 = \frac{1}{2}\left(z_1^3 + z_0^3\right)$$

When piezoelectric sensors are used as strain rate sensors, the output charge can be transformed to sensor voltage as (Ref.[6])

$$V^s(t) = \frac{1}{C} q(t) \tag{17}$$

where C is the electric capacity of sensor.

ACTUATOR EQUATION (EQUATION OF MOTION)

In this paper, we use the negative velocity feedback control. Then the applied voltage across the actuator layer can be expressed as (Ref.[8])

$$V^A = G_i i(t) = G_i \frac{dq(t)}{dt} \tag{18}$$

where G_i is the gain to provide feedback control.

The electric field intensity E_z^k can be expressed as

$$E_z^k = \frac{V^A}{h_k} \tag{19}$$

where h_k is the thickness of the actuator layer.

The mathematical statement of Hamilton's principle can be expressed as

$$\int_{t_1}^{t_2} (\delta T - \delta U + \delta W) dt = 0 \tag{20}$$

where T is the kinetic energy, U is the strain energy, and W is the work done by surface tractions. The variation of the kinetic energy is given by

$$\delta T = \int_l \{\delta \dot{u}\}^T [\overline{M}] \{\dot{u}\} b dx \tag{21}$$

where
$$\{u\} = \left[u, w, \frac{\partial w}{\partial x}, \psi \right]^T, \qquad [\overline{M}] = \begin{bmatrix} I_1 & 0 & \bar{I}_1 & \bar{I}_3 \\ 0 & I_1 & 0 & 0 \\ \bar{I}_1 & 0 & \bar{I}_5 & \bar{I}_2 \\ \bar{I}_3 & 0 & \bar{I}_2 & \bar{I}_4 \end{bmatrix}$$

and
$$(I_1, I_2, I_3, I_4, I_5, I_7) = \sum_{k=1}^{n} \int_{z_{k-1}}^{z_k} \rho_k (1, z, z^2, z^3, z^4, z^6) dz$$

$$\bar{I}_1 = -\frac{4}{3h^2} I_4, \bar{I}_2 = \frac{16}{9h^4} I_7 - \frac{4}{3h^2} I_5, \bar{I}_3 = I_2 - \frac{4}{3h^2} I_4, \bar{I}_4 = I_3 - \frac{8}{3h^2} I_5 + \frac{16}{9h^4} I_7, \bar{I}_5 = \frac{16}{9h^4} I_7$$

The variation is strain energy of beam can be expressed as

$$\delta U = \int_0^l \left(N_x \delta \varepsilon_x^0 + M_x \delta k_x^1 + P_x \delta k_x^2 + Q_{xz} \delta \gamma_{xz}^0 + R_{xz} \delta k_{xz} \right) b dx \tag{22}$$

The virtual work done by external forces is given by

$$\delta W = \int_0^l p \delta w b dx \tag{23}$$

where $p = p(x, t)$ is the uniformly distributed load.

Substituting expressions from Eqs.(21), (22) and (23) into Eq.(20), using Eqs.(13a~b), and using the derivative operator forms, the governing equation can be written as (Ref.[5])

$$\begin{bmatrix} L_{11} & L_{12} & L_{13} \\ L_{12} & L_{22} & L_{23} \\ L_{13} & L_{23} & L_{33} \end{bmatrix} \begin{Bmatrix} u \\ w \\ \psi \end{Bmatrix} = \begin{Bmatrix} \dfrac{\partial N_x^p}{\partial x} \\ p - \dfrac{4}{3h^2} \dfrac{\partial^2 P_x^p}{\partial x^2} \\ \dfrac{\partial M_x^p}{\partial x} - \dfrac{4}{3h^2} \dfrac{\partial P_x^p}{\partial x} \end{Bmatrix} \tag{24}$$

where
$$A_0 = \overline{A}_{55} - \frac{8}{h^2}\overline{D}_{55} + \frac{16}{h^4}\overline{F}_{55}, \quad B_0 = \overline{B}_{11} - \frac{4}{3h^2}\overline{E}_{11}$$
$$D_0 = \overline{D}_{11} - \frac{8}{3h^2}\overline{F}_{11} + \frac{16}{9h_4}H_{11}, \quad F_0 = \frac{4}{3h^2}\overline{F}_{11} - \frac{16}{9h^4}\overline{H}_{11}$$

and L_{ij} are the derivative operators given by

$$L_{11} = \overline{A}_{11}\frac{\partial^2}{\partial x^2} - I_1\frac{\partial^2}{\partial t^2}, \quad L_{12} = -\frac{4}{3h^2}\overline{E}_{11}\frac{\partial^3}{\partial x^3} - \bar{I}_1\frac{\partial^3}{\partial x \partial t^2}, \quad L_{13} = B_0\frac{\partial^2}{\partial x^2} - \bar{I}_3\frac{\partial^2}{\partial t^2}$$
$$L_{22} = \frac{16}{9h^4}\overline{H}_{11}\frac{\partial^3}{\partial x^3} - A_0\frac{\partial^2}{\partial x^2} + I_1\frac{\partial^2}{\partial t^2} - \bar{I}_5\frac{\partial^4}{\partial x^2 \partial t^2}, \quad L_{23} = -F_0\frac{\partial^3}{\partial x^3} - A_0\frac{\partial}{\partial x} - \bar{I}_2\frac{\partial^3}{\partial x \partial t^2}$$
$$L_{33} = -A_0 + D_0\frac{\partial^2}{\partial x^2} - \bar{I}_4\frac{\partial^2}{\partial t^2}$$

Equation (24) is subject to the following boundary condition:

$$x = 0, \text{ and } x = l: \qquad N_x = \widetilde{N}_x, \mathit{or}\ u = \widetilde{u}$$
$$x = 0, \text{ and } x = l: \qquad Q = \widetilde{Q}, \mathit{or}\ w = \widetilde{w}$$
$$x = 0, \text{ and } x = l: \qquad P_x = \widetilde{P}_x, \mathit{or}\ \frac{\partial w}{\partial x} = \frac{\partial \widetilde{w}}{\partial x}$$
$$x = 0, \text{ and } x = l: \qquad \hat{M}_x = \widetilde{\hat{M}}_x, \mathit{or}\ \psi = \widetilde{\psi}$$

where $\hat{M}_x = M_x - \frac{4}{3h^2}P_x$, $\hat{Q}_{xz} = Q_{xz} - \frac{4}{h^2}R_{xz}$, $Q = \hat{Q}_{xz} + \frac{4}{3h^2}\frac{\partial P_x}{\partial x}$, "~" denotes the known value.

METHOD OF EXACT SOLUTION

We assume that the solution for the displacement components of the simply supported beams are sought in the form

$$u = \sum_{m=1}^{\infty} u_m \cos\frac{m\pi x}{l}e^{i\omega t}, \quad w = \sum_{m=1}^{\infty} w_m \sin\frac{m\pi x}{l}e^{i\omega t}, \quad \psi = \sum_{m=1}^{\infty} \psi_m \cos\frac{m\pi x}{l}e^{i\omega t} \qquad (25a\sim c)$$

where ω is the frequency of the extend force.

The expressions (25a~c) are satisfied the boundary conditions of the simply supported beam:

$$N_x = 0, \quad w = 0, \quad P_x = 0, \quad \hat{M}_x = 0 \qquad (26a\sim d)$$

Substituting the expressions (25a~c) in Eq.(24), extending the uniformly distributed load *p*(*x*, *t*) in trigonometric series gives: $p(x,t) = \sum_{m=1}^{\infty} p_m \sin\frac{m\pi x}{l}e^{i\omega t}$, where $p_m = \frac{2}{l}\sum_{m=1}^{\infty}\int_0^l p \sin\frac{m\pi x}{l}dx$ and canceling the common factor, we can get simultaneous equations about (u_m, w_m, ψ_m). Solving these simultaneous equations, we will get the displacement of the simply supported beams. For the sensor layer, we assume the electric field E to be zero. Then, from the sensor equation, the total charge $q(t)$ will be derived. For the actuator layer, the applied electric field E will be considered. From solving the governing equations, the displacement of the beam will be derived after the feedback control.

CONCLUSIONS

In this paper, the governing equations of smart composite beams with the piezoelectric sensor and actuator, which based on higher order shear deformation theory, have been presented. The sensor and actuator equations and the arbitrary transformations of constitutive equations for smart composite structures were given. Finally, the method of exact solution for the simply supported beam was also discussed. Due to a space constraint, the numerical results will be presented in another paper.

ACKNOWLEDGEMENTS

This work was partly supported by Foundation for Research Development (FRD) of South Africa under the project: Smart Composite Structures (GUN2038139). The Peninsula Technikon Scholarship is also gratefully acknowledged. The authors are grateful to Prof. Y. Huang, the visiting professor, Dr. N. Mahomed, the HoD of Mechanical Engineering and Mr. X. Li for many helpful discussions.

REFERENCES

1. Chandra R., Chopra I., Structural Modelling of Composite Beams with Induced-Strain Actuators, *AIAA Journal*, **31**(9), pp. 1692-1701, (1993).
2. Chandrashekhapa K., Donthireddy P., Vibration Suppression of Composite Beams with Piezoelectric Devices Using a Higher Order Theory, *European Journal of Mechanics, A/Solids*, **16**(4), pp.709-721, (1997)
3. Crawley E. F., Intelligent Structures for Aerospace: A Technology Overview and Assessment, *AIAA Journal*, **32**(8), pp.1689-1699, (1994).
4. Crawley E. F., Lazarus K. B., Induced Strain Actuation of Isotropic and Anisotropic Plates, *AIAA Journal*, **29**(6), pp.944-951, (1991).
5. Huang D. and Sun B. H., Nonlinear Vibration Analysis of Smart Composite Beams, *proceedings of the 2nd South Africa Conference on Applied Mechanics, Cape Town,* Vol. 1, PP.481-492, (1998).
6. Hwang W. S. and Park H. C., Finite Element Modeling of Piezoelectric Sensors and Actuators, *AIAA Journal*, **31**(5), pp.930-937, (1993).
7. Jones R. M., Mechanics of Composite Materials, McGraw-Hill Kogakusha, Ltd, (1975).
8. Lee C. K., Theory of Laminated Piezoelectric Plates for the Design of Distributed Sensors/Actuators. Part I: Governing Equations and Reciprocal Relationships, *Journal of Acoustical Society of America*, **87**(3), pp.1144-1158, (1990).
9. Mitchell J. A., Reddy J. N., A Refined Hybrid Plate Theory for Composite Laminates with Piezoelectric Laminae, *International Journal of Solids Structures*, **32**(16), pp.2345-2367, (1995).
10. Pai P. F., Nayfeh A. H., Oh K. and Mook D. T., A Refined Nonlinear Model of Composite Plates With Integrated Piezoelectric Actuators and Sensors, *International Journal of Solids Structures*, **30**(12), pp.1603-1630, (1993).
11. Reddy J. N., A Simple Higher-Order Theory for Laminated Composite Plates, *Journal of Applied Mechanics*, **51**(12), pp.745-752, (1984).
12. Shen Y. and Yin L., Strain Sensor of Composite Plates Subjected to Low Velocity Impact with Distributed Piezoelectric Sensors: A Mixed Finite Element Approach, *Journal of Sound and Vibration*, **199**(1), pp.17-31, (1997).
13. Wang B. T., Rogers C. A., Laminated Plate Theory for Spatially Distributed Induced Strain Actuators, *Journal of Composite Materials*, **25**, pp. 43433-452, (1991).

APPENDIX

The transformed matrix

$$[T]=\begin{bmatrix} \cos^2\theta & \sin^2\theta & 0 & 0 & 2\cos\theta\sin\theta \\ \sin^2\theta & \cos^2\theta & 0 & 0 & -2\cos\theta\sin\theta \\ 0 & 0 & \cos\theta & -\sin\theta & 0 \\ 0 & 0 & \sin\theta & \cos\theta & 0 \\ -\cos\theta\sin\theta & \cos\theta\sin\theta & 0 & 0 & \cos^2\theta-\sin^2\theta \end{bmatrix}, \quad [T_0]=\begin{bmatrix} \cos\theta & -\sin\theta & 0 \\ \sin\theta & \cos\theta & 0 \\ 0 & 0 & 1 \end{bmatrix}$$

The transformed material constants

$$
\begin{aligned}
\overline{Q}_{11} &= Q_{11}\cos^4\theta + 2(Q_{12}+2Q_{66})\sin^2\theta\cos^2\theta + Q_{22}\sin^4\theta \\
\overline{Q}_{12} &= (Q_{11}+Q_{22}-4Q_{66})\sin^2\theta\cos^2\theta + Q_{12}\left(\sin^4\theta+\cos^4\theta\right) \\
\overline{Q}_{22} &= Q_{11}\sin^4\theta + 2(Q_{12}+2Q_{66})\sin^2\theta\cos^2\theta + Q_{22}\cos^4\theta \\
\overline{Q}_{16} &= (Q_{11}-Q_{12}-2Q_{66})\sin\theta\cos^3\theta + (Q_{12}-Q_{22}+2Q_{66})\sin^3\theta\cos\theta \\
\overline{Q}_{26} &= (Q_{11}-Q_{12}-2Q_{66})\sin^3\theta\cos\theta + (Q_{12}-Q_{22}+2Q_{66})\sin\theta\cos^3\theta \\
\overline{Q}_{66} &= (Q_{11}+Q_{22}-2Q_{12}-2Q_{66})\sin^2\theta\cos^2\theta + Q_{66}\left(\sin^4\theta+\cos^4\theta\right) \\
\overline{Q}_{44} &= Q_{44}\cos^2\theta + Q_{55}\sin^2\theta \\
\overline{Q}_{45} &= -Q_{44}\sin\theta\cos\theta + Q_{55}\sin\theta\cos\theta \\
\overline{Q}_{55} &= Q_{44}\sin^2\theta + Q_{55}\cos^2\theta
\end{aligned}
$$

The piezoelectric stress- and permitivity coefficient (after transformation)

$$
\begin{aligned}
\bar{e}_{31} &= e_{31}\cos^2\theta + e_{32}\sin^2\theta \\
\bar{e}_{32} &= e_{31}\sin^2\theta + e_{32}\cos^2\theta \\
\bar{e}_{14} &= e_{15}\sin\theta\cos\theta + e_{24}\cos\theta\sin\theta \\
\bar{e}_{24} &= -e_{15}\sin^2\theta + e_{24}\cos^2\theta \\
\bar{e}_{15} &= e_{15}\sin^2\theta - e_{24}\cos^2\theta \\
\bar{e}_{25} &= -e_{15}\cos\theta\sin\theta - e_{24}\sin\theta\cos\theta \\
\bar{e}_{36} &= (e_{31}-e_{32})\sin\theta\cos\theta
\end{aligned}
$$

$$
\begin{aligned}
\bar{g}_{11} &= g_{11}\cos^2\theta + g_{22}\sin^2\theta \\
\bar{g}_{12} &= -g_{11}\sin\theta\cos\theta + g_{22}\sin\theta\cos\theta \\
\bar{g}_{22} &= g_{11}\sin^2\theta + g_{22}\cos^2\theta \\
\bar{g}_{33} &= g_{33}
\end{aligned}
$$

DYNAMICS AND BUCKLING OF A MULTILAYER COMPOSITE PLATE WITH EMBEDDED SHAPE MEMORY ALLOY WIRES

W. Ostachowicz[1], M. Krawczuk[2], A. Żak[2]

[1] Institute of Fluid Flow Machinery, 14 Fiszera St, 80–952 Gdansk, Poland
[2] Institute of Fluid Flow Machinery, Poland

INTRODUCTION

The paper illustrates stress–strain relationships for a single composite lamina with embedded SMA fibres and their influence upon certain changes in natural frequencies and thermal buckling of a composite multilayer plate. Governing equations based on the finite element method are presented in the paper. The plate is modelled by plate finite elements. The elements have eight nodes with five degrees of freedom at each node (i.e. three axial displacements and two independent rotations). For both axial displacements and independent rotations biquadratic shape functions are used.

A limited number of papers concerned with natural vibration of SMA fibre–reinforced composite plates can be found in the present literature. Zhong, Chen, and Mei [8], analysed thermal buckling and postbuckling of composite plates with embedded SMA fibres using a finite element technique. Ro and Baz [4] introduced fundamental equations governing dynamic behaviour of Nitinol–reinforced plates. Applying the finite element method they studied dynamic characteristics of such structures.

In the present work a more general description of this problem is introduced. The finite element analysis results presented in this work are compared to those obtained from an analytical continuum solution.

MECHANICAL AND PHYSICAL PROPERTIES OF SHAPE MEMORY ALLOYS

Mechanical and physical properties of shape memory alloys strongly depend on temperature and initial stresses [2, 3]. Changes in temperature and initial stresses involve changes in the volume fraction of martensite in the alloys. During the martensite transformation recovery stresses appear. These recovery stresses are not only a function of alloys temperature but also depend on initial strains ε. In Fig. 1 the SMA recovery stresses versus SMA temperature for four different initial strains are presented.

It can be easily noticed that an increase in the initial strains involves higher recovery stresses in the SMA wires and simultaneously changes in the temperatures of phase transformation are also observed.

In this paper the following material properties for the SMA (Nitinol) wires are used (see also [5]): austenite start temperature T_s=37.8 °C, austenite finish temperature T_f=62.8 °C, Young's modulus E_r (from [5]), G_r=24.86 GPa for $T<T_s$, G_r=25.6 GPa for $T>T_s$, Poisson ratio ν=0.3, density ρ=6450 kg/m^3, thermal expansion coefficient α_r=10.26×10^{-6} 1/°C.

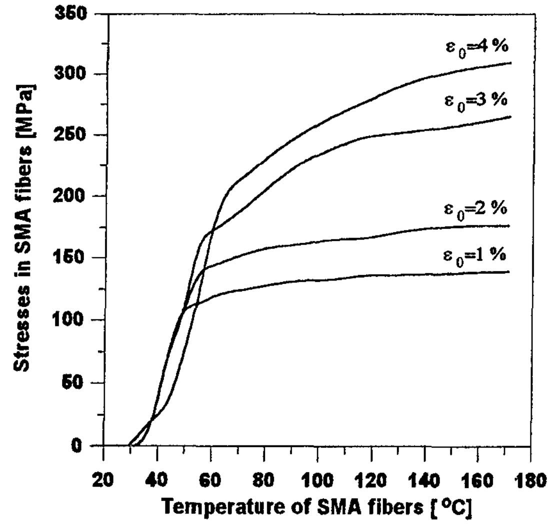

Fig. 1. Stresses in SMA fibres as a function of temperature and initial strains.

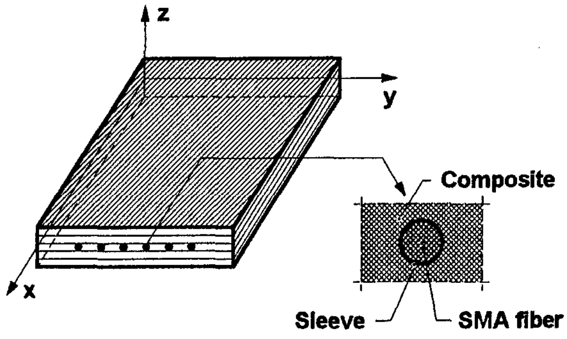

Fig. 2. A SMA fibre–reinforced multilayer composite plate.

STATE OF PROBLEM

The SMA fibre–reinforced laminated composite plate which contains embedded the SMA wires is considered, as it is shown in Fig. 2. A single composite lamina of the plate has arbitrary orientation of graphite fibres. The SMA fibres are placed in the neutral plane of the plate.

The displacements field within the single plate lamina is assumed due to the first order deformation theory. In this analysis a plate–bending quadrilateral finite element called PBQ8 [7] is used. This element has eight nodes and five degrees of freedom at each node. The shape functions of the element can also be found in [7].

$$\begin{aligned} U_e = \iint_A \Big\{ & \tfrac{1}{2} A_{11}(\partial_x u_o)^2 + A_{12}\partial_x u_o \partial_y v_o + \tfrac{1}{2} A_{22}(\partial_y v_o) + \tfrac{1}{2} D_{11}(\partial_x \overline{\alpha})^2 + \\ & + A_{44}\Big[\tfrac{1}{2}\overline{\beta}^2 + \overline{\beta}\partial_y w_0 + \tfrac{1}{2}(\partial_y w_0)^2\Big] + A_{45}\Big[\overline{\alpha}\,\overline{\beta} + \overline{\alpha}\partial_y w_0 + \overline{\beta}\partial_x w_0 + \partial_x w_0 \partial_y w_0\Big] + \\ & + A_{55}\Big[\tfrac{1}{2}\overline{\alpha}^2 + \overline{\alpha}\partial_x w_0 + \tfrac{1}{2}(\partial_x w_0)^2\Big] + A_{66}\Big[\tfrac{1}{2}(\partial_y u_0)^2 + \partial_y u_0 \partial_x v_0 + \tfrac{1}{2}(\partial_x v_0)^2\Big] + \\ & + D_{12}\partial_x \overline{\alpha}\,\partial_y \overline{\beta} + \tfrac{1}{2} D_{22}(\partial_y \overline{\beta})^2 + D_{66}\Big[\tfrac{1}{2}(\partial_y \overline{\alpha})^2 + \partial_y \overline{\alpha}\,\partial_x \overline{\beta} + \tfrac{1}{2}(\partial_x \overline{\beta})^2\Big]\Big\} dA \end{aligned} \tag{1}$$

For SMA fibre–reinforced hybrid composite plates subjected to a combined external, thermal and recovery stresses load governing equations of motion can be obtained through the principle of virtual work. For the plates which are mid–plane symmetric there is no coupling and the strain energy stored in the plates finite element is given by Eq. (1) where formulae to calculate A_{ij} and D_{ij} can be found in [6].

Work done by the in–plane forces which includes the recovery forces of the Nitinol fibres, the thermal loads induced by heating the Nitinol fibres and the external in–plane loads can be written in the following form [2]:

$$\delta V_e' = \tfrac{1}{2}h\iint_A \delta w\left[N_x(\partial_x w)^2 + N_y(\partial_y w)^2 + 2N_{xy}(\partial_x w)(\partial_y w)\right]dA \tag{2}$$

where: $N_x=P_{m,x}+P_{t,x}-F_{w,x}$, $N_y=P_{m,y}+P_{t,y}$, $N_{xy}=P_{m,xy}+P_{t,xy}$ with $P_{n,x,y,xy}$ and $P_{t,x,y,xy}$ denoting the compressive in–plane mechanical and thermal loads in x, y and xy directions. Symbol $F_{w,x}$ denotes the total tension developed in the Nitinol fibres:

$$F_{w,x} = \iint_{A_w}\left[\varepsilon_0 - \alpha_r(T-T_0)\right]E_r\, dA_w \tag{3}$$

where α_r, E_r and A_w are the thermal expansion coefficient of the SMA wires, their modulus of elasticity and their cross–sectional area, respectively. The thermal loads P_t are given by the relations:

$$\mathrm{col}[P_{t,x}, P_{t,y}, P_{t,xy}] = \sum_k \int_{h_{k+1}}^{h_k} [\mathbf{Q}_k]\,\mathrm{col}[\alpha_x, \alpha_y, \alpha_{xy}]\,\Delta T\, dz \tag{4}$$

Matrix $[\mathbf{Q}_k]$ in Eq. 4 has a well known structure and as well as formulae to calculate quantities α_x, α_y and α_{xy} may be found in [6].

The thermal loads are generated by changes in temperature ΔT of the element and are caused by both activation and deactivation processes of the Nitinol fibres. Using standard finite element formulae the inertia and stiffness matrices of the plate can be determined. The governing equation has the following form:

$$[\mathbf{M}]\{\ddot{q}\} + \left([\mathbf{K}_s] + [\mathbf{K}_r] - \Delta T\cdot[\mathbf{K}_T]\right)\{q\} = \{F\} \tag{5}$$

where $[\mathbf{M}]$ and $[\mathbf{K}_s]$ are the system mass and stiffness matrices, $[\mathbf{K}_r]$ and $[\mathbf{K}_T]$ are the geometric stiffness matrices due to recovery stress and thermal stresses, respectively. The natural frequencies ω and mode shapes $\{q^0\}$ of vibration are obtained from the eigenvalue problem. Equations governing the thermal buckling are obtained by neglecting the inertia, bending membrane–coupling, and bending force terms as:

$$\left([\mathbf{K}_s] + [\mathbf{K}_r] - \Delta T\cdot[\mathbf{K}_T]\right)\{q^0\} = \{0\} \tag{6}$$

The changes of the critical temperature ΔT are the eigenvalues which correspond to buckling modes. The temperature ΔT is considered as a steady–state temperature.

NUMERICAL CALCULATIONS

Numerical calculations were carried out for a simply supported SMA fibre–reinforced multilayer composite plate for its following dimensions: length 600 mm, width 600 mm and thickness 8 mm. The plate were consisted of 8 layers of composite material with the changing orientation of graphite fibres (0/90/90/0/0/90/90/0). The plate was modelled by 64 plate elements and the mesh size was 8×8. Each layer of the plate was made of graphite–epoxy composite (fibre: Young's modulus E_f=275.6 GPa, shear modulus G_f=114.8 GPa, density ρ_f=1900 kg/m^3, Poisson ratio ν_f=0.2, coefficients of thermal expansion α_f=24.4×10^{-6} 1/°C; matrix: Young's modulus E_m=3.43 GPa, shear modulus G_m=1.27 GPa, density ρ_m=1250 kg/m^3, Poisson ratio ν_m=0.2, coefficients of thermal expansion α_m=64.8×10^{-6} 1/°C. It was also assumed that all mechanical properties except the angle of the graphite fibres are the same for each layer.

The volume fraction of the graphite fibres in each layer was 0.2. In the present study the SMA Nitinol fibres covered only 5% of the cross sectional area of the plate. They were embedded inside the neutral plane of the plate. It was assumed that the material properties (except density, the angle of the graphite fibres and the coefficients of thermal expansion) were functions of temperature, as it is presented in Fig. 4 (see also [1]). In this study only a uniform temperature distribution in the plate was considered (see Fig. 3).

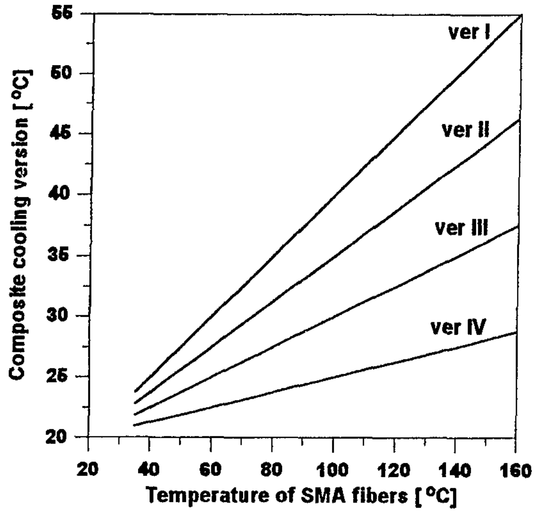

Fig. 3. Temperatures of the plate vs. temperature of SMA wires.

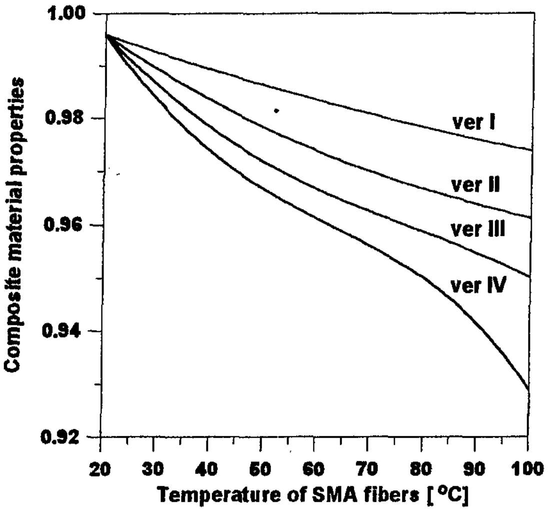

Fig. 4. Temperature dependence of composite material properties.

The results of numerical investigations illustrate influence of the SMA fibres temperature upon changes in bending natural frequencies of the analysed plate. In Figs. 5–6 the changes in the first bending natural frequencies are presented. The results of the calculations are related to those obtained for the same plate without the SMA wires. It can be clearly observed that the activation process of the SMA wires involves an increase in the bending natural frequencies. This effect rises when both temperature and initial strains are higher.

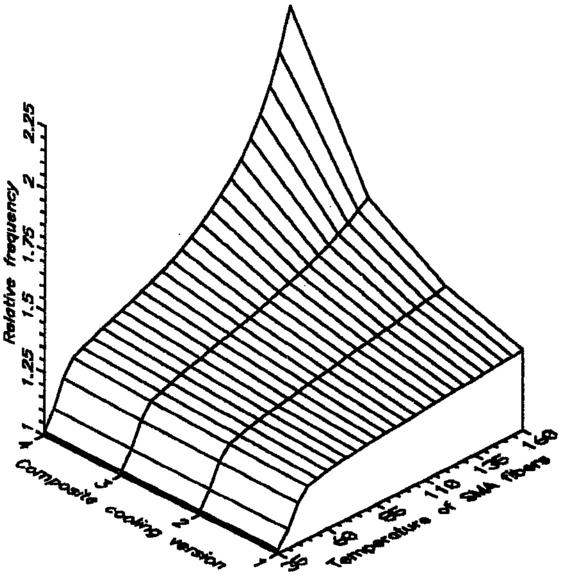

Fig. 5. Influence of SMA fibres temperature and initial strains (ε_0=1%) upon the relative change of the first natural frequency.

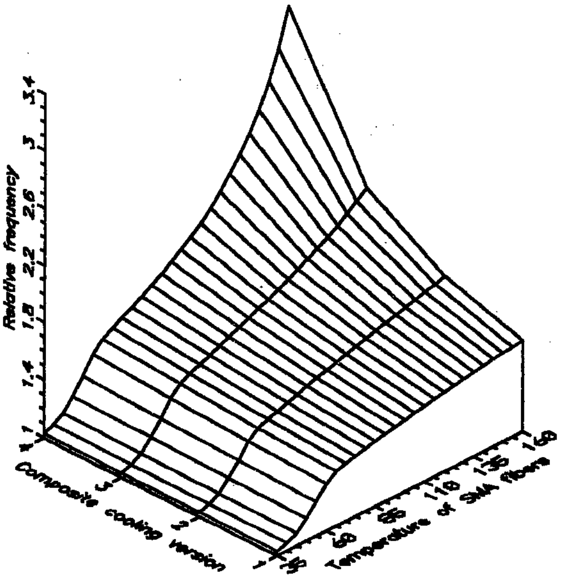

Fig. 6. Influence of SMA fibres temperature and initial strains (ε_0=4%) upon the relative change of the first natural frequency.

The results obtained in this work demonstrate the potential effectiveness of SMA fibre–reinforcement in composite structural elements in the control of vibration. The effect of SMA fibres activation on the amplitude of vibration normalised with respect to the amplitude of vibration of the uncontrolled can also be analysed.

In Figs. 7 and 8 changes in ΔT in case of the first and third bending thermal buckling are presented. The results of numerical calculations are related to those obtained for the same plate without the SMA wires. It can be clearly observed that the activation process of the SMA wires involves an increase in the critical temperature change. This effect rises when both temperature and initial strains are higher.

CONCLUSIONS

Applications of the SMA Nitinol fibres in the natural frequency analysis of composite plates have been successfully demonstrated. The fundamental equations governing behaviour of SMA fibre–reinforced multilayer composite plates have been introduced. The stress–strain relationships for a single composite lamina with embedded the SMA fibres has been presented. The finite element formulation to predict changes in natural frequencies and modes of vibration of composite laminates with the SMA fibres has also been shown in the paper.

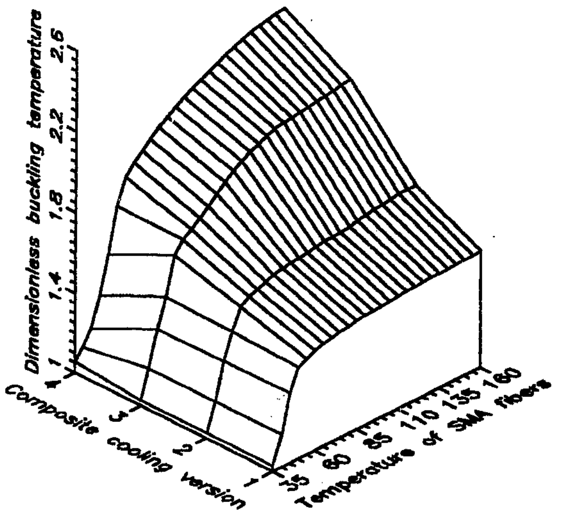

Fig. 9 Influence of SMA fibres temperature and initial strains (ε_0=1, 2, 3, and 4%) upon the relative change of the first critical temperature.

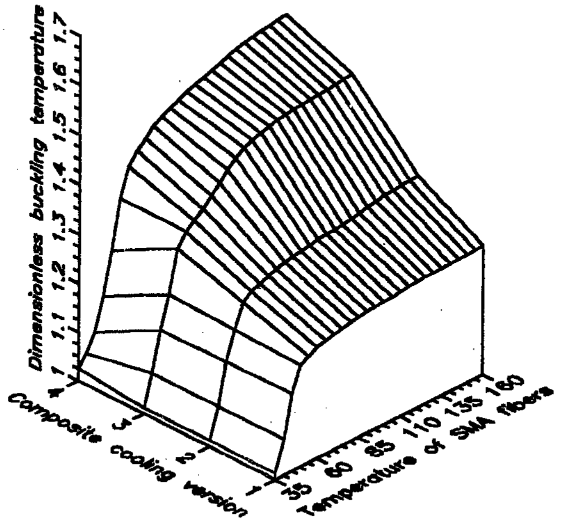

Fig. 10 Influence of SMA fibres temperature and initial strains. (ε_0=1, 2, 3, and 4%) upon the relative change of the third critical temperature

REFERENCES

[1] Baz, A., Poh, S., Ro, J., Gilheany, J. "Control of the natural frequencies of Nitinol – reinforced composite beams." *Journal of Sound and Vibration* **185** (1), pp. 171–185 (1995).

[2] Birman, V., Saravanos, D. A., Hopkins, D. A. "Micromechanics of composites with shape memory alloy fibers in uniform thermal fields." *AIAA Journal* **34** (9), pp. 1905–1912 (1996).

[3] Epps, J. J., Chopra, I. "Comparative evaluation of shape memory alloy constitutive models with test data." *Proceedings of 38th AIAA Structures, Structural Dynamics and Materials Conference and Adaptive Structures Forum*, Kissimmee, Florida, April 7–10 (1997).

[4] Ro, J., Baz, A. "Nitinol–reinforced plates, Part I–III." *Composites Engineering* **5** (1), pp. 61–106 (1995).

[5] Turner, T. L., Zhong, Z. W., Mei, C. "Finite element analysis of the random response suppression of composite panels at elevated temperatures using shape memory alloy fibers." *AIAA-94-1324-CP*, pp. 136–146 (1994).

[6] Vinson, J. R., Sierakowski, R. L. "Behaviour of Structures Composed of Composite Materials." *Martinus Nijhoff*, London (1981).

[7] Weaver, W., Johnston, P. R. „Finite Element for Structural Analysis." *Prentice Hall Inc., Englewood Cliffs*, New Jersey (1984).

[8] Zhong, Z. W., Chen, R. R., Mei, C. "Buckling and postbuckling of shape memory alloy fiber reinforced composite plates." *Buckling and Postbuckling of Composite Structures*, ASME. AD–41/PVP–233 (1984).

SOME PROBLEMS OF PIEZOELECTRIC SENSOR MECHANICS

B Sun
Department of Mechanical Engineering and
Centre for Research in Applied Technology
Peninsula Technikon, P O Box 1906, Bellville 7535, South Africa
e-mail: sunb@mecheng.pentech.ac.za

ABSTRACT In this paper, some general problems of piezoelectric sensor mechanics have been discussed. It has shown that modal sensor can not be constructed for general case of beam, plate and shell, except the case of Lee and Moon (1990). It means that distributed sensor generally detect a number of vibration modes simultaneously and can reduce but not completely vanish the control spillover. Random sensor, noise effects, finite element interpolation of sensor equation and smart finite element formulation of smart structures have also been presented. Although with emphasis on plates and beam, all results presented here are also valid for shells.

INTRODUCTION

The insatiable demand for new generations of industrial, military, commercial, medical, automotive and aerospace products have fuelled research and development activities focused on advanced materials and smart structures. This situation has been further stimulated by the intellectual curiosity of Homo Sapiens in synthesising new classes of biomimetic materials, and, of course global competition by the principal industrial nations is also a parameter in the equation governing the rate of technological progress. A fundamental axiom of this field of advanced materials is that the ultimate materials are the biological materials which are assumed to be somewhat focus of this field is to replicate these characteristics and properties in synthetic materials which can be employed in diverse scientific and technological applications.Thus by integrating the knowledge-bases associated with advanced materials, information technology and biotechnology, these three mega-technologies are facilitating the creation of a new generation of biomimetic materials and structures with inherent brains, nervous systems and actuation systems which are currently a mere skeleton compared with the anatomy perceived in the not-too-distant future. This quantum jump in materials technology will revolutionise the future in ways far more dramatic than the way the electric chip has impacted our lifestyles. These new materials are termed Smart materials or Intelligent materials and they will typical feature fibrous polymeric composite materials, embedded powerful computer chips of gallium arsenic which will be interfaced with both embedded sensors and embedded actuators by networks of embedded optical-fibre wave-guides through which large volumes of data will be transmitted at high speeds.Today's material revolution is the cornerstone of the triumvirate of mega-technologies, which comprise the essential, integrates of this embryonic field. These technologies will have a mutually symbiotic relationship and will significantly impact one another resulting in synergistic technological advances cannot be foreseen today. However, a natural consequence of advancing on these technological disciplines, will be the impending revolution in smart materials and structures.

The classes of smart materials and intelligent structures are divers and the application of them is largely unknown. However, what is known is that this new generation of materials will certainly revolutionize our quality of life as dramatically as the state-of-art materials did in the past, with stone implements triggering the Stone Age, alloys of copper and tin triggering the Bronze Age, and the smelting of iron ore triggering the Iron Age. The time-line of humankind is located at the dawn of a new era, The Smart Materials Age.

SMART STRUCTURE AND ACTIVE CONTROL

In the context of intelligent materials and structures there is considerable focus on **sensors** and **actuators** and **control capabilities**. The current generation of smart materials and structures incorporate one or more of the following features:

- *Sensors*, which are either embedded within a structural material or else, bonded to the surface of that material. Alternatively, the sensing function can be performed by a functional material, which, for example, measures the intensity of the stimulus associated with a stress, strain, electrical, thermal, radioactive, or chemical phenomenon. This functional material may, in some circumstance, also serve as a structural material.
- *Actuators*, which are embedded within a structural material or else, bonded to the surface of the material. These actuators are typically excited by an external stimulus; such as electricity in order to either changes their geometrical configuration or else change their stiffness and energy-dissipation properties in a controlled manner. Alternatively, the actuator function can be performed directly by a hybrid material, which serves as both a structural material, and also as a functional material.
- *Control capabilities*, which permit the behavior of the material to respond to an external stimulus according to a prescribed functional relationship or control algorithm. These capabilities typically involve one or more microprocessors and data transmission links, which are based upon the utilization of an automatic control theory.

The goal of creating a design that limits vibration amplitudes and duration in the presence of both shock and vibration disturbances faces limitations in the form of constraints on the choice of mass, damping, and stiffness (static deflection) values. For instance, in the design of an isolation system, it often occurs that the desired calls for a value of stiffness that results in a static deflection that is too large for the intended application. Sometimes, a given isolation design might be required to operate over a load range that is impossible to meet with a single choice of mass and stiffness. In addition, once the materials are fixed for a given system, it is difficult to change the mass and stiffness of the system more than of a few percent. Basically, the choice of the physical parameter m, c, and k determines the response of the system. The choice of these parameters to obtain a desired response is the design problem. This design procedure can be thought of as passive control (e.g., adding mass to a machine base to lower its frequency). If the constraints on mass (M), damping (C), and stiffness (K) are such that the desired response cannot be obtained by changing M, C, and K, active control may provide an attractive alternative.

Active control uses an external adjustable (or active) device, called actuator to provide a force to the device, or structure whose vibration properties are to be changed. The force applied to the structure by the actuator is dependent on a measurement of the response of the system. This is called feedback control. If the goal of the active control system is to remove unwanted vibration, the control system is called active vibration suppression, which consists of measuring the output or response of the structures to determine the force to apply to the mass to obtain the desired response. The device used to apply the force, together with the sensor used to measure the response of the mass and the electronic circuit is called the control system. The mathematical rule used to apply the force from the sensor measurement is called the control law.

Active control systems provide increased versatility and better performance in the design of vibration suppression systems. However, they do so with substantial increase in cost and potential decrease in reliability. Even in the face of increase d cost and complexity, active control methods for vibration suppression are often the only alternatives.

SENSORY ELEMENTS

It is clearly evident, therefore, to understand sensor's mechanism is essential to the full picture of smart structure. Crawley (1994). Sensory elements of smart structures must be sensitive to the mechanical states of the structure and capable of being highly distributed. The ideal sensor for a smart structure converts strain or displacement (or their temporal derivatives) directly into electrical outputs. The primary function requirements for such sensors are their sensitivity to the strain or displacement (or their time derivatives), spatial resolution, and bandwidth. Secondary requirements include the transverse and temperature sensitivity, linearity and hysteresis, electromagnetic compatibility, and size of sensor packaging. Although actuators are so large they must be explicitly accommodated in the built-in laminates, it is desirable to make sensors small enough to be placed in inter-laminar or otherwise unobtrusive positions.

Researchers [1-8, 13-19] have investigated sensor mechanism. Lee and Moon (1990) proposed various modal sensors; and Callahan and Baruh developed to segmented piezoelectric film sensor. (1995); Tzou, et al (1993) discovered membrane modal sensitivity and transverse modal sensitivity for piezoelectric shell sensor. Nevertheless, some problems are still to be reconsidered, for instance, nonlinear effects, random effects and possibility of general modal sensor. This comes to our motivation.

In this paper, some general problems of piezoelectric sensor mechanics have been discussed. It has shown that modal sensor can not be constructed for general case of beam, plate and shell, except the case of Lee and Moon (1990). It means that distributed sensor generally detect a number of vibration modes simultaneously and can reduce but not completely vanish the control spillover. Random sensor, noise effects, finite element interpolation of sensor equation and smart finite element formulation of smart structures have also been presented. Although with emphasis on plates and beam, all results presented here are also valid for shells.

WORKING PRINCIPLE AND BRIEF SUMMARY OF PIEZOELECTRIC SMART STRUCTURES

The deformation of piezoelectric structures will let sensor generate charge; the total charge developed on the surface of the sensor layer is q(t). When piezoelectric sensors are used as strain sensors, the output charge can be transformed to sensor current $i(t)=\frac{dq(t)}{dt}$, and current is converted into the open circuit sensor voltage output of controller $V(t)=-G_c i(t)$, which is actually the applied load on the actuators of smart structures given by controller. The actuator layers will deform and are result as damper of the smart structures.

The working principle of piezoelectric smart structures is illustrated in Fig.1.

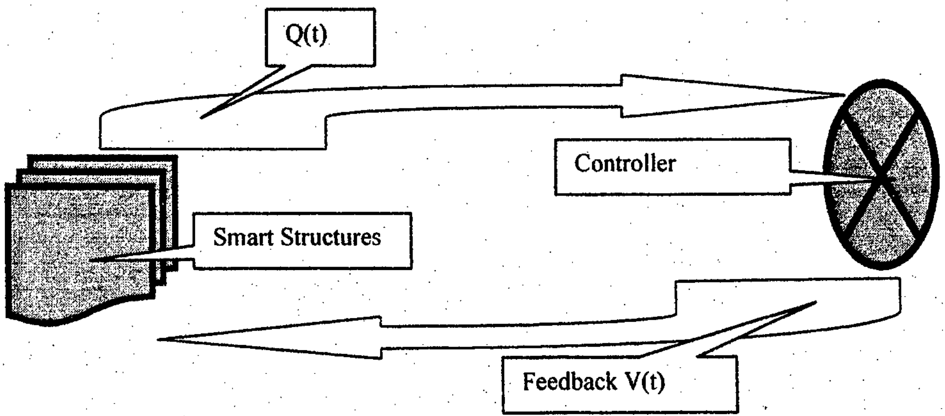

Figure 1. Smart structures working principle

According the working principle, the simulation of smart structures consists of following steps.

1. Sensor analysis - this step is to formulate sensor equation and get current I(t).

Since no external electric field is applied to the sensor layer, the electric displacement developed on the sensor surface is directly proportional to the strain acting on the sensor. If the poling direction is z for sensors with the electrodes on the upper and lower surfaces, the electric displacement is

$$D_z = e_{31}\varepsilon_x + e_{32}\varepsilon_y + e_{36}\gamma_{xy}. \tag{1}$$

The total charge on the sensor layer will be

$$q(t) = \iint_A D_z dxdy, \tag{2}$$

Where A is the domain of the sensor. The current can be obtained by

$$i(t)=\frac{dq(t)}{dt}, \text{ or } i(t) = \iint_A (e_{31}\dot{\varepsilon}_x + e_{32}\dot{\varepsilon}_y + e_{36}\dot{\gamma}_{xy})dxdy. \tag{3}$$

It can be further expressed in terms of velocity.

2. Controller analysis - this step is to design a control mechanism, or called as feedback analysis, usually, this step is simulated by introducing a series of gain G_C and negative velocity feedback control.

The input for controller is i(t), the output of the controller will be in voltage

$$V(t) = -G_c i(t). \tag{4}$$

The gain G_C plays a role as amplifier and "-" present the negative feedback control. In other word, "-G_C" represents a controller in practice.

3. Actuator analysis - this step is to formulate actuator equation, that is, the reaction forces and moment supplied by the actuator layers.

Since the actuator layers are thin, so that the electric field intensity E will be uniform for each layer. For the kth layer,

$$E_z^k = V^k / h^k, \tag{5}$$

where V^k is applied voltage across the kth layer and h^k is the thickness of the kth layer. According the definition of resultant forces and moment of laminated structures (beams, plates and shells), the contribution of actuator layers on resultant forces is

$$N^p = \sum_{k=1}^{n} (E_z^k h^k)(z_k - z_{k-1}), \tag{6}$$

and resultant moment is

$$M^p = \frac{1}{2} \sum_{k=1}^{n} (E_z^k h^k)(z_k^2 - z_{k-1}^2), \tag{7}$$

where z_k is the distance of kth layer to the reference surface of the smart structures, and number n denotes the total number of layers.

4. Smart structure analysis - this last step is to combine the above all results to formulate a governing equations by Hamilton principle, called smart structures equations (SSE).

By using Hamilton principle, the smart structure equations(SSE) can be formulated. In finite element method form, the SSE can be written as

$$M\ddot{u} + G_c C\dot{u} + Ku = F_{ext}. \tag{8}$$

This equation is quite general for linear case and it has clearly show that actuator is like an active damper. The stiffness and mass matrix are same as ordinary laminated structures. This remarkable conclusion makes the numerical calculation very easily, and all elements developed for non-smart structures can be also used to the analysis of smart structures. The only different is each element has one more degree of freedom, which is electric voltage or precisely, the gain G_C. By modal analysis, D J Inman (1996), the SSE can be transformed into standard principle coordinate form $\ddot{r}_i(t) + 2\zeta_i\omega_i\dot{r}_i(t) + \omega_i^2 r_i(t) = f_i(t)$, its solution is

$$r_i(t) = d_i \exp(-\zeta_i\omega_i t)\sin(\omega_{di}t + \phi_i) + \frac{1}{\omega_{di}}\exp(-\zeta_i\omega_i t)\int_0^t f_i(\tau)\exp(\zeta_i\omega_i\tau)\sin\omega_{di}(t-\tau)d\tau, \tag{9}$$

where $\omega_{di} = \omega_i\sqrt{1-\zeta_i^2}$, $\zeta_i = \frac{G_c C_i}{2m_i\omega_i}$, $d_i = \left[\frac{(\dot{r}_{i0} + \zeta_i\omega_i r_{i0})^2 + (r_{i0}\omega_{di})^2}{\omega_{di}^2}\right]$, $\phi_i = \tan^{-1}\frac{r_{i0}\omega_{di}}{\dot{r}_{i0} + \zeta_i\omega_i r_{i0}}$. The list of above equation is just wish to show how the gain G_C influences the damping coefficient ζ_i, frequency ω_i, amplitude d_i and phase ϕ_I.

From the steps of analysis, we can easily see that sensor analysis is essential for pick up information of the motion of structure. Without right sensor information, control of smart structures would be a dream.

SENSOR ANALYSIS - LINEAR CASE

A linear piezoelectric classical plates theory than incorporate the piezoelectric effect into the elastic laminate constitutive equation has been studied by Lee (1990), Lee and Moon (1990), Callahan and Baruh (1995), all of them assumed the in-plane displacement u and v to be negligible compared to the transverse deflection w and the output signal is generated by w only. In this paper, we will not omit the in-plane displacement, because they should be considered in the case have laminated plates, unless the sensor were in the mid-surface. Beside that, the effects of transverse deformation will be also considered because the inter-laminar shear Modula are usually much smaller than the in-plane Young's Modula, Chandra (1993, 1997), Huang and Sun (1998a,b).

If using Mindlin plates theory, the charge generated by each piezoelectric sensor is given by

$$q_r(t) = \iint_A F_r P_0 \{e\}^T \{L\}(\{u\} + z_r\{\theta\})dxdy, \quad r = 1,2,\ldots,N \tag{10}$$

This equation is generally called sensor equation which give signal output q(t); which is an average quantity over the sensor coverage. It has proved that frequency of charge $q_r(t)$ is equal to the frequency of sensors and their host structure. In which

$$\{e\} = \begin{Bmatrix} e_{31} \\ e_{32} \\ e_{36} \end{Bmatrix}, \quad \{L\} = \begin{bmatrix} \frac{\partial}{\partial x} & 0 \\ 0 & \frac{\partial}{\partial y} \\ \frac{\partial}{\partial y} & \frac{\partial}{\partial x} \end{bmatrix}, \quad \{u\} = \begin{Bmatrix} u \\ v \end{Bmatrix}, \quad \{\theta\} = \begin{Bmatrix} \theta_x \\ \theta_y \end{Bmatrix} \tag{11}$$

and $z=(z_k+z_{k-1})/2$ is the average distance from the geometric centre of the rth sensor to the mid-plane of the laminate and N is the number of piezosensors, A is the sensor coverage and is the polarization profile (Lee and Moon, 1990) and F(x,y) is Heavyside type function

$$F(x,y) = \begin{cases} 1, & \text{if } (x,y) \text{ is within the rth senso coverage} \\ 0, & \text{otherwise} \end{cases}.$$

As Tzou et al (1993) pointed out that signal output of sensor can be divided into two parts or called sensitivities: (1) transverse modal sensitivity and (2) membrane modal sensitivity. In general, the transverse modal sensitivity is defined for transverse natural modes and the membrane modal sensitivity for in-plane natural modes. But in the case of Eq(1), the transverse modal sensitivity is defined for rotation or precisely change of curvature. There is no explicit contribution from transverse deflection w; the reason is that in the sensor's constitutive equation both e_{33} and e_{34} are zero. In order to capture the contribution of w, it is suggestion to choose a piezoelectric material have no-zero e_{33} and e_{34}.

One-Dimensional Case: Composite Beam

In this case, v=0 and displacement is the only function of x, then Eq(10) simplifies to the one-dimensional sensor equation

$$q_r(t) = \int_0^a \Gamma_r(x) e_{31}(u_{,x} + z_r\theta_{x,x})dx, \quad \text{where} \quad \Gamma_r = \int_{-\frac{b}{2}}^{\frac{b}{2}} F_r P_0 dy \tag{12}$$

From linear vibration theory, we have following solution

$$u(x,t) = \sum_{m=1}^{\infty} u_m(x)\mu_m(t), \qquad \theta_x(x,t) = \sum_{m=1}^{\infty} \theta_m(x)\vartheta_m(t) \tag{13}$$

Substitute Eq(13) into Eq(12), we have

$$q_r(t) = \sum_{m=1}^{\infty} [A_m \mu_m(t) + z_r B_m \vartheta_m(t)] \tag{14}$$

where

$$A_m = e_{31} \int_0^a \Gamma_r(x) u_{m,x} dx, \qquad B_m = e_{31} \int_0^a \Gamma_r(x) \theta_{m,x} dx \tag{15}$$

A_m and B_m are constant coefficient. By using classical plate theory and omitting in-plane displacement u and v, Lee and Moon have shown that if the spatial electrode pattern of the rth lamina is proportional to the modal strain distribution along the length of the plate, one can obtains a true modal sensor based on the orthogonality of the eigenvalue-solution of the beams with respect to their stiffness. In other words, observer spillover will not be present in systems adopting this type of sensors. Further more, Lee and Moon also proposed modal actuator which excites each particular mode independently so that actuator spillover will not be an issue in one-dimensional plates actuated by this type of actuator.

Unfortunately, for Mindlin plate theory because of no general orthogonality for both u_m and rotation θ_m, to have the above modal sensor will be impossible whatever how we choose Γ_r (x). In other words, observer spillover will always be present in the system adopting Mindlin type of sensor. As a consequence, the modal actuator will be a dream in this case. Only one exceptional case, the sensor can only be used as membrane sensor if it is placed on the mid-surface, $z_r=0$. In this case, one can obtain membrane modal sensor and membrane modal actuator for beam type plates.

Two-Dimensional Case: Composite Plates

Similar to beam, vibration solution for plates is

$$\begin{aligned} u(x,t) &= \sum_{m=1}^{\infty} u_m(x)\mu_m(t), & v(x,t) &= \sum_{m=1}^{\infty} v_m(x)v_m(t), \\ \theta_x(x,t) &= \sum_{m=1}^{\infty} \theta_{xm}(x)\vartheta_{xm}(t) & \theta_y(x,t) &= \sum_{m=1}^{\infty} \theta_{ym}(x)\vartheta_{ym}(t) \end{aligned} \qquad (16)$$

Then, the charge from Eq(10) will be

$$q_r(t) = \sum_{m=1}^{\infty}\left\{A_m\mu_m(t) + C_m v_m(t) + z_r[B_m\vartheta_{xm}(t) + D_m\vartheta_{ym}(t)]\right\} \qquad (17)$$

$(A,B,C,D)_m$ are the integrated coefficients of F_r (x,y) with the mode functions of in-plane displacement u, v and rotation θ_x and θ_y in the domain of sensor coverage.

It is clear that modal sensor generally can not be constructed for plate because no orthogonality of modes.

SENSOR ANALYSIS - NONLINEAR CASE

For von Karman type of Mindlin plate, the charge of the rth sensor layer will be

$$q_r(t) = \iint_A F_r(x,y)P_r(x,y)(e_{31}\varepsilon_x + e_{32}\varepsilon_y + e_{36}\gamma_{xy})dxdy \qquad (18)$$

in which, strain components of von Karman Mindlin plate are

$$\varepsilon_x = u_{,x} + \frac{1}{2}w_{,x}^2 + z\theta_{x,x}\,,\ \varepsilon_y = u_{,y} + \frac{1}{2}w_{,y}^2,\ \gamma_{xy} = u_{,y} + v_{,x} + w_{,x}w_{,y}\,. \qquad (19)$$

For beam, Eq(18) simplifies to

$$q_r(t) = \int_0^a \Gamma_r(x)e_{31}[u_{,x} + \frac{1}{2}w_{,x}^2 + z_r\theta_{x,x}]dx \qquad (20)$$

It is clear that modal sensor generally can not be constructed for nonlinear plate because no orthogonality of modes.

DIGITAL SIGNAL PROCESSING OF SENSOR

Much of the analysis done in modal testing is performed in the frequency domain, inside the analyzer. The analyzer's task is to convert analog time-domain signals into digital frequency-domain information compatible with digital computing and then to perform the required computations with these signals. The method used to change an analog signal, q(t), into frequency-domain information is the Fourier transform. For the charge of linear Mindlin plate sensor Eq( ), the Fourier transform of the charge q(t) is denoted by Q(ω) and is defined by

$$Q_r(\omega) = \int_{-\infty}^{\infty} q_r(t)e^{-j\omega t}dt = \iint_A F_rP_0[e_{31}E_x(x,y,\omega) + e_{32}E_y(x,y,\omega) + e_{36}E_{xy}(x,y,\omega)]dxdy \qquad (21)$$

where (E_x, E_y, E_{xy}) are the Fourier transform of in-plane strain (ε_x, ε_y, γ_{xy}), respectively, and defined by

$$\begin{aligned} &E_x(x,y,\omega) = \int_{-\infty}^{\infty}(u_{,x} + z_r\theta_{x,x})e^{-j\omega t}dt,\ \ E_y(x,y,\omega) = \int_{-\infty}^{\infty}(v_{,y} + z_r\theta_{y,y})e^{-j\omega t}dt \\ &E_{xy}(x,y,\omega) = \int_{-\infty}^{\infty}(u_{,y} + v_{,x} + z_r\theta_{x,y} + z_r\theta_{y,x})e^{-j\omega t}dt \end{aligned} \qquad (22)$$

RANDOM SIGNAL ANALYSIS OF SENSOR

The transducer used to measure both the input and output during a vibration test usually contains noise, i.e., random components that make it difficult to analyze the measured data in a deterministic fashion. In addition, performing a number of identical tests and averaging the results increases confidence in a measured quantity. This is fairly common practice when measuring almost anything.

In fact, the stiffness of a signal structure is determined by multiple measurements, not just one,. Thus it is important to consider the random signal q(t). Callaham and Baruh (1995) have given an attention to this issue, but haven't given auto-correlation function and power spectral density for further random analysis.

For random signal output $q_r(t)$, we can define its auto-correlation function as

$$R_{qq}(\tau) = \lim_{T\to\infty} \int_0^T q_r(t) q_r(t+\tau) dt \tag{23}$$

The power spectral density (PSD) of the random charge is the Fourier transform of the signal's auto-correlation

$$S_{qq}(\omega) = \frac{1}{2\pi} \int_{-\infty}^{\infty} R_{qq}(\tau) e^{-j\omega\tau} d\tau . \tag{24}$$

For a smart structure system, the signal q(t) will amplified and feedback to be input of the system, To measure the noise in the signal, the coherence function is defined to be

$$\gamma^2 = \frac{|S_{xq}(\omega)|^2}{S_{xx}(\omega) S_{qq}}, \tag{25}$$

which always lie between 0 and 1. The coherence is a measurement of the noise in the signal. If it is zero, the measurement is of a pure noise; if the value of the coherence is 1, the signal x(t) and q(t) are not contaminated with noise. In which, x(t) is the response of the structures. S_{xq} is the cross-spectral density of the cross correction function of two signal x(t) and q(t).

FINITE ELEMENT FORMAT OF SENSOR EQAUTION

In practical simulation, finite element method will be dominant choice. The variation in each element can be interpolated, for element e, as

$$\begin{Bmatrix} u \\ v \\ \theta_x \\ \theta_y \end{Bmatrix} = \sum_{i=1}^{Nnode} N_i^e \begin{Bmatrix} u_i \\ v_i \\ \theta_{xi} \\ \theta_{yi} \end{Bmatrix}^e \tag{26}$$

where Nnode is the number of node of element e, N_I is the shape functions. Then the charge of the element e will be

$$q_i^e(t) = \iint F_r P_0 \begin{Bmatrix} e_{31} \\ e_{32} \\ e_{36} \end{Bmatrix}^T \begin{bmatrix} \frac{\partial}{\partial x} & 0 \\ 0 & \frac{\partial}{\partial y} \\ \frac{\partial}{\partial y} & \frac{\partial}{\partial x} \end{bmatrix} \begin{Bmatrix} u + z_r\theta_x \\ v + z_r\theta_y \end{Bmatrix} dxdy = \sum_{i=1}^{Nnode} \iint F_r P_0 \begin{Bmatrix} e_{31} \\ e_{32} \\ e_{36} \end{Bmatrix}^T \begin{bmatrix} \frac{\partial N_i^e}{\partial x} & 0 \\ 0 & \frac{\partial N_i^e}{\partial y} \\ \frac{\partial N_i^e}{\partial y} & \frac{\partial N_i^e}{\partial x} \end{bmatrix} \begin{Bmatrix} u_i + z_r\theta_{xi} \\ v_i + z_r\theta_{yi} \end{Bmatrix}^e dxdy . \tag{27}$$

In iso-parametric element space (ξ, η), Eq(27) can be rewritten as

$$q_i^e(t) = \sum_{i=1}^{Nnode} \Omega_r^e \begin{Bmatrix} u_i + z_r\theta_{xi} \\ v_i + z_r\theta_{yi} \end{Bmatrix}^e , \tag{28}$$

which are the electric degree of freedom of an element e and where the interpolation function of the charge of each element is

$$\Omega_i^e(t) = \begin{Bmatrix} e_{31} \\ e_{32} \\ e_{36} \end{Bmatrix}^T \int_{-1}^{1} \int_{-1}^{1} F_r P_0 \begin{bmatrix} \frac{\partial N_i^e}{\partial x} & 0 \\ 0 & \frac{\partial N_i^e}{\partial y} \\ \frac{\partial N_i^e}{\partial y} & \frac{\partial N_i^e}{\partial x} \end{bmatrix} J d\xi d\eta . \tag{29}$$

The feedback voltage of the element will be

$$V_r^e(t) = -G_r \frac{dq_i^e(t)}{dt} = -G_r \sum_{i=1}^{Nnode} \Omega_r^e \begin{Bmatrix} \dot{u}_i + z_r\dot{\theta}_{xi} \\ \dot{v}_i + z_r\dot{\theta}_{yi} \end{Bmatrix}^e , \tag{30}$$

which will be assembled the active damping matrix of the element included sensor. It is worth noting that the element used to sensor should not necessary have to be same as the element used to formulating host structure, although usually apply same element to both sensor and host structure.

FINITE ELEMENT FORMULATION OF A PIZOELECTRIC SMART STRUCTURES

From the above discussion, piezoelectric actuator excited by piezoelectric sensor through a controller actually plays as an active damper. In other words, the piezoelectric actuator has only contribution to system's damping but not mass and stiffness. This remarkable understood is very helpful in the FEM formulation of a smart structure. In the language of FEM, the construction of smart finite element (SFE) can be done easily, because the SFE is the only ordinary element plus one additional electric d.o.f., i.e., $q_r^e(t)$, or $V_r^e(t)$. In the numerical implementation, the only user's subroutine to be written is the active damping subroutine if using FEM package, i.e., ABAQUS.

The smart finite element is the element having "intelligent" at the element level. The smart finite element is a new concept should be studied in the future.

ACKNOWLEDGEMENT

The author would like to thank the Foundation for Research Development (FRD) for its financial support to the project: Smart Composite Structures (GUN2038139).

REFERENCE

1. Callahan, J and Baruh, H., Modal analysis using segmented piezoelectric sensors, AIAA Journal, Vol.33, No.12, December 1995.
2. Chandra R., Chopra I., Structural Modeling of Composite Beams with Induced-Strain Actuators, *AIAA Journal*, **31**(9), pp. 1692-1701, (1993).
3. Chandrashekhapa K., Donthireddy P., Vibration Suppression of Composite Beams with Piezoelectric Devices Using a Higher Order Theory, *European Journal of Mechanics, A/Solids*, **16**(4), pp.709-721, (1997)
4. Gandhi, M.V. and Thompson, B S., *Smart Materials and Structures*, Chapman & Hall, 1992.
5. Crawley E. F., Intelligent Structures for Aerospace: A Technology Overview and Assessment, *AIAA Journal*, **32**(8), pp.1689-1699, (1994).
6. Crawley E. F., Lazarus K. B., Induced Strain Actuation of Isotropic and Anisotropic Plates, *AIAA Journal*, **29**(6), pp.944-951, (1991).
7. Huang D. and Sun B., Nonlinear Vibration Analysis of Smart Composite Beams, *proceedings of the 2nd South Africa Conference on Applied Mechanics, Cape Town,* Vol. 1, PP.481-492, (1998).
8. Huang, D. and Sun B., Vibration analysis of laminated composite beams with piezoelectric layers using a higher order theory, ICCT/2, Durban, 1998.
9. Hwang W. S. and Park H. C., Finite Element Modeling of Piezoelectric Sensors and Actuators, *AIAA Journal*, **31**(5), pp.930-937, (1993).
10. Inman, D.J., *Engineering Vibration*, Prentice Hall, 1996.
11. Jones R. M., *Mechanics of Composite Materials*, McGraw-Hill Kogakusha, Ltd, (1975).
12. Lee C. K., Theory of Laminated Piezoelectric Plates for the Design of Distributed Sensors/Actuators. Part I: Governing Equations and Reciprocal Relationships, *Journal of Acoustical Society of America*, **87**(3), pp.1144-1158, (1990).
13. Lee, C.K. and Moon, F C, Modal sensors/actuators, J. Appl. Mech., ASME, 434/Vol.57, June 1990.
14. Mitchell J. A., Reddy J. N., A Refined Hybrid Plate Theory for Composite Laminates with Piezoelectric Laminae, *International Journal of Solids Structures*, **32**(16), pp.2345-2367, (1995).
15. Pai P. F., Nayfeh A. H., Oh K. and Mook D. T., A Refined Nonlinear Model of Composite Plates With Integrated Piezoelectric Actuators and Sensors, *International Journal of Solids Structures*, **30**(12), pp.1603-1630, (1993).
16. Reddy J. N., A Simple Higher-Order Theory for Laminated Composite Plates, *Journal of Applied Mechanics*, **51**(12), pp.745-752, (1984).
17. Shen Y. and Yin L., Strain Sensor of Composite Plates Subjected to Low Velocity Impact with Distributed Piezoelectric Sensors: A Mixed Finite Element Approach, *Journal of Sound and Vibration*, **199**(1), pp.17-31, (1997).
18. Tzou, H S et al, Sensor mechanics of distributed shell convolving sensors applied to flexible rings, ASME J Appl Mech, 40/Vol.115, January 1993.
19. Wang B. T., Rogers C. A., Laminated Plate Theory for Spatially Distributed Induced Strain Actuators, *Journal of Composite Materials*, **25**, pp. 43433-452, (1991).

DEVELOPMENT OF A NUMERICAL MODEL FOR THE DAMAGE IDENTIFICATION ON COMPOSITE PLATE STRUCTURES

J.V. Araújo dos Santos[1], C.M. Mota Soares[2], C.A. Mota Soares[2] and H.L.G. Pina[2]
[1] EST/IPS - Escola Superior de Tecnologia, Rua do Vale de Chaves, Estefanilha,
2910 Setúbal, Portugal
[2] IDMEC/IST, Instituto Superior Técnico, Av. Rovisco Pais,
1096 Lisboa Codex, Portugal

ABSTRACT

This paper deals with a numerical technique for the identification of damage on laminated structures. The numerical model is based on a first order shear deformation finite element. When the structure undergoes some kind of damage, its stiffness is reduced, changing the dynamic response. By considering the sensitivities of the orthogonality conditions of the mode shapes an algorithm is formulated, which calculates a damage parameter in each finite element. The damage parameter is directly related to the stiffness reduction of the damage finite element. Only the mechanical properties of the layers of the undamaged plate and the natural frequencies and mode shapes of the damage plate are required. The algorithm is applied to a laminated rectangular plate and its efficiency is demonstrated through several damage simulations.

INTRODUCTION

Detection, location and characterisation of damage in structures via techniques that examine changes in measured structural vibration response is a very important topic of research, due to increasing demands for quality and reliability. Surveys on the technical literature such as on Doebling et al [1], among others, show that in general the numerical models used are not very efficient on the identification of damage. Further, it can be verified that research work on damage identification of laminated composite structures is still very rare. The field of application of composite materials has strongly increased in the recent years, reaching several areas of application due to their versatility. Thus, efficient new numerical models, associated to experimental measured structural vibration response are required for the characterisation of damage on composite structures.

Doebling *et al* [1] have carried out a literature survey relative to methods of identification and health monitoring of structural and mechanical systems. These identification methods can be classified at three levels:

1. Verification of the presence of damage in the structure;

2. Localisation of damage;
3. Quantification of damage.

In the present work, a numerical model, which allows a level 3 characterisation is proposed, with no need of the knowledge of the localisation of it. The model is based on a first order shear deformation laminated finite element (Mota Soares *et al* [2]).

When the structure undergoes some kind of damage, the stiffness is reduced. This reduction changes the dynamic response of the damaged structure. The proposed numerical model does not need knowing previously the possible areas where damage has occurred. It also does not require the eigenfrequencies and mode shapes of the undamaged structure. It is shown that there are always enough equations to evaluate directly the damage. In the eventuality of the existence of fewer equations than unknowns, a technique of decomposition in singular values enables an iterative solution of the problem.

The theoretical bases of the model are similar to that of the updated structural analytical models by an inverse eigensensitivity method, formulated by Lin *et al* [3]. However, the present model makes use of the sensibilities of the orthogonality conditions of the mode shapes.

The model is applied to laminated rectangular plates, free in space and its efficiency and stability on the prediction of damage on small areas, as well as on very spread and large damaged zones is discussed. Two illustrative applications are here presented.

THEORY

For the descritized undamaged structure, the eigenvalue equations of motion can be written as:

$$\mathbf{K}\mathbf{q}_i = \lambda_i \mathbf{M}\mathbf{q}_i \quad \text{for} \quad i = 1,\ldots,m \tag{1}$$

where $\mathbf{K}$ and $\mathbf{M}$, are the stiffness and mass matrixes, respectively, λ_i is the ith eigenvalue, $\mathbf{q}_i$ is the ith eigenvector and m is the computed number of modes.
If the structure undergoes some kind of damage, which reduces its stiffness, equation (1) becomes:

$$\widetilde{\mathbf{K}}\widetilde{\mathbf{q}}_i = \widetilde{\lambda}_i \mathbf{M}\widetilde{\mathbf{q}}_i \quad \text{for} \quad i = 1,\ldots,m \tag{2}$$

Considering the orthogonality conditions:

$$\widetilde{\mathbf{q}}_i^{\mathrm{T}} \widetilde{\mathbf{K}}\widetilde{\mathbf{q}}_j = 0 \quad \text{for} \quad i = 1,\ldots,m \quad \text{and} \quad j = i+1,\ldots,m \tag{3}$$

and the mass normalisation of the mode shapes, the following equation can be established:

$$\widetilde{\mathbf{q}}_i^{\mathrm{T}} \widetilde{\mathbf{K}}\widetilde{\mathbf{q}}_j = \delta_{ij}\widetilde{\lambda}_i \quad \text{with} \quad \begin{cases} \delta_{ij} = 0 & \text{for } i \neq j \\ \delta_{ij} = 1 & \text{for } i = j \end{cases} \tag{4}$$

Since the damage stiffness matrix is given by $\widetilde{\mathbf{K}} = \mathbf{K} - \delta\mathbf{K}$ and on element e the corresponding perturbed matrix is $\delta\mathbf{K}_e = \delta b_e \mathbf{K}_e$, where $\delta b_e \in [0, 1[$ is the damage parameter, yields:

$$\sum_{e=1}^{N} \widetilde{\mathbf{q}}_{ie}^{\mathrm{T}} \mathbf{K}_e \widetilde{\mathbf{q}}_{je} \delta b_e = \widetilde{\mathbf{q}}_i^{\mathrm{T}} \mathbf{K} \widetilde{\mathbf{q}}_j - \delta_{ij} \widetilde{\lambda}_i \quad \text{with} \quad \begin{cases} \delta_{ij} = 0 & \text{for } i \neq j \\ \delta_{ij} = 1 & \text{for } i = j \end{cases} \tag{5}$$

where N is the number of elements.

Equations (5) are written in the compacted form as:

$$\mathbf{S}\delta\mathbf{b} = \delta\boldsymbol{\lambda} \tag{6}$$

where $\mathbf{S}(k, e) = \widetilde{\mathbf{q}}_{ie}^{\mathrm{T}} \mathbf{K}_e \widetilde{\mathbf{q}}_{je}$ is the sensitivity matrix, $\delta\mathbf{b}(e) = \delta b_e$ is the vector of damage parameters and $\delta\boldsymbol{\lambda}(k) = \widetilde{\mathbf{q}}_i^{\mathrm{T}} \mathbf{K} \widetilde{\mathbf{q}}_j - \delta_{ij} \widetilde{\lambda}_i$ is the vector of modal parameters, with $k = 1, \ldots, m(m+1)/2$ and $e = 1, \ldots, N$.

Depending on the number of mode shapes and the number of elements, three situations can occur:

1. The number of modes m is such that $M = m(m+1)/2 > N$;
2. The number of modes m is such that $M = m(m+1)/2 = N$;
3. The number of modes m is such that $M = m(m+1)/2 < N$.

In the first situation we have an overdetermined set of linear equations that can be solved by the Gauss-Jordan elimination method, since matrix **S** is not singular. The second situation is a set of equal number of linear independent equations and unknowns that can also be solved efficiently by the Gauss-Jordan elimination method. In the third situation we have fewer equations M than unknowns N and there is not a unique solution. The Gauss-Jordan elimination method fails to solve the set of equations. Using the Single Value Decomposition (SVD) it is possible to find the $N - M$ family of solutions (Maia *et al* [4], Press *et al* [5]). The physically admissible solution is the one with minimum damage $|\delta b_e|$. This solution can be obtained by an iterative process. In the first and subsequent iterations a set of M equations by N_i unknowns is solved, where N_i is the number of elements included in the i-th iteration. After each iteration, the elements with a damage parameter $\delta b_e < 0$ are eliminated. Once $N - M$ or more elements are eliminated, the damage parameter of the remaining elements can be computed with great accuracy.

APPLICATIONS

The structure chosen for this study is a symmetric cross-ply plate $[0°, 90°, 0°]$ with plane dimensions $a = 0.2$ m, $b = 0.1$ m and thickness $h = 0.002$ m. The layers have equal thickness and the material properties of each layer are presented in Table 1.

The plate is discretized in 12x12 first order shear deformation plate elements (Mota Soares *et al* [2]). Hence, there are 144 unknown damage parameters. Each element has 8 nodes with 5 degrees of freedom. Due to the symmetry of the lay-up and the materials of the layers, there are no in-plane displacements, resulting a total of 1443 degrees of freedom. Damage is simulated by a reduction in the stiffness matrix $\mathbf{K}_e$ of the e-th element.

Table 1: Mechanical properties of the layers

	Layer 1	Layer 2	Layer 3
E_1 [GPa]	100	50	100
E_2 [GPa]	10	10	10
G_{12} [GPa]	5	6	5
G_{13} [GPa]	5	6	5
G_{23} [GPa]	3	4	3
ν_{12}	0.3	0.25	0.3
ρ [kg/m^3]	1500	2000	1500

Multiple damage is simulated in elements 100, 120 and 144, with a stiffness reduction of 0.20, 0.50 and 0.05, respectively. The results are presented in Table 2. In this example, the calculations must include at least 10 modes in order to obtain a reliable computation of damage of elements 100, 120 and 144. With 9 modes, the damage in element 144 appears in adjacent element 132 (Figure 1). This is due to the large difference in the damage parameter values, 0.50 and 0.05, in elements 120 and 144, respectively. As the number of modes increases, the required number of iterations decreases.

Table 2: Damage parameter δb_e

No. of Modes, m (No. of Equations, M)	Element	100	120	144	No. of Included Elements, N_i
	Actual Value	0.2000	0.5000	0.0500	
9 (45)	Iteration 1	0.1667	0.4011	-0.0066	144
	Iteration 2	0.1966	0.4802	-	39
	Iteration 3	0.2028	0.4956	-	21
10 (55)	Iteration 1	0.1729	0.4418	0.0030	144
	Iteration 2	0.1998	0.4955	0.0378	78
	Iteration 3	0.2000	0.5000	0.0500	43
12 (78)	Iteration 1	0.1923	0.4866	0.0155	144
	Iteration 2	0.2000	0.5000	0.0500	76
16 (136)	Iteration 1	0.2000	0.5000	0.0500	144
	Iteration 2	0.2000	0.5000	0.0500	75
17 (153)	Iteration 1	0.2000	0.5000	0.0500	144

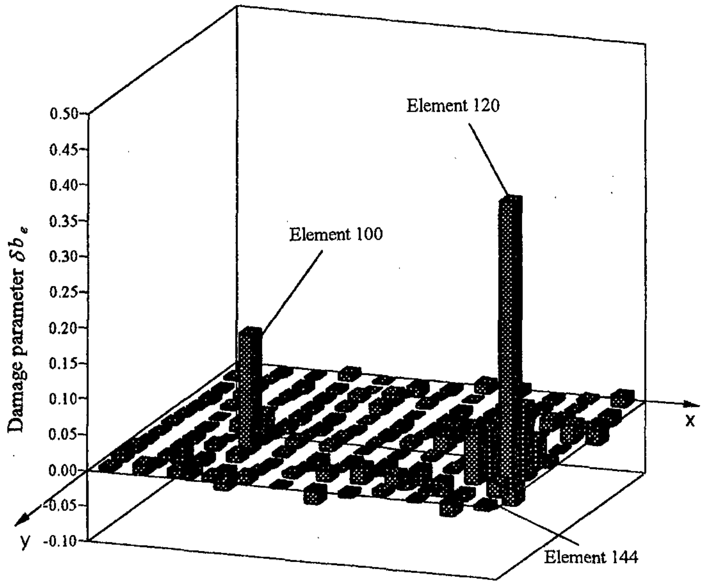

Figure 1: First iteration with 9 modes

As can be seen in Figure 2, the results are highly precise when enough equations are used.

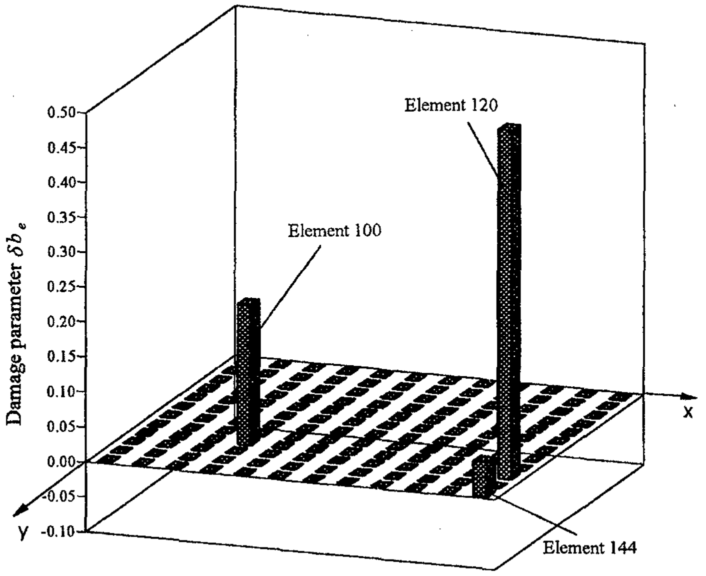

Figure 2: First iteration with 17 modes

In the second example, a 0.20 damage parameter is attributed to all elements. Figures 3a and 3b show the results for 10 and 17 modes, respectively. The results exhibit a maximum discrepancy between the actual values and the computed values inferior to 12.07% and 0.05% for 10 and 17 modes, respectively. It should be noted that this example implies no iterative process, because all elements are damaged.

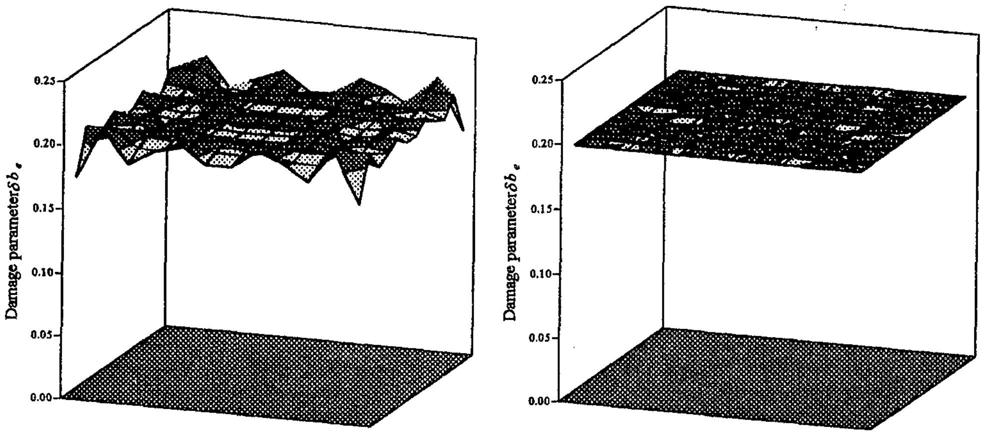

a) 10 modes b) 17 modes

Figure 3: Results for a damage parameter of 0.20 in all elements

CONCLUSIONS

A numerical model is presented for the damage identification on laminated structures, which does not need to know *a priori* the probable areas of damage. The model is applied on the characterisation of damage of plates with cross-ply laminates. When enough equations are used, the damage can be directly identified. However, when the number of equations are not sufficient, the singular value decomposition (SVD) technique can solve uniquely the problem. The two illustrative examples show the good efficiency and stability of the numerical model on the identification of damage on small areas, as well as on very spread and large damaged zones.

REFERENCES

[1] Doebling, S.W., Farrar, C.R., Prime, M.B. and Shevitz, D.W., "Damage Identification and Health Monitoring of Structural and Mechanical Systems from Changes in Their Vibration Characteristics: A Literature Review", Los Alamos National Laboratory, LA-13070-MS, (1996).

[2] Mota Soares, C.M., Freitas, M.M., Araújo, A.L. and Pedersen, P., "Identification of Material Properties of Composite Plate Specimens", *Composite Structures*, Vol.25, pp. 227-285, (1993).

[3] Lin, R.M., Lim, M.K. and Du, H., "Improved Inverse Eigensensitivity Method for Structural Analytical Model Updating", *Journal of Vibration and Acoustics*, Vol. 17, pp. 192-198, (1995).

[4] Maia, N.M.M. and Silva, J.M.M. (Editors), "Theoretical and Experimental Modal Analysis", John Wiley, (1997).

[5] Press, W. H., Flannery, B. P., Teukolsky, S. A. e Vetterling, W. T., "Numerical Recipes: The Art of Scientific Computing (FORTRAN Version)", Cambridge University Press, Cambridge (1992).

“RIOJA 95” NUMERICAL TESTING CORRELATION, AMERICA’S CUP SPANISH CHALLENGE SHIP

J. Cuartero [1], A. Pérez de Lucas [2], M. López Rodriguez [3], L. Castejón [1]

[1] University of Zaragoza
Dept.. of Mechanical Engineering
Transportation Area
C/ María de Luna 3
50015 Zaragoza, España

[2] E. N. Bazán
Paseo de la Castellana 55
Madrid
España

[3] Copa América, Desafío
Español 99
Pedro de Valdivia 10
Madrid 28006
España

INTRODUCTION

America’s Cup is one of the most exciting and amazing events on marine yachting. Extremely highly competitive and prestigious, every country in the world is quite proud of their ships challenging the last winner. Because of this craving of victory all crews try to do their best when racing. Furthermore these efforts ship’s behavior, weight, resistance and speaking in general all parameters related to design are increasing their influence on final results. Maximum effort and optimization is required to the designers trying to get the best from the ship.

It is on such situation when the Spanish committee get in touch with University of Zaragoza demanding a mathematical model capable of reproducing ship’s behavior. This model should be able to simulate by means of finite elements the structure of the “Rioja 95” the Spanish yacht.

The main task was to get an adequate finite elements model to perform different FEA in order to aim a better and optimized structure. This model should be able to simulate and to predict the results of future modifications thought to make in the ship. In order to ensure model’s performance some extensometric tests were carried out by means of 2D precision strain gauges and unidirectional strain gauges. These unidirectional strain gauges were used to measure forces along all the ropes, and 2D precision strain gauges were necessary to measure strains on 9 different points located all over the ship on strategic places. These measured strains are to be compared to the values obtained by the FEM loaded with the measured loads. This comparison should show how precise the model is and its ability to simulate actual load cases.

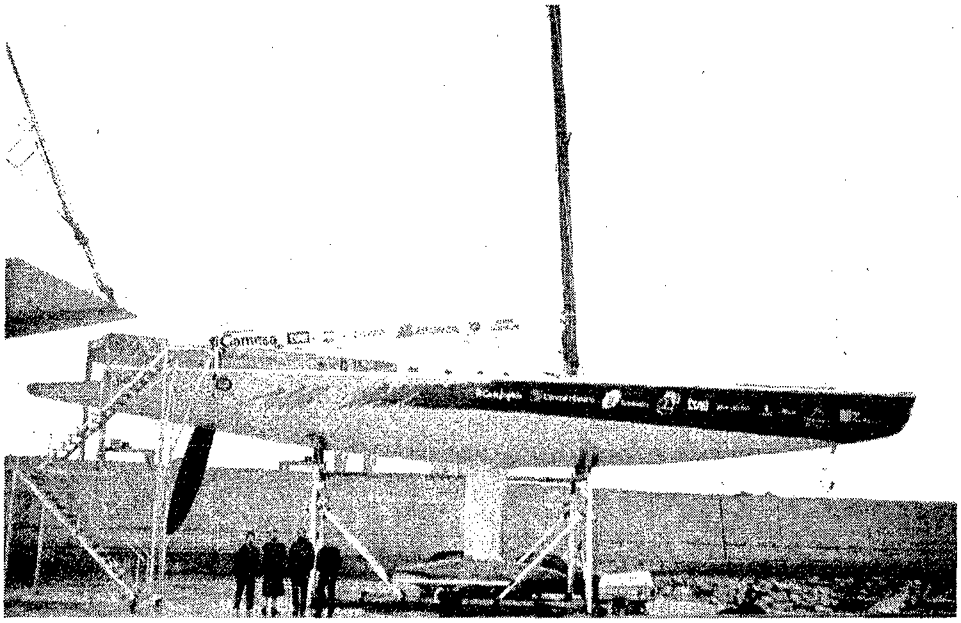

Figure 2.1 “Rioja 95” at Valencia harbour.

MATHEMATICAL MODEL.

The structure of "Rioja 95" has been simulated by means of a finite element model which consists of 19483 nodes and 19393 elements.

The distribution of elements is as follows :

- 17363 elements S4R : element S4R is a linear 4 nodes linear element.
- 436 elements S3R. : element S3R is a linear 3 nodes linear element.
- 614 elements B31 : linear bar element.
- 400 elements C3D8RH : it is 8 nodes volumetric element.
- 65 elements C3D6: 6 nodes wedge element.

The commercial code used to model and calculate the ship is ABAQUS. This code has been used for preprocessing ,ABAQUS/Pre, calculating, and postprocessing the results. The structure has been mostly meshed with 4 nodes shell elements, avoiding 3 nodes shell elements except where strictly necessary. Beam elements have been utilised to simulate the beams and profiles not possible to simulate with shells due to its geometric position or dimensions. Volumetric elements have been needed at any place where du to a great thickness volumetric elements would be the best choice to ensure an actual behaviour. A constant element dimension has been achieved ,but the mesh has been refined and optimised where necessary. The following picture shows "Rioja 95" mesh.

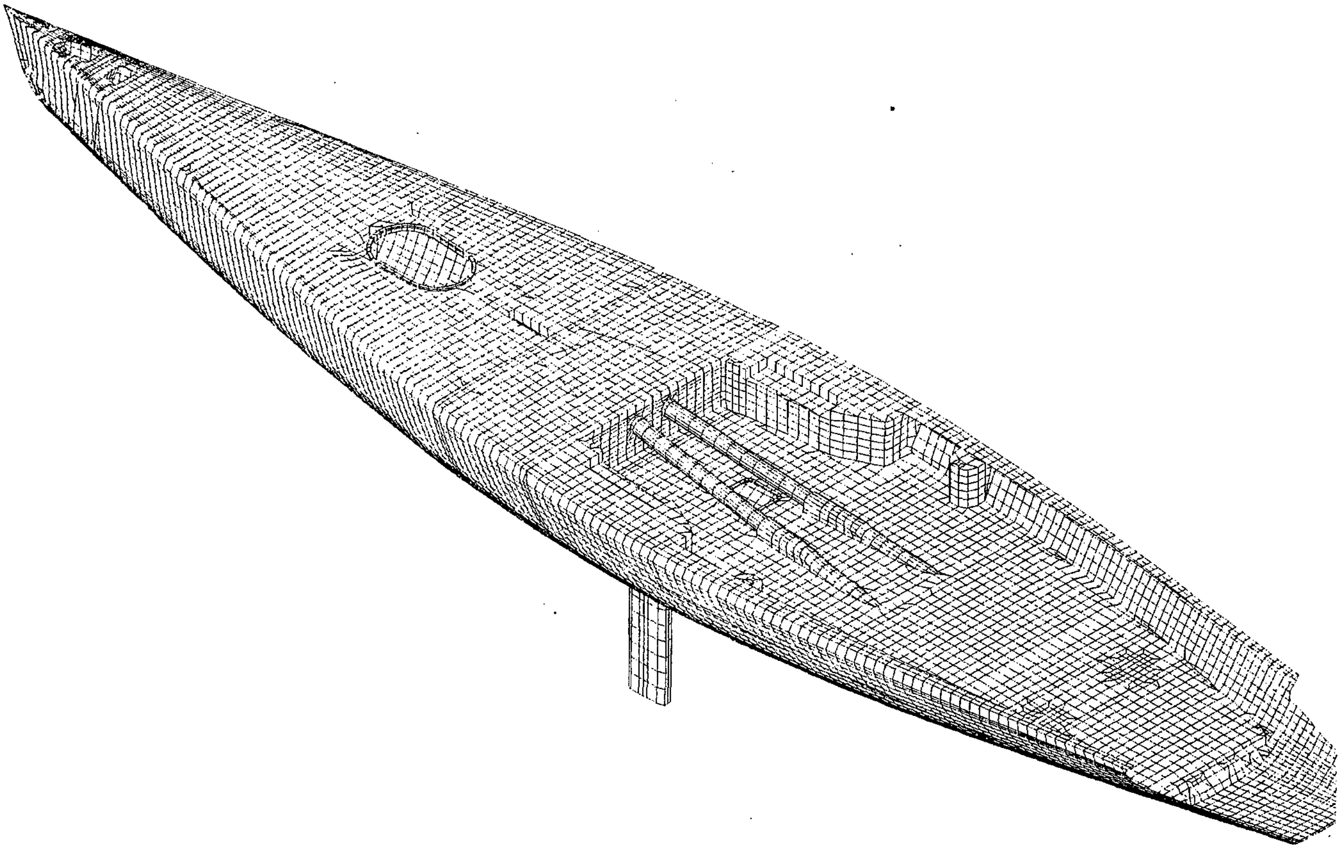

Figure 2.2 "Rioja95" finite elements mesh.

BOUNDARY CONDITIONS AND LOAD CASES

Three different load cases have been considered in order to ensure ship's model behaviour under three actual situations.

LOAD CASES 1 AND 2

Table 3.1 Load case 1

port runner 1	36000 N	starboard vertical	0 N	Stay	43400 N
starboard runner 1	31000 N	port vertical	0 N	Mast	12 Ton
port runner 2	26000 N	port diagonal	208 N		
starboard runner 2	22000 N	starboard diagonal	946 N		

1. Runners.

The value of these loads have been found by means of extensometric measurements. Unidirectional strain gauges were placed on the ropes in order to measure the load carried by that ropes. Figure 3.4 shows the applied loads at the points were runners are attached to the cockpit.

2. Loads on verticals and diagonals.

Figure 3.1 shows that loads. These loads have been calculated by considering loads found on verticals and diagonals with unidirectional strain gauges and the mast's compression load withstand. Due to this compression, verticals and diagonals withstand some stress. As these elements support a load, previous to the ship to be loaded, strain gauges do not measure the actual force supported by these elements but the loaded force. Therefore, a finite element analysis should have been carried out to find the pre stress withstand by verticals and diagonals. Once these stress values had been found, the actual force could be aimed by adding these two stresses, the one found by extensometric gauges and the one found with the performed F. E. A.

This F. E. A. have been carried out by modelling the mast and loading it. due to the great mast displacements the analysis had been to be non linear geometric analysis. Henceforth all loads are supposed to be corrected with the findings of this non linear F. E. A .Figures 3.1 and 3.2 shows the withstand force along the axis of each rope and beam and vertical displacement, respectively.

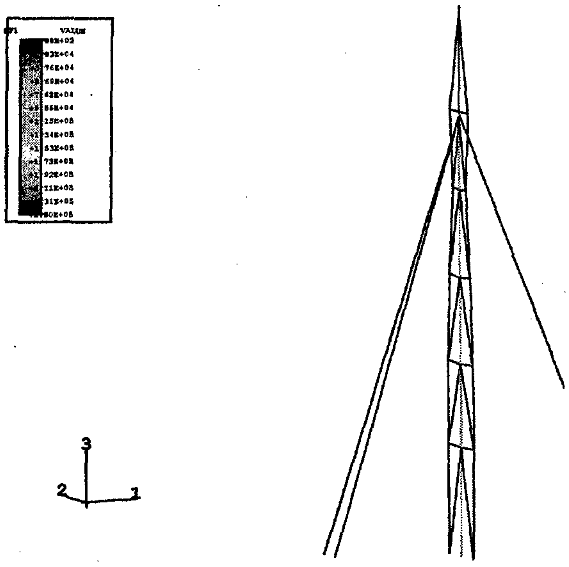

Figure 3.1

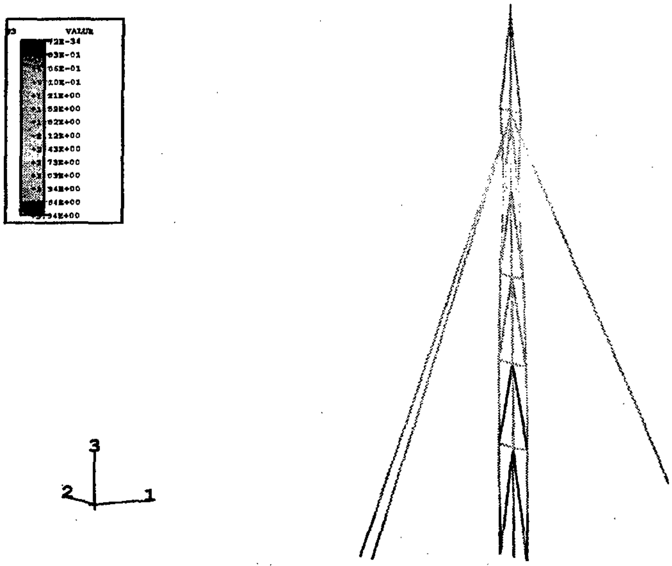

Figure 3.2

3. Stay load.
Stay carries the greatest load at the ship. That load has been determined by extensometry, with 1D strain gauge. The load and its application point is shown in figure 3.2. This load point out to a quite high mast's point.

4. Mast load.
Mast's load is the summary of all vertical loads applied to the ship, 20 Ton pre-compression load enclosed.

5. Cylinder load.
A 21 KN. load is placed on deck's cylinders. Figure 3.4 shows all loads on the cockpit.

6. Boundary conditions.
Boundary conditions are shown in Figure 3.3 . Nodes corresponding to bedsteads are restrained on 2 and 3 directions. Keel lower nodes are restrained over 1,2, and 3 directions. Due to the bedsteads and structure interaction, beams with different stiffness were placed in order to allow the structure to be assented on the bedsteads.

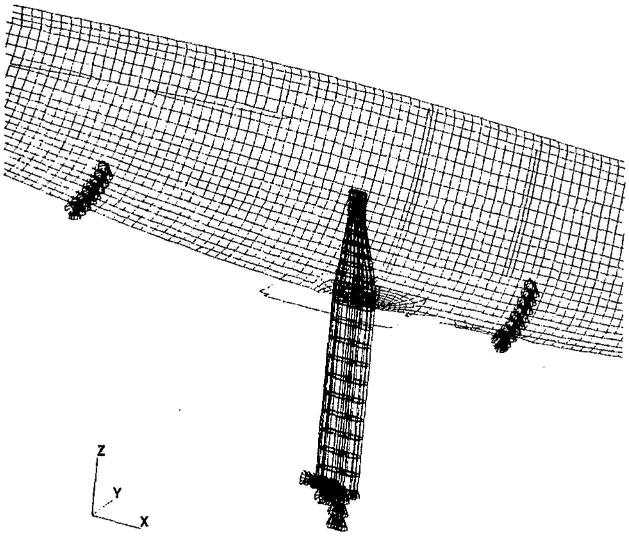

Figure 3.5

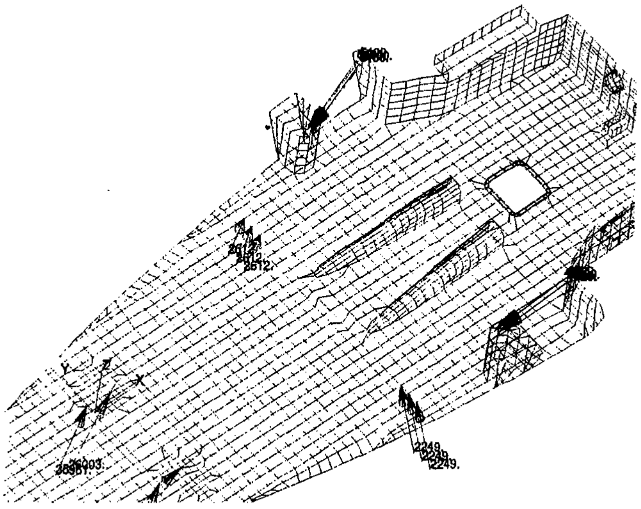

Figure 3.6

Load Case 2 is exactly the same as Case 1 except that loads on the starboard have been decreased to allow the model to show its torsion behaviour under non-symmetric load cases.

LOAD CASE 3 .Tube's compression.

1. Tubes.

15 Ton distributed load, compressing the tubes, and the same force as the reaction of that force where tubes are connected to the ship.

MATERIALS

Table 4.1 "Rioja 95" Materials

Materials/Properties	Density Kg/m^3	Ex MPa	Ey MPa	Ez MPa	Vxy	Gxy MPa
Carbon unidirectional	1500	110000	6800		0.33	4000
Carbon bi-directional	1350	51800	51800		0.03	4500
Honeycomb/A	41	0.72	1.32	2.1		
Honeycomb/B	54	0.84	1.04	4.2		
Titanium	4500	110000	110000	110000	0.3	32000
Steel	7800	210000	210000	210000	0.3	72000

RESULTS AND CONCLUSIONS

NUMERICAL RESULTS

Results are referred to the 2D strain gauges labelled from 1 to 9 , which are situated on the following points :

R1 : Ford front hull floor 2D gauge

R2 : Ford back hull floor 2D gauge

R3 : Mast bulkhead starboard strap 2D gauge

R4 : Keel bulkhead starboard flying buttress 2D gauge

R5 : Starboard middle hull 2D gauge

R6 : Aft front hull floor 2D gauge

R7 : Aft back hull floor 2D gauge

R8 : Ford deck front 2D gauge

R9 : Ford deck back 2D gauge

Measurements are shown in microstrains, and the test's day the offset varies from 0 to 30 microstrains. Bearing in mind this offset, R5 got meaning just for Case 3 , being negligible for load Case 1 and 2.

The following tables show test measurements compared to the Finite Element Analysis results on *x* (E_{11}) and *y* (E_{22}) directions.

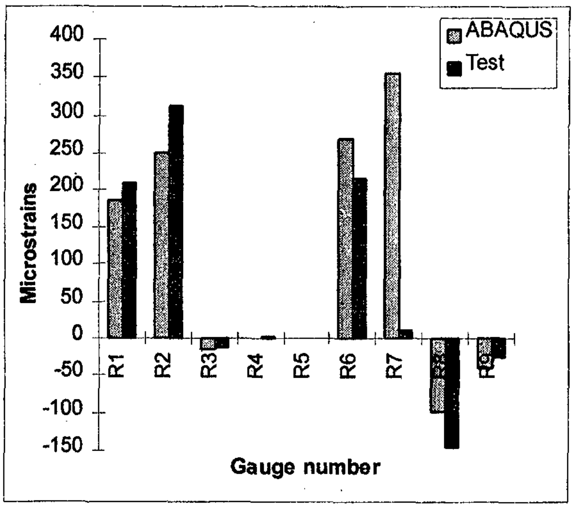

Chart 1 Load Case 1 Strains on E_{11}

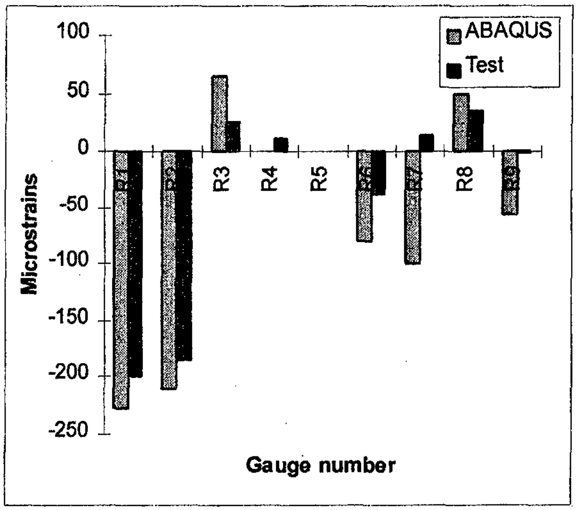

Chart 2 Load Case 1 Strains on E_{22}

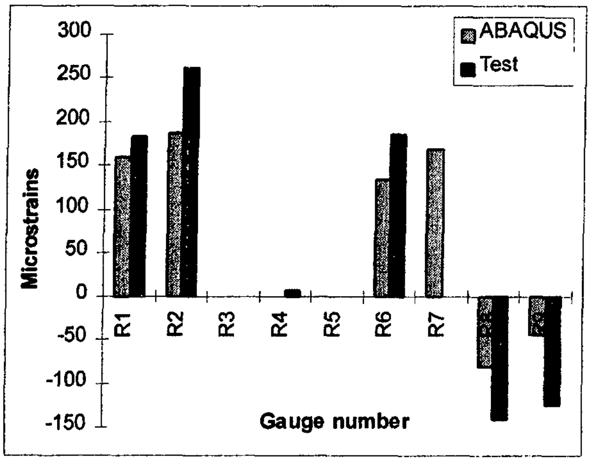

Chart 3 Load Case 1 Strains on E_{11}

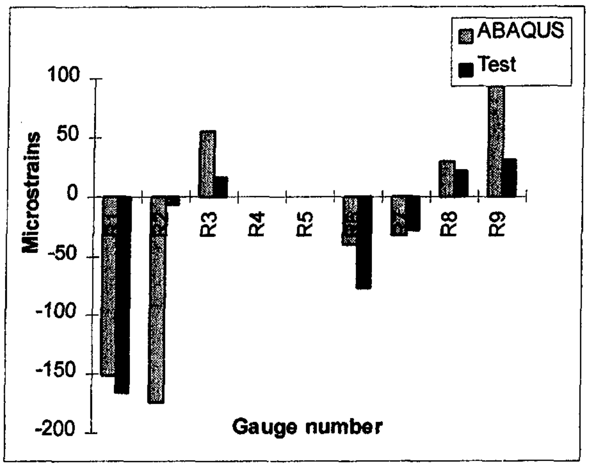

Chart 4 Load Case 2 Strains on E_{22}

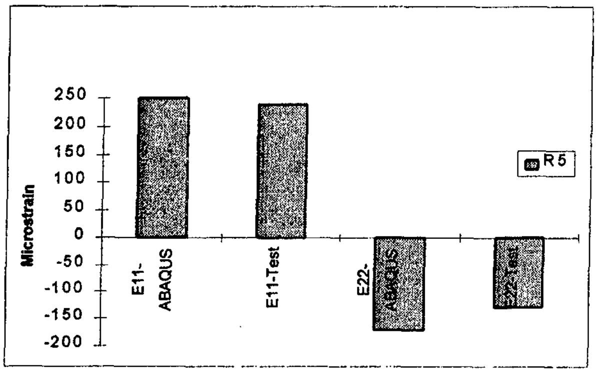

Chart 5 Load Case 3 Strains on E_{11} and E_{22}

CONCLUSIONS

The result of the correlation is excellent, test measurements are quite similar to the numerical results. This finite element model will allow to reduce considerably the scheduled test on trying different approaches to new designs. Once a reliable model is achieved, as we have done, designers are able to check every single idea they have by introducing the new concepts on the model, so that good expectations of produced consequences are known before any change would be introduced in the actual ship.

REFERENCES

[1] ABAQUS/Standard 5.6 .User's Manual I ,II ,III .
[2] "Design of marine structures in composite materials" C.S. Smith .Elsevier.
[3] "Fiberglass boat design and construction" Robert J. Scott.
[4] "Los materiales compuestos de fibra de vidrio" P. Antequera, L. Jiménez, A. Miravete.
[5] "Hull structural design ships " DNV
[6] "Design of joints and attachments in FRP ship's structures". A.R. Dodkins, R.A. Shenoi & G.L. Hawkins . Marine Structures. Elsevier.

DYNAMIC ANALYSIS OF ORTHOTROPIC SHELLS BY GRID-CHARACTERISTIC METHOD

E.G. Evseev[1] and E.V. Morozov[2]

[1]Department of Mechanics and Optimization of Processes and Structures
MATI - Russian State University of Technology
3, Orshanskaya Street, Moscow, 121351 Russia
[2]Department of Mechanical Engineering, University of Natal
4041 Durban, South Africa

INTRODUCTION

Development and justification of the numerical methods and approaches for the analysis of transitional wave processes in the thin-walled structures represent the problem that attracted an attention of many researchers over the past decades. Nevertheless, the elaboration of the efficient and universal techniques, appropriate to the field considered, is stil topical. Implementation of the explicit finite-difference methods takes the special place in this process. These methods remain quite competitive ones inspite of the wide and growing development and utilization of the powerful industrial finite-element software packages. The present paper discusses the method developed for the dynamic analysis of the othotropic shells and plates. The approach is based on the utilisation of quasilinear hyperbolic system of equations written in terms of displacements. The influence of the equation members containing large parameters is taking into account by introducing the special splitting procedure which provides the necessary level of accuracy. This procedure is applied at every step of the numerical process with respect to the time variable. The approach being implemented to the analysis of thin-walled composite structures provides the possibility to expand the domain of the computational stability for the explicit finite-difference technique.

BASIC EQUATIONS

The finite-difference schemes theory for the quasilinear second order systems of equations, presented in the following form

$$\frac{\partial \mathbf{U}}{\partial t} + \mathrm{A}(t, x, \mathbf{U}) \frac{\partial \mathbf{U}}{\partial x} = \mathbf{F}(t, x, \mathbf{U}) \qquad (1)$$

has been developed quite well for the solutions of the gas dynamics problems, magnetic hydro- dynamics problems, etc. In the system (1) $\mathbf{U}$ and $\mathbf{F}$ are the M-dimensional vectors, and A is the $M \times M$ matrix. If the system (1) is a hyperbolic one then the matrix A has M real eigenvalues λ_i and there is a full sistem of the left eigenvectors-lines ω^i, such that

$$A = \Omega^{-1}\Lambda\Omega\,, \tag{2}$$

where $\Lambda = \mathrm{diag}\|\lambda_i\|$ is the diagonal matrix, matrix Ω consists of the vector-lines ω^i, and Ω^{-1} is its inverse, i.e.,

$$\Omega^{-1}\Omega = \Omega\,\Omega^{-1} = \mathrm{E}\,,$$

where E is the unit $M \times M$ matrix.

The mixed-value problem can be formulated for the nonlinear second order system of equations which describes the dynamic behaviour of the thin-walled elastic shells of revolution on the basis of Timoshenko's model. The way of transformation from this problem to the initial-boundary-value problem for the systems similar to system (1) has been discussed in References [1, 2].

Consider the equations for modelling the dinamic axisymmetrical deformation of the orthotropic cylindrical shells of the length L as shown in Figure 1.

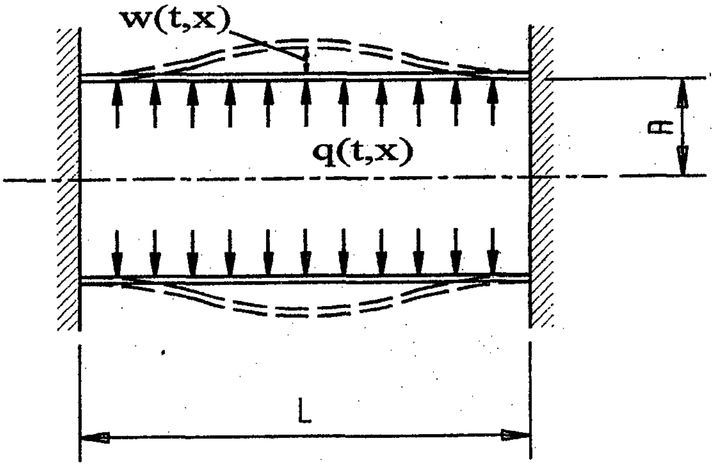

Figure 1. Orthotropic cylindrical shell

These equations can be presented in terms of unitless variables, using traditional set of notations [3, 4]:

$$\begin{aligned} &\frac{\partial^2 u}{\partial t^2} - a_1^2\frac{\partial^2 u}{\partial x^2} = b_1\frac{\partial w}{\partial x}\,,\\ &\frac{\partial^2 w}{\partial t^2} - a_2^2\frac{\partial^2 w}{\partial x^2} = b_2\frac{\partial \varphi}{\partial x} - c_2\frac{\partial u}{\partial x} - d_2\frac{\partial w}{\partial x} + e_2\,q(t,x)\,,\\ &\frac{\partial^2 \varphi}{\partial t^2} - a_3^2\frac{\partial^2 \varphi}{\partial x^2} = -b_3\frac{\partial w}{\partial x} - c_3\varphi\,, \end{aligned} \tag{3}$$

where

$$a_1^2 = \frac{1}{\alpha}a_2^2 = a_3^2 = \gamma^2\delta^2\,, \quad b_1 = \nu_2\gamma\delta^2\,, \quad b_2 = \frac{1}{12}b_3 = \alpha\gamma\delta^3\,,$$

$$c_2 = \nu_2\gamma\delta\,, \quad c_3 = 12\alpha\delta^4\,, \quad d_2 = \delta^2\frac{E_2}{E_1}\,, \quad e_2 = \gamma\delta^3\,;$$

$$\alpha = \delta^2 \frac{G_{13}(1-\nu_1\nu_2)}{E_1}, \quad \gamma = \frac{R}{L}, \quad \delta = \frac{R}{h};$$
$$x = \frac{\bar{x}}{L}, \quad u = \frac{\bar{u}}{h}, \quad w = \frac{\bar{w}}{h}, \quad t = \frac{\bar{t}ch}{R^2},$$
$$q = \frac{\bar{q}L(1-\nu_1\nu_2)}{E_1 h}, \quad c^2 = \frac{E_1}{\rho(1-\nu_1\nu_2)}.$$

After introduction of a new column-vector of unknown variables in the form

$$\mathbf{U} = \left\| \frac{\partial u}{\partial t}, \frac{\partial w}{\partial t}, \frac{\partial \varphi}{\partial t}, \frac{\partial u}{\partial x}, \frac{\partial w}{\partial x}, \frac{\partial \varphi}{\partial x}, u, w, \varphi \right\|^T$$

the system (3) can be converted into the form (1), where the hyperbolic matrix A is written as

$$\mathrm{A} = \begin{pmatrix} 0 & 0 & 0 & -a_1^2 & 0 & 0 & 0 & 0 & 0 \\ 0 & 0 & 0 & 0 & -a_2^2 & 0 & 0 & 0 & 0 \\ 0 & 0 & 0 & 0 & 0 & -a_3^2 & 0 & 0 & 0 \\ -1 & 0 & 0 & 0 & 0 & 0 & 0 & 0 & 0 \\ 0 & -1 & 0 & 0 & 0 & 0 & 0 & 0 & 0 \\ 0 & 0 & -1 & 0 & 0 & 0 & 0 & 0 & 0 \\ 0 & 0 & 0 & 0 & 0 & 0 & 0 & 0 & 0 \\ 0 & 0 & 0 & 0 & 0 & 0 & 0 & 0 & 0 \\ 0 & 0 & 0 & 0 & 0 & 0 & 0 & 0 & 0 \end{pmatrix} \tag{4}$$

and the right-hand side vector components are given by

$$\begin{aligned} F_1 &= b_1 U_5, \\ F_2 &= b_2 U_6 - c_2 U_4 - d_2 U_8 + e_2\, q(t,x), \\ F_3 &= -b_3 U_5 - c_3 U_9; \\ F_4 &= F_5 = F_6 = 0; \\ F_7 &= U_1, \quad F_8 = U_2, \quad F_9 = U_3. \end{aligned} \tag{5}$$

All of the eigenvalues of the matrix (4) may be found from the equation

$$\det\|\mathrm{A} - \lambda \mathrm{E}\| = 0$$

The corresponding real-value diagonal matrix may be written in the form

$$\Lambda = \mathrm{diag}\|0, 0, 0, a_1, -a_1, a_2, -a_2, a_3, -a_3\|.$$

The transformation matrix Ω may be determined from the following equation

$$\omega^i \mathrm{A} = \lambda_i\, \omega^i$$

Using the equation $\Omega\,\Omega^{-1} = \mathrm{E}$ we can find the corresponding inverse matrix Ω^{-1}. Finally, the hyperbolic matrix A can be presented in the form of decomposition (2).

IMPLEMENTATION OF GRID-CHARACTERISTIC METHOD

The various explicit finite-difference shemes can be used in order to solve the dynamic problem represented by the system of equations (1) with the coefficients (4) and right-hand side vector (5). In case of the constant step size of integrating with respect to the time variable Δt and coordinate variable Δx the grid-characteristic scheme can be expressed as follows

$$\begin{aligned} \mathbf{U}_i^{n+1} = \mathbf{U}_i^n + \Delta t\, \mathbf{F}_i^n - \frac{\Delta t}{2\Delta x}\left(\mathbf{U}_{i+1}^n - \mathbf{U}_{i-1}^n\right) + \\ \frac{\Delta t}{2\Delta x}\left(\Omega^{-1}|\Lambda|\Omega\right)_i^n\left(\mathbf{U}_{i+1}^n - 2\mathbf{U}_i^n + \mathbf{U}_{i-1}^n\right). \end{aligned} \tag{6}$$

According to Reference [5] this scheme demonstrates good computational characteristics. Some components of the right-hand side vector of the system (1) contain large parameters. This fact imposes quite severe constraints onto the length of the step of integrating with respect to the time variable in comparison with the well known Courant-Friedrics-Lewy condition, normally used for explicit finite difference schemes. The approach implemented in this work eliminates completely this negative influence of large parameter for considered problem. At first stage of this process we use the formulas (6) at every step in time for the homogeneous system of equations obtained from (1). The term $\Delta t\, \mathbf{F}_i^n$ in the equations (6) is substituted with the term representing external load $\Delta t\, e_2\, q_i^n$ for the second equation of the system. As a result we obtain the intermediate solution in the form of vector $\mathbf{V}$. For the next time interval the unknown variables are presented in the form of the exact closed-form solution of the following system of odinary differential equations

$$\left(\frac{d\mathbf{V}}{dt}\right)_i = \mathbf{F}(\mathbf{V}_i). \tag{7}$$

The components of the right hand side vector of this system have the form (5), where $F_2 = b_2U_6 - c_2U_4 - d_2U_8$. Finally, for each point i of the space coordinate grid we have

$$\begin{aligned} U_1^{n+1} &= V_1 + \Delta t\, b_1 V_5\,, \\ U_2^{n+1} &= V_2\cos(\sqrt{d_2}\Delta t) - (V_8 - \xi)\sin(\sqrt{d_2}\Delta t)\,, \\ U_3^{n+1} &= V_3\cos(\sqrt{c_3}\Delta t) - (V_9 - \eta)\sin(\sqrt{c_3}\Delta t)\,, \\ U_4^{n+1} &= V_4\,, \quad U_5^{n+1} = V_5\,, \quad U_6^{n+1} = V_6\,, \\ U_7^{n+1} &= V_7 + \Delta t\, V_1 + \frac{1}{2}(\Delta t)^2 b_1 V_5\,, \\ U_8^{n+1} &= (V_8 - \xi)\cos(\sqrt{d_2}\Delta t) + V_2\sin(\sqrt{d_2}\Delta t) + \xi\,, \\ U_9^{n+1} &= (V_9 - \eta)\cos(\sqrt{c_3}\Delta t) - V_3\sin(\sqrt{c_3}\Delta t) + \eta\,, \end{aligned}$$

where

$$\xi = \frac{-c_2V_2 + b_2V_5}{d_2}\,, \quad \eta = \frac{b_3V_5}{c_3}\,.$$

Using the equations analogous to (7) the contribution of the external load may be taken into acount in the similar way.

NUMERICAL RESULTS

The dynamic response of the orthotropic cylindrical shell, considered in Reference [3] (see Fig. 1), has been investigated on the basis of the discussed above method. The cylindrical shell is subjected to the axisymmetrical load $q = 1 - t/T$.The duration of the load application is changed within the following time interval $0 \leq t \leq T$. Zero initial conditions are assumed. The ends of the shell are rigidly clamped, and the appropriate boundary conditions at $x = 0$, and $x = L$ have been used. In order to simplify solution the boundary condition at $x = L$ has been substituted with the symmetry condition at $x = 0.5L$. The geometry parameters of the shell were taken as $\delta = 50$ and $\gamma = 0.5$. The duration of the loading was equal to $T = 0.01$. The space coordinate domain of the analysis has been broken into 100 intervals. Computations have been produced for the Courant numbers closed to 1.0. Some results of the calculations are shown in Figure 2.

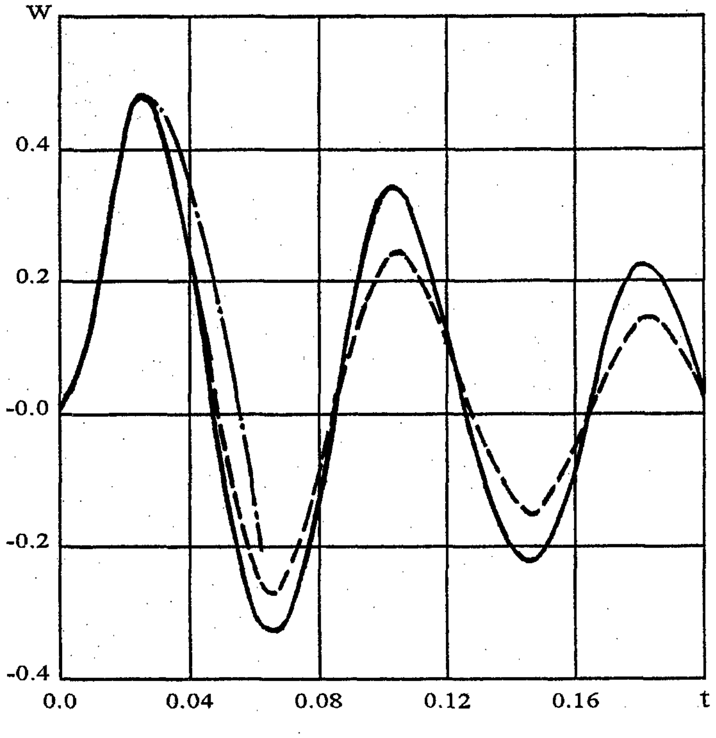

Figure 2. Dynamic deflection of the shell

The change in time of the deflection at the central cross-section of the shell is presented by solid line. The chain line corresponds to the results obtained in Reference [3]. In the close vicinity of the boundary cross-section $x = 0$ the drastic changes of the basic parameters of the solution took place. In order to eliminate this effect the special averaging procedures have been introduced within the segment of 1/20 of the shell length. The averaging has been produced using the approach described in [6]. Implementation of this procedure did not effect the solution at the central part of the shell in any significant way (see the dashed line in Figure 2.) The similar averaging technique can be applied for all of the grid nodes of the space coordinate variable x. Such an averaging leads to the overall damping of the nonphysical oscillations and makes it possible to use the scheme (6) for the analysis. However, in this case the solution fades too fast in time and it does not reflect properly the transitional dynamic processes considered in this paper.

CONCLUSIONS

The method discussed in this paper provides the stable numerical process for wide range of the values of parameters. Numerical analysis of the dynamic response of the cylindrical orthotropic shell demonstrates high efficiency and computational stability of the algorithm. The compact structure of the suggested method gives the possibility to use this technique as an analytical tool for structural design and optimisation.

ACKNOWLEDGEMENT

The financial support of the Russian Foundation for Fundamental Research (project 97-01-00856) and South African Foundation for Research Development (GUN 2034618) is gratefully acknowledged.

REFERENCES

[1] Evseev, E.G. and Semenov, A.Yu. "A method for numerical solution of the equations for the dynamics of thinn shells, based on separating out rapidly oscillating components." *Doklady AN SSSR* **310**, 4, 785–788 [*Soviet Math. Dokl.*, **41**, 1, 118–121] (1990).
[2] Evseev, E.G. and Morozov, E.V. "Nonplanar deformation of a circular thin-walled comosite bar under dynamical loading." *Izvestiya AN. Mekhanika Tverdogo Tela*, 5, 159–169 [*Mechanics of Solids*, **29**, 5, 159–169] (1994).
[3] Lugovoi, P.Z. and Meish, V.F. "On solution of axisymmetrical problems of cylindrical shells dynamics by numerical methods." *Prikladnaya Mekhanika* **22**, 1, 29–33 (1986) [in Russian].
[4] Rikards, R.B. and Teters, G.A. Stability of Composite Shells. - Zinatne, Riga (1974) [in Russian].
[5] Magomedov, K.M. and Kholodov, A.S. Grid-Characteristic Numerical Methods.- Nauka, Moscow (1988) [in Russian].
[5] Bazhenov, V.G. and Chekmarev, D.T. "Otsenka ustoichivosti yavnoi konechno-raznostnoi ckhemy "krest" resheniya nestatsionarnykh zadach teorii uprugosti i teorii obolochek." *Prikladnye Problemy Prochnosti i Plastichnosti: Algoritmizatsiya i Avtomatizatsiya Resheniya Zadach Uprugosti i Plastichnosti* (Vsevoyuznyi Mezhvuzovskii Sbornik), 15-22. - Gorkii State University, Gorkii, (1984) [in Russian].

HIGHER ORDER BOUNDARY ELEMENTS: EXACT INFLUENCE FORMULAE AND THEIR ASYMPTOTICS

M. KAYUPOV[1,2] and G. KUHN[1]

[1] Lehrstuhl für Technische Mechanik, Universität Erlangen-Nürnberg,
Egerlandstr. 5, D-91058 Erlangen, Germany
[2] E-mail: kayupov@ltm.uni-erlangen.de

INTRODUCTION

Influence functions for different stress and displacement discontinuity elements are demonstrated in [1,2]. The functions for displacement discontinuity elements allow a new formulation of the Displacement Discontinuity Method (DDM) which was presented at the ICCST'1 [3] for infinite anisotropic media and SARES'97 [4] for a finite domain with a crack. Unlike the usual DDM boundary approximation, we use coinciding displacement discontinuity boundary elements to model straight slits/cracks. Boundary conditions are satisfied at several nodal points. The nodes have the same positions for different elements. If the number of the nodes is equal to *n* then Constant, Linear, Parabolic, 3rd-order, ... , (*n*-2)-order elements, together with Left and Right Root ones, are used to solve the problem. Similar technique is employed to approximate outer boundary by stress discontinuity elements [4]. Although the above technique allows an efficient solution of the problem, it does not permit us to get accurate calculation results at points distant from higher order boundary elements.

NUMERICAL EXAMPLE

As an example, consider 10-order stress discontinuity element *AB* which is situated on the axis *Ox*. Element centre coincides with the centre *O* of the coordinate system *Oxy*. Because *A*(-1,0) and *B*(1,0), the length of the element equals two dimensionless units (L_{AB}=2). A load $g_y = [0.5(x+1)]^{10}$ is applied on the element (here *x* is the abscissa of the point on the element). We use influence functions for *k*-order stress discontinuity elements presented in the Table to model this kind of loading. Stress tensor components σ_y at points on the line x = 0.8 calculated using the functions are shown in Figure 1. Theoretically, such kind of loading should lead to the stress tensor components

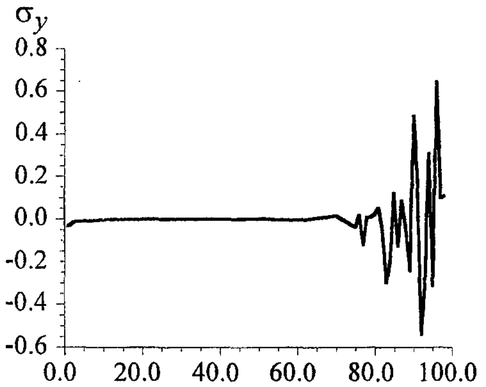

Figure 1. Stresses σ_y at points on the line x = 0.8.

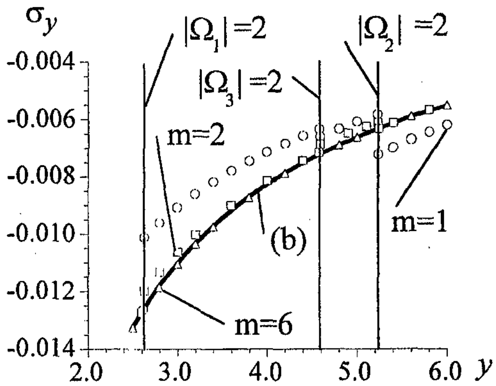

Figure 2: Stresses σ_y at points on the line x = 0.8. Analytical solution (curve b) and Taylor series approximations (separate points; entry numbers are *m*=1, *m*=2, and *m*=6, respectively).

Table. Influence functions and their Taylor series approximations

<table>
<tr><th colspan="2">Polynomially distributed stress discontinuities</th></tr>
<tr><td colspan="2">$$\mathbf{g}(t)=\sum_{k=0}^{m}\mathbf{g}_k\left(\frac{t}{L_{AB}}\right)^k, \qquad \mathbf{g}_k\equiv\mathbf{g}_k\{g_{xk},g_{yk},g_{zk}\}=\text{const}$$</td></tr>
<tr><td>Complex-valued functions</td><td>Taylor series approximations</td></tr>
<tr><td>$$\begin{aligned}\Pi_j={}&\sum_{k=0}^{m}\frac{A_{jk}}{k+1}\Bigg\{\ln\Lambda_j+\ln\Omega_j+\\&+\ln(\omega_{Bj}-\omega_{Aj})-\\&-\Omega_j^{k+1}\left[\ln\Lambda_j+\sum_{l=1}^{k+1}\frac{\Omega_j^{-l}}{l}\right]\Bigg\}\end{aligned}$$ $$\begin{aligned}\Sigma_j={}&\frac{1}{\omega_{Bj}-\omega_{Aj}}\sum_{k=0}^{m}A_{jk}\Bigg[\frac{1}{k+1}\cdot\frac{1}{\Omega_j}-\\&-\Omega_j^k\left(\ln\Lambda_j+\sum_{l=1}^{k+1}\frac{\Omega_j^{-l}}{l}\right)\Bigg]\end{aligned}$$</td><td>$$\begin{aligned}\Pi_j={}&\sum_{k=0}^{m}A_{jk}\cdot\Bigg[\frac{\ln\Omega_j+\ln(\omega_{Bj}-\omega_{Aj})}{k+1}-\\&-\sum_{l=1}^{\infty}\frac{1}{l(l+1+k)}\cdot\frac{1}{\Omega_j^l}\Bigg]\end{aligned}$$ $$\Sigma_j=\frac{1}{\omega_{Bj}-\omega_{Aj}}\sum_{k=0}^{m}A_{jk}\sum_{l=1}^{\infty}\frac{1}{(l+k)\Omega_j^l}$$</td></tr>
<tr><th colspan="2">k-order stress discontinuity element</th></tr>
<tr><td>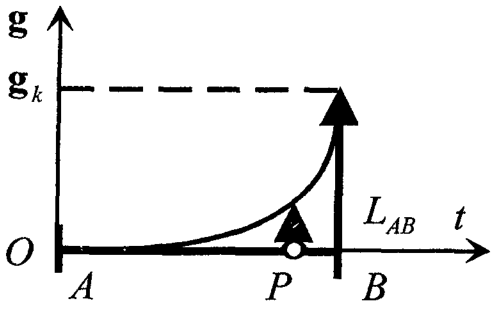
</td><td>$$\mathbf{g}(t)=\mathbf{g}_k\left(\frac{t}{L_{AB}}\right)^k,$$ $$\mathbf{g}_k\equiv\mathbf{g}_k\{g_{xk},g_{yk},g_{zk}\}=\text{const}$$</td></tr>
<tr><td>Complex-valued functions</td><td>Taylor series approximations</td></tr>
<tr><td>$$\begin{aligned}\Pi_j={}&\frac{A_{jk}}{k+1}\Bigg[\ln\Lambda_j+\ln\Omega_j+\\&+\ln(\omega_{Bj}-\omega_{Aj})-\Omega_j^{k+1}\ln\Lambda_j-\\&-\sum_{l=1}^{k}\frac{\Omega_j^{k+1-l}}{l}-\frac{1}{k+1}\Bigg]\end{aligned}$$ $$\begin{aligned}\Sigma_j={}&-\frac{A_{jk}}{\omega_{Bj}-\omega_{Aj}}\times\\&\left.\times\left(\Omega_j^k\ln\Lambda_j+\sum_{l=1}^{k-1}\frac{\Omega_j^{k-l}}{l}+\frac{1}{k}\right)\right]\end{aligned}$$</td><td>$$\begin{aligned}\Pi_j={}&A_{jk}\Bigg[\frac{\ln\Omega_j+\ln(\omega_{Bj}-\omega_{Aj})}{k+1}-\\&-\sum_{l=1}^{\infty}\frac{1}{l(l+1+k)}\cdot\frac{1}{\Omega_j^l}\Bigg]\end{aligned}$$ $$\Sigma_j=\frac{A_{jk}}{\omega_{Bj}-\omega_{Aj}}\sum_{l=1}^{\infty}\frac{1}{(l+k)\Omega_j^l}$$</td></tr>
</table>

Reverse *L*-root stress discontinuity element

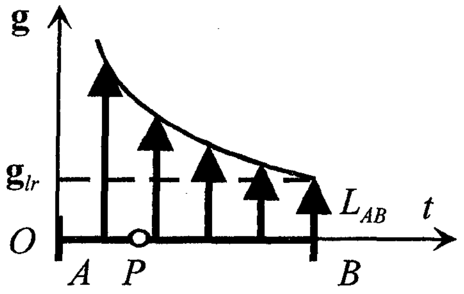

$$\mathbf{g}(t)=\mathbf{g}_{lr}\sqrt{\frac{L_{AB}}{t}},$$

$$\mathbf{g}_{lr}\equiv\mathbf{g}_{lr}\{g_{xlr},g_{ylr},g_{zlr}\}=\text{const}$$

Complex-valued functions

$$\Pi_j=2A_{jlr}\Big[\ln\Lambda_j+\ln\Omega_j-2+$$

$$+\ln(\omega_{Bj}-\omega_{Aj})-\sqrt{\Omega_j}\ln\frac{\sqrt{\Omega_j}-1}{\sqrt{\Omega_j}+1}\Big]$$

$$\Sigma_j=-\frac{A_{jlr}}{\omega_{Bj}-\omega_{Aj}}\cdot\frac{1}{\sqrt{\Omega_j}}\cdot\ln\frac{\sqrt{\Omega_j}-1}{\sqrt{\Omega_j}+1}$$

Taylor series approximations

$$\Pi_j=2A_{jlr}\Big[\ln\Lambda_j+\ln\Omega_j+$$

$$+\ln(\omega_{Bj}-\omega_{Aj})+\sum_{l=1}^{\infty}\frac{2}{2l+1}\cdot\frac{1}{\Omega_j^l}\Big]$$

Reverse *R*-root stress discontinuity element

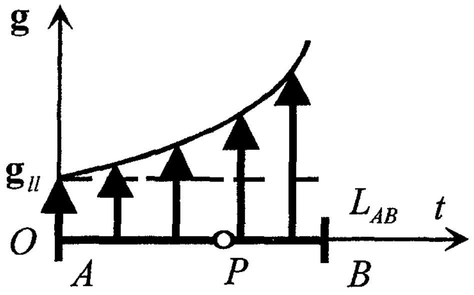

$$\mathbf{g}(t)=\mathbf{g}_{rr}\sqrt{\frac{L_{AB}}{L_{AB}-t}},$$

$$\mathbf{g}_{rr}\equiv\mathbf{g}_{rr}\{g_{xrr},g_{yrr},g_{zrr}\}=\text{const}$$

Complex-valued functions

$$\Pi_j=2A_{jrr}\Big[\ln\Omega_j+\ln(\omega_{Bj}-\omega_{Aj})-2+$$

$$+\sqrt{1-\Omega_j}\ln\frac{\sqrt{1-\Omega_j}+1}{\sqrt{1-\Omega_j}-1}\Big]$$

$$\Sigma_j=\frac{A_{jrr}}{\omega_{Bj}-\omega_{Aj}}\times$$

$$\times\frac{1}{\sqrt{1-\Omega_j}}\cdot\ln\frac{\sqrt{1-\Omega_j}-1}{\sqrt{1-\Omega_j}+1}$$

Taylor series approximations

$$\Pi_j=2A_{jrr}\Big[\ln\Omega_j+\ln(\omega_{Bj}-\omega_{Aj})-2+$$

$$+\sum_{l=1}^{\infty}\frac{2}{2l+1}\cdot\frac{1}{(1-\Omega_j)^l}\Big]$$

Polynomially distributed displacement discontinuities

$$\boldsymbol{D}(t)=\sum_{k=0}^{m}\boldsymbol{D}_k\left(\frac{t}{L_{AB}}\right)^k, \quad \boldsymbol{D}_k\equiv\boldsymbol{D}_k\{D_{\xi k},D_{\eta k},D_{zk}\}=\text{const}$$

Complex-valued functions

$$\Pi_j=\frac{L_{AB}}{\omega_{Bj}-\omega_{Aj}}\sum_{\alpha=\xi,\eta,z}(B_{\alpha j}\mu_j+C_{\alpha j})$$

$$\sum_{k=0}^{m}\Omega_j^k\left(\frac{\Omega_j^{-k-1}}{k+1}-\ln\Lambda_j-\sum_{l=1}^{k+1}\frac{\Omega_j^{-l}}{l}\right)\cdot D_{\alpha k}$$

$$\Sigma_j=-\frac{L_{AB}}{(\omega_{Bj}-\omega_{Aj})^2}\sum_{\alpha=\xi,\eta,z}(B_{\alpha j}\mu_j+C_{\alpha j})$$

$$\sum_{k=0}^{m}\Omega_j^{k-2}\left[k\Omega_j\ln\Lambda_j-\sum_{l=1}^{k+1}\left(1-\frac{k}{l+1}\right)\Omega_j^{-l}+\right.$$

$$\left.+\frac{1}{\Lambda_j}+k-1+\Omega_j^{-k}\sum_{l=1}^{2}\frac{l}{k+l}\Omega_j^{1-l}\right]\cdot D_{\alpha k}$$

Taylor series approximations

$$\Pi_j=\frac{L_{AB}}{\omega_{Bj}-\omega_{Aj}}\sum_{\alpha=\xi,\eta,z}(B_{\alpha j}\mu_j+C_{\alpha j})$$

$$\sum_{k=0}^{m}\sum_{l=1}^{\infty}\frac{1}{l+k}\cdot\frac{D_{\alpha k}}{\Omega_j^l}$$

$$\Sigma_j=-\frac{L_{AB}}{(\omega_{Bj}-\omega_{Aj})^2}\sum_{\alpha=\xi,\eta,z}(B_{\alpha j}\mu_j+C_{\alpha j})$$

$$\sum_{k=0}^{m}\sum_{l=1}^{\infty}\frac{l}{l+k}\cdot\frac{D_{\alpha k}}{\Omega_j^{l+1}}$$

k-order displacement discontinuity element

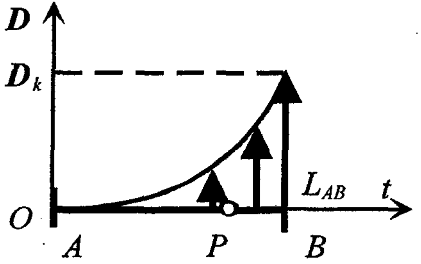

$$\boldsymbol{D}(t)=\boldsymbol{D}_k\left(\frac{t}{L_{AB}}\right)^k,$$

$$\boldsymbol{D}_k\equiv\boldsymbol{D}_k\{D_{\xi k},D_{\eta k},D_{zk}\}=\text{const}$$

Complex-valued functions

$$\Pi_j=-\frac{L_{AB}}{\omega_{Bj}-\omega_{Aj}}\times$$

$$\times\left(\Omega_j^k\ln\Lambda_j+\sum_{l=1}^{k-1}\frac{\Omega_j^{k-l}}{l}+\frac{1}{k}\right)\times$$

$$\times\sum_{\alpha=\xi,\eta,z}(B_{\alpha j}\mu_j+C_{\alpha j})\cdot D_{\alpha k}$$

$$\Sigma_j=-\frac{L_{AB}}{(\omega_{Bj}-\omega_{Aj})^2}\cdot\left[k\Omega_j^{k-1}\ln\Lambda_j+\right.$$

$$\left.+\frac{\Omega_j^{k-2}}{\Lambda_j}+\frac{1}{k-1}+\sum_{l=1}^{k-2}\frac{k-l}{l}\Omega_j^{k-1-l}\right]\times$$

$$\times\sum_{\alpha=\xi,\eta,z}(B_{\alpha j}\mu_j+C_{\alpha j})\cdot D_{\alpha k}$$

Taylor series approximations

$$\Pi_j=\frac{L_{AB}}{\omega_{Bj}-\omega_{Aj}}\sum_{l=1}^{\infty}\frac{1}{l+k}\frac{1}{\Omega_j^l}\times\cdot$$

$$\times\sum_{\alpha=\xi,\eta,z}(B_{\alpha j}\mu_j+C_{\alpha j})\cdot D_{\alpha k}$$

$$\Sigma_j=-\frac{L_{AB}}{(\omega_{Bj}-\omega_{Aj})^2}\sum_{l=1}^{\infty}\frac{l}{l+k}\frac{1}{\Omega_j^{l+1}}\times$$

$$\times\sum_{\alpha=\xi,\eta,z}(B_{\alpha j}\mu_j+C_{\alpha j})\cdot D_{\alpha k}$$

L-root displacement discontinuity element

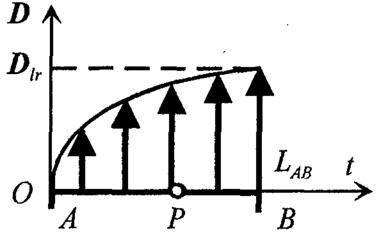

$$\boldsymbol{D}(t)=\boldsymbol{D}_{lr}\sqrt{\frac{t}{L_{AB}}},$$

$$\boldsymbol{D}_{lr}\equiv\boldsymbol{D}_{lr}\{D_{\xi lr},D_{\eta lr},D_{zlr}\}=\text{const}$$

Complex-valued functions

$$\Pi_j=-\frac{2L_{AB}}{\omega_{Bj}-\omega_{Aj}}\times$$
$$\times\left(1+\frac{1}{2}\sqrt{\Omega_j}\ln\frac{\sqrt{\Omega_j}-1}{\sqrt{\Omega_j}+1}\right)\times$$
$$\times\sum_{\alpha=\xi,\eta,z}(B_{\alpha j}\mu_j+C_{\alpha j})\cdot D_{\alpha lr}$$

$$\Sigma_j=-\frac{L_{AB}}{(\omega_{Bj}-\omega_{Aj})^2}\times$$
$$\times\left(\frac{1}{2\sqrt{\Omega_j}}\ln\frac{\sqrt{\Omega_j}-1}{\sqrt{\Omega_j}+1}+\frac{1}{\Omega_j-1}\right)\times$$
$$\times\sum_{\alpha=\xi,\eta,z}(B_{\alpha j}\mu_j+C_{\alpha j})\cdot D_{\alpha lr}$$

Taylor series approximations

$$\Pi_j=\frac{2L_{AB}}{\omega_{Bj}-\omega_{Aj}}\sum_{l=1}^{\infty}\frac{1}{2l+1}\cdot\frac{1}{\Omega_j^l}\times\cdot$$
$$\times\sum_{\alpha=\xi,\eta,z}(B_{\alpha j}\mu_j+C_{\alpha j})\cdot D_{\alpha lr}$$

R-root displacement discontinuity element

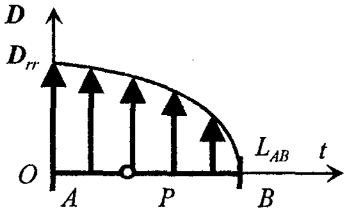

$$\boldsymbol{D}(t)=\boldsymbol{D}_{rr}\sqrt{\frac{L_{AB}-t}{L_{AB}}},$$

$$\boldsymbol{D}_{rr}\equiv\boldsymbol{D}_{rr}\{D_{\xi rr},D_{\eta rr},D_{zrr}\}=\text{const}$$

Complex-valued functions

$$\Pi_j=\frac{L_{AB}}{\omega_{Bj}-\omega_{Aj}}\left(2+\sqrt{1-\Omega_j}\ln\frac{\sqrt{1-\Omega_j}-1}{\sqrt{1-\Omega_j}+1}\right)\times$$
$$\times\sum_{\alpha=\xi,\eta,z}(B_{\alpha j}\mu_j+C_{\alpha j})\cdot D_{\alpha rr}$$

$$\Sigma_j=-\frac{L_{AB}}{(\omega_{Bj}-\omega_{Aj})^2}\times$$
$$\times\left(\frac{1}{2\sqrt{1-\Omega_j}}\ln\frac{\sqrt{1-\Omega_j}-1}{\sqrt{1-\Omega_j}+1}-\frac{1}{\Omega_j}\right)\times$$
$$\times\sum_{\alpha=\xi,\eta,z}(B_{\alpha j}\mu_j+C_{\alpha j})\cdot D_{\alpha rr}$$

Taylor series approximations

$$\Pi_j=-\frac{2L_{AB}}{\omega_{Bj}-\omega_{Aj}}\sum_{l=1}^{\infty}\frac{1}{2l+1}\cdot\frac{1}{(1-\Omega_j)^l}\times$$
$$\times\sum_{\alpha=\xi,\eta,z}(B_{\alpha j}\mu_j+C_{\alpha j})\cdot D_{\alpha rr}$$

decreasing to infinitesimal quantities at points distant from the element. We do observe this if the distances from points under consideration to the element are in the range of 20 -70 dimensionless units (ref. Figure 1). But afterwards, the calculations produce wrong results.

The analysis of the calculation technique has shown that the loss of the accuracy is dealing with specific types of the influence functions for higher order elements. As an example, consider complex valued function Σ_j for k-order stress discontinuity element (ref. the Table). We can see, that the function contains following expression:

$$\Psi = \Omega_j^k \ln \Lambda_j + \sum_{l=1}^{k-1} \frac{\Omega_j^{k-l}}{l} + \frac{1}{k} \text{ and } \lim_{\Omega_j \to \infty} \Psi = \lim_{\Omega_j \to \infty} \left[-\sum_{l=1}^{\infty} \frac{\Omega_j^{k-l}}{l} + \sum_{l=1}^{k-1} \frac{\Omega_j^{k-l}}{l} + \frac{1}{k} \right] = 0$$

However, because real computer produces very small, but still existing numerical error δ, calculating value Ω_j it is easy to show that $\lim_{\Omega_j \to \infty} \Psi = \lim_{\Omega_j \to \infty} \delta \Omega_j^{k-2} = \infty$
Thus, computer error results in numerical instability shown in Figure 1. We can avoid this problem if we use Taylor series approximations for the functions instead of the functions themselves when we conduct calculations at the distant points. For scheme of calculations presented in [4], a set of influence functions and their Taylor series approximations is shown in the Table. In the code, we do not use approximations to calculate stress functions for all root elements, constant stress and linear displacement discontinuity elements. Both stress and displacement functions are not approximated for constant displacement discontinuity element. In Figure 2, we can see that even keeping a small number of entries in the series allows a good transformation of the analytical solution into approximate one.

CONCLUSIONS

To avoid numerical instability of calculations of influence functions for higher order stress and displacement discontinuity boundary elements, it is necessary to use Taylor series approximations for the functions instead of the functions themselves if points under consideration are far enough from the elements.

ACKNOWLEDGEMENT

The work of M.A.Kayupov has been sponsored by the Alexander von Humboldt Foundation (Germany). This support is gratefully acknowledged.

REFERENCES

[1] Kayupov, M.A., Kuriyagawa, M. „Stress and displacement discontinuity boundary elements in an anisotropic medium.“ *Boundary Element Technology XI, Proceedings of the 11th Int. Conference on Boundary Element Technology: BETECH 96*, Hawaii, USA, 1996, Computational Mechanics Publications, Southampton, pp. 193-202 (1996).

[2] Kayupov, M.A., Sakurai, S., Kuriyagawa, M. „Influence functions for stress and displacement discontinuity elements in an anisotropic medium.“ *Int. J. for Numerical and Analytical Methods in Geomechanics* **21** (9), pp. 635-652 (1997).

[3] Kayupov, M.A., Sakurai, S., Kuriyagawa, M. „Higher order displacement discontinuity elements for analysis of stresses in an elastic anisotropic medium with cracks.“ *Proceedings of the First International Conference on Composite Science and Technology*, Durban, South Africa, 1996, University of Natal, Durban, pp. 235-240 (1996).

[4] Kayupov, M.A., Kuhn, G., Kuriyagawa, M., Yamaguchi, T. „A coupled BE-DD Method to Model Fracture Propagation in Rock Samples.“ *Proceedings, SARES 97: 1st Southern African Rock Engineering Symposium*, 15-16 September 1997, Johannesburg, South Africa, pp. 164-177 (1997).

FINITE ELEMENT FOR THE ANALYSIS OF VIBRATIONS OF LAMINATED COMPOSITE PLATES AND SOLID BODIES

A.V.MARCHUK V.K.PRISJAZNUK

Ukrainian Transport University, Suvorova Street No.1, Kiev, 252010, Ukraine

1.Introduction

To the analysis of achievement in development of the theories of account of laminated designs the reviews [1-7] are devoted. Exists two approaches of account of considered designs. This application of the three-dimensional theory of elasticity and item of information problems to two-dimensional.

The widest application in reduction of a three-dimensional problem to two-dimensional was found by a method of hypothesises. In a method of hypothesises there are two directions. It is the discrete-structural approach [8] and continuous-structural approach [4,9-12]. In the discrete-structural approach the order of permitting system of the equations depends on quantity of layers.

In the given work in problems of vibrations of laminated plates and solid bodies two above-stated directions are applied.

2.Problem Statement and Kinematic Model

In rectangular cartesian system of coordinates a laminated design is considered . Surfaces of section of layers parallel to obverse surfaces and surface 0xy. The layers are made from of a orthotropic material. Strains and the stresses are connected by the known equations: $\{e\} = [A]\{\sigma\}$, $\{\sigma\} = [C]\{e\}$, $\{e\} = \{e_{11}, e_{22}, e_{33}, 2e_{23}, 2e_{13}, 2e_{12}\}^T$, $\{\sigma\} = \{\sigma_{11}, \sigma_{22}, \sigma_{33}, \sigma_{23}, \sigma_{13}, \sigma_{12}\}^T$.

Summation on alphabetic indexes is made. The point at a level of indexes designates operation of differentiation. In matrix expressions matrix operations, and then summation on alphabetic indexes are in the beginning carried out.

Is entered approximation of displacements [13]

$$U_i = U_{il} f_{il} + W_{k,i} \varphi_{ik}; \tag{1}$$

$$U_3 = W_k \beta_k \quad (i, j = 1, 2; l = 1, 2; k = 1, ..., 5), \tag{2}$$

where $U_{i1}(x, y, t), U_{i2}(x, y, t)$ are displacements in tangential directions on obverse surfaces of a design; $W_1(x, y, t), W_2(x, y, t)$ are displacements in normal directions on obverse surfaces of a design; $W_3(x, y, t), W_4(x, y, t)$ are the unknown functions of the reference surface (the functions of shear); $W_5(x,y,t)$ are the unknown functions of the reference surface (the functions of drafting). The distribution functions are defined by

$$f_{i2} = \frac{\int_{a_0}^{z} dz}{\int_{a_0}^{a_n} dz}; \quad f_{i1} = 1 - f_{i2}; \quad \beta_2 = \frac{\int_{a_0}^{z} A_{33} dz}{\int_{a_0}^{a_n} A_{33} dz}; \quad \beta_1 = 1 - \beta_2;$$

$$\beta_3 = -\int_{a_0}^{z} (A_{13}C_{11} + A_{23}C_{21}) f_{12} dz + \frac{\int_{a_0}^{a_n} (A_{13}C_{11} + A_{23}C_{21}) f_{12} dz}{\int_{a_0}^{a_n} A_{33} dz} \int_{a_0}^{z} A_{33} dz;$$

$$\beta_4 = -\int_{a_0}^{z} (A_{13}C_{12} + A_{23}C_{22}) f_{12} dz + \frac{\int_{a_0}^{a_n} (A_{13}C_{12} + A_{23}C_{22}) f_{12} dz}{\int_{a_0}^{a_n} A_{33} dz} \int_{a_0}^{z} A_{33} dz;$$

$$\beta_5 = \frac{\int_{a_0}^{z} H A_{33} dz}{\int_{a_0}^{a_n} H A_{33} dz}; \quad H = \frac{\int_{a_0}^{z} F_{12} dz}{\int_{a_0}^{a_n} F_{12} dz};$$

$$F_{12} = -\int_{a_0}^{z} (C_{12} + G_{12}) f_{12} dz + \frac{\int_{a_0}^{a_n} (C_{12} + G_{12}) f_{12} dz}{\int_{a_0}^{a_n} G_{12} dz} \int_{a_0}^{z} G_{12} dz;$$

$$F_{ii} = -\int_{a_0}^{z} C_{ii} f_{12} dz + \frac{\int_{a_0}^{a_n} C_{ii} f_{12} dz}{\int_{a_0}^{a_n} G_{12} dz} \int_{a_0}^{z} G_{12} dz;$$

$$\varphi_{ik} = -\int_{a_0}^{z} \beta_k dz + \frac{\int_{a_0}^{a_n} \beta_k dz}{\int_{a_0}^{a_n} dz} \int_{a_0}^{z} dz \quad (k = 1, 2, 5);$$

$$\varphi_{i3} = \int_{a_0}^{z} (F_{i1}/G_{i3} - \beta_3) dz - \frac{\int_{a_0}^{a_n} (F_{i1}/G_{i3} - \beta_3) dz}{\int_{a_0}^{a_n} dz} \int_{a_0}^{z} dz;$$

$$\varphi_{i4} = \int_{a_0}^{z} (F_{i2}/G_{i3} - \beta_4) dz - \frac{\int_{a_0}^{a_n} (F_{i2}/G_{i3} - \beta_4) dz}{\int_{a_0}^{a_n} dz} \int_{a_0}^{z} dz.$$

3. Variational Principle

We shall receive the equation of balance of a finite element on the basis of the Gamilton variational principle.

$$\delta \int\limits_{t} (R - T - A)dt = 0. \tag{3}$$

Here

$$R = \int\!\!\int\limits_{V}\!\!\int \{u\}^T[d]^T[D][d]\{u\}dv, \tag{4}$$

where $\{u\} = \{U_1, U_2, U_3\}^T$; nonzero value the members of a matrix $[d]$ following: $d(1,1) = \partial/\partial x, d(2,2) = \partial/\partial y, d(3,3) = \partial/\partial z, d(4,1) = \partial/\partial y, d(5,2) = \partial/\partial x, d(6,1) = \partial/\partial z, d(7,3) = \partial/\partial x, d(8,2) = \partial/\partial z, d(9,2) = \partial/\partial y$; nonzero value the members of a symmetric matrix $[D] : D(1,1) = C_{11}, D(1,2) = C_{12}, D(1,3) = C_{13}, D(2,2) = C_{22}, D(2,3) = C_{23}, D(3,3) = C_{33}, D(4,4) = G_{12}, D(4,5) = G_{12}, D(5,5) = G_{12}, D(6,6) = G_{13}, D(6,7) = G_{13}, D(7,7) = G_{13}, D(8,8) = G_{23}, D(8,9) = G_{23}, D(9,9) = G_{23}$.

$$T = \int\!\!\int\limits_{V}\!\!\int \{u\}^T[d_t]^T[D_t][d_t]\{u\}dv, \tag{5}$$

where nonzero value the members of a matrix $[d_t] : d_t(1,1) = \partial/\partial t, d_t(2,2) = \partial/\partial t, d_t(3,3) = \partial/\partial t$; where nonzero value the members of a matrix $[D_t] : D_t(1,1) = \rho, D_t(2,2) = \rho, D_t(3,3) = \rho$;

$$A = \int\!\!\int\limits_{S} \{u\}^T\{q\}ds, \tag{6}$$

where $\{q\} = \{q_1, q_2, q_3\}^T$-external load vector.

We substitute the equations for displacements (1) and (2) in the equations (4), (5) and (6).

$$R = \int\!\!\int\limits_{V}\!\!\int \{\bar{w}\}^T[d_f]^T[\bar{F}]^T[d]^T[D][d][F][d_f]\{w\}dv; \tag{7}$$

$$T = \int\!\!\int\limits_{V}\!\!\int \{\bar{w}\}^T[d_f]^T[\bar{F}]^T[d_t]^T[D_t][d_t][F][d_f]\{w\}dv; \tag{8}$$

$$A = \int\!\!\int\limits_{S} \{\bar{w}\}^T[d_f]^T[\bar{F}]^T\{q\}ds, \tag{9}$$

where $\{w\} = \{U_{1l}, \{U_{2l}, W_k\}^T$; nonzero value the members of a matrix $[d_f] : d_f(1,1) = 1, d_f(2,2) = 1, d_f(3,3) = 1, D_f(4,3) = \partial/\partial x, d_f(5,3) = \partial/\partial y$; nonzero value the members of a matrix $[F] : F(1,1) = f_{1l}, F(1,4) = \varphi_{1k}, F(2,2) = f_{2l}, F(2,5) = \varphi_{2k}, F(3,3) = \beta_k, F(4,3) = \psi_k$; In matrixes $[\bar{F}]$ and $\{\bar{w}\}$ the indexes l, k are replaced on Indexes $\bar{l}, \bar{k} (\bar{l} = 1, ..., 6; \bar{k} = 1, ..., 3)$.

We set approximation in the plan of unknown functions U_{il} known polynomial functions of the first degree,W_k polynomial functions of the fourth degree [11]. We shall present such approximation in the matrix form:

$$\{w\} = [N]\{P\}, \tag{10}$$

where $[N]$ are matrix polynomial functions;
$\{P\} = \{U_{1l}(x_1, y_1), U_{1l}(x_2, y_2), U_{1l}(x_3, y_3), U_{1l}(x_4, y_4), U_{2l}(x_1, y_1), U_{2l}(x_2, y_2), U_{2l}(x_3, y_3), U_{2l}(x_4, y_4), W_k(x_1, y_1), \partial W_k(x_1, y_1)/\partial y, -\partial W_k(x_1, y_1)/\partial x, W_k(x_2, y_2), \partial W_k(x_2, y_2)/\partial y, -\partial W_k(x_2, y_2)/\partial x, W_k(x_3, y_3), \partial W_k(x_3, y_3)/\partial y, -\partial W_k(x_3, y_3)/\partial x, W_k(x_4, y_4), \partial W_k(x_4, y_4)/\partial y, -\partial W_k(x_4, y_4)/\partial x\}$, $x_m, y_m (m = 1, ..., 4)$ are coordinate of units of rectangular finite element.

4.Finite Element

Let us substitute the equation (10) in the equation (7), (8), (9). We vary and receive the equations of balance of a finite element

$$\begin{aligned}
&\int_t \Big(\int\int_V\int [N]^T[d_f]^T[\bar{F}]^T[d]^T[D][d][F][d_f][N]\{P\}dv - \\
&- \int\int_V\int [N]^T[d_f]^T[\bar{F}]^T[d_t]^T[D_t][d_t][F][d_f][N]\{P\}dv\Big)dt = \\
&= \int_t \Big(\int\int_S [N]^T[d_f]^T[\bar{F}]^T\{q\}ds\Big)dt.
\end{aligned} \tag{11}$$

5.Numerical Results and Conclusion

We consider a four-layer (0/90/0/90) square solid body. The lamina properties are assummed to be

$E_1^{(1)}/E_2^{(1)} = 40$; $E_2^{(1)} = E_3^{(1)}$; $\nu_{12}^{(1)} = 0,25$; $\nu_{13}^{(1)} = 0,25$; $\nu_{23}^{(1)} = 0,25$; $G_{12}^{(1)}/E_2^{(1)} = 0,6$; $G_{13}^{(1)}/E_2^{(1)} = 0,6$; $G_{23}^{(1)}/E_2^{(1)} = 0,5$;. Thickness of layers identical. The relation of length by height: $l/h = 5$. On a quarter of a plate a uniform grid is put finite elements (5 * 5). The boundary conditions on the middle plane are the following: $U_3(x, 0, z) = 0; U_3(0, y, z) = 0; U_2(a/2, y, z) = 0; U_1(x, a/2, z) = 0$.

We consider the following variants of a design:

1. Rigid contact of layers. The bottom surface free (V1).
2. Rigid contact of layers. The bottom surface is fixed (V2).
3. Slippery contact of layers. The bottom surface free (V3).
4. Slippery contact of layers. The bottom surface is fixed (V4).

Is applied two variants of account:

1. The design on thickness is simulated by one finite element (M1). In this case the slippery contact is simulated by a thin layer with the following characteristics: $E_1^{(pr)} = E_3^{(1)}/1000$; $E_2^{(pr)} = E_1^{(pr)}$; $E_3^{(pr)} = E_3^{(1)}$; $\nu_{21}^{(pr)} = \nu_{12}^{(pr)} = 0,25$; $\nu_{31}^{(pr)} = \nu_{32}^{(pr)} = 0$; $G_{12}^{(pr)} = 0,6E_3^{(1)}/1000$; $G_{13}^{(pr)} = G_{12}^{(pr)}/1000$; $G_{23}^{(pr)} = G_{12}^{(pr)}/1000$; $h^{(pr)} = h/100$.

2. Each layer of a design is broken on thickness on five finite elements (M2).

Results of account $(\omega(\rho h^2/E_2^{(1)})^{1/2})$ are given in table

Source	*V1*	*V2*	*V3*	*V4*
M1	0,4189	1,5706	0,1801	1,5952
M2	0,4242	1,6645	0,1751	1,6337

The account of the first variant (V1) design on other models gives the following results: 0,42719 [14] and 0,44694 [4].

Finite element intended for the decision of problems of vibration of laminated plates and bodies is constructed. Rigid and slippery contact of layers is allowed. The considered example demonstrates sufficient accuracy of an offered finite element.

References

[1] Grigoluk E.I., Kogan F.A. A Modern Condition of the Theory Laminated Shells., J. Soviet applied mechanics, Vol.6, No.8, 1972, pp.3-17 (in Russian).

[2] Grigorenko Ya.M., Vasilenko A.T. Methods of Account of Shells. The Theory of Account of Shells Variable Rigidity. -Kiev, Naukova dumka, Vol.4, 1981, 544 p. (in Russian).

[3] Dudchenko A.A., Lurie S.A. and Obrascov I.F. Multilayered anisotropic plates and shells. Results of the science and engineering. Mechanics of a solid body.-Moscow, 1988, vol.15, pp.3-68 (in Russian).

[4] Reddy J.N., Khdeir A.A. Application of the Various Theories of plates to Buckling and Vibrations Laminated Composite Plates, AIAA Journal, Vol.12, No.12, 1989, pp.1808-1817.

[5] Kapania R.K., Raciti S. Recent Advances in the Analysis of Laminated Beams

and Plates, Part I, Sher Effects and Buckling, AIAA Journal, Vol.27, No.7, 1989, pp.923-934.

[6] Kapania R.K., Raciti S. Recent Advances in the Analysis of Laminated Beams and Plates, Part II, Vibrations and Wave Propagation, AIAA Journal, Vol.27, No.7, 1989, pp.935-946.

[7] Grigorenko Ya.M., Gulyaev V.I. Nonlinear Problems of the Theory of Shells and Methods of their Solution (Review), J. Soviet applied mechanics, Vol.27, No.10, 1991, pp.3-23 (in Russian).

[8] Bolotin V.V., Novichkov Yu.N. Mechanics of Laminated Designs. -Moscow, Mechanical Engineering, 1980, 372p. (in Russian).

[9] Ambartsumian S.A. Theory of Anisotropic Plates. J.E.Ashton, Technomic Publication Company, Stamford, CT, 1970.

[10] Rasskasov, A.O., Sokolovskaya I.I. and Shul'ga N.A. The Theory and Accont of Laminated Ortotropic Plates and Shells.-Kiev, Hight School, 1986, 191p. (in Russian).

[11] Piskunov V.G., Verizenko V.E., Prisjaznuk V.K., Sipetov V.S. and Karpilovski V.S. Calculation of Inhomogeneous Shells and Plates by Finite Element Methods.-Kiev, Hight School, 1987, 200p. (in Russian).

[12] Piscunov V.G., Verijenko V.E. and Adali S. Transverse Shear and Normal Deformation Higer-Order Theory for the Solution of Dynamic Problems of Laminated Plates and Shells. Int. J. Solids Structures, Vol.31, No.24, pp.3345-3374.

[13] Marchuk A.V. Generation of Sampled- and Continuously-Structural Approaches to Formation of Mathematical Model of Calculation of Laminated Plates and Solid Masses, Mechanics of Composite Materials, Vol.32, No.3, 1996, pp.377-387 (in Russian).

[14] Noor A.K. Free Vibrations of Multilayered Composite Plates, AIAA Journal, Vol.11, 1973, pp. 1038-1039.

SOFTWARE FOR THE SIMULATION AND THE CONTROL OF THE FILAMENT WINDING OF ELLIPSOIDAL STRUCTURES

ATANGANA ATEBA, ESSOH NGOME H,
KINGUE SOBGOUM J., DZONANG A. D.

Ecole Normale Supérieure D'Enseignement Technique,
Département du Génie Mécanique,
Laboratoire de Mécanique Appliquée et des Composites,
Université de Douala,
B.P. 1872 Douala Cameroun.

INTRODUCTION

The software we present is destined for the simulation of winding ellipsoidal structures and to prepare data and programmes for the control of the filament winding machine by a numerical control unit. Such strutures present many applications :

- basket for field (in Africa)
- blades
- canals

The advantages of the the filament winding process to manufacture vessels are well known [1] :

- large structures can be built ;
- cost can be reduced with high productivity ;
- high quality can be achieved, due to the use of continuous fibres.

Our technique is limited to thermosetting resins [2], the glass fibres are impregnated during the winding process, before being wound on the mandrel. The system we use is composed of :

- a filament winding machine ;
- a micro-computer with a special sofware ;
- a numerical control unit.

The numerical control unit is an industrial modular unit, able to control up to eight axes. It uses its own low-level programming language [3]. It can be programmed directly from its keyboard or can be loaded with externally prepared data and programmes through a RS-232 interface. For complex sequences, direct programmation reveals too complicated and external preparation of control programmes necessary.

PRESENTATION OF THE SOFTWARE

The purpose is to simulate the winding process at a micro-computer screen, and to prepare data and programmes destined for the numerical control unit, to control the filament winding machine. The main movements are : - the rotation of the mandrel aroundits longitudinal axis (ox), - the longitudinal translation of the feed-eye X_E, - the transversal transversal of the feed-eye Y_E, the vertical translations of the feed-eye Z_E, and the rotation of the feed-eye around its transversal axis of movement Φ. The synchronisation of these five movements allows the winding process to take place.

Analysis

A mathematical analysis has been done in order to determine the rotation of the mandrel β_0 and the feed-eye location E [4]. M is the deposit point, it is the point at which the fibre takes off the mandrel (Fig. 1).

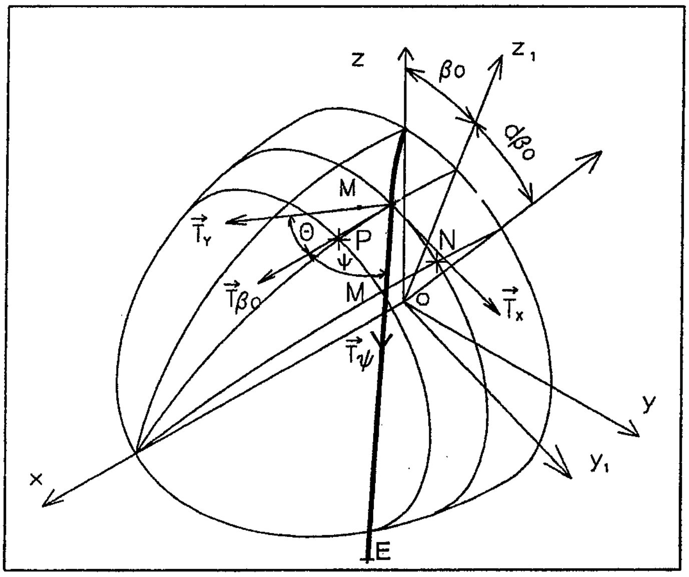

Figure 1 : Defining the geometrical parameters

Where : $\vec{T}\beta_0$ - the tangent unit vector to the meridian at point M, $\vec{T}_x$ - the tangent unit vector to the parallel at point M, $\vec{T}_\psi$ -the tangent vector to the geodesic at point M, $\vec{T}_y$

- the tangent unit vector to the normal at point M, β_0 - the rotation of the mandrel around its longitudinal axis, E - the location of the feed-eye, ψ - the winding angle.

The location of the feed-eye, for a constant cross section, is defined by its coordinates E $\left(X_E,\ Y_E,\ Z_E\right)$, such as :

$$\begin{cases} X_E = x - \lambda\, cos\,\psi \\ Y_E = \left(u + \dfrac{\lambda u_0\, sin\,\psi}{H}\right) sin\,\theta_d - \dfrac{\lambda\, sin\,\psi}{Hu^2} cos\,\theta_d \\ Z_E = \left(u + \dfrac{\lambda u_0\, sin\,\psi}{H}\right) cos\,\theta_d + \dfrac{\lambda\, sin\,\psi}{Hu^2} sin\,\theta_d \end{cases} \tag{1}$$

Where : λ-a constant distance from E to M, θ_d-the angle between (o, x, z) and (o, x, z_1), u-a parameter depending on the cross section, H-a parameter depending on the cross section. We have $(y/b)^2 + (z/c)^2 = 1$, and :

$$u_0 = \left(\frac{1}{c^2} - \frac{1}{b^2}\right) sin\,\theta_d\, cos\,\theta_d \tag{2}$$

$$u = \frac{1}{\sqrt{\dfrac{cos^2\,\theta_d}{c^2} + \dfrac{sin^2\,\theta_d}{b^2}}}, \tag{3}$$

$$\mathrm{H} = \sqrt{\frac{\cos^2\theta_\mathrm{d}}{\mathrm{c}^4} + \frac{\sin^2\theta_\mathrm{d}}{\mathrm{b}^4}} \tag{4}$$

The rotation of the feed-eye aroundits transversal axis of movement is given by the angle Φ such as :

$$tg\Phi = \frac{cos\,\psi}{-\left(\dfrac{sin\,\theta_d}{u^2} + u_0\, cos\,\theta_d\right)\dfrac{sin\,\psi}{H}} \tag{5}$$

Programming

The software developed on an IBM/PC micro-computer with graphical features that control the following parameters :

- the mandrel rotation β_0 ;
- the longitudinal movement of the feed-eye X_E ;
- the transversal movement of the feed-eye Y_E ;

-the vertical movement of the feed-eye Z_E ;

- the rotation of the feed-eye around its transversal axis Φ .

The software is written in Turbo-Pascal language. The programme generates a file in which the necessary parameters to the numerical control unit are stored. When operating the machine, this file has to be loaded in the control unit through the RS-232 interface.

Simulation

The simulation starts by showing the geometry of the mandrel in a three dimensionnal window on the screen. The winding process is displayed cycle by cycle up to full coating of the mandrel (Fig. 2).

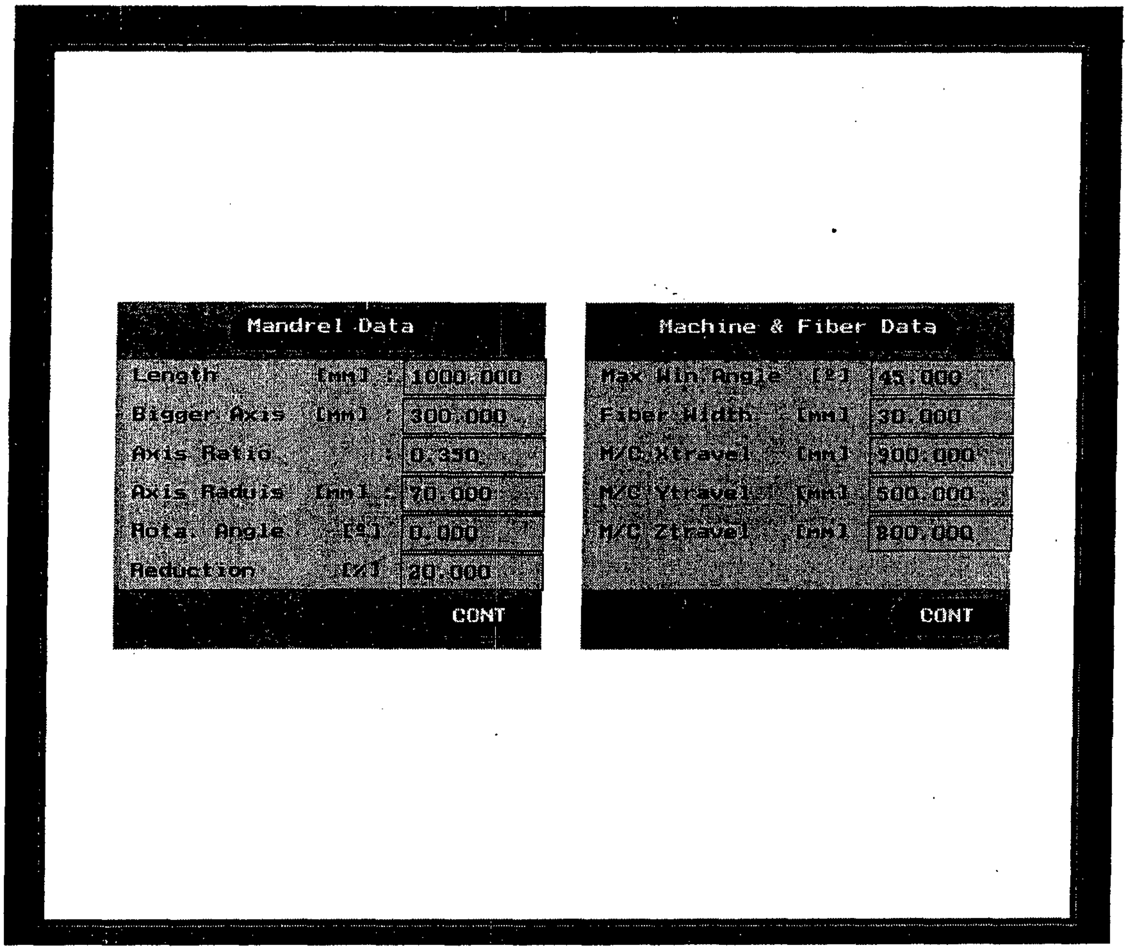

Mandrel Data

Length [mm] : 1000.000
Bigger Axis [mm] : 300.000
Axis Ratio : 0.350
Axis Raduis [mm] : 70.000
Rota. Angle [º] 0.000
Reduction [%] 20.000

Machine & Fiber Data

Max Win.Angle [º] 45.000
Fiber Width [mm] 30.000
M/C Xtravel [mm] 900.000
M/C Ytravel [mm] 500.000
M/C Ztravel [mm] 800.000

Figure 2-a : Winding data

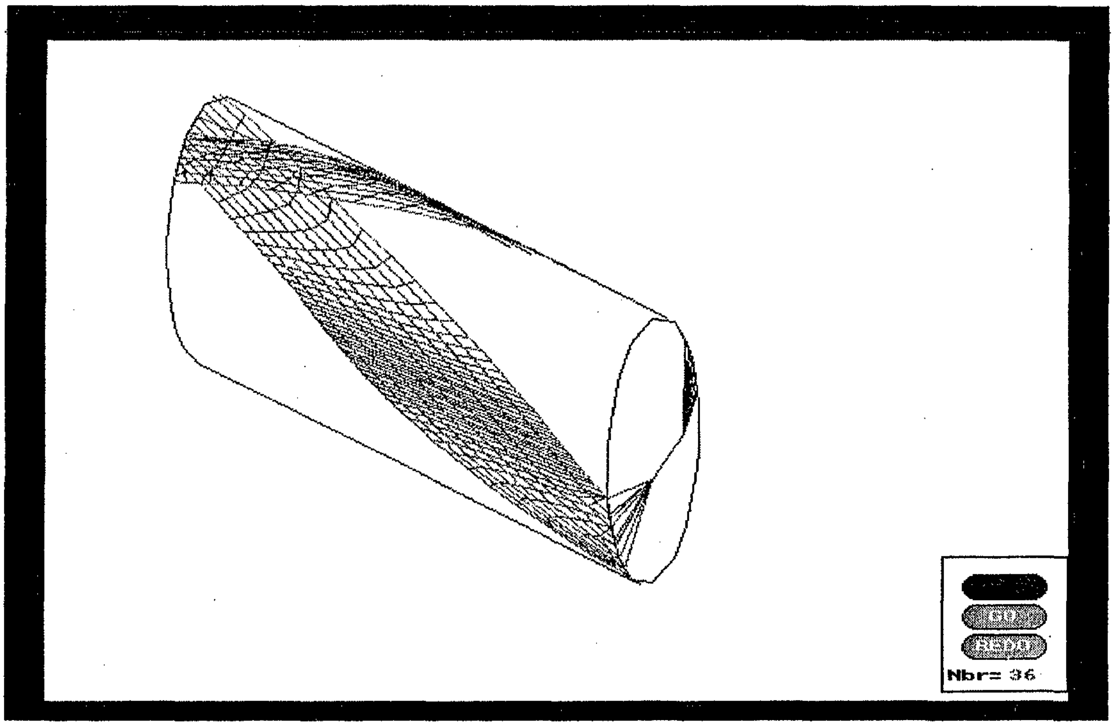
GO
REDO
Nbr= 36

Figure 2-b : The structure after five cycles wound

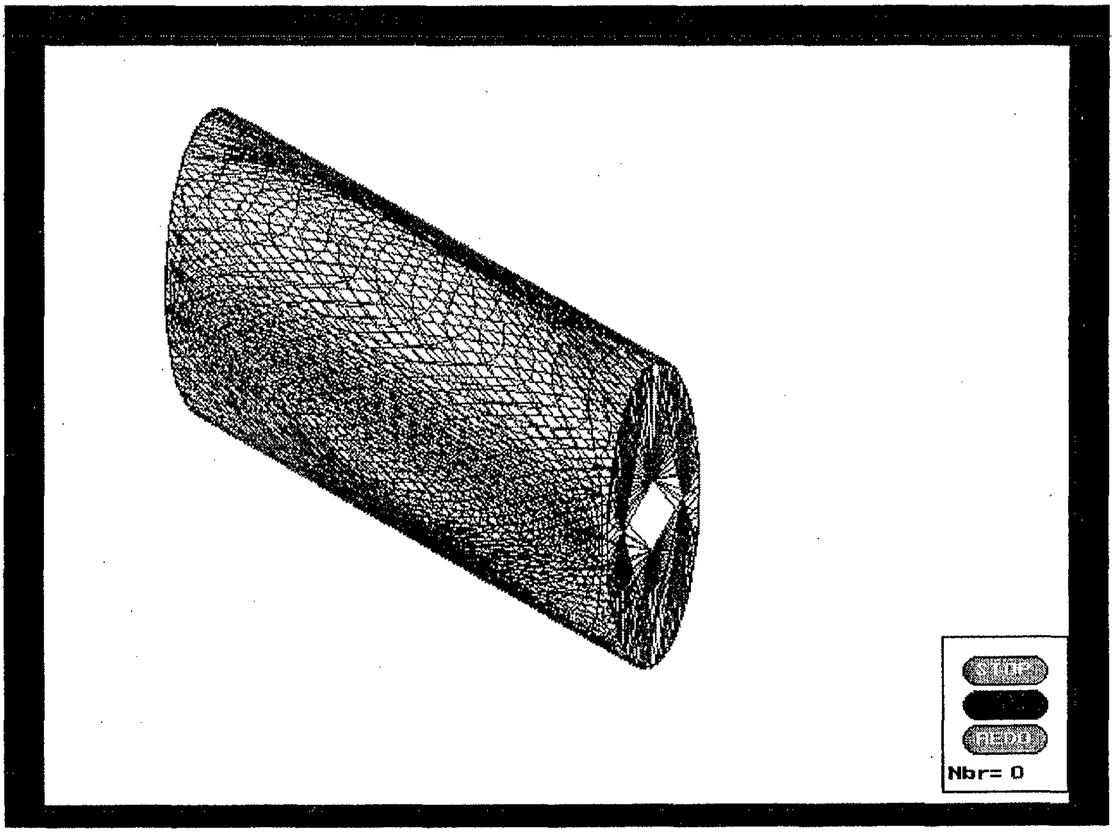
STOP
REDO
Nbr= 0

Figure 2-c : Complete simulation of the process

CONCLUSION

In this paper, we have presented a software for simulation and control of a filament winding system, developed for manufacturing ellipsoidal vessels in thermosetting fibre composites. The software controls five parameters used for the placement of the fibre on the mandrel. A graphical representation of the fibre placement provides the user with a convenient simulation of the whole system. The software generates data subsequently loaded in a numerical control unit, which controls the machine.

REFERENCES

[1] Peters S.T., Humphrey W.D., Forral R.F., "Filament winding composite structure fabrication", Sampe, Covina, 1991.

[2] Rosato D.V., Grove C.S., "Filament Winding : its development, manufacturing, applications and design", Polymer Engineering and Technology, Interscience, 1984.

[3] Gecalstom, "Mise en service", Cyber 3000/ PVD 3382, 1990.

[4] Valiron G. "Théorie des surfaces-Théorèmes généraux", Cours d'analyse mathématique - Equations fonctionnelles - Applications, 2e édition, Masson et Cie, pp 429-473, 1950

QUICK-WELDING IN FILAMENT WINDING OF THERMOPLASTIC PREPREGS

ATANGANA ATEBA[1], BELINGA ESSOMBA P.[1],
PEKEKO P. G.[1], SAMBA N.P.[1], FOUDA J.B.[1] , OWONO A.[2].

[1] Ecole Normale Supérieure d'Enseignement Technique,
Laboratoire de Mécanique Appliquée et des Composites,
Université de Douala,
B.P. 1872 Douala, Cameroun.

[2] Département de Physique.
Université de Yaoundé-1, Cameroun

INTRODUCTION

Filament winding composite structures fabrication requires welding while winding for thermoplastics resins, or heating in an oven after the winding process for thermosetting resins. Welding while winding can be obtained using a heating mandrel, or a heating head moving after the fibre deposit point on the mandrel. The last method poses a problem for the welding speed and the synchronization of the mandrel, the feed-eye and the heating head movements [1]. If the winding machine is simultaneously controlled in both speed and displacement, the welding speed regulating is easy. If controlling of the machine is limited to block by block displacements, the movements of motorized axes, although they are synchronized, remain random in their way of varying from one block to another ; that is the case of the numerical control unit "CYBER 3000", the one we use.

The filament winding machine is a prototype specially built for research purpose. It has been designed as a 5-axis machine [2] with a mandrel and a heating head associated to the feed-eye. The prepregs used are preimpregnated of thermoplastic resins. Quick-welding is the best if the resin melting state is reached in both the prepreg roving coming from the feed-eye and the underlining layer on the mandrel ; furthermore the welding pressure must be sufficient.

THE HEATING SYSTEM

It is an ultrasound heating head. The mandrel, in metallic alloy, has a circular cross-section. The maximal temperature generated by the ultrasound heating head is about 400° C. When operating, the movements of components are associated such as the contacting point between the heating head and the structure wound is the deposit point on the mandrel. It appears a fall of temperature due to the contacting point speed ; that fall is accentuated with the increasing deposit speed. Knowing the total fibre length L wound during one cycle and the allocated time T, we can determine the medium speed to introduce in the numerical control unit V_{moy}.

Determination of the fibre length

The mandrels present variation of cross-section, which makes difficult the determination of the fibre length ; only that variation of section will be analysed here (Fig. 1).

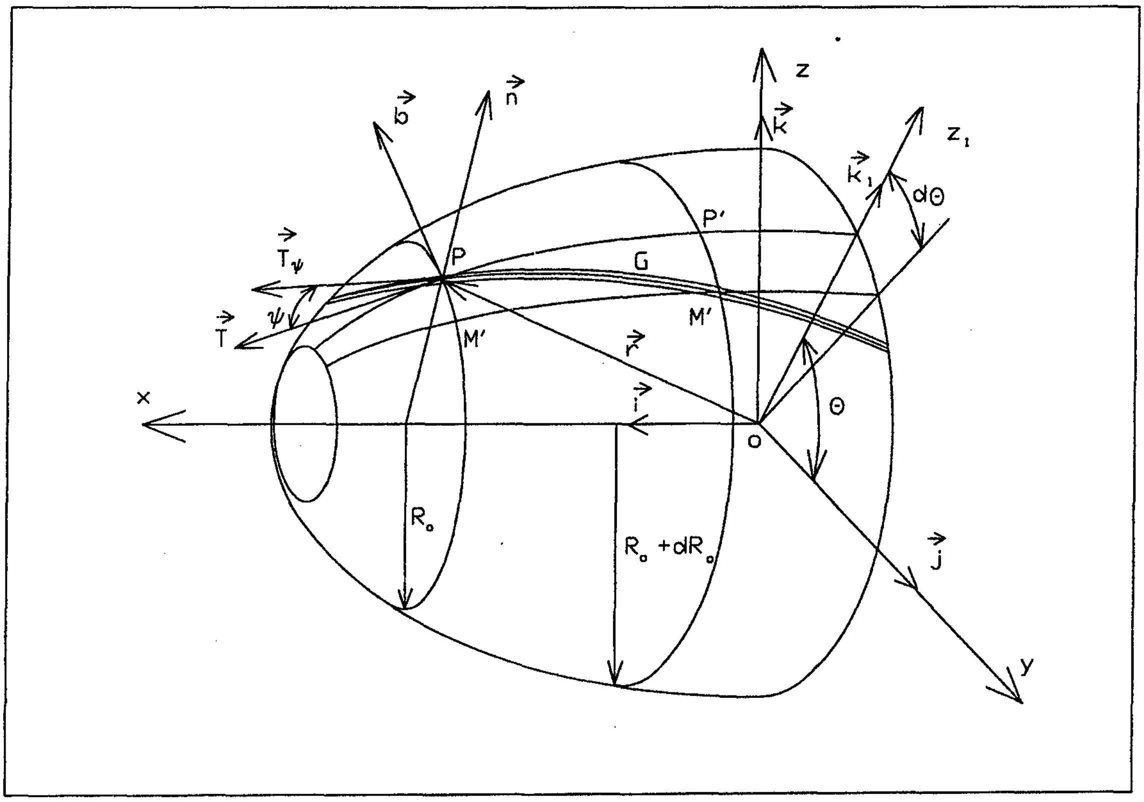

Figure 1 : Revolution surface

Where : P-the deposit point, G-geodesic line, $\vec{T}$-the tangent unit vector to the meridian at point P, $\vec{b}$-the tangent unit vector to the parallel at point P, $\vec{T}_\psi$-tangent vector to the geodesic line at point P, R_0-the mandrel radius at point P, φ-the winding angle with $\varphi = \left[\vec{T}, \vec{T}_\psi\right]$.

The element of fibre length is given by :

$$dL = \frac{R_0}{R_f}\sqrt{\frac{x'^2 + 1}{R_0^2 - R_f^{\ 2}}}.dR_0 \tag{1}$$

Where : x'-the derivative of x compared with R_0-,$x' = dx / dR_0$. Integrating dL for one cycle, R_f-the mandrel radius at the end closure of the dome. we will have the total length of the fibre L.

Determination of the welding medium speed :

$$V_{moy} = \frac{L}{T} \tag{2}$$

Where : V_{moy}., L and T are defined above.

WELDING PRESSURE

The welding pressure allows to improve machanical characteristics of the structure built, it is obtained by tightening the fiber and varies from 0.1 to 1 MPa to make removal easier from the mandrel. In helical winding the winding angle ψ varies from 20 to 80 degrees ; the welding pressure is given by :

$$P = \frac{T \sin^2\psi}{R_0 l} \tag{3}$$

Where : T-the fibre tension, ψ-the winding angle is defined by the tangent vector to the meridian and the roving direction at point M (the deposit point),R_0--the mandrel radius at point M, l-the roving width (Fig. 2).

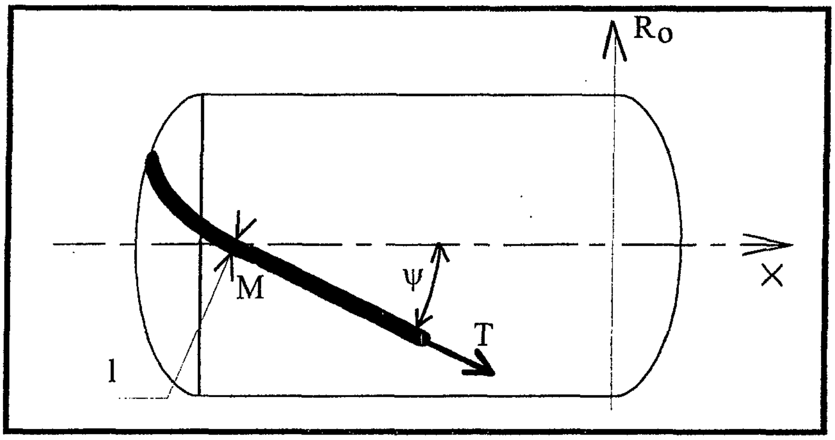

Figure 2 : A mandrel with the roving under tension

In circonferencial winding, where y ≈ 90°, we have the pressure formulated by J. L. Tisne [3] :

$$P = \frac{T}{R_0 l} \tag{4}$$

CONCLUSION

Welding composite revolution structures while winding poses the problem of continuity of the weld due to the discontinuity of the deposit point movement in block by bloc displacement. However, that problem can be solved by limiting the maximal welding speed. The structure obtained must be heated in an oven after having been covered by a fine layer of resin in solution to eliminate porosity. The welding speed using ultrasound heating system remain low, about few meters per minute.

REFERENCES

[1] Atangana, A., Aivazzadeh, S., Verchery, G., "Simulation and control of a filament winding machine with heating device for thermoplastic prepregs", Composites modelling and processing science-V3, pp 423-429, 1993.

[2] Atangana, A. J., "A 5-axes filament winder with software control", Composite science and technology, S. Adali and V.E. Verijenko, pp 19-24, 1996.

[3] Tisne, J.L., "Bobinagedes fibres continues imprégnées de résine thermoplastique", Composite 3, pp 121-128,1986.

INTEGRALLY STIFFENED RTM COMPOSITE PANEL

V. S. AVVA, R. L. SADLER, and K. N. SHIVAKUMAR

Department of Mechanical Engineering
North Carolina Agricultural and Technical State University
1601 E. Market St., Greensboro, NC 27411 USA

INTRODUCTION

It is known that composite parts with considerable geometric complexity and close dimensional tolerances can be fabricated with high fiber volume, low void content and low scrap, and a dependable fiber architecture by using resin transfer molding (RTM) process[1-4]. The RTM fabrication also allows parts to be manufactured with fiber volume ratios comparable to those achievable with traditional autoclave processing techniques. The present work addresses a technique utilized in obtaining an integrally stiffened composite flat panel using sixteen plies of W5-322 (Fiberite, Inc.,) plain weave carbon fabric with a high temperature PR-500 (3M Co.,) epoxy matrix. To maintain the shape of the stiffener, a Rohacell® rigid foam core is inserted in the mold prior to the RTM process takes place. The composite component fabrication incorporates a complex geometric configuration starting with the mold design followed by RTM processing. The design of the part was based on an assumed generic stiffened panel geometry. The part was sized to be compatible with existing RTM equipment.

APPROACH

The PR-500 epoxy resin is an advanced epoxy packaged as a one component system especially formulated for RTM. It is compatible with our Graco Heated RTM Supply Pump (Figure 1). Since the matrix is a thick paste at room temperature, the pumping and plumbing system must be controlled at an elevated temperature. A mold design (not shown) was selected that follows the contour of the finished stiffened panel (Figure 2). The mold was held in a compression press during the RTM process because the liquid matrix was to be held at 150 psi during the fabrication process. The press platens keep the mold closed and minimize the deflection of the mold components at this hydraulic pressure as well as affect a vacuum- and fluid- seal.

MATERIALS AND FABRICATION

The matrix chosen for this project was PR-500 Epoxy Resin produced and marketed by the 3M Company. It is a proprietary one-component epoxy resin especially formulated for the fabrication of advanced composites by the RTM process. It is a high strength epoxy with exceptionally good mechanical properties, especially under wet conditions. The Graco Heated RTM Supply Pump (Figure 1) was designed for injecting the matrix material into an RTM mold. The matrix contains a powdered curing ingredient suspended in the thick epoxy matrix paste. The powder melts at approximately 280^{0}F. The latent cure system must be melted before it reaches the fiber preform., otherwise the preform would filter the powder out of the matrix before it dissolves in the epoxy. This feature was particularly useful for the RTM process because it allowed the matrix to be pumped through the plumbing before the matrix was activated by dissolving the powdered ingredient. Therefore, the matrix plumbing between the pump and the mold was almost all reusable between injection cycles without cleaning.

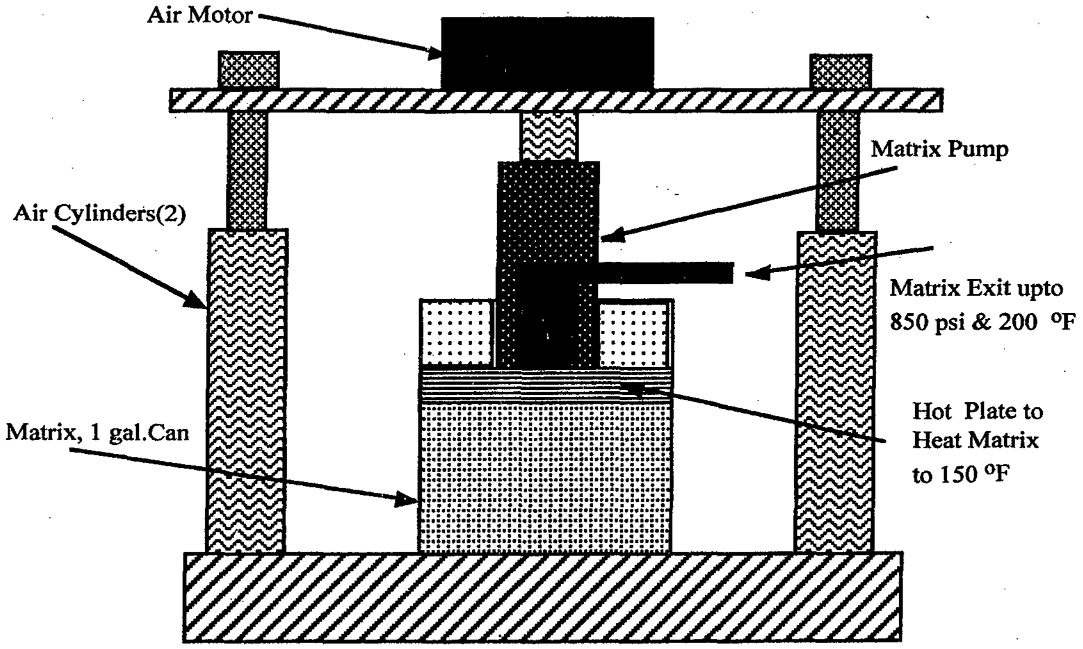

Figure 1. Graco Heated RTM Supply Pump

The reinforcement chosen was W5-322 plain weave carbon fiber fabric (16 layers) provided by Fiberite, Inc. After a few initial trials with several foam densities, a Rohacell® 71 WF (Rohm Tech Inc.,) rigid foam core (3.2 lb./cubic ft) was found to maintain the final projected shape and contour of the stiffener. The foam core was inserted between the 8th and 9th plies in the mold prior to the RTM process.

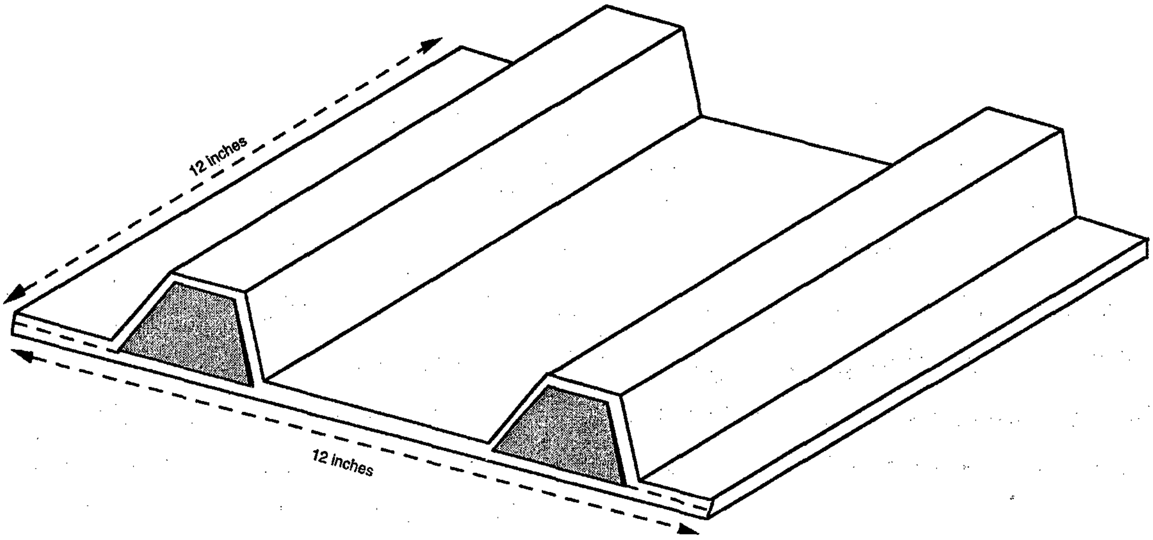

Figure 2. Integrally Stiffened RTM Panel

The matrix and vacuum plumbing system is illustrated in Figure 3. The mold was placed in the compression press and the copper tubing was assembled as shown. Copper tubing, 1/4 inch outer diameter with 37 degree flared tube fittings, was used throughout. At the time of assembly, a small amount of vacuum grease was applied to each joint to enhance the vacuum seal. All of the plumbing on the matrix entrance side of the mold was wrapped with electrical heating tape and adjusted to 150^0 F. The plumbing temperature on the matrix exit side of the mold was set at 200^0 F. The exit side of the mold contained a shut-off valve, a matrix trap, vacuum gage and a vacuum pump. The entrance side of the mold contained a shut-off valve, a needle valve and the Graco Heated RTM Supply Pump.

The plumbing was vacuum tested to determine if the system was vacuum tight. This was accomplished by closing the inlet valve, opening the outlet valve and turning on the vacuum pump. After the vacuum reached about 30 inches of Mercury, the vacuum pump was turned off and the vacuum gage was observed for vacuum leaks. If the gage indicated a leak of over one inch in 15 minutes, the plumbing connections were retightened and retested. A vacuum tight plumbing system is required for a successful RTM molding cycle.

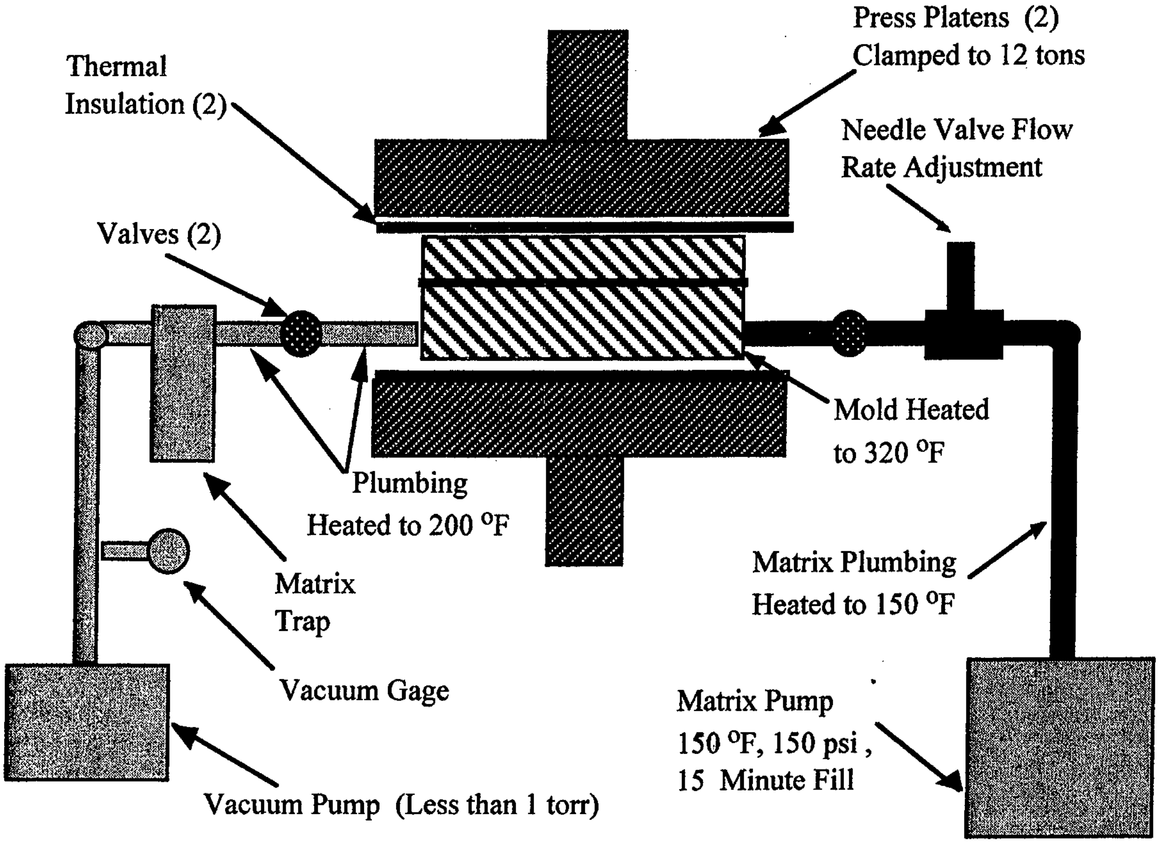
Press Platens (2)
Clamped to 12 tons
Thermal
Insulation (2)
Needle Valve Flow
Rate Adjustment
Valves (2)
Mold Heated
to 320 °F
Plumbing
Heated to 200 °F
Matrix
Trap
Matrix Plumbing
Heated to 150 °F
Vacuum Gage
Matrix Pump
150 °F, 150 psi,
15 Minute Fill
Vacuum Pump (Less than 1 torr)

Fig. 3: Injection Set-up Showing Plumbing Arrangement

The preform was constructed of sixteen layers (eight under and another eight over the 'core') of W5-322 carbon fiber plain weave fabric stacked in a quasi-isotropic sequence. The dimensions of the layers in the transverse direction to the core in the stiffened panel were adjusted appropriately to fit the mold cavity precisely.

The set-up and conditions illustrated in Fig. 3 are used to inject the matrix. A coat of mold release was applied to all surfaces of the mold. The O'ring and the O'ring groove were cleaned, lubricated with vacuum grease, and assembled. The preform was placed into the mold cavity with the compression press. The vacuum pump, heat to matrix plumbing, heat to Graco wiper plate assembly and heat to the mold were turned on and allowed to stabilize. Thermocouples were attached to various locations in the matrix plumbing- and mold-equipment. The mold temperature was set at 320^0 F, the matrix in-let plumbing and Graco wiper plate assembly temperatures were set at 150^0 F and the matrix out-let plumbing was set at 200^0 F.

Before commencing the matrix injection, the vacuum seal was rechecked to determine if the plumbing joints continued to seal at elevated temperature. If a leak was found, it was repaired and rechecked. The compressed air to the Graco was adjusted to 40 psi with the needle valve closed. The air to the air cylinders was set at 10 psi and the air to the matrix pump was set at 22 psi. The vacuum pump was turned off. The needle valve was slowly opened and the frequency of the pump stroke was observed and the needle valve adjusted to provide one stroke per minute. When the matrix was observed to flow into the matrix trap, the matrix exit valve was closed and the matrix pump increased the liquid matrix pressure to 150 psi. The exit valve was opened briefly two times to "burp" a small amount of matrix through the mold. Finally, the matrix was pressurized to 150 psi and held for 60 minutes. This pressurization reduced the size of any remaining air voids and matrix polymerization shrinkage.

The mold was held at 320^0 F for two hours as recommend by the matrix manufacturer to achieve a full cure. The mold halves were separated at the cure temperature of 30^0 F and the part was removed from the mold at room temperature.

The preceding demonstration has served to illustrate the feasibility of fabricating a two-stiffener panel without any 'bonding' of the stiffeners as is customary in the 'autoclaved' processing. The new RTM technology could prove to be very cost-effective in processing and fabricating geometrically complex components. Further, it is shown that a light weight foam could be used to 'retain' the shape of complex parts. Mechanical properties of the stiffened panels are being evaluated and they will be reported later.

ACKNOWLEDGMENTS

The authors wish to thank the Office of Naval Research, Department of the Navy, USA for providing financial support through a research grant No. N00014-95-0649. Dr. Yapa Rajapakse is the Scientific Officer.

REFERENCES

[1] V. S. Avva, R. L. Sadler, K. N. Shivakumar, D. Dunn., S. E. Jessup and C. Ingram., "Comparative studies on Laminated and Textile Composites"., AIAA/ ASME/ASCE/AHS/ASC 38th SDM Conference., April 7-10 1997, Hyatt Orlando, Kissimmee, Florida.

[2] R. L. Sadler and V. S. Avva., "Fabricating Affordable Composites" AIAA/ ASME/ AHS/ ASC 38th SDM Conference., April 7-10, 1997, Kissimmee, FL.

[3] V. Sarma Avva and Robert L. Sadler., "Processing Approaches to Fabricate Low Cost Composites"., 56th Annual International Conference on Mass Properties Engineering., Hosted by Seattle Chapter of Society of Allied Weight Engineers, Inc., May 19-21, 1997., Seattle, WA.

[4] V. S. Avva, R. L. Sadler, K. N. Shivakumar, and J. R. Campbell., "Resin Transfer Molding of Complex Textile Composite Components"; July 14-18, 1997, ICCM-11, Queensland, Australia.

OPTIMISATION OF COMPOSITE CURING PROCESS FOR MINIMUM RESIDUAL STRESS

A. K. Gopal[1], S. Adali[2] and V. E. Verijenko[2]

[1] CSIR Miningtek
P.O. Box 91230 Auckland Park, 2006
South Africa

[2] Department of Mechanical Engineering
Uniiversity of Natal
Durban, 4041, South Africa

INTRODUCTION

A major problem encountered in the processing of composite materials is the inducement of residual stresses. The detrimental effect of these stresses demands the development of an optimisation scheme for the minimisation of residual stresses in the processing of composite materials. To accomplish this objective, a residual stress process model should incorporate viscoelastic material response, chemical and thermal shrinkage effects and mechanical property development during cure. Previous works have used either elastic models [1,2] or have restricted the analysis to the cooldown phase of the cure cycle [3,4]. Additionally, most of the analyses are limited to either thermally induced strains solely or chemically induced strains solely.

PROBLEM STATEMENT

The constituent materials of the composite react differently to the changes in environmental conditions encountered during processing. Chemically, the reinforcing fibres are affected very little during the process cycle. The polymer matrix on the other hand will contract during crosslinking by as much as 6% in thermosets. There are thermally induced deformations as well. The reinforcing fibres show very little thermal deformation during cooldown due to their highly oriented structure. The polymer matrix on the other hand has a higher coefficient of thermal expansion, typically an order of magnitude or more. After processing, the composite must be well-bonded and continuous, therefore these deformations are balanced internally within the composite by the inducement of residual stresses. Processing induced residual stresses can be high enough to cause cracking within the matrix even before mechanical loading [5]. This microcracking adversely affects the strength of the material and exposes the fibres to chemical degradation [1].

The case of a $[0°/90°]_T$ cross-ply laminate is considered. The cure kinetics response is modeled by the Bogetti and Gillespie [6] equation, viz.

$$\frac{d\alpha}{dt} = A\exp\left(\frac{-\Delta E}{RT}\right)(1-\alpha)^n \alpha^m \tag{1}$$

where A is the frequency factor, ΔE is the activation energy, R is the universal gas constant, T is the temperature and m and n are cure kinetics exponents.

The laminate non-mechanical strains are composed of chemical strains and thermal strains. The longitudinal chemical strains are taken to be zero since the fibres do not experience chemical strains during the process cycle.

$$e_2{}^c = \beta_1 + \beta_2 10^{(\beta_3 \alpha)} \qquad \alpha \le \alpha^c \tag{2a}$$

$$e_2{}^c = e_2{}^{cf} \qquad \alpha > \alpha^c \tag{2b}$$

where e_j is the non-mechanical laminate strain, e^c is the laminate chemical strains, β_1, β_2, and β_3 are empirical transverse chemical shrinkage strain modeling coefficients and exponent respectively, α^c is the degree of cure when chemical shrinkage is complete and $e_2{}^{cf}$ is the final transverse chemical shrinkage strain.

The thermal strains can be modeled using the longitudinal and transverse thermal expansion coefficients [7].

$$e_i{}^T = \alpha_i (T - T_0) \tag{3}$$

where e^T is the laminate thermal strain α_i is the thermal expansion coefficient and T_0 is the initial stress free temperature.

The transverse modulus dependence on degree of cure is modeled by the following expression [8]:

$$\bar{E}_{22i}(\alpha) = E \qquad 0 \le \alpha < \alpha^* \tag{4a}$$

$$\bar{E}_{22i}(\alpha) = a_0 + a_1 \alpha + a_2 \alpha^2 \qquad \alpha^* \le \alpha \tag{4b}$$

where E_{22i} is the initial transverse modulus, E is the uncured transverse modulus, α^* is the degree of cure at initial transverse modulus development, ans a_0, a_1 and a_2 are the transverse modulus modeling parameters.

The longitudinal modulus and major Poisson's ratio are assumed to be linearly dependent on degree of cure as indicated from experimental testing, [7]. Thus,

$$\bar{E}_{11}(\alpha) = \bar{E}_{11i} + (\bar{E}_{11f} - \bar{E}_{11i})\alpha \tag{5}$$

$$\bar{\nu}_{12}(\alpha) = \bar{\nu}_{12i} + (\bar{\nu}_{12f} - \bar{\nu}_{12i})\alpha \tag{6}$$

where E_{11} is the longitudinal modulus, E_{11i} is the uncured longitudinal modulus, E_{11f} is the fully cured longitudinal modulus, ν_{12} is the major Poisson's ratio, ν_{12i} is the uncured major Poisson's ratio and ν_{12f} is the fully cured major Poisson's ratio.

The determined mechanical properties are then used to calculate the elastic compliances which are in turn used to calculate the time-dependent stiffnesses. The transverse compliance is taken as the only time-dependent compliance. With the strains and stiffnesses determined throughout the laminate the moment resultants can be calculated to be [8]

$$M_1(t) = -M_2(t) = h^2 \int_0^t F\{\alpha(\tau), [\xi(t) - \xi(\tau)]\}(e_1(\tau) - e_2(\tau))\, d\tau \tag{7}$$

where F is given by

$$F(\alpha,t) = \frac{[Q_{12}{}^{2}(\alpha,t) + Q_{11}(\alpha,t)Q_{22}(\alpha,t)]}{[Q_{11}(\alpha,t) + Q_{22}(\alpha,t) + 2Q_{12}(\alpha,t)]} \tag{8}$$

Since Equation (7) is a history dependent integral, the degree of cure, $\alpha(\tau)$, is represented as a function of τ and not the current time, t, hence the use of shift factors and reduced times, $\xi(t)$ and $\xi(\tau)$, which are given by

$$\xi(t) = \int_0^t \frac{ds}{a_T[T(s)]} \tag{9a}$$

$$\xi\tau) = \int_0^\tau \frac{ds}{a_T[T(s)]} \tag{9b}$$

where a_T is the shift factor

$$a_T(T) = \exp(\frac{B_1}{T} - B_2) \tag{10}$$

and B_1 and B_2 are empirical shift factor modeling parameters.

NUMERICAL RESULTS AND DISCUSSION

Parametric Study

When considering the input requirements of the chosen process model, it is observed that the only parameters that the engineer has control over are the initial stress free temperature and the applied temperature profile.

Cooldown gradient investigation

An analysis of the Figures presented in [8] indicate that the residual moment and hence residual stress profiles follow closely the applied temperature profile. Also evident is that the greatest increase in residual moment occurs during the cooldown phase of the cure cycle. Investigation of the this gradient shows that the residual stresses decrease initially with increasing gradient, up to a point of optimum gradient where the stress is the lowest and thereafter begins increasing with further increase in gradient. The possible change in stress observed is 63%.

First to second dwell temperature rise

Analysing the temperature-moment diagram [8] again results in the observation that there is also an increase in residual moment (stress) in the period of temperature change from the first to second dwell temperatures. Analysis of this observation yields a surprising result; the residual stresses in the composite decrease with increasing gradient. The lowest stress achieved occurs at a gradient that constitutes an almost instantaneous jump. Investigation indicates a possible decrease in residual stresses of 30%. The results observed in this investigation has a second advantage; the steep gradient shortens the processing time of the cure cycle which impacts on the production rate of manufacturing and hence the cost of manufacture of the product.

Rate of increase of temperature to first dwell

There is no evidence in the temperature-moment figure [8] to support any investigation of the temperature gradient to the first dwell temperature. Realisation, however, of the fact that the residual stress response is history dependent (viscoelastic) indicates that every change in the applied temperature can have an effect on the final residual stress value, even if there is no effect at the time of change. The results of the study of the effect of this temperature gradient yields a result similar to the previous set in that the residual stresses decrease with increasing gradient. An instantaneous jump amounts to a possible decrease in residual stress of 37%. There is also the second advantage of a reduced processing time for lower residual stresses.

Pre-heating response

The last of the control parameters is the initial stress free temperature. Normally, in most industrial cure cycles, the initial stress free temperature is room temperature. However, the materials can be pre-heated separately before being combined to form the composite and allowing curing to commence. Investigation of the effect of pre-heating, however, yields only a 1.3% decrease in stress for a pre-heating temperature difference of 104 °C. The additional expenses incurred in pre-heating the individual materials will not be justified by the small decrease in residual stresses.

The trends observed in the parametric study is evident in both plies of the laminate. The figures quoted, however, apply to the upper surface of the 0° orientated ply.

Optimising the cure cycle

Having obtained the required tools, it now becomes possible to develop an optimised curing cycle by combining the results of the parametric study (disregarding any pre-heating of component materials). The optimised cycle is shown in Figure 1, along with the cure response. When the resultant stress history is compared to the resultant stresses of the actual implemented cycle the significance in the decrease becomes evident. The implemented cure cycle is simulated using data from [7] and yields a final residual stress of 71.2 Mpa while the optimised cure cycle results in a final stress of 48 Mpa i.e a 32.5% decrease. The other important reduction is that of the cycle time. The processing time decreases from 425 minutes for the implemented cycle to 339 minutes for the optimised cure cycle. The optimised cycle may, however, be difficult to implement due to the almost instantaneous temperature changes. In these cases, the most rapid practical temperature change should be applied.

CONCLUSION

The modeling of the processing environment in composite materials poses a complex problem, hence a judicious choice of assumptions and simplifications has to be made in order to keep complexity to a minimum while keeping the model accurate. The inherent assumption that the temperature field is uniform through the thickness of the composite plate in the solution of the cure kinetics equations restricts the model to thin laminates. Additionally, the heat source should be of a uniform nature as in the radiant heating of composites in an autoclave environment or for hot presses. The matrix system is restricted to thermosetting, polymers in which the cure kinetics can be modeled by an Arrhenius type equation. The material should also be thermorheologically simple, thus obeying time-temperature superposition. Linear viscoelastic behaviour is assumed. All assumptions inherent in lamination theory are inclusive in the model. Moisture absorption during processing has been neglected. The accuracy of the implemented model is verified using test data from the experimental study conducted by White and Hahn [7]. Optimisation of the cure cycle has facilitated an important realisation; implementation of an optimised cycle can result in higher strength materials as well as reduced composites manufacturing costs.

REFERENCES

1. Hahn, H. T. 1984. "Effects of Residual Stresses in Polymer Matrix Composites," *Journal of Astronautical Sciences,* 32(3):253
2. Hahn, H. T. and N. J. Pagano. 1975. "Curing Stresses in Composite Laminates," *Journal of Composite Materials*, 9:9 1.
3. Harper, B. D. and Y. Weitsman. 1985. "On the Effects of Environmental Conditioning on Residual Stresses in Composite Laminates," *International Journal of Solids and Structures*, 21:907.
4. Weitsman, Y. 1979. "Residual Thermal Stresses Due to Cooldown of Epoxy-Resin Composites," *Journal of Applied Mechanics*, 46:563.
5. Doner, D. R. and R.C. Novak.1969. "Structural Behaviour of Laminated Graphite Filament Composites," *24th Annual Technical Conference, SPI, Inc.,No.*2d
6. Bogetti, T. A. and J. W. Gillespie, Jr. "Processing Induced Stress and Deformation in Thick-Section Thermosetting Composite Laminates," CCM Report 89-2 1, University of Delaware, August, 1989.
7. White, S. R. and H. T. Hahn. 1992. "Process Modeling of Composite Materials: Residual Stress Development During Cure. Part 2. Experimental Validation," *Journal of Composite Materials*, 26(16):2423-2453.
8. White, S. R. and H. T. Hahn. 1992. "Process Modeling of Composite Materials: Residual Stress Development during Cure. Part 1. Model Formulation," *Journal of Composite Materials*, 26(16): 2402-2422

FIGURES

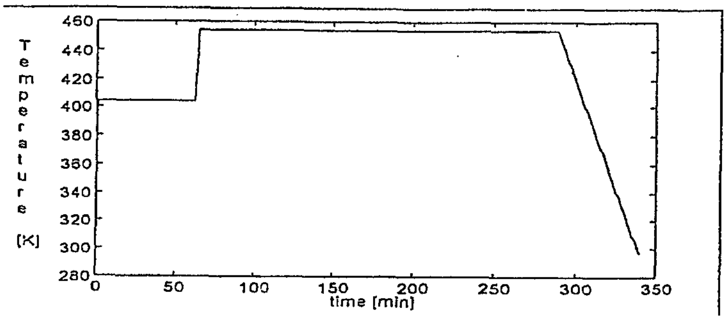

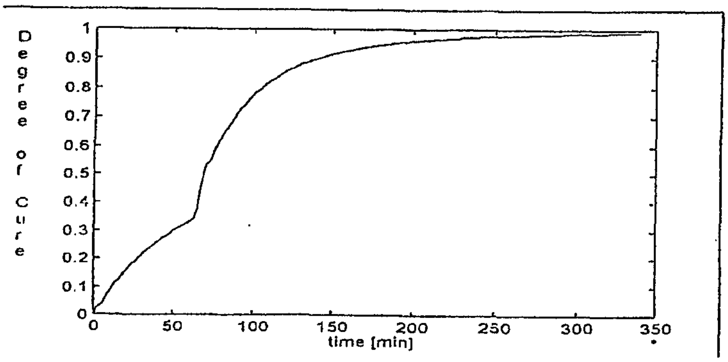

Figure 1 : Optimum Cure Cycle and Response

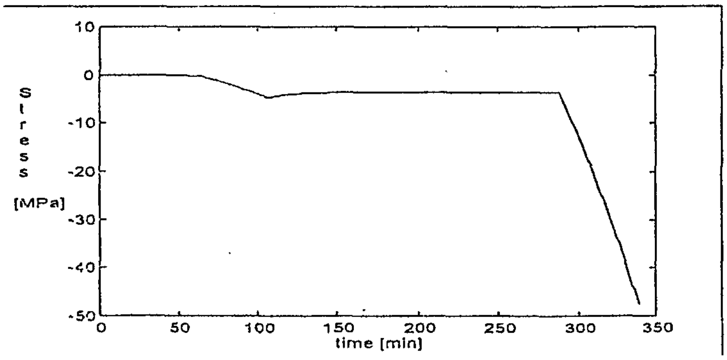

Figure 2 : Residual Upper Surface Stress vs. Time : Optimum Cure Cycle

Six Axes Fittings Winder: High Speed Production of 'T' and Elbow Parts

by
W. Shawn Kozak
Composite Machines Company

Presented by
John E. Green

There are a great many advantages to using FRP piping in the industrial world. Fiberglass pipes have excellent corrosion resistance, making them invaluable to the chemical and oil producing companies. The high performance to weight ratio allows high pressure lines to be run easily. Once an FRP pipe line has been properly installed it will have a far longer life span than its metal competitors. The typical steel pipeline has over 5 times the maintenance costs over a twenty year period. Unfortunately, the main drawback to completely switching over to fiberglass reinforced plastics for every major piping application has been the initial material and installation costs. While great strides have been made in recent years to bring the costs of the long lengths of straight tube more price competitive with current metal pipes, the individual elbow, 'T' and 'Y' fitting are still far more expensive. Modern fitting winding methods are capable of producing these fitting at a more economical rate.

There are several major problems with the current methods of manufacturing FRP fittings. Often times, mandrels are simply placed on a rotating fixture while an experienced operator gently guides the resin coated fibers or tape into the correct orientation. This is a very slow and labor intensive process, relying on the skill of individual operators to produce consistent part quality. Material is overused to cover inaccuracies in the pattern, and the actual laminate structure of the completed part can only be estimated. Because of this, wall thickness is usually far thicker than required for pressure rating. These operators are also continuously exposed to the toxic resins.

There are several firms winding fittings on two or three axis computer controlled filament winding machines. There have been several adequate patterns developed, especially for elbows, that run quite well, if a little slow, on these machines. The manufacture of 'T' fittings has even been attempted on 4 axis CNC machines. Unfortunately, to position the fiber or tape properly, quite a number of extra moves need to be added to the pattern, adding to the wind time. For 'T' parts especially, there is often still some manual intervention required. The triangular area where the tubes join is very difficult to wind over. The program generally needs to be stopped while the operator lays a triangular shaped piece of bi-axial cloth into the area. Winding with woven tape (which is the preferred method of production) is extremely difficult with only 4 axes because the tape twists and rolls on itself.

FRP pipe manufacturers have struggled with these problems for many years. The first step is generating the correct winding patterns. CADWIND software, by MATERIAL S.A. in Belgium, for creating non-linear winding patterns has been widely used in the aerospace and high performance composite fields. CADWIND software that can completely wind a 'T' fitting with tape has been around several years, and seen some use in Europe. CADWIND has several initial advantages for any type of fitting. Unlike metal and plastic, the mechanical properties of fiber reinforced plastic depends on the fiber orientation in the laminate (anisotropic). The winding process does not allow every possible winding angle. CADWIND determines the maximum laminate strength limited by the winding angles and develops a stable winding path on the mandrel. The system can predict at every point on the surface the laminate thickness and fiber orientation as well as the total part weight and fiber/resin usage. CADWIND also allows the end user to perform a finite element analysis on the newly generated fitting. A 'T' fitting that is just a computer concept can be pressure tested and impact tested before it is manufactured full scale, saving valuable production time. Once the optimal fiber path has been determined, it needs to be translated into machine movement.

Most pipe manufacturers have been reluctant to invest time and money into designing their own custom machinery necessary to run these complicated winding patterns. Often these cumbersome pieces of equipment can only wind one of two types of fittings, and sit idle after producing their quota. Composite Machines Company has developed a line of six axis CNC winding machines supported by CADWIND generated winding patterns that are capable of tremendously boosting fitting production. While it is not possible to wind every fitting on one machine, the three machine sizes can accommodate the majority of manufacturing needs. The small machine can handle up to 8.0 inch fittings. The intermediate machine works best for 8.0 inch to 16.0 inch pipe. The large fittings winder is capable of winding up to 24.0 inch elbow and 'T' fittings.

The heart of these winding machines is the CNC machine control system. All six axis are servo controlled, providing quick, accurate movement. The control system takes into account machine accelerations and speed as well as the stroke limitation of the various axes, to produce a smooth winding pattern. The pattern allows the machine to lay the fibers along the calculated fiber path while avoiding collisions between the mandrel and the delivery eye in the shortest possible winding time.

Figure 1 provides a general sketch of the relative position of each of the six axes. The first computer controlled winding axis is the overhead turntable. This axis rotates in a horizontal plane below the machine frame. The large shaft is constrained by angular thrust bearings and supports the ground beam from which the headstock and tailstock arms are mounted. These arms are adjustable in and out from the machine center and allow for different mandrel lengths. This axis allows for the circumferential winding of the leg of the 'T' fitting as well as orients the mandrel at the correct angle for the center section crossover winding.

The headstock arm contains the spindle drive for the second axis. It has a 3 jaw chuck to easily engage a wide variety of tooling. The spindle axis allows the main tube of both 'T' and elbow fittings to be wound in a conventional manner. The opposing end of the mandrel is supported by an adjustable live center or a quick release pneumatic collet mounted in the tailstock arm. This axis needs to be well powered and accurate. Both 'T' and elbow mandrels are unbalanced along this axis. This unbalanced load creates additional force that needs to be compensated for by the servo motor as the mandrel is accelerated and decelerated. The spindle motor drive needs to be particularly accurate because as the mandrel spins in one direction, the position error is cumulative. A homing proximity sensor on the spindle itself allows the machine to re-calibrate itself during the homing sequence.

The horizontal or X axis is common on almost every filament winding machine. Driven by a chain, it allows for rapid traverse and quick accelerations for low angle winding and crossover winding. This axis typically limits the maximum fiber feed rate of the machine on extremely low angle winding. This feed rate is normally determined by fiber wet-out in the resin station, and generally determines the wind time of the entire part.

Axis 3, the radial carriage, moves in and out toward the center of the fitting (Y direction). This axis of motion allows the delivery point to closely follow the surface of the mandrel being wound. The radial carriage allows the cross over angle to change in the wound radius that joins the tube with the leg. This axis has a much longer stroke than on a typical filament winding machine for manufacturing pipe. The delivery point should be capable of traveling from the center of the turntable and spindle rotations back away from the mandrel such that the delivery point can clear the swinging headstock and tailstock. This long radial carriage needs to be structurally stiff in order to keep the delivery eye in constant relation with the moving sections of the X,Y,Z carriages, and place the fiber along the path expected.

The leg of the 'T' fitting projects downward while it is being circumferentially wound. In order to allow helical winding on this surface as well as place fiber or lay tape into the triangular intersection of the fitting, the fifth, or vertical (Z) axis is necessary. The stroke of this axis needs to travel from slightly above the top surface of the 'T' mandrel in the leg down position all the way below the bottom of the leg. Once again, gravity has an effect on the servo motor acceleration. There needs to be some form of counterbalance to even out the load seen at the motor whether it is lifting or lowering the radial carriage in to position. This counterbalance, while it loads the motor in the lowering situation, is crucial for smooth servo performance.

Last, the rotating eye (sixth axis), controls the fiber band or tape twist. This eye is typically fitted with a comb bar (for fiber only)at the eye entrance and a smooth delivery bar is the last contact point before the mandrel. As the mandrel is positioned properly by the other axes, the eye is rotated such that the delivery bar is constantly maintained parallel to the mandrel surface. In addition to preventing twists and kinks, laying the fiber band/tape down as flat as possible on the surface helps maintain consistent fiber performance in the laminate without lumps or hollows where the bandwidth has compressed or spread.

When all six axes function together as a team, the results are quite impressive. Once the mandrel shape has been input into the pattern generation software, the optimal fiber path can be determined. This pattern is then downloaded into the machine control system. A minimal amount of minor modifications are sometimes needed to prove the pattern on the actual mandrel. The part can then be wound using pre-impregnated material or by mounting a resin bath on the radial carriage of the machine. In field tests, a 16.0 inch elbow mandrel was completely wet wound in just 27 minutes, approximately 40% less time than the identical mandrel could be done by hand. This was then repeated over and over again, producing identical fittings with identical resin and fiber usage and very similar laminate quality and burst strength.

Overall Machine Layout

6 AXES FITTINGS WINDER

(FIGURE 1)

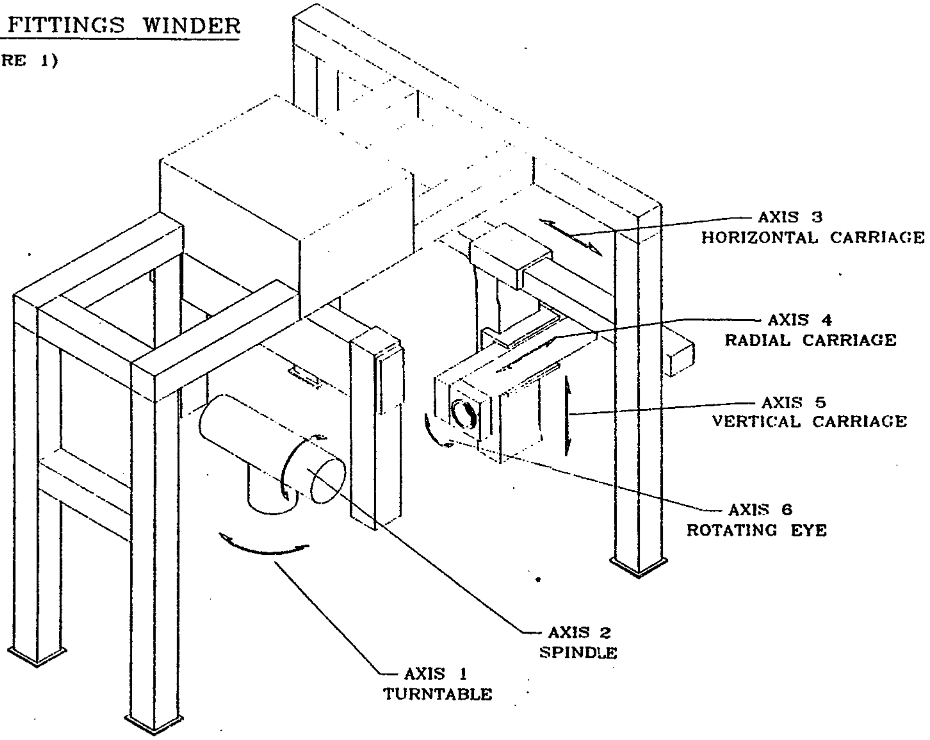
AXIS 3
HORIZONTAL CARRIAGE
AXIS 4
RADIAL CARRIAGE
AXIS 5
VERTICAL CARRIAGE
AXIS 6
ROTATING EYE
AXIS 2
SPINDLE
AXIS 1
TURNTABLE

Composite Machines Company

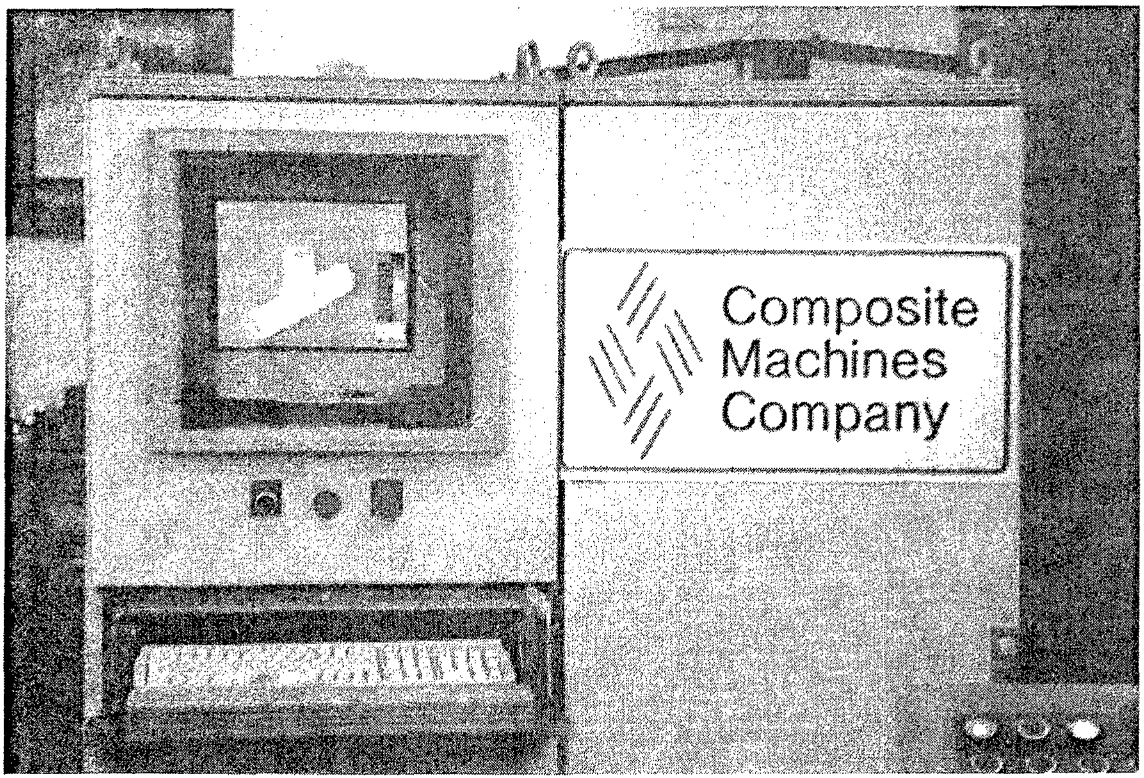
Composite
Machines
Company

FIGURE 2: COMPUTER CONTROL CABINET WITH 'T' PATTERN DISPLAYED

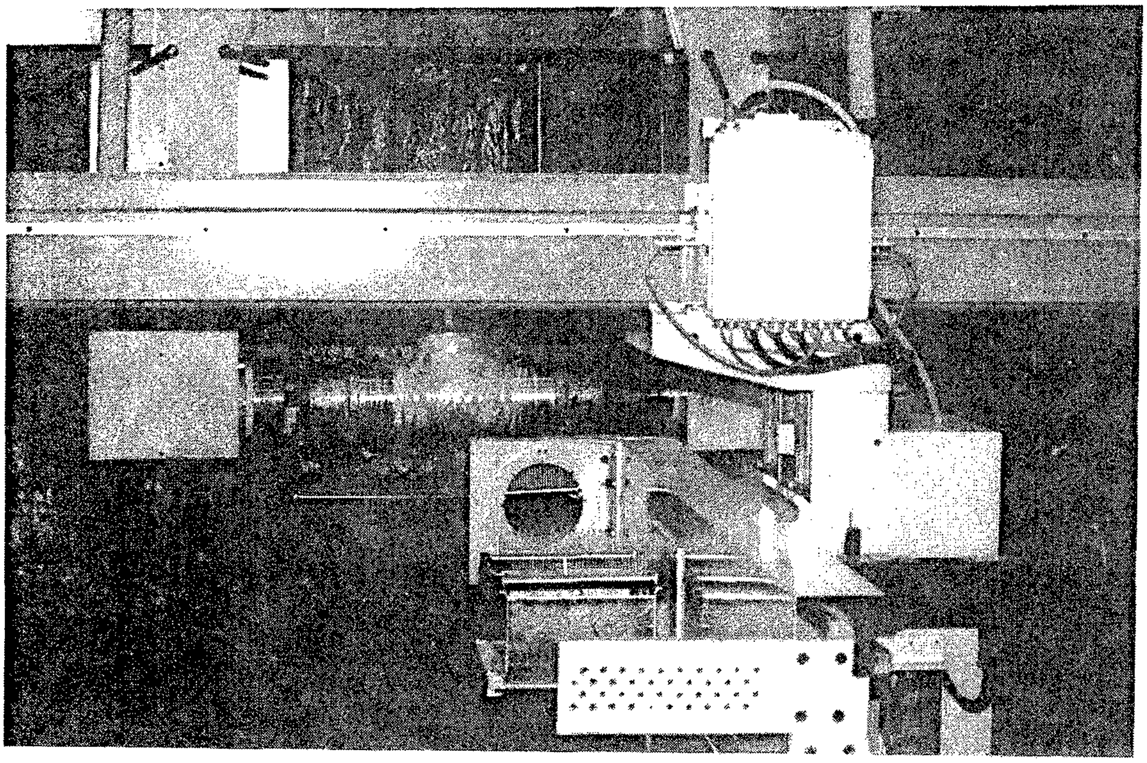

FIGURE 3: 'T' FITTING BEING WOUND

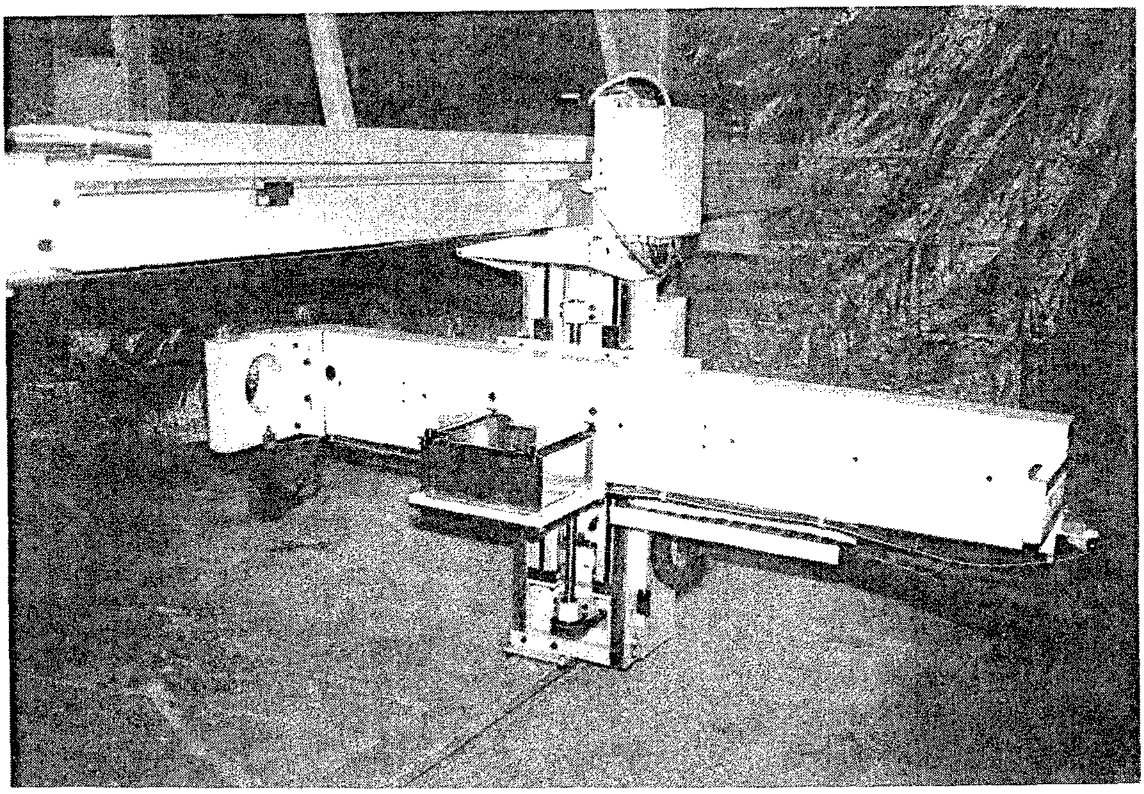

FIGURE 4: SIDE VIEW OF CARRIAGE ASSEMBLY

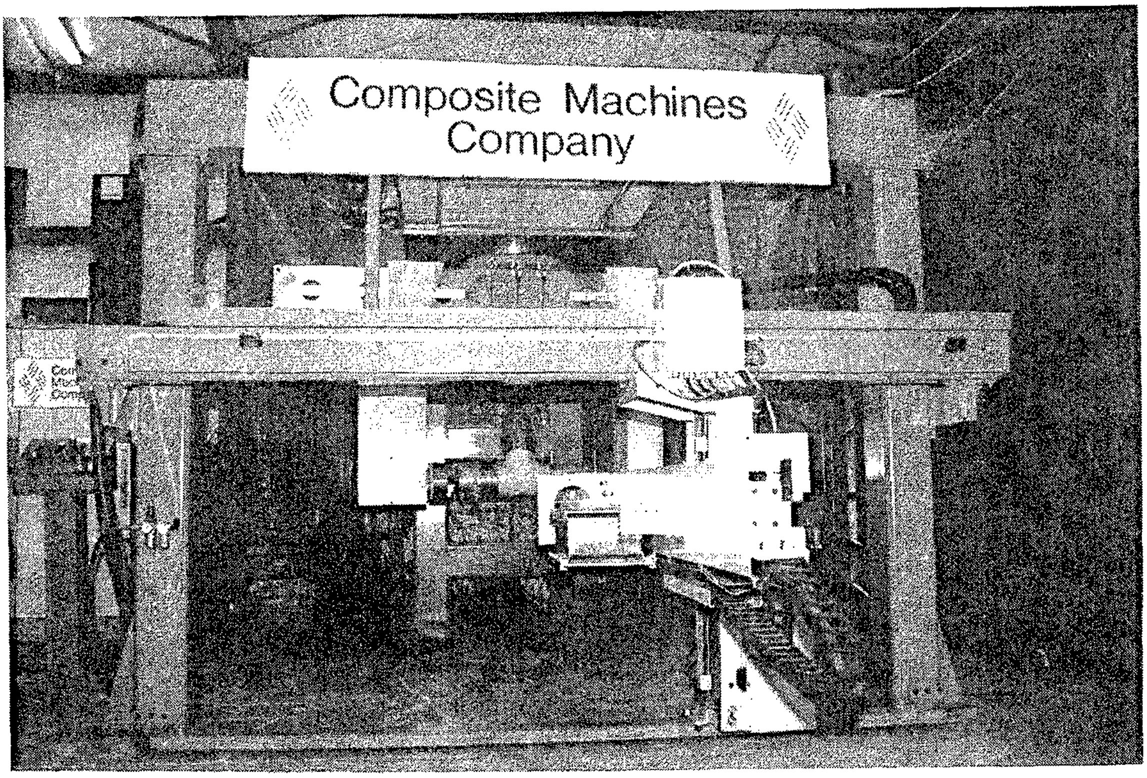

Composite Machines
Company

FIGURE 5: 6 AXES FITTINGS WINDER

FABRICATION AND MECHANICAL PROPERTIES OF GLASS FIBER REINFORCED POLYESTER FILLED WITH COPPER PARTICLES - PART I

A. C. SEIBI[1] and S. AL-ZADJALI[2]

[1] Department of Mechanical Engineering, Sultan Qaboos University, P.O.Box33, Al Khod 123, Oman.
[2] Mechanical Engineer, Oman Refinery Co., P.O. Box 13, Mina Al-Fahl 116, Oman

INTRODUCTION

Rotational molding is a manufacturing technique used to produce hollow articles made from plastic powder placed in molds heated up to 250 °C. In rotational molding, plastic powder is placed in the mold and heated from 250 - 300 °C for a period of 10 to 15 minutes. During the heating period, the mold is rotated at a constant speed of 20 rpm about two axes at a right angle to each other followed by air and water spray cooling. Although rotational molding presents a low pressure process and its cycle duration is slow compared to injection or blow molding, it can produce very large, thick walled articles (e.g. water tanks) which are not economically feasible by any other technique.

Most common molds, traditionally used in industry, are made of steel or aluminum. Production of metal molds involves a long process and is time consuming (3-4 weeks per medium to large size molds). In practice, this process is not economically feasible implying that better alternatives must be sought especially if the molds are intended for production of customized items.

Recently, Amiantit Oman, a local Omani company, is exploring the potential use of Glass Reinforced Plastics (GRP) as molds in rotational molding intended for production of customized items. However, since GRP is a good heat resistant, its thermal conductivity can be improved by incorporation of copper powder as a filler in GRP materials. Use of molds made from GRP/Copper materials will cut the cost tremendously by reducing the number of days taken to produce molds with the same characteristics as other conventional materials (steel and aluminum). Therefore, before proceeding with the fabrication of such molds, an experimental investigation related to the effect of the addition of copper powder to GRP on the thermomechanical properties of such composite material is required. The present paper, therefore, is intended to study the effect of the volume fraction of copper powder incorporated in GRP material on the thermomechanical properties of the developed GRP/Copper composite.

EXPERIMENTAL STUDY

GRP/Copper flat plates of 400x400x4 mm made of four layers of random glass fiber mixed with polyester resin and copper powder were fabricated using Hand Lay-up manufacturing technique. Seven volume fractions of copper powder, ranging from 5 to 30% with increments of 5%, were used in fabricating the GRP/Copper plates. The fabrication process involved the use of a drilling fluid mixer to initially mix the polyester resin and copper powder for 10 minutes followed by the addition of chopped fibers to the polyester/filler slurry to be heated up to 80 °C for 30 minutes. During heating, the slurry is mixed well in order to obtain a uniform mixture as well as reduce the resin viscosity. The mixture is then poured inside a mold and a roller was used to flatten the layers and get rid of entrapped air. A flat steel plate was then placed on top of the slurry to apply a constant pressure for 2-3 hours in order to obtain 3-5 mm GRP/Copper composite thick laminates. The laminates were then left for curing at room temperature. A flowchart showing the procedure for fabrication of GRP/Copper laminates is shown in Figure 1. Similar steps were performed for plates made of GRP/Copper materials using woven fibers except that only the polyester/copper powder was mixed and poured on top of woven fiber mats.

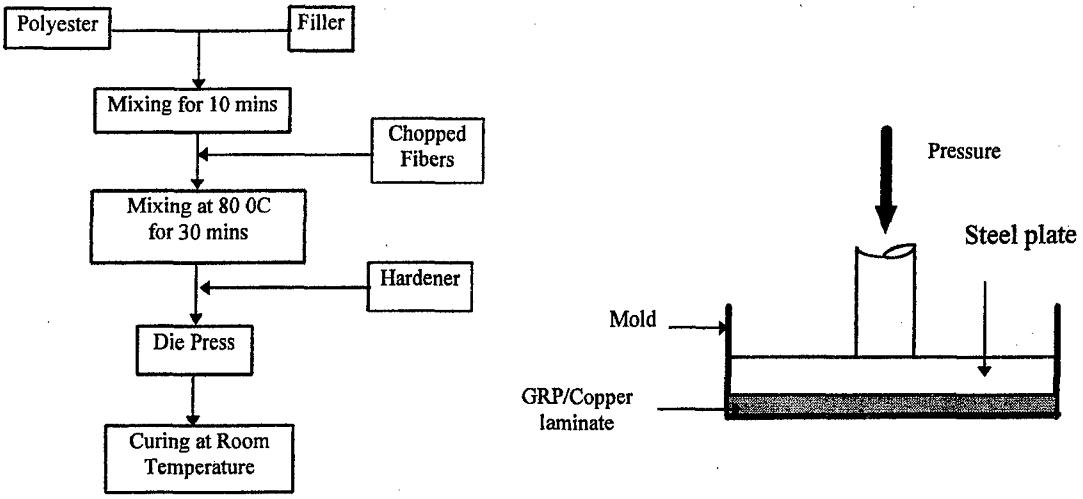
Polyester
Filler
Mixing for 10 mins
Chopped Fibers
Mixing at 80 0C for 30 mins
Hardener
Die Press
Curing at Room Temperature
Pressure
Steel plate
Mold
GRP/Copper laminate

a) Fabrication process

b) Die press

Fig. 1 Fabrication process of flat GRP/Copper Plates

Test specimens for tensile, compression, shear, and flexural testing are cut according to the ASTM and JIS standard test methods. The tensile and flexural specimens were cut according to JIS K 7054 and JIS K7055, respectively; whereas, the compression and shear samples were cut according to JIS K 7056 and ASTM D 4255-83, respectively. In this paper, only the testing fixtures of the shear (see Fig. 2) and compression (see Fig. 3) are included. All tests were conducted using a Lloyd M30K testing machine at a rate of 2 mm/min. An X-Y plotter was used to plot the resulting load-deflection curves for different volume fractions. In addition, disc samples of GRP/Copper composites were cut to measure the coefficient of thermal conductivity using a thermal conductivity measuring device.

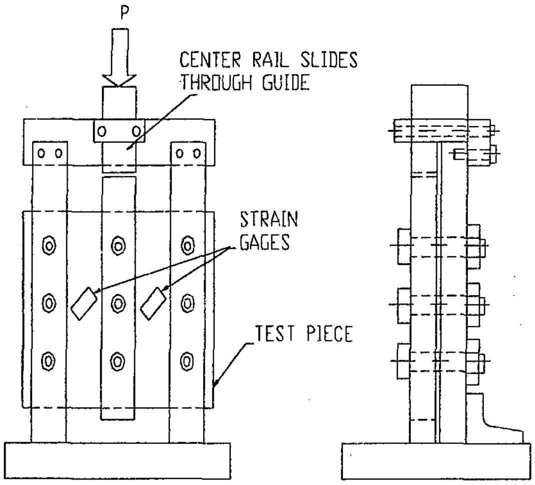
P
CENTER RAIL SLIDES THROUGH GUIDE
STRAIN GAGES
TEST PIECE

Fig. 2 Three rail shear test

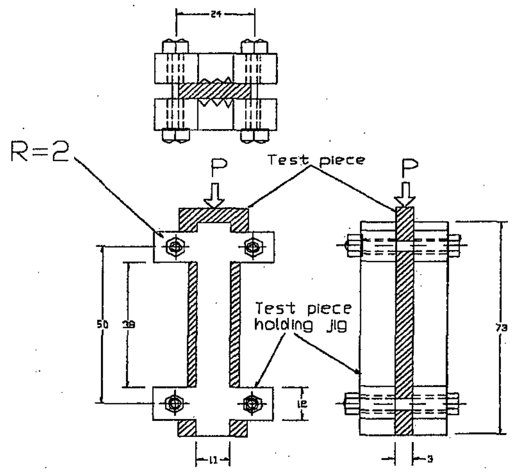
24
R=2
P
Test piece
P
Test piece holding jig
50
38
73
12
11
3

Fig. 3 Compression test fixture

RESULTS AND DISCUSSION

Tensile, flexural, compressive, shear, and thermal conductivity tests were conducted according to standard test methods. These tests are intended to determine the failure strength and stiffness of GRP materials filled with copper powder of different volume fractions for each test. The general behavior of the load-deflection curves is linear up to failure, followed by a sharp drop in the load. In general, addition of copper powder, up to 30% volume fraction, makes a considerable contribution to the change of strength and stiffness.

Figures 4 to 7 show the strength versus copper volume fraction for all tests. Figure 4 shows that the flexural strength decreases as the copper volume fraction increases for both woven and random GRP/Copper materials. In addition, it is observed that the flexural strength for both materials is equal for volume fractions higher than 15%. The reduction in strength can be attributed to the inclusion large copper particles that act as stress raisers in the composite.

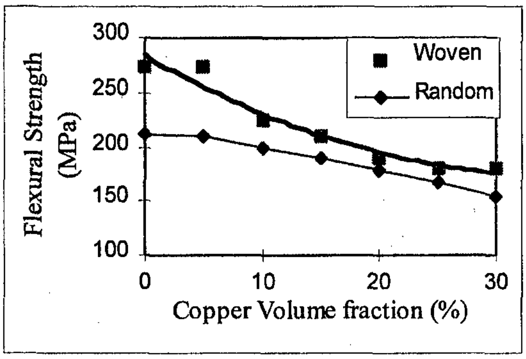

Fig.4 Flexural strength vs. volume fraction

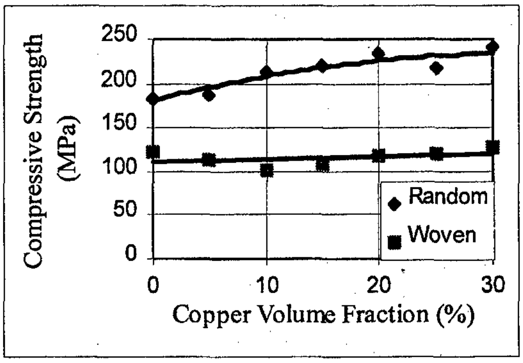

Fig.5 Compressive strength vs. volume fraction

A typical compressive strength versus copper volume fraction are presented in Figure 5. From this figure, it can be seen that the compressive strength for woven fiber is not affected by the addition of copper powder up to 30% volume fraction. However, the compressive strength increases for random fibers as the volume fraction of copper increases. In all cases, random fibers have higher compressive strength than woven fibers since random fibers behave as an isotropic material.

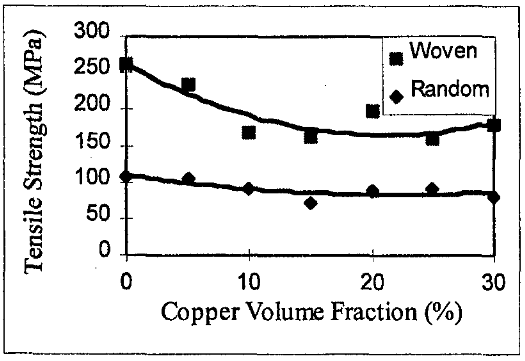

Fig. 6 Tensile strength vs. volume fraction

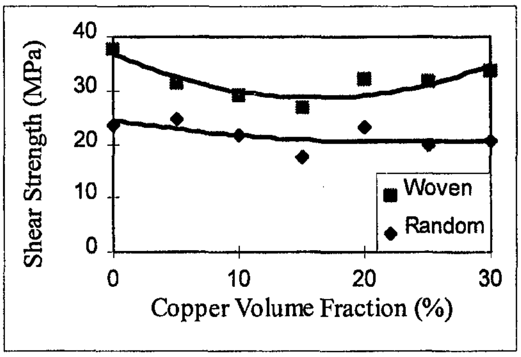

Fig. 7 Shear strength vs. volume fraction

Figure 6 shows the tensile strength as a function of copper volume fraction for both random and woven GRP/Copper. It is clear that the addition of copper powder up to 30% does not affect the tensile strength of random fibers, as compared to woven fibers which shows a decrease as the volume fraction of copper is increased.

Figure 7 shows the shear strength versus copper volume fraction for random and woven fibers. It can be seen that for random fibers the shear strength shows a slight decrease with the addition of copper powders. However, the shear strength for woven fibers decreases up to 15% of copper content followed by an increase in strength. It is observed that for random GRP/Copper cracks propagate at 45° with respect to the longitudinal axis, however for woven GRP/Copper no cracks were observed except inter-laminar delamination.

Figures 8 and 9 show fractured shear specimens of both random and woven fibers. For random GRP/Copper, cracks are observed to propagate at 45^0 to the longitudinal axis; however, for woven GRP/Copper no cracks are observed except inter- laminar delamination.

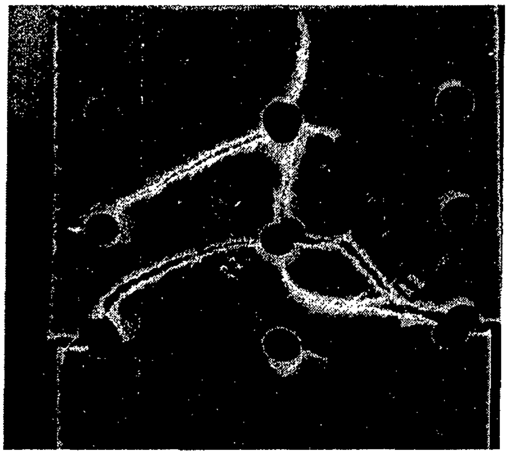

Fig. 8 Fractured shear specimen (Random)

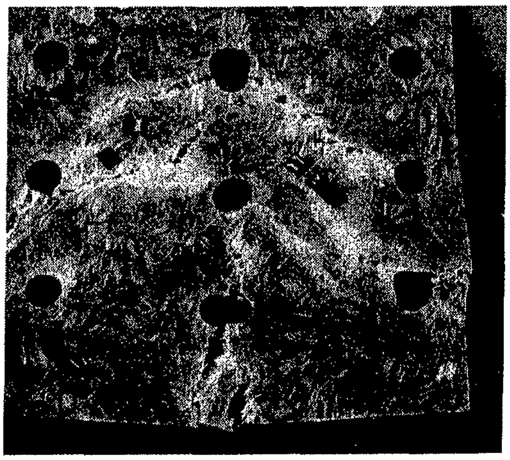

Fig. 9 Fractured shear specimen (Woven)

Figure 11 shows the coefficient of thermal conductivity versus copper volume fraction. The figure shows that the presence of copper particles in the composite increases the thermal conductivity of GRP materials. It can be seen that random fibers provide higher thermal conductivity than woven fibers at 30% copper content.

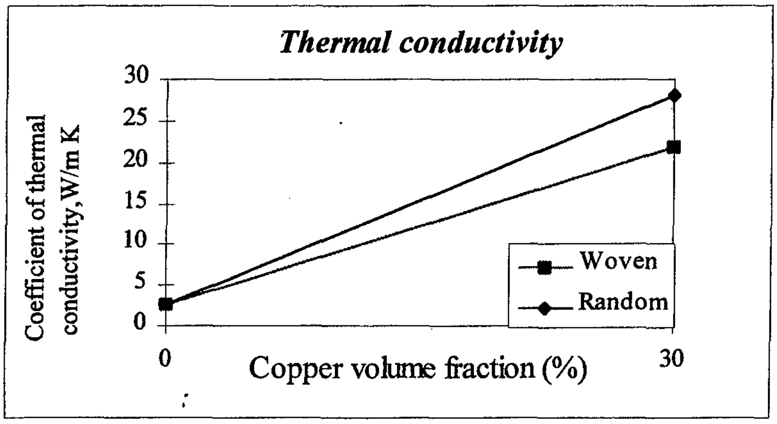

Figure 11. Thermal conductivity test

CONCLUSIONS

An Experimental investigation of GRP/Copper was performed. It was observed that, in general, the incorporation of copper particles improves the thermal conductivity of the material and reduces its strength. A follow-up study related to the design of GRP/Copper molds using finite element analysis is being undertaken.

ACKNOWLEDGMENT

The authors thank the Management of Amiantit Oman for giving facilities to the writers to carry out the research work.

REFERENCES

1. Leslie N Phillips., (1989), " Design with Advanced Composite Materials ", The Design Council, United Kingdom.

2. R. J. Crawford., (1987), " Plastics Engineering ", Maxwell Macmillan, United Kingdom.

3. R. W. Dyson., (1990), " Engineering Polymers ", Chapman & Hall, New York.

4. Ronald F. Gibson., (1994), " Principles of Composite Material Mechanics ", McGraw-Hill, United States of America.

5. Peter Child., (1987), " Vehicle Fabrications in GRP" , Billing & Sons Ltd, United Kingdom.

6. Derek Hull., (1981), " An Introduction to Composite Materials ", Cambridge University, United Kingdom.

7. F. R. Jones., (1994), " Handbook of Polymer-Fibre Composites, Longman ", England.

8. William F. Smith., (1990), " Principles of Materials Science and Engineering ", McGraw-Hill Publishing, United States.

Cost Comparison of RTM Hand-Lay and Cast Tooling

G. Veldsman, A.H. Basson[1]
Department of Mechanical Engineering,
University of Stellenbosch,
Stellenbosch, South Africa

NOMENCLATURE

A	Surface area of mould		(m^2)	Equation 1,3,7,8,9
A_P	Flat surface area of mould		(m^2)	Equation 13
A_G	Curved surface area of mould		(m^2)	Equation 13
B	Index: 1 if specific corner exist 0 if specific corner doesn't exist			Equation 14,15,16,17
L_B	Labour, Cenulite & Mastercore backing		(seconds)	Equation 19
L_C	Total labour, fast cast		(seconds)	Equation 5
L_{C1}	Labour, measuring and mixing fast cast		(seconds)	Equation 2
L_{C2}	Labour, casting fast cast system		(seconds)	Equation 4
L_{CI}	Labour laminating inside corners		(seconds)	Equation 15
L_{CO}	Labour, laminating outside corners		(seconds)	Equation 14
L_{CIF}	Labour, laminating filleted inside corners		(seconds)	Equation 17
L_{COF}	Labour, laminating filleted outside corners		(seconds)	Equation 16
L_{HL}	Total laminating labour		(seconds)	Equation 18
L_{HLT}	Total labour for hand-lay tooling		(seconds)	Equation 20
L_G	Labour, applying gelcoat		(seconds)	Equation 3,12
L_L	Labour, laminating flat and curved areas, surface vial and CSM		(seconds)	Equation 13
M_B	Total material cost Cenulite & Mastercore backing		(1998 Rand)	Equation 10
M_C	Total material cost - fast cast system		(1998 Rand)	Equation 1
M_F	Total material cost for fibres		(1998 Rand)	Equation 9
M_G	Total material cost for gelcoat		(1998 Rand)	Equation 7
M_{HL}	Total material cost for Hand-Lay Tooling		(1998 Rand)	Equation 11
M_R	Total material cost Resin		(1998 Rand)	Equation 8
P_C	Price/litre for fast cast system	(R82.34)	(1998 Rand)	Equation 1
P_{CSM}	Price/m^2 for 450g/m^2 CSM	(R8.20)	(1998 Rand)	Equation 9
P_F	Price/kg for Cenulite	(R2.05)	(1998 Rand)	Equation 10
P_G	Price/kg for vinyl ester gelcoat	(R54.95)	(1998 Rand)	Equation 1,7
P_M	Price/m^2 for MasterCore	(R201.00)	(1998 Rand)	Equation 10
P_R	Price/kg for vinyl ester tooling resin	(R32.00)	(1998 Rand)	Equation 8
P_S	Price/m^2 for Surface Vail	(R2.80)	(1998 Rand)	Equation 9
S	Circumference of mould		(m)	Equation 8,10
S_C	Length of specific corner type		(m)	Equation 14,15,16,17
t_G	Applied gelcoat thickness		(mm)	Equation 1,7
T_C	Lead time fast cast tooling		(seconds)	Equation 6
T_{HLT}	Lead time hand-lay tooling		(seconds)	Equation 20
V_C	Volume to be cast		(litre)	Equation1,2,4

---

[1] Correspondence should be sent to Prof. A.H. Basson,
Dept. of Mech. Eng., Univ. of Stellenbosch, Private Bag X1, Matieland 7602, South Africa
Email : ahb@ing.sun.ac.za

1.Introduction

Resin Transfer Moulding (RTM) tooling can be subdivided into four main categories: hand-lay tooling, machined tooling, plated tooling and cast tooling. These categories can further be grouped into:

i) Small- to medium-volume production tooling (Hand-Lay and Cast Tooling);

ii) Medium- to high-volume production tooling (Plated and Machined Tooling).

The main focus of this paper is to compare the two types of RTM tooling systems in the small- to medium- volume production category, on a cost basis. The conclusions in this paper are based on labour and material costs of RTM tooling manufactured in-house.

Hand-Lay tooling refers to a tooling system which is build-up by applying layer after layer of glass cloth impregnated with resin backed up by a steel frame. The "Plastech" method was used to construct the hand-lay tooling.

Cast Tooling refers to a tooling system that is cast onto the pattern in one or more shots. It consists of a resin that is highly filled with a filler material, usually aluminium. The "Atlas M130" system was used to construct the cast tooling.

The conclusions in this paper are based on cost comparisons done on the following two products:

i) Bell-mouth air intake;

ii) Centrifugal fan housing.

It was found that three of the major design parameters influencing the cost effectiveness of the two systems are:

i) The surface area of the tool;

ii) Tool complexity;

iii) The aspect ratio of the tool.

Cost estimation models (making use of the design parameters mentioned above) make it possible for designers to choose between the two tooling systems for a particular product. The models also determine the lead times necessary for constructing the moulds.

2. Fast Cast Tooling

The model presented here is based on the Atlas M130 system [1]. The Atlas M130 system is a methacrylate-based two-component resin filled with aluminium. After the addition of the hardener, the system sets up quickly at room temperature and a self-induced exotherm cures the mould. Two formulations were developed for different applications: the standard formulation (60% aluminium powder and 40% resin by weight) and a highly filled formulation (85% aluminium and 15% resin by weight). The cost model presented in this paper applies to the 85/15 formulation, used as a backing behind a vinyl ester tooling gel coat.

2.1 Cost Model - Fast Cast Tooling

The cost model is based on time studies done on moulds produced in-house. The manufacturing process was broken down into set-up for casting, pre-casting operations, casting and demoulding; the times for each process recorded. After statistical analysis of the data, the following equations were derived.

2.1.1 Material Cost - Fast Cast Tooling

The material cost is only a function of the volume to be cast and can be determined as follows:

$$M_C = P_C \times V_C + P_G \times (1.2)^2 \times A \times t_G \qquad (1)$$

2.1.2 Labour Cost - Fast Cast Tooling

The following equation determines the labour required and the labour cost can be calculated by dividing L_C by 3600 and multiplying the result by an hourly rate.

$$L_{C1} = 46.7 \times V_C + 684.4 \qquad (2)$$

$$L_G = 353.0 \times A + 261.8 \qquad (3)$$

$$L_{C2} = 278.3 \times V_C + 88.2 \qquad (4)$$

$$L_C = L_{C1} + L_G + L_{C2} + 475 \qquad (5)$$

$$T_C = L_C + 8985 \qquad (6)$$

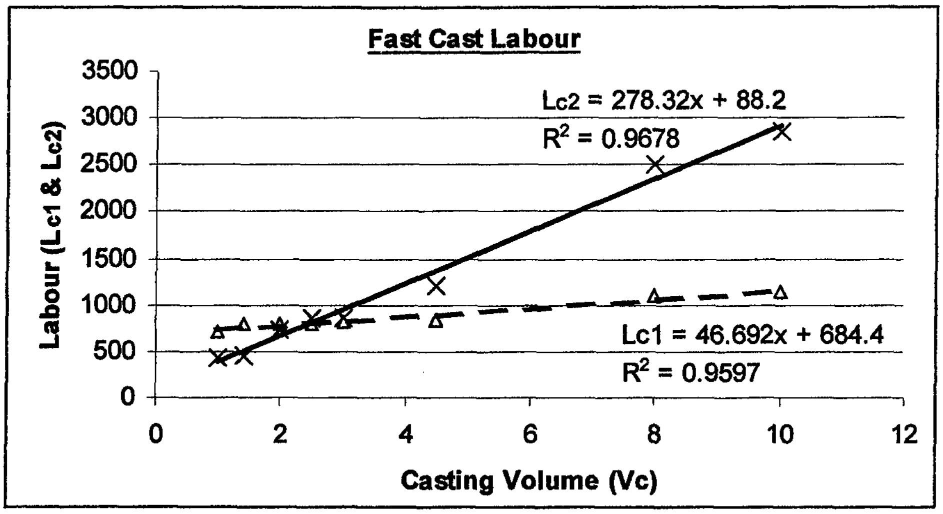

Figure 1: Fast Cast Labour

3. Hand-Lay Tooling

The hand-lay tooling system is based on the "Plastech" or "Allan Harper" method for constructing composite RTM tooling [2]. The method is used by SANI in South Africa as well as various overseas companies. It is a vinyl ester-based system comprising of tooling gel coat, 7 layers of 450 g/m^2 chopped strand mat (csm), mineral filler backing blocks (mastercore), another 2 layers of 450g/m^2 csm and lastly a floating steel frame. The cost models presented here are based on time studies done on moulds produced in-house.

3.1 Cost Model - Hand-lay Tooling

The cost model for the hand-lay tooling system again comprises a material cost component and a labour component. Only the direct cost for producing the mould is provided for and cost models for the pattern and other related processes will follow. Earlier models can be found in Veldsman et al., 1996 [3] and Veldsman, 1995 [4]. All costs are for one mould half.

3.1.1 Material Cost - Hand-Lay Tooling

Only the final equations for the material costs are given and costs for inserts and seals were not taken into account.

$$M_G = 1.44 \times A \times t_G \times P_G \quad (7)$$

$$M_R = (2.59 \times A + 0.057 \times S) \times P_R \tag{8}$$

$$M_F = (1.1 \times P_S + 9.9 \times P_{CSM}) \times A \tag{9}$$

$$M_B = (0.47 \times A + 0.048 \times S) \times P_F + 0.9 \times A \times P_M \tag{10}$$

$$M_{HL} = M_G + M_R + M_F + M_B \tag{11}$$

3.1.2 Labour Cost - Hand-Lay Tooling

The complexity of the tool plays an important role in determining the final manufacturing cost of the moulds. Kim, 1991 [5] defines a complexity index for composite cost modelling based on the assumptions that the process can be modelled as a first-order system. For our first-order model we defined complexity as a function of:

i) Percentage of surface area being flat;

ii) Percentage of surface area being curved;

iii) Total length of sharp corners;

iv) Total length of filleted corners.

The model also distinguishes between inside and outside corners (see Figure 2).

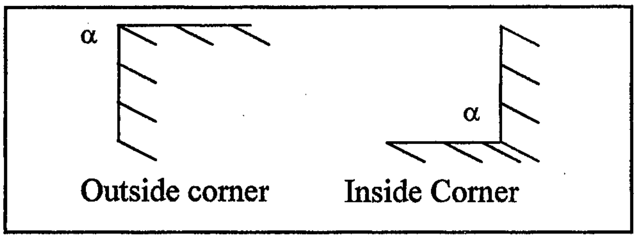

Figure 2: Different Corners

$$L_G = 353.0 \times A + 261.8 \tag{12}$$

$$L_L = 12639.55 \times A_P + 28016.95 \times A_G + 6010.07 \tag{13}$$

$$L_{CO} = B \times (360.22 + 2876.19 \times S_C) \tag{14}$$

$$L_{CI} = B \times (542.73 + 1283.99 \times S_C) \tag{15}$$

$$L_{COF} = B \times (283.21 + 1835.25 \times S_C) \tag{16}$$

$$L_{CIF} = B \times (52.81 + 1275.12 \times S_C) \tag{17}$$

$$L_{HL} = L_L + L_{CO} + L_{CI} + L_{COF} + L_{CIF} \quad (18)$$

$$L_B = 242.45 + 4356.4 \times A \quad (19)$$

$$L_{HLT} = L_G + L_{HL} + L_B \quad (20)$$

$$T_{HLT} = L_{HLT} + 61920 \quad (21)$$

The labour cost can be determined by dividing L_{HLT} by 3600 and multiplying it with an hourly rate.

4. Conclusion

By making use of the above the designer can determine the costs as well as the lead times necessary for producing moulds with the two systems. He can define the cost in terms of design parameters such as surface area, complexity (flat or curved areas, corners etc.), and volume. By using this in conjunction with cost models for fabrication of welded assemblies, as published by Schuster, 1997 [6], he can make a choice between the two systems. For small complex geometries, where the lead time is important cast tooling will probably be the most cost effective, whereas for larger moulds hand-lay tooling might be more cost effective.

5. References

[1] Atlas M130 Data sheet, AMT Cape Town, South Africa, Tel. +27 (0)21 5112669

[2] Plastech TT, RTM mould construction handbook, Gunnislake, U.K., Tel. +44 (0)1822 832621

[3] Veldsman, G., Basson, A.H., Van der Westhuizen, J. "Composite Mould Design and Cost Estimation for RTM" Proceedings of ICCST/1, pp571-576 (1996).

[4] Veldsman, G., "Aspects of Design for Manufacturing for RTM" M.Eng. Thesis, Dept. of Mech. Eng., Univ. of Stellenbosch, Stellenbosch (1995).

[5] Kim, C.E., "Composite Cost Modeling: Complexity" M.Eng. Thesis, Dept. of Mech. Eng., MIT, (1991).

[6] Schuster, H.R., "A computer Aid for Specification Development Conceptual Design and Manufacturing Cost Estimation in Mechanical Design" Ph.D. Thesis, Dept. of Mech. Eng., Univ. of Stellenbosch, Stellenbosch (1997).

VOID FORMATION DURING RESIN FILM INFUSION PROCESS AND OPTIMUM TEMPERATURE PROFILE.

V.E. Verijenko, S.Adali, I.B. Sevostianov

Department of Mechanical Engineering, University of Natal,
4001 Durban, South Africa.

INTRODUCTION

The resin film infusion (RFI) method to produce composite structures has been developed to overcome the problems encountered in the resin transfer moulding. These problems include low fibre content, necessity of using expensive matched moulds, long distances for resin to flow to fill out the fibrous preform, and void formation. The RFI process compresses the preform and draws the resin through it producing high quality composite parts from a wide range of fibre and resin combinations. However, flaws that may originate from the process can severally degrade the material properties of structures obtained by RFI. One major imperfection arises if voids are formed in the resin during manufacturing. The voids may occur at different stages of the process and a thorough understanding of the mechanisms of void formation requires several aspects of the process to be taken into account. There has been a number of studies in recent years explaining the void formation in composites and offering ways of reducing the void content [1-6]. It is generally accepted that one of the most common features of voids is that they are formed at the resin flow front [4-6].

The objective of the research presented in this paper is to develop a mathematical model of pore formation during RFI process. An analytical model is developed to describe cavitation conditions in the resin. This approach leads to an understanding of the influence of temperature on bubbles formation. The use of non-linear equation of filtration allows to define pressure distribution inside viscous liquid resin. The fibres which form the woven fabric are assumed to behave as linearly elastic bodies and the resin as a non-Newtonian viscous fluid. Based on the results obtained from this model it the optimum temperature profile for this process is obtained.

FRACTURE OF LIQUIDS

When the tension in a liquid becomes rather high, it becomes possible for a bubble to nucleate homogeneously. This process is called cavitation, or fracture of the liquid. Fisher [7] showed that the rate of nucleation of bubbles I_V is given by the following equation:

$$I_V = \frac{N_A kT}{V_M h} exp\left[-\left(Q + \frac{16\pi\gamma^3_{LV}}{3(P-p_V)^2} \right) \Big/ kT \right] \qquad (1)$$

where N_A is Avogadro's number, k is Boltzmann's constant, h is Planck's constant, V_M is molar volume of liquid, Q is activation energy for molecular transport across the liquid/vapour interface, T is absolute temperature, γ_{LV} is liquid/vapour interface energy, p_V is the pressure of vapour in the bubble; P is the stress in the liquid (which is equal in magnitude to the pressure, but opposite in sign; thus P is positive, when the liquid is in tension). The nucleation rate I_V has significant dependency on P, as illustrated in Figure 1. The pressure changes by only about 10% as I_V varies by six orders of magnitude, so the fracture pressure is quite well defined; moreover it is weakly dependent on Q. Cavitation occurs at such a high tension, that $P >> p_V$, so the vapour pressure can be neglected. Therefore letting $Q = 0$ and $p_V = 0$ and choosing a detectable nucleation rate of $I_V = 1\text{x}10^6 m^{-3} s^{-1}$, the fracture stress is accurately approximated as

$$P^* \approx \sqrt{\frac{16\pi\gamma_{LV}^3}{3kT\,ln\left(10^{-6} N_A kT / V_M h\right)}} \tag{2}$$

since the logarithmic term varies little for different liquids, equation (2) can be further approximated by

$$P^*\left(GPa\right) \approx 19.8\gamma_{LV}^{3/2} / T^{1/2} \tag{3}$$

where γ_{LV} is in $N\,m$ and T is in K. The corresponding critical nucleus size for bubble is

$$r^* = \frac{2\gamma_{LV}}{P^*} \approx \sqrt{\frac{3kT\,ln\left(10^{-6} N_A kT / V_M h\right)}{4\pi\gamma_{LV}}} \tag{4}$$

or

$$r^*\left(nm\right) = 0.16\sqrt{T / \gamma_{LV}} \tag{5}$$

Bubbles with radii larger than r^* grow, while smaller bubbles shrink.

The typical temperature conditions which is used in RFI process and corresponding dependencies for P^* and r^* are shown in Figure 2. It is quite clear that cavitation is more likely to occur when resin infusion is performed at higher temperatures.

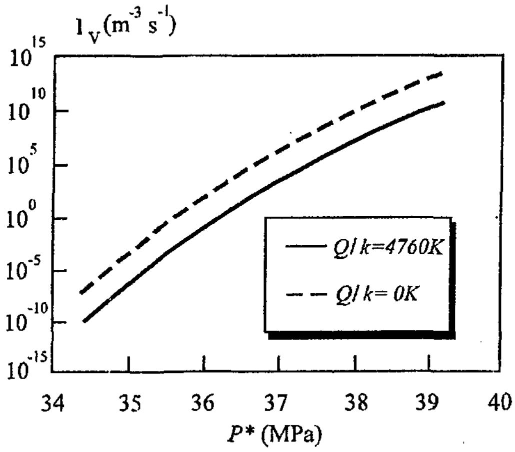

Figure 1. Homogeneous nucleation rate at $T=400$ K calculated from Eq. (1) for epoxy resin

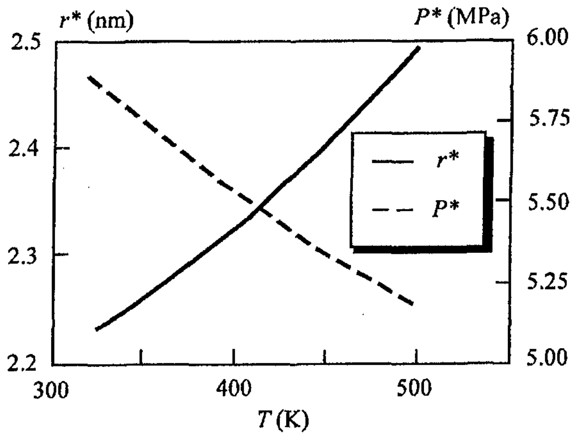

Figure 2. Effect of temperature on r^* and P^* for epoxy resin.

PRESSURE IN THE INJECTED RESIN

Let us consider the resin film injection through the pores of rigid network with a uniform pore size r_p as shown in Figure 3. In Figure 3(a) no resin flux is occurring. The liquid resin penetration into the woven material is initiated by reducing the tension P which develops in the liquid according to the Gibbs-Thompson equation:

$$P = -(RT/V_M)\ln(p_V/p_0) \qquad (6)$$

where R is the ideal gas constant, p_V is the partial pressure of the vapour and p_0 is its equilibrium value. If the contact angle θ between the resin and network is less than 90°, fingering menisci start to form in the mouths of the pores at the resin front as soon as the liquid resin begins to propagate as in Figure 3(b). The radius of the meniscus is related to the tension in the resin by Laplace's equation:

$$P = -2\gamma_{LV}/r_m \qquad (7)$$

where r_m is the radius of curvature of the meniscus.

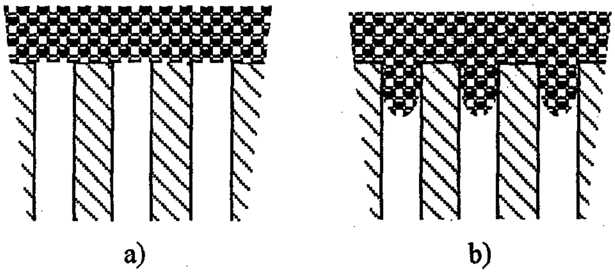

Figure 3. Schematic of a woven material with uniform pores: (a) before penetration of the resin film; (b) after resin fingering.

The flow of resin through the woven material j_r obeys Darcy's law, *viz.*,

$$j_r = \frac{D}{\eta}\nabla P \qquad (8)$$

where D is the permeability of the woven material η is the viscosity of the resin and ∇P indicates the pressure gradient. Mathematically the problem of the resin flux through the woven material is a variation of the well known Stephan's problem. Thus, an additional equation to describe the resin film penetration into the woven material is required to solve this moving boundary problem. Denoting the coordinate of the interface as $h(t)$, the following equation can be used [8]

$$\nabla P = -\frac{\eta(1 + C_s(0)P_C/K_W - C_s(0))}{D}\frac{dh(t)}{dt}, \quad \text{when } x_3 = h(t) \qquad (9)$$

where K_W is bulk modulus of the woven material, $C_S(0)$ is initial concentration of the solid phase and P_C is a critical value of pressure at the resin front.

Using equations (8) and (9) the following equation for the pressure field in the resin can be derived

$$\frac{\partial P(x_3,t)}{\partial t} - \frac{K_L}{\eta K_W}\nabla\cdot\left(D\nabla P(x_3,t)\right) + \frac{D}{\eta}(\nabla P)^2 = 0 . \tag{10}$$

In obtaining equation (10) it was taken into account that the permeability D of the woven material changes with the solid concentration and it was also assumed that the bulk modulus of the liquid is essentially less than that of the solid. The solution of (10) has to satisfy the following boundary condition:

$$\frac{D}{\eta}\nabla P(0,t) = j_{ext} \tag{11}$$

where j_{ext} denotes the external flux.

METHOD OF SOLUTION

A basic outline of the numerical procedure is shown in Figure 4. Starting with the resin film located at the top of the woven material a boundary condition is specified. These may be given in terms of constant pressure at a point (Dirichlet), inlet velocity through the side of an element (Neumman) or a flow rate at a point. The Dirichlet boundary condition was used in the recent study. A Flow Analysis Network [9] technique is then used to calculate the free surface location at a new time step. After each time step the free-surface boundary conditions are reset, and the governing equations are solved for new pressure values using Finite Element Method. Once the new pressure solution is known, the process is repeated untill the woven material is saturated completely.

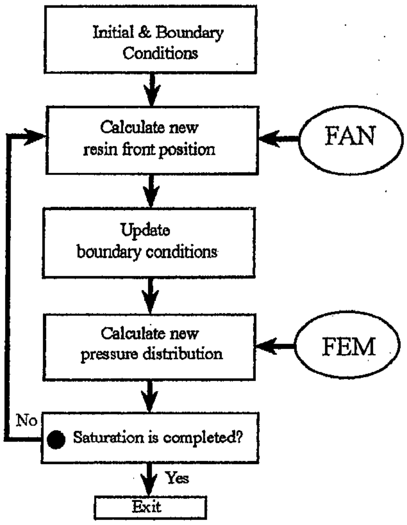
Initial & Boundary Conditions
Calculate new resin front position
FAN
Update boundary conditions
Calculate new pressure distribution
FEM
No
Saturation is completed?
Yes
Exit

Figure 4. Flow chart of the numerical algorithm

NUMERICAL RESULTS AND DISCUSSION

The viscosity of the resin depends significantly on the temperature of the process. The dependence from [10] was used in the recent study, *viz.*

$$\eta(T) = \eta_0\, exp\left(\frac{\varsigma}{T} + \kappa\alpha\right) \tag{12}$$

where μ, ς, and κ are constants which have to be obtained from the experiment; α denotes the degree of cure and T is the temperature at which the process takes place. As an example, the data obtained by Kang *et al.* [10] were used, *i.e.* $\alpha = 0.2$, k = 26.89, ς=1034.

For simplicity, external pressure was not considered in this analysis. However, it can be taken into account by superposition. The following mechanical parameters were used in the study for resin and solid woven material: viscosity η_0=5.5x10^{-5} Pa.s; critical pressure P_C=280 MPa; compressibility modulus of resin K_L=130 Mpa; initial volume fraction of fibres $C_S(0)$=0.5; permeability of the woven material D= 1.42x10^{-12} m^2; bulk modulus of the woven material K_W = 4.2 GPa; poisson's ratio of the woven material ν=0.25.

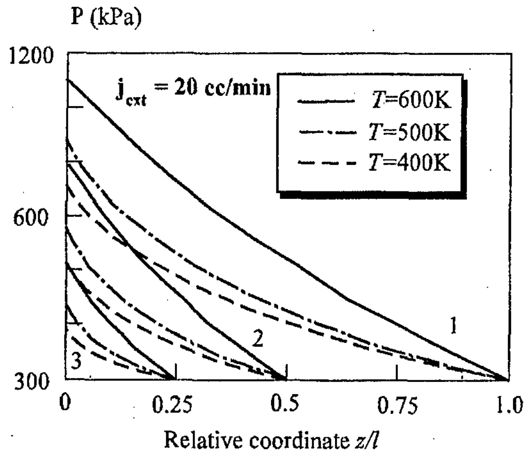

Figure 5. Pressure distribution along the preform thickness:
1-$t=t_f$, 2-$t=0.5t_f$, 3- $t=0.25\ t_f$

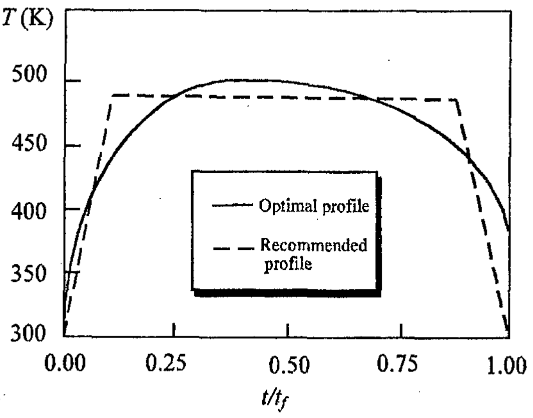

Figure 6. Optimum temperature profile for epoxy resin.

The pressure distribution along the plate thickness is presented in Figure 5 at different times for various temperatures. t_f is the time at which the preform is completely saturated. In the present study isothermal conditions of the process was assumed for simplicity. The temperature decrease during RFI process has two effects. On the one hand, it reduces the pressure in the resin since the resin viscosity becomes lower. On the other hand it also reduces the cavitation pressure P^*. Therefore a minimax problem has to be solved to determine the optimal temperature profile of the process with the pressure P being minimized and the cavitation pressure P^* being maximized. For simplicity, the resin cure is not considered in this study. Thus only two parameters are significant: the pressure field and the thickness of the saturated zone of woven material. A basic criterion to compute the optimum temperature profile can be formulated as the maximization of the relation P^*/P. The corresponding plot is presented in Figure 6. The value used for liquid/vapour interface energy is $\gamma_{LV} = 3\times10^{-2}\ Nm$. The dotted line corresponds to the recommended regime which also have to be convenient for the manufacturer.

CONCLUSIONS

An analytical model was developed for resin film infusion process which is used for autoclave processing of composite structures with a high fibre volume content. The model was used to simulate the RFI process and to study the void formation during the process. These defects reduce the strength of the fibre composite component manufactured by this process and can even lead to the premature failure of the component. Microdamage formation is governed by the pressure distribution in the resin infused into the fibrous preform. Pressure is related to the rate of infusion, preform permeability and resin viscosity and it is governed by Darcy's law.

In the present study it was assumed that the compressibility coefficient of fibres is essentially higher than that of the resin. However, fibrous preform, which may be considered as a porous medium, is assumed to be sufficiently compressible. Due to the moving front of the resin, the problem can be stated as a moving boundary problem which becomes a particular case of a well known Stephan's problem. This problem was solved by finite element method using flow analysis network. Analytical model for the cavitation pressure is developed. It is shown that temperature variation leads to change in the capillary pressure as well as in the cavitation pressure. The minimax problem was solved in order to obtain the optimal temperature profile for the process.

ACKNOWLEDGEMENTS

Partial financial assistance for this research was provided by Kentron, a division of Denel, through a project awarded to the Centre for Composite Materials and Structures at the University of Natal.

REFERENCES

1. Lundström, T.S., Gebart, B.R. and Lundemo, C.Y. Void formation in RTM.// *J. Reinforced Plastics and Composites*, 1993, **12**, 1339-1349.

2. Lundström, T.S. Measurement of void collapse during resin transfer moulding.// *Composites Part A.*, 1997, **28A**, 201-214.

3.Hayward, J.S. and Harris, B. Effect of process variables on the quality of RTM moulding.//*SAMPE J.*, 1990, **26**, 39-46.

4. Mahale, A.D., Prud'Homme, R.K. and Rebenfeld, L. Quantitative measurement of voids formed during liquid impregnation of nonwoven multifilament glass networks using an optical visualisation technique.//*Polymer Engineering and Science*, 1992, **32**, 319-326.

5. Lundström, T.S. and Gebart, B.R. Influence from process parameters on void formation in resin transfer molding.// *Polymer Composites*, 1994, **15**, 25-33.

6. Patel, N. and Lee, L.J. Effects of fibre mat architecture on void formation and removal in liquid composite molding.// *Polymer Composites*, 1995, **16**, 386-389.

7. Crank, J., *Free and Moving Bounary Problems*, Clarendon Press, Oxford, 1982.

8.Fisher, J.C. Nucleation of vapor bubbles in liquid.// *J. Appl. Phys*, 1948, **19**, 1062-1074.

9. Phelan Jr., F.R. Simulation of the injection process in resin transfer molding.// *Polymer Composites*, 1997, **18**, 460-476.

10. Kang, M.K., Lee, W.I., Kim, T.W., Kim, B.S., and Jun, E. Numerical simulation of resin transfer mold filling process.// In: *Proc. 10th Int. Conf. on Composite Materials*, Whistler, Canada, August 1995, ***III***, 253-260.

THEORETICAL FOUNDATIONS FOR NONDESTRUCTIVE DETECTION OF CRACKS IN CERAMIC MATRIX COMPOSITES BASED ON SURFACE TEMPERATURE

Larry W. Byrd
Wright-Patterson Air Force Base
Dayton, Ohio, USA

Victor M. Birman
Engineering Education Center
University of Missouri-Rolla, St. Louis, Missouri, USA

Abstract

Ceramic matrix composites are processed at high temperatures and experience significant residual thermal stresses upon cooling to room temperature. These stresses often result in matrix cracking prior to the application of external loads. Matrix cracks may also appear as a result of thermomechancial loading. It is important to detect these matrix cracks which affect the structural response using a nondestructive technique. The method proposed in this report is based on measurements of the surface temperature of a ceramic matrix material subjected to cyclic stresses. The elevated surface temperature is due to friction between the fibers and the matrix that occurs in the presence of bridging matrix cracks. The solution presents a relationship between surface temperature and matrix crack spacing that can be used to identify the extent of the damage.

Introduction

The fact that ceramic matrix composites (CMCs) are processed at a high temperature implies significant thermally-induced residual stresses. These stresses can result in damage even before the material is subject to an external load. For example, Bischoff et al.[1] and Nishiyama et al.[2] observed post-processing cracking in CMCs. Additional cracks are formed when the material is subject to monotonous or cyclic tensile loads. Elevated operational temperatures may also contribute to the process of matrix cracking. The cracks usually form a regular pattern with the spacing that can be assumed constant. Long cracks perpendicular to the fibers, similar to those observed by Marshall and Evans[3] and other investigators, are called "bridging cracks", because the fibers bridge the cracks without breaking. It is important to be able to determine the extent of matrix damage because, although matrix cracks do not significantly degrade the strength and stiffness of the material in the fiber direction, they are detrimental to those in the transverse direction and allow oxygen induced embrittlement[4-7].

In the presence of matrix cracks, the fibers slide relative to the matrix in the regions adjacent to the cracks when the material experiences dynamic loading. This is accompanied with an increase of temperature due to friction between the fibers and the matrix as observed by Holmes and his associates[8,9]. Cho et al.[10] developed a solution that related the interfacial shear stress to the rise of temperature of the specimen. It was suggested that the interfacial shear stress along the fiber-matrix interface can be monitored as a function of temperature. In the present paper, the analytical foundation is developed for prediction of the spacing of matrix cracks (and the interfacial shear stress) as a function of the surface temperature for a unidirectional CMC. This technique can be applied to a nondestructive testing of CMC components.

Analysis

The purpose of the present solution is to determine a relationship between the matrix crack spacing in a unidirectional CMC and its surface temperature during a nondestructive dynamic test. The amplitudes of cyclic stresses are assumed below the matrix cracking limit of the material so that cycling does not change the matrix crack spacing. The solution assumes the mode of cracking employed in the theories of Aveston-Cooper-Kelly[11] and Budiansky-Hutchnison-Evans[12], i.e. long, regularly spaced cracks. Shown in Fig. 1, the problem is formulated in terms of the crack spacing (s), the length of the sliding distance (x_0), and a distribution of stresses in the fibers and the matrix.

The solution involves the following steps. First, the modulus of elasticity of the material is determined as a function of the interfacial shear stresses, matrix crack spacing and the residual thermal stresses in the fiber using a modified approach of Pryce and Smith[13]. Residual thermal stresses are evaluated accounting for the effect of temperature on the properties of the constituent materials. Then the experimental findings of Karandnikar and Chou[14] are used to justify a simple relationship between the modulus of elasticity and the matrix crack spacing.

Combining these two solutions, the modulus of elasticity can be eliminated giving a single equation relating the matrix crack spacing to the interfacial shear stress. An energy balance is employed, as suggested by Cho et al.[10], to obtain a relationship between the surface temperature and the interfacial shear stress. This procedure enables the evaluation of both the shear stress and the matrix crack spacing as functions of the surface temperature.

A distribution of stresses in a specimen subjected to an external stress σ_c is shown in Fig. 1. This distribution corresponds to a partial slip, i.e., $2x_0 < s$. Adjacent cracks are located at $x = 0$ and $x = s$. The stresses in the fibers and the matrix can be evaluated based on their values at the points A and B:

$$\sigma_{fA} = \frac{\sigma_c}{V_f}; \quad \sigma_{fB} = \frac{\sigma_c E_f}{E_c} + \sigma_f^T; \quad \sigma_{mA} = 0; \quad \sigma_{mB} = \frac{\sigma_c E_m}{E_c} + \sigma_m^T \tag{1}$$

where the subscripts "f" and "m" refer to the fibers and matrix, respectively, V_f is the volume fraction of the fibers, E_f, E_m and E_c are the moduli of elasticity of the fibers, matrix and undamaged composite, respectively, and σ_f^T and σ_m^T are the residual thermal post-processing stresses outside the slippage region. During cycling the composite stress σ_c varies continuously, thus the stresses given by eqns. (1) represent instantaneous values, although dynamic (viscous) effects are not included in the present analysis.

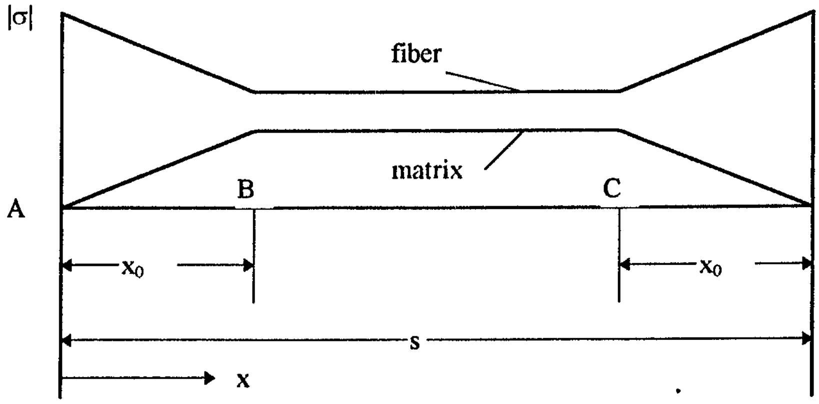

Fig. 1. Distribution of stresses in the fibers and in the matrix between two cracks during cycling (not to scale).

Force equilibrium at each cross sections is satisfied. In the slippage region, the stresses in the fiber and the matrix are linear functions of the distance from the plane of the crack, i.e., x. The stress in the fiber is[12]:

$$\sigma_f = \frac{\sigma_c}{V_f} - \frac{2\tau x}{r} \tag{2}$$

where r is the fiber radius and τ is the interfacial shear stress which is approximated as a constant. The stress in the matrix within the slippage region is

$$\sigma_m = \left(\sigma_c \frac{E_m}{E_c} + \sigma_m^T\right)\frac{x}{x_0} \; ; \; x_0 = \frac{r}{2\tau}\left(\sigma_c \frac{V_m E_m}{V_f E_c} - \sigma_f^T\right) \tag{3}$$

where x_0 is the half-length of the slippage region given by Pryce and Smith[13] and V_m is the matrix volume fraction. The residual thermal stresses in the fiber and in the matrix can be found from the force equilibrium at an arbitrary cross section, i.e.,

$$E_f V_f (\varepsilon - \alpha_f \Delta T_{po}) + E_m V_m (\varepsilon - \alpha_m \Delta T_{po}) = 0 \tag{4}$$

Here α_f and α_m are the coefficients of thermal expansion of the fibers and the matrix, and ΔT_{po} is the difference between the processing and operating temperatures. The strain, ε, can be immediately evaluated from eqn. (4). However, considering the fact that the processing temperature of CMCs is usually above 1200°C, it is necessary to account for an effect of the temperature on the properties of the materials of the fibers and the matrix. In this case, the strain will be found in eqn. (5).

$$\varepsilon = \int_{T_p}^{T_0} \frac{E_f(T)V_f\alpha_f(T) + E_m(T)V_m\alpha_m(T)}{E_f(T)V_f + E_m(T)V_m} dT \tag{5}$$

The integration is carried out from the processing (T_p) to the operating (T_0) temperature. The residual stresses in the region that is not affected by the slip are found as

$$\sigma_f^T = E_f(T_o)\int_{T_p}^{T_o} \frac{E_mV_m(\alpha_m - \alpha_f)}{E_fV_f + E_mV_m} dT \; ; \quad \sigma_m^T = E_m(T_o)\int_{T_p}^{T_o} \frac{E_fV_f(\alpha_f - \alpha_m)}{E_fV_f + E_mV_m} dT \tag{6}$$

The instantaneous modulus of elasticity of the material is evaluated by modifying the approach adapted by Pryce and Smith[13]. The instantaneous mean strain in the fiber is found by averaging the strains over the spacing length:

$$\bar{\varepsilon}_f = \frac{2x_0\varepsilon_{AB}}{s} + \frac{s - 2x_0}{s}\varepsilon_{BC} = \frac{x_0}{s}\left[\frac{\sigma_c(2V_fE_f + V_mE_m)}{V_fE_fE_c} + \frac{\sigma_f^T}{E_f}\right] + \frac{s - 2x_0}{s}\left(\frac{\sigma_c}{E_c} + \frac{\sigma_f^T}{E_f}\right) \tag{7}$$

The mean residual strain is found from an analog of eqn. (7) where the mean strain in the region AB is given by $\sigma_f^T/2E_f$, while the strain within the region BC is σ_f^T/E_f (see Fig. 2). Accordingly,

$$\bar{\varepsilon}_f^T = \frac{s - x_0}{s}\frac{\sigma_f^T}{E_f} \tag{8}$$

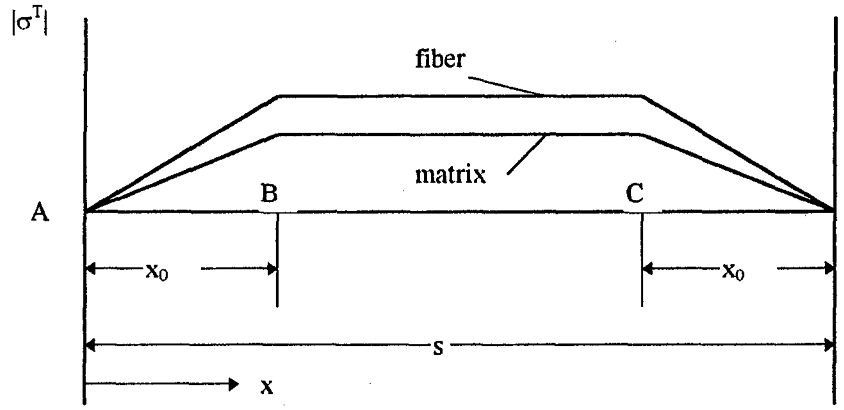

Fig. 2. Thermal residual stresses in a unidirectional material with matrix cracks (not to scale).

The additional strain associated with cyclic loading can now be found as a difference of the strains given by eqns. (7) and (8), i.e.,

$$\bar{\varepsilon} = \left[1 + \frac{r}{2s\tau}\frac{\left(\sigma_c\frac{V_mE_m}{V_fE_c} - \sigma_f^T\right)V_mE_m}{V_fE_f}\right]\frac{\sigma_c}{E_c} \tag{9}$$

The instantaneous modulus of elasticity is determined as:

$$E = \frac{d\sigma_c}{d\bar{\varepsilon}} = \left[1 + \frac{r}{2s\tau}\frac{E_m V_m}{E_f V_f}\left(2\sigma_c \frac{E_m V_m}{E_c V_f} - \sigma_f^T\right)\right]^{-1} E_c \tag{10}$$

This will be used with the experimental findings of Karandikar and Chou[14] who showed that the change of the modulus of a unidirectional Nicalon fiber CAS matrix composite is a linear function of the matrix crack density (1/s):

$$\Delta E = E_c - E = k_1 + k_2(1/s) \tag{11}$$

where k_1 and k_2 are constants. For Nicalon fiber CAS matrix, k_1 = -6.7350 GPa and k_2 = 6.2754 GPa·mm. The present approach to the solution remains valid as long as an arbitrary analytical relationship ΔE = f(s) is available. Combining eqns. (10) and (11) yields the relationship between the interfacial shear stress and the matrix crack spacing:

$$\tau = \left[\frac{E_c - k_1 - k_2/s}{k_1 + k_2/s}\right]\left[\frac{r}{2s}\frac{E_m V_m}{E_f V_f}\left(2\sigma_c \frac{E_m V_m}{E_c V_f} - \sigma_f^T\right)\right] \tag{12}$$

The interfacial shear stress is related to the surface temperature of the specimen by considering the equilibrium between the rate of the steady state heat loss from a unit volume of the specimen and the rate of work performed by the interfacial friction within this volume. The former quantity was presented in the paper of Cho et al.[10] for the general case where the flow loss occurs through conduction in the fiber direction and free convection and radiation from the surface. In this paper conduction along the fiber direction and radiation were neglected. The rate of the heat loss from the element with the surface area A_s (including both surfaces of the specimen) and the volume $V = A_s t/2$ where t is the thickness becomes

$$\dot{q} = \left[h(T_s - T_a)\right]\frac{2}{t} \tag{13}$$

In eqn. (13), T_s and T_a are the surface and ambient air temperatures, respectively, h is the heat transfer coefficient. The heat transfer coefficients from the surfaces of a representative element can be estimated using standard relations for heat transfer due to natural convection (see, for example, Incropera, F.P. and DeWitt, D.P., "Fundamentals of Heat and Mass Transfer," 4th edition, Wiley, New York, 1996).

The work produced by the interfacial friction on the slippage length of one fiber as it is loaded is given by Cho et al.[10]

$$W = 2\int_0^{x_0}(2\pi r)\tau(u_f - u_m)dx \tag{14}$$

where u_f and u_m are dynamic components of the axial displacements of the fiber and the matrix due to cyclic loading that are functions of the x-coordinate. Note that the upper limit of integration given by eqn. (4) is affected by the magnitude of the interfacial shear stress. The difference between dynamic components of the axial fiber and matrix displacements can be found as

$$u_f - u_m = \frac{1}{2}[\delta\varepsilon_f(x) - \delta\varepsilon_m(x)](x_0 - x) \tag{15}$$

where $\delta\varepsilon_f$ and $\delta\varepsilon_m$ are the dynamic strains at the cross section x. This equation reflects the fact that the fiber and the matrix experience identical axial displacements at $x = x_0$, and the change of the length of the element $(x_0 - x)$ can be found as the mean strain within this element multiplied by its length.

The dynamic strain in the fiber is determined as a difference between the total and residual strains. The former can be found from eqn. (2) but it is more convenient to use the following expression that immediately follows from Fig. 1:

$$\varepsilon_f(x) = \left[\frac{\sigma_c}{V_f} - \left(\frac{\sigma_c}{V_f} - \frac{\sigma_c E_f}{E_c} - \sigma_f^T\right)\frac{x}{x_0}\right] E_f^{-1} \qquad (16)$$

The latter strain is of course (see Fig. 2), $(\sigma_f^T/E_f)(x/x_0)$.

Now the dynamic components of the strains in the fibers and in the matrix can be found as:

$$\delta\varepsilon_f(x) = \left[\frac{1}{V_f} - \left(\frac{1}{V_f} - \frac{E_f}{E_c}\right)\frac{x}{x_0}\right]\frac{\sigma_c}{E_f}; \qquad \delta\varepsilon_m(x) = \frac{x}{x_0}\frac{\sigma_c}{E_c} \qquad (17)$$

Substituting dynamic strains given by eqns. (17) into eqn. (15) and integrating eqn. (14) one obtains:

$$W = \frac{2\pi r \tau \sigma_c}{3 V_f E_f} x_0^2 \qquad (18)$$

Note that the composite stress in eqn. (18) represents the maximum stress during the cycle, while the minimum stress is assumed equal to zero. In the case of a stress ratio different from zero, the composite stress should be replaced with the stress range. The rate of the frictional energy dissipation per unit volume can be found as recommended by Cho et al.[10], i.e.,

$$\dot{w} = 2fW/(\pi r^2 s/V_f) \qquad (19)$$

where f is the frequency of loading and the factor "2" in the numerator accounts for the fact that equal amounts of energy are generated during the loading and unloading phases of each cycle. Then a relationship between the matrix crack spacing and the interfacial shear stress can be obtained from the requirement that the rate the heat loss given by eqn. (13) must be equal to the rate of the frictional energy dissipation according to eqn. (19). This relationship should be considered together with eqn. (12) to specify both the interfacial shear stress as well as the matrix crack spacing.

Results

A parametric study of the model was undertaken with E_m = 100GPa and E_f = 200GPa. The heat transfer coefficient was approximated as a constant h = 6W/m^{2}K. The coefficients of thermal expansion were assumed constant with values of $\alpha_f = 3(10^{-6})°C^{-1}$ and $\alpha_m = 4.5(10^{-6})°C^{-1}$. The difference between the processing and use temperature was assumed to be 600°C. The fiber radius was 10μm. The surface temperature rise, $\Delta T = T_s - T_a$, was then calculated for V_f = .35, f = 10Hz and σ_c = 200 MPa. The form of the empirical relation in eqn. (11) places some restraints on the values of the s. For ΔE to remain positive, s should be less than .932mm which is in agreement with the recommendation Karadikar et al.[14]. There is also a minimum crack spacing which can be calculated from eqn. (3) once the shear stress has been determined. The slippage half length x_0 cannot be greater than s/2 or the analysis is invalid. For this study for σ_c = 200MPa, the minimum crack spacing is on the order of .085mm. This is considerably smaller than minimum value used in Figure 3. As seen in Figure 3, ΔT increases as the crack spacing decreases. This is expected as a result of increasing damage and sliding between the matrix and fibers as the crack density increases.

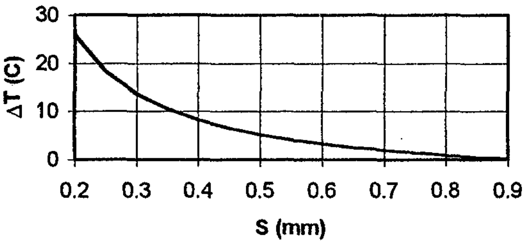

Fig. 3. ΔT as a function of crack spacing V_f=.35, f = 10Hz, σ_c = 200MPa

Discussion and Conclusions

The solution presented in this report outlines the theoretical background for a nondestructive detection of the presence and density of matrix cracks in unidirectional ceramic matrix composites. The density of the matrix cracks and the interfacial shear stress can be evaluated using this solution, based on the measurement of the surface temperature of the component subjected to periodic loading. The solution is obtained in a closed-form, i.e., it is accurate as long as the basic assumptions incorporated into the analysis are valid. In particular, these assumptions include the form of matrix cracking, i.e. long bridging cracks, and the presumed analytical relationship between the change of the modulus of elasticity and the matrix crack spacing. However, these assumptions are justified by available experimental evidence.

Acknowledgements

This paper was written with the support of the Air Force Office of Scientific Research (Contract F49620-93-C-0063) and Wright Laboratory.

References

1. Bischoff, E., Ruhle, M., Sbaizero, O. and Evans, A.G., Microstructural studies of the interface zone of a SiC-fiber-reinforced lithium aluminum silicate glass-ceramic. *Journal of the American Ceramic Society*, 1989, **72**, 741-745.
2. Nishiyama, K., Umekawa, S.,Yuasa, M. and Fukumoto, I., Effect of fiber coating on interfacial phenomena in tungsten-fiber/boron carbide composites. *Proc. Fourth Japan-US Conf. Composite Mater.*, 1988, Technomic, Lancaster, PA, pp. 776-788.
3. Marshall, D.B. and Evans, A.G., Failure mechanisms in ceramic-fiber/ceramic-matrix composites. *Journal of the American Ceramic Society*, 1985, **68**, 225-231.
4. Wetherhold, R.C. and Zawada, L.P., Fractography of glasses and ceramics. Eds. Frechete, V.D. and Varner, J.P., *Ceramic Transactions*, 1991, Vol. 17, American Ceramic Society, Westerville, Ohio, p. 391.
5. Zawada, L.P. and Wetherhold, R.C., The effect of thermal fatigue on a SiC fibre/aluminsilicate glass composite. *Journal of Materials Science*, 1991, **26**, 648-654.
6. Kahraman, R., A microdebonding study of the high-temperature oxidation embrittlement of a cross-ply glass-ceramic/SiC composite. *Composites Science and Technology*, 1996, **56**, 1453-1459.
7. Westwood, M.E,, Webster, J.D., Day, R.J., Hayes, F.H. and Taylor, R., Review. Oxidation protection for carbon fibre composites. *Journal of Material Science*, 1996, **31**, 1389-1397.
8. Holmes, J.W. and Shuler, S.F., Temperature rise during fatigue of fibre-reinforced ceramics. *Journal of Materials Science Letters*, 1990, **9**, 1290-1291.
9. Holmes, J.W. and Cho, C., Experimental observations of frictional heating in fiber-reinforced ceramics. *Journal of the American Ceramic Society*, 1992, **75**, 929-938.
10. Cho, C., Holmes, J.W. and Barber, J.R., Estimation of interfacial shear in ceramic composites from frictional heating measurements. *Journal of the American Ceramic Society*, 1991, **74**, 2802-2808.
11. Aveston, J. and Kelly, A., Theory of multiple fracture of fibrous composites. *Journal of Material Science*, 1973, **8**, 352-362.
12. Budiansky, B., Hutchinson, J.W. and Evans, A.G., Matrix fracture in fiber-reinforced ceramics. *Journal of Mechanics and Physics of Solids*, 1986, **34**, 167-189.
13. Pryce, A.W. and Smith, P.A., Matrix cracking in unidirectional ceramic matrix composites under quasi-static and cyclic loading. *Acta Mettalurgica et Materialia*, 1993, **41**, 1269-1281.
14. Karandikar, P.G. and Chou, T.-W., Microcracking and elastic moduli reductions in unidirectional Nicalon-CAS composite under cyclic fatigue loading. *Ceramic Engineering & Science Proceedings*, 1992, **13**, 882-888.

ON CONTINUUM APPROXIMATION IN COMPRESSIVE FRACTURE THEORY FOR METAL MATRIX COMPOSITES: ASYMPTOTIC ACCURACY

IGOR A. GUZ

Timoshenko Institute of Mechanics, Nesterov str. 3, 252057 Kiev, Ukraine

INTRODUCTION

There are two different approaches to description of phenomena in mechanics of composites. One of them is based on the model of piecewise-homogeneous medium, when behaviour of each component of material is described by three-dimensional equations of solid mechanics provided certain boundary conditions are satisfied at the interfaces. This approach enables to investigate in the most rigorous way phenomena in the composite microstructure. However, due to the complexity its application is restricted to a very small group of problems. The other approach, or continuum theory, involves significant simplifications. Within the continuum theory a composite is simulated by homogeneous anisotropic material with effective constants, by means of which physical properties of the original material, shape and concentration of components are taken into account. Continuum theory may be applied when the scale of investigated phenomenon (for example, the wavelength of the mode of stability loss l) is considerably smaller than that of material structure (say, the layer thickness h), i.e.

$$l >> h \qquad (1)$$

The approach based on the model of the piecewise homogeneous medium is free from such restrictions and is, therefore, an exact one.

The wide usage of the continuum theory, based on its simplicity in comparison with the model of piecewise-homogeneous medium, puts into consideration the questions of its accuracy and of its domain of applicability. The answer to it may be given only by comparison of the results delivered by both continuum theory and the exact approach, based on the model of the piecewise-homogeneous medium. The last imposes no restrictions on the scale of investigated phenomena and, therefore, has a much larger domain of applicability than the first one. The results obtained within continuum theory must follow from those obtained using the model of piecewise-homogeneous medium if the ratio between the scale of structure and the scale of phenomena tends to zero, i.e. when

$$hl^{-1} \to 0 \qquad (2)$$

If this is the case, the continuum theory may be considered as asymptotically accurate one.

The present investigation is devoted to substantiation of the continuum theory of fracture [4] in compression for laminated composite materials with periodical structure. Within the scope of this theory [4] the moment of stability loss in the structure of material - internal instability according to [1] - is being treated as the beginning of fracture process. By the present time investigations of the continuum theory accuracy, from the model of piecewise-homogeneous medium point of view, have been done only for the problems of statics and wave propagation [2, 9]. But, there are no such investigations for problems on stability loss in composite structure yet.

Basing on the results [5-8] obtained using the model of piecewise-homogeneous medium and three-dimensional linearised theory of deformable bodies stability (TLTDBS) [3], asymptotic accuracy of the continuum theory of plastic fracture is examined in this paper for composites with metal matrix. The investigation is carried out for small pre-critical strains for three-dimensional (non-axisymmetrical and axisymmetrical) as well as for plane problems. Consideration of small strains only is justified, since fracture of composite materials with metal matrix usually happens under small deformations.

ASYMPTOTIC ANALYSIS

Let us consider very briefly the asymptotic analysis of solutions of the stability problems for layered composites in compression. Let composite consist of alternating layers with thicknesses $2h_a$ and $2h_m$, which are simulated respectively by compressible elastic transversally isotropic and elastic-plastic incompressible solids. Thickness of the latter (matrix) is assumed to be larger one. (Henceforth all values referred to these layers will be labelled by indices a and m). Suppose also that the material is compressed in plane of the layers by "dead" loads applied at infinity in such a manner that equal deformations along each layer are provided. The detailed problem statement and solution within the scope of exact approach (i.e. using model of piecewise-homogeneous medium and equations of TLTDBS) for the above materials are given in [7, 8] and for materials with other properties of layers in [5, 6]. It is worth noting that in the case of elastic-plastic layers the generalised concept of continuing loading, which allows to neglect variations of loading and unloading zones during the stability loss, is utilised.

To perform the asymptotic analysis we should apply the condition of applicability of the continuum theory (2) to all formulae of [7, 8] and calculate the limits analytically under this condition, which yields

$$\alpha_a \to 0, \quad \alpha_m \to 0, \quad \text{where} \quad \alpha_a = \pi h_a l^{-1}, \quad \alpha_m = \pi h_m l^{-1}$$

$$\cosh \frac{\alpha_a}{\xi_j^a} \to 1, \quad \sinh \frac{\alpha_a}{\xi_j^a} \to \frac{\alpha_a}{\xi_j^a}, \quad j=2,3$$

$$\cosh \frac{\alpha_m \Re \xi_2^m}{\left|\xi_2^m\right|^2} \to 1, \quad \sinh \frac{\alpha_m \Im \xi_2^m}{\left|\xi_2^m\right|^2} \to \frac{\alpha_m \Im \xi_2^m}{\left|\xi_2^m\right|^2}, \quad \cos \frac{\alpha_m \Re \xi_2^m}{\left|\xi_2^m\right|^2} \to 1, \quad \sin \frac{\alpha_m \Im \xi_2^m}{\left|\xi_2^m\right|^2} \to \frac{\alpha_m \Im \xi_2^m}{\left|\xi_2^m\right|^2} \qquad (3)$$

On substitution of (3) into characteristic determinants derived in [7, 8] for four considered modes of stability loss we get

- for the 1st mode of stability loss

$$\det\left\|\beta'_{pq}\right\| \equiv -\left(\xi_2^{a^{-2}} - \xi_3^{a^{-2}}\right)\overset{a}{\omega}_{1111}\left(\overset{a}{\omega}_{1133}+\overset{a}{\omega}_{1313}\right)\frac{\Re\overset{m}{\xi}_2\Im\overset{m}{\xi}_2}{\left|\overset{m}{\xi}_2\right|^4}\times$$

$$\times\left[\left(\frac{h_m}{h_a}\,\overset{a}{\omega}_{3113}+\overset{m}{\kappa}_{3113}\right)\left(\frac{h_m}{h_a}\,\overset{m}{\kappa}_{1331}+\overset{a}{\omega}_{1331}\right)-\frac{h_m}{h_a}\left(\overset{a}{\omega}_{1313}-\overset{m}{\kappa}_{1313}\right)^2\right]=0 \qquad (4)$$

- for the 2nd mode of stability loss

$$\det\left\|\beta'_{pq}\right\| \equiv -\left(\xi_2^{a^{-2}} - \xi_3^{a^{-2}}\right)\overset{a}{\omega}_{1111}\overset{a}{\omega}_{3113}\left(\overset{a}{\omega}_{1133}+\overset{a}{\omega}_{1313}\right)\frac{\Re\overset{m}{\xi}_2\Im\overset{m}{\xi}_2}{\left|\overset{m}{\xi}_2\right|^4}\left(\overset{m}{\kappa}_{1331}\overset{m}{\kappa}_{3113}\right)^{1/2}=0 \qquad (5)$$

- for the 3rd mode of stability loss

$$\det\left\|\beta'_{pq}\right\| \equiv -\left(\xi_2^{a^{-2}} - \xi_3^{a^{-2}}\right)\frac{\overset{a}{\omega}_{3113}}{\overset{a}{\xi}_2\overset{a}{\xi}_3}\left(\overset{a}{\omega}_{1133}+\overset{a}{\omega}_{1313}\right)\frac{\Re\overset{m}{\xi}_2\Im\overset{m}{\xi}_2}{\left|\overset{m}{\xi}_2\right|^4}\left(\overset{m}{\kappa}_{1331}\overset{m}{\kappa}_{3113}\right)^{1/2}\times$$

$$\times\left[\frac{h_m}{h_a}\left(\frac{h_m}{h_a}\,\overset{a}{\omega}_{3333}+2\overset{a}{\omega}_{1133}+\overset{m}{\kappa}_{3333}+\overset{m}{\kappa}_{1111}-2\overset{m}{\kappa}_{1133}-2\overset{m}{\kappa}_{1313}\right)+\overset{a}{\omega}_{1111}\right]=0 \qquad (6)$$

- for the 4th mode of stability loss

$$\det\left\|\beta'_{pq}\right\| \equiv \left(\xi_2^{a^{-2}} - \xi_3^{a^{-2}}\right)\frac{\overset{a}{\omega}_{1111}\overset{a}{\omega}_{3113}}{\overset{a}{\xi}_2\overset{a}{\xi}_3}\left(\overset{a}{\omega}_{1133}+\overset{a}{\omega}_{1313}\right)\frac{\Re\overset{m}{\xi}_2\Im\overset{m}{\xi}_2}{\left|\overset{m}{\xi}_2\right|^4}=0 \qquad (7)$$

Characteristic equations (4)-(7) correspond to the 1st, 2nd, 3rd and 4th modes of stability loss for the case of biaxial compression (non-axisymmetrical problem). Henceforth only this problem is analysed. Consideration of other problem statements (plane problem in the case of uniaxial compression, axisymmetrical problem in the case of biaxial compression) has proved to lead to the same conclusions.

Let us examine characteristic equations (4)-(7). It was proved in [4] that for approved models of layers

$$\Re\xi_j^{am^2} > 0,\ j=1,2,3;\quad \Im\xi_1^{am^2}=0,\quad \Im\xi_2^{a^2}=\Im\xi_3^{a^2}=0,\quad \xi_2^{m^2}=\overline{\xi_3^{m^2}} \qquad (8)$$

Besides that, the roots of characteristic equations, which correspond to the considered phenomenon of internal instability, must depend on properties of both alternating layers, i.e. on the ratio h_a/h_m. This feature was discussed, for example, in [6-8]. Given the above-said and condition (6), one can observe that characteristic equations (5) and (7), which correspond respectively to the 2nd and 4th modes of stability loss, do not have such roots and, therefore, do not describe the internal instability in the long-wave approximation.

Using formulae of [3, 4], components of tensor **ω**, **κ** may be expressed as

$$\omega^{a}_{1111}=A^{a}_{11}+\sigma^{0\,a}_{11},\quad \omega^{a}_{3333}=A^{a}_{33},\quad \omega^{a}_{1133}=A^{a}_{13},\quad \omega^{a}_{1313}=\mu^{a}_{13},\quad \omega^{a}_{1331}=\mu^{a}_{13}+\sigma^{0\,a}_{11},\quad \omega^{a}_{3113}=\mu^{a}_{13}$$

$$\kappa^{m}_{1111}=A^{m}_{11}+\sigma^{0\,m}_{11},\quad \kappa^{m}_{3333}=A^{m}_{33},\quad \kappa^{m}_{1313}=\mu^{m}_{13},\quad \kappa^{m}_{1331}=\mu^{m}_{13}+\sigma^{0\,m}_{11},\quad \kappa^{m}_{3113}=\mu^{m}_{13} \tag{9}$$

Substitution of (9) into characteristic equation (4), which corresponds to the 1st mode of stability loss, yields for the roots which depend on h_a/h_m

$$\left(1+\frac{h_a}{h_m}\right)^2\mu^{a}_{13}\mu^{m}_{13}+\left(\sigma^{0\,a}_{11}+\frac{h_m}{h_a}\sigma^{0\,m}_{11}\right)\left(\mu^{a}_{13}+\frac{h_m}{h_a}\mu^{m}_{13}\right)=0 \tag{10}$$

Introducing effective values of stresses $\langle\sigma^{0}_{11}\rangle$ and parameters $\langle\mu_{13}\rangle, \langle A_{11}\rangle$ in the moment of stability loss by well-known formulae

$$\langle\sigma^{0}_{11}\rangle=\sigma^{0\,a}_{11}S_a+\sigma^{0\,m}_{11}S_m,\quad \langle\mu_{13}\rangle=\mu^{a}_{13}\mu^{m}_{13}(\mu^{a}_{13}S_m+\mu^{m}_{13}S_a)^{-1},\quad \langle A_{11}\rangle=A^{a}_{11}S_a+A^{m}_{11}S_m \tag{11}$$

where

$$S_a=\frac{h_a}{h_a+h_m},\quad S_m=\frac{h_m}{h_a+h_m} \tag{12}$$

we can obtain from equation (10) that

$$(\Pi^{-}_{1})_T\equiv-\langle\sigma^{0}_{11}\rangle=\langle\mu_{13}\rangle \tag{13}$$

This coincides with the results derived within the scope of continuum theory of plastic fracture for laminated composites [4] given $(\Pi^{-}_{1})_T$ denotes the theoretical strength limit.

As to characteristic equation (6), which corresponds to the 3rd mode of stability loss, we observe that in long-wave approximation this mode yields higher critical stresses than the 1st mode and, therefore, along with the 2nd and 4th modes may be excluded from consideration. Indeed, on substitution of (11), (12) into (6) we get

$$-\langle\sigma^{0}_{11}\rangle=\langle A_{11}\rangle+S_aS_m(A^{a}_{13}-A^{m}_{13})^2(A^{m}_{33}S_a+A^{a}_{33}S_m)^{-1} \tag{14}$$

From the condition of uniqueness of solution of a linear problem for orthotropic bodies it follows [3, 4] that

$$A^{a}_{33}>0,\quad A^{m}_{33}>0 \tag{15}$$

Besides that, real constructive composite materials show higher compressive than shear strength, i.e.

$$\langle A_{11}\rangle>\langle\mu_{13}\rangle \tag{16}$$

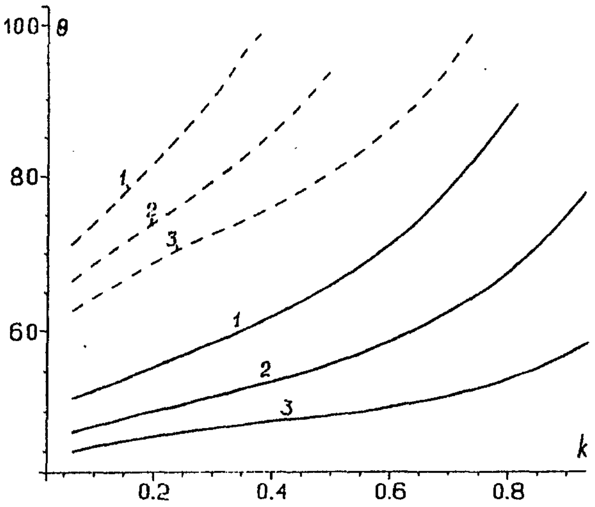

Fig. 1

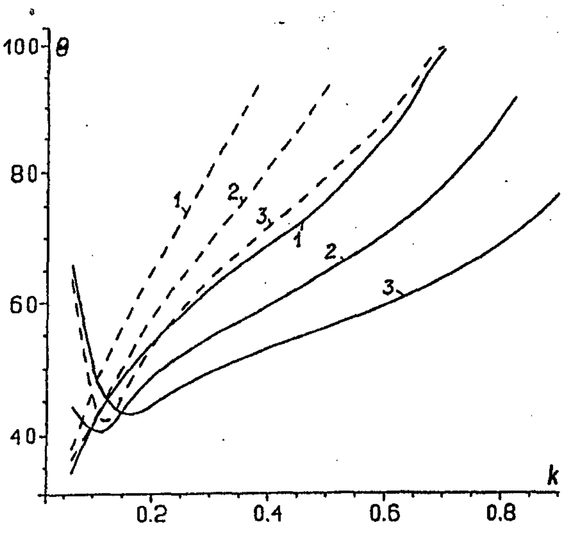

Fig. 2

And, finally, on substitution of (15), (16) into (14) we obtain

$$-\left\langle \sigma_{11}^{0} \right\rangle = \left\langle A_{11} \right\rangle + S_a S_m \left(A_{13}^{a} - A_{13}^{m} \right)^2 \left(A_{33}^{m} S_a + A_{33}^{a} S_m \right)^{-1} > \left\langle A_{11} \right\rangle > \left\langle \mu_{13} \right\rangle \qquad (17)$$

Inequalities (17) clearly show that critical stresses (13) corresponding to the 1st mode of stability loss, are always smaller than those corresponding to the 3rd mode of stability loss (14).

NUMERICAL RESULTS

Now, using the results of the previous section, the accuracy of the continuum theory can be calculated. Values of critical strains (or other critical parameters, e.g. critical stresses) calculated within the scope of exact approach may be found in numerous publications, e.g. [8]. Following these papers values of critical strains for the 1st mode of stability loss under the condition of applicability of the continuum theory (2) are easily obtained. Some papers even show them explicitly. Comparing the above-mentioned values of critical parameters the asymptotic accuracy of the continuum theory of fracture for metal matrix composites in compression can be estimated and conclusions about reasonability of utilisation of this theory can be made properly.

As an example, let us consider a composite consisting of alternating layers of a linear-elastic isotropic compressible filler, which constitutive equation is as follows

$$\sigma_{ij}^{0} = \delta_{ij} \frac{E\nu}{(1+\nu)(1-2\nu)} \varepsilon_{mm}^{0} + \frac{E}{1+\nu} \varepsilon_{ij}^{0} \qquad (18)$$

and an elastic-plastic incompressible matrix with power-mode dependence between equivalent stress and strain in the form

$$\sigma_I^0 = A(\varepsilon_I^0)^k \tag{19}$$

Values of parameter θ (i.e. the ratio of results obtained in the context of exact approach and continuum theory expressed in percentage) calculated following [8] are given on Fig. 1 and Fig. 2 as dependences on parameter k for biaxial and uniaxial compression, respectively. In so doing, values of other parameters were taken as it follows: $\nu = 0.21$; A/E=0.0001 (curves 1), 0.000325 (curves 2), 0.001 (curves 3); $h_a/h_m = 0.02$ (continuous curves on Fig. 1), 0.05 (hatched curves on Fig. 1), 0.03 (continuous curves on Fig. 2), 0.06 (hatched curves on Fig. 2),

CONCLUSIONS

It is rigorously proved for laminated metal matrix composites that the results of the continuum theory of plastic fracture follow as a long-wave approximation from those for the 1st mode of stability loss obtained using the model of piecewise-homogeneous medium. Therefore, the asymptotic accuracy of the continuum theory of plastic fracture for laminated composites in compression is established. The above conclusions were obtained for the cases of biaxial as well as uniaxial compression along layers.

REFERENCES

[1] Biot, M.A. Mechanics of Incremental Deformations. Wiley, New York, USA (1965).

[2] Brekhovskih, L.M. Waves in Laminated Media. Nauka, Moscow (1979). (In Russian)

[3] Guz, A.N. Fundamentals of Three-Dimensional Theory of Deformable Bodies Stability. Vyshcha Shkola, Kiev (1986). (In Russian)

[4] Guz, A.N. Mechanics of Fracture of Composite Materials in Compression. Naukova Dumka, Kiev (1990). (In Russian)

[5] Guz, A.N. and Guz, I.A. "Three-dimensional problems of the stability theory of laminated compressible composite materials". *Theor. and Appl. Mech.* **25**, pp.1080-1085 (1988).

[6] Guz, I.A. "Spatial nonaxisymmetric problems of the theory of stability of laminar highly elastic composite materials". *Soviet Appl. Mech.* **25**, pp.24-32 (1989).

[7] Guz, I.A. "Three-dimensional nonaxisymmetric problems of the theory of stability of composite materials with metallic matrix". *Soviet Appl. Mech.* **25**, pp.1196-1201 (1989).

[8] Guz, I.A. "Internal instability of laminated composites with a metal matrix". *Mech. Comp. Mater.* **26**, pp.762-767 (1990).

[9] Rytov, S.M. "Acoustic properties of small-scale-laminated medium". *Acoustic Journal.* **2**, pp.71-83 (1956). (In Russian)

NONLINEAR FRACTURE ANALYSIS OF HYBRID POLYMER COMPOSITE MATERIALS AND STRUCTURES

E.V. Morozov[1], S.A. Sylantiev[2], E.G. Evseev[2], and H.G. Lessmann[2]

[1] Department of Mechanical Engineering, University of Natal, 4041 Durban, South Africa
[2] Department of Mechanics and Optimisation of Processes and Structures,
MATI - Russian State University of Technology, 3 Orshanskaya Street, Moscow, 125351
Russia

INTRODUCTION

Fracture analysis and prediction of the tolerable defect size play a significant role in the damage-tolerant design for laminated composite structures. Damage-tolerant design for composite structural elements should take into consideration the types of defects possibly occurring during manufacture or service life such as scratches, impact damaged areas, and cracks. Most of the methods and techniques developed in this area were based on the linear approach and principles of linear elastic fracture mechanics. At the same time the development of failure process in the laminated composites quite often exhibits the features of nonlinear behaviour. In particular, these mechanisms of failure could be observed for composites composed of the combinations of cross-ply laminates (i.e., combinations of 0^0 and 90^0 plies), angle ply laminates (combinations of $+\phi$ and $-\phi$ plies), and unidirectional laminates (all 0^0 plies). The situation becomes more complicated in case of implementation of a hybrid composites. Normally, the hybrid composites are used to provide the necessary damage propagation resistance. This property is essential for such applications as aircraft components, helicopter rotor blades, impact resistant structure, etc. The application of the methods of nonlinear fracture mechanics to the analysis of the hybrid polymer composites and structural components is discussed in this paper. The technique is based on the combination of the nonlinear J-contour integral approach and evaluation of the stress intensity factors of hybrid composite materials.

NONLINEAR FRACTURE CHARACTERISTICS OF COMPOSITES

Description of the severity of conditions at a crack tip in a non-linear material can be produced on the basis of J-contour integral approach [1]. The J-contour integral can be interpreted as the potential energy release rate per unit crack opening displacement. In this case we can express the J-contour integral in terms of such experimentally measured parameters as load and displacement for notched specimens subjected to monotone loading [2]

$$J = -\int_0^{\delta} \frac{\partial P}{\partial a}\Big|_{\delta} d\delta = \int_0^{\delta} \frac{\partial P}{\partial b}\Big|_{\delta} d\delta \qquad (1)$$

where P is the load per unit thickness t, a is the half crack length, δ is the load point displacement due to notch opening, h is the specimen width, and $b=h-a$.. The methods for obtaining critical values J_{cr} of J-contour integral are based on the experimental examinations of the notched specimens subjected to the tensile and bending loading. In case of bending the load P can be presented in the following form [3]

$$P = \frac{b^2}{h} F(\delta / h, a / h) \tag{2}$$

Function $F(\delta / h, a / h)$ is determined from the fracture test records [1,2]. Substituting this exdpression for P into equation (1), we can present the J-integral as:

$$J = \frac{2b}{h}\int_0^{\delta} F d\delta - \frac{b^2}{h^3}\int_0^{\delta} \frac{\partial F}{\partial (a/h)} d\delta \tag{3}$$

From the analysis of experimental results on the nonlinear fracture behaviour of composites the following relationship may be obtained

$$\frac{\partial F}{\partial (a/h)} = \alpha F(a/h) \tag{4}$$

The value of the coefficient α may be found by comparing the experimental fracture diagrams obtained for the two geometrically identical specimens with different crack size

$$\alpha = \frac{(P_2 - P_1)h}{(a_2 - a_1)P_1} \tag{5}$$

Typical fracture diagrams are presented in Figure 1.

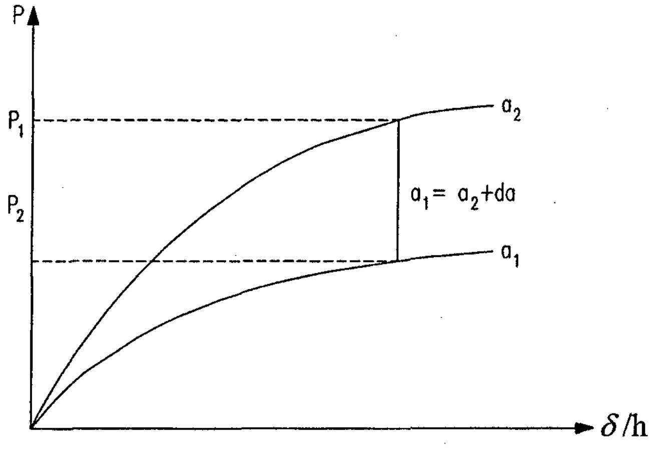

Figure 1. Fracture diagrams for two specimens with the cracks of different lengths.

Taking into account the equations (2) and (5) the critical value J_{cr} can be expressed in the form

$$J_{cr}=\frac{1}{t}\left(\frac{2}{b}+\frac{1}{h(a_2-a_1)}\right)\int_0^{\delta_c}P_1 d\delta-\frac{1}{ht(a_2-a_1)}\int_0^{\delta_c}P_2 d\delta \qquad (6)$$

The following representation of the load per unit thickness t can be used in case of tensile loading [2]

$$P=bF(\delta/h,a/h)$$

Using the procedure similar to outlined above for bending the following equation for J_{cr} can be derived for the tensile stress state

$$J_{cr}=\frac{1}{bt}\int_0^{\delta_c}P_1 d\delta-\frac{1}{ht(a_2-a_1)}\int_0^{\delta_c}(P_2-P_1)d\delta \qquad (7)$$

The critical values of J- integral characterise the material crack resistance and can be used as a means to estimate the maximum defect size for a given stress or the maximum permissible stress for a given intrinsic defect size. Further application of the J -contour integral approach is to convert determined above values of J_{cr} to equivalent stress intensity factors K_{Ic}. It is well known that J -integral is related to the crack opening displacement. The following equation can be used to relate the fracture toughness parameters

$$K_I^2=BJ \qquad (8)$$

where K_I is the stress intensity factor, and B -is the toughness parameter of composite.

STRESS INTENSITY FACTORS FOR HYBRID LAMINATES

Consider a hybrid composite laminate of thickness h. The laminate is composed of N orthotropic layers made of different materials. Each layer has a constant thickness h_i so that $h=\sum_{i=1}^{N}h_i$ .The fibre angles are oriented symmetrically with respect to the middle surface of the laminate. The coordinate axes are x ,y, and z, where z is perpendicular to the laminate plane with the origin lying in the middle surface . The stresses in the coordinate axes are given by

$$[\sigma]=[A][\varepsilon] \qquad (9)$$

where $[\sigma]=(\sigma_x,\sigma_y,\tau_{xy})^T$, $[\varepsilon]=(\varepsilon_x,\varepsilon_y,\gamma_{xy})^T$,

$$[A]=\begin{pmatrix}A_{11} & A_{12} & A_{16}\\ A_{12} & A_{22} & A_{26}\\ A_{16} & A_{26} & A_{66}\end{pmatrix}$$

and A_{mn} are the stiffness coefficients of the laminate given by

$$A_{mn}=\frac{1}{h}\sum_{i=1}^{N}Q_{mn}^{(i)}h_i \quad (m,n=1,2,6),$$

and $\varepsilon_x, \varepsilon_y$, and γ_{xy} denote the normal and shear strains. The constitutive equations for the *i*th layer are presented as follows

$$[s^{(i)}] = [Q_{mn}^{(i)}][\varepsilon]$$

where $[s^{(i)}] = (\sigma_x^{(i)}, \sigma_y^{(i)} \tau_{xy}^{(i)})^T$ denotes the stress vector in the *x-y* coordinate system. The stiffness coefficients $Q_{mn}^{(i)}$ for the separate layer are given by the known relationships expressed in terms of the mechanical characteristics of the unidirectional layers and parameters of fibre orientation [5]. The laminate stresses $[\sigma]$ are related to the stresses acting in the *i*th layer in the following way

$$\sigma_x = \frac{1}{h}\sum_{i=1}^{N} \sigma_x^{(i)} h_i \qquad \sigma_y = \frac{1}{h}\sum_{i=1}^{N} \sigma_y^{(i)} h_i \qquad \tau_{xy} = \frac{1}{h}\sum_{i=1}^{N} \tau_{xy}^{(i)} h_i \tag{10}$$

The laminate contains a through crack of length $2a$ at the centre. The crack is oriented under right angle to the loading direction and tensile stress σ_x correspondingly. In this case the stress intensity factor is presented as

$$K_I = \sigma_x \sqrt{a} Y \tag{11}$$

where Y is a correction function that depends on the notched specimen geometry. Similarly, for the separately considered *i*th layer the stress intensity factor is defined as

$$K_I^{(i)} = \sigma_x^{(i)} \sqrt{a} Y \tag{12}$$

Stresses $\sigma_x^{(i)}$ can be expressed in terms of the stresses σ_x using the equations (9), (10) [5]. As a result the stress intensity factor for *i*th layer may be determined from (12) as follows

$$K_I^{(i)} = \sigma_x h \sqrt{a} Y (Q_{11}^{(i)} A_{22} - Q_{12}^{(i)} A_{12}) / \Delta \tag{13}$$

where $\Delta = A_{11} A_{22} - A_{12}^2$. Substituting equation (13) into (10) and subsequently into equation (11) yields the stress intensity factor for the laminate in the following form

$$K_I = \frac{1}{h}\sum_{i=1}^{N} K_I^{(i)} h_i \tag{14}$$

This equation relates the stress intensity factor of the laminate to the stress intensity factors of the constituting layers. Taking into account the results presented above and following the approach discussed in Reference [4] we can, finally, express the equation (8) as follows

$$J_I = K_I^2 \{A_{11} A_{22} / \Delta[(A_{11} / A_{12})^{1/2} + A_{12} / A_{22} + \Delta / (2 A_{66} A_{22})]\}^{1/2} \tag{15}$$

The analogous equation may be obtained on the basis of similar approach in case of bending loading.

EXPERIMENTAL CRACK RESISTANCE CHARACTERISTICS OF HYBRID COMPOSITES

The central notched specimens of rectangular cross-section were subjected to a tensile test. The directions of loading and reinforcement orientation did not coincide in some cases in order to facilitate the exposure of the nonlinear fracture behaviour. Besides, some of the organic-based materials revealed the non-linearity due to the nature of organic fibres themselves. The edge notched beams made of hybrid materials were used as a specimens for bending tests. Fracture diagrams were registered by means of the high speed shooting technique. Using these results the corresponding J - integrals have been calculated. The following materials have been tested: glass satin fabric/epoxy-phenol plastic EF32-301; unidirectional glass/epoxy composite EDT-10; unidirectional glass/epoxy-phenol plastic VMS-6; hybrid glass-carbon/epoxy-phenol composite reinforced with the glass fabric T-25 (VM) (4 outer layers) and carbon fibre tape LU-3 (7 inner layers); hybrid carbon/epoxy (UKN-500) and organic/epoxy (SVM) composite; unidirectional glass/epoxy plastic T-25(VM). The results of the experiments and calculations are presented in Table 1 (ϕ is the angle of reinforcement orientation).

DAMAGE TOLERANCE OF HELICOPTER ROTOR BLADE

On the basis of the theoretical approach discussed and experimental results obtained for various types of composites the prediction of the tolerable defect sizes has been produced for the composite helicopter blade. The blade was made of hybrid composite material consisting of 16 layers ($\phi = 0^\circ$) and 4 layers ($\phi = 45^\circ$) of T-25 (VM) and 13 layers of LU-3 ($\phi = 0^\circ$). The fibre angles of the layers were oriented symmetrically with respect to the middle surface of the blade wall. The basic set of the mechanical constants of the unidirectional materials involved has been obtained from the

Table 1. Crack resistance characteristics

Material	K_{IC} N/mm $^{3/2}$	J_{IC} N/mm
1. EF32-301 $\phi = 0^\circ$	808	42.6
2. T-25 (VM) $\phi = 0^\circ$ $\phi = 45^\circ$	1500 910	142 87.4
3. EDT-10 $\phi = 5^\circ$	1770	375
4. VMS-6 $\phi = 0^\circ$ $\phi = 25^\circ$ $\phi = 65^\circ$	2250 1460 837	519 336 39.5
5. LU-3, $\phi = 0^\circ$	873	63.3
6. T-25 (VM)+LU-3	1180	-
7. SVM + UKN	-	87.8
8. T-25 (VM) (bending)	-	212

experiments and the corresponding values of $Q_{mn}^{(i)}$ have been calculated. The cross-section of the blade with the working stress of 110 MPa has been identified using the results of the numerical stress analysis. The width of this cross-section of the blade was equal to 220 mm. Using this information and equations (13), (14), and (15) the calculations have been produced for various crack sizes. The results of the computations showed that the maximum allowable crack size was 140 mm (64% of the blade width) for the layer made of T-25 (VM) with ($\phi = 0°$). The critical crack size was equal to 186 mm (85% of the blade width) for the layer made of the same material and angle of reinforcement orientation ($\phi = 45°$). The maximum allowable crack size was found to be of 9.6 mm for the layer made of LU-3, and the critical crack length for the through defect in the blade wall as a whole has been estimated as 73.6 mm.

CONCLUSIONS

The nonlinear fracture behaviour of composite materials should be taken into account in the process of damage-tolerant design. The approach to the nonlinear fracture analysis of hybrid composites discussed in this paper is based on the combination of J -contour integral technique and methods of nonlinear fracture mechanics. The theoretical and experimental results presented in this work demonstrate the possible way of the damage tolerance estimation of composite structural components. The method can be used for fracture analysis and prediction of the tolerable defect size. The designer may take an advantage of this to tailor the mechanical properties distribution over the structure and material combinations in correspondence with the obtained estimates.

ACKNOWLEDGEMENT

The financial support of the Russian Foundation for Fundamental Research (Project 97-01-00856) and South African Foundation for Research Development (GUN 2034618) is gratefully acknowledged.

REFERENCES

[1] Rice, J.R. *Fracture,* Vol. II, ed. by H. Liebowitz, Academic Press, New York (1968).

[2] Ernst, H.A., Paris, P.C., and Landes, J.D. “Estimations on J - integral and tearing modulus from a single specimen test record”, *ASTM STP* **743** (1981).

[3] Rice, J.R., Paris, P.C., and Merkle, G.T. “Some further results of J- integral analysis and estimates.” *ASTM STP* **536** (1973).

[4] Sih, G.C., Paris, P.C., and Irwin, G.R.. “On crack in recti-lineary anisotropic bodies.” *International Journal on Fracture Mechanics* **1,** 3 (1965).

[5] Vorobey, V.V., Morozov, E.V., Tatarnikov, O.V. *Analysis* of *Termoloaded Composite Structures.* Moscow, Mashinostroenie (1992).

A NEW APPROACH TO FATIGUE ANALYSIS IN COMPOSITES BASED ON RESIDUAL STRENGTH DEGRADATION

D. REVUELTA[1], J. CUARTERO[1], A. MIRAVETE[1], R. CLEMENTE[1]

[1] Dept. of Mechanical Engineering, University of Zaragoza, C/ María de Luna, 3, 50015, Zaragoza, Spain

INTRODUCTION

Composite materials applied to transportation are usually subjected to cyclic loads that extend for periods of time longer than the ones traditionally studied. Therefore, it seems necessary to define a prediction model which would extend its range beyond the traditional 10^6 cycles of the S-N curves. This paper develops a prediction model based on the residual strength degradation of composites when subjected to cyclic loads.

FATIGUE THEORIES BASED ON RESIDUAL STRENGTH DEGRADATION

HYPOTHESIS

Composite fatigue theories based on residual strength degradation are based on three assumptions:

1) The static strength follows a two-parameter Weibull distribution

$$P(\sigma_e) = \exp\left[-\left(\frac{\sigma_e}{\beta}\right)^{\alpha}\right] \tag{1}$$

where α and β are the shape and scale parameters of the Weibull distribution. A maximum-likelihood estimation method is used in order to determine both parameters from the static data.

2) Residual strength, σ_r, after n cycles of constant amplitude alternating load is related to the initial static strength, σ_e, through a deterministic equation.

$$\frac{d\sigma}{dn} = -AB\sigma_a^{1/A}\sigma^{1-1/A} \tag{2}$$

where σ, σ_a, A and B are the instantaneous material strength, the maximum applied load, and two dimensionless functions that do not depend on σ.

3) Fatigue failure takes place when the residual strength decreases to the maximum cyclic applied load, i.e., $\sigma_r = \sigma_a$.

FIRST APPROACH

Like A and B are independent from σ, Equation (2) can be integrated to yield:

$$\sigma_r^{1/A} = \sigma_e^{1/A} - B\sigma_a^{1/A}(n-1) \qquad (3)$$

where integration limits are chosen to provide that, if failure takes place over the first cycle, the residual strength, σ_r, equals to the initial static strength, σ_e. Equation (3) may be rewritten as:

$$\sigma_e = \sigma_a\left[\left(\frac{\sigma_r}{\sigma_a}\right)^{1/A} + B(n-1)\right]^A \qquad (4)$$

Assumption 3) stated that fatigue failure takes place when $\sigma_r = \sigma_a$. Therefore:

$$\sigma_e = \sigma_a[1+(N-1)B]^A \qquad (5)$$

where N are the cycles to failure when the applied cyclic stress is σ_a. Equation (5) describes the S-N curve of the material as a function of the two mentioned before dimensionless functions, A and B. These two parameters adopt different forms which may even include the dependence upon the stress ratio, R. However, test data for different stress ratio was not available, so only two fatigue models were assumed depending on the shape of A and B. The two models considered in this paper are:

Model	**A**	**B**
M1	A_0	1
M2	A_0	B_0

Model 1 is the most commonly used power law, where B = 1, that results in a straight line when plotting the S-N curve on a log-log plot. This model is the simplest one, being broadly used by Ran Kim (Ref. [1, 4]). Model 2 is the wearout model, where A and B are constants, and has been used by Sendeckyj and co-workers (Ref. [2, 5-9]). Fatigue theory parameters may be obtained by different estimation procedures, as regression analysis. If the possibility of failure during the first cycle is disregarded, then the life distribution can be obtained by substituting Equation (5) into Equation (1), to get:

$$P(N) = \exp\left[-\left(\frac{N-\Delta}{\beta_f}\right)^{\alpha_f}\right] \qquad (5)$$

where $\alpha_f = A\alpha$; $\beta_f = \frac{(\beta/\sigma_a)^{1/A}}{B}$; $\Delta = -(1-B)/B$

Finally, the residual strength distribution can be obtained by substituting Equation (3) into Equation (1), to yield:

$$P(\sigma_r) = \exp\left\{-\left[\left(\frac{\sigma_r}{\beta}\right)^{1/A} + \left(\frac{\sigma_a}{\beta}\right)^{1/A} B(n-1)\right]^{\alpha A}\right\} \qquad (6)$$

Equation (5) resembles a three-parameter Weibull distribution. Ran Kim (Ref. [1]) uses this resemblance to formulate his residual strength degradation model. However, he does not take into account the influence of more-than-one parameter S-N curves. It is observed through experimental tests that the shape parameter, $\alpha_f = \alpha A$, does not depend upon the applied stress level in fatigue tests. Therefore, it may be inferred that a combined shape parameter exists for the whole fatigue distribution in the material. This parameter is figured out by normalizing the cycles for each stress level over the corresponding pooled Weibull scale parameter, β_i, for that stress level. Maximum-likelihood method may be used again to calculate the combined shape parameter once the data have been normalized.

On the other hand, Equation (5) defines β_f as $(\beta / \sigma_a)^{1/A}/B$. The β_f parameter is the scale parameter of a Weibull distribution. Then, due to the own nature of the distribution, this parameter means the value of the characteristic life of the distribution. In the case of fatigue, the characteristic life is the fatigue life, N.

$$\beta f \cong N \tag{7}$$

The life N is found out from the S-N curve equation, Equation (5). Introducing these changes onto Equations (5) and (6), the new residual strength distribution and fatigue life distribution equations for each fatigue model are obtained:

$$P(\sigma_r) = \exp\left\{-\left[\left(\frac{\sigma_r}{\beta}\right)^{\alpha/\alpha_f} + \frac{(n-1)}{(\sigma_e/\sigma_a)^{1/A}}\right]^{\alpha_f}\right\}$$

Model M1, Equation (8)

$$P(\sigma_r) = \exp\left\{-\left[\left(\frac{\sigma_r}{\beta}\right)^{\alpha/\alpha_f} + \frac{(n-1)}{\frac{(\sigma_e/\sigma_a)^{1/A}-1}{B}+1}\right]^{\alpha_f}\right\}$$

Model M2, Equation (9)

$$P(N) = \exp\left[-\left(\frac{N-\Delta}{(\sigma_e/\sigma_a)^{1/A}}\right)^{\alpha_f}\right]$$

Model M1, Equation (10)

$$P(N) = \exp\left[-\left(\frac{N-\Delta}{\frac{(\sigma_e/\sigma_a)^{1/A}-1}{B}+1}\right)^{\alpha_f}\right]$$

Model M2, Equation (11)

Theoretical curves described by Equations (8) and (9) are presented together with the experimental residual strength data for different fatigue lives and applied stresses, for three different material systems: a glass fibre reinforced polyester, a glass fibre reinforced epoxy, and a carbon fibre reinforced epoxy. Probabilities of survival for the residual strength data are obtained through the median rank formula, f(x) = 1 - (i - 0.3) / (n + 0.4), where i is the ith test specimen for a sample size of n specimens.

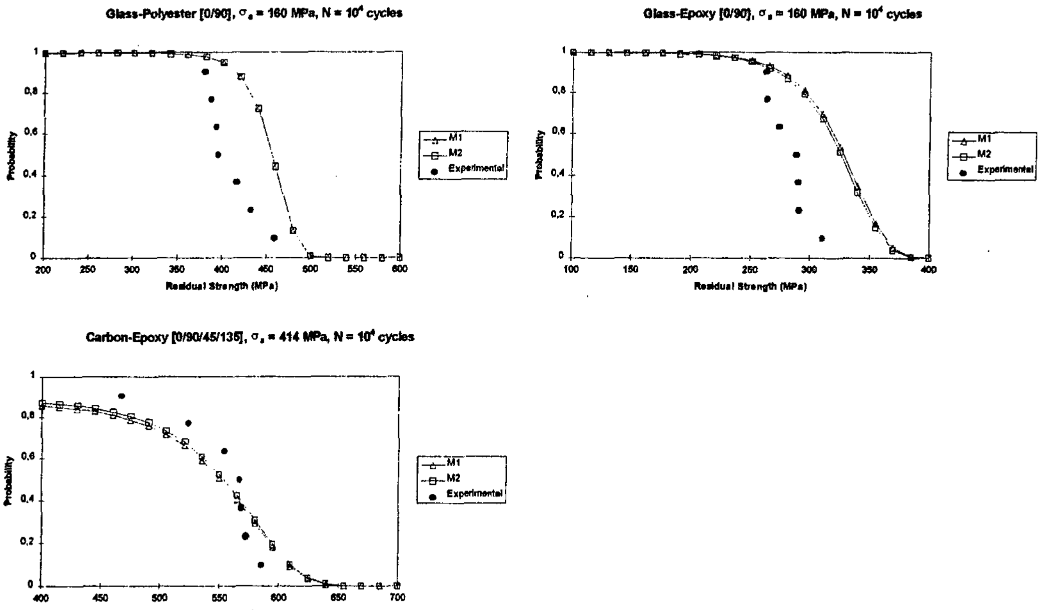

Fig. 1. Residual Strength Distributions

It is noticed that, for glass fibre reinforced composites, experimental data appear to be located to the left of the theoretical prediction. Therefore, Equations (8) and (9) are not a good prediction method.

In the case of the carbon fibre reinforced composite, the model seems to fit more satisfactorily to the experimental data. A possible explanation about this divergence between glass and carbon fibre may be the worse glass composite fatigue behaviour than carbon composites, which translates into a greater data dispersion. Thus, it was necessary to revise the statistical parameter determination procedure by introducing confidence bounds which may be able to issue a safe design value.

SECOND APPROACH (PROBABILISTIC)

The great existing divergence between the theoretical prediction and the experimental data made necessary the revision of the probabilistic procedures for estimating the shape and scale parameters, α and β, for both Weibull distributions, fatigue and static distributions.

Fortunately, maximum likelihood method issues the advantage that confidence bounds may be calculated for the α and β estimations.

If $\overline{\beta}$ means the Weibull scale parameter estimation issued from the static data through the maximum likelihood method - Equation (10) -, the 95% confidence bound for the scale parameter, β, may be obtained from:

$$P(\tilde{\alpha}\ln(\tilde{\beta}/\beta) < l^{*}_{0,95}) = 0{,}95 \qquad (12)$$

where $\bar{\alpha}$ is the shape Weibull parameter estimation from the static strength distribution, and $l^{*}_{0,95}$ is the statistic critical value that verifies Equation (12).

If $\underline{\beta}$ names the lower limit of the 95% confidence bound, then:

$$\underline{\beta} = \tilde{\beta}\ \exp[-(l^{*}_{0,95}/\tilde{\alpha})] \qquad (13)$$

Admissible value B, X_B, is a fatigue design value for a material. It is defined by the probabilistic assessment that is 95% reliable the statement that the probability of survival of the admissible value B is 90%. Thus, admissible value B, X_B, may be obtained from:

$$P(X_B) = \exp[-(X_B/\tilde{\beta})^{\tilde{\alpha}}] = 0{,}90 \quad \Rightarrow \quad X_B = \underline{\beta}\,[-\ln(0{,}90)]^{1/\tilde{\alpha}} \qquad (14)$$

The admissible value X_B is introduced in the formulation instead of β to get:

In fatigue, the lower limit for the confidence bound is obtained at 95% certainty for each stress level; afterwards, the admissible value X_{Bi} is calculated for each stress level. Fatigue data is then normalised by X_{Bi} to get the shape and scale parameter of the fatigue life distribution.

The admissible value X_B is introduced in the formulation instead of β to get:

$$P(\sigma_r) = \exp\left\{-\left[\left(\frac{\sigma_r}{X_B}\right)^{\alpha/\alpha_f} + \frac{(n-1)}{(\sigma_e/\sigma_a)^{1/A}}\right]^{\alpha_f}\right\} \qquad P(\sigma_r) = \exp\left\{-\left[\left(\frac{\sigma_r}{X_B}\right)^{\alpha/\alpha_f} + \frac{(n-1)}{\frac{(\sigma_e/\sigma_a)^{1/A}-1}{B}+1}\right]^{\alpha_f}\right\}$$

Model M1, Equation (15) Model M2, Ecuación (16)

Equations (15) and (16) are plotted with the residual strength experimental data, their probabilities of survival obtained through the median rank formula. At last, fatigue life distributions are plotted according to Equations (10) and (11).

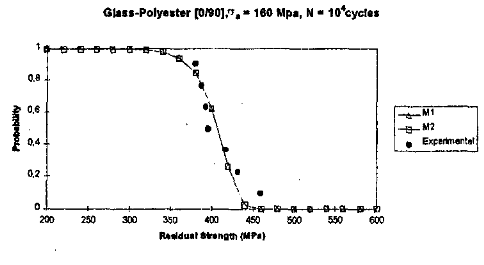

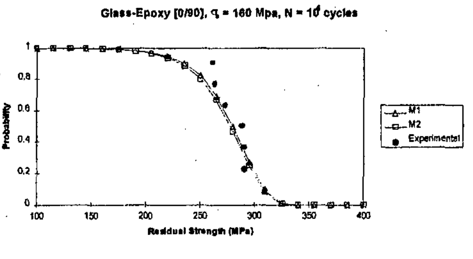

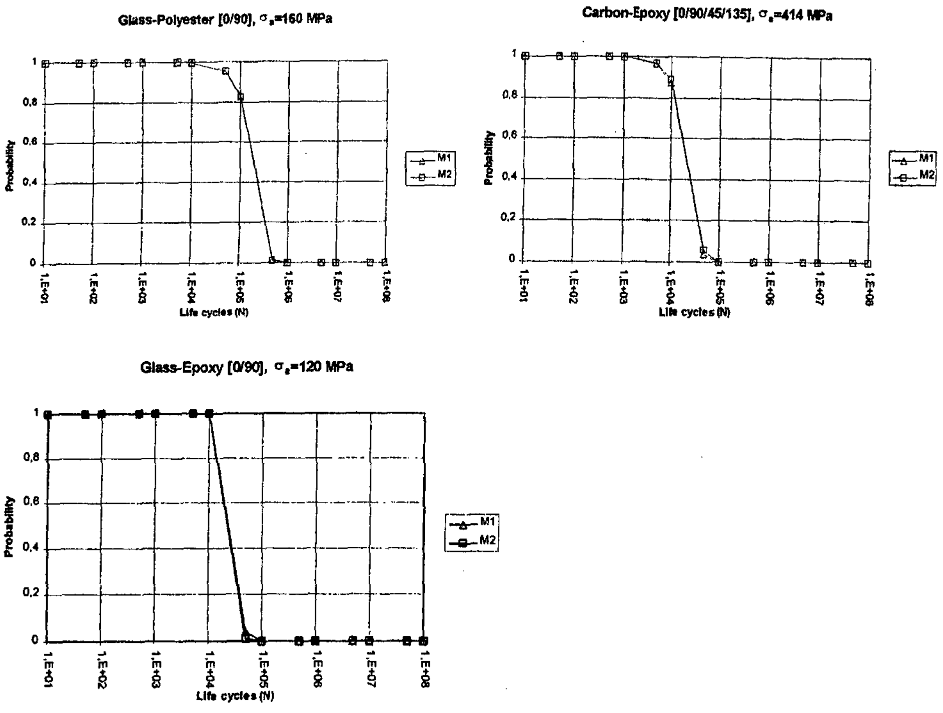

Fig. 2. Residual Strength Curves (probabilistic approach) and Fatigue LifeDistributions

CONCLUSIONS

- It has been shown that the Weibull distribution also models the fatigue response of polymeric matrix composites.
- The introduction of more complex fatigue models than the traditionally used linear model to characterise the S-N curve does not yield a significant better fit of the curves to the experimental data.
- The introduction of confidence bounds and admissible design values in the fatigue parameters estimation procedures is necessary in glass fibre reinforced composites.
- The use of confidence bounds in carbon fibre reinforced composites does not appear to be needed, maybe due to the better fatigue response of this kind of composites.

REFERENCES

1. Kim, R.Y., Donaldson, S.L., 'Life prediction of glass/vinylester and glass/polyester composites under fatigue loading', *ICCM*, **10**, 1995.
2. Sendeckyj, G.P., Reifsnider, K.L., (Ed.), 'Life prediction for resin-matrix composite materials', *Composite Materials Series*, **Vol. 4, 10**, p.431, Elsevier Science Publishers, 1991.

IMPACT PERFORATION OF THIN STIFFENED CFRP PANELS

M. S. Found, I. C. Howard and A. P. Paran
SIRIUS, Department of Mechanical Engineering,
University of Sheffield, Sheffield, UK

INTRODUCTION

Due to the lack of adequate predictive methods for determining the damage tolerance of composite structures many present design tend to be conservative such that the potential weight-saving is not achieved. Improvements in resistance to impact damage may be obtained with the use of a thin membrane to absorb the energy with structural stiffness being provided by other means. Previously this has often involved the use of a honeycomb core with CFRP skins to provide a sandwich section. However in service such structures, if damaged, prove difficult to repair. Therefore the use of local stiffeners has been recognised as an alternative means of providing structural stiffness for thin membranes [1-5].

Whilst there are no known references on the impact perforation of stiffened panels attempts to model perforation of CFRP plain panels have been undertaken by a number of workers based on energy considerations. Cantwell and Morton [6] showed that elastic deformations, delaminations and shear-out were the main mechanisms, whilst Delfosse and Poursartip [7] identified the proportions of matrix damage and fibre damage absorbed at perforation. This paper suggests a means of predicting the impact perforation threshold energy based on the static perforation energy associated with a static indentation test. CFRP T-stiffened panels are subjected to dropweight impact and static indentation tests and comparisons made with plain panels of similar lay-up.

EXPERIMENTAL

CFRP panels nominally 300 x 300 mm, stiffened with three parallel T-blades of 100 mm pitch were supplied by Hurel-Dubois UK. The blades measured 25 mm wide x 12.5 mm deep and the webs were produced from two plies back-to-back with the ends bent at 90° to form a single thickness for the flange. Plain panels of the same three-ply lay-up were also supplied for comparison. The material was a five-harness satin weave carbon fibre preimpregnated with an epoxy resin designated 914C-713-40 and supplied by Hexcel Composites. The panels were laid up in three plies as (0/90, ±45, 0/90) and 0/90 stiffeners added, each panel being moulded in one shot by Hurel-Dubois at a nominal 58% fibre volume fraction.

An instrumented dropweight impact rig, described in Refs. [8, 9], was used for both static indentation tests and low velocity impact tests. The panels were clamped to the same ring pressure using two annular rings ranging from 100 to 300 mm internal diameter, the lower ring having slots to accept the webs of the stiffeners. Dropweight impact tests were conducted from a height of 0.5 m to produce an impact velocity of the impactor of about 3 m/s. The impact forces and displacements were obtained from data that was processed through a digital low-pass filter set at a cut-off frequency of 3.5 kHz [9]. Static indentation and impact tests were performed on the stiffened panels at three different locations namely; in the bay between the stiffeners, at the toe of stiffeners and directly in-line with stiffeners. Damage was assessed using x-radiography and microscopy techniques in order to determine the principal failure mechanisms of backface cracking, delamination and permanent indentation of the frontface.

RESULTS AND DISCUSSION

Figure 1 shows typical force-displacement plots for plain and stiffened panels of 100 mm diameter obtained from static indentation tests. Note that for panels of this size, indentation between the stiffeners is very similar to indentation on a plain panel since only a small length of the toes of adjacent stiffeners are encompassed within the test diameter. The sudden load reduction of the stiffened panel is associated with a vertical crack in the web of the stiffener immediately below the point of contact of the indentor. However, the load increases again as the rest of the panel responds at reduced stiffness, but still greater than that of a plain panel, to produce a maximum force of more than twice that of a plain panel. The second damage load identifies onset of damage in the panel in the form of backface cracking and remains dominant up to about the average peak force when delaminations become dominant. At the start of the downside of the load-displacement plot fibre fracture is significant leading to perforation of the panel. The fractured portion of the web appeared to obstruct the progress of the indentor and impeded the perforation of the panel. Figure 2 shows the influence of increasing the test panel size up to 300 mm such that testing at a position between the stiffeners is now different to the response of a plain panel. Whilst the peak force is similar for the plain panel and for testing between the stiffeners of a stiffened panel a greater indentor displacement is required to perforate the plain panels. Hence the static perforation energy is higher for the plain panels due to their ability to store more energy. Comparing Figures 1 and 2 shows that increasing the panel diameter makes the panels more compliant reducing the peak force on the stiffener but increasing the displacement and perforation energy.

Figure 3 shows a plot of normalised peak force for indentation on the stiffener for the 300 mm panel identified in Figure 2. Often the peak force is not clearly defined and therefore an average peak force is determined. This is obtained from the area under the force-displacement curve from the second damage load to the corresponding position on the downside of the plot. The second damage load is identified by the small change in the upside of the plot and is associated with damage in the panel which occurs at approximately 85% of the peak force. Note that the first damage load is associated with cracking of the web of the stiffener. Also shown in Figure 3 is the normalised work done by the indentor during the test. The static perforation energy of the panel may be estimated in terms of maximum work done by the indentor to produce upperbound and lowerbound values. The former is obtained from the crossover of the two plots in Figure 3 which occurs at approximately 82% of the maximum work done by the indentor to give an estimated static perforation energy of 5.58 J when the panel is tested in-line with the stiffener. The lower value is determined from the work done by the indentor at the median displacement associated with the average peak force which occurs at approximately 60% of the maximum work done to produce an estimated static perforation energy of 4.12 J.

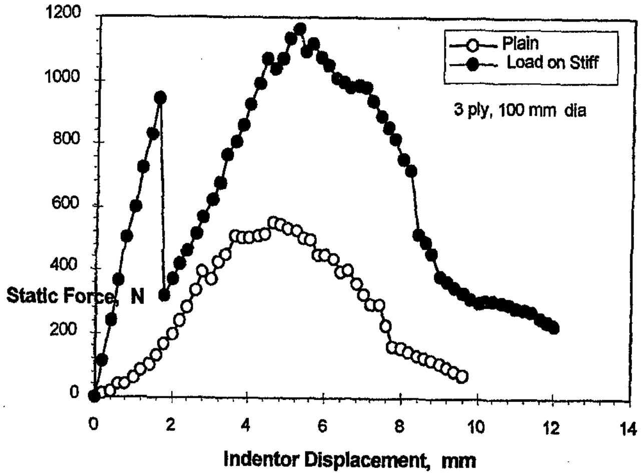

Figure 1.

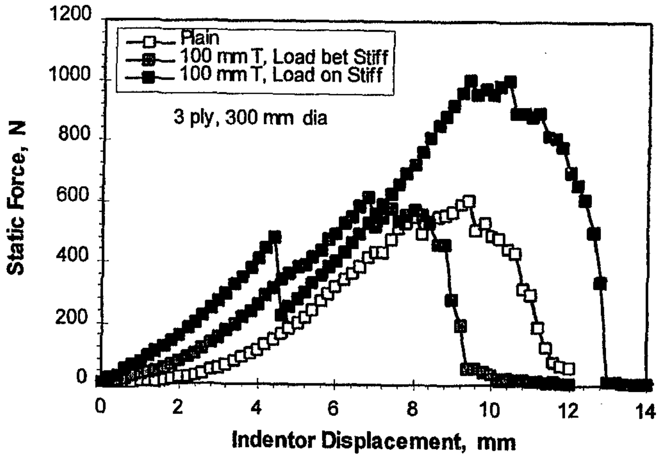

Figure 2.

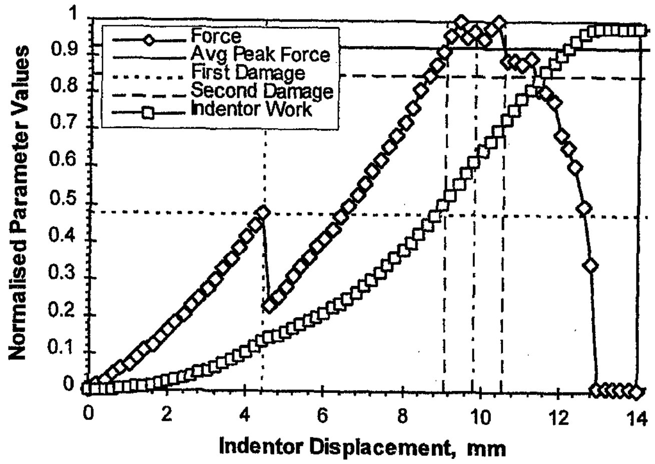

Figure 3.

Table 1. Comparison of lower and upperbound static perforation energies with impact perforation energies for 300 mm panels

Panel type and indentor location	Plain panel	Stiffened panel	
		between stiffeners	on stiffener
Static perforation energy J	1.82 2.50	1.85 2.44	4.12 5.58
Impact perforation energy J	2.75	2.73	5.62

The static perforation energy also appears to be related to the impact perforation threshold as shown in Table 1. The upperbound values of the static perforation energy appear to give a reasonable estimate of the impact perforation threshold energy. We have previously presented [8] energy maps as a means of identifying the different mechanisms that develop from initial damage to perforation for plain panels subjected to impact. In this paper Figures 4 to 6 represent energy maps relating to the principal failure mechanisms of stiffened panels compared with plain panels of 300 mm diameter. Figure 4 shows that whilst the maximum backface crack length is not significantly different for each of the test conditions, that when tested in-line with a stiffener the largest damage occurs at a much higher energy and that the perforation energy is also greater. The backface cracking presented in Figure 4 refers to damage in the actual panel. For a stiffened panel subjected to impact on a stiffener, there is additionally a vertical crack in the web of the stiffener which occurs prior to damage in the panel as earlier identified for the static case. Figures 5 and 6 for delamination area and permanent indentation of the frontface of the panels respectively, show similar trends to those identified in Figure 4 for backface cracking. They confirm that stiffened panels subjected to impact between the stiffeners behave in a similar manner to that of plain panels.

CONCLUSIONS

Static indentation and dropweight impact tests have been conducted on thin CFRP blade-stiffened panels and comparisons made with similar plain panels. The static perforation energy may be estimated from the work done by the indentor and the values used to estimate the impact perforation threshold energy. The response of stiffened panels loaded between the stiffeners is similar to that of plain panels. As expected, the perforation energy is significantly increased when tests are conducted in-line with the stiffeners. The principal failure mechanisms of backface cracking, delamination and permanent indentation of the frontface have been identified and represented in the form of energy maps. For panels loaded in-line with a stiffener the maximum damage levels occur at higher energies than for the other panel conditions, however, the damage is preceded by vertical cracking of the web of the stiffener.

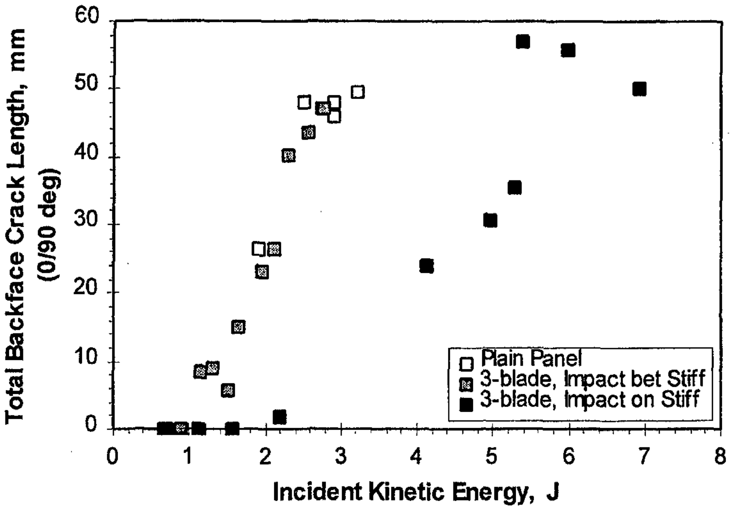

Figure 4.

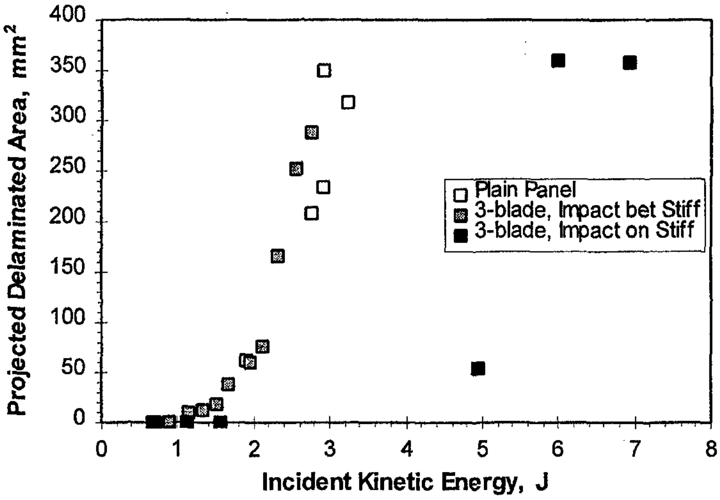

Figure 5.

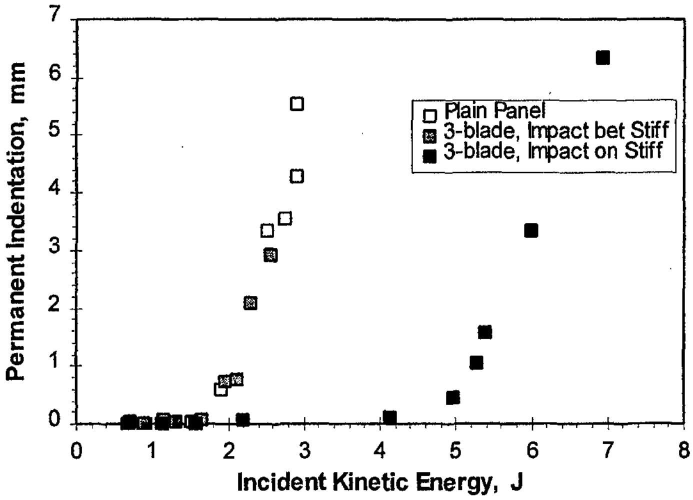

Figure 6.

REFERENCES

[1] Found, M. S., Howard, I. C. and Paran, A. P. Impact behaviour of stiffened CFRP sections. Composite Structures, 39, 3-4, pp. 229-235 (1997).

[2] Wiggenraad, J. F. M., Aoki, R., Gadke, M., Greenhalgh, E., Hachenberg, D., Wolf, K. and Bubl, R. Damage propagation in composite structural elements - analysis and experiments on structures. Composite Structures, 36, pp. 173-186 (1996).

[3] Greenhalgh, E., Bishop, S. M., Bray, D., Hughes, D., Lahiff, S. and Millson, B. Characterisation of impact damage in skin-stringer composite structures. ibid, pp. 187-207.

[4] Gadke, M., Geier, B., Goetting, H-C, Klein, H., Rohwer, K. and Zimmermann, R. Damage influence on the buckling load of CFRP stringer-stiffened panels. ibid, pp. 249-275.

[5] Stevens, K. A., Ricci, R. and Davies, G. A. O. Buckling and postbuckling of composite structures. Composite Structures, 26, pp. 189-1999 (1995).

[6] Cantwell, W. J. and Morton, J. Impact perforation of carbon fibre reinforced plastic. Composite Science and Technology, 38, 2, pp. 119-141 (1990).

[7] Delfosse, D. and Poursartip, A. Energy-based approach to impact damage in CFRP laminates. Composites, 28A, pp. 647-655 (1997).

[8] Found, M. S., Howard, I. C. and Paran, A. P. Size effects in thin CFRP panels subjected to impact. Composite Structures, 38, 1-4, pp. 599-607 (1997).

[9] Found, M. S., Howard, I. C. and Paran, A. P. Interpretation of signals from dropweight impact tests. Composite Structures, in press (1998).

DAMAGE DEVELOPMENT ASSESSMENT IN GRP PIPES UNDER BIAXIAL LOADING CONDITIONS

L. Gołaski[1], J. Schmidt[2] and I.Baran[2].

[1] Kielce University of Technology
[2] Foundry Research Institute, Zakopiańska 73 str., Krakow, Poland

INTRODUCTION

In most of failure criteria which are used to predict the strength of laminates under any anticipated loading conditions the behavior of single lamina is not included. However it is obvious that at the beginning failure processes start in single lamina as a part of laminate. Therefore there is a strong need to improve the method of laminate strength prediction on the basis of strength data determined on monolayer composite. For these purposes more information about damage accumulation in laminate during loading is necessary. It should be noticed that most of damage parameters for laminates (remaining strength, changes in stiffness modules, dumping or any other „characteristic damage parameters") do not indicate the „critical events" in fracture processes because these parameters depend on loading modes as a rule. Therefore an approach where the damage accumulation is analyzed „in situ" in reference to the strength of single lamina seems to be useful. To follow the development of damage accumulation in composites, an acoustic emission method was applied with success for both composites and laminates under different loading modes [1,2,3,4,5,6]. However, to detect the critical events in failure of laminates, a more comprehensive analysis of AE signals is necessary. In this paper the results of AE signals analysis produced during failure of polyester glass fiber reinforced laminates in reference to failure criterion is presented.

MATERIALS AND TREATMENT

The tested laminate was four layer cross ply one. This laminate makes up the wall of filament pipes wound at $\phi = \pm 54°44'$. Fiberglass Ltd. Superwind 20/70 E glass fiber was used. The resin was a terephtalic polyester resin Impol T400. The average volume fraction of fibers was $V_f \sim 0.5$. The tubular specimens were subjected to seven different loading modes. The pipes were loaded up to the loss of loading capacity. This loss of loading capacity depends on loading modes and rather does not coincide with the sample collapse. The strength data of tested laminate are given in papers [2,7].

On the basis of these results, an attempt was made to develop the failure envelope. For this reason the Tsai - Wu [4] criterion was applied which is given by formula:

$$(- 1131\sigma_1 + 971\sigma_2 + 5.15\,\sigma_1^2 + 11.7\sigma_2^2 - 12.51\sigma_1\sigma_2) * 10^{-5} = 1 \qquad (1)$$

The failure envelope described by Eqn.1, is shown in Fig.1. The black spots concern the experimental data.

To investigate the mechanisms which took place in laminate during loading it is important to know the properties of single lamina. The single lamina reinforced with undirected fibers may be considered as a transversely isotropic material. For such materials stress components are defined with respect to the symmetry axis. They are: normal stress parallel to fiber $\sigma_{//}$ normal stress perpendicular to fiber $\sigma_{\perp}$ and shear stress referred to the fiber and perpendicular direction $\tau_{\#}$. To determine these stress components for single lamina at fracture, hoop wound pipes were loaded in tension, compression, torsion and internally pressurized. During tension and torsion of hoop wound pipes, acoustic emission was recorded in order to estimate the beginning of failure. The AE activity was evaluated as RMS voltage. The hoop wound pipe in tension exhibits linear stress - strain character and no acoustic emission was observed up to failure at stress $\sigma_{\perp}$=14 MPa. Samples under torsion exhibit nonlinear shear stress - angular deformation plot and the beginning of fracture indicated by AE took place at shear stress $\tau_{\#}$ ~18 MPa. Significant increasing in AE activity at shear stress $\tau_{\#}$ ~35 MPa suggests changes in failure mechanism.

To estimate the beginning of fracture in single lamina, when it is a part of the laminate, the stress components in lamina should be known for any anticipated loading modes. These components were computed for biaxial loading applied in the symmetry axis of laminate (axial and hoop direction in tubular specimens). Stress calculations were made using Puck solution [8]. For considered laminate the stress components in lamina in dependence on applied loading are as below [7]:

$$\begin{aligned} \sigma_{||} &= 0.972\sigma_H + 0.414\sigma_A + 1.549\tau_A \\ \sigma_{\perp} &= 0.027\sigma_H + 0.582\sigma_A + 0.650\tau_{AH} \qquad (2) \\ \tau_{\#} &= 0.363\sigma_H - 0.500\sigma_A + 0.117\tau_{AH} \end{aligned}$$

where: σ_H-stress in hoop direction of pipe, σ_A-stress in axial direction of pipe
τ_{AH}-stress referred to axial direction of pipe.

To estimate fracture in single lamina as a part of laminate, the maximum stress criterion was applied. Thus, it was assumed that the failure takes place when one of stress components in the lamina is equal to its critical value. When these critical stress components are introduced into left hand side of equations (2), the failure criteria for the beginning of failure processes in single lamina are obtained. These criteria are superposed on Tsai - Wu criterion in Fig.1. The dot lines represent the beginning of fracture while the solid lines parallel to them - the final fracture under shear. The other two straight lines represent fracture due to the normal stress perpendicular to the fiber - positive and negative, respectively. It is expected that failure processes are started at stress levels enough high to exceed any of the critical stress for single lamina.

In this analysis, to follow the failure processes of cross ply pipes, and to detect the beginning of fracture an acoustic emission technique was applied. For AE events data acquisition, the acoustic emission processor GACEK with broad band sensor was used. The acoustic emission behavior of tested laminate was changed significantly in accordance to the loading mode. As an example, the loading and acoustic emission intensity plotted against time for specimen in tension is shown in Fig.2, while in Fig.3 the intensity of acoustic emission for pipe in compression is given. As it can be seen in Fig. 2, the beginning of AE starts at stress σ_A ~26 MPa, which corresponds to $\sigma_{\perp}$ ~ 13 MPa and $\tau_{\#}$ ~ 13 MPa. Because normal stress $\sigma_{\perp}$ is close to its critical stress $\sigma_{\perp T}$ it seems that cracking due to this stress component took place. Intensive AE starts at σ_A~ 56 MPa when shear stress exceeds its critical value for the beginning of shear fracture. At the same time whitening of pipe as a result of matrix fiber debonding is observed. This damage results in decreasing of loading capacity of samples. Some fiber rotation towards specimen axis was observed which indicates that delamination took place.

During axial compression, acoustic emission was observed when the shear stress $\tau_{\#}$ was of the range from 20 to 50 MPa. The compressive stress $\sigma_{\perp}$ perpendicular to fibers was well below its critical values, thus cracking due to shear could take place. This was confirmed by single white lines parallel to fibers which appeared at the same time as AE. Only limited number of events was detected. Intensive AE took place during final failure. After sample collapse, damage of laminate by shear can be seen.

DISCUSSION

For all applied loading modes, the acoustic emission started when the normal stress perpendicular to fibers or shear stress parallel to fibers were equal to their critical value determined for single lamina. At the beginning the observed AE was a burst type and the number of acoustic events was limited. Intensive AE activity was observed at higher loading levels for selected loading modes. They are axial tension, biaxial tension and, in a less degree, hoop tension. High acoustic emission was accompanied by whitening of pipe walls. These phenomena occurred in samples in axial and biaxial tension when both stress components in lamina normal to fibers and shear parallel to fibers exceeded their critical values. The strong acoustic emission for these two loading modes resulted from intensive cracking of laminae and fibers matrix decoupling. In addition, for samples under axial and hoop tension some fibers rotation towards axis of sample was observed. This suggests that delamination has some contribution to AE, too. Details concerning results of acoustic emission analysis of failure processes in tested laminate is given elsewhere [6].

A coincidence of the beginning of acoustic emission activity with critical stress in single lamina attained in tested laminate suggests that lamina properties and failure mechanisms in lamina are particularly relevant to the prediction of laminate failure. The simple analysis of AE signals provided data for damage development intensity and accumulation analysis, however it is not possible to detect the critical events in failure process. Therefore an attempt has been made to apply multiparameter recognition of AE signals for more detailed analysis of failure process. For this purpose PAC MISTRAS AE processor has been applied. Four broad band sensors were located near the pipe ends. The pipes were smoothly pressurized at constant rate equal to 0.6 bar/s. The events summation, events rate, energy summation, energy rate, events duration and RMS voltage have been recorded vs. pressure. Selected results for pipe loaded in M II are given in Fig.4. As it can be seen in Fig.4(a) scr.1-4 events summation and events rate are the same for both channels. However, when energy and energy rate vs. pressure is taken it can be seen the diagrams for both channels are different (see Figs. 4(b) scr.28-31). The differences result from different distances between each sensor and the point where failure processes take place. Therefore to evaluate, with the help of acoustic emission, the critical load corresponding to the most intensive failure processes, a number of AE parameters should be taken into consideration. As an example, a three dimensional the diagrams are shown for pipe loaded in Mode II and in Mode III where number of counts vs. pressure and AE signals amplitude is given (see Figs. 4(c)).

CONCLUSIONS

The tests of laminate after failure process examined with the help of acoustic emission technique together with signs of damage observation show that failure processes involved different mechanisms according to the loading modes and applied loading. It should be noticed that the major axis of failure ellipse is nearly parallel to envelopes resulting from critical shear stress condition. The observed discrepancies between lower branch of Tsai - Wu criterion and shear stress criterion may be caused by friction between fibers during their reorientation.

The acoustic emission activity indicated that failure mechanisms depends strongly on loading mode.

Multiparameter analysis of AE signals can be useful to determine loading range where the failure process is the most intensive.

REFERENCES

[1] Gołaski, L., Kumosa, M., Hull, D. "On acoustic emission testing of filament wound pipes under repeated loading." *J. Acoust. Emission* 1, pp.95 - 101 (1982).
[2] Gołaski L., Hull D., Kumosa M. "Acoustic emission from filament wound pipes under long term loading conditions." *Proc. IV Int. Conf. Mechanical Behaviour of Materials*, Pergamon Press, Oxford Vol.1, pp.557 - 563 (1983).
[3] Gołaski L., Figiel A. „Testing stresss corrosion of glass reinforced plastic with acoustic emission monitorning" *J. Acoust. Emission* 4, pp.182 - 185 (1985).
[4] Gołaski L., Schmidt L. "Fracture Toughness Test of Short Fibrę Composites, Journal of Theoretical and Applied Mechanics 32, pp.261 - 272 (1994).
[5] Gołaski L., Schmidt J., Kujawinska M., Salbut L. *"Fracture phenomena and strain distribution at the vicinity of crack tip in short fibre composites"*, Proc. 10th Int. Conference on Experimental Mechanics", Lisbon 1994, Ed: J.F. Silva, A.A. Balkema, Rotterdam, pp.1307 - 1312 (1994).
[6] Gołaski L., Ono K. *"Acoustic emission analysis of laminate failure mechanisms with reference to failure criteria"*, Int .Conf. Acoustic Emission from Composites Materials 5, Sundswall, Sveden, ASNT Columbus pp.170 - 175 (1995).
[7] Gołaski L *"Failure Behaviour of laminates under combined loading conditions"*, EC Paris - Kielce UT Joint Seminary on Failure of Advanced Materials, Paris November 1994, Ed.D. Francois and L. Gołaski, TUK Publisher, pp. 37 - 62 (1996).
[8] Puck A. *"Zur Beanspruchungund Verformung von GFK - Mehrschichtenverbund - Bauelementen"*, Kunstoffe 57, pp. 284 - 293, 573 - 582 and 965 - 973 (1967).

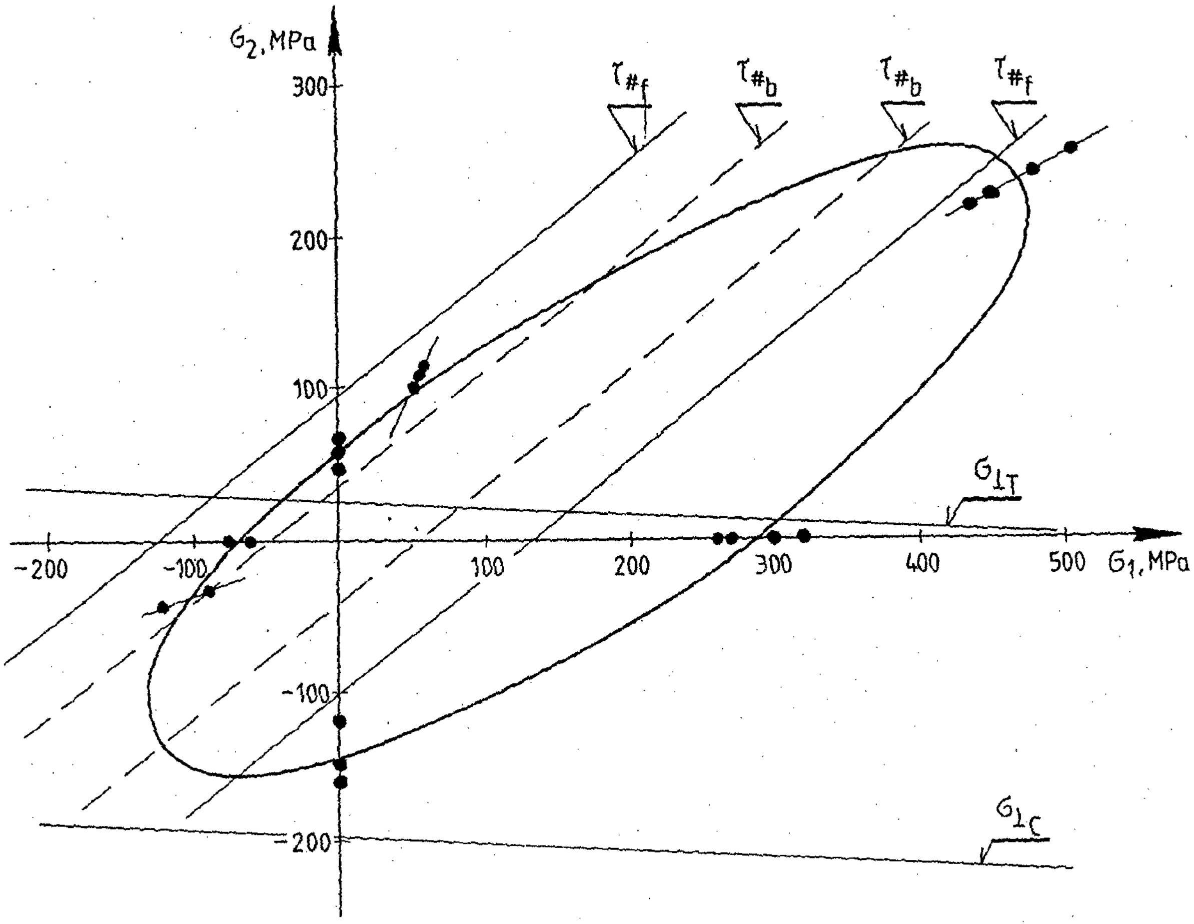

Fig. 1. Failure envelope for tested laminate

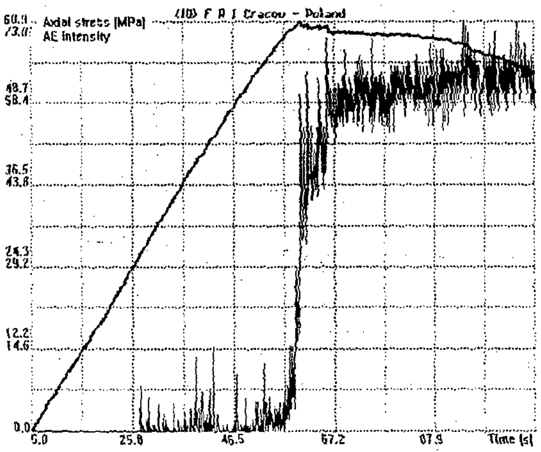

Fig. 2. Intensity of acoustic emission and load vs. time plots for laminate pipe under axial tension

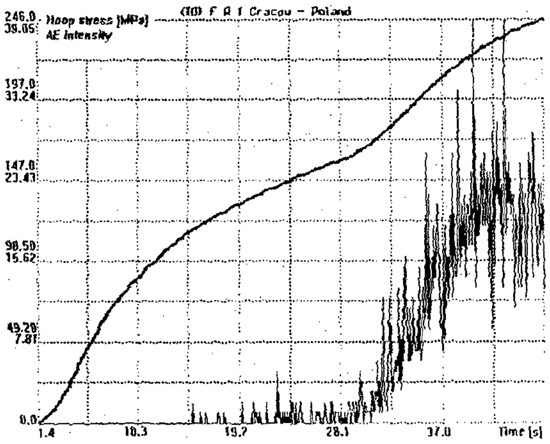

Fig. 3. Intensity of acoustic emission and load vs. time plots for laminate pipe under axial compression

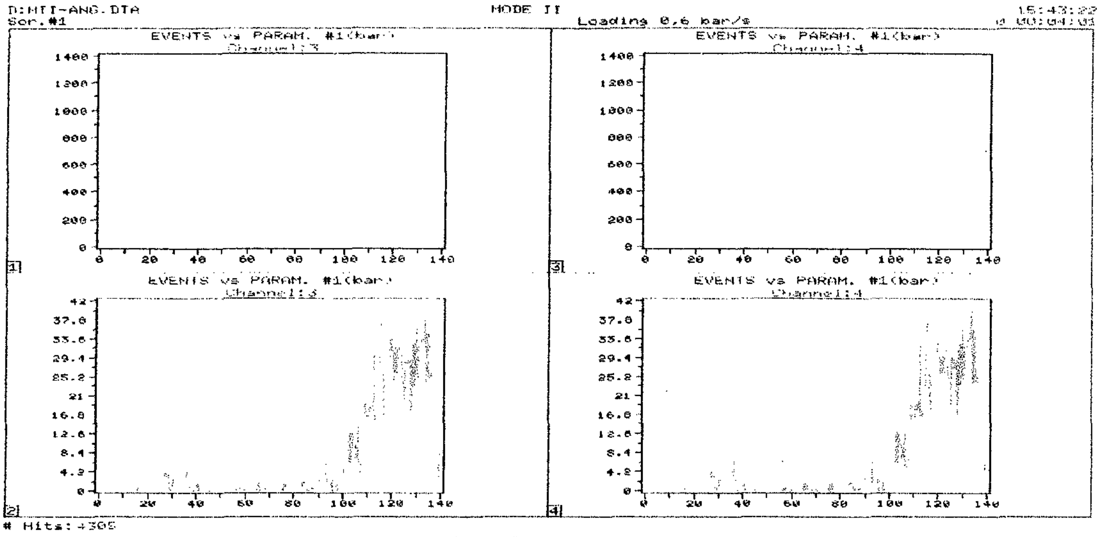

a) number of AE events scr.1,3
intensity of AE events scr.2,4

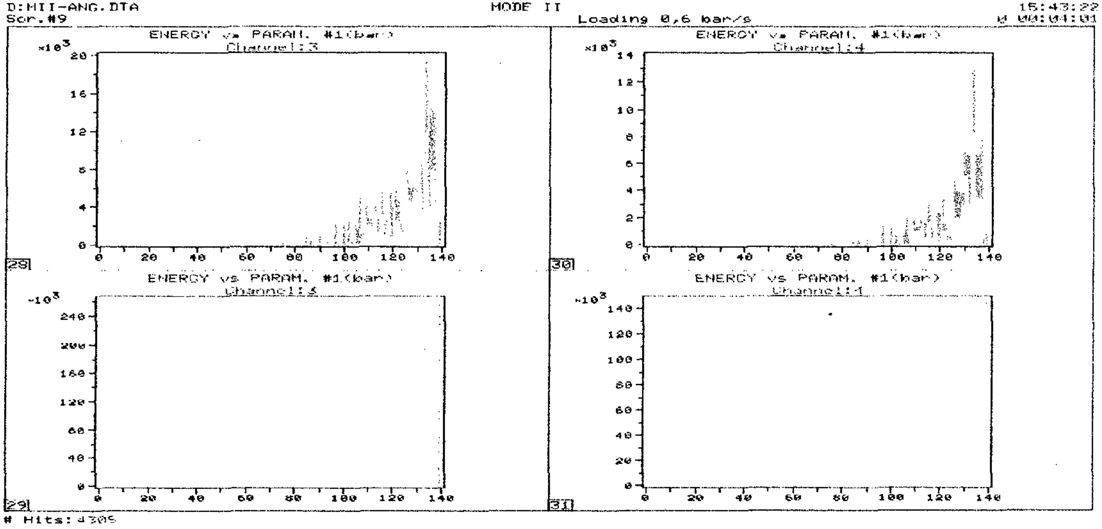

b) energy of AE signals summation scr,29,31
energy intensity of AE signals scr.28,30

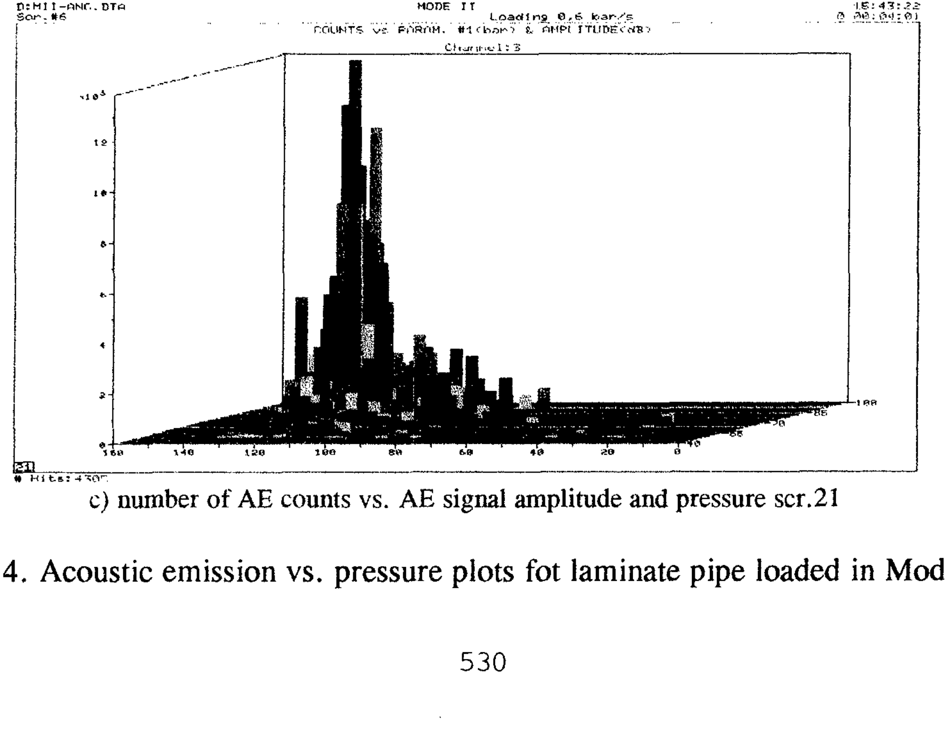

c) number of AE counts vs. AE signal amplitude and pressure scr.21

Fig. 4. Acoustic emission vs. pressure plots fot laminate pipe loaded in Mode II

EFFECT OF TRIGGER GEOMETRY ON ENERGY ABSORPTION IN COMPOSITE PROFILES.

M. A. Jiménez, A. Miravete, E. Larrodé and D. Revuelta.
C. P. S. Ingenieros Industriales. Universidad de Zaragoza
Área de Ingeniería e Infraestructura de los Transportes. Dept. de Ingeniería Mecánica
C/ María de Luna 3, 50015 Zaragoza, España

ABSTRACT.

This paper presents an experimental study on the energy absorption capability of two different composite profiles; both are realised in glass-polyester pultrusion. One of the profiles is a unidirectional box section, whilst the other, an I section, consists of alternating layers of mat and fabric. For each one of the two profiles, six different trigger geometries are analysed. The results show that the I profile is a good candidate for being considered for energy absorption applications. It is also concluded that when studying a trigger geometry, slight modifications of it (as the bevel angle of a bevel trigger) can result on important variations of the results.

INTRODUCTION.

The specific energy absorption levels obtained during the progressive axial crushing of organic matrix composite material profiles are comparable to, or higher than, those obtained during progressive axial folding of steel or aluminium profiles[1,2]. This fact makes composite materials a good choice for the design of crash energy absorption elements.

Most of the studies on the energy absorption of composite profiles under axial crushing have been focused on closed section profiles, while there are much less data on open section profiles[2,4-7]. This paper presents an experimental study on the progressive axial crushing of an open profile: a I section, which is realised on glass/polyester pultrusion consisting of mat and fabric alternating layers. A box section, made of unidirectional pultrusion, has also been tested in order to have reference values to evaluate the I profile. The effects of different trigger geometries are analysed for both studied profiles.

AXIAL PROGRESSIVE CRUSHING.

The failure of a composite profile under axial compressive loading occurs usually in a catastrophic manner unless a progressive failure triggering mechanism is provided. This triggering mechanism consists most of the times of machining an special geometry in one of the edges of the profile. The trigger geometry originates a localised failure area as result of stress concentration; afterwards, the local failure area progressively extends. Figure 1 shows the typical load/displacement curves for catastrophic and progressive axial compressive failure of a composite profile.

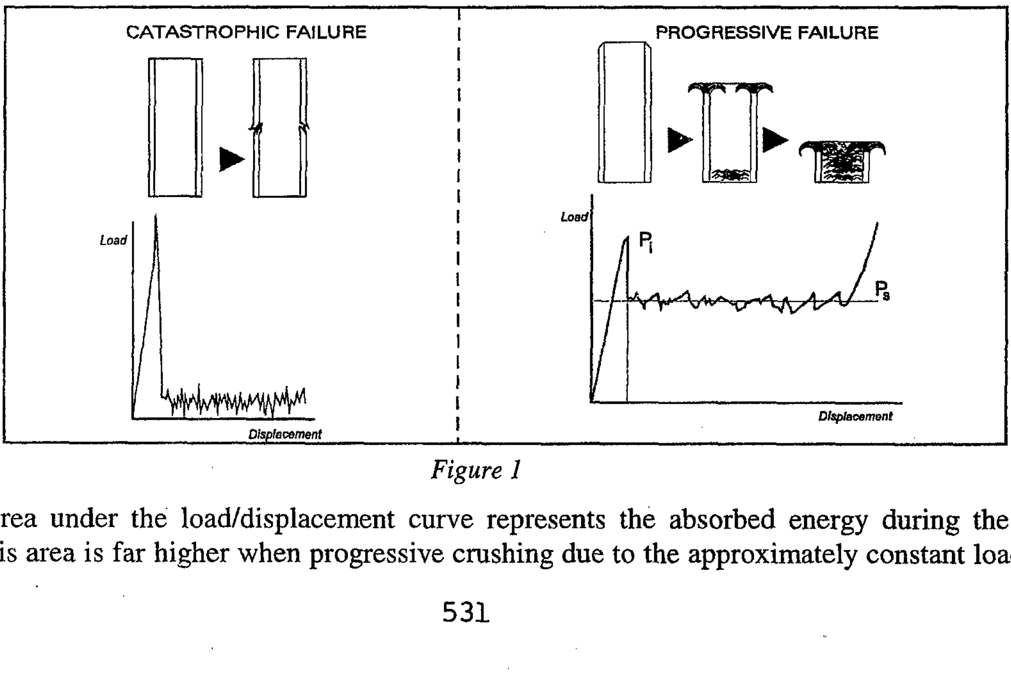

Figure 1

The area under the load/displacement curve represents the absorbed energy during the failure process. This area is far higher when progressive crushing due to the approximately constant load under which failure progresses; this is the reason why a trigger mechanism is required to get a high energy absorption level.

The energy absorption capability of a profile is measured with the specific energy absorption (E_s), which is defined as: $E_s = P_s/(\rho \cdot A)$, where A is the area of the section of the profile, P_s is the sustained load, and ρ is the density of the material.

When using a profile to protect an structure by absorbing crash energy is important to limit the loads that the profile transmits, to avoid damage of the rest of the structure. Therefore, when selecting the trigger geometry for an energy absorption element is not only important to have into account the sustained load during crushing, but also the maximum load level which is reached along it. It is also important to pay attention in figure 1 to the last section (final ascending part) of the progressive crushing curve, it corresponds to an uncontrolled load increase that may occur in closed profiles as result of failed material blocked inside the profile.

DESCRIPTION OF PROFILES AND TRIGGER .

An sketching of each one of the two sections that have been analysed is shown in figure 2. The material in both sections is E-glass/polyester. The nominal weight content of glass is 65% for the box section and 50% for the I section. The box section is realised in unidirectional pultrusion with an outer layer of mat, and also a mat layer at the interior of the flanges. The I section consists of mat and plain fabric alternating layers, with an small amount of unidirectional material which is the minimum required by the pultrusion process.

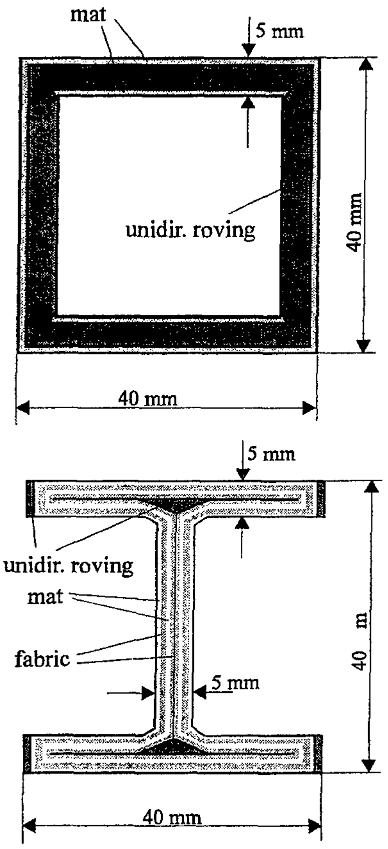

Figure 2

For each one of the two profiles, two different trigger geometry types have been analysed. Figure 3 shows these trigger geometries and the name that is used to reference each one of them. For each type of trigger geometry it has been considered the modification of the angle that defines it with values of 30°, 45° and 60°. Hence, six different trigger geometries (two types of trigger and three angles for each type) have been studied for each profile.

The type T trigger geometry represents a modification of the "tulip type" trigger which is usually referred in literature[7]. This modification has been chosen to simplify the machining in order to assure reliable values of the angle that defines the geometry.

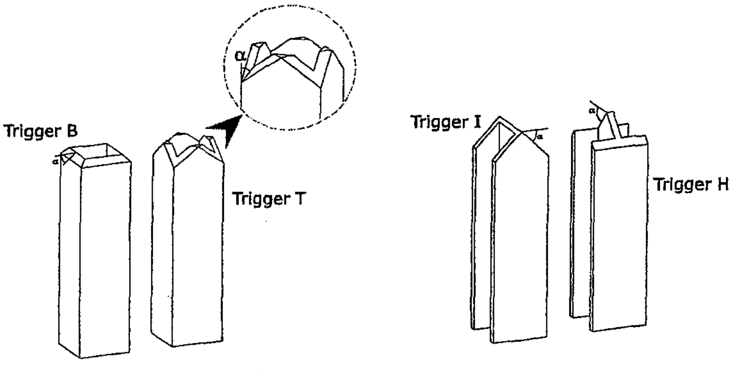

Box section profile

I section profile

Figure 3

TESTING AND RESULTS.

As result of the combination of trigger types and angles, six different trigger geometries are defined for each profile; these will be referred by the combination of the names in figure 3 and the angle value; so, as an example, B-30 makes reference to a bevel trigger geometry (see figure 3) with a bevel angle of 30°.

The crushing tests were carried out in an Instron installation with a loading capacity of 100 kN. Two steel plates were adapted to the installation. The specimens, 15 cm long, were crushed between the plates at a constant speed of 0.21 mm/s up to a relative displacement of 9 cm. Figure 4 shows a picture of the testing of one of the I section profiles.

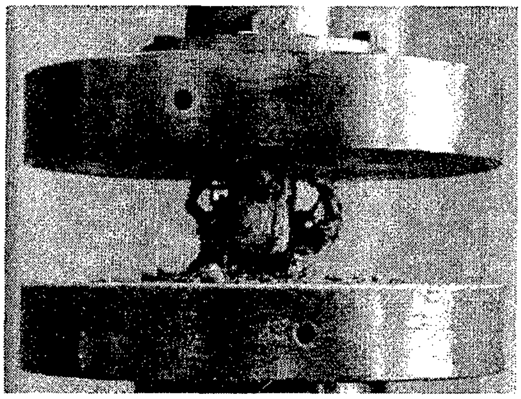

Figure 4

The load/displacement curves have been saved in numerical files through a digital oscilloscope Fluke 105. These numerical files have been used to calculate the maximum load peaks and sustained loads, and from them the specific energy absorption. Figure 5 shows one of the three curves corresponding to each one of the tested trigger geometries for each section profile. Figure 6 is equivalent, but is this case it corresponds to the I section profile.

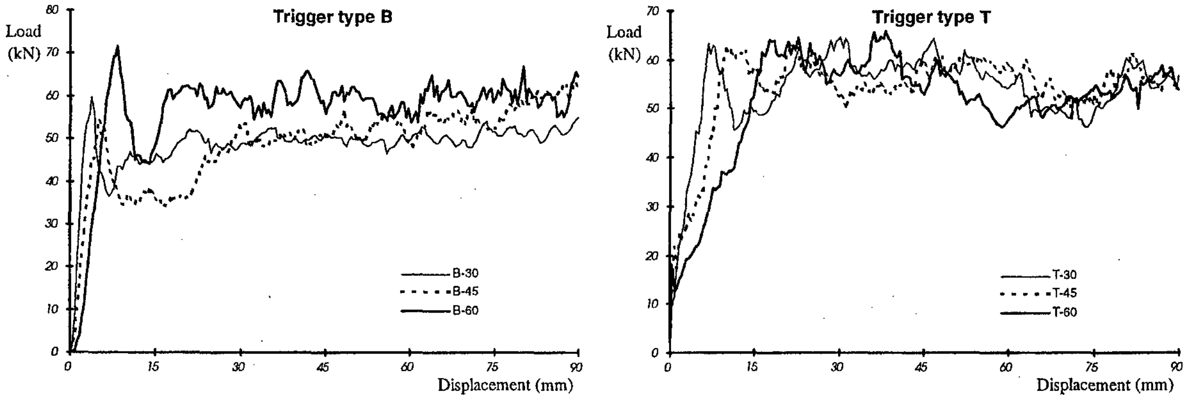

Figure 5

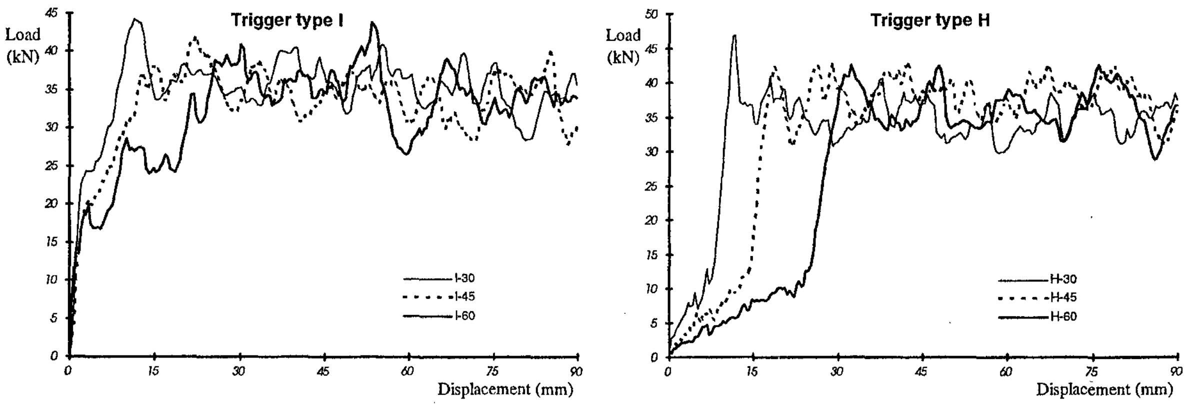

Figure 6

The figure 7 is included as an example of the differences between the curves obtained from equal samples, given that these differences are not substantial, the curves in figure 5 and figure 6 can be taken as representative of each trigger geometry for comparison porpoises. Moreover, the low dispersion of results in terms of load peaks and sustained loads, allows to obtain from each series of equal samples averaged values that can be considered as representative of a given profile and trigger geometry.

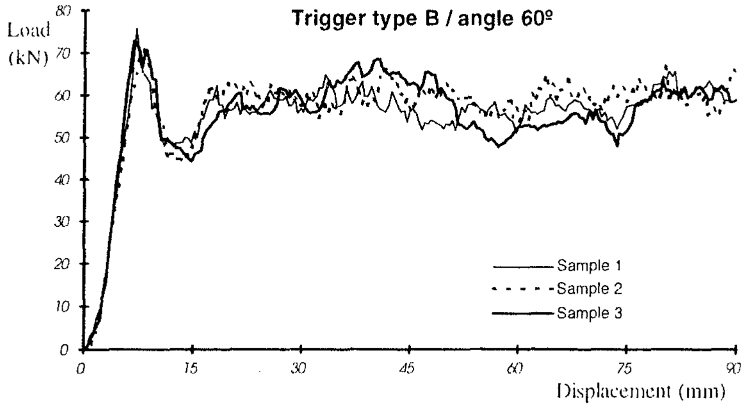

Figure 7

After testing, the samples were longitudinally cut to carry out a visual inspection of the crushed zone. In the case of the box section, the inspected sectioned samples showed no difference in the type of failure and level of damage depending on trigger type or angle. Figure 8 corresponds to a box section which has been tested with a B-60 trigger. It can be seen how the outer layers of mat have delaminated. The delaminated mat has fractured while bending, so finishing in the roll shape that can be appreciated in the figure. The presence of some unidirectional fibres in the delaminated mat layer prevents it from separating from the rest of the specimen. Fragmentation of fibres and resin has also occurred, resulting in a rest of material debris.

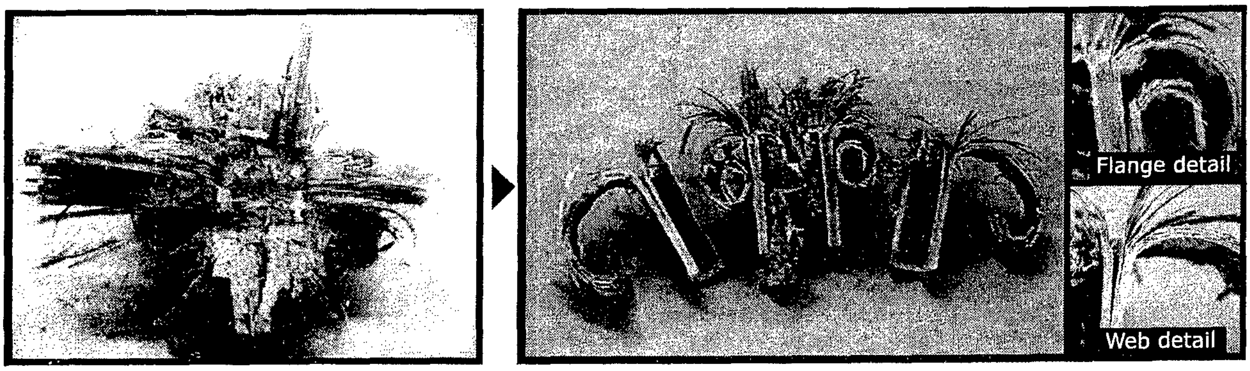

Figure 8

The unidirectional fibres have split in multiple groups inwards and outwards the profile. In the webs of the profile this splitting is associated to the progression of a main central crack; while, in the flanges, the presence of the interior mat (not present in the webs) avoids the onset and growing of a main central crack.

The curves for the type T trigger indicate that the variation of the angle does not affect to the sustained load level, so indicating than after the formation of the crush front it progresses in a constant manner, but in the case of the B trigger type, the load/displacement curves show big differences depending on the trigger angle. Anyway after the crush process, the sectioned samples corresponding to B type trigger show the same type of failure and level of damage, independently of the angle, and without difference respect to the T type triggers.

The trigger geometries B-30 and B-45 generate at the first stages of the crush process a higher level of damage (longer length of main central cracks in webs) than the B-60 trigger and than the T triggers, but as the crush proceeds this level reach the same value than in the other cases. This fact is related to the important load reduction which is observed in the B type triggers curves after the initial load peak. This load reduction is associated to the tearing of the box corners, shown in figure 7 for one of the B-60 samples. After the sudden onset of the corner cracks, the length of these cracks decreases as crush progresses and so the load increases again. With the B-30 and B-45 triggers longer cracks are formed during corners tearing, this results in longer inner cracks that afterwards reduce progressively their length until the final stable value of load is reached.

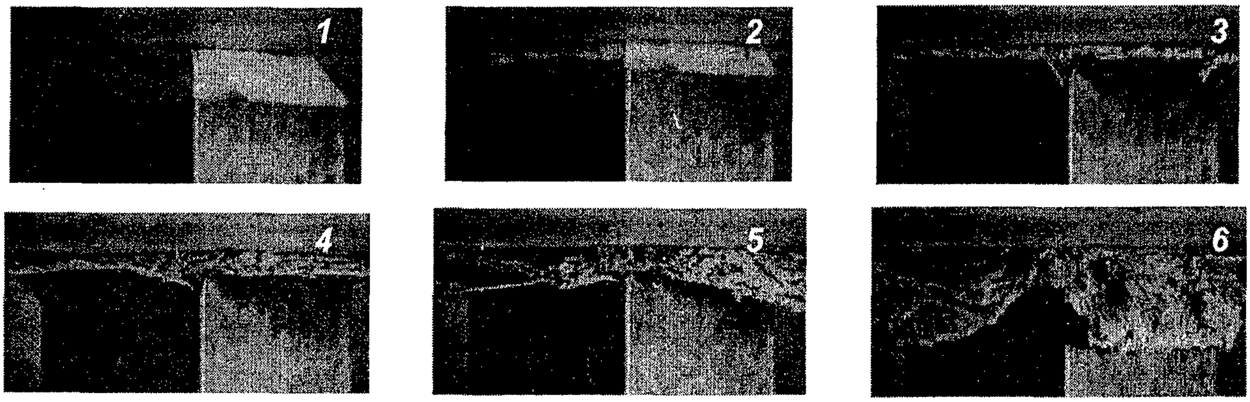

Figure 7

Figure 8 corresponds to a section of the web of a I section sample tested with a H-60 trigger, there are not differences respect to the other trigger types and angles used for the I section. The delamination between the alternating layers of mat and fabric and the formation of a main central crack in the centre of the section can be observed in the picture. In the flanges of the profile the same type of failure than in the webs has been observed. In the I section samples, and as a difference respect to the box section, the transverse fracture lines which appear during bending of the delaminated material extend through the whole material thickness and the failed material separates from the rest of the specimen.

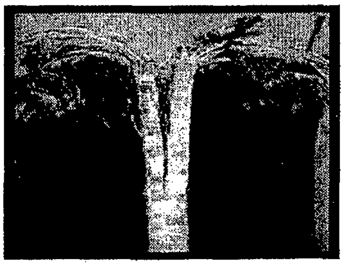

Figure 8

SPECIFIC ENERGY ABSORPTION LEVELS.

The average values of the sustained crushing loads and of the maximum loads reached during the process are shown in table 1. The results in table 1 show that for the I section profile, with either trigger types I and H, and independently of the trigger angle, the same level of energy absorption is obtained (37-39 J/gr). There is not either important modification of the maximum load of the crushing process depending on the trigger type or angle.

Box section	Max. load (kN)	E_s (J/gr)
B - 30	61.4	35.8
B - 45	59.6	35.7
B - 60	74.7	44.8
T - 30	66.7	42.0
T - 45	64.6	43.0
T - 60	69.6	43.5

I section	Max. load (kN)	E_s (J/gr)
I - 30	43.1	38.0
I - 45	42.0	37.8
I - 60	44.0	37.0
H - 30	47.7	39.0
H - 45	43.2	39.8
H - 60	44.2	39.7

Table 1

In the box section, the trigger type and the angle show a very important influence in the level of energy absorption. For the T trigger the specific energy absorption is around 43 J/gr independently of the angle; while on the other hand, with the B trigger a level close to 45 J/gr (higher than with the T trigger) is obtained with an angle of 60°, without getting more than 36 J/gr with angles of 30° and 45°. Moreover, in the B trigger the angle also affects notably the maximum load value which is reached during crushing.

In terms of specific energy absorption the best result from all the trigger geometries studied for both profiles is that of the B-60; with this trigger the energy absorption of the box profile is over 15% higher than that which is obtained with any of the trigger types used in the I section profile, but the maximum loads are also a 60% higher. Also, and thinking of the possibilities of practical application to an energy absorbing element, it has to be notice that with the I section profile the problem of uncontrolled load increasing due to material blockage at the interior of the profile would never occur.

CONCLUSIONS

The I section mat/fabric pultrusion profile shows, independently of the trigger geometry, an energy absorption level which results very interesting if compared with that of the box section unidirectional pultrusion profile. The energy absorption capability of the I section profile is only 15% smaller than with the best trigger configuration of the box section profile while limits the maximum loads during crushing process to a value which is 60% smaller. Also the I section profile, as an open section profile, do not present problems of uncontrolled load increase as result of failed material blocking the crush process.

In the case of the box section unidirectional pultrusion profile the trigger geometry has a very important influence in the results. When a bevel trigger is used, different bevel angles give place to a difference of 25% in the specific energy absorption level. In literature, many of the analysis of trigger geometries consider only different geometry types but without analysing variations of the angle for a give geometry and, as it has been shown, this could result in misleading conclusions.

Bibliography

[1] D. Hull, "Axial crushing of fiber reinforced composite tubes", in Structural Crashworthiness (Eds. N. Jones and T. Wierzbicki), Butterworths, Boston, 1983, pp. 118-135.

[2] P. H. Thornton, P. J. Edwards. "Energy Absorption in composite tubes", *J. Comp. Mater.,* 16 pp.521-45 (1982)

[3] E. Larrodé, M. A. Jiménez , S. Baselga. "Absorción de energía en vehículos mediante materiales compuestos de matriz orgánica". *Actas del I Congreso Nacional de Materiales Compuestos - Sevilla 1995.* p. 233-238

[4] P.H. Thornton, "The Crush behaviour of Galss Fiber Reinforced Plastic Sections", J. of Composites Science and Technology, Vol. 27 (1986) p. 199-223.

[5] N. K. Gupta et al, "An Analysis of Axial Crushing of Composites Tubes", J. of Composite Materials, Vol 31. No.13 p. 1262-1286

[6] G. L. Farley. "Energy absorption of composite materials", *J. Comp. Mater.*, 17 pp. 267-79 (1983)

[7] P. H. Thornton. "Effect of trigger geometry on energy absorption of composite tubes". *Proc.. ICCM-V*, pp 1183-99 (1985)

EXPERIMENTAL VALIDATION OF REFINED MODELS OF COMPOSITE PLATES

M. KARAMA, S. MISTOU, J.P. FAYE, S. CAPERAA & J. LACASSAGNE

LGP ENIT, Chemin d'Azereix, BP1629, 65016 Tarbes Cedex, France
Telephone +33 (0)5 62 44 27 26, Fax +33 (0)5 62 44 27 08, E-mail moussa@enit.fr

INTRODUCTION

Using plate models proves to be a convenient method for the resolution of three dimensional problems when two dimensions are higher than the third one. With this method only a minimal number of elements are needed to represent the model and determine how it behaves by recreating the displacement field in the third direction.
The ability of composite materials to allow important stresses along certain directions avoids designing massive parts, which represents gains in weight, costs (material or development), and performance. In this way, it becomes necessary to develop adapted tools for the analysis of structures using this kind of material. In fact, for advanced composites, transverse shear plays an important role because the ratio of the elastic modulus to the shear modulus is high. Then the mechanical behaviour of laminated composite structures is directly modified.
The aim is to define adequate reliable models for simple and fast modelling of composite structures like plates. Indeed, various plate models will be compared to numerical simulation and to experimental results through displacement, strain and stress fields. The experimental model is composed of a clamped rectangular laminate plate under uniformly distributed pressure.

APPROXIMATION MODEL

The studied models will be defined from the following displacement field :

$$\begin{aligned} U_\alpha(x_1,x_2,x_3,t) &= u_\alpha(x_1,x_2,t) - x_3 w_{,\alpha}(x_1,x_2,t) + f(x_3)\gamma_\alpha(x_1,x_2,t) \\ U_3(x_1,x_2,t) &= w(x_1,x_2,t) \end{aligned} \quad (1)$$

The fifth variational unknowns are the membrane displacement in the α direction u_α, the transverse displacement w, and the rotation γ_α. The models differ from the definition of the $f(x_3)$ function which represents the transverse shear. The $f(x_3)$ function defines the relative displacement fields for the currently existing models :

- $f(x_3) = 0$, Kirchhoff-Love theory [1],
- $f(x_3) = x_3$, Reissner-Mindlin theory [2],
- $f(x_3) = x_3\left(1 - \frac{4x_3^2}{3h^2}\right)$, Reddy-Liu model [3],
- $f(x_3) = \frac{h}{\pi}\sin\frac{\pi x_3}{h}$, Touratier model [4].

GOVERNING EQUATIONS

From the virtual power principle, the motion equations and the natural boundary conditions can be obtained. The calculations are made in small perturbations. The principle is :

$$\int_{\Omega} \rho U^{*T} \ddot{U} d\Omega = -\int_{\Omega} \overline{\overline{D}}^{*T} : \overline{\overline{\sigma}} d\Omega + \int_{\Omega} U^{*T} f d\Omega + \int_{\Gamma} U^{*T} \hat{F} d\Gamma$$

The governing equations are :

$$\begin{aligned}
&-D_{11}w_{,1111} - 2(D_{12} + 2D_{66})w_{,1122} - D_{22}w_{,2222} + d_{11}\gamma_{1,111} \\
&+(d_{12} + 2d_{66})(\gamma_{1,122} + \gamma_{2,211}) + d_{22}\gamma_{2,222} + q = 0 \\
&-d_{11}w_{,111} - (d_{12} + 2d_{66})w_{,122} + \widetilde{D}_{11}\gamma_{1,11} + (\widetilde{D}_{12} + \widetilde{D}_{66})\gamma_{1,12} \\
&+\widetilde{D}_{66}\gamma_{1,22} - \widetilde{A}_{55}\gamma_1 = 0 \\
&-d_{22}w_{,222} - (d_{12} + 2d_{66})w_{,211} + \widetilde{D}_{22}\gamma_{2,22} + (\widetilde{D}_{12} + \widetilde{D}_{66})\gamma_{2,21} \\
&+\widetilde{D}_{66}\gamma_{2,11} - \widetilde{A}_{44}\gamma_2 = 0
\end{aligned} \tag{2}$$

with,

$$\widetilde{D}_{\mu\nu}, d_{\mu\nu}, D_{\mu\nu} = \int_{-h/2}^{h/2} C_{\mu\nu}(x_3^2, x_3 f(x_3), f^2(x_3)) dx_3,$$

$$\widetilde{A} = \int_{-h/2}^{h/2} C_{\mu\nu} f^2(x_3) dx_3, \quad \mu\nu = 11,22,12,66.$$

BOUNDARY PROBLEM

The boundary problem determination as shown in Navier introduced Timoshenko [5] or Srinivas and Rao [6], proposes solutions for a clamped plate under a constant pressure which are established within the Kirchhof-Love theory and do not allow to take into account the refined models. The solutions proposed by Levy and developed by Idlbi [7] can yield results from refined models but only in the case of a two-edge simply supported plate under sinusoïdal load.

To find an analytical solution for clamped plates one has to simplify the solutions. A method for the minimization of errors such as Galerkine's can lead to a solution in that particular case. To approach the solution of a field φ, which represents the unknowns w or γ_α, a sum of linearly independent functions verifying the boundary conditions can be used such as :

$$\varphi = \sum_i \alpha_i . \varphi_i \tag{3}$$

where the coefficients α_i are linearly independent. The method for the minimization of errors could be employed in the following way :

$$\int_D \left[A\left(\sum_{k=1}^{N} \alpha_k . \varphi_k \right) - q \right] . \varphi_i dD = 0 \quad \text{with} \quad i = 1,...,N \tag{4}$$

A(...) represents the differential operator, and φ_i the weighting function.

If the operator is linear, which is the case of the differential stability equation in the studied plate, one obtains a linear system in which α_k can be deduced. This model presents the advantage of establishing only one stability equation in the studied area. The φ function is chosen so as to verify the boundary conditions (x_1=0,a ; x_2=0,b) :

$$\varphi(x_1,x_2)=\sum_{i=2}^{N}\alpha_i(x_1-a)^i.x_1^i.(x_2-b)^i.x_2^i \tag{5}$$

The results for a clamped square steel plate (a=b=0.5m, h=0.025m) shows a good convergence of the solution (Table 1).

Models	$\overline{w}$	error (%)
Exact solution	890.70	ref.
Navier	846.70	4.93
Galerkin (present)	852.48	4.29

Table 1. Transverse displacement in the middle of the plate for different models

$$\overline{w}=\frac{G.w(x_1,x_2)}{h.q}$$

So as to have a reference numerical solution, a finite element analysis will be used. This approach is realized on the Abaqus software with elements S8R (1024 el.). The convergence of the results obtained by this model is verified for the values of transverse displacement and stresses. The results are compared to the exact solution (Table 2).

h	$\overline{w}$ (exact)	$\overline{w}$ (Abaqus)
0.025	890.7	891.9
0.05	62.83	63.19
0.07	18.64	18.83
0.1	5.61	5.70

Table 2. Transverse displacement in the middle of the plate for different thickness

EXPERIMENTAL SET-UP

The mechanical properties of the material are issued from a ultrasound method. This method is based on the propagation of longitudinal and transverse ultrasound waves in different directions in order to evaluate their velocities. The studied plate is composed of glass fiber associated with a polyester resin.

The mechanical properties are :

E_1=16.798GPa, E_2=18.022GPa, E_3=8876MPa,
G_{23}=2160MPa, G_{12}=3358MPa, G_{13}=5203MPa,
ν_{23}=0.414, ν_{32}=0.202, ν_{13}=0.449, ν_{31}=0.237, ν_{12}=0.245, ν_{21}=0.262.

A bending test (Figure 1) allows the measurements of the behaviour of clamped plates submitted to an uniformly distributed load (pressure).

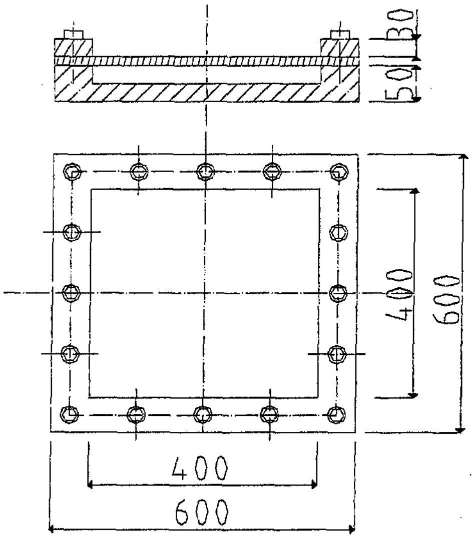

Figure 1. Test-bed for plates under pressure

DISPLACEMENT RESULTS

The first part of our experimental studies rests on the case of an isotropic plate (a=b=0.4m, h=0.006m) submitted to a 2 bars pressure. The small perturbation hypothesis is verified in our measurements.

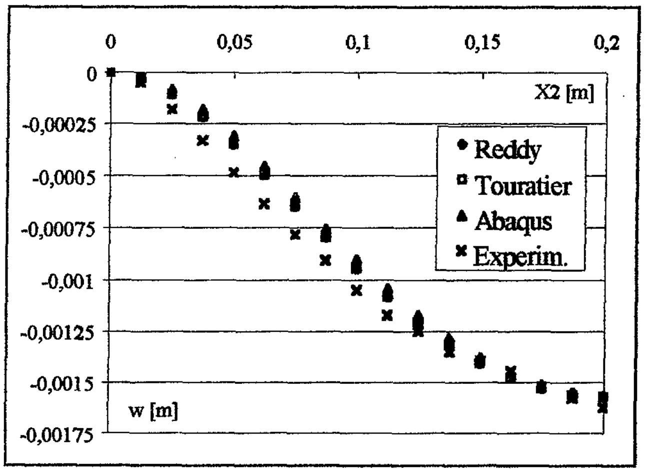

Figure 2. Transverse displacement between an edge and the middle of the isotropic plate for $x_1=a/2$

This first comparison shows the homogeneity of the different models in determining the deflection of the plate (Figure 2). The experimental values have been measured with the help of a tridimensional measuring machine. The values are quite good, especially in the middle of the plate.

Then the orthotropic material described above is tested. The dimension are : a=b=0.4m, h=0.013m. The small perturbation hypothesis is verified in our tests.

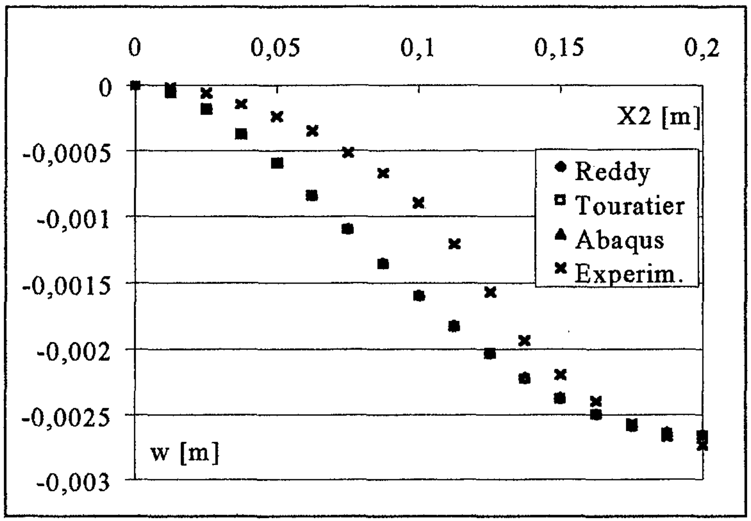

Figure 3. Transverse displacement between an edge and the middle of the orthotropic plate for $x_1=a/2$

On this figure (Figure 3) one can note the coherence of the different models for the transverse displacements especially in the middle of the plate. The difference between experimental values and theoretical results can be explained by the heterogeneity of the structure and by the effect of the deformations introduced on the clamping of the plate.

STRAIN RESULTS

The plates have been fitted out with strain gauges on the top surface. A small chain is used in order to get information on the edge effects (Figure 4).

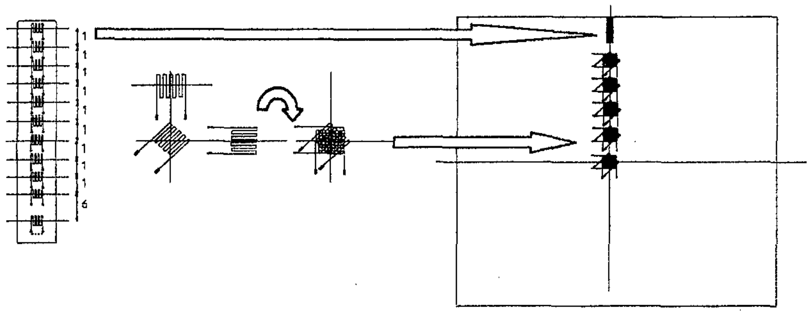

Figure 4. Instrumentation for strain measurements

The figures 5-6 shows the coherence between experimental and numerical results in the middle of the plate as well as the convergence of all models. The measurements taken on the edge zone present good results for the isotropic plate, but a difference appears for the orthotropic plate. This can be explained by the transverse sensitivity of the strain gauges.

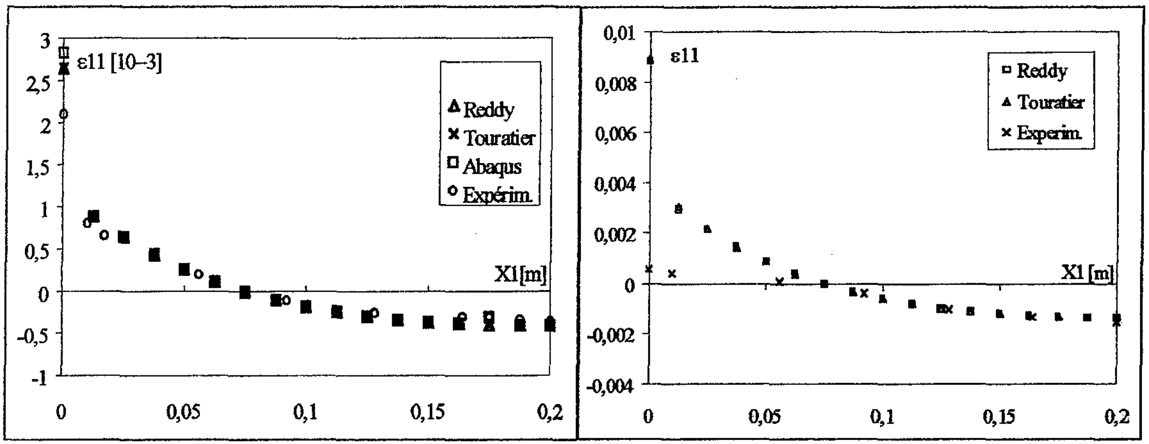

Figure 5-6. Distribution of the deformation for an isotropic and an orthotropic plate

CONCLUSION

The experimental tests have been realized to validate the refined plate models. They show the difficulty of obtaining accurate and reliable results. In fact, the experimental parameters which have an effect on measurements are large and their influences are identified with difficulty. In our case, the clamped boundary condition leads to deformations which affect the behaviour of the plate on the edge zone. On the other hand, the measuring system used involves an average effect on the values which reduce the research phenomenon.

This work is focused on the research of boundary conditions and load types in order to minimize the difference between experimental and theoretical results. Then free edge boundary conditions could be considered.

Finally, the validation of differences noted down in the determination of the unknowns by the considered models, requires developed techniques (ie. photoelasticimetry) in order to highlight the distribution of stress and strain through the thickness of the composite plate.

REFERENCES

[1] Love, A.E.H. (1934). *A Treatise on the Mathematical Theory of Elasticity*, 4th Edn. Cambridge University Press.

[2] Reissner, E. (1945). On Transverse Bending of Plates Including the Effect of Transverse Shear Deformation, *Int. J. Solids Structures* 11(5), 569-573.

[3] Reddy, J.N. (1984). A Simple Higher-Order Theory for Laminated Composite Plates. *J. Appl. Mech.* 51, 745-752.

[4] Touratier, M. (1991). An Efficient Standard Plate Theory. *Int. J. Eng. Sci.* 29(8), 901-916.

[5] Timoshenko, S. and Woinowsky-Krieger (1989). *Theory of Plates and Shells*. Mc Graw-Hill.

[6] Srinivas, S. and Rao, A.K. (1970). Bending, Vibration and Buckling of Simply Supported Thick Orthotropic Rectangular Plates and Laminates, *Int. J. Solids Structures* 6, 1463-1481.

[7] Idlbi, A. (1995). *Comparaison de théories de plaque et estimation de la qualité des solutions dans la zone bord*. Thesis, ENSAM, Paris.

WHAT WE CAN EXPECT FROM ULTRASONIC METHOD FOR COMPOSITE MATERIALS

Edouard G. Nesvijski
Center of Technology, Federal University of Santa Maria
Campus Universitario, Santa Maria, RS, Brazil

INTRODUCTION

Nondestructive methods of materials evaluation are a reliable part of practical testing of physical properties of composite materials. In a wide range of different methods of nondestructive testing (NDT) ultrasonic methods occupies one of the leading places. Ultrasonic methods were mostly developed for characterization of metals and alloys. During the last several decades composites have begun to substitute such traditional materials as metals, alloys, wood, and ceramics. And previously developed ultrasonic methods and instrumentation have been applied for new materials. But such a direct compilation has brought a number of discrepancies connected with estimation of the main characteristics of composites, such as modules of elasticity, strength, and crack resistance. An attempt to explain some problems of ultrasonic characterization of the materials is made in this work.

ELASTIC MODULES OF COMPOSITES

Elastic modules are the most important characteristics of composites. They are calculated parameters in analytical apparatus of physical theory of damage and fracture of structural materials. Elastic modules are included into all formulae of solid mechanics and serve for design calculations of structures, machines, and devices [1]. Unlike other characteristics of solids, elastic modules are very sensitive to structural properties of composites. For example, for polymer composites a slight change of composition of one of the components can give a considerable change of elastic modules of the material. Existing experimental methods for estimation of elastic modules of different structures of composites obtained by destructive and nondestructive methods give a noticeable dispersion of data. Majority of researchers and practicians try to explain that by imperfect instrumentation or procedure of application. Therefore, a number of theories of solids, for example for polycrystals, describe elastic characteristics as a range of modules [2].

$$M^* = M_0 \pm \sum_k M_k \; U_k \qquad (1)$$

where M_k – modules, U_k – weight coefficients, and $k = 1,2,\ldots,\infty$

Other sources give special significance to testing temperature, porosity of specimens or anisotropy of materials [3, 4]. Stress is also considered as a reason of data dispersion during tests. Modules of the third degree are often used for compensation of stress impact [5]. Modules for multicomponent composite materials have complex character. They depend on the modules of each of the components and their combination and volume proportions of the elements. We can also take for consideration regular composites, where components have a determined succession of components, for example fiberglass and composites with random combination of components for example concrete (Fig. 1).

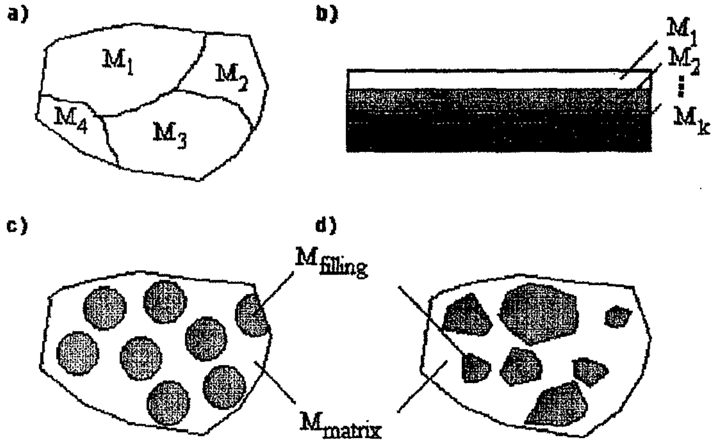

Fig.1. Multicomponent materials: a – multifaced; b – maltilayered; c – two-component with regular filling; d – two component with irregular filling, where $M_{filling}$ – module of filling, M_{matrix} – module of matrix, M^* – effective modules and $k = 1,2,\dots,\infty$ – number of components of composite material

There are several theoretical analytical approaches for estimation of an average module for such materials [6]. But it is more important for calculation of safety and reliability of structures to estimate value limits of modules for these composites. For example it is possible to take a two-component material for demonstration of relationship of modules of each of the components with their resulting value of modules for the material. Composite matrix-filling material may serve for this purpose. In this case homogeneous matrix with module M_1 and a random filling with module M_2 are investigated. An approach based on “Hill’s fork” may be used for analysis of such a material. This approach describes composite material as a stochastic elastic model and gives solution only for top M_{top} and bottom M_{bot} limits depending on volume proportions of matrix V_{matrix} and filling $V_{filling}$ Distribution of filling in matrix may be considered as uniformed random distribution [7] (Fig.1c).

Hashin and Shtrikman investigate a mathematical model of composite with stochastic distribution of filling in matrix [8] (Fig. 1d). Effective modules M^* are considered for two-component material with random distribution of filling in matrix. Filling may be of any shape and its volume in the matrix may be very large. As a result this approach, comparing with the previously mentioned one, gives more precise value limits for elastic modules of composite material with a good practical correlation.

The following formulae may be applied for calculation of the top limit of the resulting effective volume module $K_{top}{}^*$

$$K_{TOP}{}^* = K_1 + \frac{V_2(K_2 - K_1)}{1 + V_1\alpha_1(K_2 - K_1)} \tag{2}$$

and for the bottom limit of the module $K_{bot}{}^*$

$$K_{bot}{}^* = K_2 + \frac{V_1(K_1 - K_2)}{1 + V_2\alpha_2(K_1 - K_2)} \tag{3}$$

To calculate the top and bottom limits of effective shear module G^* the following formulae may be applied, for $G_{top}{}^*$

$$G_{top}{}^* = G_1 + \frac{V_2(G_2 - G_1)}{1 + V_1\beta_1(G_2 - G_1)} \tag{4}$$

and $G_{bot}{}^*$

$$G_{bot}{}^* = G_2 + \frac{V_1(G_1 - G_2)}{1 + V_2\beta_2(G_1 - G_2)} \tag{5}$$

Where coefficients $\alpha_1, \alpha_2, \beta_1, and \beta_2$ are

$$\alpha_1 = \frac{3}{3K_1 + 4G_1}; \alpha_2 = \frac{3}{3K_2 + 4G_2}; \beta_1 = \frac{6(K_1 - 2G_1)}{5G_1(3K_1 + 4G_2)}; \beta_2 = \frac{6(K_2 - 2G_2)}{5G_2(3K_2 - 4G_2)} \tag{6}$$

and V_1, V_2 - volumes of matrix and filling.

It should be noticed that average values of modules were not found. So, it may be assumed that they do not exist as a clear defined statistical characteristics such as mode, median, and average value for elastic modules of composites. There is a schematic representation of effective module limits in the Fig. 2. Combination of volume modules K^* and Young modules E^* give value of all other linear modules. For modules of higher degree (for example, Murnaghan module) other approaches may be applied.

Taking formulae (2) - (6) it is possible to conclude that for two-component material with hard matrix and soft filling (light filling concrete) elastic modules shift to the bottom limits, and for material with soft matrix and hard filling (heavy filling concrete) elastic modules shift to the top limits of their values.

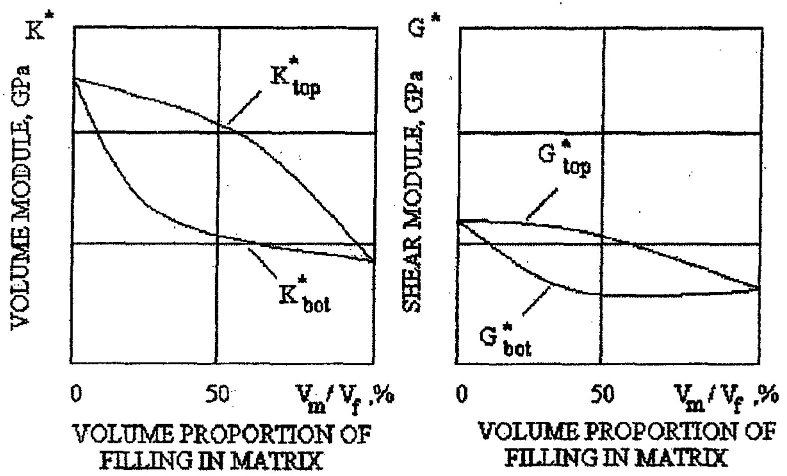

Fig. 2. Computer simulation of limits of effective elastic modules: K^* – volume module, E^* – Young modules, V_m / V_f – volume proportion of filling in matrix for two-component composite material, where $K_1 = 60 MPa, K_2 = 20 MPa, \mu^* = 0.25$

Hashin-Shtrikman model is developed to describe materials with porous matrix. The following relations for effective modules taking into account porosity parameter *Por* may be applied for characterization of ceramics, concrete and some other composites: for volume module $K_{por}{}^*$ [4]

$$K_{por}{}^* = K^* \left[1 - \frac{3}{2} \cdot \frac{(1-\mu^*) \cdot Por}{(1-2\mu^*)} \right] \tag{7}$$

for shear module $G_{por}{}^*$

$$G_{por}{}^* = G^* \left[1 - \frac{15(1-\mu^*) \cdot Por}{7-5\mu^*} \right] \tag{8}$$

for Young module $E_{por}{}^*$

$$E_{por}{}^* = E^* \left[1 - \frac{(1-\mu^*) \cdot (27+15\mu^*) \cdot Por}{2(7-5\mu^*)} \right] \tag{9}$$

for pores of ellipse shapes. For pores of a circular shape it is possible to use a more simple formula:

$$E_{por}{}^{*} = E^{*}\left[1 - \frac{15(1-\mu^{*})\cdot Por}{(7-5\mu^{*})+2(4-5\mu^{*})}\right] \quad (10)$$

where μ^{*} – effective Poisson ratio.

It is possible to conclude that reduction of the matrix elastic properties M connected with increase of porosity Po that affects effective modules of the whole composite material with random structure widening their bottom limits.

ULTRASONIC CHARACTERIZATION OF COMPOSITES

Special properties of composites that can be determined by their elastic modules are described above. If we accept ultrasonic wave velocity as a main parameter for characterization of materials, then we may expect that these properties be displayed in ultrasonic testing data. Velocity data dispersion characterizes top and bottom limits of elastic modules values and at the same time includes errors connected with measuring procedures. These errors give additional extension of module “fork” and hinder classification of materials with similar properties.

Usage of ultrasonic testing for estimation of strength of composites is connected with additional problems basing on absence of analytical relation between strength and elastic modules for all known materials. Several attempts were made to build a regression relation between strength and elastic modules, and some positive results were obtained. In these cases “fork” of top and bottom strength limits widen due to statistical correlation between the investigating parameters and depends on closeness between elastic modules of the material and its strength.

Ultrasonic estimation of cracking under loads connected with change of elastic modules of material due to development of macro and micro cracks and pores, from one side, and, from the other side, with special effects of diffraction and refraction of acoustic waves on inhomogeneities of composites. Sometimes these effects unite and considerably change wave velocity e.g. modules estimation, sometimes they conflict with one another and do not give a possibility to estimate stress for characterization of composites.

CONCLUSION

Special insight into the problems of ultrasonic characterization of composite material properties, such as modules of elasticity, strength, and cracking is presented in this paper. Some difficulties and dead end problems based in the notion of effective elastic modules that should be taken into account during analysis of data received by ultrasonic testing of composites are shown. But these disadvantages are connected with traditional analysis of ultrasonic velocity and amplitude for materials evaluation. Right now new approaches to data analysis basing on signal processing, pattern recognition, fuzzy logic, and neural network tools give an opportunity to develop ultrasonic testing methods and overcome their disadvantages. That is why we can expect positive results of future development and application of ultrasonic methods for NDT of composites.

REFERENCES

[1] Frantsevich, I.N., Voronov, F.F., Bakuta, S.A. Elastic Constants and Elastic Modules of Metals and Nonmetallic Materials, Naukova Dumka, Kiev, Ukraine, 1982.

[2] Voit, W. Lehrbuch der Kristallphysik, Springer, Leipsig, Germany, 1928.

[3] Griffith, D.S. The Phenomenon of Rapture and Flow in Solids, Phyl.Tans.of the Royal Society of London, Ser.A, V.221, pp. 127-135, 1921.

[4] Hashin, Z. Relations between Young Modules and Temperature, J.Appl.Mech, 29, pp. 143-147, 1962.

[5] Murnaghan, F.D. Finite Deformation of an Elastic Solid, Amer.J.Math., 59, pp. 235-320, 1937.

[6] Köster, W. Elastische Eigenschoften in Max Hansen, Z.f.Metallkunde, 5, N 4, p. 149, 1948.

[7] Hill, R. The Elastic Behavior of Crystalline Aggregate, Proc. Phys. Soc. A., 65, pp. 349-354, 1952.

[8] Hashin, Z, Shtrikman, S. A Variational Approach to Theory of the Elastic Behavior of Multifaced Materials, J.Mech.and Solids, 11, pp. 127-135, 1963.

ON THE APPLICATION OF THE ACOUSTIC EMISSION AND INFRARED THERMOGRAPHY TO FRACTURE PROCESS EVALUATION IN SHORT FIBRE REINFORCED PLASTICS

J.Schmidt, I.Baran.

Foundry Research Institute, Zakopiańska 73 str., Krakow, Poland

INTRODUCTION

The composite materials comprising a brittle matrix made of plastic reinforced with short fibres, manufactured in the process of injection are characterised by structural anisotropy, due to the distribution of fibres obtained in the course of the technological process. Consequently, what we obtain is a material or an element whose resistance and toughness are the result of an interaction of the regions characterised by different orientation of the reinforcing phase. The formation of fractures in material of this type is a very complex process. Considering to material anisotropy settlement of the initiation processes and joining of creating processing has particular sense both on diagnostic of made from this material object as well for fracture toughness allocation. It has been assumed that different crack events shell produce different acoustic signals of which analysis allows to identificate of essential cracking steps. Acoustic emission method is not able to present of the region in which the crack occurs therefore simultaneously the thermal picture of the crack tip area was recorded as a function of loading.

The aim of our investigation was to describe the effect of microstructure on fracture mechanism in phenolic short glass fibre reinforced composites. The samples CT were machined from 5 mm thick sheets, in L-T and T-L crack orientation in respect to the mould filling direction.

The compact samples configurations are : W/A = 48/24, W/B = 48/5.

The samples were tension loaded using computer controlled Schenck systems, and the crack opening was measured by 10 mm clip gauge. In the loading system an additional protection was provided to eliminate the possible loss of specimen stability. The variations in temperature field within the area of crack development were recorded by an AGA 680 camera equipped with a numerical system of image recording.

The AE signals produced during loading were together with load and displacement recorded by PAC Mistras 2001 system.

RESULTS

The multi-ply structure of the examined material is well visible on a geometrical model of the orientation of a structure-reinforcing phase, revealed by microscopic examinations (Fig.1).

For this type of structure the measurement of fracture toughness K_Q basing on the values of the crack- initiating load, determined according to the laws of the linear fracture mechanics, has no physical justification since the process of fracture is not occurring simultaneously in each layer.

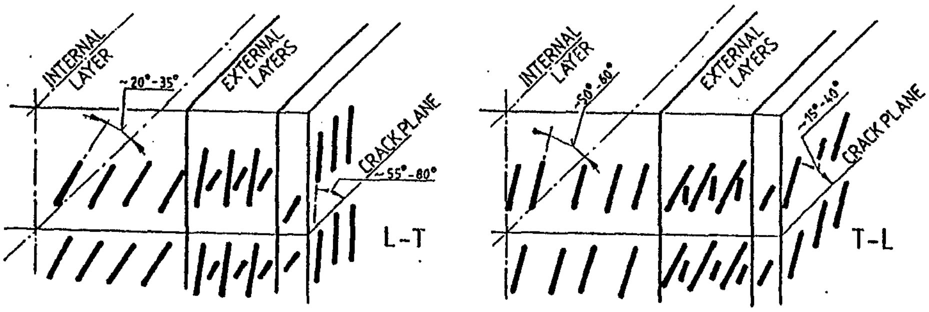

Fig.1. Model of structural geometry

Figures 2 show the curves of the loading versus crack opening for both structure orientations; they also serve for computation of the fracture toughness K_Q (in accordance the approach of linear fracture mechanics [1]). Diagram is completed by differential parameter duration to load. The tests performed for both structure orientations, i.e. L-T and T-L, enable the determination of an effective critical load corresponding to the initiation of fracture process, combining the observed effect of thermomechanical coupling and variations in acoustic emission. The image of the thermal effect on the loading process are presented for examples in figure 3. Basing on realise experiments, as the parameters best describing the fracture process the following ones were selected: the duration of emission signals, the rise time describing an increment in the signal value up to its a maximum level, and the number of events. For structure orientation L-T the recorded changes in acoustic emission are presented in Figures 4. For structure orientation T-L the AE parameters are shown in Figures 5.

ANALYSIS

The main aim of the application in loading tests of various measuring methods is to determine the value of the effective load at which the fracture process is initiated. The observations of the temperature field enable an evaluation of the increase in plastic strain near the crack tip, revealed by temperature increase up to achievement of the state of maximum temperature increment to cause crack development. In view of the structural constitution of both the L-T and T-L specimens orientations, and especially the fibre orientation in external layers, the processes of crack development are different. In the case of L-T orientation the increase of strain is caused the initially effect of heat dissipation (the change of temperature near the crack tip $\Delta t=0,4$ K) and cause the rapid formation of a long crack. In the case of T-L orientation a short crack appears in the external layer at the crack tip with unfavourable orientation to the normal load (the maximum change in temperature Δt=0,9 K) and as soon as its development has been arrested, the second full structure crack branching caused by loading in the central zone of structure is formed.

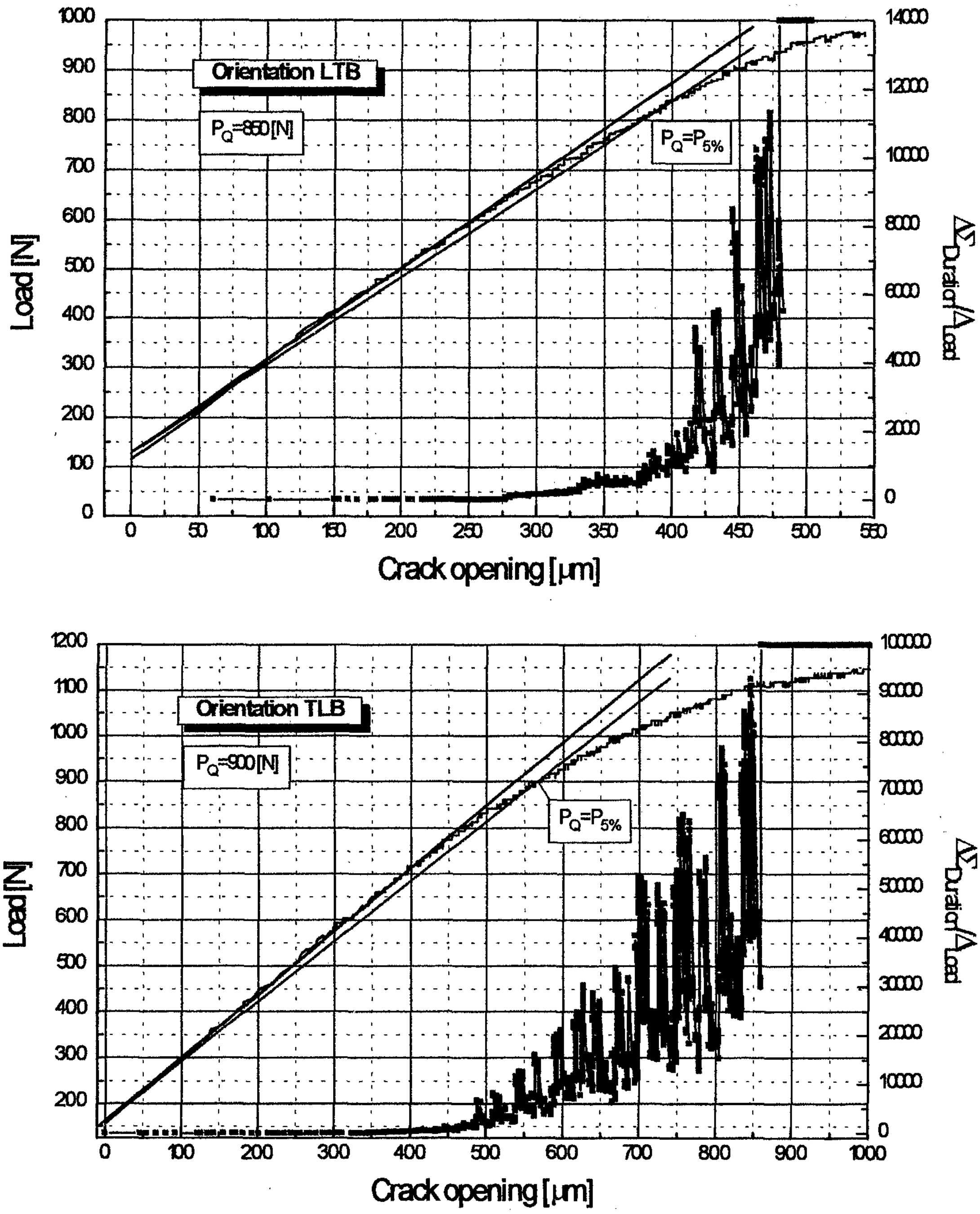

Fig.2. Load and AE parameter plot versus crack opening.

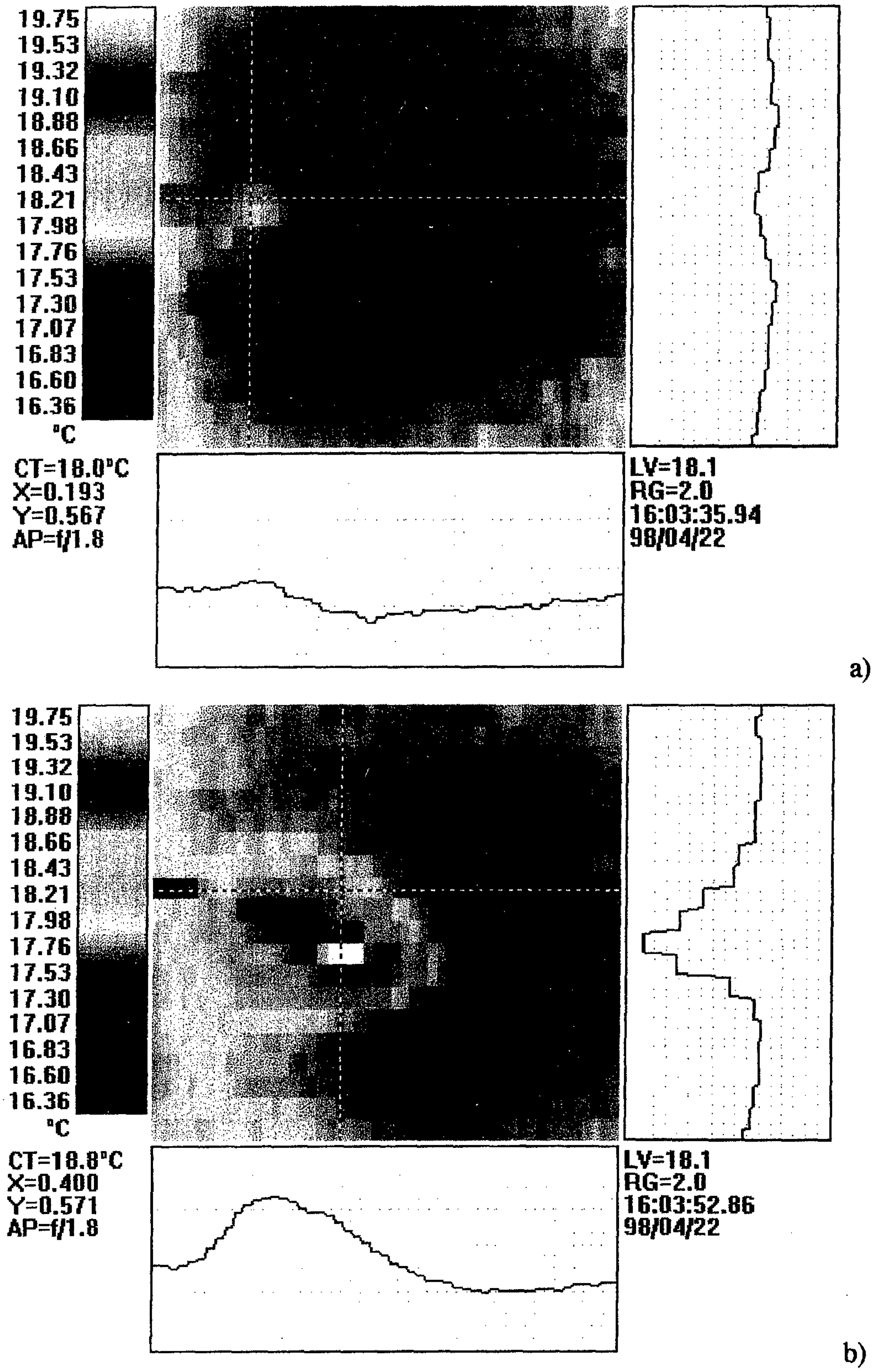

Fig.3. Sample with T-L orientation. Example of the thermal image to fracture process evaluation in the crack tip with marked lines of temperature level.

a) at stress initiation of first crack

b) development of second crack (maximum load)

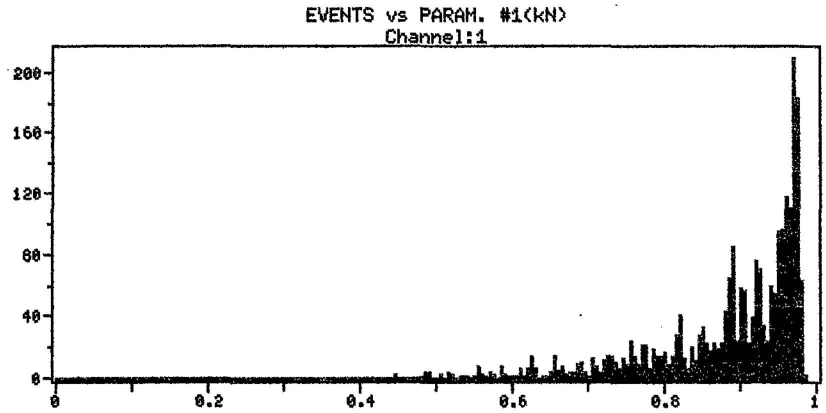

Fig.4. L-T orientation: History of acoustic emission events and rise time versus load [kN]

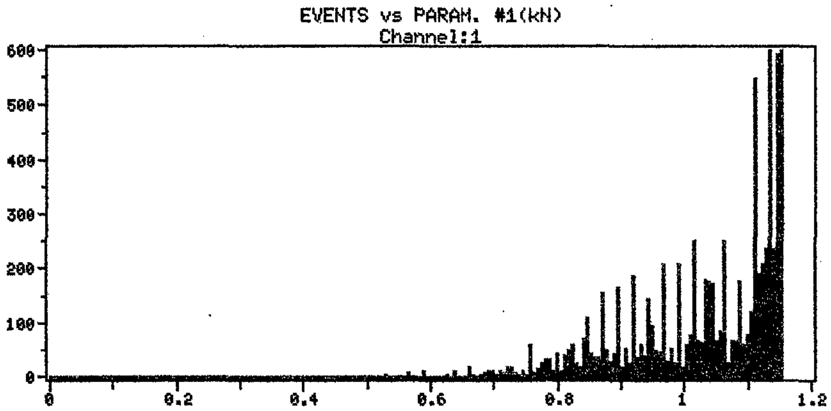

Fig.5. T-L orientation: History of acoustic emission events and rise time versus load [kN]

When the crack development is caused the loss of structural stability, the dissipation process is expressed by an increase of the zone temperature by 2,4 K. Since outside the zone of an increase in plastic strain, along the plane of fracture, the volume of structure changes due to an elastic deformation of the matrix, the superficially changing zone of reduced temperature is visible for both structures (-0,2 K). To make the recorded changes in the signals of acoustic emission, the parameters corresponding to the fracture mechanisms which occur during loading were analysed. For the examined structure the critical parameter has proved to be the process of the coalescence of microdeformations to form linear cracks and the process of pulling out of fibres [2]. The fracture process is initiated separately in individual layers of the specimen with different fibre orientation at various levels of loading, while the strength of structure is due to a combined effect of the operating mechanisms. In the process of loading, the change duration parameter within a broad band of amplitude and the time of the signal amplitude increase satisfactorily represent the load level rise or the crack tip opening critical for a stability of this process. From the point of view of an effective evaluation of the failure process, this period should be regarded as a critical one for the crack growth. In the case of structure with L-T orientation this state corresponds to a load of 880 N. The process of failure starts in the internal layer of the structure characterised by an orientation unfavourable in relation to the normal load. In the case of structure with T-L orientation, the critical level corresponds to a load of 970 N. The process of heat dissipation corresponding to increase in strain near the crack tip is also corresponding to the deformation of a superficial layer.

In the structure of orientation L-T the process of failure in the external layer characterised by a high strength relative to the applied load occurs not earlier but only after a failure in the central zone has taken place, thus increasing the effect of dissipation at a level of 920 N. In the structure of orientation T-L the beginning of failure reduces the strength of the external layer and the process of dissipation in the crack tip is noted to occur very distinctly at the load level of 980 N, according to the critical level determined by acoustic emission. In this crack tip two cracks are initiated. The first crack is in the external layer is arrested; the second crack is critical for the stability of the specimen.

CONCLUSIONS

The analysis of the failure process in the structure described here has revealed some serious obstacles in proper assessment of the critical state of loading during fracture toughness K_Q test. The multi-ply structure, in which during deformation various mechanisms of fracture are acting, requires for a correct choice of the crack initiating load, apart from the rules of linear mechanics, also the rules of the experimental mechanics.

It seems that the proposed here, complementary to each other, methods of acoustic emission and thermomechanical coupling give real chances for an effective evaluation and proper choice of the critical load value under the conditions of the crack formation and growth. The small differences in the critical load value determined by the methods of the linear fracture mechanics and by the experiments are a consequence of the effect of strain and of an additional effect of the phase constituents. The application of the effect of thermomechanical coupling in testing of the strain state in sub-surface zones enables an evaluation of the elastic strain state of the composite matrix and of the plastic strain state which is responsible for the heat dissipation effect. The application in the studies of the degree of structure damage of the systems of acoustic emission gives the possibility of a multi-parameter assessment of the state of composite structure, but the condition indispensable here is an exact knowledge of this structure construction [3].

REFERENCIS

1.Williams J.G.: *A linear elastic fracture mechanics (LEFM) standard for determination K_C and G_C for plastics*, ESIS Polymers and Composites Task Group, London, 1991;

2.Go³aski L., Schmidt J., Kujawinska M., Salbut L. "*Fracture phenomena and strain distribution at the vicinity of crack tip in short fibre composites*", Proc. 10th Int. Conference on Experimental Mechanics", Lisbon 1994, Ed: J.F. Silva, A.A. Balkema, Rotterdam, 1994;

3.Schmidt J.: *Acoustic emission failure testing of short fibre composites with fibre-ply distribution*, Joint Polish-French Symposium on Advanced Materials, Paris, 1994.

AUTHOR INDEX

Adali, S 227, 265, 383, 389, 463, 489
Adanur,S 101
Ahmad Fuad,M Y........51
Ait-Kadi, ...57
Albano, C 63, 107
Al-Qureshi, H A 69
Al-Zadjali, S 477
Amateau , M F 157
Araujo Santos, J V 417
Ashida, F 17
Atangana, A J 447, 453
Avva, V S 457
Azarova, T 89
Banks, W M 295
Baran, I 525, 549
Basson, A H 483
Becker, W 201
Belinga, E P 453
Belostotsky, I 307
Birman, V 495
Blomert, D 75
Bodger, R 271
Brieu, M 139
Brito, Z 113
Bruch Jr, J C 227
Burihyn, S G 365
Byrd, L B 495
Caperaa, S 537
Castejon, L 253, 423
Chen, M 319
Chigarev, A V 301
Clemente, R 253, 513
Cuartero, J 423, 513
Das, P S 325
Devries, F 139
Dumontet, H 313
Duvaut, G 233
Dzonang, A D 447
Essoh, N H 447
Evseev, E G 429, 507
Faryna, M 169
Faye, J P 537
Feldman, E 307
Foster, E 325
Fouda, J B 453
Found, M S 519
Galileev, S M 345
Gaofeng, Q 175
Golaski, L 525
Gonzales, J 107
Gopal, A K 463
Goryk, A V 333
Gubin, N N 345
Gurtovy, O G 207
Guz, I A 501
Haberko, K 169
Howard, L C 519
Huang, D 395
Ichazo, M 107
Ilyuschenko, A 89
Jeelani, S 325
Jimenez, M A 253, 531
Jonson, D 287
Ju, D Y 181
Kalamkarov, A L 239
Kandeil, A Y 119
Karama, M 537
Kashtalian, M 353
Kayupov, M A 435
Kingue, S J 447
Kozak, W S 469
Kravchuk, A S 301
Krawczuk, M 403
Krawiec, Z 259
Krikanov, A A 245
Kuhn, G 435
Lacassagne, J L 537
Lapusta, Yu N 145
Larrode, E 253, 531
Le Bris, N 313
Lee, R 319
Lene, F 139, 313
Lessmann, H G 507
Levin, V M 151
Li, Z 319
Librescu, L 1
Lopez Rodriguez, M 423
Lyakhov, A L 333
Mahfuz, H 325
Marchuk, A V 441
Marquez, L 63
Matrosov, A V 345

AUTHOR INDEX

McCullough, R L ... 133
Mingjing, T ... 175
Miravete, A ... 513, 531
Miroshnichenko, I N ... 345
Mistou, S ... 537
Morozov, E V ... 359, 429, 507
Mota Soares, C A ... 417
Mota Soares, C M ... 417
Muc, A ... 213, 259
Navas, R ... 107
Nesvijski, E G ... 543
Noda, N ... 17
Nor Azlan, M R ... 51
Okoli, O I ... 125
Ostachowicz, W ... 403
Owono, A P ... 453
Papaspyrides, C D ... 133
Paran, A P ... 519
Parra, C ... 107
Paskaramoorthy, R ... 187
Pedzich, Z ... 169
Pekego, P G ... 453
Perera, R ... 107
Perez de Lucas, A ... 423
Phoenix, S L ... 3
Pina, H L G ... 417
Pinzelli, R ... 75
Piskunov, V G ... 333, 365
Polyakov, V A ... 219
Pompe, W ... 151
Prisjaznuk, V K ... 441
Pyda, W ... 169, 195
Rahmad, S ... 51
Rahman, M ... 325
Rasskazov, A A ... 365
Revuelta, D ... 513, 531
Richter, A ... 389
Ronca, G ... 63
Rosales, C ... 107
Rossikhin, Y A ... 339
Russell, J A ... 295
Sadek, I S ... 227
Sadler, R L ... 457
Samba, N P ... 453
Sanchez, G ... 113
Sato, Y ... 83
Schmidt, J ... 525, 549
Schnick, T ... 89
Seibi, A C ... 157, 477
Sevostianov, I B ... 151, 265, 489
Shenouda, S S ... 95
Shitikova, M V ... 339
Shivakumar, K N ... 457
Silva, J L G ... 69
Simelane, P S ... 371
Slinchenko, D ... 265
Sloss, J M ... 227
Smith, G F ... 125
Steinhauser, S ... 89
Sun, B ... 371, 395, 409
Swanson, S R ... 163
Sylantiev, S A ... 507
Tauchert, T R ... 17, 383, 389
Terrel, G ... 233
Tong, P ... 319
Urbina, C ... 107
Varelidis, P C ... 133
Vasiliev, V V ... 31
Veldsman, G ... 483
Verijenko,V 17, 265, 383, 389, 463, 489
von Klemperer, C J ... 271
Vuksanovic, D ... 377
Walker, M ... 277, 287
Wielage, B ... 89
Xu, B ... 101
Yousefi, A ... 57
Yujiu, S ... 175
Zahran, R R ... 95, 119
Zak, A ... 403
Zuchara, P ... 213